Transactions of the ASME

Journal of Heat Transfer

Published Quarterly by The American Society of Mechanical Engineers
VOLUME 102 • NUMBER 4 • NOVEMBER 1980

EDITORIAL STAFF
Editor, **J. J. JAKLITSCH, JR.**
Production Editor, **STELLA ROBINSON**
Editorial Prod. Asst., **BETH DARCHI**

HEAT TRANSFER DIVISION
Chairman, **C. L. TIEN**
Secretary, **C. J. CREMERS**
Senior Technical Editor, **K. T. YANG**
Technical Editor, **B. T. CHAO**
Technical Editor, **D. K. EDWARDS**
Technical Editor, **M. EPSTEIN**
Technical Editor, **J. S. LEE**
Technical Editor, **V. E. SCHROCK**
Technical Editor, **R. SIEGEL**

POLICY BOARD, COMMUNICATIONS
Chairman and Vice-President
I. BERMAN

Members-at-Large
J. W. LOCKE
J. E. ORTLOFF
M. J. RABINS
W. J. WARREN

Policy Board Representatives
Basic Engineering, **F. LANDIS**
General Engineering, **C. F. PHILLIPS**
Industry, **J. E. ORTLOFF**
Power, **R. E. REDER**
Research, **G. P. COOPER**
Codes and Stds., **L. L. ELDER**
Nom. Com. Rep., **J. W. LOCKE**

Business Staff
345 E. 47th St.
New York, N. Y. 10017
(212) 644-7789
Mng. Dir., Publ., **C. O. SANDERSON**

OFFICERS OF THE ASME
President, **CHARLES E. JONES**
Exec. Dir. & Sec'y, **ROGERS B. FINCH**
Treasurer, **ROBERT A. BENNETT**

Journal of Heat Transfer (ISSN 0022-1481) is edited and published quarterly at the offices of The American Society of Mechanical Engineers, United Engineering Center, 345 E. 47th St., New York, N. Y. 10017. ASME-TWX No. 710-581-5267, New York. Second-class postage paid at New York, N. Y., and at additional mailing offices.

CHANGES OF ADDRESS must be received at Society headquarters seven weeks before they are to be effective. Please send old label and new address.

PRICES: To members, $30.00, annually; to nonmembers, $60.00. Single copies, $20.00 each. Add $5.00 for postage to countries outside the United States and Canada.

STATEMENT from By-Laws. The Society shall not be responsible for statements or opinions advanced in papers or . . . printed in its publications (B13, Par. 4).

COPYRIGHT © 1980 by the American Society of Mechanical Engineers. Reprints from this publication may be made on condition that full credit be given the TRANSACTIONS OF THE ASME, JOURNAL OF HEAT TRANSFER, and the author, and date of publication be stated.

INDEXED by the Engineering Index, Inc.

ANNOUNCEMENTS

TECHNICAL PAPERS

(*Continued on page 597*)

Downloaded 04 Feb 2011 to 194.85.80.107. Redistribution subject to ASME license or copyright; see http://www.asme.org/terms/Terms_Use.cfm

TECHNICAL NOTES

DISCUSSION

ERRATA

C. A. C. Altemani
E. M. Sparrow
Fellow ASME

Department of Mechanical Engineering,
University of Minnesota,
Minneapolis, Minn. 55455

Turbulent Heat Transfer and Fluid Flow in an Unsymmetrically Heated Triangular Duct

Experiments were performed to determine entrance-region and fully developed heat transfer characteristics for turbulent airflow in an unsymmetrically heated equilateral triangular duct; friction factors were also measured. Two of the walls were heated while the third was not directly heated. The resulting thermal boundary conditions consisted of uniform heating per unit axial length and circumferentially uniform temperature on the heated walls. Special techniques were employed to minimize extraneous heat losses, and numerical finite-difference solutions played an important role in both the design of the apparatus and in the data reduction. The thermal entrance lengths required to attain thermally developed conditions were found to increase markedly with the Reynolds number and were generally greater than those for conventional pipe flows—a behavior which can be attributed to the unsymmetric heating. The fully developed Nusselt numbers were compared with circular tube correlations from the literature, from which it was shown that the hydraulic diameter is not fully sufficient to rationalize the circular and noncircular duct results. However, excellent Nusselt number predictions were obtained by employing the Petukhov-Popov correlation in conjunction with the measured friction factors for the triangular duct. This approach may have general applicability for predicting noncircular duct heat transfer. The friction factor results also affirmed the inadequacies of the hydraulic diameter but supported a general noncircular duct correlation available in the literature.

Introduction

The use of noncircular ducts in heat exchange devices is motivated by a variety of potential benefits. For example, noncircular configurations have enabled the development of highly compact heat exchangers. A novel application of noncircular ducts is of current interest in connection with air-operated flat plate solar collectors. Inasmuch as airflow heat transfer coefficients are much lower than those of water flow, the circular tubes that are common in water-operated collectors have to be replaced with a duct configuration which affords greater heat transfer surface area. One such configuration is formed when the collector plate is a corrugated surface consisting of a succession of V grooves. When the corrugated plate rests on the underside insulation of the solar collector, an array of triangular ducts is created which constitute the passages for the airflow.

The research to be reported here is concerned with turbulent flow and heat transfer in a triangular duct. Although the initial motivation for the work was the aforementioned solar application, it was performed as a fundamental experimental study of convective heat transfer in a noncircular duct. Indeed, the experiments were carried out with a view to providing research results of impeccable quality which can serve as a standard against which analysis can be compared, as well as for direct input to design. The results were actually employed in this way in the latter portion of the paper. There, the well-known Petukhov-Popov circular-tube heat transfer correlation [1] was generalized to noncircular ducts by employing both the present heat transfer and friction factor data; the analytical-computational model of [2] for turbulent airflow in triangular ducts was also tested by comparison with the data.

The experiments were performed utilizing a sharp-cornered equilateral triangular duct, two walls of which were heated, while the third wall was not directly heated. The geometrical configuration and the heating arrangement were designed to yield a standard thermal boundary condition—uniform heat input per unit axial length and circumferentially uniform temperature on the heated walls. In the design of the apparatus, numerical finite-difference solutions were employed to aid in the selection of wall thicknesses, in the positioning of heating wire, and in the placement of thermocouples. Once the experimental data had been obtained, finite-difference solutions enabled evaluation of the heat leakage from the directly heated walls of the duct to the unheated wall; heat losses to the environment were also determined by finite differences.

Heat-transfer-related measurements were made which yielded both entrance region and fully developed heat transfer coefficients, as well as thermal entrance lengths. Pressure distributions were also measured, both for isothermal and nonisothermal conditions, from which friction factors were deduced. The experiments encompassed the Reynolds number range from 4000 to 60,000. In the low Reynolds number range, auxiliary data runs were made to explore the possible presence of natural convection effects. Air was the working fluid in all cases.

The relevant literature on turbulent heat transfer in triangular ducts will now be briefly reviewed. In an early investigation of equilateral ducts [3], average heat transfer coefficients for the duct as a whole were measured at high heating rates such that circumferential temperature variations of up to 55°C (100°F) were encountered. Later, in [4], measurements of heat transfer and friction characteristics were made in a narrow isosceles duct having an apex angle of 11.46 deg. Although the duct was 116 hydraulic diameters in length, thermally developed conditions were generally not attained. Somewhat more recently, experiments were performed in a rounded-corner equilateral triangular duct with a corner radius of curvature equal to 15 percent of the duct hydraulic diameter [5]. Intense heating rates were employed in those experiments, which resulted in a decrease of the Reynolds number from entrance to exit of as much as 50 percent. The foregoing citations encompass the available experimental literature on heat transfer.

The most complete study of turbulent fluid flow phenomena in equilateral triangular ducts is that of [2], which included both experiments and analytical-numercial predictions (based on the Buleev mixing length and turbulence kinetic energy model). The numerical solutions were extended to predict heat transfer coefficients, but without experimental confirmation.

Contributed by the Heat Transfer Division for publication in the JOURNAL OF HEAT TRANSFER. Manuscript received by the Heat Transfer Division March 21, 1980.

The Experiments

The experiments were performed in an open-loop airflow circuit which took air from a building-wide system and ultimately discharged it to the atmosphere. Along its path of flow, the air first encountered a succession of control and regulator valves and a filter, after which it was metered by one of two calibrated sharped-edged orifices which were respectively employed for high and low flow rates. It was then ducted to a plenum chamber fitted with baffles and a flow straightener—the plenum served as a transition from the circular tubing of the upstream piping system to the downstream triangular cross section.

The air exiting the plenum passed into an unheated equilateral triangular duct (made of plexiglass) which served as a hydrodynamic development section. The development section mated with the electrically heated test section. Both sections were of identical internal dimensions; side of triangle = 3.97 cm (1.56 in.), hydraulic diameter = 2.29 cm (0.902 in.). The respective axial lengths of the development and test sections were 53 and 106 hydraulic diameters. After passing through the test section, the air was thermally mixed in a specially designed mixing chamber, from which it was ducted to an outside exhaust.

The key components of the experimental apparatus will now be described. The description will highlight the novel measures that were employed to thermally isolate the heated test section in order to minimize possible extraneous heat losses or gains; another focus is the role of computer modeling as an adjunct to the apparatus design. Details of the apparatus and its design, beyond those given here, may be found in [6].

Heated Test Section. The triangular duct which served as the test section consisted of two relatively thick metallic walls and a thinner wall of a lesser conducting material. A cross-sectional view showing the duct wall configuration is presented in Fig. 1. The metallic walls were of aluminum, with a thickness of 0.952 cm (0.375 in.). The choice of aluminum of this thickness, taken together with the adopted heating method, was made with a view toward obtaining axially uniform heating and circumferentially uniform temperature on the two heated walls.

Heating was accomplished by means of electrical resistance wire embedded in longitudinal grooves machined in the outer face of each aluminum wall (see Fig. 1). Numerical finite-difference solutions of a model of this heating arrangement were employed to demonstrate that for the chosen wall material, wall thickness and heater-groove spacing, and for expected values of the heat transfer coefficient, uniform temperature is attained on the face of the wall that is in contact with the airflow. A generalized version of the analytical model is available in [7] along with representative results.

The third wall of the duct (i.e., the lower wall as pictured in Fig. 1) was made of plexiglass—chosen because of its moderately low thermal conductivity, light weight, surface smoothness, and availability in many sizes. The design objective for this wall was to approximate, as closely as possible, a zero heat flux surface. In practice, heat conduction across the surfaces of contact between the lower wall and the heated walls operates to oppose this objective. Both the size of the contact surface and thickness (0.318 cm, 0.125 in.) of the plexiglass wall were chosen as small as possible relative to mechanical constraints such as strength, wall flatness, and avoidance of leaks. To guide the trade-off between these mechanical constraints and the aforementioned heat transfer objective, the effects of both contact size and wall thickness on the heat flow via the plexiglass into the fluid were examined by means of finite-difference solutions detailed in Chapter 4 of [6]. The quantitative extent of this indirect heating of the fluid will be presented in the Results section of the paper.

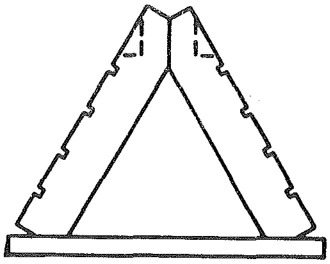

Fig. 1 Cross section of the heated test section

To facilitate the assembly of the duct, bevels were painstakingly cut into the edges of the aluminum walls as indicated in Fig. 1. The bevels extended along the entire 244-cm (8-ft.) length of the duct. The two aluminum walls were held together along their upper extremities by screws and nuts positioned at 10-cm (4-in.) intervals (the recesses for the screws and nuts are indicated by dashed lines in Fig. 1). Fastening of the aluminum side walls to the plexiglass bottom wall was accomplished by nylon screws positioned at the same interval—nylon being chosen to minimize heat conduction. To insure a leak-free seal, silicone rubber was packed into the V-shaped grooves at the intersections of the walls.

Thermocouples were installed at 14 axial stations along the test section. The use of the relatively thick-walled aluminum provided the options of surface mounting (on the rear face) or of embedding the thermocouples within the wall. The latter has the apparent advantage of placing the point of measurement closer to the inner surface of the wall, where the temperature value is desired, but also may cause a disturbance of the temperature field in the wall. Rear-face mounting also has both advantages and disadvantages. To resolve the issue, computational models were made for both situations (Chapter 4 of [6]), taking account of conduction in the wall, in the thermocouple leads, and in the insulation around the duct. These computations showed that wall embedding gives rise to a slightly more accurate temperature measurement and argued strongly for the use of iron-constantan wire rather than copper-constantan wire.

The thermocouples in the heated walls were positioned in drill holes which penetrated to within 0.19 cm (0.075 in.) of the inner surface. Prior to the insertion of the thermocouples, the holes were filled with a paste of copper-oxide cement, which subsequently hardened around the inserted thermocouples (copper-oxide cement is a moderately good heat conductor and an excellent electrical insulator). Three to five thermocouples were circumferentially distributed in the aluminum walls at each instrumented axial station. The coordinates of these stations will be evident from the data to be presented later.

At these same stations, a row of thermocouples was positioned along the spanwise centerline of the lower (plexiglass) wall. Owing to the thinness of this wall, external surface mounting of the thermocouples was the only viable option. Good thermal contact between the thermocouple junctions and the wall was ensured by the use of copper

Nomenclature

f = friction factor, equation (4)
h = local circumferential-average heat transfer coefficient
$\hat{h}$ = heat transfer coefficient for convection at lower wall
D_h = hydraulic diameter
k = thermal conductivity of air
k_p = thermal conductivity of plexiglass
$\dot{m}$ = mass flow rate
Nu = Nusselt number, hD_h/k
P = wetted perimeter of flow cross section
P_q = wetted perimeter of heated walls
Pr = Prandtl number
p = static pressure
Q' = local rate of heat transfer per unit length from heated walls to fluid
Q'_t = total rate of heat transfer per unit length from all walls to fluid
Re = Reynolds number
T = temperature
T_b = bulk temperature
$\hat{T}_b$ = bulk temperature for convection at lower wall
T_{bi} = bulk temperature at inlet
T_w = wall temperature
$\bar{u}$ = mean velocity
x = axial coordinate
x_{ent} = entrance length
μ = viscosity
ν = kinematic viscosity
ρ = density

oxide cement, whereas tape and epoxy were employed for strength and positive positioning.

For the determination of the axial pressure distribution along the duct, seven taps were installed in a row in one of the aluminum walls at a streamwise interval of ten hydraulic diameters. The tap in a given cross section was located at the circumferential midpoint of its host wall.

The instrumentation for the temperature and pressure readings will be described shortly.

Prior to the final assembly of the test section, the inner surface of the aluminum walls was hand polished to a high degree of smoothness. Special precautions were taken to eliminate burrs or other irregularities adjacent to the pressure tap holes.

Hydrodynamic Development Section; Mixing Box. As was noted earlier, the heated test section was preceded by a 53 diameters long unheated hydrodynamic development section. The development section was an equilateral triangular duct with inner dimensions identical to those of the test section. It was assembled from three pieces of plexiglass, two of which were bevelled in a manner identical to that for the aluminum walls of the test section. The assembly procedures were the same as for the test section, and the final assembled cross section is, with the exception of the heater wire grooves, well portrayed by Fig. 1.

The two side walls of the development section were 1.25 cm in thickness (½ in.), whereas the lower wall was 0.318-cm (0.125-in.) thick. It may be noted that the latter dimension is identical to the thickness of the plexiglass lower wall of the test section. In fact, to facilitate the assembly of the system, the test-section lower wall was designed to extend upstream, and thus to serve as the downstream end of the lower wall of the development section.

To monitor upstream thermal events, three thermocouples were installed in the wall of the development section (1, 10, and 20 diameters upstream of the test section). Two additional thermocouples, 10 and 20 diameters from the test section, were passed through the plexiglass wall into the airflow. These thermocouples, whose readings were always identical, yielded the inlet bulk temperature for the test section.

A mixing box was positioned at the downstream end of the test section for the determination of the exit bulk temperature. In view of the asymmetric heating of the airflow, the conventional three- or four-disk mixing box, with either centrally or peripherally positioned throughflow holes in the consecutive disks, is not sufficient for the mixing task. Instead, a special mixing box was designed to promote large scale transverse and circumferential motions (complete drawings are available in [6]). Thermocouple traverses immediately downstream of the mixing box indicated temperature uniformity to within 1 or 2 μV. For the actual temperature measurement of the mixed airflow, two thermocouples were employed, each installed in a six-legged star-shaped copper structure that spanned the cross section of the mixing box at its downstream end.

Minimization of Extraneous Heat Losses. The special measures employed to minimize extraneous heat losses will now be described. The need for extra care in the present experiments stems from the use of a thick-walled heated duct. Direct face-to-face contact of the upstream and downstream edges of the duct with the walls of the development section and of the mixing box would provide active conduction paths for heat loss and, therefore, the cross sections of those paths must be minimized. We will deal here with the adopted measures for curbing heat losses from the heated test section to the hydrodynamic development section, to the mixing box, and to the surroundings.

Consider first the mating between the aluminum walls of the test section and the corresponding plexiglass walls of the hydrodynamic development section. As shown in Fig. 2, full-face contact was avoided in favor of contact between a thin lamina A, which extends downstream from the plexiglass wall, and the aluminum wall. To prepare for this arrangement, a lap-like recess, 1.27-cm (0.5-in.) long and with a depth of approximately 0.046 cm (0.018 in.), was machined at the downstream end of the plexiglass wall. Then, a 2.54-cm (1-in.)-long phenolic lamina A was cemented into the recess, and the resulting surface was finished smooth. The forward edge of the phenolic extended 1.27 cm (0.5 in.) beyond the plexiglass, and it was this edge that contacted the aluminum.

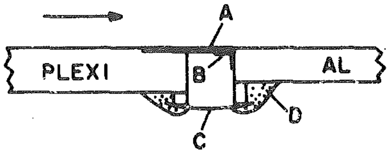

Fig. 2 *Arrangement for minimizing heat conduction at the upstream end of the test section*

To avoid leaks at the contact, a thin (0.005 cm, 0.002 in.) pressure-sensitive tape B was pressed in place as shown in Fig. 2. The main defense against leaks was made on the outer face of the walls. Here, a thicker plastic sheet C bridged between the two walls, with an airtight seal being achieved with silicone rubber D. To hold the just-described arrangement in place, a pair of narrow isolated plexiglass struts (not shown in the figure) bridged the gap just under the plastic sheet C.

Direct contact between the two aluminum walls and their upstream plexiglass counterparts was avoided by the aforementioned arrangement. With regard to the lower, not-directly-heated, wall of the test section (i.e., the plexiglass wall), it extends continuously upstream into the hydrodynamic development section. To minimize conduction along this wall, a spanwise cut was made from the outside surface which reduced the wall thickness to half the original value of 0.318 cm (0.125 in.). This cut was made at the cross section at which the heating was initiated.

Attention will now be turned to the measures used to minimize extraneous heat transfer between the downstream end of the test section and the mixing box. One of these measures was to reduce the conduction cross section of the aluminum walls by making a spanwise cut in each wall just upstream of the mixing box. The wall thickness at the location of the cut was 0.1 cm (0.040 in.) rather than the original thickness of 0.953 cm (0.375 in.). In addition, a spanwise cut was made in the lower (plexiglass) wall which locally reduced its thickness by a factor of two. Also, on the face of the mixing box which mated with the test section, numerous crater-like holes were drilled to reduce the cross section for heat conduction.

The measures for minimizing heat losses from the duct to the environment will now be discussed. To avoid heat conduction through structural supports, the entire assembly consisting of the hydrodynamic development section, the test section, and the mixing box was suspended by 0.043-cm (0.017-in.) dia nylon line at five axial stations. The nylon line was carefully monitored for stretch and sag, and none was encountered after an initial break-in period.

The aforementioned assembly was positioned within an insulated chamber of cross sectional dimensions 25 × 25 cm (10 in. × 10 in.). The chamber walls were of styrofoam, leaving a hollow cavity 10 × 15 cm (4 × 6 in.) for the apparatus. Silica aerogel powder insulation, which has a thermal conductivity less than that of air, was poured into the cavity around the apparatus.

The other parts of the piping system were lagged with fiberglass insulation.

Other Instrumentation. All thermocouples were made from 30-gage, calibrated iron and constantan wire. After installation of the thermocouples, they were led out of the insulation enclosure in a single bundle which terminated in a thermocouple junction box which contained connectors and switches. The box also contained aluminum bars and insulation to promote temperature uniformity. Thermocouple emfs were read with a Hewlett-Packard 3465A digital multimeter with a smallest digit of 1 μV.

For the test section pressure distribution, the pressure signals were sensed by a Baratron solid-state capacitance-type meter capable of being read to as low as 10^{-3} torr. The Baratron provided a digital output which was read by the aforementioned HP multimeter.

The test section power input was regulated to ensure constancy and was read by a specially calibrated electrodynamometer wattmeter with a full-scale accuracy of 0.25 percent.

Data Reduction

The main objective of the data reduction procedure was to yield axially local heat transfer coefficients for the heated walls of the triangular duct, both in the thermal entrance region and in the thermally developed region. The coefficients to be determined will represent circumferential average values at each axial station. Friction factors will also be deduced from the measured pressure distributions.

The local circumferential-average heat transfer coefficient for the heated walls is defined here as

$$h = (Q'/P_q)/(T_w - T_b) \tag{1}$$

where Q' is the rate of convective heat transfer per unit axial length from the heated walls to the fluid, and P_q is the wetted perimeter of the heated walls. The temperatures T_w and T_b respectively represent the values for the heated wall and the bulk. It is worthy of note that all of the wall-embedded thermocouples (i.e., in the aluminum walls) at any axial station gave temperature readings within 0.02°C of each other. Therefore, the heated walls may be regarded as being circumferentially uniform in temperature. All quantities in equation (1) pertain to a given axial station x.

In equation (1), only T_w is directly measured, whereas Q' and T_b are obtained from the data reduction procedure (P_q is equal to 7.92 cm (3.12 in.)). The starting point in the determination of Q' is the electric power dissipated in the resistance wire situated in the longitudinal grooves on the rear faces of the aluminum walls.[1] Two corrections were applied to the power dissipation per unit length in order to obtain Q'. One of these is for the heat loss from the duct outer surfaces to the environment via conduction through the insulation. The other is for the heat which flows by conduction from the heated walls into the plexiglass wall (i.e., the lower wall) and then passes into the airstream by convection at that wall. The latter heat flow is, in fact, not a heat loss; rather, it causes a rearrangement of the surface locations at which heat enters the airstream.

The determination of these two corrections involved a lengthy computation which is described in detail in [6] and will be discussed here only in broad terms. For the heat loss through the insulation, a two-dimensional, finite-difference conduction network was set up to accommodate the irregular solution domain encompassing the outer walls of the triangular duct and the somewhat irregular rectangular boundaries of the two zones of insulation (silica aerogel and styrofoam). The temperature inputs needed for these finite-difference solutions included the surface temperatures of the aluminum and plexiglass walls and the temperature of the air in the surroundings. Of these, the temperatures of the aluminum and of the surroundings were known from direct measurement, but the plexiglass surface temperature varies with spanwise position and only the mid-span value is available from measurement. The needed spanwise temperature distribution was obtained from the calculated temperature field in the plexiglass wall, the determination of which will now be described.

As already noted, heat is conducted into the plexiglass wall through its surfaces of contact with the heated aluminum walls and then flows by convection into the airstream. A fine-grid, two-dimensional finite-difference conduction network was superposed on the plexiglass wall to facilitate determination of the temperature distribution and the convection heat transfer. This computation was elevated from the routine by a philosophical issue related to the convective boundary condition.

To explore this issue, let y denote the direction normal to the inner surface of the plexiglass wall. Then, at that surface

$$-k_p(\partial T/\partial y) = \hat{h}(T - \hat{T}_b) \tag{2}$$

where k_p is the thermal conductivity of the plexiglass. The quantities $\hat{h}$ and $\hat{T}_b$ respectively represent the heat transfer coefficient and bulk temperature that are relevant to the convective heat transfer at the plexiglass surface. A careful study of the problem reveals that either $\hat{h}$ or $\hat{T}_b$ must be provided as input and, with that, the solution will yield the other of the two via an iterative procedure which makes use of the measured temperature at the mid-span point on the rear face of the wall. The solution also makes use of the measured temperature of the aluminum walls, which is assumed to prevail at the interface with the plexiglass wall.

Both options were explored. In one, $\hat{h}$ was taken equal to the average heat transfer coefficient at the heated walls of the duct, while $\hat{T}_b$ was treated as an unknown. In the other, $\hat{T}_b$ was set equal to the bulk temperature for the cross section as a whole and $\hat{h}$ was the unknown. There was little practical effect of using one option versus the other, as reflected in the fact that the extreme difference in the resulting heat transfer coefficients for the *heated walls* was only three percent.

For the authors, the first option is more satisfying on physical grounds and, therefore, it has been used for the final data-reduction computations. We do not believe that the bulk temperature T_b, which is primarily set by the heat transfer rates at the aluminum walls, has very much influence on the rate of convective heat transfer at the plexiglass wall;[2] in a real sense, T_b is quite remote from the plexiglass wall. Furthermore, considering the similarity of the flow pattern adjacent to all three walls, it is not unreasonable to use the same h at the plexiglass wall as at the other walls.

The numerical solutions for the plexiglass wall yield the rate at which heat passes out of the heated walls at the surfaces of contact with the plexiglass. This, in turn, completes the determination of Q' for equation (1). These computations were performed at each instrumented axial station. The foregoing description was intended to sketch the broad outlines of the computation procedure, but not to reproduce the details given in [6].

The bulk temperature appearing in equation (1) was computed by a step-by-step marching procedure that moved downstream along the duct, making use of the net heat transfer to the airstream at each station.

The effects of axial heat conduction in the aluminum walls were also examined. It was found that within the accuracy of the temperature instrumentation, significant effects of axial conduction could not be identified except at the most upstream stations at low Reynolds numbers. Owing to the uncertainty of the axial conduction corrections (i.e., large changes in $\partial^2T/\partial x^2$ in response to small temperature uncertainties), the questionable data points will be omitted from the forthcoming presentation of results (see uncertainty analysis in Chapter 5 of [6]).

Once the local heat transfer coefficient had been determined from equation (1), the local Nusselt number was evaluated from

$$\mathrm{Nu} = hD_h/k \tag{3}$$

where D_h is the hydraulic diameter of the duct (2.29 cm, 0.902 in.) and k is the thermal conductivity of the airstream at the local bulk temperature.

The measured axial pressure distributions yielded, in each case, a straight line on a p versus x diagram, the slope of which was determined from a least-squares fit. This information was recast in dimensionless form via the friction factor

$$f = (-dp/dx)D_h/\tfrac{1}{2}\rho\bar{u}^2 \tag{4}$$

where $\rho\bar{u}^2$ was evaluated at the midpoint of the axial length over which p was measured.

The heat transfer and friction factor results are parameterized by the Reynolds number Re defined as

$$\mathrm{Re} = \bar{u}D_h/\nu = 4\dot{m}/\mu P \tag{5}$$

in which $\dot{m}$ is the mass flow rate and P is the perimeter of the walls which bound the flow cross section. For the actual evaluation of Re,

---

[1] The wattmeter reading was corrected to take account of ohmic dissipation in small segments of heating wire that lay outside the grooves. Also, thermocouple lead losses, which were ~0.1 percent, were prorated uniformly along the duct.

[2] The calculated convective heat transfer rate at the plexiglass wall ranged from three to ten percent of the total convective input to the air over the Reynolds number range from 59,000 to 4000 (see Table V, p. 136 of [6]).

the rightmost term of equation (5) was used, with μ at the local bulk temperature.

In general, property variations did not play a major role in the results. The maximum wall-to-bulk temperature difference was about 10°C (18°F), and the maximum bulk temperature rise from inlet to exit was of the same general magnitude.

Results and Discussion

The main focus of the presentation that follows will be the heat transfer results. Friction factors will also be presented, and they will be employed in correlating the fully developed heat transfer coefficients. To avoid interrupting the smooth flow of the heat transfer presentation, initial attention will be directed to the friction factor results.

Friction Factors. The friction factor results are plotted as a function of the Reynolds number in Fig. 3, where the open circles represent the isothermal data and the blackened circles correspond to the heat transfer runs. These two sets of data are nearly coincident and show the trend of f decreasing with Re that is typical of flow in smooth ducts.

Three literature correlations are shown in the figure in order to provide a comparison with the present results. The two uppermost curves respectively represent the Blasius and Prandtl circular tube correlations, which were applied here by employing the hydraulic diameter as the characteristic dimension. The comparison shows that the hydraulic diameter concept is not sufficient to rationalize the difference between the tube and triangular duct geometries, leaving an accuracy gap for f of 10 to 15 percent. The lower curve represents a general noncircular duct friction factor correlation [8] which was specialized to the present configuration. In the range of Re >7000, the present data agree with the correlation within two percent, on the average, thereby affirming its validity for the equilateral triangular duct. Since the correlation was developed for fully turbulent flow, the larger deviations at lower Reynolds numbers are not unexpected.

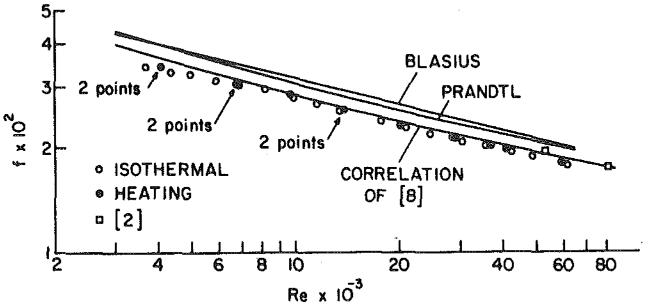

Fig. 3 Friction factor results

The square data symbols, which represent experimental results from [2], lie slightly above the present data. Finite difference solutions were also performed in [2] for the Reynolds number range between 40,000 and 300,000. For Reynolds numbers between 40,000 and 60,000, the predicted friction factors are about two percent lower than those given by the correlation of [8], which means almost exact agreement between the predictions and the present data. This agreement lends support to the computational model used in [2].

Temperature Distributions. Heat transfer data runs were made for eight Reynolds numbers between 4000 and 59,000. The measured axial temperature distributions display an interesting evolution in shape as a function of the Reynolds number, which is fully documented in [6]. Here, it will be sufficient to show results for two Reynolds numbers, one high and one low (59,130 and 6740), in order to illustrate the trends, and Figs. 4 and 5 have been prepared for this purpose.

In these figures, the temperature is made dimensionless in the form

$$(T - T_{bi})/(Q'_t/k) \qquad (6)$$

In this expression, T_{bi} is the inlet bulk temperature and k is the thermal conductivity of the air at the mean bulk temperature. The quantity Q'_t is the total rate of heat transfer to the air per unit axial length, encompassing contributions from the directly heated walls and from the indirectly heated lower wall. Since T_{bi}, Q'_t, and k are fixed constants for each data run, the axial variation of the dimensionless group of equation (6) is a true reflection of the axial temperature variation.

In each figure, there are three sets of data points. The uppermost set depicts the temperature variation along the heated walls (as noted earlier, the temperature of the heated walls is circumferentially uniform). The other two sets, both of which are in the lower part of the figure, respectively depict the calculated values of the bulk temperature and the measured temperatures along the midspan of the rear face of the lower wall.

Attention may first be turned to the high Reynolds number results, Fig. 5. The temperature distribution on the heated wall displays a classical pattern that reflects the uniform heating condition—namely, an initial rapid rise that evolves into an ascending straight line which parallels the temperature rise of the bulk. The bulk temperature itself departs only very slightly from a straight line, the departures being due to slight variations in the heat losses along the duct. The region in which there is parallelism between the heated-wall and bulk temperatures grows larger as the Reynolds number decreases.

Figure 5 also shows that the midspan temperatures on the lower wall fall below the bulk temperature at the higher Reynolds numbers, and this relationship continues to prevail for all Re $> 10{,}000$. There

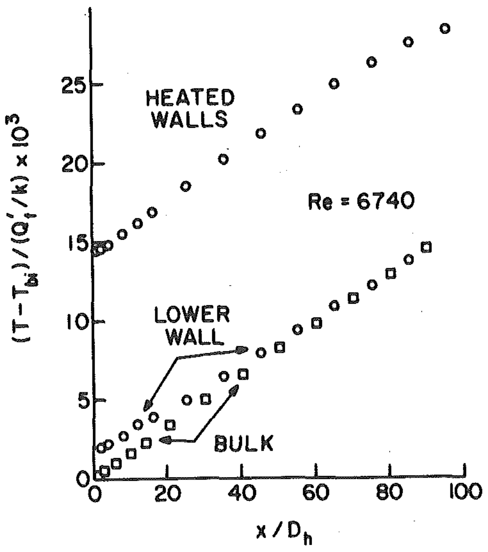

Fig. 4 Axial temperature distributions, Re = 6740

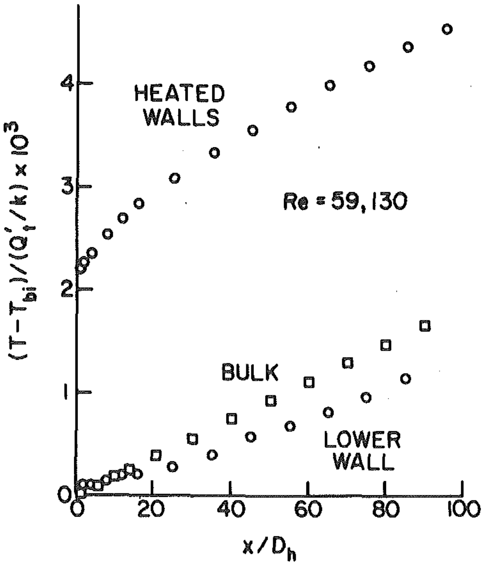

Fig. 5 Axial temperature distributions, Re = 59,130

is a tendency for the two distributions to become parallel at the most downstream stations. That the temperature of the lower wall is relatively low at these Reynolds numbers is indicative of the low rate at which heat is conducted into the lower wall from the directly heated walls. This low rate of conduction is the result of the relatively efficient convective heat transfer from the directly heated walls to the airstream, which makes the conduction leakage path to the plexiglass relatively unattractive.

The fact that the rear-face midspan temperature of the lower wall falls below the corresponding bulk temperature should not be taken as an indication that heat is being transferred from the airstream to the wall. In the lower part of the flow cross section, there is a zone of relatively low-temperature air (i.e., temperatures lower than the bulk temperature). It is the temperatures of the air in that zone, rather than the bulk temperature, which controls the magnitude and direction of the convective heat transfer at the lower wall.

The temperature distributions for Re = 6740 (Fig. 4) are quite different from those for Re = 59,130 which were just discussed. These differences evolve progressively with decreasing Reynolds number, as is evidenced in the successive figures presented in [6]. The main characteristics of the low Reynolds number distributions are: (1) parallelism between the heated-wall and bulk temperature distributions that is in force along most of the length of the duct, (2) temperatures on the lower wall that exceed the bulk temperature, and (3) a droop of the heated-wall temperature distribution near the downstream end of the duct.

The first of these characteristics implies a very short thermal development length, and we will return to this matter shortly when the Nusselt number results are presented. The second and third characteristics indicate the strengthened role of heat conduction which results from the less efficient convective heat transfer at the directly heated walls when the Reynolds number is low. Thus, the droop in the heated-wall temperatures at the downstream end of the duct is due to extraneous conduction to the mixing box. Furthermore, conduction from the heated walls into the lower wall is responsible for the elevation of the latter's temperature above the bulk.

Nusselt Numbers and Thermal Entrance Lengths. Circumferential-average Nusselt numbers for the heated walls have been determined at a succession of axial stations by employing the data reduction procedures described earlier. These results are presented in Fig. 6, where the Nusselt number is plotted against the dimensionless axial coordinate x/D_h ($x = 0$ corresponds to the beginning of the heated test section). The figure displays axial distributions for eight Reynolds numbers in the range from 4070 to 59,130. Supplementary data runs for the two lowest Reynolds numbers and for Re $\simeq$ 29,000 yielded results so close to those in the figure that they could not be plotted separately.

Examination of the figure shows the expected trend whereby higher Nusselt numbers correspond to higher Reynolds numbers. Also, the curves for the higher Reynolds numbers display the classic developmental pattern characterized by relatively high heat transfer coefficients near the inlet which decrease smoothly throughout the thermal entrance region and ultimately attain an axially unchanging fully developed value. It is, however, interesting to note that at these Reynolds numbers, the entrance length, as measured in terms of the hydraulic diameter, is rather long; in fact, fully developed conditions are just barely achieved. As the Reynolds number decreases, the length of the entrance region decreases markedly. (Note that at the two lowest Reynolds numbers, data affected by axial conduction have not been presented).

For a quantitative characterization, the thermal entrance length may be defined as the axial location at which the heat transfer coefficient approaches to within five percent of its fully developed value. Entrance lengths corresponding to this definition are presented in Fig. 7, where the marked increase with Reynolds number is clearly evident. To obtain perspective about these results, the relevant literature may be examined. For triangular-duct heat transfer, no entrance lengths were determined in [3] (only average coefficients were measured), while in [5] the large property-related Reynolds number variations along the duct make the definition of an entrance length quite uncertain. In [4], for a small apex-angle triangular duct, very large entrance lengths were encountered.

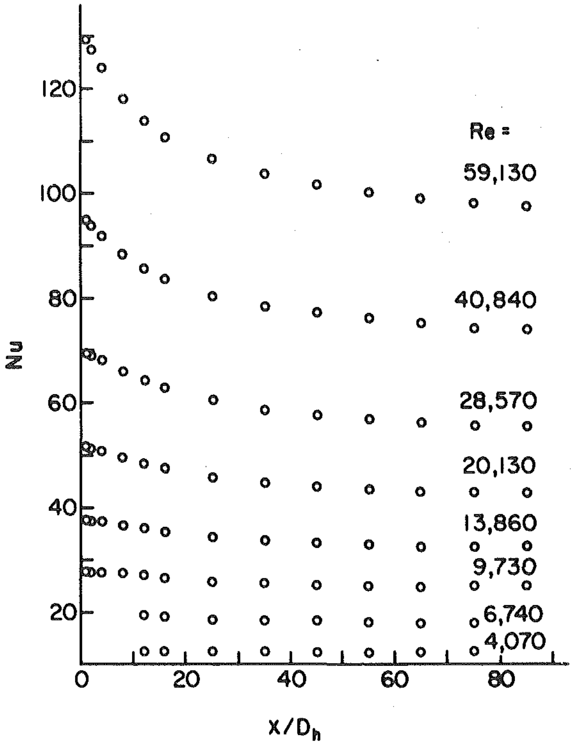

Fig. 6 Axial distributions of the Nusselt number

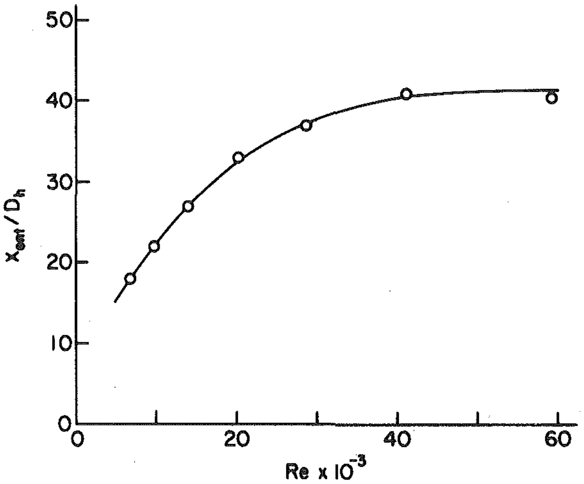

Fig. 7 Thermal entrance lengths based on a five percent approach of Nu to its fully developed value

Also relevant are the experiments of [9] involving turbulent airflow in a circular tube heated on only half of its circumference. There, it was found that the thermal entrance lengths were considerably greater than those for a circumferentially uniformly heated tube; furthermore, the entrance lengths increased markedly with Reynolds number, as in the present experiments.

From the foregoing, it can be concluded that nonuniform heating increases the length of the thermal entrance region. The noncircular geometry of the duct cross section may also be a contributing factor.

Fully Developed Nusselt Numbers. It is relevant to compare the fully developed Nusselt numbers to literature information and to seek the best possible correlation. From the literature, we take the venerable Dittus-Boelter correlation and the newer Petukhov-Popov correlation [1], respectively

$$\mathrm{Nu} = 0.023\mathrm{Re}^{0.8}\mathrm{Pr}^{0.4} \qquad (7)$$

and

$$\mathrm{Nu} = (f/8)\mathrm{Re}\mathrm{Pr}/(1.07 + 12.7(\mathrm{Pr}^{2/3} - 1)(f/8)^{1/2}) \qquad (8)$$

where

$$f = (1.82 \log_{10}\mathrm{Re} - 1.64)^{-2} \qquad (9)$$

Both of these correlations were developed for circular tubes and are specified to be applicable for $\mathrm{Re} > 10{,}000$.

Equations (7–9) have been evaluated using the hydraulic-diameter Reynolds numbers and are compared with the present data in Fig. 8. For $\mathrm{Re} > 10{,}000$, the Dittus-Boelter equation overpredicts the data by about 30 percent, while the Petukhov-Popov equation is about 15 percent above the data.[3] Although this comparison adds further confirmation of the superiority of the Petukhov-Popov correlation relative to that of Dittus-Boelter, it also demonstrates that the hydraulic diameter does not provide an adequate rationalization of the noncircular geometry.

In considering the causes of less-than-successful performance of the literature correlations, specifically Petukhov-Popov, note may be taken of Fig. 3 which indicates that the circular-tube friction factor results deviate from those of the equilateral triangular duct, even when the hydraulic diameter is employed. This suggests the use of the measured triangular-duct friction factors as input to the Petukhov-Popov equation (8), replacing the circular-tube friction factor equation (9). When this is done, a duct-specific Petukhov-Popov prediction is obtained, as shown in Fig. 9 along with the experimental data. For $\mathrm{Re} > 10{,}000$, the duct-specific prediction agrees with the data in the 1–5 percent range. This level of agreement is actually better than that achieved when the Petukhov-Popov correlation is compared with circular tube data.

Although a fully certain recommendation cannot be made at this time, it appears reasonable, when employing the Petukhov-Popov correlation for a noncircular duct, to input the friction factors for that duct, provided that they are available.

As an alternative correlation of the present data, a power-law fit yields

$$\mathrm{Nu} = 0.019\mathrm{Re}^{0.781} \qquad (10)$$

to an accuracy of about four percent.

The present data will now be compared with the results of the turbulent-flow finite-difference solutions of [2]. For these solutions, the thermal boundary condition was circumferentially uniform temperature (on all three walls) and axially uniform heat input. Numerical results are reported only for $\mathrm{Re} > 40{,}000$. Comparison with the present data for the two highest Reynolds numbers yields agreement within four percent (the prediction being high). This excellent level of agreement lends support to the analytical model and its numerical implementation.

Natural Convection Effects. Out of concern for possible natural convection effects, supplementary data runs were made for each of the two lowest Reynolds numbers such that the Grashof number was varied by a factor of two, from 6×10^3 to 1.3×10^4. The Grashof number variation had no detectable effect on the Nusselt number [6], and it was thus concluded that natural convection effects were negligible.

Concluding Remarks

The experiments reported here were designed with unusual care and attention to detail in order to provide research results of such quality as to serve as a standard against which analysis can be compared. Special techniques were employed to minimize extraneous heat conduction. Numerical finite-different solutions played an important role in both the design of the apparatus and in the data reduction.

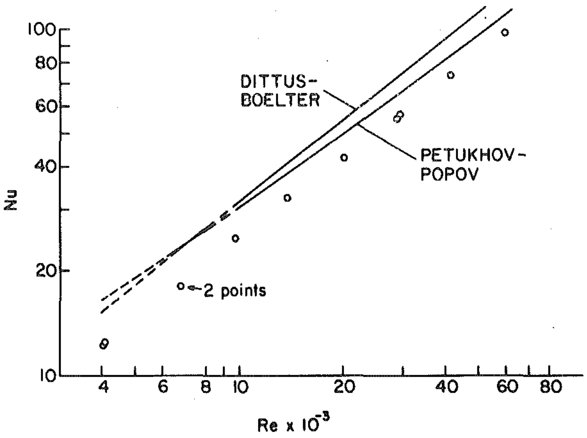

Fig. 8 *Fully developed Nusselt numbers and comparisons with literature correlations*

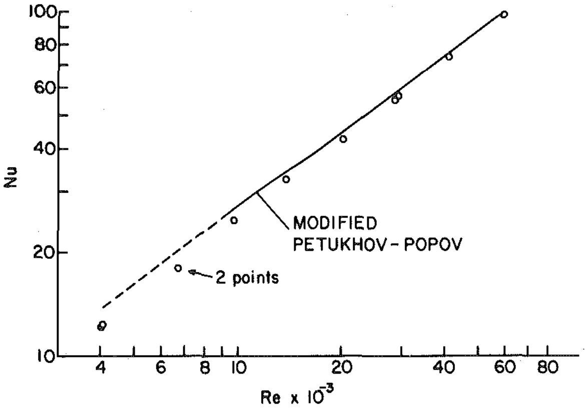

Fig. 9 **Comparison of measured fully developed Nusselt numbers with the Petukhov-Popov correlation evaluated with the measured friction factors as input**

The friction factor data underscored the fact that the hydraulic diameter is not completely successful in bringing circular tube correlations into agreement with noncircular duct results. The data did, however, support the predictions of a general noncircular duct correlation [8] as well as those from numerical solutions of a modeled turbulent flow [2].

Nusselt numbers were determined both in the thermal entrance region and in the fully developed region of the duct. The length of the entrance region increased markedly with Reynolds number. Entrance lengths, based on a five percent approach to fully developed conditions, ranged from 18 to 40 hydraulic diameters over the Reynolds number range from 6700 to 57,000. These lengths are greater than those for conventional duct flows (for air) and are believed to reflect the unsymmetric heating.

The experimentally determined fully developed Nusselt numbers were compared with both the Dittus-Boelter and Petukhov-Popov circular tube correlations (applicable for $\mathrm{Re} > 10{,}000$), with the hydraulic diameter replacing the tube diameter. Although the latter correlation yielded better agreement with the data than did the former, it was still about 15 percent high. When the measured friction factors were used as input to the Petukhov-Popov equation, agreement between prediction and experiment to better than five percent was attained. This finding suggests that for a noncircular duct, the Petukhov-Popov equation be evaluated with the friction factor specific to that duct. The present data also support the Nusselt number predictions of [2] obtained via finite-difference solutions of a modeled turbulent flow.

Acknowledgment

This research was performed under the auspices of the Office of Naval Research (contract No. N00014-79-C-0621). Scholarship support was accorded to C.A.C. Altemani by CNPq and UNICAMP, both Brazilian Institutions.

---

[3] The Sleicher-Rouse correlation [10] is within about one-half percent of Petukhov-Popov.

References

1 Petukhov, B. S., "Heat Transfer and Friction in Turbulent Pipe Flow with Variable Physical Properties," *Advances in Heat Transfer,* Vol. 6, Academic Press, 1972, pp. 503–564.

2 Aly, A. M. M., Trupp, A. C., and Gerrard, A. D., "Measurements and Prediction of Fully Developed Turbulent Flow in an Equilateral Triangular Duct," *Journal of Fluid Mechanics,* Vol. 85, 1978, pp. 139–149.

3 Lowdermilk, W. H., Weiland, W. F., and Livingood, J. N. B., "Measurement of Heat Transfer and Friction Coefficients for Flow of Air in Non-Circular Ducts at High Surface Temperatures," NACA RM E53J07, 1954.

4 Eckert, E. R. G. and Irvine, T. F., "Pressure Drop and Heat Transfer in a Duct with Triangular Cross Section," ASME JOURNAL OF HEAT TRANSFER, Vol. 82, 1960, pp. 125–138.

5 Campbell, D. A., and Perkins, H. C., "Variable Property Turbulent Heat and Mass Transfer for Air in a Vertical Rounded Corner Triangular Duct," *International Journal of Heat and Mass Transfer,* Vol. 11, 1968, pp. 1003–1012.

6 Altemani, C. A. C., "Turbulent Heat Transfer and Fluid Flow Characteristics for Air Flow in an an Unsymmetrically Heated Triangular Duct," Ph.D. Thesis, Department of Mechanical Engineering, University of Minnesota, Minneapolis, Minn., 1980.

7 Sparrow, E. M., and Altemani, C. A. C., "On Attaining Isothermal Convectively Cooled Surfaces with Rear-Side, Discrete Groove-Embedded Heaters," *Numerical Heat Transfer,* Vol. 2, 1979, pp. 129–136.

8 Malak, J., Hejna, J., and Schmid, J., "Pressure Losses and Heat Transfer in Non-Circular Channels with Hydraulically Smooth Walls," *International Journal of Heat and Mass Transfer,* Vol. 18, 1975, pp. 139–149.

9 Knowles, G. R. and Sparrow, E. M., "Local and Average Heat Transfer Characteristics for Turbulent Airflow in an Asymmetrically Heated Tube," ASME JOURNAL OF HEAT TRANSFER, Vol. 101, 1979, pp. 635-641.

10 Sleicher, C. A., and Rouse, M. W., "A Convenient Correlation for Heat Transfer to Constant and Variable Property Fluids in Turbulent Pipe Flow," *International Journal of Heat and Mass Transfer,* Vol. 18, 1975, pp. 677–683.

H. M. Soliman
Assistant Professor,
Mem. ASME

T. S. Chau
Research Associate.

A. C. Trupp
Associate Professor.

Department of Mechanical Engineering,
University of Manitoba,
Winnipeg, Manitoba,
Canada R3T 2N2

Analysis of Laminar Heat Transfer in Internally Finned Tubes with Uniform Outside Wall Temperature

An analysis is presented for fully developed laminar convective heat transfer in tubes with internal longitudinal fins and uniform outside wall temperature. The governing momentum and energy equations were solved numerically, with the influence of fin conductance accounted for by a single parameter. The distributions of fin temperature, fluid temperature and local heat flux (both at the fin and unfinned surfaces) are presented. These are shown to be strongly dependent on finned tube geometry and, in some cases, on the fin conductance parameter as well. Based on average heat transfer per unit area, the various fins proved more effective than the unfinned surfaces. Values for overall Nusselt number indicated significant heat transfer enhancement over smooth tube conditions.

Introduction

This work is a continuation of the analysis of laminar, fully developed fluid flow and heat transfer in tubes with internal longitudinal fins. The results of earlier studies by the present authors and others, have included the velocity distribution and friction factor [1, 2], the temperature distribution and Nusselt number [3, 4], and the influence of fin conductance on the heat transfer characteristics [5]. These heat transfer results corresponded to the wall condition of constant heat flux, axially, and uniform temperature, circumferentially. This boundary condition is relevant to many practical situations including electric heating, nuclear heating, and counter flow heat exchangers with equal heat-capacity rates for the two streams [6]. This paper presents heat transfer results corresponding to the second fundamental wall condition, namely that of constant temperature axially as well as circumferentially, which has immediate applications for equipment such as condensers and evaporators.

Several experimental investigations dealing with pressure drop and heat transfer in internally finned tubes have been reported. These studies have involved various geometries with both straight and twisted fins and a range of flow situations encompassing single and two-phase (boiling and condensation) flows. Most of the single phase studies have dealt with turbulent flow and only a few consider laminar flow [7–9]. Reference to the results of these three investigations will be made later, however it is important to state here that none of them provided experimental data corresponding to the present combination of flow and boundary conditions.

The tube geometry used in this study is similar to the one used earlier by Soliman and Feingold [2, 4]. A variable number of straight fins is evenly distributed around the circumference of the tube. Fin sides are radial flanks and the tips coincide with a circular arc concentric with the axis of the tube. This geometry has the advantage of being close to real finned tube configurations while coinciding with the cylindrical coordinate system. Within the fins, the temperature is assumed uniform circumferentially, but variable in the radial direction. For the present study, the governing momentum and energy equations were solved numerically using a finite difference approach. Distributions of local heat flux at the tube wall and along the sides of the fins, as well as temperature distributions and overall heat transfer characteristics are presented.

Analysis

Due to geometrical symmetry of the flow domain as shown in Fig. 1, solutions for the governing equations were sought only between $\theta = 0$ and $\theta = \gamma$. Assuming uniform fluid properties and negligible viscous dissipation within the fluid, the momentum equation reduces to

$$\frac{1}{r}\frac{\partial}{\partial r}\left(r\frac{\partial u}{\partial r}\right)+\frac{1}{r^2}\frac{\partial^2 u}{\partial \theta^2}=\frac{1}{\mu}\frac{dp}{dx}. \tag{1}$$

Nondimensionalizing, using quantities defined in the Nomenclature, results in

$$\frac{1}{R}\frac{\partial}{\partial R}\left(R\frac{\partial U}{\partial R}\right)+\frac{1}{R^2}\frac{\partial^2 U}{\partial R^2}=-1. \tag{2}$$

Equation (2) was solved subject to the boundary conditions $U = 0$ on the solid walls, $\partial U/\partial\theta = 0$ on the symmetry lines, and $\partial U/\partial R = 0$ at the center-line of the tube. The resulting velocity distributions are functions of the number of fins M, relative fin height H, and half fin angle β. The following range of geometrical parameters was covered.

$$4 \le M \le 32,$$

$$0.2 \le H \leqslant 0.8, \text{ and}$$

$$\beta = \pi/60 \text{ rad (3 deg)}.$$

The single β value represents a typical value for internally finned tubes already manufactured and tested [7, 10].

The solution of equation (2) was obtained by finite differences using a grid with 20 subdivisions in the radial direction and ten subdivisions in the circumferential direction. The density of points was increased near the tube wall, fin side, and fin tip due to steep gradients at these locations. Trials with finer grids were conducted for different tube

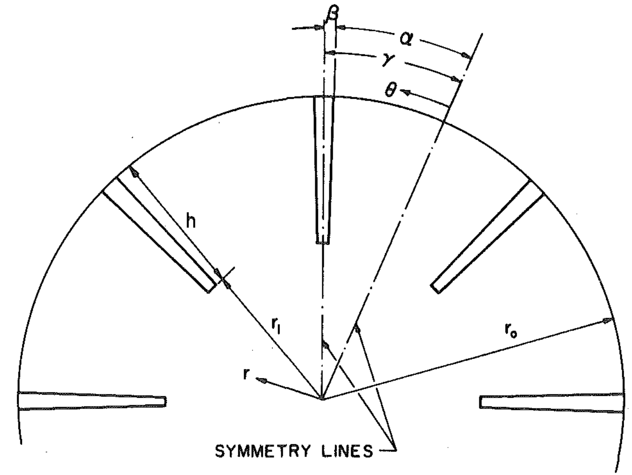

Fig. 1 Tube geometry

Contributed by the Heat Transfer Division for publication in the JOURNAL OF HEAT TRANSFER. Manuscript received by the Heat Transfer Division December 19, 1979.

geometries and the resulting changes in velocity values were too small to justify the increased computation cost.

For a smooth tube with radius r_0, the friction factor and Reynolds number are normally defined as: $f = (-dP/dx)r_0/(\rho u_b^2)$, and $\mathrm{Re} = \rho u_b(2r_0)/\mu$, respectively. In terms of mass flow rate $\dot{m}$, these definitions take the form

$$f = (\pi^2 \rho r_0^5/\dot{m}^2)(-dP/dx), \tag{3a}$$

and

$$\mathrm{Re} = 2\dot{m}/(\pi r_0 \mu). \tag{3b}$$

Equations (3) were used for correlating the friction factor results of internally finned tubes because they provide a basis for comparison with smooth tubes and a dimensionless measure of the influence of internal finning on the pressure gradient for the same r_0, ρ, μ, and $\dot{m}$. The product $f\mathrm{Re}$ can be placed in the following dimensionless form

$$f\mathrm{Re} = (\pi/A_f)(2/U_b), \tag{4}$$

where A_f is the dimensionless flow area expressed as

$$A_f = a_f/r_0^2 = \pi - M\beta\,(1 - R_i^2).$$

Calculated results of $f\mathrm{Re}$ were compared with the analytical results reported by Soliman and Feingold [2] as an additional test for the adequacy of the present mesh size. This resulted in an agreement between the two values to within 1 percent for all tube geometries considered. The above numerical results were then used as input to the heat transfer problem.

For a fully developed temperature profile and negligible axial conduction, the energy equation reduces to

$$\frac{1}{r}\frac{\partial}{\partial r}\left(r\frac{\partial T}{\partial r}\right) + \frac{1}{r^2}\frac{\partial^2 T}{\partial \theta^2} = \frac{\rho c_p}{k_f}u\frac{\partial T}{\partial x}. \tag{5}$$

In addition, the axially invariant temperature profile can be written in terms of dimensionless temperature as

$$\phi(r,\theta) = \frac{T(x, r, \theta) - T_w}{\bar{q}_w(x)\, r_0/k_f}. \tag{6}$$

Using definitions (3, 4), and (6), equation (5) takes the following nondimensional form.

$$\frac{1}{R}\frac{\partial}{\partial R}\left(R\frac{\partial \phi}{\partial R}\right) + \frac{1}{R^2}\frac{\partial^2 \phi}{\partial \theta^2} = f\mathrm{Re}\; U\phi/\phi_b \tag{7}$$

Thermal boundary conditions applicable to equation (7) are

$$\phi = 0 \qquad \text{at } R = 1, 0 \le \theta \le \alpha, \tag{8a}$$

$$\frac{\partial \phi}{\partial \theta} = 0 \qquad \text{at } 0 \le R \le 1, \theta = 0, \tag{8b}$$

$$\frac{\partial \phi}{\partial \theta} = 0 \qquad \text{at } 0 \le R \le R_i, \theta = \gamma, \tag{8c}$$

$$\frac{\partial \phi}{\partial \theta} = KR\frac{\partial}{\partial R}\left(R\frac{\partial \phi}{\partial R}\right) \qquad \text{at } R_i < R < 1, \theta = \alpha, \tag{8d}$$

and

$$\frac{\partial \phi}{\partial R} = 0 \qquad \text{at } R = 0. \tag{8e}$$

Condition (8*a*) is a direct consequence of definition (6), while conditions (8*b*, 8*c*), and (8*e*) are due to symmetries in the flow domain. Relation (8*d*) was obtained from a one-dimensional heat balance on the fin, where the fin conductance parameter (K), is defined as $K = \beta k_s/k_f$. For the limiting case of infinite fin conductivity (i.e., 100 percent fin efficiency), K approaches infinity and the temperature becomes uniform within the fin and equal to the base temperature T_w. Consequently, when solving for this limiting case, condition (8*d*) was replaced by,

$$\phi = 0 \qquad \text{at } R_i \le R \le 1, \theta = \alpha.$$

As will be shown, this situation results in the best overall heat transfer performance for any tube geometry.

In addition to the above boundary conditions, zero heat flux was assumed at the tips of the fins. In other investigations, this assumption was adopted for convenience, (e.g., Soliman [5] and Sparrow, et al. [11]). The decision to use it here was made in order to establish a correspondence between the present results and those in [5], keeping in mind that it would cause a small decline in the predicted heat transfer performance because of the decrease in the effective heat transfer area.

The solution of energy equation (7) together with boundary conditions (8) is subject to the three geometrical parameters M, H, and β, in addition to the fin conductance parameter K. Since the evaluation of ϕ depends on the bulk temperature ϕ_b in the right hand side of equation (7), an iterative procedure was developed as follows.

1 The values of ϕ and the corresponding ϕ_b for the case of constant heat input axially and uniform temperature circumferentially were obtained by solving the applicable energy equation [5], which has the form

$$\frac{1}{R}\frac{\partial}{\partial R}\left(R\frac{\partial \phi}{\partial R}\right) + \frac{1}{R^2}\frac{\partial^2 \phi}{\partial \theta^2} = f\mathrm{Re}\ \mathrm{U}. \tag{9}$$

The solution of (9), subject to boundary conditions (8), was performed numerically using the mesh described earlier. The results of this step served the following two purposes: (i) they provided a first trial for the solution of equation (7); and, (ii) they established further confidence in the adequacy of the chosen mesh since it was found that the computed values of ϕ_b were always within 1 percent of the analytical results [5].

2 The results of step (1) were substituted into the right hand side of equation (7), which was then solved numerically for new values of ϕ. Based on these, a new value for ϕ_b was calculated and all results were again placed in the right hand side of equation (7).

Nomenclature

A_f = dimensionless flow area of the tube, a_f/r_0^2
a_f = flow area of the tube
c_p = specific heat at constant pressure
f = friction factor, equation (3*a*)
H = dimensionless fin height, h/r_0
h = fin height
$\bar{h}$ = average heat transfer coefficient at solid-fluid interface
K = fin conductance parameter, $\beta k_s/k_f$
k_f = thermal conductivity of fluid
k_s = thermal conductivity of fin
M = number of fin
$\dot{m}$ = mass flow rate of fluid
Nu = Nusselt number, equations (10)
P = pressure
Q = total heat transfer rate at solid-fluid interface
$\bar{q}$ = average heat flux, $Q/[2M(\alpha r_0 + h)]$
q_B = local heat flux at unfinned surface
$\bar{q}_B$ = average heat flux at unfinned surface
q_f = local fin heat flux
$\bar{q}_f$ = average fin heat flux
$\bar{q}_w$ = average heat flux at outer tube-wall, $Q/(2\pi r_0)$
R = dimensionless radial coordinate, r/r_0
R_i = dimensionless radial coordinate at tip of fin
r = radial coordinate
r_0 = radius of tube
Re = Reynolds number, equation (3*b*)
T = temperature
T_b = bulk temperature
T_w = tube-wall temperature
U = dimensionless velocity, $u/[(r_0^2/\mu)(-dP/dx)]$
U_b = dimensionless bulk velocity
u = axial velocity
u_b = bulk velocity
x = axial coordinate
α = half the angle between the flanks of two adjacent fins
β = half the angle subtended by one fin
γ = half the angle between the centre-lines of two adjacent fins
θ = angular coordinate
μ = dynamic viscosity
ρ = density
ϕ = dimensionless temperature, equation (6)
ϕ_b = dimensionless bulk temperature

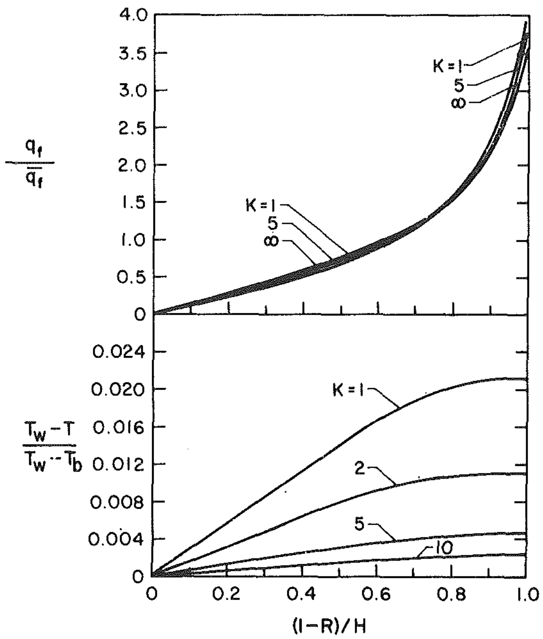

Fig. 2(a) **Fin temperature and local heat flux distributions for $M = 8$ and $H = 0.2$**

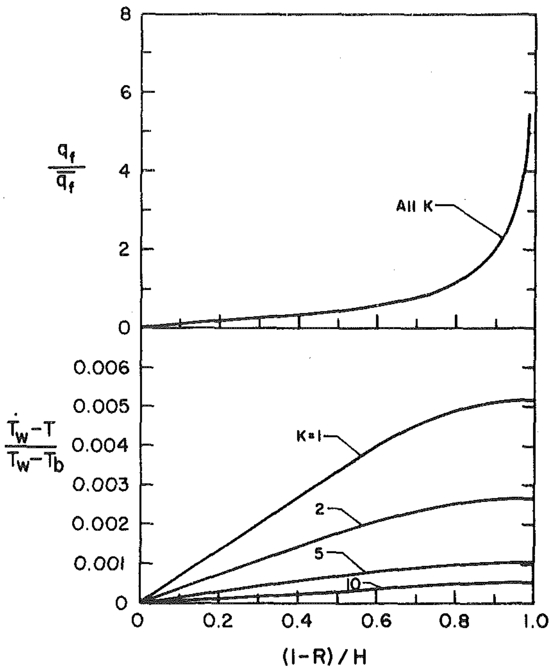

Fig. 2(b) **Fin temperature and local heat flux distributions for $M = 24$ and $H = 0.2$**

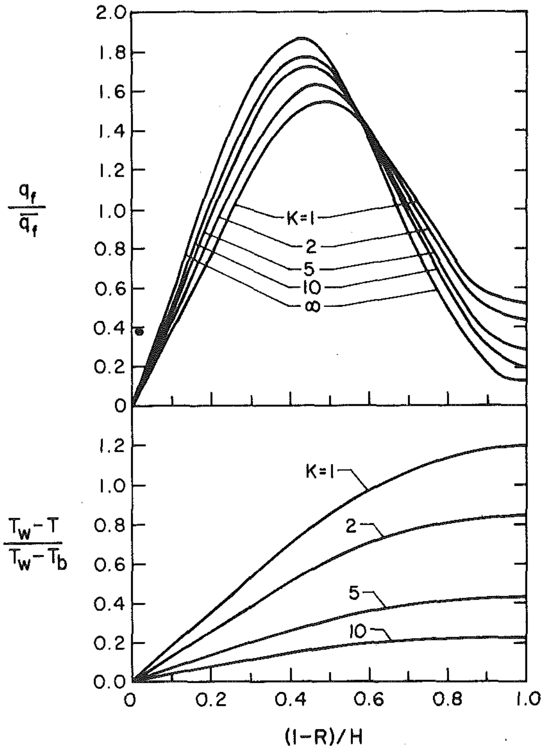

Fig. 2(c) **Fin temperature and local heat flux distributions for $M = 8$ and $H = 0.8$**

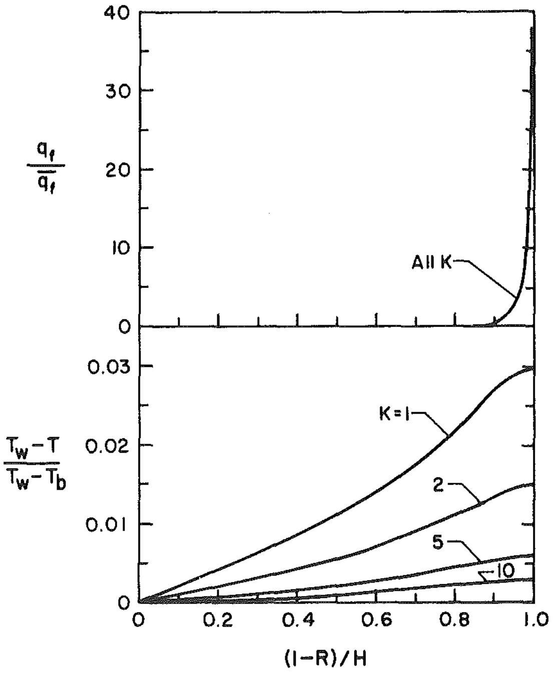

Fig. 2(d) **Fin temperature and local heat flux distributions for $M = 24$ and $H = 0.8$**

3 Step (2) was repeated until all values of ϕ and ϕ_b converged to six significant figures.

Finally, the heat transfer results were readily obtained from the converged solutions to the temperature fields.

Results and Discussion

Heat transfer results of both local and average nature were obtained for a wide range of finned tube geometries. A selected sample of the local distributions of fin temperature and heat flux, tube-wall heat flux, and fluid temperature is presented in Figs. 2–5. Values pertaining to the overall heat transfer characteristics are listed in Table 1, covering the entire investigated range of geometrical and fin conductance parameters. As stated earlier, all the present results correspond to a half fin angle $\beta = \pi/60$ radians.

Local Fin Temperature and Heat Flux. Local fin temperature and heat flux distributions corresponding to four selected tube geometries are presented in Figs. 2(*a,b,c,d*). Each graph shows (where practical) the plots corresponding to $K = 1, 2, 5, 10$, and ∞. The local heat flux is normalized using the average heat flux along the fin side ($\bar{q}_f$), while the local fin-to-base temperature difference is plotted relative to the bulk-to-base temperature difference. Attention is focused first on heat flux distributions, followed by a discussion on temperature distributions.

For tubes with a small number of short fins, the typical variation

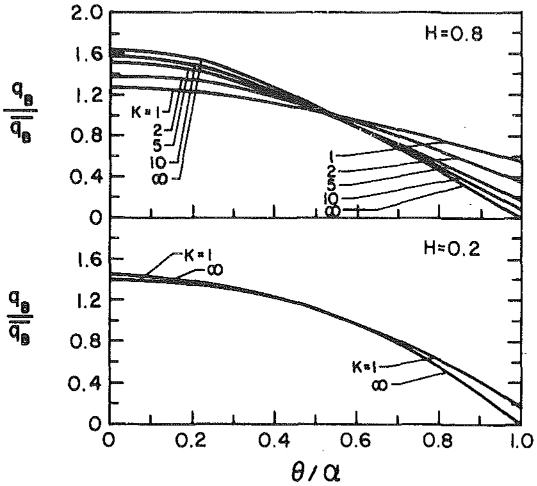

Fig. 3(a) Unfinned surface heat flux distribution for $M = 8$

of local fin heat flux is as shown in Fig. 2(*a*) for the case $M = 8$ and $H = 0.2$. The heat flux increases from zero at the base to a maximum at the edge of the fin tip. The fin conductance parameter has only a very minor effect on the values of $q_f/\bar{q}_f$. For the same relative fin height, increasing the number of fins to $M = 24$ results in the heat flux distribution shown in Fig. 2(*b*). Again, the value of K continues to have a negligible effect on the heat flux distribution, and most of the heat transfer occurs near the end of the fin. To comprehend the results of Figs. 2(*a,b*), we have to consider the velocity variation around the fin. At the corner formed by the fin and the tube-wall, the fluid velocity is very small resulting in small heat transfer coefficients and consequently small heat fluxes. As we move along the fin towards the tip, increasing velocities are encountered which contribute to an increasing heat flux with a maximum at the end of the fin.

To complete the sample presentation of local fin heat flux, the distributions for tubes with long fins ($H = 0.8$) are shown in Fig. 2(*c*) for a small fin number ($M = 8$) and in Fig. 2(*d*) for a large fin number ($M = 24$). Figure 2(*c*) shows that for a small number of long fins, $q_f/\bar{q}_f$ starts from zero at the base, reaches a maximum almost midway along the fin, and then decreases as we move towards the tip. Again, this behaviour is a direct result of the velocity distribution. For this tube geometry, it was shown in [2] that in the bay between two adjacent fins, equivelocity lines form closed loops resulting in small velocities near the base and tip of the fin and a maximum around the middle. As the number of fins increases, the resistance to the flow between the fins increases and an increasing portion of the flowing mass is pushed towards the core area of the tube. The limiting case of a large number of long fins is exemplified by the results in Fig. 2(*d*) where only a small area around the tip of the fin is participating in heat transfer.

One interesting deduction can be made from the above results concerning the hypothesis of a uniform heat transfer coefficient along the side of the fin. This assumption, often used for the evaluation of fin efficiency (e.g., [7]), would lead to a fin heat flux distribution starting from a maximum at the base and decreasing monotonically to a minimum at the tip. Since none of the considered tube geometries produced such a distribution, it is obvious that this assumption is inapplicable. A similar conclusion was reached by Sparrow, et al. [11] for shrouded fin arrays.

The dimensionless temperature distributions within the fin for the above mentioned tube geometries are presented in the lower portions of Figs. 2(*a–d*). Consistently, the wall-to-fin temperature difference increases from zero at the base to a maximum at the tip. Also, at any location within the fin, the dimensionless temperature decreases as the fin conductance parameter increases up to the limiting case of $K = \infty$ at which $(T_w - T)/(T_w - T_b) = 0$ everywhere within the fin. Comparing the results of Figs. 2(*a*) and 2(*b*), or those of Figs. 2(*c*) and 2(*d*), we notice that the increase in the number of fins from $M = 8$ to $M = 24$ resulted in a decrease in the dimensionless temperatures. This is due to a corresponding increase in the value of $(T_w - T_b)$, indicating

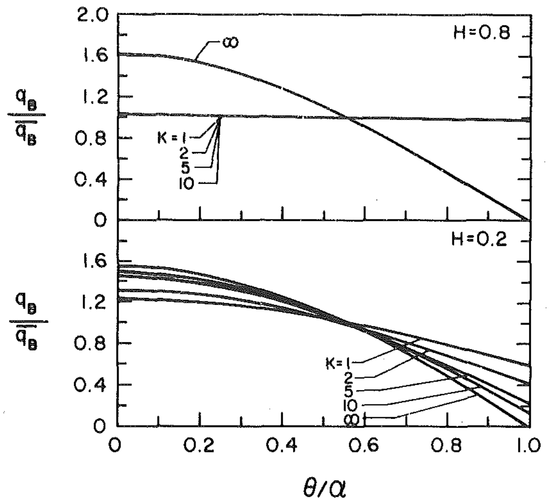

Fig. 3(b) Unfinned surface heat flux distribution for $M = 24$

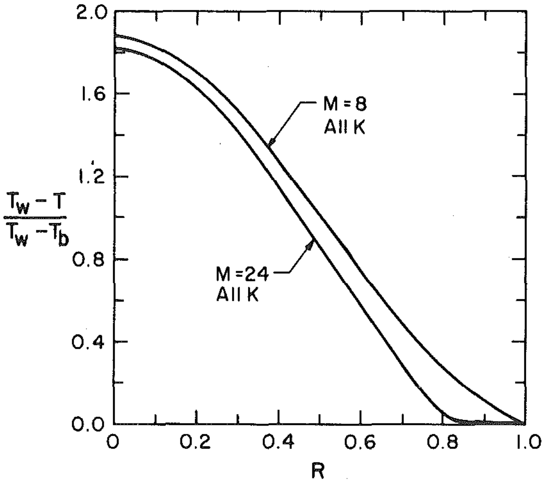

Fig. 4(a) Temperature distribution along $\theta = 0$ for $H = 0.2$

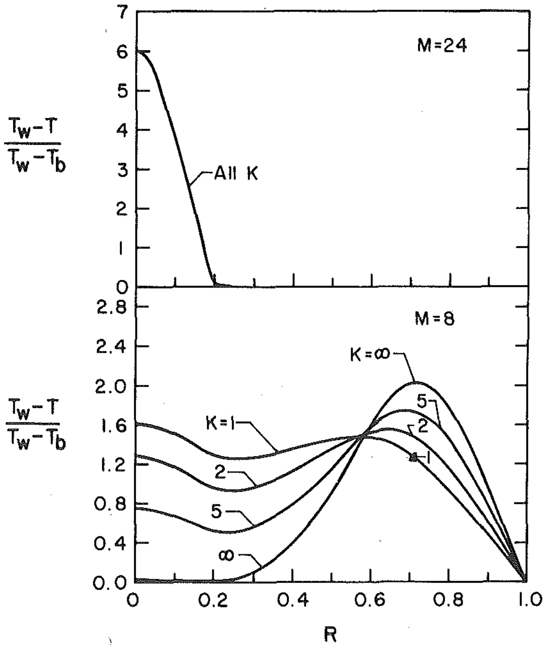

Fig. 4(b) Temperature distribution along $\theta = 0$ for $H = 0.8$

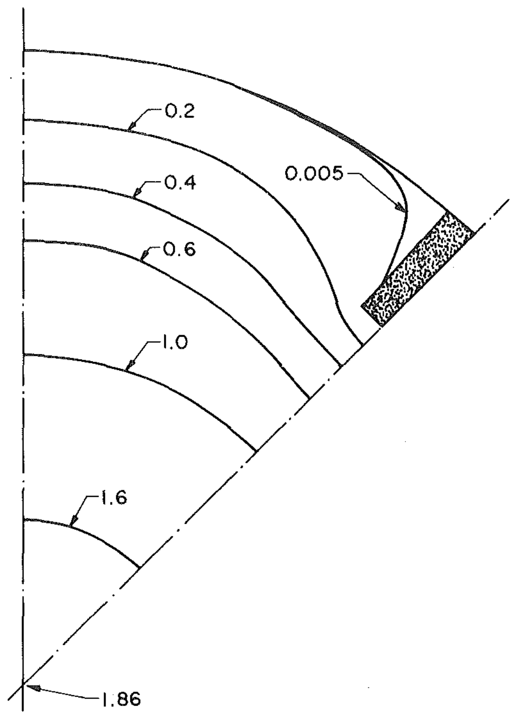

Fig. 5(*a*) Isotherms $(T_w - T)/(T_w - T_b)$ for $M = 4$, $H = 0.2$, and $K = 5$

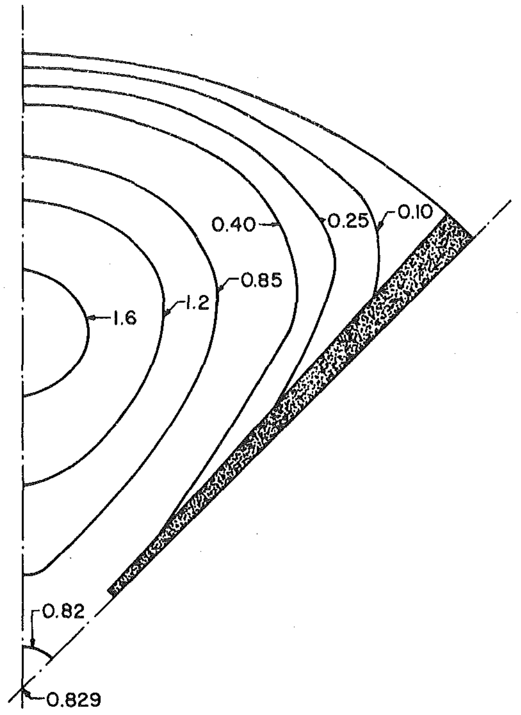

Fig. 5(*b*) Isotherms $(T_w - T)/(T_w - T_b)$ for $M = 4$, $H = 0.8$, and $K = 5$

Table 1 Overall heat transfer results ($\beta = \pi/60$ rad)

H	K	$M = 4$		$M = 8$		$M = 16$		$M = 24$		$M = 32$	
		$\bar{q}_f/\bar{q}$	Nu	$\bar{q}_f/\bar{q}$	Nu	$\bar{q}_f/\bar{q}$	Nu	$\bar{q}_f/\bar{q}$	Nu	$\bar{q}_f/\bar{q}$	Nu
	1	1.616	3.792	1.698	3.834	1.560	3.738	1.367	3.674	1.225	3.658
0.2	5	1.698	3.813	1.768	3.865	1.594	3.763	1.378	3.686	1.228	3.659
	10	1.709	3.816	1.778	3.870	1.598	3.766	1.380	3.688	1.228	3.660
	∞	1.721	3.819	1.787	3.874	1.603	3.770	1.381	3.689	1.228	3.660
	1	1.451	4.454	1.493	4.480	1.308	3.911	1.185	3.718	1.112	3.664
0.4	5	1.666	4.691	1.631	4.714	1.345	3.999	1.194	3.748	1.114	3.673
	10	1.699	4.729	1.651	4.749	1.350	4.011	1.195	3.753	1.114	3.674
	∞	1.734	4.770	1.672	4.787	1.356	4.023	1.196	3.757	1.115	3.676
	1	1.233	6.650	1.311	7.689	1.202	5.132	1.123	4.095	1.075	3.761
0.6	5	1.551	8.231	1.483	8.806	1.232	5.322	1.129	4.139	1.076	3.772
	10	1.606	8.557	1.509	8.978	1.236	5.349	1.130	4.145	1.076	3.773
	∞	1.666	8.930	1.536	9.157	1.240	5.376	1.131	4.151	1.076	3.775
	1	1.032	8.579	1.140	14.59	1.176	8.729	1.107	5.232	1.065	4.092
0.7	5	1.311	12.46	1.381	19.60	1.200	9.055	1.111	5.278	1.065	4.101
	10	1.352	13.48	1.422	20.23	1.203	9.098	1.112	5.284	1.065	4.102
	∞	1.390	14.77	1.465	20.81	1.206	9.143	1.112	5.290	1.065	4.103
	1	0.846	9.254	0.913	17.56	1.131	29.95	1.096	11.97	1.057	6.071
0.8	5	1.084	13.66	1.032	29.55	1.175	31.43	1.098	12.04	1.057	6.078
	10	1.113	14.77	1.036	32.29	1.178	31.56	1.098	12.05	1.057	6.079
	∞	1.136	16.09	1.033	35.29	1.180	31.68	1.098	12.06	1.057	6.080

a drop in the overall effectiveness of the heat transfer surface.

Local Unfinned-Surface Heat Flux. The variation of heat flux along the tube-wall between $\theta = 0$ and $\theta = \alpha$ (See Fig. 1) is illustrated in Fig. 3(*a*) for tubes with small M and in Fig. 3(*b*) for tubes with large M. Values of q_B are nondimensionalized using the average unfinned-surface heat flux $\bar{q}_B$. As a general trend, $q_B/\bar{q}_B$ has a maximum value at $\theta = 0$ (midway between two fins) and decreases to a minimum at $\theta = \alpha$ (base of fin). This form of variation is expected since the fin base is surrounded by almost stagnant fluid. Another feature which prevails for all tube geometries is that the variation in q_B becomes larger as K increases. This is also explainable since a higher K results in smaller fluid-to-wall temperature differences near the fin base and consequently a decrease in q_B there.

In regard to a possible assumption of uniform heat transfer coefficient along the unfinned surface, it is noted that this is valid only for tubes with a large number of long fins. This is evident from the results of Fig. 3(*b*) for $M = 24$ and $H = 0.8$, where $q_B/\bar{q}_B$ is almost uniform for all finite values of K. The reason for this is that for such geometries the fluid velocity in the gaps between the fins is so small that the dominant mode of heat transfer between the unfinned surface and the fluid is conduction.

Local Fluid Temperature. The influence of internal finning and of the fin conductance parameter on the fluid temperature is presented in Figs. 4(*a,b*). In these figures, the radial distributions of $(T_w - T)/(T_w - T_b)$ along the symmetry line $\theta = 0$ are plotted for the four tube geometries considered above. From our numerical results, we can also supplement the findings of Figs. 4 with the fact that the K-effect on the temperature distribution along any angular position is similar in trend to that along $\theta = 0$.

For tubes with short fins ($H = 0.2$), Fig. 4(*a*) shows that the fin conductance parameter has no effect on the dimensionless temperature distribution. Values of $(T_w - T)/(T_w - T_b)$ decrease radially from a maximum at the center-line to zero at the tube wall. The only distinguished difference in distribution between small and large numbers of fins is that for a large number of fins (e.g., $M = 24$) the wall-to-fluid temperature difference in the gaps between fins drop to very small values. This is consistent with heat flux and fin temperature results presented earlier.

Dimensionless temperature distributions are markedly different for tubes with long fins ($H = 0.8$). First of all, for a small number of fins ($M = 8$), the fin conductance parameter has a strong influence on the radial distribution of $(T_w - T)/(T_w - T_b)$, as shown in Fig. 4(b). At any value of K, the dimensionless temperature has two maximal values, one at the center-line of the tube and the second located somewhere in the gap between two fins. The global maximum can be either one of these two values depending on the magnitude of K. For a large number of fins, the radial temperature distribution takes on a completely different form as shown in Fig. 4(b) for $M = 24$. In the gap between two fins, the fluid-to-wall temperature difference is very small, and this difference increases to a maximum at the center-line of the tube. This form of temperature profile is attributed to the corresponding velocity distribution described earlier. The fin conductance parameter has no noticeable effect on the temperature distribution for this geometry.

For completeness, the isotherms $(T_w - T)/(T_w - T_b)$ were plotted over the whole flow domain and are shown in Fig. 5(a) for tubes with short fins and in Fig. 5(b) for tubes with long fins. The main distinguishing features between the two cases is the existence of closed loops in Fig. 5(b). This is consistent with the results of Fig. 4(b), and also with the velocity results reported in [2] where closed loop equivelocity lines were shown to exist for these geometries.

Overall Heat Transfer. The parameter which is commonly used as a measure of the overall performance of any heat transfer surface is the Nusselt number. In the present work, Nusselt number is defined as

$$\mathrm{Nu} = \frac{\bar{h}\,(2r_0)}{k_f}, \quad \text{where} \quad \bar{h} = \frac{\bar{q}_w}{T_w - T_b}.$$

Substituting, we get

$$\mathrm{Nu} = \frac{2r_0\bar{q}_w}{k_f\,(T_w - T_b)}, \tag{10a}$$

and in dimensionless form

$$\mathrm{Nu} = -\,2/\phi_b. \tag{10b}$$

Definition (10) results in values for Nu which can be used for comparing the average wall heat flux $\bar{q}_w$ of different tubes (finned or smooth) at the same r_0, k_f, and $(T_w - T_b)$. Thus, numerical values of Nu reflect influence of internal finning on the overall heat transfer performance. For smooth tubes, equations (10) reduce to the well known value Nu = 3.657.

Calculated values of Nu are listed in Table 1 for the range of tube geometries, using $K = 1, 5, 10$, and ∞ for each geometry. As a general trend, values of Nu for all finned tubes exceed that of a smooth tube irrespective of the value of K. Of course, the magnitude of heat transfer enhancement over smooth tube conditions depends on M, H, and K. From the results of Table 1, we can easily see that for any tube geometry the value of Nu increases as K increases. Again, the extent of the K-influence on Nu depends on the tube geometry. For example, $(\mathrm{Nu})_{K=1}/(\mathrm{Nu})_{K=\infty}$ has the value 0.70 for $M = 8$ and $H = 0.7$, as compared to 0.99 at $M = 16$ and $H = 0.2$. It is also interesting to note that for any combination of H and K, the value of Nu first increases with an increase in M up to an optimum value after which any further increase in M will result in a decrease in Nu. The magnitude of M at which this optimum Nu occurs increases as the relative fin height increases. To help in visualizing this behaviour we should point out that for any combination of H and K, there are two limiting values of M at which Nusselt number approaches 3.657. These limiting values are $M = 0$ (smooth tube), and $M = 60$, which correspond to the situation where the gaps between the fins disappear and the geometry reduces to a smooth tube with a thick wall. Finally, comparing the present results with those reported by Soliman [5], we conclude that for all tube geometries Nusselt numbers for uniform temperature axially are lower than for uniform heat flux axially. For example, for $K = \infty$, the present Nu results (25 cases) averaged 67 percent of those reported in [5] with a range of 26 to 84 percent. The corresponding ratio for smooth tubes is also 84 percent, hence it follows that enhancement over smooth tube conditions due to internal finning is relatively less for uniform outside wall temperature than for the uniform heat flux boundary condition. The present variations of Nu with M, H, and K are fairly similar to those reported in [5]. A notable difference is that for a given H, the present Nu values peak at lower M values than in [5]. Optimal Nu values for the two boundary conditions occurred in the same general neighborhood $-H = 0.8$ for both, but $M = 11$ for the present results versus $M = 16$ for [5].

Another parameter relevant to the present geometry is the ratio $\bar{q}_f/\bar{q}$ (included in Table 1) where $\bar{q}_f$ is the average heat flux at the sides of the fins and $\bar{q}$ is the overall average heat flux at the solid-fluid interface excluding the fin tips. This ratio serves as an indicator of the effectiveness of the fin as a heat transfer surface. As may be seen from these results in Table 1, for values of H up to and including 0.7, the fin surface is a more effective heat transfer surface than the tube-wall surface for the whole range of M and K considered. The same conclusion is true for $H = 0.8$, except for $K = 1$ at $M = 4$ and 8.

Concluding Remarks

Earlier analyses of laminar, fully developed, forced convective heat transfer in internally finned tubes [3–5] were concerned with the wall condition of constant heat flux axially and uniform temperature circumferentially. The present analysis considers the second fundamental boundary condition of an isothermal wall, both axially and circumferentially. The governing momentum and energy equations were solved numerically, taking into consideration radial conduction within the fins. Local and average heat transfer results were calculated for a combined range of relative fin heights ($0.2 \leq H \leq 0.8$), number of fins ($4 \leq M \leq 32$), and a half fin angle $\beta = \pi/60$ radians. For each tube geometry, the heat transfer performance was sought at different values of the fin conductance parameter K. The following conclusions can be drawn from the results of the present investigation.

1 The distribution of local heat flux at the side of the fin and along the unfinned surface is strongly dependent on the values of M and H. The hypothesis of uniform heat transfer coefficient along the fin, often used for the calculation of fin efficiency, proved inapplicable for all geometries considered. Along the unfinned surface, this assumption is valid only for tubes with a large number of long fins (e.g., $M = 24$ and $H = 0.8$).

2 The fluid temperature within tubes with short fins ($H < 0.4$) has a single maximum value located at the center-line, whereas with long fins the fluid temperature is characterized by the existence of closed loop isotherms.

3 The fin side is a more effective heat transfer surface than the unfinned tube-wall.

4 Internal finning provides substantial heat transfer enhancement over smooth tube conditions. Nusselt numbers (equation (10)) are dependent on M, H, and K and exceed 3.657 by up to a factor of close to 10. The present values of Nu are consistently lower than their counterparts for the boundary condition of uniform axial heat input [5].

Unfortunately, comparison of the present results with experimental results available in the literature was not possible due to lack of common geometrical, flow, or boundary conditions. As pointed out earlier, only three experimental studies [7–9] have dealt with laminar flow in internally finned tubes. Watkinson, et al. [7] used several tubes with spiral and straight fins and applied uniform temperature at the outer wall by a steam jacket. However, they presented average heat transfer results over a certain tube length without distinction between the developing and fully developed regions. The finned tubes used by Soliman and Feingold [8] all had spiral fins. Marner and Bergles [9] reported local heat transfer data for different augmented test sections corresponding to the two fundamental wall conditions. However, their large scale constant wall temperature tests did not involve tubes with straight fins. The need for more experimental results at specified wall conditions, flow situations (developing and fully developed), and using a wide range of tube designs is quite obvious.

Finally, it is appropriate to emphasize that whereas the present study has dealt solely with heat transfer, the advantage of enhanced heat transfer over smooth tube conditions is always accompanied by the penalty of higher pressure drop [2]. The present results plus those in [5] are being examined to determine optimal configurations under a variety of operating conditions and objectives. This optimization study is expected to be available for publication shortly.

Acknowledgment

The authors gratefully acknowledge the support provided for this research by the Natural Sciences and Engineering Research Council of Canada.

References

1 Nandakumar, K., and Masliyah, J. H., "Fully Developed Viscous Flow in Internally Finned Tubes," *The Chemical Engineering Journal*, Vol. 10, 1975, pp. 113–120.

2 Soliman, H. M., and Feingold, A., "Analysis of Fully Developed Laminar Flow in Longitudinal Internally Finned Tubes," *The Chemical Engineering Journal*, Vol. 14, 1977, pp. 119–128.

3 Masliyah, J. H., and Nandakumar, K., "Heat Transfer in Internally Finned Tubes," ASME JOURNAL OF HEAT TRANSFER, Vol. 98, 1976, pp. 257–261.

4 Soliman, H. M., and Feingold, A., "Analysis of Heat Transfer in Internally Finned Tubes Under Laminar Flow Conditions," *Proceedings of the Sixth International Heat Transfer Conference*, Vol. 2, 1978, pp. 571–576.

5 Soliman, H. M., "The Effect of Fin Material on Laminar Heat Transfer Characteristics of Internally Finned Tubes," Symposium on Advances in Enhanced Heat Transfer, The 18th National Heat Transfer Conference, 1979, pp. 95–102.

6 Shah, R. K., and London, A. L., "Thermal Boundary Conditions and Some Solutions for Laminar Duct Flow Forced Convection," ASME JOURNAL OF HEAT TRANSFER, Vol. 96, 1974, pp. 159–165.

7 Watkinson, A. P., Miletti, D. L., and Kubanek, G. R., "Heat Transfer and Pressure Drop of Internally Finned Tubes in Laminar Oil Flow," ASME Paper No. 75-HT-41, 1975.

8 Soliman, H. M., and Feingold, A., "Heat Transfer, Pressure Drop, and Performance Evaluation of a Quintuplex Internally Finned Tube," ASME Paper No. 77-HT-46, 1977.

9 Marner, W. J., and Bergles, A. E., "Augmentation of Tubeside Laminar Flow Heat Transfer by Means of Twisted-Tape Inserts, Static-Mixer Inserts, and Internally Finned Tubes," *Proceedings of the Sixth International Heat Transfer Conference*, 1978, Vol. 2, pp. 583–588.

10 Carnavos, T. C., "Cooling Air in Turbulent Flow With Internally Finned Tubes," AIChE Paper, Presented at the 17th National Heat Transfer Conference, Salt Lake City, Utah, Aug. 1977.

11 Sparrow, E. M., Baliga, B. R., and Patankar, S. V., "Forced Convection Heat Transfer From a Shrouded Fin Array With and Without Tip Clearance," ASME JOURNAL OF HEAT TRANSFER, Vol. 100, 1978, pp. 572–579.

E. M. Sparrow
Fellow ASME

M. Charmchi
Department of Mechanical Engineering,
University of Minnesota,
Minneapolis, Minn. 55455

Laminar Heat Transfer in an Externally Finned Circular Tube

An analysis has been carried out for laminar heat transfer in a circular tube subjected to an axially periodic variation of the external heat transfer coefficient (or of its dimensionless counterpart, the Biot number). This thermal boundary condition serves to model flow in a tube fitted with a regularly spaced array of annular fins. It was found from numerical solutions that external finning yields substantial heat transfer enhancement compared with an unfinned tube, especially when the Biot number of the unfinned tube is low. The degree of enhancement is quite insensitive to the period of the Biot number variation provided that the overall proportions of the unfinned and finned surface are maintained and the Biot number level is also maintained. An increase in the interfin spacing tends to diminish the enhancement. A constant-Biot-number model intended to approximate the heat transfer results for the periodic-Biot-number case was devised and tested. The predictions of this simplified model are especially accurate at low Biot numbers. The results of the laminar flow analysis have suggested ways of modeling turbulent heat transfer in externally finned tubes.

Introduction

There are many engineering applications where a fluid flowing in a tube is subjected to a thermal boundary condition which varies in a periodic manner along the flow direction. Perhaps the most visible application is the externally finned tube, where the fins are uniformly spaced annular or square plates affixed to (or integral with) the outside surface of the tube. Finned tubes of this type are encountered, for example, in residential or institutional space heating.

Each fin can be regarded as an enhancement device which brings about a local increase of the heat transfer coefficient for convective exchange between the fin base area and the ambient. This view can be illustrated by noting that the fin heat transfer rate Q_f can be related to the fin base area A_{fb} and the temperatures T_{fb} and T_∞ at the fin base and in the ambient

$$Q_f = h\phi A_{fb}(T_{fb} - T_\infty) \tag{1}$$

where ϕ is the fin effectiveness and h is the heat transfer coefficient which would prevail at the outer surface of the tube in the absence of the fins. Under normal conditions, the numerical value of ϕ is very much larger than one. The quantity $h\phi$ can be regarded as an effective heat transfer coefficient between the fin base and the ambient.

The foregoing discussion serves to motivate a model for analyzing the heat transfer characteristics of a forced convection flow in a pipe having a regularly spaced array of fins attached to its outer surface. The pipe flow can be regarded as being subjected to an external convective boundary condition, with an external heat transfer coefficient which varies periodically along the flow direction. The periodic variation will be idealized here as a succession of high and low values, respectively modeling the successive finned and unfinned portions of the tube (see Fig. 1, lower diagram). This model is a limiting case in that it does not take account of the possible smoothening effects of axial conduction in the tube wall. The ramifications of accounting for axial conduction will be discussed at the end of the paper.

It appears that pipe flows subjected to an axially periodic external heat transfer coefficient have not heretofore been analyzed in the published literature. Recently, problems involving either axially periodic prescribed wall temperature or axially periodic prescribed heat flux have been studied [1], but the methods developed for those cases do not apply to the case under consideration here. In the absence of a viable analytical method, a numerical method has been employed.

The solutions are carried through the entire thermal entrance region and are terminated when thermally developed conditions are attained. In this regard, it should be noted that the thermally developed regime in an axially periodic system is altogether different from that in a conventional pipe or duct flow, where the heat transfer coefficient and the shape of the temperature profile are axially unchanging [2]. For the present case, thermal development was defined in terms of average heat transfer coefficients for the successive finned and unfinned portions of the tube. When each of these average coefficients attained a constant value, independent of axial position, thermal development was regarded as having been attained.

The solutions were carried out for laminar flow. For each solution, a minimum of four independent dimensionless parameters must be specified. In view of the large number of parameters and of the extreme demands of the computational task, a full parametric exploration is unrealistic. Rather, the parameters were varied systematically in order to reveal the key trends in the results. In addition, an approach was made to correlating the heat transfer characteristics for finned and unfinned tubes. In this connection, supplementary finite

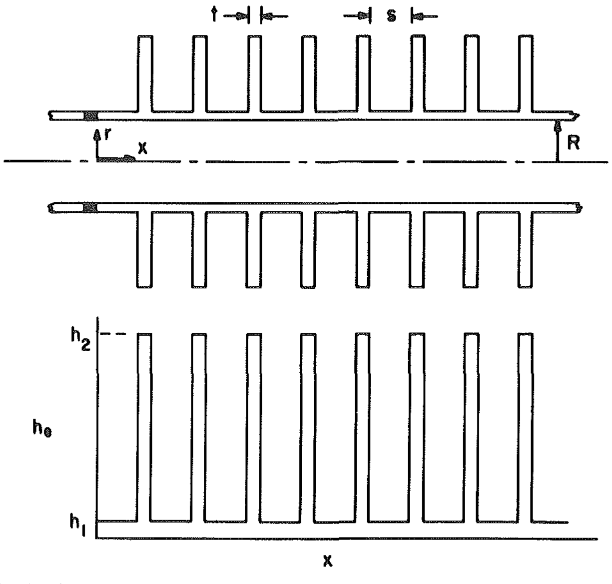

Fig. 1 Schematic of an externally finned tube (upper diagram) and model adopted for the external heat transfer coefficient (lower diagram)

Contributed by the Heat Transfer Division for publication in the JOURNAL OF HEAT TRANSFER. Manuscript received by the Heat Transfer Division March 14, 1980.

difference solutions were carried out for tubes with uniform external heat transfer coefficients (i.e., no fins).

Analysis

The description of the analysis is facilitated by reference to Fig. 1. The upper portion of the figure is a schematic diagram of an externally finned tube showing the coordinates and dimensional nomenclature, while the lower portion displays the model adopted for the heat transfer at the outside surface of the tube. As discussed earlier, the external heat transfer coefficient h_e at the successive unfinned and finned portions of the tube is modeled as a periodic distribution of low and high values, respectively designated as h_1 and h_2 in Fig. 1.

In considering the analysis of the tube flow, it may be noted that the adopted numerical solution method can deal equally well with the heat transfer problem for a developing velocity profile or for a fully developed velocity profile. Since the former situation involves the specification of an additional prescribable parameter (the Prandtl number), over and above the basic set of four parameters, the present solutions will be carried out for a hydrodynamically developed flow. For this same reason, the thermal resistance of the tube wall will not be dealt with explicitly but rather will be regarded as being accounted for in h_1 and h_2.

With the foregoing as background, the problem to be treated here will now be defined. We consider a fluid entering a tube with a fully developed laminar velocity profile and a uniform temperature T_o. In the course of its flow through the tube, the fluid exchanges heat with an external environment at temperature T_∞ via a streamwise-periodic external heat transfer coefficient h_e. The goal of the work is to determine the heat transfer rates which occur under the influence of the periodic external boundary condition and, if possible, to relate these results to those for tube flows with a streamwise-uniform external heat transfer coefficient.

To arrive at a formulation involving the minimum number of parameters, the following dimensionless variables are introduced

$$X = (x/R)/\mathrm{Pe}, \quad \eta = r/R, \quad \theta = (T - T_o)/(T_\infty - T_o) \tag{2}$$

where $\mathrm{Pe} = \bar{u}D/\alpha$ is the Peclet number. With these variables, the streamwise lengths s and t of Fig. 1 which define the successive regions of low and high external heat transfer coefficient become, in dimensionless terms,

$$\sigma = (s/R)/\mathrm{Pe}, \quad \tau = (t/R)/\mathrm{Pe} \tag{3}$$

Furthermore, the dimensionless counterparts of the external heat transfer coefficients h_1 and h_2 (the successive low and high values) are Biot numbers[1] Bi_1 and Bi_2

$$\mathrm{Bi}_1 = h_1R/k, \quad \mathrm{Bi}_2 = h_2R/k \tag{4}$$

The four dimensionless quantities σ, τ, Bi_1, and Bi_2 constitute the four parameters which must be prescribed for each solution.

With the Poiseuille velocity distribution $u/\bar{u} = 2(1 - \eta^2)$ and with the variables of equation (2), the dimensionless energy equation can be written as

$$(1 - \eta^2)\partial\theta/\partial X = (1/\eta)\partial/\partial\eta\,[\eta(\partial\theta/\partial\eta)] \tag{5}$$

The axial diffusion term has been omitted because the Peclet number range of interest here exceeds the threshold (Pe = 50) below which axial diffusion has a detectable effect. In addition, equation (5) includes the assumptions of constant fluid properties and negligible viscous dissipation.

At the tube wall ($r = R$), the convective interchange between the tube flow and the ambient takes the mathematical form

$$-k\partial T/\partial r = h_e(T - T_\infty), \quad \text{or} \quad -\partial\theta/\partial\eta = (h_eR/k)(\theta - 1) \tag{6}$$

The periodic boundary condition involving Bi_1 and Bi_2 then becomes

$$-\partial\theta/\partial\eta = \mathrm{Bi}_1(\theta - 1), \quad n(\sigma + \tau) < X < n(\sigma + \tau) + \sigma \tag{7}$$

$$-\partial\theta/\partial\eta = \mathrm{Bi}_2(\theta - 1), \quad n(\sigma + \tau) + \sigma < X < (n + 1)(\sigma + \tau) \tag{8}$$

in which $n = 0, 1, 2, \ldots$. At the tube inlet ($x = 0$), the $T = T_o$ boundary condition becomes $\theta = 0$ in the transformed variables.

The equations set forth in the preceding paragraphs were solved by adapting the Patankar-Spalding method [3]. This is a fully implicit finite difference scheme which marches the solution steadily along the tube, starting at $x = 0$. The computational task required to obtain the solutions was especially demanding because of the nature of the boundary conditions (7) and (8). In particular, the periodic abrupt changes in Bi require a fine distribution of grid points in both x and r for their accommodation. The effects of these abrupt changes are more strongly felt in the initial portion of the tube, where the largest differences prevail between the fluid bulk temperature T_b and the ambient temperature T_∞. Consequently, it was necessary to use extremely small axial steps in that region.

The grid was laid out with 220 points spanning the cross section $0 \le \eta \le 1$, with a greater concentration near the tube wall. For the axial grid layout, the computations were begun with a uniform step size of $\Delta X = 10^{-6}$ or 0.5×10^{-6} depending on the parameters. This step size was maintained until the rate of axial change had diminished to a level at which the step could be safely increased (usually by a factor of two). The decision to increase the step size was made by examining average Nusselt numbers for the successive low- and high-Bi segments of the tube. A change in step was made when the resulting segment-to-segment differences in the average Nusselt numbers were less than one percent, both for the low-Bi and high-Bi segments. Subsequent step size increases were made using the same criterion.

The streamwise marching of the solution was continued until the aforementioned average Nusselt numbers for the low and high-Bi segments became constant, independent of axial position. This occurred in the range of X values between 0.2 and 0.4, depending on the parameters. The number of axial grid points ranged from 50,000 to

Nomenclature

Bi = external Biot number, h_eR/k
Bi_1 = Biot number for unfinned surface, h_1R/k
Bi_2 = Biot number for finned surface, h_2R/k
c_p = specific heat
D = tube diameter
h_e = external heat transfer coefficient
h_1 = coefficient for unfinned surface
h_2 = coefficient for finned surface
k = thermal conductivity
$\dot{m}$ = mass flow rate
Nu = local Nusselt number for tube flow
$\overline{\mathrm{Nu}}_1$ = average tube-side Nusselt number for unfinned segment
$\overline{\mathrm{Nu}}_2$ = average tube-side Nusselt number for finned segment
Pe = Peclet number, $\bar{u}D/\alpha$
Q = rate of heat transfer between $x = 0$ and $x = x$
$Q_{\max}$ = maximum heat transfer rate, $\dot{m}c_p(T_\infty - T_o)$
R = tube radius
r = radial coordinate
s = interfin spacing
T = temperature
T_{bx} = local bulk temperature
T_o = entering fluid temperature
T_∞ = ambient temperature
t = fin thickness
u = axial velocity component
$\bar{u}$ = mean velocity
X = dimensionless axial coordinate, $(x/R)/\mathrm{Pe}$
x = axial coordinate
α = thermal diffusivity
η = dimensionless radial coordinate, r/R
θ = dimensionless temperature, $(T - T_o)/(T_\infty - T_o)$
σ = dimensionless interfin spacing, $(s/R)/\mathrm{Pe}$
τ = dimensionless fin thickness, $(t/R)/\mathrm{Pe}$

---

[1] The characteristic dimensions in the Biot number can be selected with a certain degree of arbitrariness. Since the Biot number represents a ratio of thermal resistances, the radius R was selected rather than the diameter D because it is believed that R/k is a better measure of the thermal resistance of the tube flow than is D/k.

95,000, corresponding to total numbers of grid points (radial times axial) ranging from about ten to twenty million.

To verify the solution methodology, comparisons were made with the eigenvalue solution of [4] for constant Biot number. With only ten eigenvalues available, that solution is limited to the downstream portion of the tube. In that region, the local Nusselt numbers from the present solutions agreed to within 0.01 percent with those from the eigenvalue solution.

The main result that will be extracted from the solutions is the rate of heat transfer from the fluid flowing in the tube. If $\dot{m}$ denotes the mass rate of fluid flow and T_{bx} is the bulk temperature at a streamwise station x, the rate of heat transfer for the section of the tube between $x = 0$ and $x = x$ is

$$Q = \dot{m}c_p(T_{bx} - T_o) \qquad (9)$$

A dimensionless representation for Q can be obtained by noting that the maximum possible rate of heat transfer occurs when $T_{bx} = T_\infty$, a condition which is fulfilled as $x \rightarrow \infty$. If

$$Q_{\max} = \dot{m}c_p(T_\infty - T_o) \qquad (10)$$

then

$$Q/Q_{\max} = (T_{bx} - T_o)/(T_\infty - T_o) = \theta_{bx} \qquad (11)$$

In the main, the results will be reported in terms of the $Q/Q_{\max}$ ratio. The dimensionless bulk temperature appearing in equation (11) was evaluated from its definition as

$$\theta_{bx} = 2\int_0^1 (u/\bar{u})\theta\eta d\eta \qquad (12)$$

Average Nusselt numbers for the successive low and high Biot number sections (1 and 2, respectively) of the tube were determined from

$$\overline{\mathrm{Nu}}_1 = \bar{h}_1 D/k, \quad \bar{h}_1 = \int_\sigma qdX \Big/ \int_\sigma (T_{wx} - T_{bx})dX \qquad (13)$$

$$\overline{\mathrm{Nu}}_2 = \bar{h}_2 D/k, \quad \bar{h}_2 = \int_\tau qdX \Big/ \int_\tau (T_{wx} - T_{bx})dX \qquad (14)$$

The integrals appearing in the numerators and denominators of the $\bar{h}$ equations respectively yield the average heat flux and average wall-to-bulk temperature difference per section. Values of $\overline{\mathrm{Nu}}_1$ and $\overline{\mathrm{Nu}}_2$ were determined at all of the successive sections.

Results and Discussion

As was noted earlier, the superabundance of parameters and the very lengthy computations make it unrealistic to undertake a full-blown parametric investigation. Rather, a sequence of typical cases was selected in order to illuminate the heat transfer response to variations of the parameters. A listing of the investigated cases characterized by a periodically varying external heat transfer coefficient is presented in Table 1. Some finite difference solutions were also performed for the case of uniform external Biot number; these will be described shortly.

With respect to Table 1, case 1 may be regarded as a baseline case. It is characterized by an interfin spacing that is three times the fin thickness and by an effective fin heat transfer coefficient that is fifty times that of the external coefficient on the unfinned surface of the tube. Case 2 explores the effect of changing the general level of the external coefficient (i.e., of both h_1 and h_2) while maintaining the same fin thickness, the same interfin spacing, and the ratio of h_2 to h_1. The intent of case 3 is to study the effect of changing the h_2/h_1 ratio. In case 4, the interfin spacing is increased to seven times the fin thickness (compared to three times for the baseline case).

Table 1 Parameter values

Case	τ	σ	Bi_1	Bi_2	Bi (equation (15))
1	10^{-4}	3τ	1	50	53/4
2	10^{-4}	3τ	5	250	265/4
3	10^{-4}	3τ	1	20	23/4
4	10^{-4}	7τ	1	50	57/8
5	0.5×10^{-4}	3τ	1	50	53/4
6	0.5×10^{-4}	3τ	0.1	5	5.3/4

All of the foregoing cases correspond to a fixed dimensionless fin thickness. For case 5, both the fin thickness and the interfin spacing are reduced to half their former values; this changes the spatial period of the variation but leaves unchanged the actual extent of finned and unfinned surfaces. For this same fin arrangement, case 6 re-examines the effect of changing the level of the external resistance, this time to sufficiently low values so that the external resistance is controlling, as would occur with an internal liquid flow and an external gas flow.

To complement and provide perspective for the results of cases 1–6, finite difference solutions based on a constant Biot number were carried out. These included Biot numbers of 0.1, 1, and 5, which correspond to unfinned-tube counterparts of cases 1–6. Also included were Biot numbers given by

$$\mathrm{Bi} = (\sigma \mathrm{Bi}_1 + \tau \mathrm{Bi}_2)/(\sigma + \tau) \qquad (15)$$

These Biot numbers correspond to the spatial mean of Bi_1 and Bi_2.

As an alternative to the spatial-mean Biot number of equation (15), a force-fit approach might have been taken. In such an approach, a succession of constant Biot number solutions would have been run until a Bi value is found which yields a satisfactory fit with the results of the variable Biot number case in question. This approach is extremely costly with regard to computer time. It would have practical merit only if the force-fit Biot nunbers could be correlated with Bi_1, Bi_2, σ, and τ. The existence of such a correlation can only be explored by solving a larger number of cases than has been considered here. For this reason, the alternate approach was not employed.

As noted at the end of the preceding section, the main focus of the presentation of results will be the rate of heat transfer Q between $x = 0$ and any streamwise station x, with the ratio $Q/Q_{\max}$ being used to obtain a dimensionless representation. These heat transfer results will be presented from two distinct perspectives. The first focuses on the relationship between the results for streamwise-periodic Bi and those for uniform Bi. Comparisons will be made which show the degree of heat transfer enhancement due to finning. Other comparisons will illustrate how well the results for periodic Bi can be approximated by those for uniform Bi. In the second part of the presentation, the $Q/Q_{\max}$ results for the various cases 1–6 of Table 1 will be compared among themselves in order to illustrate the role of the parameters.

Representative results for the average heat transfer coefficients for the successive finned and unfinned portions of the tube will also be presented in the form of axial distributions. These distributions will provide perspective on the length of the thermal entrance region.

Relationship between results for periodic and constant Bi. Figures 2–6 have been prepared to show the relationship between the $Q/Q_{\max}$ results for streamwise-periodic Biot number and for constant Biot number. In each figure, the periodic Biot number results are portrayed by a solid line, while those for constant Biot number are drawn as dashed lines. The lower of the constant Biot number lines corresponds to the value of the Biot number Bi_1 on the unfinned portions of the tube. The extent to which the finned-tube line lies above this lower line indicates the degree of heat transfer enhancement achieved by finning.

The upper of the constant Biot number lines corresponds to the spatial mean of Bi_1 and Bi_2 as given by equation (15). In the absence of solutions for the periodic case, heat transfer results corresponding to this type of average Biot number might be considered as a first approximation for those for a periodic Biot number. The comparisons presented in Figs. 2–6 enable conclusions to be drawn about the quality of the approximation.

In all of these figures, $Q/Q_{\max}$ is plotted as a function of the dimensionless streamwise coordinate $(x/R)/\mathrm{Pe}$. Figure 2 conveys results both for cases 1 and 5 since the constant Bi comparison curves for both these cases are the same. Results for cases 2, 3, 4, and 6 are presented separately in Figs. 3–6.

If attention is first turned to Fig. 2, it is seen that there is substantial heat transfer enhancement due to external finning. The enhancement,

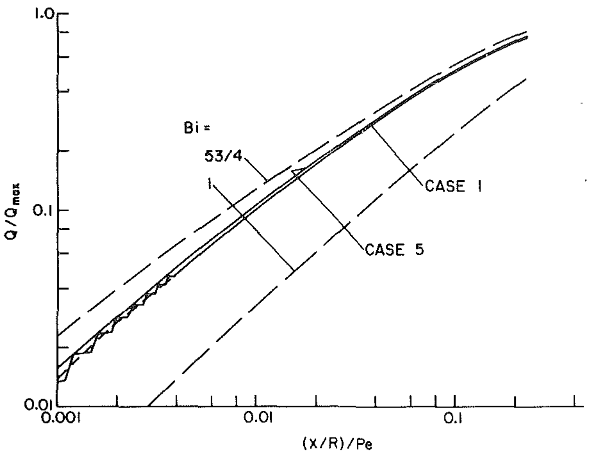

Fig. 2 Relationship between heat transfer results for axially periodic and axially uniform Biot number, cases 1 and 5

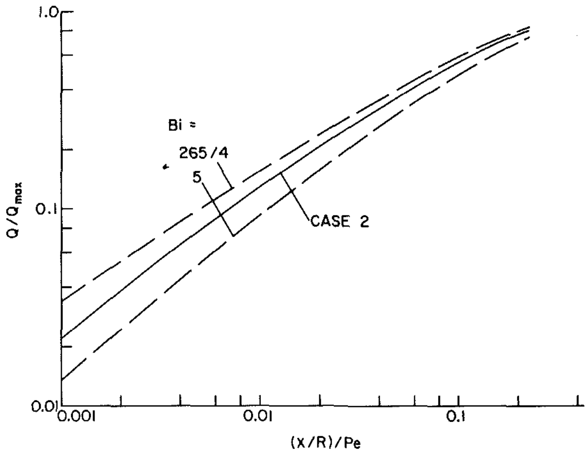

Fig. 3 Relationship between heat transfer results for axially periodic and axially uniform Biot number, case 2

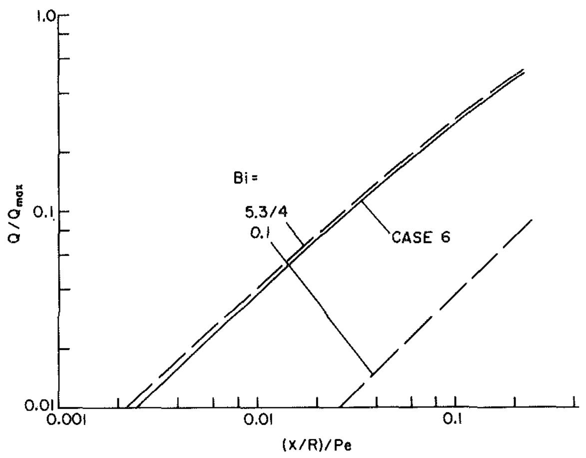

Fig. 4 Relationship between heat transfer results for axially periodic and axially uniform Biot number, case 6

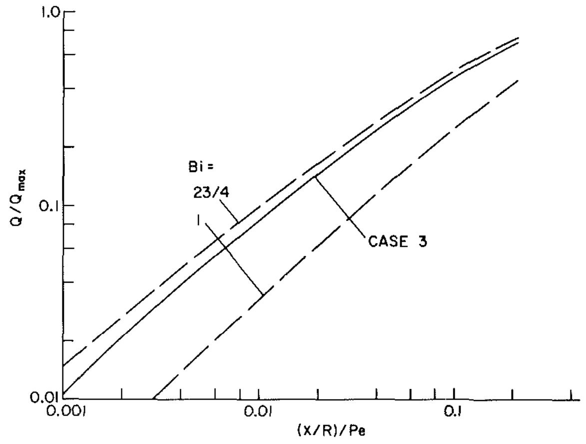

Fig. 5 Relationship between heat transfer results for axially periodic and axially uniform Biot number, case 3

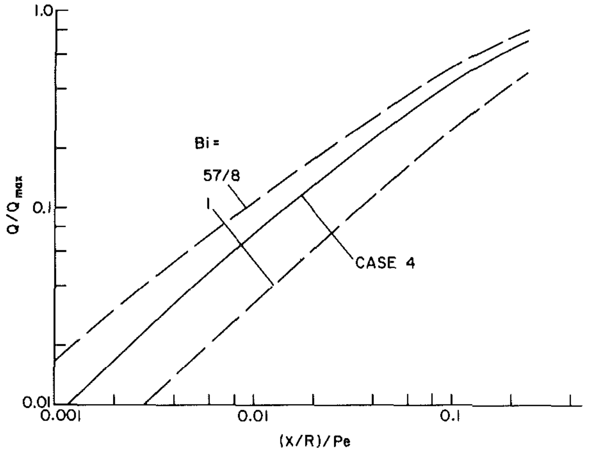

Fig. 6 Relationship between heat transfer results for axially periodic and axially uniform Biot number, case 4

which can be identified by the vertical separation distance between the solid line for the finned tube case and the lower dashed line for the unfinned tube, tends to diminish somewhat with increasing downstream distance (i.e., for longer tubes). This trend is physically plausible and reflects the fact that the fluid tends toward thermal saturation (i.e., $T_{bx} \rightarrow T_\infty$) as it flows through the tube. The general level of heat transfer enhancement in evidence in the figure is in the range of two to four times that for the unfinned case. These findings hold for both cases 1 and 5, which differ with respect to the streamwise period of the Biot number variation but have identical finned and unfinned surface areas and identical Biot number levels.

The next issue to be addressed in Fig. 2 is the matter of how well the results for the finned tube can be approximated by the results for a constant Biot number based on the spatial average of Bi_1 and Bi_2. In considering this issue, it may be noted that the $Q/Q_{\max}$ curve for the finned tube case is not altogether smooth owing to the periodic rapid changes of the external heat transfer coefficient. The departures from smoothness are illustrated for case 1 in the figure. As can be seen there, the non-smoothness is confined to the most upstream portion of the tube and dies away with increasing downstream distance. The nonsmoothness can be very effectively smoothed in the mean by passing a curve through the $Q/Q_{\max}$ values at the successive midpoints of the unfinned sections, as is illustrated by the short-dashed line in Fig. 1. From now on, only smoothed curves will be considered.

The results for cases 1 and 5 are so close that they bear a common relationship to the candidate constant-Biot-number approximating curve (the comparison between cases 1 and 5 will be elaborated later). For these cases, the candidate constant Biot number is $((3)(1) + (1)(50))/(3 + 1) = 53/4$. As seen in the figure, the approximating curve overestimates the heat transfer for the finned tube. The greatest overestimation occurs in the immediate neighborhood of the heated inlet, and thereafter the approximating curve is increasingly more accurate. For example, at axial stations beyond the point where $Q/Q_{\max} \sim 0.1$, the approximating curve is accurate to 20 percent and better, and ten percent accuracy is achieved at the point where $Q/Q_{\max} \sim 0.5$.

The less than complete success of the constant-Biot-number approximating curve is due to the fact that the thermal resistance of the tube flow (i.e., the tube-side resistance) is not included in the averaging process used to determine the candidate constant Bi (see equation (15)). The omission of such thermal resistances was intentional in that such information would not be known in the absence of detailed solutions of the finned-tube problem. Rather, a candidate constant Biot number was sought which is based only on a priori known information, as in equation (15).

Attention may now be turned to Fig. 3 (i.e., to case 2), the Biot number values for which are greater than those of Fig. 2 by a factor of five. Inspection of Fig. 3 shows that finning gives rise to only modest enhancement in this case. This is because in the presence of relatively high external heat transfer coefficients, the thermal resistance of the tube flow tends to play an important role. In particular, the effect of a decrease in external resistance, as occurs when fins are employed, is muted by the relatively large tube-side resistance. If the Biot number of the unfinned tube were very high, then finning would have essentially no effect on the heat transfer. As before, Fig. 3 also shows that the greatest enhancement occurs for relatively short tubes; the enhancement is about 40 percent when $Q/Q_{\max} \sim 0.1$ and 15 percent when $Q/Q_{\max} \sim 0.5$.

The candidate constant-Biot-number approximation, which corresponds to $\mathrm{Bi} = 265/4$, yields results whose accuracy is similar to that in evidence in Fig. 2. For Biot numbers much larger than those of Fig. 3, it is expected that all three curves would be nearly coincident and would approximate that for uniform wall temperature.

As a study in contrasts with respect to Fig. 3, the results for case 6 are presented in Fig. 4. Case 6 corresponds to a relatively low value of Bi_1, so that the external resistance controls the rate of heat transfer. Therefore, the diminution of the external resistance which occurs when fins are employed should have a significant effect on the heat transfer, and that this is so can be verified by examination of Fig. 4. Heat transfer enhancement by an order of magnitude is in evidence in the figure.

The figure also shows that the constant-Biot-number approximating curve ($\mathrm{Bi} = 5.3/4$) yields results of very high accuracy in this case. This is because the omission of the tube-side resistance in the evaluation of the candidate constant Bi value (equation (15)) ceases to be an approximation when the tube-side resistance is small. Thus, the constant Biot number model serves as an altogether satisfactory means of obtaining heat transfer results for periodically varying Bi, when Bi is small.

Although the foregoing findings were obtained for laminar tube flows, they suggest expectations for turbulent tube flows. In general, because of the higher heat transfer coefficients, the tubeside resistance of a turbulent flow is substantially lower than that of a corresponding (same fluid, same tube diameter) laminar flow. Therefore, in the case of a turbulent tube flow, the likelihood that the external resistance controls the heat transfer is greater than that for a laminar tube flow. Consequently, the characteristics in evidence in Fig. 4 should be applicable to turbulent tube flows, namely, substantial enhancement due to finning and accurate predictions of finned-tube heat transfer by a constant Biot number model.

A further exploration of the effect of Biot number can be made by examining Fig. 5, where results are shown for case 3. To place these results in perspective, they may be compared with those for case 1 (Fig. 2). The specified conditions (Table 1) for the two cases differ only in that $\mathrm{Bi}_2/\mathrm{Bi}_1 = 50$ for case 1 while $\mathrm{Bi}_2/\mathrm{Bi}_1 = 20$ for case 3, with Bi_1 being the same; the geometrical parameters are also the same. For these conditions, it is reasonable to expect that in case 3 the heat transfer enhancement due to finning will be less than that in case 1. On the other hand, since Bi_1 and Bi_2 are less different in case 3 than in case 1, a constant Biot approximation is expected to be more accurate for the former than for the latter.

These expectations may be appraised by examining and comparing Figs. 5 and 2. From the comparison, it is seen that both expectations are qualitatively fulfilled, but certain clarifying comments are in order. The first is that the degree of heat transfer enhancement is only modestly reduced as $\mathrm{Bi}_2/\mathrm{Bi}_1$ is decreased from 50 to 20 (the ratio of Q_{finned} to Q_{unfinned} is reduced by 10 to 15 percent). This insensitivity can be attributed to the control exercised by the tube-side resistance when Bi_2 becomes large. The second observation is that the constant-Biot-number approximating curve for case 3 is accurate to 15 percent and better for $Q/Q_{\max} \geq 0.1$.

Attention may next be turned to geometry effects. It was already shown in Fig. 2 (cases 1 and 5) that the period of the streamwise variation plays a minor role as long as the actual amount of finned and unfinned surface remains the same. Another geometrical issue is considered in Fig. 6, where results for case 4 are presented. For this case, the interfin spacing is seven times the fin thickness, in contrast to case 1 where the spacing is three times the thickness. The Biot numbers Bi_1 and Bi_2 are the same in both cases.

Comparison of Figs. 2 and 6 shows that the greater interfin spacing and the consequent decrease in the amount of tube surface that is finned diminishes the enhancement due to finning. Thus, the ratio of Q_{finned} to Q_{unfinned} for case 4 is 15 to 25 percent lower than for case 1. Notwithstanding this, enhancements on the order of a factor of two are in evidence in Fig. 6. The accuracy of the constant-Biot-number approximating curve for case 4 is not very satisfactory, the error being about 40 percent at $Q/Q_{\max} \sim 0.1$. Thus, when the interfin spacing is relatively large, the linear surface area weighting of Bi_1 and Bi_2, as employed in equation (15), tends to give too much weight to the fin (i.e., to Bi_2).

The main findings obtained from Figs. 2 to 6 will be reassembled in the Concluding Remarks section at the end of the paper.

Comparisons among Finned-Tube Results. The presentation and discussion of the previous section was focused on establishing relationships between finned-tube and unfinned-tube heat transfer results. Attention is now focused on comparisons among the finned-tube results themselves.

Biot number effects for a fixed geometry are shown in Figs. 7 and 8. In Fig. 7, the geometry is defined by a dimensionless fin thickness τ of 10^{-4} and a dimensionless spacing $\sigma = 3\tau$. For Fig. 8, $\tau = 0.5 \times 10^{-4}$ and $\sigma = 3\tau$.

For the discussion of Fig. 7, it is convenient to regard case 1 as a baseline case. Compared with case 1, the higher Biot numbers of case 2 (higher by a factor of five) lead to modest increases in heat transfer—about 30 percent for $Q/Q_{\max} \sim 0.1$ and about ten percent for $Q/Q_{\max} \sim 0.5$. Similarly, the reduction of Bi_2 from 50 to 20 (case 1 to case 3) causes only a moderate heat transfer response. This lack of sensitivity may be rationalized by noting that all the Biot numbers that pertain to Fig. 7 are in the intermediate and high range, signalling the presence of a significant tube-side resistance. It is the tube-side resistance that mutes the heat transfer response to changes in Biot number.

In contrast, Fig. 8 displays a substantial heat transfer response to Biot number changes.[2] This figure corresponds to the same extent of finned and unfinned surfaces as Fig. 7 but to a different period of the Biot number variation. The reason for the sensitivity evidenced in Fig. 8 is the relatively low value of Bi_1 for case 6. This low Bi_1 value means that the external resistance controls the heat transfer, so that changes of external resistance have a strong impact.

Changes in the geometrical aspects of the imposed periodic Bi variation are considered in Fig. 9. All cases appearing in this figure have the same Bi_1 and Bi_2 values. The results for cases 1 and 5 have already been interpreted as indicating that the heat transfer is not very sensitive to the period of the imposed Bi variation, provided that the extent of the finned and unfinned areas remain unchanged. The case with the shorter period, case 5, displays slightly higher rates of heat transfer. For case 4, compared with case 1, the extent of the finned surface is reduced by a factor of two. The heat transfer drops moderately—by 15 to 25 percent. At higher levels of Biot number, the reduction in fin coverage would have had a lesser effect, while a much greater effect would have been registered at low levels of Biot number.

Segment-Averaged Nusselt Numbers. Average heat transfer coefficients for the successive finned and unfinned portions of the tube were evaluated in accordance with equations (13) and (14). Representative results, corresponding to case 1, are presented in Fig. 10. In the figure, $\overline{\mathrm{Nu}}_1$ denotes the average Nusselt number for the unfinned

---

[2] The Biot number changes in Fig. 8 are not quite the same as those of Fig. 7, but this does not affect the essential trends.

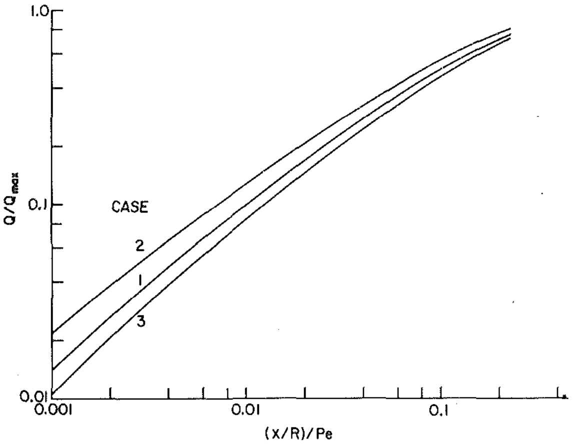

Fig. 7 Comparisons among heat transfer results for axially periodic Biot number; fixed geometry cases 1, 2, and 3

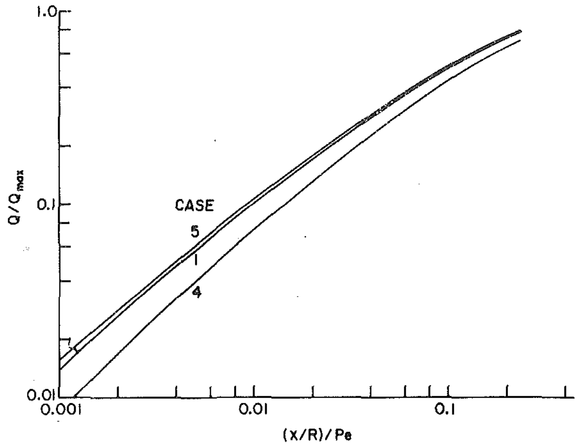

Fig. 9 Comparisons among heat transfer results for axially periodic Biot number; variable geometry cases 1, 4, and 5

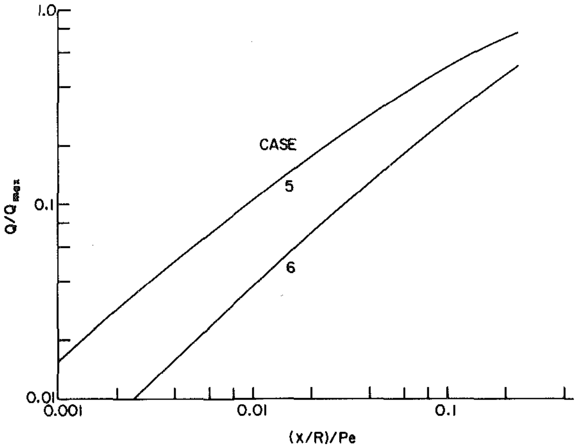

Fig. 8 Comparisons among heat transfer results for axially periodic Biot number; fixed geometry cases 5 and 6

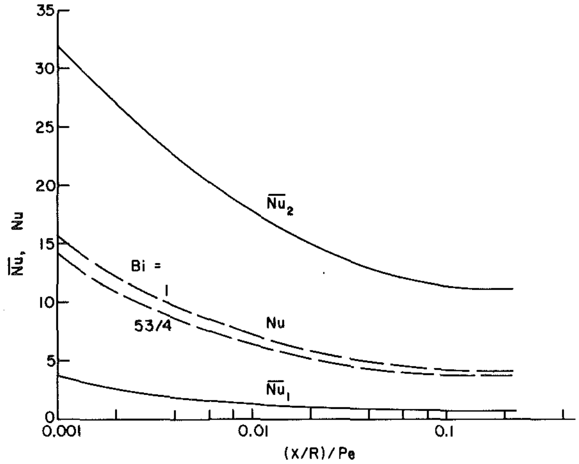

Fig. 10 Representative average heat transfer coefficients for successive finned and unfinned portions of the tube, case 1

segments of the tube and $\overline{\mathrm{Nu}}_2$ denotes the average Nusselt number for the finned segments. These values were plotted at the respective mid-points of the successive segments, and then the plotted points were interconnected with a smooth curve to provide continuity. Also shown in the figure, for reference purposes, are the local Nusselt numbers Nu for the unfinned tube for constant Biot numbers Bi = 1 and 53/4

The figure shows that the average Nusselt numbers for the finned portions of the tube are very much higher (by an order of magnitude) than those for the unfinned portions. Both $\overline{\mathrm{Nu}}_1$ and $\overline{\mathrm{Nu}}_2$ decrease with increasing downstream distance, and finally level off in the neighborhood of $(x/R)/\mathrm{Pe} \sim 0.1$. Thereafter, $\overline{\mathrm{Nu}}_1$ and $\overline{\mathrm{Nu}}_2$ are constant, thereby signalling the attainment of the periodic thermally developed regime as discussed in the Introduction.

The Nu versus x distributions for the constant Biot number cases Bi = 1 and 53/4 lie between the $\overline{\mathrm{Nu}}_1$ and $\overline{\mathrm{Nu}}_2$ curves, but no clear relationship is apparent. The fact that $\overline{\mathrm{Nu}}_2$ is much higher than the constant-Biot-number Nusselt number is the result of the substantially higher heat transfer rates at the finned sections. These same high heat transfer rates are responsible for the low values of $\overline{\mathrm{Nu}}_1$, since the fluid arriving at an unfinned section has, in effect, been highly preheated (or precooled).

It is uncertain how information about $\overline{\mathrm{Nu}}_1$ and $\overline{\mathrm{Nu}}_2$, if available, might be useful in practical design calculations. For this reason, the axial distributions of $\overline{\mathrm{Nu}}_1$ and $\overline{\mathrm{Nu}}_2$ are not presented here for the other cases. However, for completeness, the fully developed values are listed in Table 2.

Concluding Remarks

The main findings which have emerged from the presentation of results will now be brought together. It was found that heat transfer enhancement due to external finning is greatest for short tubes and diminishes as the tube length increases. Enhancements in the range of two to four times the unfinned-tube heat transfer were typically encountered.

When the Biot number of the unfinned tube is relatively high, only modest heat transfer enhancement due to finning occurs. On the other hand, for low values of the unfinned-tube Biot number, there are great possibilities for enhancement. The degree of enhancement is little affected by a change in the period of the Biot number variation when the proportions of finned and unfinned surfaces are maintained for fixed values of Bi_1 and Bi_2. If the interfin spacing is increased (resulting in a decrease in the finned surface), the enhancement decreases, with the extent of the decrease being affected by the Biot number.

With a view to finding a means of circumventing the lengthy calculations for the periodic Biot number case, a constant Biot number solution which gives comparable heat transfer results was sought. In order that such an approach be useful for design, the constant Biot number was based on a priori known information—Bi_1, Bi_2, fin thickness and interfin spacing (see equation (15)). The constant-Biot-number approximating curve was found to generally overestimate the finned-tube heat transfer, with the largest deviations near the inlet and lesser deviations at larger downstream distances. Typical deviations are 20 to 25 percent at $Q/Q_{\max} \sim 0.1$ and ten percent at

Table 2 Fully developed Nusselt numbers

Case	$\overline{\mathrm{Nu}}_1$	$\overline{\mathrm{Nu}}_2$
1	0.7536	11.23
2	1.770	8.839
3	1.074	10.82
4	1.336	16.51
5	0.6553	11.75
6	0.3657	13.32

$Q/Q_{\max} \sim 0.5$. For small Biot numbers, the constant Bi approximation is an excellent representation of the heat transfer results for periodic Biot number. When the Biot number is large, both the constant-Biot-number and periodic-Biot-number results tend to merge with those for uniform wall temperature.

The quality of the constant-Biot-number approximation is about the same for finned tubes of different Biot-number periods, provided that the fin coverage and the Biot number level are maintained. However, an increase in the interfin spacing degrades the quality of the approximation.

Although the analysis and results are for laminar tube flow, certain conclusions can also be drawn for turbulent flows in externally finned tubes. In general, the tube-side (i.e., internal) thermal resistance of a turbulent tube flow is substantially smaller than that of a laminar tube flow. Therefore, the external resistance will play a more decisive role in the former than in the latter. On this basis, it may be expected that external finning will be even more effective for a turbulent tube flow than for laminar tube flow. Furthermore, the present results for low-Biot-number laminar flows suggest that the heat transfer to an externally finned turbulent flow can be well approximated by that of a constant-Biot-number model.

As was noted in the Introduction, the model used here for the external heat transfer coefficient represents a limiting case. Depending on the tube wall thickness and thermal conductivity, axial heat conduction in the wall will tend to smear out the abruptness of the changes between h_1 and h_2. To determine the extent of such smearing would necessitate that the conduction problem for the tube wall and the fin be solved simultaneously with that for convection in the flowing fluid. In addition to the generally enlarged scope of the computations, the solution of such a coupled problem would have a different numerical character from that of the convective heat transfer problem that has been solved in this paper.

The present solution is a marching solution (starting at $x = 0$ and marching to larger x), so that the solution at any given axial station is unaffected by happenings at larger x. On the other hand, in the coupled problem, axial conduction in the wall tends to carry information upstream as well as downstream, with the result that the solution at a given axial station is affected by happenings at larger x. As a consequence, a marching-type solution is precluded and, instead, the entire field (i.e., all axial stations) has to be solved simultaneously. Such a numerical solution, while possible in principle, is extremely demanding in computer time and storage. Its demands are well beyond the computational capabilities available to the authors.

Acknowledgment

The research reported here was performed under the auspices of the Office of Naval Research (contract no. N00014-79-C-0621).

References

1 Patankar, S. V., Liu, C. H., and Sparrow, E. M., "The Periodic Thermally Developed Regime in Ducts with Streamwise Periodic Wall Temperature or Heat Flux," *International Journal of Heat and Mass Transfer,* Vol. 21, 1978, pp. 557–566.

2 Kays, W. M. , *Convective Heat and Mass Transfer,* McGraw-Hill, New York, 1966, pp. 104–106.

3 Patankar, S. V. and Spalding, D. B., *Heat and Mass Transfer in Boundary Layers,* Intertext Books, London, 1970.

4 Hsu, C. J., "Exact Solution to Entry-Region Laminar Heat Transfer with Axial Conduction and the Boundary Condition of the Third Kind," *Chemical Engineering Science,* Vol. 23, 1968, pp. 457–468.

J. L. Woods
Department of Agricultural Engineering,
University of Newcastle upon Tyne,
Newcastle upon Tyne, England

W. D. Morris
Professor,
Department of Engineering Design
and Manufacture,
University of Hull, England

A Study of Heat Transfer in a Rotating Cylindrical Tube

The paper reports the results of a numerical solution for laminar fluid flow and heat transfer in the developed region of a tube rotating about a parallel axis. The results cover a wide range of Prandtl number and the eccentricity and Coriolis effects are included in the solution. By transforming the variables in the governing equations, it is shown that the Rayleigh and Reynolds numbers only occur as the product Ra Re, and at large Prandtl number an asymptotic solution is defined by the product Ra Re Pr and the eccentricity alone. The numerical solution of the full governing equations confirms this and indicates that for sufficiently large radius of rotation Nu = f(Ra Re Pr) is a good approximation over a wide range of Prandtl number. The Fanning friction factor is better described by Gr Re. The solution is compared with other analyses and experimental data for air, water, and glycerol.

Introduction

Fluid which is constrained to flow in a rotating duct is influenced by inertial effects which can significantly alter the flow field in relation to the stationary duct situation. If the duct wall is heated, the convective mechanism, which controls energy transfer to the fluid, is also interactively influenced by the rotation and it is with this effect that the present paper is mainly concerned. In addition to their intrinsic academic interest, this class of rotating flow problems is particularly important in the design of certain energy conversion machines where it is often necessary to cool components which are rotating in a hostile thermal environment in order to maintain a commercially acceptable machine life.

The investigation considers the effect of buoyancy on laminar flow and heat transfer in the developed region of a uniformly heated circular tube, rotating about on axis parallel to itself. At large radii of rotation, the phenomenon is analogous to gravitational buoyancy in a uniformly heated horizontal tube. The solution therefore presents a correction to the Nusselt solution for the case of the horizontal tube.

The first theoretical solutions to the problem were presented by Morton [1] and Morris [2]. They used a perturbation technique to solve the governing equations and their solutions were valid for weak secondary flows. With the aid of experimental observations on the horizontal tube using air, Mori and Nakayama [3] developed a solution for strong secondary flows. The solution was based on the division of the flow and temperature fields into a central core region and a boundary layer region along the wall. Their solution at low Prandtl number was confirmed by Woods and Morris [4] but at high Prandtl number their assumptions on the flow and temperature fields break down. Siegworth, et al. [5] generated a solution for a Prandtl number approaching infinity, demonstrating that the axial velocity profile remains in its parabolic form in this situation and does not display a core and boundary layer region structure.

This paper presents a numerical solution of the problem which requires no assumptions as to the structure of the flow and temperature fields to simplify the governing equations. The solution is therefore able to span the full range of Prandtl numbers between the solutions of Mori and Nakayama and Seigworth, et al. In order to simplify the problem for ease of solution, the additional effects of eccentricity and Coriolis terms have been largely ignored to date. The numerical solutions examines these effects.

Experimental heat transfer data is available for a wide range of Prandtl number. Results are available for air in the horizontal tube and air, water and glycerol in the rotating tube. The data are converted to a common notation and compared with the numerical and other solutions. This is designed to coordinate information available in this field.

Formulation of the Equations

Consider steady laminar flow in a cylindrical tube of radius, a, rotating with uniform angular velocity, Ω about an axis parallel to the central axis of the tube and displaced a distance, H, from it. The motion of the fluid is referred to the cylindrical polar frame, r, θ, z, which is fixed relative to the tube. The velocities in these respective directions are u, v and w. The angular co-ordinate is defined as positive in the direction of rotation and the axial co-ordinate as positive in the direction of flow.

The following assumptions are made in order to make the problem more amenable to analysis. All properties of the fluid are taken to be uniform with the exception of density in its interaction with the rotational acceleration terms. The density is assumed to vary linearly with temperature via the usual volume expansion coefficient, β. The flow is studied far enough downstream for entry effects to be absent. The tube wall is considered of sufficiently high conductivity for there to be no circumferential temperature variation at the wall. Under these circumstances a similarity solution exists. As the temperature at all locations in the developed region is increasing linearly, the temperature relative to the local wall value is independent of axial location.

The assumptions of linear density variation in the buoyancy terms and all other fluid properties constant render the theory more valid as the temperature range decreases. Therefore strong secondary flow effects, due to large values of the terms, Ω, H, a and β rather than large temperature gradients are better described by the theory.

Details of the formulation of the governing equations in the general form presented here have been presented by Morton [1], Morris [2] and Woods and Morris [4]. These equations are therefore presented in their final dimensionless form. The axial momentum and vorticity transport equations become

$$\nabla^2 W + \frac{1}{x}\frac{\partial(\psi, W)}{\partial(x, \theta)} + 4\,\mathrm{Re}_p = 0 \tag{1}$$

and

$$\nabla^2 \xi + \frac{1}{x}\frac{\partial(\psi, \xi)}{\partial(x, \theta)} - \mathrm{Ra}\left(\frac{1}{\mathrm{x}}\frac{\partial \eta}{\partial \theta}\cos\theta + \frac{\partial \eta}{\partial x}\sin\theta + \epsilon\frac{\partial \eta}{\partial \theta} - \frac{\epsilon}{J}\frac{1}{x}\frac{\partial(\psi, \eta)}{\partial(x, \theta)}\right) = 0, \tag{2}$$

the stream function and vorticity are related by the equation,

$$\nabla^2 \psi + \xi = 0 \tag{3}$$

and the energy equation becomes

$$\nabla^2 \eta + \frac{\mathrm{Pr}}{x}\frac{\partial(\psi, \nu)}{\partial(x, \theta)} + W = 0, \tag{4}$$

where

$$\frac{\partial(\psi\ )}{\partial(x, \theta)} = \frac{\partial \psi}{\partial x}\frac{\partial}{\partial \theta} - \frac{\partial \psi}{\partial \theta}\frac{\partial}{\partial x},$$

Contributed by the Heat Transfer Division for publication in the JOURNAL OF HEAT TRANSFER. Manuscript received by the Heat Transfer Division September 11, 1978.

$$\nabla^2 = \frac{1}{x}\frac{\partial}{\partial x}\left(x\frac{\partial}{\partial x}\right) + \frac{1}{x^2}\frac{\partial^2}{\partial\theta^2}.$$

The nondimensional stream function, ψ is defined

$$\frac{\partial\psi}{\partial r} = \frac{v}{\nu}, \frac{\partial\psi}{\partial\theta} = \frac{-ru}{\nu} \tag{5}$$

and the dimensionless axial pressure gradient, Re_p is written in the form

$$\mathrm{Re}_p = -\frac{a^3}{4\nu^2\rho}\frac{\partial p}{\partial z}, \tag{6}$$

so that for the nonrotational case it becomes equal to the mean flow Reynolds number. The remaining variables are defined in the Nomenclature. The boundary conditions at the tube wall can be written

$$\frac{\partial\psi}{\partial x} = \frac{\partial\psi}{\partial\theta} = W = \eta = 0 \tag{7}$$

Properties of the Equations

It would appear at first sight that it is necessary to specify the five parameters Ra, Re_p, Pr, ϵ and J in order to define a particular solution for the flow and temperature fields. However these five parameters may be reduced to four by means of the following transformations. Let

$$\psi' = \mathrm{Pr}\,\psi,\ \xi' = \mathrm{Pr}\,\xi,\ \eta = \eta/\mathrm{Re}_p,\ W' = W/\mathrm{Re}_p$$

which, on substitution into equations (1–4) gives

$$\nabla^2 W' + \frac{1}{\mathrm{Pr}}\frac{1}{x}\frac{\partial(\psi', W')}{\partial(x,\theta)} + 4 = 0 \tag{8}$$

$$\begin{aligned}\nabla^2\xi' &+ \frac{1}{\mathrm{Pr}}\frac{1}{\mathrm{x}}\frac{\partial(\psi',\xi')}{\partial(x,\theta)} \\ &- \mathrm{Ra}\,\mathrm{Re}_p\,\mathrm{Pr}\left(\frac{1}{x}\frac{\partial\eta'}{\partial\theta}\cos\theta + \frac{\partial\eta'}{\partial x}\sin\theta\right. \\ &\left. + \epsilon\frac{\partial\eta'}{\partial\theta} - \frac{\epsilon}{\mathrm{Pr}\,J}\frac{1}{\mathrm{x}}\frac{\partial(\psi',\eta')}{\partial(x,\theta)}\right) = 0\end{aligned} \tag{9}$$

$$\nabla^2\psi' + \xi' = 0 \tag{10}$$

$$\nabla^2\eta' + \frac{1}{x}\frac{\partial(\psi',\eta')}{\partial(x,\theta)} + W' = 0 \tag{11}$$

This formulation indicates that the Rayleigh number and pseudo-Reynolds number do not occur independently, but only in a product form. Thus it is only necessary to specify the four parameters Ra Re_p, Pr, ϵ and J to describe the flow and related temperature field.

A further interesting features emerges by examining the influence of Prandtl number. As the Pradtl number becomes large, equations (8) and (9) approach the assymptotic form

$$\nabla^2 W' + 4 = 0 \tag{12}$$

$$\nabla^2\xi' - \mathrm{Ra}\,\mathrm{Re}_p\,\mathrm{Pr}\left(\frac{1}{x}\frac{\partial\eta'}{\partial\theta}\cos\theta + \frac{\partial\eta'}{\partial x}\sin\theta + \epsilon\frac{\partial\eta'}{\partial\theta}\right) = 0 \tag{13}$$

whereas equations (10) and (11) remain as before. We see immediately from equation (12) that rotation does not influence the axial velocity field in the limiting case of large Prandtl number fluids, so that the axial velocity retains the parabolic form associated with Poiseuille flow. Therefore rotation does not affect flow resistance with fluids of high Prandtl number. For this limiting case equation (13) also demonstrates that only two parameters are necessary to describe the solution, namely the product Ra Re_p Pr and the eccentricity, ϵ. It is interesting to note that the Coriolis terms are no longer significant.

Equations (1–4) are elliptic and may be solved numerically using the generalised procedure proposed by Gosman, et al. [6]. The application of this solution procedure to the present problem and the detailed manipulation required are given by Woods and Morris [4] and Woods [7]. In principle the partial differential equations are replaced by an approximate set of nonlinear algebraic equations which are subsequently solved using an iterative procedure. Care was necessary in using the procedure to ensure convergence of the solution and in this respect criteria presented by Varga [8] for the iterative solution of a set of linear algebraic equations proved satisfactory guidelines.

When the numerical solution had converged to an acceptable level of accuracy, the usual pipe flow Reynolds number, Re, the Fanning friction factor f, and the Nusselt number, Nu, were determined by numerical integration of the axial velocity and temperature fields according to the definitions cited below.

$$\mathrm{Re} = \frac{2}{\pi}\int_0^{2\pi}\int_0^1 Wx\,dx\,d\theta \tag{14}$$

$$f = \frac{16\mathrm{Re}_p}{\mathrm{Re}} \tag{15}$$

$$\mathrm{Nu} = \frac{\mathrm{Re}}{2}\,\frac{\displaystyle\int_0^{2\pi}\left.\frac{\partial\eta}{\partial x}\right|_{x\,=\,1} d\theta}{\displaystyle\int_0^{2\pi}\int_0^1 W\eta\,x\,dx\,d\theta} \tag{16}$$

Results and Discussion

The Analogous Horizontal Tube. In this analysis, the horizontal tube situation is simulated by putting ϵ, the ratio of tube radius to radius of rotation, equal to zero. The results of the numerical solution for this case are presented in Fig. 1. These results are based on the solution of the full governing equations (1–4). However, in the light of the preceding analysis that indicated an asymptotic solution at high Prandtl number, the results are plotted against the parameter, Ra Re Pr. The results confirm the existence of the asymptotic solution. It is interesting to note that the asymptotic solution is a good approximation over a wide range of Prandtl number.

As for the asymptotic solution, Siegworth, et al.'s analysis for large

Nomenclature

a = tube radius
f = friction factor, equation (15)
H = eccentricity
J = rotational Reynolds number, $\Omega a^2/2\nu$
Nu = Nusselt number, equation (16)
p = pressure
Pr = Prandtl number
r = radial co-ordinate
Ra = rotational Rayleigh number, $H\Omega^2\beta\tau a^4/\alpha\nu$
Re = through flow Reynolds number, $2w_m a/\nu$
Re_p = Reynolds number based on gradient of p, equation (6)
t = time
T = temperature
u = radial velocity component
v = tangential velocity component
w = axial velocity component
W = nondimensional axial velocity component, wa/ν
x = nondimensional radial co-ordinate r/a
z = axial co-ordinate
Ω = angular velocity component
ρ = density
ξ = axial vorticity component, $-\nabla^2\psi$
β = expansion coefficient
ν = kinematic viscosity
θ = angular co-ordinate
ψ = nondimensional stream function, equations (5)
ν = nondimensional temperature, $(T_w - T)/\tau a$ Pr
ϵ = eccentricity parameter, a/H
τ = axial temperature gradient
α = thermal diffusivity

Subscripts

c = tube center line value
m = mean value
w = wall condition
0 = nonrotating condition

Superscript

′ = transformed variables

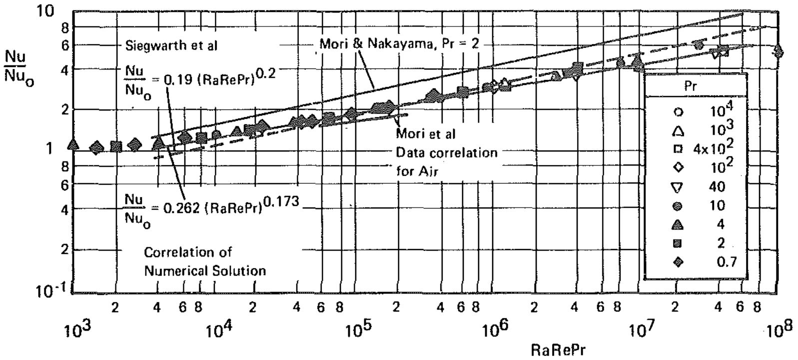

Fig. 1 The numerical solution for Nusselt number, $\epsilon = 0$

Prandtl number eliminated the terms convecting momentum from the governing equations by means of dimensional reasoning and experimental observation. Their integral method solution can be written

$$\frac{\mathrm{Nu}}{\mathrm{Nu}_0} = 0.19\,(\mathrm{Ra\,Re\,Pr})^{0.2} \tag{17}$$

This is in good agreement with the results presented here. Correlating the numerical solution gives the modified equation

$$\frac{\mathrm{Nu}}{\mathrm{Nu}_0} = 0.262\,(\mathrm{Ra\,Re\,Pr})^{0.173} \tag{18}$$

over the range

$$4 \times 10^3 \leqslant \mathrm{Ra\,Re\,Pr} \leqslant 10^8$$
$$0.7 \leqslant \quad \mathrm{Pr} \quad \leqslant 10^4$$

It should be noted that this is merely a convenient approximation over that particular range. As can be seen from Fig. 1, the numerical solution also describes the weak secondary flow behavior as the solution approaches the Nusselt value, Nu_0. In addition, there is some variation with Pr as well as with Ra Re Pr and the numerical solution predicts this.

Mori and Nakayama's solution for a Prandtl number of 0.7 can be written

$$\frac{\mathrm{Nu}}{\mathrm{Nu}_0} = 0.182\,(\mathrm{Ra\,Re\,Pr})^{0.2} \tag{19}$$

This is in surprisingly good agreement with the high Prandtl number solutions, considering the difference in assumptions. On the scale of Fig. 1, equation (19) can be considered coincident with Siegworth, et al.'s solution. At a Prandtl number of 2 the solutions do not agree due to the breakdown in the assumption of a core and boundary layer distribution for axial velocity at increasing Prandtl number. Again in Fig. 1, the solution is compared with the heat transfer data of Mori et al for air in the developed region of a horizontal tube. The agreement is good and indicates that the assumptions necessary for the analysis do not invalidate application. Mori, et al. also measured the temperature and axial velocity distributions across the vertical and horizontal tube diameters. These are compared with the numerical solution in Fig. 2 and confirm the results.

In Fig. 3 the results for flow resistance are presented. The parameter Gr Re is found to be more effective in collapsing the data than Ra Re. Therefore at a given Ra Re value increasing Pr decreases the buoyancy effect and f approaches f_0 as predicted by the asymptotic solution. The comparison with Mori and Nakayama confirms their solution at low Prandtl numbers and for strong secondary flows.

Eccentricity and Coriolis Effects. The effect of eccentricity on the temperature and flow fields is illustrated in Fig. 4. Coriolis terms are eliminated by setting $J = 10^9$. When $\epsilon = 10$ the tube is rotating at a radius of one tenth the tube radius. Although the temperature and flow fields are considerably modified relative to the $\epsilon = 0$ distributions (4), the effect on the overall parameters, Nu and f is not great, as shown in Fig. 5. Even at ϵ, values approaching unity the effect is not dramatic.

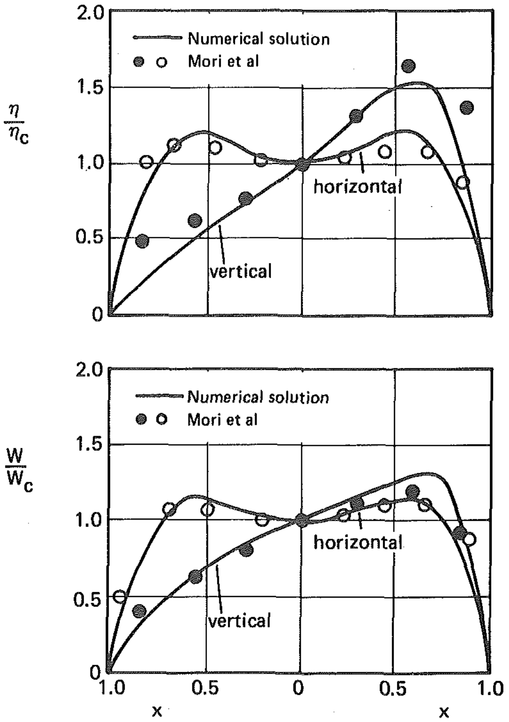

Fig. 2 A comparison between the numerical solution and the axial velocity and temperature distributions measured by Mori, et al. [9] on a horizontal heated tube (horizontal diameter, Re = 2850, Ra = 56.8, Pr = 0.7 and vertical diameter, Re = 2700, Ra = 49.7, Pr = 0.7)

The Coriolis terms cause the temperature and flow fields to become asymmetric. This is illustrated in Fig. 6. The Coriolis term, Ra $\epsilon^{J/x}$ $\partial(\psi, \eta)/\partial(x, \theta)$ in equation (2) indicates that the effect increases as ϵ increases and as J decreases for a given Rayleigh number. This effect of rotational Reynolds number on Nu and f is shown in Fig. 7. Mori and Nakayama's analysis predicts the opposite, that the Coriolis effect increases with increasing J. Their analysis is based on the secondary flow interacting with rotation directly. In the formulation of the equations presented here direct interaction does not appear. Coriolis terms not including the temperature effect form a conservative field and do not effect the flow pattern. It is the interaction of the Coriolis accelerations and temperature field that modifies the flow.

Comparison with Rotating Tube Data. The sources of the data are Morris [2], Woods [7] and Sakamoto and Fukui [11]. Table 1 indicates the range of variables and fluids studied.

One of the results which emerged from the theoretical analysis described earlier was the fact that the high Prandtl number solution could be extended with good approximation to include gas-type flows. It is convenient therefore to compare the experimentally determined heat transfer results with the product Ra Re Pr as shown in Fig. 8. In this figure the increase in developed region Nusselt number is shown

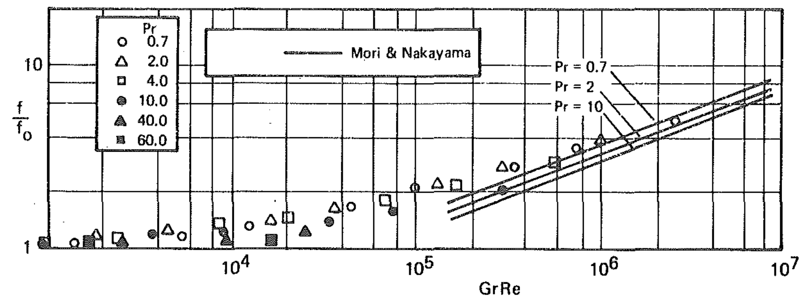

Fig. 3 The numerical solution for the friction coefficient, $\epsilon = 0$

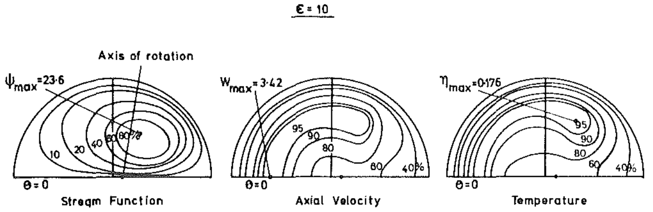

Fig. 4 Velocity and temperature distributions as predicted by the numerical solution illustrating the eccentricity effect ($RaRe_p = 10^6$, $Pr = 2$, $J = 10^9$)

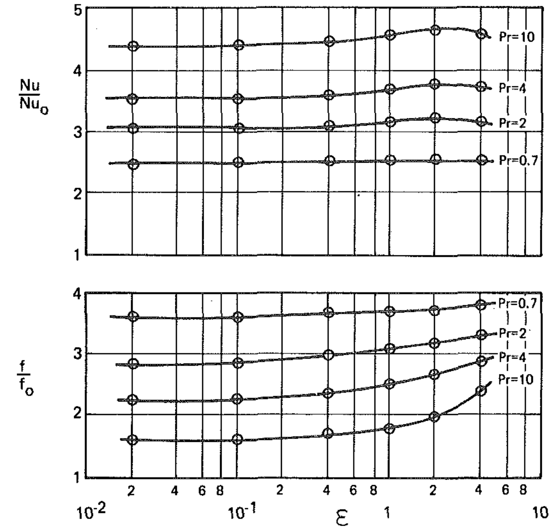

Fig. 5 The effect of eccentricity on the numerical solution for bulk Nusselt number and friction coefficient ($RaRe_p = 10^6$, $J = 10^9$)

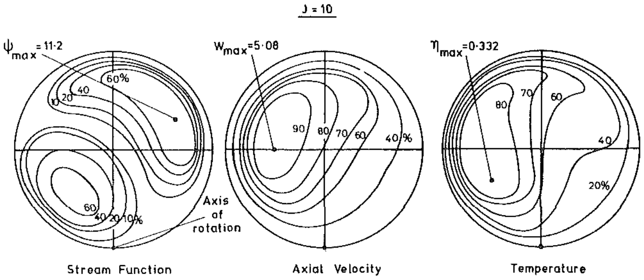

Fig. 6 Velocity and temperature distribution as predicted by the numerical solution illustrating the Coriolis effect ($RaRe_p = 10^6$, $Pr = 2$, $\epsilon = 1$)

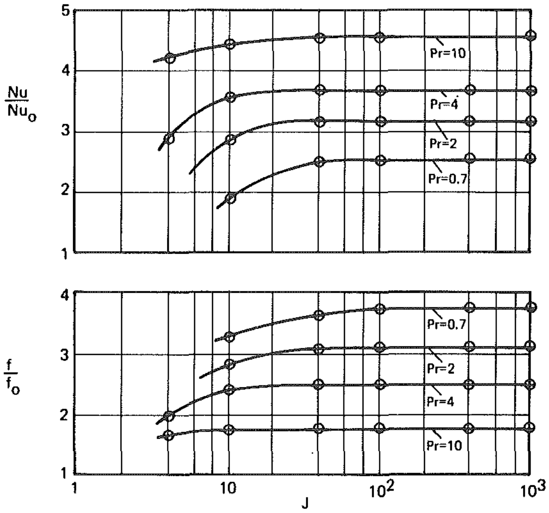

Fig. 7 The effect of coriolis accelerations on the numerical solution for bulk Nusselt number and friction coefficient ($RaRe_p = 10^6$, $\epsilon = 1$)

Table 1 Sources of experimental data

Source	Fluid	Length/diameter ratio of test section	Eccentricity Parameter (ϵ)	Ra Re range
Morris [10]	Water	48	0.021	$10^3 - 6 \times 10^6$
Morris [10]	100 percent Glycerol	48	0.021	$2 \times 10^{-1} - 4 \times 10^2$
Woods [4]	Air	48	0.021	$10^4 - 6 \times 10^6$
		96	0.011	$10^4 - 6 \times 10^6$
Sakamoto and Fukui [11]	Air	20–24	0.05	$0 - 1.6 \times 10^8$

for all three fluids for which experimental data are available. Also shown is the high Prandtl number solution resulting from the present analysis for $\epsilon = 0$. This eccentricity value was selected for the theoretical comparison since as demonstrated earlier, the range of eccentricities used for the experiments was unlikely to have a significant effect.

The scatter of the data indicates the problem of entry region effects in rotational work where long heated sections and settling lengths are not easily constructed. The data do, however, form an envelope around the solution. It is interesting to note that the low Reynolds number glycerol data, which would exhibit the shortest entry region, appear to follow the data closest.

The asymmetric temperature profile produced as a consequence of rotation results in a corresponding circumferential variation in local heat flux at the wall of the tube. Sakamoto and Fukui [11] assessed this circumferential variation of flux using the well known analogy between heat and mass transfer. These authors measured the rate of naphthalene transfer from a coated inner tube wall for a variety of

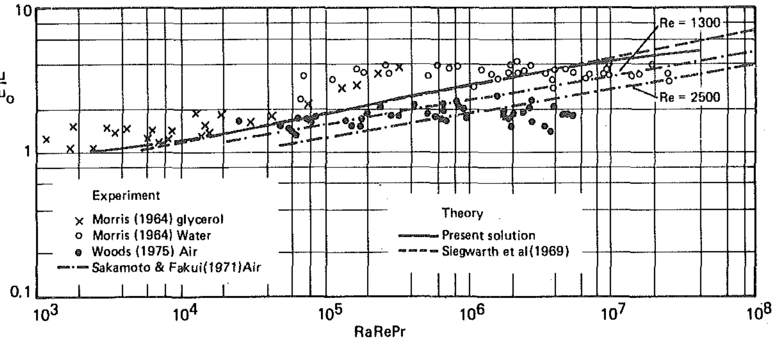

Fig. 8 Comparison between theoretical and experimental data

rotational conditions. Figure 9 shows, for a typical set of operating conditions, the variation of mass transfer detected. For convenience the ordinate in Fig. 9 is the normalized flux compared to maximum value which occurs at the outermost radial location. Also shown in Fig. 9, for the same conditions at which the experimental data were taken, is the variation of heat flux predicted from the present solution technique. The agreement is good with exactly the same pattern of behavior being shown.

Conclusions

The use of a numerical technique has enabled a more general solution of the equations than was previously possible. Simplifying assumptions for the flow and temperature fields are not required as the fields are predicted. This has enabled a wide range of Prandtl number to be explored and the eccentricity and Coriolis effects to be incorporated.

By transforming the variables it has been demonstrated that the Rayleigh and Reynolds numbers do not occur independently but as a product, Ra Re. In addition, at sufficiently large Prandtl number an asymptotic solution is approached which is defined by only two variables, Ra Re Pr and ϵ. This was confirmed by solving the full general equations for a given eccentricity ($\epsilon = 0$, the horizontal tube) and a range of Prandtl number. This demonstrated that $Nu = f(\text{Ra Re Pr})$ not only at large Pr but at values as low as the gas range. This enabled a simplified correlation to be proposed which agrees well with Siegworth, et al.'s solution for Nusselt number at large Prandtl number.

At the gas end of the Prandtl number range, the numerical solution is in good agreement with Mori and Nakayama's solution for heat transfer and flow resistance. The comparison with the experimental data of Mori, et al. for air in a horizontal tube confirms the theoretical predictions for heat transfer and the internal flow and temperature fields.

The effects of eccentricity and Coriolis terms on the internal flow and temperature fields have been demonstrated. It is particularly useful to observe the structure of these fields theoretically, as to measure them experimentally would be difficult. Eccentricity has been shown not to have a great effect on heat transfer and flow resistance even when the radius of rotation approaches the tube radius. For a given Rayleigh number, the Coriolis effect increases with ϵ and decreases with J. This conflicts with Mori and Nakyama's solution. The values of J at which the effect becomes significant are far lower than would be anticipated in most applications.

The comparison with rotational data probably indicates the problem of entry effects as the tube is necessarily short for practical reasons. Although the results are assuring in that they form an envelope around the theoretical solution, the gravitational data make comparison easier.

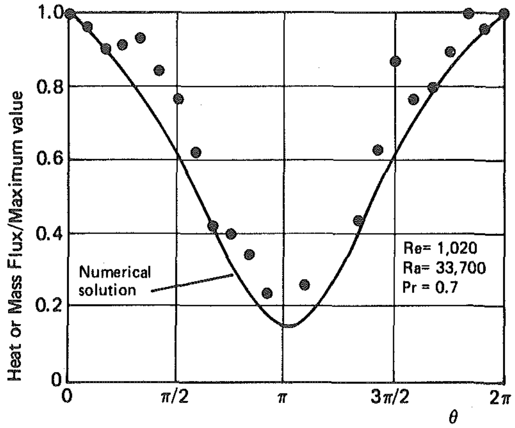

Fig. 9 A comparison between the numerical solution for the circumferential heat transfer distribution and results of Sakamoto and Fukui [11] for the sublimation of napthalene

References

1 Morton, B. R., "Laminar Convection in Uniformly Heated Horizontal Pipes at Low Rayleigh Number," *Quarterly Journal of Mechanics and Applied Mathematics*, Vol. 12, 1959, p. 410.

2 Morris, W. D., "Laminar Convection in a Heated Vertical Tube Rotating about a Parallel Axis," *Journal Fluid Mechanics*, Vol. 21, part 3, 1965, p. 453.

3 Mori, Y., and Nakayama, W., "Forced Convective Heat Transfer in a Straight Pipe Rotating about a Parallel Axis (1st Report, Laminar Region)," *International Journal of Heat Mass Transfer*, Vol. 11, 1967, p. 1179.

4 Woods, J. L., and Morris, W. D., "An Investigation of Laminar Flow in the Rotor Windings of Directly-Cooled Electrical Machines," *JMES* (*I Mech E.*)., Vol. 16, 6, p. 408.

5 Siegwarth, D. P., Mikesell, R. D., Readal, T. C., and Hanratty, T. J., "The Effect of Secondary Flow on the Temperature Field and Primary Flow in a Heated Horizontal Tube," *International Journal of Heat Mass Transfer*, Vol. 12, 1969, p. 1535.

6 Gosman, A. D., Pun, W. M., Runchal, A. K., Spalding, D. B., and Wolfshtein, M. W., "Heat and Mass Transfer in Recirculating Flows," Internal Publication, Thermo-Fluids Section, Imperial College of Science and Technology, SF/R/3, 1968.

7 Woods, J. L., "Heat Transfer and Flow Resistance in a Rotating Duct System," D. Phil. thesis, University of Sussex, 1976.

8 Varga, R. S., *Matrix Iterative Analysis*, Prentice-Hall International, London, 1962.

9 Mori, Y., Futagami, K., Tokuda, S., and Nakamara, M., "Forced Convective Heat Transfer in Uniformly Heated Horizontal Tubes," *International Journal of Heat Mass Transfer*, Vol. 9, 1966, p. 453.

10 Morris, N. D., "Heat Transfer Characteristics of a Rotating Thermosyphon," Ph.D thesis, Dept. of Mech. Eng., University of Wales (Swansea), 1964.

11 Sakamoto, M., and Fukui, S., "Convective Heat Transfer of a Rotating Tube Revolving about an Axis Parallel to Itself," Electric and Nuclear Engineering Laboratory, Tokyo Shibaura Electric Co. Ltd., Kawasaki, Japan, 1971.

M. A. I. El-Shaarawi
Lecturer.

A. Sarhan
Assistant Lecturer.

Mechanical Engineering Department,
Alazhar University,
Nasr City, Cairo, Egypt

Free Convection Effects on the Developing Laminar Flow in Vertical Concentric Annuli

Coupled energy and momentum boundary layer equations have been numerically solved for the problem of combined forced-free laminar convection in the entrance region of vertical concentric annuli. Both upflow and downflow of a fluid with Pr = 0.7 are considered under the thermal conditions of one wall being isothermal and the other adiabatic. Results for the development of velocity profiles, axial distance at which the axial velocity gradient normal to the wall vanishes, pressure drop, and heat transfer characteristics are presented at various values of the parameter Gr/Re ranged from −700 to 1500.

Introduction

In many engineering applications, heating usually starts at the duct entrance or at some point where the flow has not yet become hydrodynamically fully developed. However, few papers in the literature have dealt with the problem of combined forced-free laminar flow with simultaneously developing hydrodynamic and thermal boundary layers. Lawerence and Chato [1] obtained a numerical solution to the boundary-layer-type equations for the developing combined forced-free laminar flow in a vertical tube with a uniform velocity profile at the entrance and a constant wall heat flux. Zeldin and Schmidt [2] presented numerical results for the developing combined forced-free laminar flow in an isothermally heated vertical tube. Savakar [3] and Quintiere and Mueller [4] considered the developing mixed laminar flow between vertical parallel plates. The only published theoretical investigation handling the developing laminar flow with temperature-dependent physical properties in vertical concentric annuli seems to be that of Shumway and McEligot [5]. In their investigation, the thermal boundary conditions of constant heat flux at one wall, while the other wall is kept either adiabatic or isothermal at the inlet fluid temperature, were considered. They presented numerical results for the local Nusselt number and pressure drop in an annulus of 0.25 radius ratio and concluded that "the flow development dominates the uniform entry problem and the effects of property variation are less striking." The possibility of flow reversal at high heat transfer rates was not considered in their investigation and neither developing axial nor developing radial velocity profiles were presented.

The available experimental investigations for the determination of the convective heat transfer parameters, in the combined forced-free laminar flow regime, and/or the effect of superimposed natural convection on the stability of forced laminar flows are normally in tubes [1, 2, 6–13]. Very limited experimental data on combined forced-free convective heat transfer in vertical annuli are available in the literature [14, 15].

The lack of either theoretical or experimental data concerning the problem of combined forced-free laminar annular flow with simultaneously developing hydrodynamic and thermal boundary layers, and the practical importance of this problem in the field of nuclear reactors at periods of low power operation [11], motivated the present work. In the present study, combined forced-free laminar flow with a flat velocity profile at the entrance of concentric annuli has been investigated for two boundary conditions; namely, case (O) in which the outer wall is isothermal while the inner wall is adiabatic and case (I) in which the inner wall is isothermal while the outer wall is adiabatic.

Governing Equations and Method of Solution

Assuming steady, axisymmetric, laminar, boundary layer flow of a Newtonian fluid, with no internal heat generation, with constant physical properties except the density which only varies in the gravitational body force term according to the Boussinesq approximation, and neglecting viscous dissipation, compression work and axial conduction of heat, the dimensionless conservation equations of mass, momentum and energy in the entry region of a vertical annulus are respectively as follow

$$\frac{\partial U}{\partial Z}+\frac{\partial V}{\partial R}+\frac{V}{R}=0, \tag{1}$$

$$V\frac{\partial U}{\partial R}+U\frac{\partial U}{\partial Z}=-\frac{\partial P}{\partial Z}\pm\frac{\mathrm{Gr}}{\mathrm{Re}}\frac{T}{4(1-N)^2}+\frac{\partial^2 U}{\partial R^2}+\frac{1}{R}\frac{\partial U}{\partial R}, \tag{2}$$

$$V\frac{\partial T}{\partial R}+U\frac{\partial T}{\partial Z}=\frac{1}{\mathrm{Pr}}\left(\frac{\partial^2 T}{\partial R^2}+\frac{1}{R}\frac{\partial T}{\partial R}\right). \tag{3}$$

The plus and minus signs in the buoyancy term of equation (2) apply respectively to upward and downward flows, taking into account that the body force acts in the negative z-direction in case of an upward flow and vice versa in case of a downward flow.

Since the r-momentum equation has been eliminated due to the boundary layer simplifications, an additional equation becomes mathematically necessary and it is possible, under the linearization numerical technique of Bodoia and Osterle [16, 17], to compensate for the lack of such an equation by using the following dimensionless integral continuity equation

$$\int_N^1 RU\,dR=\frac{1}{2}(1-N^2) \tag{4}$$

Equations (1–3) are three equations in four unknowns, (U, V, P and T) subject to the following boundary conditions.

for $Z \geqslant 0$ and $R = N$, $U = V = 0$ and $\dfrac{\partial T}{\partial R} = 0$ for case (O) or $T = 1$ for case (I),

for $Z \geqslant 0$ and $R = 1$, $U = V = 0$ and $T = 1$ for case (O) or $\dfrac{\partial T}{\partial R} = 0$ for case (I),
for $Z = 0$ and $N < R < 1$, $U = 1$ and $T = 0$ (flat velocity and temperature profiles),
at $Z = 0$, $P = 0$. (5)

Equations (1–4), subject to the boundary conditions (5), have been numerically solved in [18] by means of the linearized implicit finite-difference scheme of Bodoia and Osterle [16]. This linearized numerical technique depends on the application of equations (2–4) at each cross section with the values of V, in equations (2) and (3), as known values taken from the previous axial step, i.e., equations (2–4) are considered three equations in three unknowns (U, P and T).

Contributed by the Heat Transfer Division for publication in the JOURNAL OF HEAT TRANSFER. Manuscript received by the Heat Transfer Division December 17, 1979.

Then, after numerically calculating U, P and T at each cross section, the correct values of V at the cross section are calculated by means of equation (1) with the known values of U.

Due to space limitations and since the main aim of this paper is to present results not available in the literature, the reader may refer to [18] for the details of the method of solution or may refer to [17] as the present finite-difference scheme is a direct extension to that scheme described in [17].

Range of Validity of the Boundary-Layer Flow Model

Since substantial radial momentum transfer is known to exist very near to the channel entrance, and since the boundary layer simplifications (which neglect all radial forces in comparison with the forces in the axial direction) are used in deriving the governing equations of the present flow model, one would expect the present numerical solutions to be applicable beyond a short distance from the annulus entrance. For developing flows in circular tubes, Worsoe-Schmidt and Leppert [19] estimated the order of magnitude of the neglected terms, due to the boundary layer assumptions, and concluded that the boundary layer model is indeed valid as long as $2z/D \text{ Re Pr} \geqslant 10^{-3}$. Transforming this restriction to the present nomenclature, we get $Z \geqslant 2 \times 10^{-3} (1 - N)^2 \text{Pr}$.

Wang and Longwell [29] obtained a solution for the complete governing equations in the entry region of parallel plate channels at a Reynolds number of 300. They concluded that both the overall pressure drop and the hydrodynamic development length predicted by the boundary layer methods are in reasonable agreement with their results. However, the boundary layer theory is not appropriate for obtaining the velocity profiles and the pressure gradients near the channel entrance.

Considering the results of [29], calculated for Re = 300 with the more realistic boundary condition of $U = 1$ at $z = -\infty$, the velocity gradient at the wall shows agreement within 1 percent with that of Schlichting's boundary layer solution at a dimensionless axial distance (based on channel hydraulic diameter) of 0.2083325. Taking into account Re = 300, this latter dimensionless axial distance is again, with Pr = 0.7, very nearly equivalent to the same value of $2z/D \text{ Re Pr} = 10^{-3}$ given by [19].

The annular flow bears resemblance to the flow in parallel plate channels as $N \rightarrow 1$, and to the flow in circular tubes as $N \rightarrow 0$. Therefore, the restriction of $2z/D \text{ Re Pr} \geqslant 10^{-3}$, given by [19] and concluded from the results of [29], and which by transformation to the present nomenclature may be written as $Z \geqslant 2 \times 10^{-3} (1 - N)^2 \text{Pr}$, is a valid restriction on the applicability of the boundary layer assumptions for the present investigation. However, another restriction, concerned with the presence of flow reversals, would be clarified in next sections.

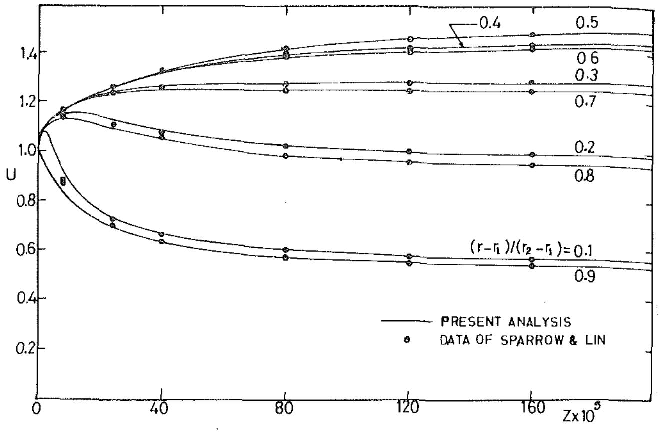

Fig. 1 Comparison between the results of the present analysis and those of [20], $N = 0.8$, $\text{Gr/Re} = 0$

Results and Discussion

To check the adequacy of the present numerical solution, a special computer run was made for a radius ratio 0.8 with Gr/Re = 0. Figure 1 shows, for the axial velocity development, a comparison between the results of the present work and those obtained by the analytical method of Sparrow and Lin [20] after plotting various points taken from the curves of [20] on the corresponding curves in the figure. It is clear from this figure that, in general, the present results are in excellent agreement with those of [20] especially for $Z \geqslant 4 \times 10^{-4}$. The small difference between the two sets of results at $Z < 4 \times 10^{-4}$ comes mainly from the fact that in this region the curves of [20] corresponding to $(r - r_1)/(r_2 - r_1) = 0.1$ and 0.9, 0.2 and 0.8, etc. tend to coincide with each other; i.e., the velocity profiles become more symmetrical about the mid-point of the gap. However, the present results predict that asymmetry of the velocity profiles exist from the early stages of the development, the velocity profile being symmetrical only at the annulus entrance where it is uniform. It should be noted that, even though boundary layer assumptions and linearization of the inertia terms exist in both analyses, the effect of linearization in the present analysis has always been reduced, especially in the early stages of development, by using very small axial steps near the entrance, the axial step being increased several times as the flow moves away from the entrance.

Nomenclature

c = specific heat of fluid at constant pressure
D = hydraulic diameter of annulus, $2(r_2 - r_1)$
g = gravitational body force per unit mass
h = local heat transfer coefficient based on area of heated surface,

$$-k \frac{\partial t}{\partial r}\bigg|_{\text{wall}} \bigg/ (t_m - t_w)$$

k = thermal conductivity of fluid
L = ratio between hydraulic development length and annulus hydraulic diameter
N = annulus radius ratio, r_1/r_2
p = pressure of fluid at any cross section
p_m = pressure defect at any cross section, $p - p_s$
p_{mfd} = fully developed pressure defect, $(p - p_s)_{fd}$
p_0 = pressure of fluid at annulus entrance
p_s = hydrostatic pressure, $\mp \rho_0 g z$
P = dimensionless pressure defect, $(p_m - p_0)/\rho_0 \bar{u}^2$
P_{fd} = fully developed dimensionless pressure defect, $(p_{mfd} - p_0)/\rho_0 \bar{u}^2$
r = radial coordinate
r_1 = inner annulus radius
r_2 = outer annulus radius
R = dimensionless radial coordinate, r/r_2
t = fluid temperature at any point
t_m = mixing cup temperature over any cross section,

$$\int_{r_1}^{r_2} utr\, dr \bigg/ \int_{r_1}^{r_2} ur\, dr$$

t_0 = fluid temperature at annulus entrance
t_w = isothermal wall temperature
T = dimensionless temperature, $(t - t_0)/(t_w - t_0)$
T_m = dimensionless mixing cup temperature, $(t_m - t_0)/(t_w - t_0)$
u = axial velocity component
$\bar{u}$ = mean axial velocity,

$$\int_{r_1}^{r_2} ur\, dr \bigg/ \int_{r_1}^{r_2} r\, dr$$

u_0 = entrance velocity
U = dimensionless axial velocity, $u/\bar{u}$
v = radial velocity component
V = dimensionless radial velocity, $\rho_0 v r_2/\mu$
z = axial coordinate
Z = dimensionless axial coordinate, $2z(1 - N)/r_2 \text{Re}$
Z_0 = dimensionless hydrodynamic development length
Z_r = dimensionless axial distance at which the velocity gradient normal to the wall vanishes
β = volumetric coefficient of thermal expansion
ρ = fluid density, $\rho_0[1 - \beta(t - t_0)]$
ρ_0 = fluid density at inlet fluid temperature
μ = dynamic viscosity of fluid
Re = Reynolds number, $\rho_0 D \bar{u}/\mu$
Pr = Prandtl number, $\mu c/k$
Gr = Grashof number, $\rho_0^2 g \beta (t_w - t_0) D^3/\mu^2$
Nu = local Nusselt number, hD/k

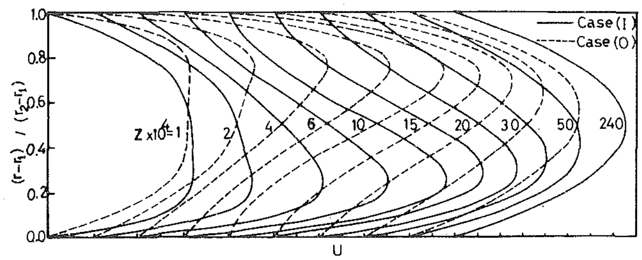

Fig. 2(*a*) Development of axial velocity profiles, $N = 0.9$, Pr = 0.7, Gr/Re = 500

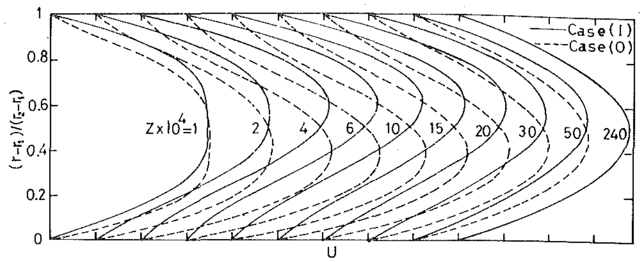

Fig. 2(*b*) Development of axial velocity profiles, $N = 0.9$, Pr = 0.7, Gr/Re = −200

Table 1 Critical distance Z_r at which the velocity gradient normal to the wall vanishes and the hydrodynamic development length Z_0, Pr = 0.7

	Thermal Boundary Condition (I)					
	$N = 0.9$			$N = 0.5$		
Gr/Re	$Z_r \times 10^4$	$Z_0 \times 10^2$	$L^+ \times 10^2$	$Z_r \times 10^4$	$Z_0 \times 10^2$	$L^+ \times 10^2$
−700	0.63	NI	NI	13.3	NI	NI
−600				17.2	NI	NI
−500	1.08	NI	NI	23.5	69.45	69.45
−400	1.70	NI	NI	37.0	65.50	65.50
−300	3.30	1.562	39.05	NFR	60.04	60.04
−200	NFR	1.396	34.90	NFR	51.31	51.31
−100	NFR	1.118	27.95	NFR	38.20	38.20
0	NFR	0.059	1.475	NFR	1.68	1.68
100	NFR	0.878	21.95			
200	NFR	1.092	27.58	NFR	20.60	20.60
300	NFR	1.223	30.40			
400	NFR	1.312	32.80			
500	NFR	1.387	34.75	NFR	42.70	42.70
700	9.40	1.514	37.85			
800	7.66	1.566	39.15	NFR	56.80	56.80
900	6.80	NI	NI			
1000	6.25	NI	NI	23.9	64.20	64.20
1200	5.52	NI	NI	18.5	70.50	70.50
1300	5.30	NI	NI	17.7	73.00	73.00
1400				17.0	75.50	75.50
1500	4.90	NI	NI	16.6	78.02	78.02
1600				16.1	NI	NI

	Thermal Boundary Condition (0)		
	$N = 0.9$		
−200	NFR	1.203	30.075
200	NFR	1.042	26.05
500	NFR	1.332	33.30
800	6.8	1.481	37.025

NFR—Neither flow reversal nor zero velocity gradient normal to the wall occur.
NI—Numerical instability occurs before the flow reaches full development.

Figures 2(*a*) and 2(*b*) represent samples of the developing axial velocity profiles U corresponding to some values of the parameter Gr/Re for both boundary conditions (I) and (O) with Pr = 0.7. It is clear from these figures that when the free convection aids the forced flow (i.e., positive Gr/Re for heating with upflow or cooling with downflow) the fluid accelerates near the heated boundary and decelerates near the opposite insulated wall. The developing axial velocity profiles deviate increasingly from the corresponding isothermal (or constant density) profiles until a cross section of a maximum velocity distortion, at which the slope of the profile ($\partial U/\partial R$) at the insulated wall becomes a minimum is reached. As the axial distance increases further, the axial velocity profile recovers and approaches the fully developed isothermal profile as the fluid temperature approaches the isothermal wall temperature.

On the other hand, when the free convection opposes the forced flow (i.e., negative Gr/Re for heating with downflow or cooling with upflow) the buoyancy force tends to retard the fluid near the heated boundary and accelerates it near the opposite adiabatic wall. In such a case the maximum velocity profile distortion occurs when the slope of the profile at the heat transfer boundary reaches its minimum value. Therefore, in this case a possibility of flow reversal occurs near the heat transfer boundary while such a flow reversal may occur near the insulated wall if the natural convection is aiding the forced flow.

With a reversed flow the slope of the axial velocity profile at the wall, near which the flow reversal occurs, is negative. However, it is important to know, for each value of the parameter Gr/Re, the critical distance Z_r, at which the velocity gradient normal to the wall vanishes ($\partial U/\partial R\,|_{\text{wall}} = 0$), since under such a condition boundary layer separation may occur and the boundary layer assumptions might no further be applicable [21]. This critical distance is given in Table 1 for all the computer runs which are available at the moment of writing this paper.

It is clear from this table that, in general, such a critical condition only occurs at large absolute values of Gr/Re and that, for a given annulus, the distance Z_r decreases as the absolute value of Gr/Re increases. Also, for the same value of Gr/Re, Z_r decreases as the annulus radius ratio increases and it has, for a given annulus, a smaller value with thermal condition (O) than with thermal condition (I). This latter prediction can physically be attributed to the greater velocity profile distortions which exist, at the same dimensionless axial distance Z, with thermal boundary condition (O) than with thermal boundary condition (I) due to the bigger heated surface area associated with the former boundary condition than with the latter.

Another important length given in Table 1 is the dimensionless hydrodynamic development length Z_0 defined as the distance required for the axial velocity profile to approach within ±0.5 percent of its fully developed value [22]. The dimensionless constant "L^+" given in Table 1 is equal to L/Re, where L is the ratio between the hydrodynamic development length and the annulus hydraulic diameter. It is clear from Table 1 that, for a given annulus, the hydrodynamic development length Z_0 increases with the absolute value of the parameter Gr/Re. This is to be expected since the distortion of the velocity profiles increases by increasing the absolute value of Gr/Re and hence the distance required for recovery and approaching the fully developed profile increases.

Table 1 also shows that, in general, for cases where neither flow reversal nor zero velocity gradient normal to the wall occur over the entire development length, the computer program was able to obtain the hydrodynamic development length Z_0. On the other hand, it was expected that, due to numerical stability (the reader may refer to [23] and [24] for details of numerical stability), the step-by-step numerical scheme would not handle anything but uni-directional laminar flow problems [16, 17]. However, in the present work it has succeeded in obtaining converged numerical solutions until full development for some cases with a reversed flow occurring over a certain portion of the hydrodynamic development length. Indeed, at large absolute values of Gr/Re, where appreciable flow reversals exist, converged numerical solutions could always be obtained until the critical distance Z_r after which the solution starts to diverge from the laminar solution, normally after a further axial distance with a reversed flow existing. This divergence appears as the radial velocity component starts to increase instead of decaying as in the laminar flow solution. It may be worth mentioning here that similar solution divergences have been reported by Sherwin and Wallis [14, 25] and Zeldin and Schmidt [2]. Also, experiments with hydrodynamically fully developed pipe flows (e.g., [8]) indicate that with free convection aiding the forced flow transition to unsteady flows occurs only beyond a stable reversed flow region while with natural convection opposing the forced flow such a transition occurs suddenly.

Figure 3 shows the development of the radial velocity component in an annulus of $N = 0.9$ for both thermal boundary conditions (I) and (O) with Pr = 0.7 and Gr/Re = 200. Comparing the radial velocity development in this figure with its development for the case of pure forced convection given in [17] and [22], the drastic effect of free convection on the development of that velocity component could easily be seen.

Effect of Free convection on Laminar Pressure Drop and Heat Transfer Characteristics. Figure 4 presents some numerical results of dimensionless pressure P against the dimensionless axial distance Z for $N = 0.9$ at various values of the parameter Gr/Re with Pr = 0.7. It is clear from this figure that with positive values of Gr/Re (i.e., the free convection aids the forced flow) the power required to pump the fluid until a certain distance from the entrance through a given annulus is less than that required in the absence of free convection. On the other hand, when the free convection opposes the forced flow (i.e., negative values of Gr/Re) the power needed is higher than that in the the purely forced convection case.

Another important point to be mentioned is that at large values of the dimensionless axial distance Z the flow approaches full development. Taking into account that at full development the inertia terms on the left hand side of equation (2) vanish, $\partial P/\partial Z$ = constant and $T = 1$, it could easily be proved that the linear variation of the fully developed dimensionless pressure (P_{fd}) with Z is according to the following equation

$$P_{fd} = \pm \frac{\mathrm{Gr}}{\mathrm{Re}} \frac{Z}{4(1-N)^2} - \frac{8Z}{1 + N^2 + (1 - N^2)/\ln N} \tag{6}$$

At large values of Z, the present numerical predictions showed that the variation of P with Z becomes linear and parallel to the straight lines given by equation (6). This means that, for each value of Gr/Re and at large values of Z (where the flow approaches full development), the difference between the dimensionless pressure P and the dimensionless fully developed pressure P_{fd} (which would be obtained if the flow were hydrodynamically and thermally fully developed right from the annulus entrance) approaches a constant value which is known as "the fully developed pressure drop increment" [20]. Therefore, Fig. 4 only concentrates on that distance near to the annulus entrance before the variation of P with Z becomes linear and parallel to the straight lines given by equation (6).

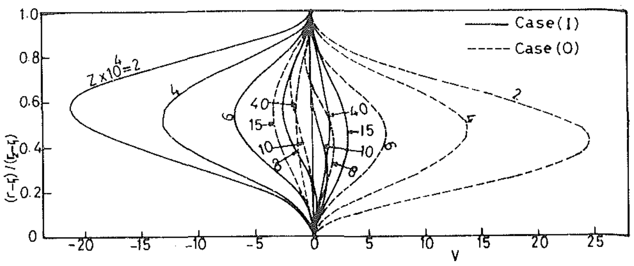

Fig. 3 **Development of radial velocity component, $N = 0.9$, Pr = 0.7, Gr/Re = 200**

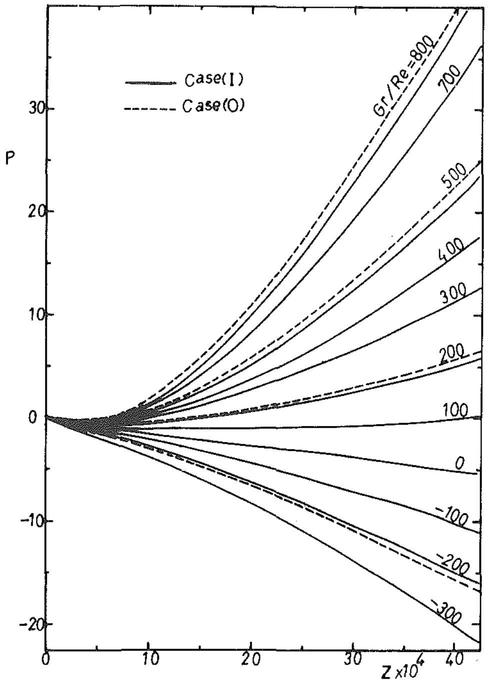

Fig. 4 **Effect of Gr/Re on the pressure drop, $N = 0.9$, Pr = 0.7**

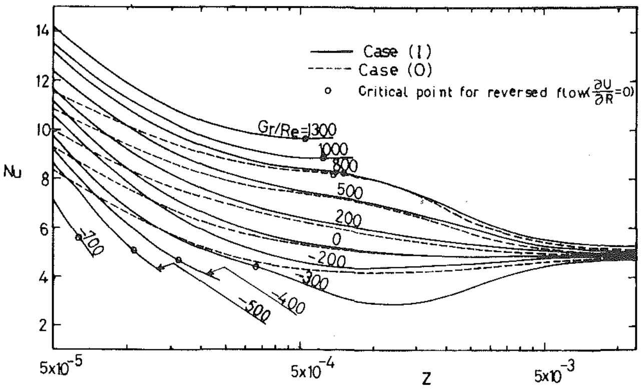

Fig. 5 **Local Nusselt number against axial distance, $N = 0.9$, Pr = 0.7**

Figure 5 gives, for $N = 0.9$, the variation of the local Nusselt number with the dimensionless axial distance Z at various values of the parameter Gr/Re with Pr = 0.7, while Fig. 6 gives such a variation for the mixing cup temperature T_m. It is clear from these two figures that with positive values of Gr/Re (i.e., free convection aids the forced flow) both T_m and Nu are higher, for the same Z, than their corresponding values of the purely forced convection case (Gr/Re = 0) and vice versa with negative values of Gr/Re. This is attributed to the higher velocities near the heated surface, and hence the decrease in the thickness of the developing boundary layer on that boundary, in case of an aiding free convection. However, since the fully developed laminar velocity profile for both pure forced convection and mixed convection cases is the same as the isothermal laminar velocity profile, the mixed

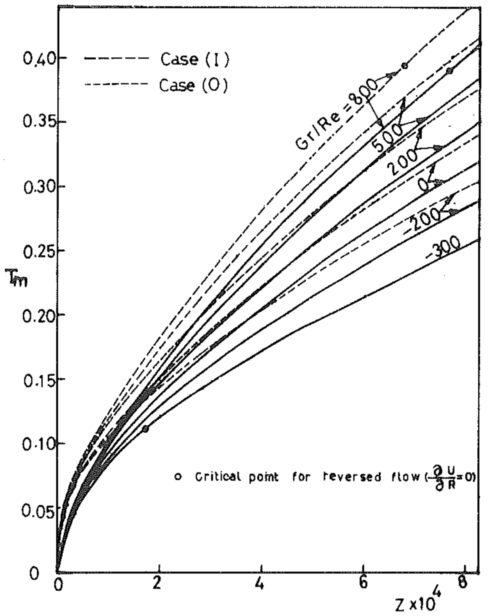

Fig. 6 Mixing cup temperature against axial distance, N = 0.9, Pr = 0.7

convection Nusselt number approaches, at large values of Z and for all values of Gr/Re, the same fully developed values which could be obtained from the series solutions of the well known classical Graetz problem. This provides an analytical check on the numerical solutions to be obtained. The present numerical predictions showed that, at large values of Z and for all values of Gr/Re, the local Nusselt number for $N = 0.9$ with thermal boundary conditions (I) and (O) approaches the values 4.941 and 4.778, respectively. Also, the corresponding predicted numerical value for $N = 0.5$ with thermal boundary condition (I) is 5.715, which is within 0.4 percent of the value 5.738 obtained by series solutions of the classical Graetz problem [26, 27].

It could be seen from Fig. 5 that, at any dimensionless axial distance Z, Nu is very nearly a linear function of Gr/Re. This is in agreement with the results of Zeldin and Schmidt [2] for developing pipe flows.

The unusual behavior found by Marner and McMillan [28] concerning the increase of Nu, near the point of maximum velocity profile distortion, with increasing axial distance has also been obtained in the present work, especially with negative values of Gr/Re. However, it should be cautioned that such an unusual behaviour occurs in the present work only beyond the critical distance for reversed flow Z_r, which is indicated on the curves given in Fig. 5.

It should be noted that the variation of Nu with Z for large absolute values of Gr/Re, given in Fig. 5, is shown up to the axial distance after which the solution starts to diverge. Referring to this figure and also to Table 1, it can be seen that this divergence only happens after the critical distance Z_r is reached. Since, as previously mentioned, the boundary layer assumptions might not be applicable beyond that critical distance [21], use of such a figure may only be limited up to that critical distance (circuled points in the figure).

Finally, to show a case for the importance of the present results and to discuss the practical applications for which the reported range of Z and Gr/Re would be important, let us consider a double-pipe heat exchanger with an upflow of air in its annular gap and a condensing steam inside its core pipe. Owing to the very low thermal resistance of the condensing steam in comparison with the thermal resistance of the flowing air, the inner wall temperature of such a double-pipe heat exchanger would be very nearly equal to the saturation temperature of the condensing steam. Given a condensing steam absolute pressure of 4000 kp/m^2, which is a reasonable figure for a process steam pressure bled from a power station, the inner wall temperature t_w would be nearly 75.42°C. Assuming an inlet ambient air temperature t_0 of 27°C, then $(t_w - t_0) \simeq 48.42$°C, $\mu/\rho_0 \simeq 15.7 \times 10^{-6}$ m^2/s, $1/\beta = (t_0 + 273) = 300$ K, and hence for an annulus of $N = 0.5$ with $r_2 = 0.05$ m the Grashof Number Gr $\simeq 8 \times 10^5$. Therefore, for a flow of air with Re = 1600, the parameter Gr/Re $\simeq$ 500, and from Table 1 $Z_0 = 0.427$ i.e., $z_0 = 34.16$ m. This example shows that under such possible practical conditions, the flow is in the combined forced-free laminar regime, the distance required to approach the fully developed flow conditions is very large, and hence the hydrodynamic and heat transfer characteristics should be estimated from the solutions of the developing combined forced-free laminar flow.

Concluding Remarks

The present investigation showed the significant effects of a superimposed free convection on the hydrodynamic and heat transfer characteristics of a developing laminar annular flow. Data, not available in the literature, have been given for the hydrodynamic development length, pressure drop, and heat transfer parameters under the thermal boundary conditions of one wall being isothermal and the opposite wall adiabatic. When the free convection opposes the forced flow (i.e., heating with downflow or cooling with upflow) there exists a possibility of flow reversal near the heated boundary while such a flow reversal may occur near the insulated wall if the free convection is aiding the forced flow. The critical distance at which such a flow reversal, and hence boundary layer separation, may occur has also been given.

Acknowledgment

The financial support of Alazhar University, which allowed us to carry out this investigation on the ICL 1900 computer of Cairo University, is gratefully acknowledged.

References

1 Lawrence, W. T., and Chato, J. C., "Heat Transfer Effects on the Developing Laminar Flow Inside Vertical Tubes," ASME JOURNAL OF HEAT TRANSFER, Vol. 88, No. 2, May 1966, pp. 214–222.

2 Zeldin, B., and Schmidt, F. W., "Developing Flow with Combined Forced-Free Convection in an Isothermal Vertical Tube," ASME JOURNAL OF HEAT TRANSFER, Vol. 94, No. 2, May 1972, pp. 211–223.

3 Savakar, S. D., "Developing Forced and Free Convective Flows Between Two Semi-Infinite Parallel Plates," Fourth International Heat Transfer Conference, Vol. IV, Paper No. Nc 3.8, Paris 1970.

4 Quintiere, J., and Mueller, W. K., "An Analysis of Laminar Free and Forced Convection Between Finite Vertical Parallel Plates," ASME JOURNAL OF HEAT TRANSFER, Vol. 95, No. 1, Feb. 1973, pp. 53–59.

5 Shumway, R. W., and McEligot, D. M., "Heated Laminar Gas Flow in Annuli with Temperature-Dependent Transport Properties," *Nuclear Science and Engineering*, Vol. 46, 1971, pp. 394–407.

6 Jackson, T. W., Harrison, W. B., and Boteler, W. C., "Combined Free and Forced Convection in a Constant-Temperature Vertical Tube," *Trans. ASME*, Vol. 80, 1958, pp. 739–745.

7 Hallman, T. M., "Experimental Study of Combined Forced and Free Laminar Convection in a Vertical Tube," NASA TN D-1104, 1961.

8 Scheele, G. F., and Hanratty, T. J., "Effect of Natural Convection on Stability of Flow in a Vertical Pipe," *Journal of Fluid Mechanics*, Vol. 14, Part 2, 1962, pp. 244–256.

9 Kemeny, G. A., and Somers, E. V., "Combined Free and Forced Convective Flow in Vertical Circular Tubes-Experiments with Water and Oil," ASME JOURNAL OF HEAT TRANSFER, Vol. 84, 1962, pp. 339–346.

10 Scheele, G. F., and Hanratty, T. J., "Effect of Natural Convection Instabilities on Rates of Heat Transfer at Low Reynolds Numbers," *AIChE Journal*, Vol. 9, No. 2, 1963, pp. 183–185.

11 Dalle Donne, M., and Bowditch, F. H., "High Temperature Heat Transfer," *Nuclear Engineering*, Vol. 8, Jan. 1963, pp. 20–29.

12 Greene, H. L., and Scheele, G. F., "Effect of Fluid Viscosity on Combined Free Forced Convection Flow Phenomena in Vertical Pipes," *AIChE Journal*, Vol. 16, No. 6, 1970, pp. 1039–1047.

13 Greif, R., "An Experimental and Theoretical Study of Heat Transfer in Vertical Tube Flows," ASME JOURNAL OF HEAT TRANSFER, Vol. 100, No. 1, Feb. 1978, pp. 86–91.

14 Sherwin, K., and Wallis, J. D., "Combined Natural and Forced Laminar Convection for Upflow Through Heated Vertical Annuli," Heat and Mass Transfer by Combined Forced and Natural Convection, Thermodynamics and Fluid Mechanics Conference, Institute of Mechanical Engineers, 1972, pp. 1–5.

15 Rao, T. L. S., and Barrow, H., "Experimental Study of Combined Free and Forced Laminar Convection in Asymmetrically Heated Two-Dimensional Aiding Flow," *Wärme und Stffübertragung*, Vol. 5, 1972, pp. 127–133.

16 Bodoia, J. R., and Osterle, J. F., "Finite Difference Analysis of Plane Poiseuille and Couette Flow Developments," *Applied Scientific Research*, Section A, Vol. 10, 1961, pp. 265–276.

17 Coney, J. E. R., and El-Shaarawi, M. A. I., "Finite Difference Analysis for Laminar Flow Heat Transfer in Concentric Annuli with Simultaneously Developing Hydrodynamic and Thermal Boundary Layers," *International*

Journal for Numerical Methods in Engineering, Vol. 9, 1975, pp. 17–38.

18 Sarhan, A., and El-Shaarawi, M. A. I., "Combined Forced-Free Laminar Convection in the Entrance Region of Concentric Annuli," Internal Report, Mechanical Engineering Department, Alazhar University, Cairo.

19 Worsoe-Schmidt, P. M., and Leppert, G., "Heat Transfer and Friction for Laminar Flow of Gas in a Circular Tube at High Heating Rate," *International Journal of Heat and Mass Transfer,* Vol. 8, 1965, pp. 1281–1301.

20 Sparrow, E. M., and Lin, S. H., "The Developing Laminar Flow and Pressure Drop in the Entrance Region of Annular Ducts," ASME *Journal of Basic Engineering,* Vol. 86, No, 4, 1964, pp. 827–834.

21 Schlichting, H., *Boundary Layer Theory,* Fourth Edition, McGraw Hill, New York, 1962, pp. 31, 113, 245, 260

22 Coney, J. E. R., and El-Shaarawi, M. A. I., "Developing Laminar Radial Velocity Profiles and Pressure Drop in the Entrance Region of Concentric Annuli," *Nuclear Science and Engineering,* Vol. 57, No. 2, June 1975, pp. 1969–174.

23 Bodoia, J. R., PhD thesis, Carnegie Institute of Technology, July 1959.

24 Carnahan, B., Luther, H. A., and Wilkes, J. O., *Applied Numerical Methods,* John Wiley & Sons, New York, pp. 449–475.

25 Sherwin, K., and Wallis, J. D., "A Theoretical Study of Combined Natural and Forced Laminar Convection for Developing Flow Down Vertical Annuli," Fourth International Heat Transfer Conference, Vol. IV, Paper No. Nc 3.9, Paris, 1970.

26 Lundberg, R. E., McCuen, P. A., and Reynolds, W. C., "Heat Transfer in Annular Passages. Hydrodynamically Developed Laminar Flow with Arbitrarily Prescribed Wall Temperature and Heat Fluxes," *International Journal of Heat and Mass Transfer,* Vol. 6, 1963, pp. 495–529.

27 Shah, R. K., and London, A. L., "Laminar Flow Forced Convection Heat Transfer and Flow Friction in Straight and Curved Ducts—A Summary of Analytical Solutions," Technical Report No. 75, Department of Mechanical Engineering, Stanford University, Stanford, Calif. Nov. 1971.

28 Marner, W. J., and McMillan, H. K., "Combined Free and Forced Laminar Convection in a Vertical Tube with Constant Wall Temperature," ASME JOURNAL OF HEAT TRANSFER, Vol. 92, No. 3, Aug. 1970, pp. 559–562.

29 Wang, Y. L., and Longwell, P. A., "Laminar Flow in the Inlet Section of Parallel Plates," *AIChE Journal,* Vol. 10, No. 3, May 1964, pp. 323–329.

E. M. Sparrow
Department of Mechanical Engineering,
University of Minnesota,
Minneapolis, Minn. 55455
Fellow ASME

M. Faghri[1]
Department of Mechanical Engineering,
Tehran University of Technology,
Tehran, Iran

Natural Convection Heat Transfer from the Upper Plate of a Colinear, Separated Pair of Vertical Plates

The effect of a buoyant boundary layer spawned by a heated vertical plate on the natural convection heat transfer from an upper colinear vertical plate has been determined analytically. The interplate spacing was varied parametrically, as were the relative temperatures and relative lengths of the two plates; the Prandtl number was equal to 0.7 for all cases. Heat transfer at the upper plate was found to be affected both by the preheating and by the finite velocity imparted to the fluid by the first plate, respectively tending to degrade and to enhance the heat transfer. The upper-plate heat transfer was compared to that of an otherwise identical vertical plate, but with the lower plate absent. When the temperatures of the upper and lower plates are the same, the overall upper-plate heat transfer is less than that of its single-plate counterpart for small interplate spacings, with the opposite relationship at larger spacings. If the temperature of the upper plate is substantially below that of the lower plate, the overall heat transfer is degraded. On the other hand, heat transfer enhancement generally occurs when the upper plate is relatively hot. In general, the heat transfer from relatively short upper plates is very sensitive to the presence of the lower plate, with a lessening sensitivity with increasing plate length. The computed temperature and velocity profiles demonstrated that near the leading edge of the upper plate, a new boundary layer develops within the already existing boundary layer spawned by the first plate.

Introduction

Since the pioneering work of Lorenz [1] in 1881, there has been an outpouring of papers dealing with external-flow natural convection (e.g., about vertical plates or horizontal cylinders). A modest sampling of this literature may be found in [2–4]. A careful examination of the available literature has shown that, aside from a handful of papers, all of this work was concerned with natural convection about single bodies (e.g., a single plate or a single cylinder). In reality, there are many instances where natural convection flows induced by one body wash other bodies which are, themselves, generators of natural convection flows. The present research is concerned with such interacting natural convection flows and their analytical treatment.

It is interesting to consider the processes which shape the heat transfer response of a body which is washed by an upstream-induced natural convection flow. The existence of a finite-velocity approach flow tends to increase the rate of heat transfer from the body relative to that for the same body situated in an otherwise quiescent environment. On the other hand, the approach flow has been preheated by the upstream body (or bodies), so that the temperature difference between the body and the flow is diminished compared with the case of the quiescent, isothermal environment. The diminution in temperature difference tends to decrease the heat transfer, both directly as well as indirectly due to a diminution of the bouyancy force.

Thus, the two novel features related to the upstream-induced natural convection flow tend to affect the heat transfer from the body in conflicting ways. The outcome of the conflict depends on a variety of factors including the streamwise (i.e., vertical) and transverse distances between the bodies and the relative temperatures of the bodies. For example, intuitive expectations can be projected about the role of the streamwise separation distance. For this, note may be taken of the behavior of the buoyant plume spawned when a natural-convection vertical-plate boundary layer departs the trailing edge of the plate. It was shown [5] that with increasing vertical distance from the trailing edge, the velocities in the central region of the plume increase while the temperatures decrease. In light of the discussion of the prior paragraph, it follows that a body situated in the central region of the plume will experience higher heat transfer rates as it is positioned progressively farther above the trailing edge. These expectations will be revisited when the results of the present analysis are presented.

The literature on interacting natural convection flows is very sparse, and a search revealed only three papers on the subject [6–8], all dealing with experiments involving two or more convectively interacting horizontal cylinders. It appears that there has been no prior analytical study of interacting natural convection flows; the present work is directed toward such a study.

The physical situation selected for analysis is depicted in Fig. 1 which portrays a pair of colinear vertical plates separated by a space S. The lower plate, which is of length L_1, is maintained at a uniform temperature T_{w1}, and the upper plate, of length L_2, is maintained at T_{w2}. Both T_{w1} and T_{w2} are greater than the ambient temperature T_∞, so that there is a natural convection upflow. Furthermore, both faces of each plate are at the same temperature, giving rise to an identical

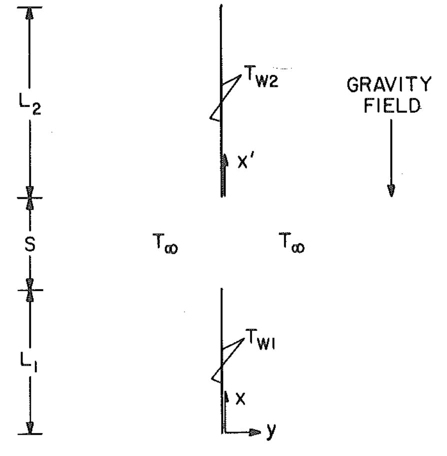

Fig. 1 Schematic diagram of a colinear, separated pair of vertical plates

---

[1] Work performed when the author was an adjunct associate professor at the University of Minnesota.

Contributed by the Heat Transfer Division for publication in the JOURNAL OF HEAT TRANSFER. Manuscript received by the Heat Transfer Division December 14, 1979.

flow field adjacent to each face of the plate. The plates are sufficiently thin so that neither trailing-edge or leading-edge flow separation occurs.

The boundary layer which develops along the lower plate becomes a buoyant plume as it flows upward through the space S. Thus, the fluid arriving at the leading edge of the upper plate has a finite velocity and a temperature which, owing to heat transfer at the first plate, exceeds T_∞. The temperature and velocity profiles in the plume are bell-shaped, with the respective maximum values at any streamwise station occurring at the symmetry line ($y = 0$). In what follows, these profiles will be referred to as boundary layer profiles, although strictly speaking, they are better described as shear layer profiles.

When the upmoving fluid encounters the upper plate, new boundary layers, embedded within the already existing velocity and temperature profiles of the plume, develop. The development of new boundary layers within already existing boundary layers is one of the novel features of the present problem. The resolution of this phenomenon is computationally very demanding, as will be documented shortly.

The primary objective of the numerical solutions is to determine the local and average heat transfer rates on the upper plate. These results will be ratioed with the corresponding natural convection heat transfer rates for a single plate situated in a quiescent, isothermal environment. Temperature and velocity profiles in the fluid adjacent to the upper plate are also presented to illustrate the boundary layer within a boundary layer phenomenon.

The solutions were obtained for dimensionless plate-to-plate separation distances S/L_1 ranging from zero to two. Another parameter that was varied during the computations is the ratio of the temperatures of the plates, $(T_{w2} - T_\infty)/(T_{w1} - T_\infty) \equiv \theta_{w2}$. This parameter was assigned values of 0.5, 1, and 2. Cases with $S/L_1 = 0$ and $\theta_{w2} \neq 1$ correspond to a continuous vertical plate with a step change in wall temperature. In addition to S/L_1 and θ_{w2}, the plate length ratio L_2/L_1 was also employed to parameterize the average heat transfer results. The Prandtl number for all cases was fixed at 0.7 with air in mind.

The present analysis bears a filial relationship to prior analyses of natural-convection vertical-plate flows with discontinuous boundary conditions, of which [5] and [9–11] are representative.

Analysis and Solution

The analytical model to be employed here is based on the boundary layer equations for natural convection flow and heat transfer. Although the boundary layer model is inexact in the immediate neighborhood of the leading edge of a plate, the heat transfer results at downstream surface locations are of high accuracy when the Rayleigh number is not too small. Deviations from boundary layer behavior may also occur at the trailing edge of the plate, but, in common with leading edge effects, their range of influence is limited [9]. To avoid entanglement with non-boundary-layer effects associated with the trailing edge, the minimum separation distance S, for those cases where $S > 0$, will be taken as $0.5L_1$. The issue of nonboundary-layer effects at the trailing edge does not arise for the limiting case of $S = 0$. It is also reasonable to expect that the wake shed by the lower plate will be more stable when the upper plate is present than when it is absent. This is because the upper plate provides a definite place to which the wake can attach, whereas otherwise it tends to wander.

To begin the analysis, dimensionless variables are introduced as follows.

$$X = x/L_1, \quad Y = y[g\beta(T_{w1} - T_\infty)/\nu^2 L_1]^{1/4} \tag{1}$$

$$U = u/[g\beta(T_{w1} - T_\infty)L_1]^{1/2}, \quad V = v/[g\beta(T_{w1} - T_\infty)\nu^2/L_1]^{1/4} \tag{2}$$

$$\theta = (T - T_\infty)/(T_{w1} - T_\infty) \tag{3}$$

Note that the length L_1 and temperature $(T_{w1} - T_\infty)$ of the first plate have been chosen as the length and temperature scales, respectively. In terms of these variables, the mass, momentum, and energy equations for natural convection boundary layer flow take the form

$$\frac{\partial U}{\partial X} + \frac{\partial V}{\partial Y} = 0 \tag{4}$$

$$U\frac{\partial U}{\partial X} + V\frac{\partial U}{\partial Y} = \theta + \frac{\partial^2 U}{\partial Y^2} \tag{5}$$

$$U\frac{\partial \theta}{\partial X} + V\frac{\partial \theta}{\partial Y} = \frac{1}{\Pr}\frac{\partial^2 \theta}{\partial Y^2} \tag{6}$$

The foregoing equations contain one parameter, the Prandtl number. A second parameter, S/L_1, enters the problem via the boundary conditions.

On the surfaces of both plates, the velocity components U and V are zero. Each of the plates is isothermal, but the respective temperatures, T_{w1} and T_{w2}, may be different, so that in terms of θ,

$$\theta = \theta_{w1} = 1, \quad \theta = \theta_{w2} \tag{7}$$

for the first and second plates, respectively. In the interplate gap, symmetry conditions apply on the line that is colinear with the plates; the conditions are

$$V = \partial U/\partial Y = \partial\theta/\partial Y = 0 \text{ for } Y = 0 \text{ and } 1 < X < (1 + S/L_1) \tag{8}$$

The boundary layer velocity and temperature profiles approach the ambient values $U = \theta = 0$ at sufficiently large Y. These same ambient conditions prevail at the leading edge of the first plate but, for computational convenience, they were replaced by alternative specifications for U and θ as will be described shortly.

From the foregoing discussion, it is evident that the problem involves three distinct zones distinguished by specific boundary conditions, namely, $0 \leq X \leq 1$, $1 < X < (1 + S/L_1)$, and $X > (1 + S/L_1)$. Note that the length L_2 of the second plate need not be specified in the definition of the solution domain. This is because the boundary layer model limits streamwise information transfer to the positive x-direction, so that downstream events have no effect at upstream positions. Any streamwise station x on the second plate can, if desired, be regarded as $x' = L_2$.

Although the velocity and temperature fields adjacent to the first plate admit a similarity solution, those in the interplate gap and adjacent to the second plate are nonsimilar. For computational effi-

Nomenclature

g = acceleration of gravity
h = local heat transfer coefficient on upper plate
h^* = local coefficient on counterpart single plate
$\bar{h}$ = average heat transfer coefficient on upper plate
$\bar{h}^*$ = average coefficient on counterpart single plate
k = thermal conductivity
L_1 = length of lower plate
L_2 = length of upper plate
Pr = Prandtl number
Q = surface-integrated heat transfer rate on upper plate
Q^* = value of Q for counterpart single plate
q = local heat flux at location x' on upper plate
q^* = value of q at location x' on counterpart single plate
S = interplate spacing
T = temperature
T_{w1} = surface temperature of lower plate
T_{w2} = surface temperature of upper plate
T_∞ = ambient temperature
U,V = dimensionless velocities, equation (2)
u,v = velocity components
X,Y = dimensionless coordinates, equation (1)
x = coordinate measured from leading edge of lower plate
x' = coordinate measured from leading edge of upper plate
y = transverse coordinate
β = coefficient of thermal expansion
θ = dimensionless temperature, $(T - T_\infty)/(T_{w1} - T_\infty)$
θ_{w2} = dimensionless upper-plate wall temperature, $(T_{w2} - T_\infty)/(T_{w1} - T_\infty)$
ν = kinematic viscosity

ciency, a single numerical scheme was used for the entire solution domain, and no special note was taken of the similarity solution for the first plate, except for checking and comparison.

The solutions were obtained by a marching procedure, starting at the leading edge of the first plate, traversing the length of that plate and the interplate gap, and then moving upward along the second plate. The actual computations were carried out by the Patankar-Spalding method [12]. This is a fully implicit finite difference scheme, a special feature of which is that a dimensionless stream function $\omega = (\psi - \psi_i)/(\psi_o - \psi_i)$ is used as the transverse coordinate. The quantities ψ_i and ψ_o respectively designate the values of the stream function at the inner and outer edges of the boundary layer. In the present problem, $\psi_i = 0$ but ψ_o varies with X as the boundary layer entrains fluid in the course of its development (the calculation of the entrainment rates is described in [12]).

The finite difference grid spans the range $0 \leq \omega \leq 1$ at all X, so that as the boundary layer thickness varies, the grid automatically follows the variations. This feature is highly advantageous for conventional boundary layers, for instance, for the boundary layer on the lower plate. However, it has to be employed with care when a new boundary layer develops within a thicker, already existing boundary layer, as occurs on the second plate in the present problem. The basis of the potential difficulty is that the ω coordinate is tied to the already existing boundary layer, as is the distribution of the grid points in the ω direction. Therefore, unless special care is taken, there will be too few points adjacent to the plate surface to accurately resolve the development of the new boundary layer.

After extensive testing and checking, a grid layout was determined which yielded high accuracy in all aspects of the solutions, including resolution of the new boundary layer on the second plate. The grid layout encompassed the following features:

1 Five hundred points in the range $0 \leq \omega \leq 1$. This number is about five times as great as that used for conventional boundary layers.

2 Nonuniform deployment of the grid points in the ω-direction with the highest concentration near the wall (or the symmetry line). The grid point distribution is expressed by

$$\omega_i = [(i - 1)/(N - 1)]^{2.75} \tag{9}$$

where N is the total number of transverse grid points ($N = 500$ in the present instance).

3 A highly refined and carefully deployed grid point distribution in the X-direction. For example, in the immediate neighborhood of the leading edge of the second plate, a step size $\Delta X = 10^{-8}$ was employed, and in the streamwise length from the leading edge ($x' = 0$) to $x'/L_1 = 0.01$ there were 4000 streamwise stations. All told, 3000 streamwise stations were used on the first plate, 1000–4000 in the interplate gap (depending on S/L_1), and about 13,000 on the second plate between $x'/L_1 = 0$ and 5.

As an accuracy test, the present Nusselt number prediction for the first plate was compared with the literature value as obtained from a similarity solution. The deviation between the two results was one in the fourth significant figure (~0.03 percent), and it is a moot question as to which result should be regarded as being more accurate.

The Patankar-Spalding method requires that velocity and temperature profiles be given at the streamwise station at which the marching procedure is initiated. For this purpose, profiles from the integral momentum-energy solution ([13] pp. 312–315) were employed. The calculations were initiated at $X = 6 \times 10^{-10}$. In view of this very small value of X, the approximations in the input profiles had no influence on the results at downstream stations.

Results and Discussion

The presentation and discussion of results will be subdivided into three parts: overall heat transfer, local heat transfer, and temperature and velocity profiles. These results pertain to the upper plate of the two-plate array. It is unnecessary to present results for the lower plate because they are identical to literature information for the conventional isothermal vertical plate. The parameters to be used for the presentation of the results will now be discussed.

At any surface location x' on the second plate, the local heat flux is given by

$$q = -k(\partial T/\partial y)_0 = -k(T_{w1} - T_\infty)^{5/4}(g\beta/\nu^2 L_1)^{1/4}(\partial\theta/\partial Y)_0 \tag{10}$$

and, for a plate of length L_2 and unit width, the overall rate of heat transfer from one side is

$$Q = \int_0^{L_2} q\, dx' \tag{11}$$

These quantities are to be compared to the values of corresponding quantities for a plate that is in all ways identical to the upper plate (wall temperature = T_{w2}, ambient temperature = T_∞, length = L_2), except that the lower plate is absent. This reference case will be identified by an asterisk, so that the ratios of interest are q/q^* and Q/Q^*.

The reference quantities q^* and Q^* are readily determined from literature information. For laminar natural convection about an isothermal vertical plate, the local Nusselt number is expressed as

$$\mathrm{Nu}_x/\mathrm{Gr}_x{}^{1/4} = \phi(\mathrm{Pr}) \tag{12}$$

so that

$$q^* = k(T_{w2} - T_\infty)^{5/4}(g\beta/\nu^2 x')^{1/4}\phi \tag{13}$$

and

$$Q^* = k(T_{w2} - T_\infty)^{5/4}(g\beta/\nu^2)^{1/4} L_2{}^{3/4}(4\phi/3) \tag{14}$$

With the foregoing, the q/q^* and Q/Q^* ratios follow as

$$\frac{q}{q^*} = \left(\frac{T_{w1} - T_\infty}{T_{w2} - T_\infty}\right)^{5/4} \cdot \frac{(x'/L_1)^{1/4}\,[-(\partial\theta/\partial Y)_0]}{\phi} \tag{15}$$

$$\frac{Q}{Q^*} = \left(\frac{T_{w1} - T_\infty}{T_{w2} - T_\infty}\right)^{5/4} \frac{I(L_2/L_1)}{(L_2/L_1)^{3/4}(4\phi/3)} \tag{16}$$

where

$$I(L_2/L_1) = -\int_0^{L_2/L_1} (\partial\theta/\partial Y)_0\, d(x'/L_1) \tag{17}$$

Since q, q^*, Q, and Q^* correspond to the same wall-to-ambient temperature difference and the latter pair pertain to the same plate length, it follows directly that

$$q/q^* = h/h^*, \quad Q/Q^* = \bar{h}/\bar{h}^* \tag{18}$$

where h and $\bar{h}$ denote local and average heat transfer coefficients.

The derivative $(\partial\theta/\partial Y)_0$ and its integral I were determined during the course of the numerical solutions, thereby enabling the q/q^* and Q/Q^* ratios to be evaluated. For the special case of $S = 0$ and $\theta_{w2} = 1$ (i.e., $T_{w2} = T_{w1}$), it is easily shown that

$$q/q^* = [(x'/L_1)/(1 + x'/L_1)]^{1/4} \tag{19}$$

$$Q/Q^* = [(1 + L_2/L_1)^{3/4} - 1]/(L_2/L_1)^{3/4} \tag{20}$$

The results to be presented here are for $\mathrm{Pr} = 0.7$, for which $\phi = 0.4995/\sqrt{2} = 0.3532$.

Overall Heat Transfer. The results for the overall heat transfer rate and/or the average heat transfer coefficient are, perhaps, of most direct practical utility, and they are, therefore, presented first. In Figs. 2 and 3, Q/Q^* ($= \bar{h}/\bar{h}^*$) is plotted as a function of the dimensionless interplate separation distance S/L_1 for various fixed lengths of the upper plate. These plate lengths are expressed in terms of the ratio L_2/L_1, which has been assigned values of 0.25, 0.5, 1, 2, and 5. Figure 2 conveys results for the case where $(T_{w2} - T_\infty)$ is half of $(T_{w1} - T_\infty)$, while Fig. 3 contains information for two cases—one where T_{w2} and T_{w1} are equal and the other where $(T_{w2} - T_\infty)$ is twice $(T_{w1} - T_\infty)$.

Inspection of these figures reveals that the heat transfer at the upper plate can either be greater or less than its single-plate counterpart, depending on the geometrical and thermal parameters. In this regard, consider first the case of $T_{w2} = T_{w1}$ (upper set of curves in Fig. 3). For this case, it is seen that the upper-plate heat transfer rate is lower than that of its single-plate counterpart at small separation distances, i.e., $Q/Q^* < 1$. However, with increasing separation distance, the upper-plate heat transfer rate increases relative to the counterpart value so that $Q/Q^* > 1$ at sufficiently large separation distances. Under these conditions, the presence of the lower plate actually serves as an augmentation device with respect to the heat transfer performance of the upper plate.

This behavior can be made plausible for referring to the ideas set forth in the Introduction. There, it was noted that the presence of the lower plate induces streamwise velocities in the fluid approaching the second plate but also tends to preheat the fluid. These factors tend to have opposite effects on the upper-plate heat transfer. Since the velocities increase as the fluid traverses the interplate gap whereas the temperature excess diffuses away, the temperature excess tends to be more important for small gaps while the velocity-of-approach is of greater importance for larger gaps. Thus, since the temperature excess tends to diminish the upper-plate heat transfer while the velocity-of-approach tends to increase the heat transfer, the trends in evidence in Fig. 3 are fully plausible.

Further examination of the results for $\theta_{w2} = 1$ indicates that both the magnitude of the Q/Q^* ratio and its variation with separation distance are markedly influenced by the length L_2 of the upper plate. When L_2/L_1 is large, the departures of Q/Q^* from unity are small and, furthermore, Q/Q^* is quite insensitive to separation distance. Therefore, the heat transfer performance of a long upper plate differs only slightly from that of its single-plate counterpart. On the other hand, when L_2/L_1 is small, the departures of Q/Q^* from unity are appreciable, and its variation with separation distance is significant.

In considering these findings, it is reasonable to expect that a short upper plate will be sensitive to conditions in the approach flow. This is because it provides too short a length of run to neutralize these initial influences and develop velocity and temperature fields that are characteristic of itself. Thus, if some feature of the approach flow tends to degrade heat transfer (i.e., preheating), the upper-plate heat transfer performance will be degraded. If, on the other hand, the approach flow tends to enhance heat transfer (i.e., due to relatively high velocity), the plate will display enhanced heat transfer performance.

A long plate, on the other hand, provides a sufficient length of run so that the velocity and temperature fields over most of the plate are little influenced by the characteristics of the approach flow. Thus, Q/Q^* should differ only slightly from unity over the entire range of separation distances.

Attention may now be turned to the other results of Figs. 2 and 3, namely, to cases where $T_{w2} \neq T_{w1}$. Consider first the situation treated in Fig. 2, $(T_{w2} - T_\infty) = \frac{1}{2}(T_{w1} - T_\infty)$. In this case, when viewed from the standpoint of an observer situated on the upper plate, the approach flow is significantly preheated. Indeed, for small separation distances, the fluid arriving at the leading edge of the upper plate may be at a higher temperature than that of the plate itself. Consequently, in a region adjacent to the leading edge, heat will be transferred from the fluid to the plate surface (i.e., negative heat transfer). Even if such a heat transfer reversal does not occur, the severe preheating of the fluid strongly inhibits heat flow from the fluid to the surface.

In light of these remarks, the results presented in Fig. 2 appear quite reasonable. In general, $Q/Q^* \leq 1$ for the range of parameters investigated. Furthermore, for short upper plates and small interplate separation distances, Q/Q^* is negative. Thus, the presence of a relatively hot lower plate can severely degrade the heat transfer performance of the upper plate, and this is the main message of the figure. The trends of Q/Q^* with L_2/L_1 and S/L_1 are the same as those already identified and rationalized for the case of $\theta_{w2} = 1$.

The other investigated case where $T_{w2} \neq T_{w1}$ is that of $(T_{w2} - T_\infty) = 2(T_{w1} - T_\infty)$. In this instance, when viewed from the perspective of an observer on the upper plate, the preheating effect is unimportant because of the plate's elevated temperature. Therefore, the potential heat transfer degradation due to preheating should be minor. With regard to the magnitude of the velocity approaching the upper plate, it is governed by the lower plate and by the size of the interplate gap. Therefore, the upper-plate heat transfer enhancement due to velocity-of-approach should not be very different from that for the case where $T_{w2} = T_{w1}$ (i.e., for the case of $\theta_{w2} = 1$).

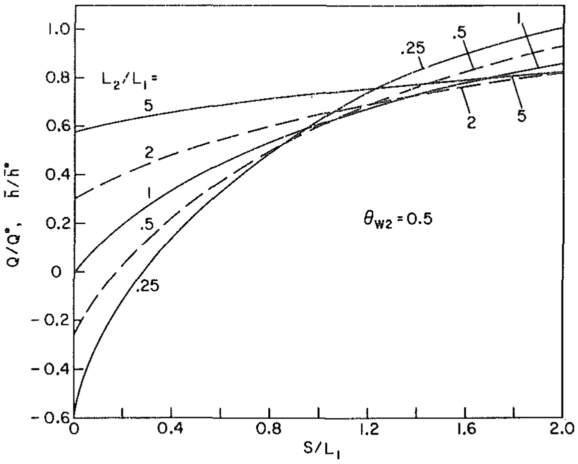

Fig. 2 Comparison of overall heat transfer at the upper plate with its single-plate counterpart, $(T_{w2} - T_\infty)/(T_{w1} - T_\infty) = 0.5$

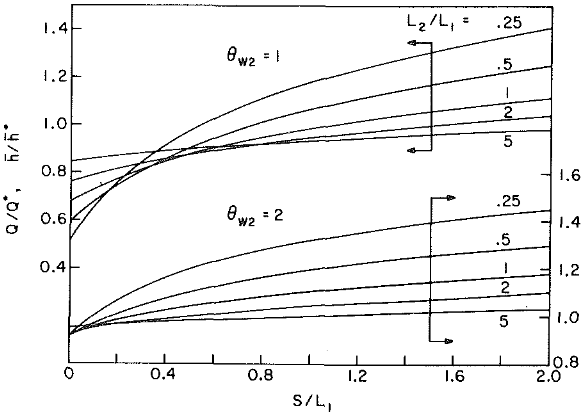

Fig. 3 Comparison of overall heat transfer at the upper plate with its single-plate counterpart, $(T_{w2} - T_\infty)/(T_{w1} - T_\infty) = 1$ and 2

These expectations are borne out in Fig. 3 (lower graph). There, it is seen that $Q/Q^* \sim 1$ for small spacings, indicating a negligible effect of preheating. For larger spacings, the Q/Q^* values are not very different from those for the $\theta_{w2} = 1$ case.

An overview of the results of Figs. 2 and 3 indicates that the temperature level of the upper plate appears to play a stronger role when $T_{w2} < T_{w1}$ than when $T_{w2} > T_{w1}$. Shorter upper plates are more sensitive than are longer plates to the presence of a lower plate. Larger gaps provide the opportunity for upper-plate heat transfer enhancement compared to a counterpart single plate, and such enhancement is actually realized except when $(T_{w2} - T_\infty)$ is substantially smaller than $(T_{w1} - T_\infty)$.

The absence of prior work on stacked plates precludes any direct comparisons of the results presented in the foregoing. It is, however, interesting to make trendwise comparisons with the available experimental information for stacked horizontal cylinders [6–8]. In [6], only a single operating condition was examined so that no trends can be identified. In [7] and [8], the qualitative effect of intercylinder spacing was found to be the same as the interplate spacing effect identified earlier in this paper. Specifically, at small intercylinder spacings, the presence of the lower cylinder gave rise to reduced heat transfer on the upper cylinder; at large spacings, the heat transfer was augmented. The other parametric explorations undertaken here, i.e., systematic variations of second-body temperature and length, were not included in the prior works.

Local Heat Transfer. The local heat transfer results are plotted in Figs. 4 and 5 for parametric values of θ_{w2} equal to 0.5 and to 1 and 2, respectively. In these figures, the ordinate q/q^* compares the local heat flux at a streamwise station x' on the upper plate with that at the same station on an identical single plate. These results are plotted against the streamwise coordinate x' which measures distances along the upper plate from its leading edge. A logarithmic scale is used on the abscissa to enable details of the q/q^* versus x' distributions to be shown for small x' values. The curves in each figure are parameterized by the dimensionless separation distance S/L_1.

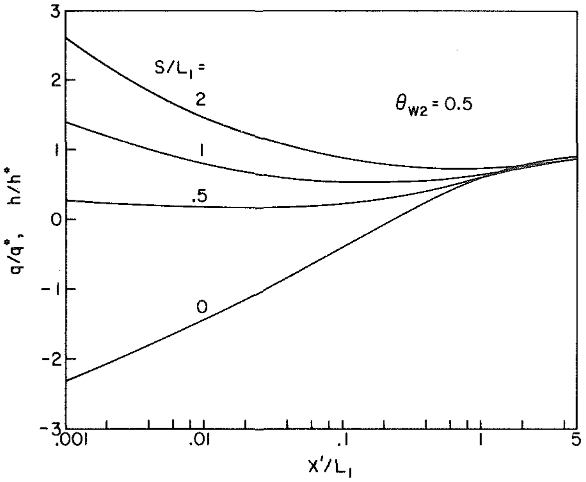

Fig. 4 Comparison of local heat flux at the upper plate with its single-plate counterpart, $(T_{w2} - T_\infty)/(T_{w1} - T_\infty) = 0.5$

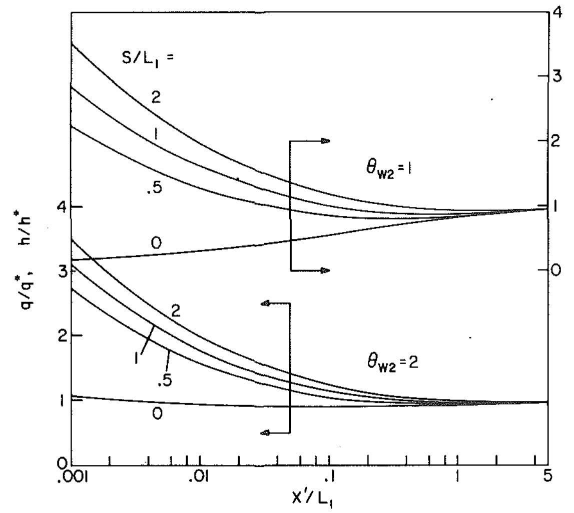

Fig. 5 Comparison of local heat flux at the upper plate with its single-plate counterpart, $(T_{w2} - T_\infty)/(T_{w1} - T_\infty) = 1$ and 2

In appraising these figures, note should be taken of the positioning of the various curves with respect to the $q/q^* = 1$ line. The latter is the demarcation between augmented or degraded local heat transfer on the upper plate compared with its single-plate counterpart. With the $q/q^* = 1$ line as a reference and from the distinct differences in the curve shapes, it is evident that the results for the intermediate and large interplate spacings are of a different nature from those for small spacings (the $S = 0$ case is taken to be representative of small spacings).

In general, at intermediate and large spacings, q/q^* starts with values well in excess of unity at small x' and decreases with increasing x'. On the other hand, at small spacings (except for large θ_{w2}), the initial values of q/q^* are well below unity and then increase with x'. In all cases, the curves tend toward unity as x' increases.

It is plausible to expect that with increasing distance downstream from the leading edge, the flow and temperature fields adjacent to the upper plate tend to "forget" the existence of the flow approaching the leading edge from below. Therefore, the tendency of q/q^* to approach unity at large x' is entirely reasonable. However, near the leading edge, q may be markedly affected by the approach flow. At large and intermediate spacings, the velocities of approach are sufficiently large so as to enhance the values of q relative to q^*. On the other hand, for small spacings, the preheating of the approach flow by the first plate tends to degrade q. The effect of the preheating is most marked when $\theta_{w2} < 1$. As θ_{w2} increases, the heat transfer degradation decreases, as can be seen by successive examination of the graphs for $\theta_{w2} = 0.5$, 1, and 2 in Figs. 4 and 5.

Development of Temperature and Velocity Profiles. Earlier in the paper, mention was made of the phenomenon of a new boundary layer growing within an already existing boundary layer. This phenomenon will now be illustrated with the aid of temperature and velocity profiles from the numerical solutions. Figures 6(a) and 6(b) respectively display temperature and velocity profiles that are typical of those encountered when a non-zero gap exists between the upper and lower plates (the specific profiles are for $S/L_1 = 1$ and $\theta_{w2} = 1$).

Attention may first be focused on the temperature results of Fig. 6(a). In the inset at the upper right, the temperature distribution in the fluid just upstream of the leading edge of the upper plate (i.e., at $x'/L_1 = 0^-$)is shown.This profile is bell-shaped, as expected. The portion of the profile immediately adjacent to the plate surface, in the range $0 \leq Y \leq 0.1$, is plotted in the main part of the figure. Within the scale of the figure, this portion of the profile is a horizontal line; it is seen to be the base line of the set of curves plotted in the main part of the figure. The other curves of the set represent temperature profiles at a succession of axial stations immediately downstream of the leading edge (note the exceedingly small values of x'/L_1).

From the figure, it is seen that in the first temperature profile (at

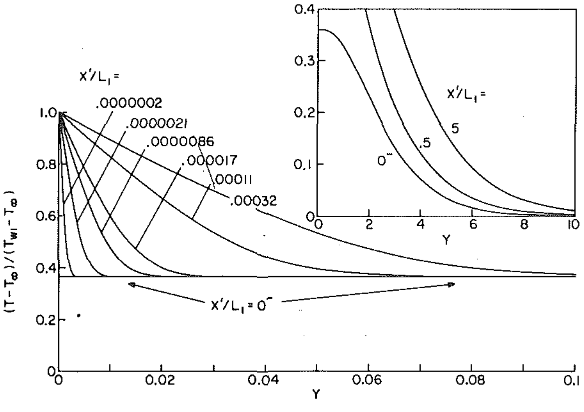

Fig. 6(a) Temperature profiles in the fluid adjacent to the upper plate, $S/L_1 = 1$ and $\theta_{w2} = 1$

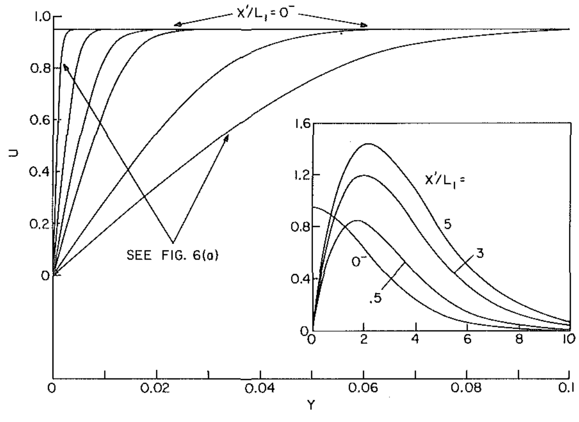

Fig. 6(b) Velocity profiles in the fluid adjacent to the upper plate, $S/L_1 = 1$ and $\theta_{w2} = 1$

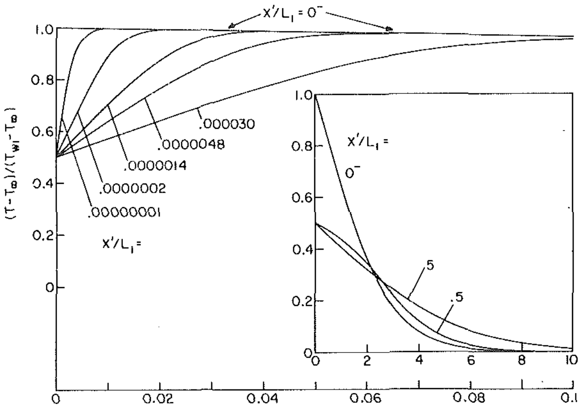

Fig. 7(*a*) Temperature profiles in the fluid downstream of a step decrease in wall temperature, $S/L_1 = 0$ and $\theta_{w2} = 0.5$

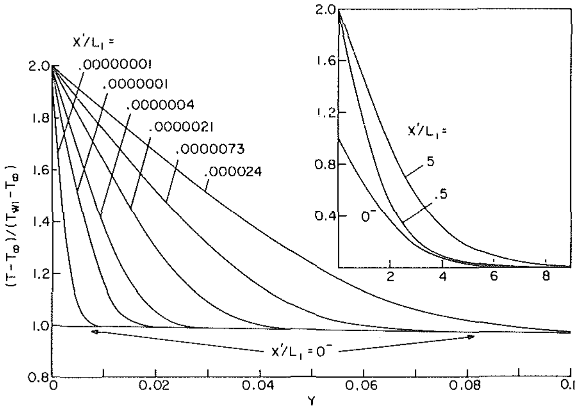

Fig. 7 (*b*) Temperature profiles in the fluid downstream of a step increase in wall temperature, $S/L_1 = 0$ and $\theta_{w2} = 2$

$x'/L_1 = 0.0000002$), θ drops sharply from its value $\theta = 1$ at the wall and then blends into the profile for $x'/L_1 = 0^-$. The second profile drops somewhat less sharply and also blends into the $x'/L_1 = 0^-$ profile, with the blending at a somewhat larger value of Y. This trend continues as the thickness of the new boundary layer increases with increasing x'/L_1. The growth of the new thermal boundary layer within the existing thermal boundary layer is vividly displayed by these profiles.

In the highly restricted range of x'/L_1 dealt with in the main portion of the figure, the new boundary layer does not penetrate very far into the old boundary layer. However, when a larger range of x'/L_1 is considered, as in the inset of Fig. 6(*a*), it is evident that the new boundary layer ultimately engulfs the old one.

The velocity profiles that are the counterparts of the just-discussed temperature profiles are shown in Fig. 6(*b*). The structure of this figure is similar to that of Fig. 6(*a*). The velocity profile at $x'/L_1 = 0^-$ is shown in its entirety in the inset, while the inner region between $Y = 0$ and $Y = 0.1$ is plotted in the main part of the figure, where it appears as a horizontal line at the top. The message conveyed by Fig. 6(*b*) reinforces that of Fig. 6(*a*).

In the limiting case of $S = 0$ (no gap), the response of the boundary layer to a step change of temperature at $x'/L_1 = 0$ is somewhat different from that illustrated in Figs. 6(*a*) and 6(*b*). For one thing, the plate surface is physically continuous, so that there are no dramatic changes in the velocity boundary layer in the neighborhood of $x'/L_1 = 0$. Furthermore, the temperature profile at $x'/L_1 = 0^-$ is not bell-shaped; rather, it has the form characteristic of the conventional natural-convection vertical-plate boundary layer.

Profiles illustrating the thermal boundary layer development downstream of $x'/L_1 = 0$ for the $S = 0$ case are presented in Figs. 7(*a*) and 7(*b*) for $\theta_{w2} = 0.5$ and $\theta_{w2} = 2$, respectively. In the first of these figures, the temperature profile at $x'/L_1 = 0^-$ is shown both in the inset at the right and at the top of the main portion of the figure. Note that in contrast with Fig. 6(*a*), this profile is not horizontal in the range between $Y = 0$ and $Y = 0.1$. This difference reflects the distinction between a bell-shaped symmetric profile and one where a temperature gradient must exist at $Y = 0$ to accommodate the wall heat transfer. Notwithstanding this difference, the development of the new thermal layer within the existing one is similar to that of Fig. 6(*a*). Of particular interest is the temperature profile at $x'/L_1 = 0.5$ shown in the inset. This profile is seen to have an S-shape, reflecting the strong effect of the preheating of the fluid upstream of $x'/L_1 = 0$.

To complete the presentation, attention may be turned to the results of Fig. 7(*b*) for the case of the step increase of temperature at $x'/L_1 = 0$. Here, as in Fig. 7(*a*), the $x'/L_1 = 0^-$ profile is seen to be slightly sloping even in the expanded Y scale of the main part of the figure. The growth of the new thermal boundary layer is as in the previous figures. The inset shows that the downstream temperature profiles are free of inflections, testifying to the fact that the upstream heating does not play a significant role.

Concluding Remarks

The natural convection heat transfer characteristics of the upper plate of a vertical, colinear two-plate array are affected by two attributes of the fluid flow spawned by the lower plate. One of these, the preheating of the fluid, tends to reduce the upper-plate heat transfer. The other, the finite velocity imparted to the fluid, tends to increase the heat transfer. The dominance of one or the other of these factors depends on the relative temperatures of the plates, the size of the interplate gap, and, for the overall heat transfer performance, the relative lengths of the plates.

Prime attention was focused on the overall heat transfer at the upper plate and the relationship to that of an otherwise identical vertical plate, but with the lower plate absent. When the temperatures of the upper and lower plates are the same, the upper-plate heat transfer is less than that of its single-plate counterpart for small interplate separations, with the opposite relationship at larger separations. If the upper-plate temperature is substantially smaller than that of the lower plate, the preheating effect brings about a degradation of the upper-plate heat transfer which is accentuated at small interplate spacings. Indeed, at small spacings and for short upper plates, heat may flow from the fluid to the plate even though $T_{w2} > T_\infty$. When the upper plate is hotter than the lower plate, preheating is unimportant and the velocity-of-approach effect generally enhances the heat transfer, especially at larger interplate spacings.

In general, the overall heat transfer for the upper plate is very sensitive to the presence of the lower plate when the upper plate is relatively short. The sensitivity diminishes as the relative length of the upper plate increases.

With regard to the local heat flux at the upper plate, the influence of the lower plate dies away at sufficiently large distances downstream from the leading edge. However, near the leading edge, the local heat flux is very sensitive to the attributes of the approach flow.

The temperature and velocity profiles illustrate how the boundary layer on the upper plate grows within the already existing boundary layer spawned by the lower plate. In the immediate neighborhood of the leading edge, the new boundary layer does not penetrate very far into the existing boundary layer. With increasing downstream distance, the new boundary layer ultimately engulfs the old one. When the preheating is important, the temperature profiles in the fluid adjacent to the second plate may be inflected (S-shaped).

Acknowledgment

This research was performed under the auspices of the National Science Foundation (grant ENG-7518141 A01) and with support to M. Faghri from the Iranian Ministry of Education. The authors gratefully acknowledge the valuable suggestions of Professor S. V. Patankar. The involvement of Professor T. S. Chen at an early stage of the work is also acknowledged with gratitude.

References

1 Lorenz, L., "Ueber das Leitungsvermögen der Metalle für Wärme und Electricität," *Annalen der Physik und Chemie,* Vol. 13, 1881, pp. 582–606.

2 Ede, A. J., "Advances in Free Convection," in *Advances in Heat Transfer,* Vol. 4, 1967, pp. 1–64.

3 Churchill, S. W. and Chu, H. H. S., "Correlating Equations for Laminar and Turbulent Free Convection from a Vertical Plate," *International Journal of Heat and Mass Transfer,* Vol. 18, 1975, pp. 1323–1329.

4. Churchill, S. W., and Chu, H. H. S., "Correlating Equations for Laminar and Turbulent Free Convection from a Horizontal Cylinder," *International Journal of Heat and Mass Transfer,* Vol. 18, 1975, pp. 1049–1053.

5 Sparrow, E. M., Patankar, S. V., and Abdel-Wahed, R. M., "Development of Wall and Free Plumes Above a Heated Vertical Plate," ASME JOURNAL OF HEAT TRANSFER, Vol. 100, 1978, pp. 184–190.

6 Eckert, E. R. G., and Soehngen, E. E., "Studies on Heat Transfer in Laminar Free Convection with the Zehnder-Mach Interferometer," AF Technical Report 5747, United States Air Force, Air Material Command, Wright-Patterson Air Force Base, Ohio, 1948.

7 Lieberman, J., and Gebhart, B., "Interactions in Natural Convection from an Array of Heated Elements, Experimental," *International Journal of Heat and Mass Transfer,* Vol. 12, 1969, pp. 1385–1396.

8 Marsters, G. F., "Array of Heated Horizontal Cylinders in Natural Convection," *International Journal of Heat and Mass Transfer,* Vol. 15, 1972, pp. 921–933.

9 Hardwick, N. E. and Levy, E. K., "Study of the Laminar Free-Convection Wake Above an Isothermal Vertical Plate," ASME JOURNAL OF HEAT TRANSFER, Vol. 95, 1973, pp. 289–294.

10 Kelleher, M., "Free Convection from a Vertical Plate with Discontinuous Wall Temperature," ASME JOURNAL OF HEAT TRANSFER, Vol. 93, 1971, pp. 349–356.

11 Yang, K. T., and Jerger, E. W., "First-Order Perturbations of Laminar Free-Convection Boundary Layers on a Vertical Plate," ASME JOURNAL OF HEAT TRANSFER, Vol. 86, 1964, pp. 107–115.

12 Patankar, S. V., and Spalding, D. B., *Heat and Mass Transfer in Boundary Layers,* Second ed., Intertext Books, London, 1970.

13 Eckert, E. R. G., and Drake, R. M., Jr., *Heat and Mass Transfer,* McGraw-Hill, New York, 1959.

R. Anderson
A. Bejan
Assoc. Mem. ASME

Department of Mechanical Engineering,
University of Colorado,
Boulder, Colo. 80309

Natural Convection on Both Sides of a Vertical Wall Separating Fluids at Different Temperatures

This paper describes an analytical study of laminar natural convection on both sides of a vertical conducting wall of finite height separating two semi-infinite fluid reservoirs of different temperatures. The countercurrent boundary layer flow formed on the two sides is illustrated via representative streamlines, temperature and heat flux distributions. The net heat transfer between reservoirs is reported for the general case in which the wall thermal resistance is not negligible relative to the overall reservoir-to-reservoir thermal resistance.

Introduction

The engineering importance of heat transfer by natural convection is widely recognized. For example, in the area of energy conservation in buildings natural convection is often responsible for prohibitively large heat leaks to the environment. This and many other applications have stimulated a strong interest in the phenomenon, reflected in an impressive volume of research at the fundamental and applied level.

A central natural convection geometry in many applications is the transfer of heat across a vertical wall separating two semi-infinite fluid reservoirs at different temperatures (see Fig. 1). This problem is of fundamental importance for a variety of reasons. From the insulation engineering point of view, it is important to know the net heat transfer rate across solid walls and windows separating a warm room from a colder environment. From the point of view of fundamental research in heat transfer and fluid mechanics, it is important to understand the interaction of two convective systems coupled across a partially conducting wall.

In spite of the importance of coupled flows, the existing work on natural convection is centered on the study of surfaces with specified heat flux or temperature distributions. We are familiar with only a few examples which allow the heat flux and temperature distribution to be determined by the interaction between adjacent boundary layers [1, 2]. Recently, the first author developed an approximate solution based on the hypothesis that the wall heat flux is uniform [3]. This analysis is outlined in the Appendix. The only other attempt to analyze the configuration shown in Fig. 1 appears to be due to Lock and Ko who reported a numerical solution for heat transfer valid in the limit where the solid wall thermal resistance is negligible [4].

Our objective in this paper is to present an analytical solution for the problem of two countercurrent free convective flow fields separated by a vertical plate with a wide range of conductive resistance. The great advantage of an analytical approach is that the parametric dependence of the heat transfer mechanism is considerably more visible than in a numerical solution. To our knowledge, the present report contains the only analysis and results applicable to situations in which the solid wall thermal resistance is not negligible relative to the two boundary layer resistances formed on either side of the wall.

Mathematical Formulation

In dimensionless form, the equations expressing conservation of mass, momentum and energy for each boundary layer shown in Fig. 1 are

$$\frac{\partial u}{\partial x} + \frac{\partial v}{\partial y} = 0 \tag{1}$$

$$\frac{1}{\mathrm{Pr}} \frac{\partial}{\partial y}\left(u \frac{\partial u}{\partial x} + v \frac{\partial u}{\partial y}\right) = \frac{\partial t}{\partial y} + \frac{\partial^3 u}{\partial y^3} \tag{2}$$

$$u \frac{\partial t}{\partial x} + v \frac{\partial t}{\partial y} = \frac{\partial^2 t}{\partial y^2} \tag{3}$$

$$x = \frac{X}{H} \tag{4}$$

$$y = Y/\ell \tag{5}$$

$$t = [T - (T_H + T_C)/2]/(T_H - T_C) \tag{6}$$

The height of the wall, H, is used as length scale in the vertical direction. The horizontal length scale of the boundary layers is ℓ, while T_H and T_C are the dimensional temperatures of the hot and cold fluids. It can be shown via dimensional analysis that [5]

$$\ell = [\nu \alpha H / \beta g \Delta T]^{1/4} \tag{7}$$

while the vertical velocity scale is $\alpha H/\ell^2$

In writing equations (1–3) the terms involving viscous dissipation and gravity work have been ignored. It was assumed that the Boussinesq approximation applies, i.e., that the bouyancy force is proportional to the local temperature difference. The dependence of all other physical properties upon temperature was neglected.

The appropriate boundary conditions in the horizontal (y) direction are

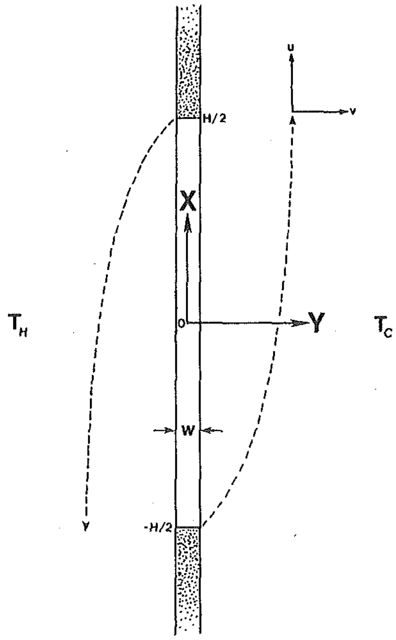

Fig. 1 Schematic of vertical conducting wall with natural convection boundary layers on either side

---

Contributed by the Heat Transfer Division for publication in the JOURNAL OF HEAT TRANSFER. Manuscript received by the Heat Transfer Division December 3, 1979.

$$u = v = 0 \text{ at } y = \pm w/2 \tag{8}$$

$$t = \mp 1/2 \text{ at } y = \pm \infty \tag{9}$$

In addition, at any given vertical position (x) the heat flux entering the left face of the plate must equal the flux leaving the right face,

$$\left(\frac{\partial t}{\partial y}\right)_{y=-w/2,x} = \left(\frac{\partial t}{\partial y}\right)_{y=w/2,x} = \frac{k_w}{k_f}\left(\frac{\partial t}{\partial y}\right)_{\text{wall}} \tag{10}$$

An important observation is that the governing equations and boundary conditions (1–10) remain unchanged after simultaneously changing the sign of u,v,x,y and t. Therefore, the temperature and velocity fields are centro-symmetric with respect to the origin of the x–y coordinate system shown in Fig. 1,

$$u(x,y) = -u(-x,-y), \tag{11}$$

$$v(x,y) = -v(-x,-y) \tag{12}$$

$$t(x,y) = -t(-x,-y). \tag{13}$$

Equations (1–3) are difficult to treat analytically due to the nonlinearity in the convection part of the energy equation. One way to circumvent this difficulty is to linearize the energy equation according to the modified Oseen technique developed by Gill [5]. In a recent note Bejan [6] showed that Gill's technique produces excellent overall heat transfer results. Linearization is accomplished by regarding v and $\partial t/\partial x$ in equation (3) as unknown functions of altitude, $\bar{v}(x)$ and $\bar{t}'(x)$.

Consider the limit Pr → ∞, in which the boundary layer equations become

$$\partial u/\partial x + \partial v/\partial y = 0 \tag{14}$$

$$\partial t/\partial y + \partial^3 u/\partial y^3 = 0 \tag{15}$$

$$(\bar{t}')u + (\bar{v})\frac{\partial t}{\partial y} = \frac{\partial^2 t}{\partial y^2} \tag{16}$$

As shown in the Appendix and Fig. 8, the Pr → ∞ approximation is acceptable in the case of fluids with Prandtl number of order one or greater. Eliminating t between equations (15) and (16) leads to a fourth order ordinary differential equation in $u(x,y)$. The solution to this equation has the general form

$$u = \sum_{n=1}^{4} A_n(x)e^{\lambda_n(x)y} \tag{17}$$

where λ_n are the roots of the characteristic equation

$$\lambda^3(\lambda - \bar{v}) + \bar{t}' = 0 \tag{18}$$

Applying the boundary conditions and symmetry properties, equations (8–13), we obtain

$$u_C = \frac{-(t_0 - Q + 1/2)}{(\lambda_1{}^2 - \lambda_2{}^2)}\left(e^{\lambda_1(y-w/2)} - e^{\lambda_2(y-w/2)}\right) \tag{19}$$

$$t_C = \frac{(t_0 - Q + 1/2)}{(\lambda_1{}^2 - \lambda_2{}^2)}\left(\lambda_1{}^2e^{\lambda_1(y-w/2)} - \lambda_2{}^2e^{\lambda_2(y-w/2)}\right) - 1/2 \tag{20}$$

$$u_H = \frac{-(t_0 + Q - 1/2)}{(\xi_1{}^2 - \xi_2{}^2)}\left(e^{-\xi_1(y+w/2)} - e^{-\xi_2(y+w/2)}\right) \tag{21}$$

$$t_H = \frac{(t_0 + Q - 1/2)}{(\xi_1{}^2 - \xi_2{}^2)}\left(\xi_1{}^2e^{-\xi_1(y+w/2)} - \xi_2{}^2e^{-\xi_2(y+w/2)}\right) + 1/2 \tag{22}$$

In the above equations $t_0(x)$ is an unknown function representing the temperature distribution along the midplane $y = 0$. For reasons discussed in detail by Gill [5], $\lambda_{1,2}$ are the roots with negative real parts. In addition

$$\xi_{1,2} = -\lambda_{1,2}(-x) \tag{23}$$

and

$$Q = \left|\frac{w}{2}\left(\frac{\partial t}{\partial y}\right)_{\text{wall}}\right|. \tag{24}$$

Since $\lambda_{1,2}$ and $\xi_{1,2}$ are all solutions of equation (18) we can write

$$(\lambda - \lambda_1)(\lambda - \lambda_2)(\lambda + \xi_1)(\lambda + \xi_2) = 0 \tag{25}$$

Expanding result (25) and comparing it with equation (18) we obtain

$$\bar{v}(x) = \lambda_1 + \lambda_2 - (\xi_1 + \xi_2) \tag{26}$$

$$\bar{t}'(x) = (\lambda_1\lambda_2)(\xi_1\xi_2) \tag{27}$$

$$\xi_1\xi_2 + \lambda_1\lambda_2 = (\lambda_1 + \lambda_2)(\xi_1 + \xi_2) \tag{28}$$

$$(\lambda_1\lambda_2)(\xi_1 + \xi_2) = (\xi_1\xi_2)(\lambda_1 + \lambda_2) \tag{29}$$

The solution is simplified if we define two new functions of x, p(even) and q(odd),

$$p = \lambda_1 + \lambda_2 + \xi_1 + \xi_2 \tag{30}$$

$$q = \frac{\bar{v}}{p} \tag{31}$$

Combining these definitions with equations (26–29) allows expressions for $\lambda_{1,2}$ and $\xi_{1,2}$ in terms of the unknown functions $p(x)$ and $q(x)$

$$\lambda_1 + \lambda_2 = 1/2\, p(1 + q) \tag{32}$$

$$\xi_1 + \xi_2 = 1/2\, p(1 - q) \tag{33}$$

$$\lambda_1\lambda_2 = 1/8\, p^2(1 - q^2)(1 + q) \tag{34}$$

$$\xi_1\xi_2 = 1/8\, p^2(1 - q^2)(1 - q) \tag{35}$$

$$\lambda_{1,2} = 1/4\, p(1 + q)[1 \pm i\sqrt{1 - 2q}] \tag{36}$$

$$\xi_{1,2} = 1/4\, p\,(1 - q)[1 \pm i\sqrt{2q + 1}] \tag{37}$$

Functions p and q can be determined from the heat flux continuity constraint, equation (10), and the condition that the linearized solution (19–22) must satisfy the energy equation in intergral form

$$\frac{d}{dx}\left(\int_0^\infty u t dy\right) + |vt|_0^\infty = \left|\frac{\partial t}{\partial y}\right|_0^\infty \tag{38}$$

As parameter w approaches zero, the vertical wall becomes a thin membrane whose face-to-face temperature difference is negligible compared with the overall ΔT between the fluid reservoirs. Substituting $w = 0$ into equations (19–22) and utilizing the heat flux constraint (10) we find

$$\frac{(1/2 - t_0)[(\xi_1 + \xi_2)^2 - \xi_1\xi_2]}{(\xi_1 + \xi_2)} = \frac{(1/2 + t_0)[(\lambda_1 + \lambda_2)^2 - \lambda_1\lambda_2]}{(\lambda_1 + \lambda_2)} \tag{39}$$

Nomenclature

Bi_x = wall local Biot number, h_xW/k_w
g = gravitational acceleration
Gr = Grashof number, Ra/Pr
H = wall (window) height
K = constant of integration
ℓ = horizontal length scale, equation (7)
Nu = Nusselt number, hH/k_f
p = even function of x, equation (30)
Pr = Prandtl number
q = odd function of x, equation (31)
Q = wall temperature drop, equation (24), $\mathrm{Bi}_x/2$

Ra = Rayleigh number, $g\beta H^3\Delta T/(\alpha\nu)$
T = temperature
u = vertical velocity
v = horizontal velocity
W = wall thickness
X = vertical position
Y = horizontal position
α = thermal diffusivity
β = coefficient of thermal expansion
ν = kinematic viscosity
ψ = streamfunction
ω = wall parameter, equation (53)

Subscripts

C = ambient conditions on the cold (right) side of the plate
f = fluid
H = ambient conditions on the hot (left) side of the plate
w = wall
0 = conditions at midplane of plate
∞ = ambient conditions on either side of plate

The integral energy constraint (38) applied to each side of the membrane yields

$$\frac{d}{dx}\left[\frac{(t_1 + ½)^2}{(\lambda_1 + \lambda_2)^3}\right] = \frac{2(t_0 + ½)(\lambda_1^3 - \lambda_2^3)}{(\lambda_1^2 - \lambda_2^2)} \tag{40}$$

$$\frac{d}{dx}\left[\frac{(t_0 - ½)^2}{(\xi_1 + \xi_2)^3}\right] = \frac{2(t_0 - ½)(\xi_1^3 - \xi_2^3)}{(\xi_1^2 - \xi_2^2)} \tag{41}$$

In terms of p and q, equation (39) can be written as

$$t_0 = -q/(1 + q^2). \tag{42}$$

Finally, writing equations (40) and (41) in terms of p and q, adding side by side and integrating the result once yields

$$p = [(1 - q)^7 + (1 + q)^7]^{1/3}/[K(1 - q^2)(1 + q^2)^{2/3}] \tag{43}$$

Parameter K appearing in equation (43) is an arbitrary constant of integration. Substitution of equation (43) into equation (40) produces a first order ordinary differential equation for the unknown function $x(q)$,

$$\frac{dx}{dq} = [-112\,K^4(1 + q^2)^{5/3}(1 - q^2)^5]/[(1 - q)^7 + (1 + q)^7]^{7/3}. \tag{44}$$

The boundary conditions necessary for solving (44) are based on the approximation that the vertical velocity and horizontal temperature gradient are zero at the beginning of the two boundary layers.

$$u = 0 \text{ at } 0 \leq y \leq \infty, x = -½ \tag{45}$$

$$u = 0 \text{ at } -\infty \leq y \leq 0, x = +½ \tag{46}$$

$$\frac{\partial t}{\partial y} = 0 \text{ at } y = 0, x = \pm ½ \tag{47}$$

Condition (45) can be satisfied if $t_0 = -½$ or, $\lambda_{1,2} \rightarrow \infty$ when $x = -½$. This is equivalent to setting $q = 1$ in expression (42).

$$q = +1, t_0 = -½ \text{ at } x = -½ \tag{48}$$

Applying similar arguments to the descending boundary layer in the hot fluid leads to the result

$$q = -1, t_0 = ½ \text{ at } x = ½ \tag{49}$$

Since t_0 is an odd function of q in (42) it is also an odd function of x, hence

$$t_0 = 0, q = 0 \text{ at } x = 0. \tag{50}$$

Wall with Finite Thickness

A procedure similar to that used for the thin membrane was also applied to the more general case of finite w. Substitution of equations (19–22) into equation (10) yields

$$t_0 = -q(1 - 2Q)/(1 + q^2) \tag{51}$$

$$Q = -\omega p(1 - q^2)^2/[16(1 + q^2) - 2\omega p(1 - q^2)^2] \tag{52}$$

$$\omega = \frac{W}{H}\frac{k_f}{k_w}\,\mathrm{Ra}^{1/4}. \tag{53}$$

As shown in the Nomenclature, $2Q$ is the wall local Biot number, Bi_x. When the energy integral (38) is applied to the cold side one finds

$$\frac{d}{dx}\{(t_0 - Q + ½)^2/[p^3(1 + q)^3]\} = -Q/2\omega. \tag{54}$$

Adding this result to the corresponding energy integral for the hot side and integrating once produces

$$\frac{(1 - q)^7 + (1 + q)^7}{[4(1 + q^2) - \frac{\omega}{2}p(1 - q^2)^2]^2 p^3(1 - q^2)^3} = \frac{K^3}{16} \tag{55}$$

where K is a constant of integration. The value of this constant was determined by integrating equation (54) numerically, trying different values for K until conditions (48–50) were satisfied. The resulting function $K(\omega)$ is listed in Table 1. An important value in this table is $K(0) = -0.6362$ which corresponds to the thin wall limit; this value can also be obtained by integrating equation (44) subject to conditions (48–50).

Results

Figures 2(a,b) illustrate a set of representative streamlines and isotherms obtained in the thin wall limit ($\omega = 0$). The streamfunction ψ was defined in the usual way by writing $u = \partial\psi/\partial y$ and $v = -\partial\psi/\partial x$. As in Fig. 1, the warm reservoir is on the left side of the picture. The streamlines reveal a descending boundary layer on the warm side coupled with a centrosymmetric ascending boundary layer on the cold side. In the vicinity of the solid wall ($y = 0$) the isotherms are nearly parallel, particularly in the central region. This feature implies that the heat flux is nearly constant along the wall, as shown by the curve $\omega = 0$ in Fig. 6. The slight tilt of the isotherms indicates that the boundary layers transfer heat from the upper left to the lower right across the thin wall.

The wall temperature distribution resulting from the coupled flows is summarized in Figs. 3 and 4. In Fig. 3 we plotted the temperature distribution in the mid-plane ($y = 0$) of the vertical wall, for a series

Table 1 Constant K and overall heat transfer rate $\mathrm{Nu/Ra}^{1/4}$ as a function of ω

ω	K	$\lvert\mathrm{Nu/Ra}^{1/4}\rvert$
0	−0.6362	0.2575
0.2	−0.6232	0.2422
0.4	−0.6113	0.2285
0.6	−0.6004	0.2164
0.8	−0.5903	0.2057
1.0	−0.5809	0.1961
2.0	−0.5422	0.1594
4.0	−0.4891	0.1170
6.0	−0.4529	0.0929
8.0	−0.4259	0.0773
10.0	−0.4047	0.0663
20.0	−0.3390	0.0389

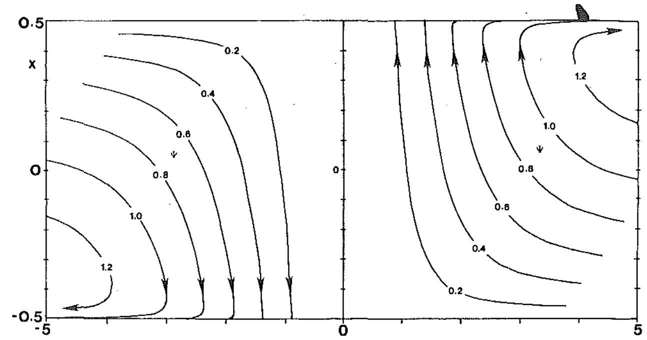

Fig. 2(a) Streamline pattern

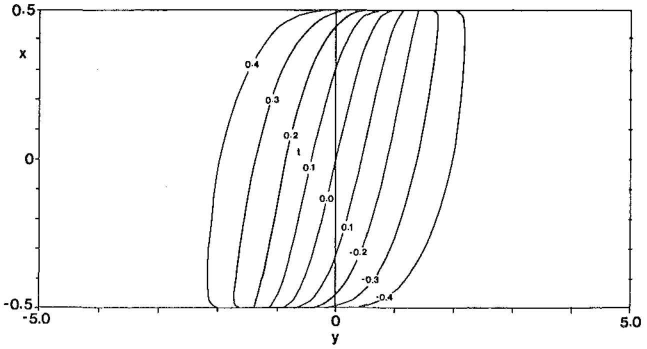

Fig. 2(b) Temperature field, in the thin wall limit ($\omega = 0$)

Fig. 2

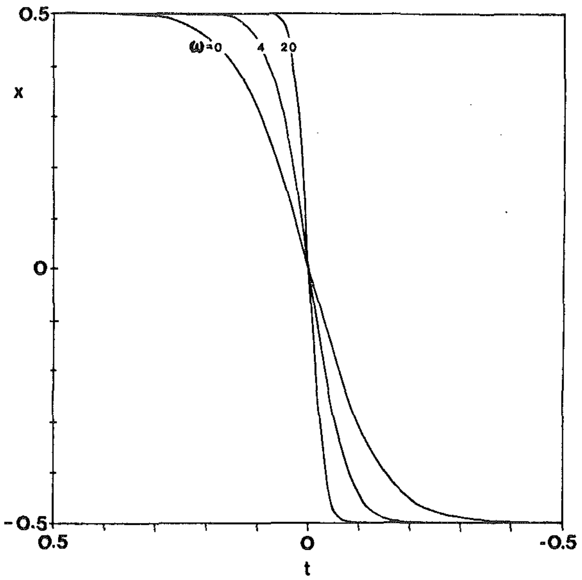

Fig. 3 Temperature distribution in mid-plane ($y = 0$)

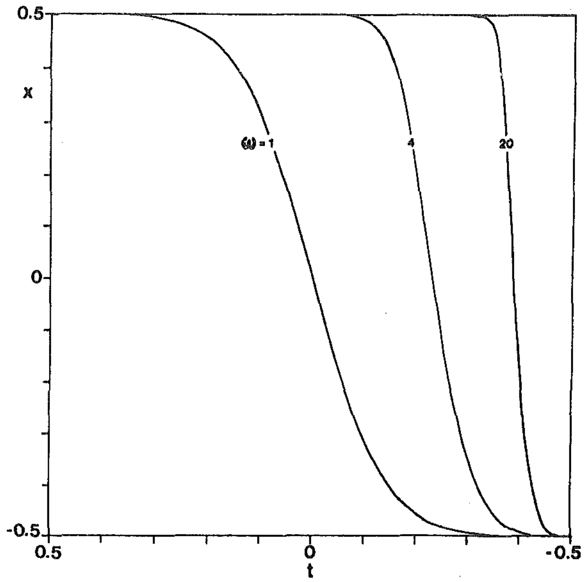

Fig. 4 Temperature distribution over the solid surface facing the cold reservoir

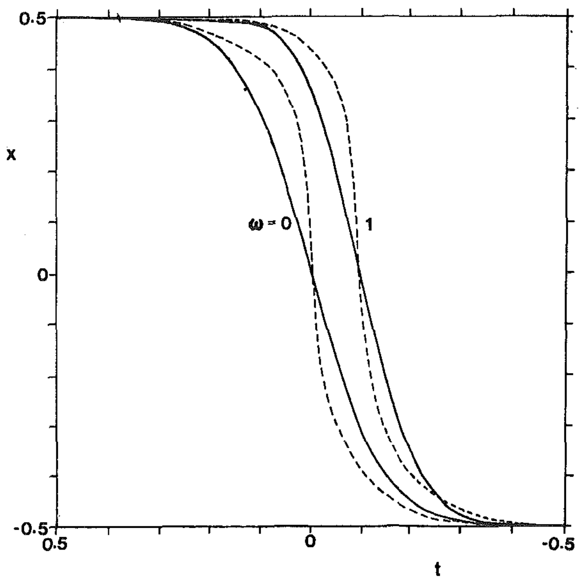

Fig. 5 Comparison of the present result (——) for surface temperature against the numerical solution of Lock and Ko (- - -)

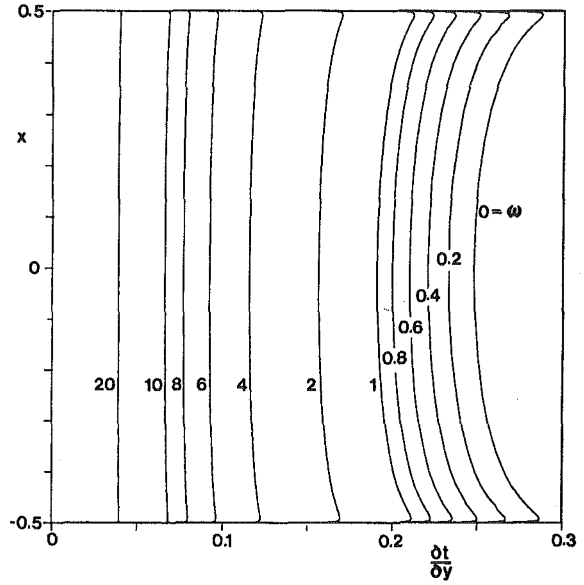

Fig. 6 The distribution of heat flux along the vertical wall

of values of thickness parameter ω. The mid-plane temperature becomes more and more uniform as the wall thermal resistance increases, i.e., as the thermal contact between the two boundary layers deteriorates. Figure 4 shows the corresponding temperature distribution on the surface facing the cold reservoir; the results for the surface facing the warm reservoir are readily obtained by rotating Fig. 4 by 180 deg. It is clear that as the wall becomes thicker the surface-to-surface temperature difference increases to the point where, for $\omega = 20$, it is roughly 80 percent of the reservoir-to-reservoir temperature difference.

In their numerical study of the same phenomenon, Lock and Ko [4] graphed results for Pr = 0.72 and a limited range of wall thickness, ω. In Fig. 5 we compare our results for cold side surface temperature with the results of Lock and Ko, for $\omega = 0$ and $\omega = 1$. The two solutions agree in an average sense, although the numerical solution [4] describes a relatively more uniform surface temperature in the central region of the plate. The constant flux solution developed in the Appendix predicts that the surface temperature distribution will become more nearly isothermal as Pr → 0. Hence, the discrepancy between the two sets of curves on Fig. 5 is attributed to the different Prandtl numbers used in each investigation.

The wall heat flux is presented in Fig. 6 as the horizontal temperature gradient $(\partial t/\partial y)_{y=\omega/2}$. The heat flux decreases as the thickness parameter ω increases. This effect is to be expected since a thicker wall means more effective insulation between the two reservoirs.

Regardless of ω, the wall heat flux is nearly uniform over most of the height H. This observation is the basis for the constant heat flux analysis [3] summarized in the Appendix. In this analysis the wall heat flux is assumed independent of vertical position x and the natural convection problem of Fig. 1 is reconstructed by piecing together two Sparrow and Gregg [7] solutions for convection along a vertical constant heat flux surface, via pure conduction through a wall of finite thickness. The cold surface temperature distribution predicted by the constant heat flux analysis is presented in Fig. 7 vis-a-vis results based on the analysis developed in this paper. The agreement is excellent expecially as ω increases, which is the limit where the constant heat flux assumption is more appropriate.

Overall Heat Transfer

Defining the heat transfer coefficient in terms of the average heat flux through the wall and the total temperature difference between fluid reservoirs

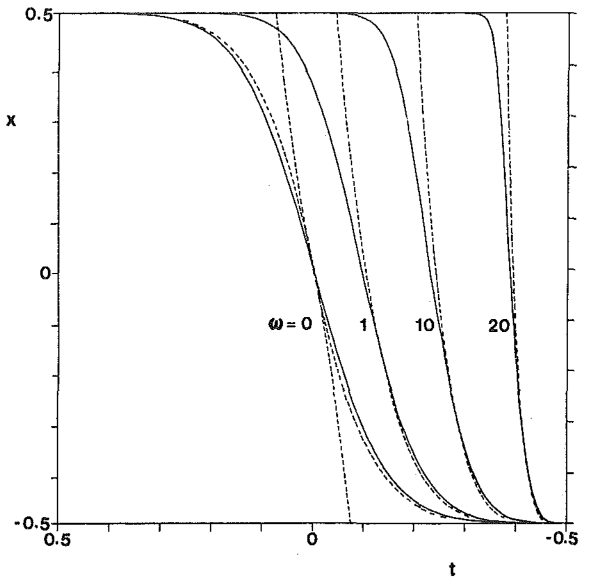

Fig. 7 Comparison of the present result for cold surface temperature (——) against the result based on the constant heat flux approximation (- - -)

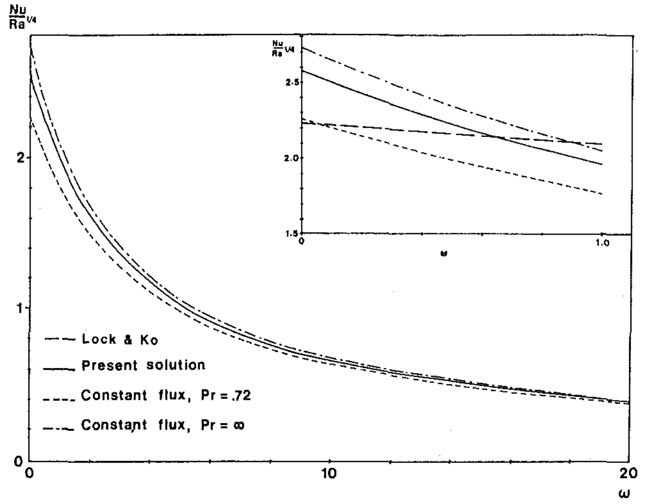

Fig. 8 Dependence of total heat transfer rate on wall resistance parameter ω

$$h = \bar{q}/\Delta T = \frac{k_f}{\Delta T}\overline{\left(\frac{\partial T}{\partial Y}\right)}_{y=w/2} = \frac{k_f}{\ell}\overline{\left(\frac{\partial t}{\partial y}\right)}_{y=w/2} \tag{56}$$

the Nusselt number can be written as

$$\mathrm{Nu} = \frac{Hh}{k_f} = \frac{H}{\ell}\overline{\left(\frac{\partial t}{\partial y}\right)}_{y=w/2} = \mathrm{Ra}^{1/4}\overline{\left(\frac{\partial t}{\partial y}\right)}_{y=w/2}. \tag{57}$$

Figure 8 shows the Nusselt number predicted by our solution and the estimate based upon the constant flux approximation for Pr = 0.72 and Pr → ∞. The agreement between the two solutions is excellent over the entire ω range of interest. The ratio $\mathrm{Nu}/\mathrm{Ra}^{1/4}$ decreases substantially as the wall thickness increases from 0 to 10. Recalling that the present solution was obtained in the limit Pr → ∞ and that the constant heat flux result is Pr dependent, Fig. 8 demonstrates that the overall heat transfer rate is a weak function of Pr provided Pr is of order one or greater. Representative values for $\mathrm{Nu}/\mathrm{Ra}^{1/4}$ for the present solution are shown in Table 1.

Overall heat transfer calculations in the range examined by Lock and Ko are presented in the inset of Fig. 8. The numerical result [4] predicts a weaker dependence on wall thickness than either the present solution or the constant heat flux analysis.

Concluding Remarks

In this paper we analyzed the fundamentals of laminar free convective heat transfer across a vertical wall sandwiched between two fluid reservoirs at different temperatures. In order to gain some insight into the fluid mechanics and basic heat transfer mechanism we constructed an analytical solution based on the Oseen linearization approach without making assumptions about the heat flux or temperature distribution at the wall. We were able to illustrate streamlines and isotherms for the flow field. We also presented results for the distribution of temperature and heat flux along the vertical wall. The effect of increasing wall thermal resistance was documented.

The engineering importance of this study is that it reports means for estimating the reservoir-to-reservoir heat transfer for cases in which the thermal resistance of the wall is not negligible. Prior to our study, the heat transfer literature contained information on overall heat transfer only in the limited range $0 < \omega < 1$. Another conclusion of our study is that the vertical wall can be approximated as a constant flux surface and that the overall heat transfer rate is relatively independent of Prandtl number, for Pr of order 1 or larger.

Acknowledgment

This work was supported in part by NSF Grant ENG 78-20957. The authors thank Professors B. Gebhart and J. C. Mollendorf of the State University of New York at Buffalo, for their comments and for pointing out the existence of reference [4].

APPENDIX

Constant Heat Flux Analysis

Sparrow and Gregg [7] report the following wall temperature distribution for a constant flux surface

$$T_w - T_\infty = f(\mathrm{Pr})\left(\frac{q}{k_f}\right)^{4/5} X^{1/5}\left[\frac{g\beta}{\nu^2}\right]^{-1/5} \tag{A1}$$

where T_w and T_∞ are the dimensional temperatures at the wall and at infinity, and X is the distance measured from the start of the boundary layer. The temperature at $X = H/2$ on the surface facing the cold fluid is

$$\frac{T_H + T_C}{2} + \frac{W}{2}\frac{k_f}{k_w}\overline{\left(\frac{\partial T}{\partial Y}\right)}_{Y=W/2}. \tag{A2}$$

Substituting this for T_w in (A1) and rearranging we find

$$q^{4/5} = \frac{\Delta T}{2}\left(1 + \omega\overline{\left(\frac{\partial t}{\partial y}\right)}_{y=w/2}\right)({k_f}^{4/5})\left(\frac{g\beta}{\nu^2}\right)^{1/5} \Big/ [(H/2)^{1/5} f(\mathrm{Pr})] \tag{A3}$$

which, in combination with (A1), yields

$$\frac{T_w - T_\infty}{\Delta T} = \frac{1}{2}\left(1 + \omega\overline{\left(\frac{\partial t}{\partial y}\right)}_{y=w/2}\right)\left(\frac{X}{H/2}\right)^{1/5} \tag{A4}$$

Defining h as $q/\Delta T$, the Nusselt number is

$$\mathrm{Nu} = \frac{hH}{k_f} = \frac{1}{2[f(\mathrm{Pr})]^{5/4}}\mathrm{Gr}^{1/4}\left(1 + \omega\overline{\left(\frac{\partial t}{\partial y}\right)}_{y=w/2}\right)^{5/4} \tag{A5}$$

Sparrow and Gregg [7] report a solution for $f(\mathrm{Pr})$ derived using the Karman-Pohlhausen method,

$$\left(\frac{1}{f(\mathrm{Pr})}\right)^{5/4} = \frac{2^{5/4}\,\mathrm{Pr}^{1/2}}{(360)^{1/4}\,(0.8 + \mathrm{Pr})^{1/4}} \tag{A6}$$

Substituting now (A6) into (A5) we obtain

$$\mathrm{Nu} = \left[\frac{\mathrm{Pr}}{0.8 + \mathrm{Pr}}\right]^{1/4}\frac{\mathrm{Ra}^{1/4}}{(180)^{1/4}}\left[1 + \omega\overline{\left(\frac{\partial t}{\partial y}\right)}_{y=w/2}\right]^{5/4}. \tag{A7}$$

Since

$$h = \frac{k_f}{\Delta T}\overline{\left(\frac{\partial T}{\partial Y}\right)} = \frac{k_f}{\ell}\overline{\left(\frac{\partial t}{\partial y}\right)}_{y=w/2} \tag{A8}$$

Table A1 $Nu/Ra^{1/4}$ for constant heat flux solution

	$Nu/Ra^{1/4}$	
ω	$Pr = 0.72$	$Pr = \infty$
0	0.226	0.273
0.2	0.214	0.256
0.4	0.203	0.241
0.6	0.194	0.227
0.8	0.185	0.215
1.0	0.177	0.205
2.0	0.147	0.165
4.0	0.110	0.120
6.0	0.088	0.095
8.0	0.074	0.079
10.0	0.064	0.067
20.0	0.038	0.039

we can write

$$Nu = Ra^{1/4}\overline{\left(\frac{\partial t}{\partial y}\right)}_{y=w/2}. \tag{A9}$$

Combining (A9) and (A7) results in

$$\overline{\left(\frac{\partial t}{\partial y}\right)}_{y=w/2} = \left(1+\omega\overline{\left(\frac{\partial t}{\partial y}\right)}_{y=w/2}\right)^{5/4}\left[\frac{Pr}{(0.8+Pr)(180)}\right]^{1/4} \tag{A10}$$

Equation (A10) was solved numerically to establish the relationship between $\overline{\partial t/\partial y}_{y=w/2}$ and ω. Temperature distributions for the constant flux approximation are shown in Fig. 7 and the variation of $Nu/Ra^{1/4}$ with ω is shown in Fig. 8. Values for $(\overline{\partial t/\partial y})$ are shown in Table A1. Note that $|\partial t/\partial y|$ decreases with Pr. Equation (A4) implies a wall temperature distribution which is more isothermal in the central region of the plate for small values of Pr.

References

1 Kelleher, M. D., and Yang, K. T., "A Steady Conjugate Heat Transfer Problem with Conduction and Free Convection," *Applied Science Research*, Vol. 17, 1967, pp. 249–269.

2 Lock, G. S. H., and Gunn, J. C., "Laminar Free Convection from a Downward-Projecting Fin," ASME JOURNAL OF HEAT TRANSFER, Vol. 90, No. 1, Feb. 1968, pp. 63–70.

3 Anderson, R., "Heat Transfer through a Thin Membrane Bounded by Fluids with Different Temperatures," term paper, course M.E. 563, (M. C. Branch and D. R. Kassoy, instructors) University of Colorado, May 16, 1979.

4 Lock, G. S. H., and Ko, R. S., "Coupling through a Wall between Two Free Convective Systems," *International Journal of Heat and Mass Transfer*, Vol. 16, 1973, pp. 2087–2096.

5 Gill, A. E., "The Boundary-Layer Regime for Convection in a Rectangular Cavity," *Journal of Fluid Mechanics*, Vol. 26, 1966, pp. 515–536.

6 Bejan, A., "Note on Gill's Solution for Free Convection in a Vertical Enclosure," *Journal of Fluid Mechanics*, Vol. 90, 1979, pp. 561–568.

7 Sparrow, E. M., and Gregg, J. L., "Laminar Free Convection for a Vertical Surface with Uniform Surface Heat Flux, *Trans ASME*, Vol. 78, 1956, pp. 435–440.

Onset of Natural Convection from a Suddenly Heated Horizontal Cylinder

J. R. Parsons, Jr.
Assistant Professor,
Department of Mechanical Engineering,
University of Tennessee,
Knoxville, Tenn.

J. C. Mulligan
Professor,
Department of Mechanical and Aerospace Engineering,
North Carolina State University,
Raleigh, NC 27650

A study of the onset of transient natural convection from a suddenly heated, horizontal cylinder of finite diameter is presented. The termination of the initial conductive and "locally" convective heat transfer regime which precedes the onset of global natural convection is treated as a thermal stability phenomenon. An analysis is presented wherein the effects of finite cylinder diameter, cylinder heat capacity, and cylinder thermal conductivity are included in calculations of the convective delay time. A simple experimental apparatus is described and data presented. The thermal stability analysis is confirmed experimentally and data is presented which indicates localized natural convection prior to global motion.

Introduction

There is a large body of transient natural convection literature concerned with problems involving vertical elements. In these cases, the transient following a step change in wall temperature or heat flux is known to consist of three relatively distinct regimes. The initial regime is characterized by pure conduction. Then fluid motion begins as the diffusion of heat from the body establishes variations in the density field. Finally, the convection currents become established and dominate the heat transfer.

Few studies have been carried out which attempt to define the typical characteristics of the transient free convection from horizontal cylinders, spheres, and other bluff geometries. Only three experimental investigations, for example, have been performed which deal directly with the transient free convection from a horizontal cylinder. These investigations of Ostroumov [1], Vest and Lawson [2], and Parsons and Mulligan [3] have dealt with the phenomena of heat transfer overshoot and convective delay for the case of suddenly heated fine wires. In the work of Ostroumov, an optical technique was used to observe the transient pattern of the temperature field around a fine wire, and a resistance bridge was used to measure the actual temperature response of the wire. A delay in the convective motion was observed optically in that the isotherms around the wire appeared to remain approximately concentric for a certain time before they were distorted by convective motion. This "delay time" was empirically correlated against the power input to the wire. A global type theory for predicting this delay time was then sketched wherein a certain volume of liquid, characterized by the penetration depth of the temperature field, must be heated until its buoyancy overcomes the viscosity of the surrounding liquid at which point it breaks away from the wire. This development, however, was left incomplete. Vest and Lawson went further by actually formulating this concept for the prediction of the delay time based on the hypothesis that the governing mechanism is that of thermal stability. An analogy was drawn with the classical Bénard problem of a fluid layer heated from below, with the conduction regime breaking down at a critical Rayleigh number defined on the basis of temperature penetration depth. Excellent agreement was obtained with their optically observed delays.

The stability theory was also confirmed by the authors [3] for the fine wire case using actual wire temperature versus time measurements and a comparison with an analytical conduction solution. It was also observed that some modifications of the theory would allow an extension to other important applications. Notably, the theory as developed for fine-wire work has the severe limitation of only being applicable in the case of small diameter wires with essentially infinite thermal conductivity and negligible thermal capacity, conditions seldom met in real physical situations. The primary purpose of the present work is to present an extension of the stability theory for the more general case of finite diameter cylinders with general heat transfer properties and to present the results of an experimental verification of the extended theory.

Theory

When a horizontal cylinder is subjected to sudden constant heating, the heat transfer to the surrounding medium is initially by pure conduction. The thermal stability hypothesis is that the conduction regime breaks down and global convective motion begins when the conduction temperature field penetrates to a certain critical depth. This concept, as applied here, pertains strictly to the flow conditions occurring at the top of the cylinder and presumes no motion of the fluid for a certain period of time.

While there is considerable experimental evidence to support this lack of global motion for a fine wire, a consideration of the physical situation for a cylinder of finite diameter suggests that on the sides of the cylinder the fluid is unstable as soon as any temperature gradient is generated. The density gradient normal to the direction of gravity should therefore produce a local circulation starting immediately. The global stability theory utilized here rests on the assumption that local circulations at the side of the cylinder, if and when they occur, are small in effect until some minimum temperature gradient is exceeded and do not, themselves, significantly alter the temperature distribution within the solid cylindrical material from that which would exist if the external heat transfer were by pure radial conduction. The observation of such small local movement has been beyond the objectives of prior work, although a major objective in the present experimental work.

It is assumed here that the process occurring at the uppermost point on a heated cylinder is essentially the thermal stability problem of a fluid layer heated from below. The Bénard problem represented by a constantly imposed temperature difference across a horizontal layer with one fixed and one free boundary has an instability which occurs at a critical Rayleigh number of approximately 1100 [4]. While the Bénard instability criteria may not be perfectly representative of the physical boundary conditions of the present problem, a computational procedure employing it was found to be successful by Vest and Lawson. In the present analysis a comparable procedure is employed wherein the critical Rayleigh number is evaluated from the expression

$$\mathrm{Ra}_\delta = g\beta(T_w - T_\infty)_e\, \delta^3 \rho_2{}^2 c_2 / k_2 \mu \qquad (2)$$

where δ is the penetration distance of the conductive temperature field into the surrounding medium and $(T_w - T_\infty)_e$ is an equivalent temperature differential. The latter quantity is computed by constructing a linear temperature distribution from the surface to δ which, when

---

Contributed by the Heat Transfer Division for publication in the JOURNAL OF HEAT TRANSFER. Manuscript received by The Heat Transfer Division February 29, 1980.

integrated, yields the same value as the integrated exact temperature distribution from the surface to δ. Thus, $(T_w - T_\infty)_e$ represents twice the average temperature excess in the penetration zone. It should be noted that the theory does not require the initial numerical specification of Ra_δ and that, in fact, this value could await empirical determination. However, there is sufficient experience [1–3] with fine wire data to warrant the assumption of the value of 1100.

In computing the actual $T(t)$ profile Vest and Lawson used an approximate solution for the temperature distribution in the surrounding fluid and an analysis applicable specifically to very fine wires which did not require allowances for the heat capacity or thermal conductivity of the cylinder itself. For this more general case of a fluid surrounding a cylinder of radius, a, $r > a$, which is subjected to a step change in input heat rate at $t = 0$, the temperature distribution is given by Carslaw and Jaeger [5] as

$$T - T_\infty = \frac{\alpha q'}{\pi^2 k_2} \int_0^\infty (1 - exp(-\tau u^2)) \left\{ J_0\left(\frac{ur}{a}\right) [uY_0(u) - \alpha Y_1(u)] - Y_0\left(\frac{ur}{a}\right) [uJ_0(u) - \alpha J_1(u)] \right\} \frac{du}{u^2 \Delta(u)} \quad (2)$$

where

$$\Delta(u) = [uJ_0(u) - \alpha J_1(u)]^2 + [Y_0(u) - \alpha Y_1(u)]^2 \quad (3)$$

for the case of finite cylinder heat capacity but infinite cylinder thermal conductivity, and

$$T - T_\infty = \frac{2q'\kappa_2^{1/2}}{\pi^2 a^2} \int_0^\infty (1 - \exp(-\kappa_1 u^2 t)) J_1(ua).$$

$$[J_0(\kappa_3 ur)\phi(u) - Y_0(\kappa_3 ur)\,\psi(u)] \frac{du}{u^3[\phi^2(u) + \psi^2(u)]} \quad (4)$$

where

$$\psi(u) = k_1 \kappa_2^{1/2} J_1(au) J_0(\kappa_3 au) - k_2 \kappa_1^{1/2} J_0(au) J_1(\kappa_3 au) \quad (5)$$

$$\phi(u) = k_1 \kappa_2^{1/2} J_1(au) Y_0(\kappa_3 au) - k_2 \kappa_1^{1/2} J_0(au) Y_1(\kappa_3 au) \quad (6)$$

for the case of a cylinder with general properties. In the present theory, these expressions determine the variation of the temperature distribution in the surrounding fluid with time for prescribed values of the linear heating rate, material properties, and cylinder diameter. These profiles are then averaged and the quantity $(T_w - T_\infty)_e$ determined versus time, which then allows the computation of the time required to exceed $\mathrm{Ra}_\delta = 1100$ under various conditions. This time is referred to as the convective delay time.

Experiments

Experiments were designed and conducted to verify the previous theory as well as clarify the existence of local convective motion prior to global instability. The apparatus consisted of a 0.632 ± .0013 cm dia mild steel rod, 37.1 cm long, which was mounted in a test chamber constructed of fiberglass coated plywood and covered with styrofoam sheet for insulation purposes. The diameter of the rod was determined by multiple measurements with a precision micrometer. The rod was heated by applying direct current from an 18 V, 500 amp power supply. The power supply output voltage could be varied to regulate power to the rod. A power dissipating resistor consisting of a copper coil in a water bath was constructed to absorb excess power.

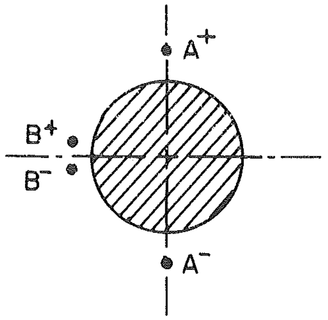

Fig. 1 **Cylinder cross-section and thermocouple locations**

The rod was mounted in two phenolic-board supports 31.8 cm apart, and fine thermocouple wire was strung along the rod between these supports. The location of the thermocouples is shown in Fig. 1. Thermojunctions labeled $A+$ and $A-$ were formed at the top and bottom of the rod, one junction 0.16 cm above the rod and the other the same distance below. Since the bottom junction served as a reference the thermocouple output represented a difference between the temperature above and below the cylinder at mid-cylinder. The purpose of this measurement was to determine the instant of global fluid motion and thus provide data necessary to confirm the stability analysis of large diameter cylinders.

In configuration B, the two thermojunctions were moved to the side of the rod, approximately 0.25 mm off the rod surface, with one junction 0.38 mm above the midplane and the other the same distance below. The purpose of these experiments was to observe local fluid motion or "washing" of the cylinder sides speculated to occur prior to global fluid motion. In the experiments a deliberate effort was made to avoid the spurious indications which can sometimes be attributed to thermocouple unresponsiveness. Small 36 AWG wire was used and thermojunctions with a bead diameter of approximately 1-½ wire diameters were formed by welding. The junctions were then always used in pairs to indicate a deviation. The actual placement of the junctions relative to the surface of the cylinder was determined using a gauge measure and nominally accurate to within the micrometer accuracy of 0.025 mm.

Preliminary experiments were performed to determine the behavior of the system upon sudden and constant internal heating. Both the current delivered by the power supply and the voltage drop across the rod were measured during the transient and were found to remain constant to within ±2 percent during the period of interest (initial 10 s). Some variations were expected because of finite capacity of the power supply and heating effects of both the rod and power dissipating resistor. However, because the temperature rise of the rod during the transient experiments was slight and only of the order of several degrees, the electrical resistance of the rod and the internal

Nomenclature

a = radius of cylinder
Bi = Biót number, hd/k_1
c = specific heat at constant pressure
d = diameter of cylinder
g = gravitational acceleration
Gr = Grashof number, $g\beta(T_w - T_\infty) d^3\rho_2{}^2/\mu^2$
h = convective heat transfer coefficient, $q'/\pi d(T_w - T_\infty)$
k = thermal conductivity
k^* = thermal conductivity parameter, k_2/k_1
Nu = Nusselt number, hd/k_2
Pr = Prandtl number, $c_2\mu/k_2$
q' = cylinder linear heat rate
r = radial coordinate from centerline of cylinder
Ra = Rayleigh number, Gr·Pr
Ra* = modified Rayleigh number based on heat rate, Ra·Nu
Ra_δ = Rayleigh number based on penetration depth δ
t = time
T = temperature
T_w = cylinder wall temperature
T_∞ = bulk fluid temperature
α = heat capacity parameter, $2\rho_2 c_2/\rho_1 c_1$
β = coefficient of thermal expansion of fluid
δ = penetration depth of temperature field around cylinder
κ = thermal diffusivity, $k/\rho c$
$\kappa_3 = \sqrt{\kappa_1/\kappa_2}$
μ = dynamic viscosity of fluid
ρ = density
τ = Fourier number, $4\kappa_2 t/d^2$
τ_D = Fourier number at the onset of significant convection, referred to as delay time

Subscripts

1 = a property of the cylinder
2 = a property of the surrounding medium

heat generation within the rod were considered essentially constant. The external convective heat transfer, however, varied during the course of the transient. The electrical resistance of the rod was determined from these measurements to be 0.00232 ± 0.00006 Ω. During a typical test run, then, a sudden and constant current was imposed on the rod and the thermocouple output monitored on a high speed oscillograph. The error inherent in detecting the onset of fluid motion from the thermocouple trace was estimated to be ±10 percent. The voltage drop across the rod was also monitored and the power input calculated using the known resistance of the rod. Between test runs the test chamber was closed and 1–2 hr allowed for the air inside to become quiescent.

Results and Discussion

The temperature response of the two thermocouple arrangements shown in Fig. 1 are illustrated for a typical test run in Fig. 2. The temperature difference from the top to the bottom of the rod (thermocouple A) remained at zero for a distinct number of seconds after power was applied and then abruptly moved away from zero, marking the point at which the onset of significant global convective motion occurred. Confirmatory runs were made with the thermocouple junctions both closer and farther away from the cylinder surface than the 0.16 cm used for the majority of the test runs. These data demonstrated the expected behavior that once global fluid motion is initiated, the change to significant convective motion is essentially instantaneous. No experimentally significant difference in delay time was detected between the different thermocouple spacings.

In configuration B, wherein the two thermojunctions were moved to the side of the cylinder, localized motion was detected in the form of slight but distinct temperature differences starting essentially instantaneously after power was applied, significantly prior to the delay time. These results are illustrated in Fig. 2. While this behavior may lower the local cylinder wall temperature by a small amount, this effect was not found to be significant in altering the pure conductive instigation of global fluid motion governed by the stability of the fluid at the top of the cylinder. If the local washing was of sufficient magnitude to disrupt the stability mechanism, then the trace of thermocouple A would be expected to depart from zero much less abruptly, and at roughly the same time as the thermocouple B trace. Clearly, this does not happen.

Analytical results describing the global stability phenomenon were developed by numerically integrating the temperature response equations (2–6) for a general property cylinder. These expressions were solved for the delay time at which $\text{Ra}_\delta = 1100$, this critical Rayleigh number having been previously verified as applicable to the fine wire case. The results are shown in Figs. 3 and 4. The effect of diameter alone was removed by using the nondimensional Fourier number and modified Rayleigh number for time and heat rate, respectively. The delay time was found to be very sensitive to the ratio of the heat capacities of the cylinder and media α and relatively insensitive to the ratio of thermal conductivities k^*.

The dimensionless delay time τ_D is plotted in Fig. 3 as a function of dimensionless heat rate Ra* with the heat capacity ratio α as a parameter. The line labeled $\alpha \to \infty$ is equivalent to the expression given by Vest and Lawson for negligibly small wires. The effect of finite size of the cylinder in terms of allowing for its heat capacity is clearly shown. Values of α for various pertinent combinations of cylinder and medium materials are shown in Table 1. Typical values are 0.001 for a metallic conductor in air and 2.0 for a metal cylinder in water. It is apparent that the retarding effect of heat capacity is significant for very fine wires in air or gaseous media as shown by the marked deviation from the $\alpha \to \infty$ line even for very small Ra*.

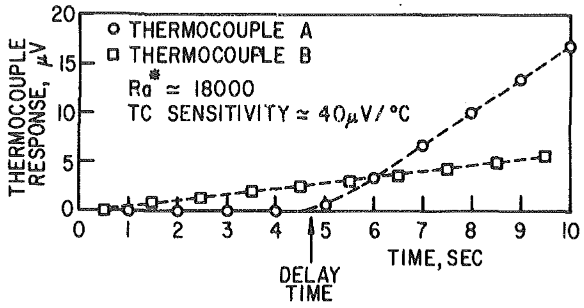

Fig. 2 Thermocouple response for a typical test run

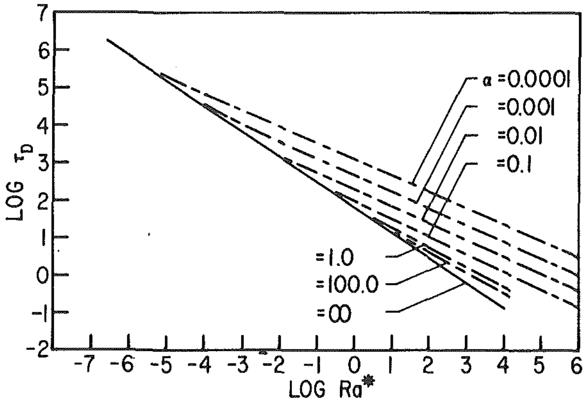

Fig. 3 Correlation of the convective delay time and Rayleigh number with the heat capacity ratio as parameter

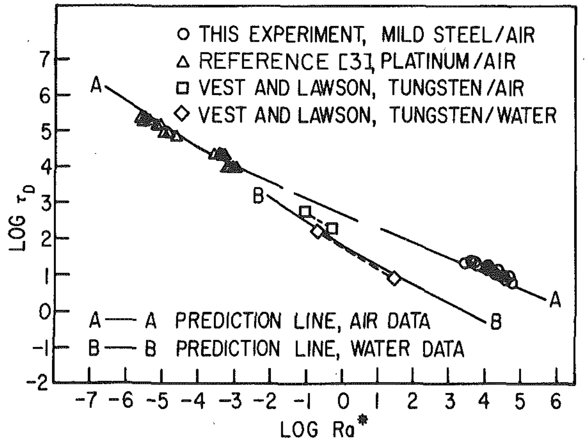

Fig. 4 ***Comparison of the convective delay correlation with available data***

Figure 4 compares the analysis to the available data. Shown are the wire data of Vest and Lawson (0.203 mm dia tungsten), the wire data of Parsons and Mulligan (0.030 and 0.127 mm dia platinum), and the cylinder data of the present experiment (6.32 mm dia mild steel). The prediction line A-A for air data is shown disjointed because the value of α was slightly different for comparison with each data set due to the different cylinder materials. The agreement of the data from this experiment—the air data of Parsons and Mulligan, and the water data of Vest and Lawson—is seen to be excellent. The deviation of the data from the prediction is approximately ±20 percent, which is considered to be quite good taking into account the extreme range of parameters considered. The air data of Vest and Lawson are not in as close agreement. The theory would predict that the heat capacity of their wire could have delayed convection more than it apparently did. A possible explanation is the greater percentage inaccuracy which would be expected in air data relative to the water data due to the difficulty in measuring the much shorter air delay times with a fixed precision technique.

It was concluded from a thorough comparison of the analysis using the general equations (4–6) in place of the infinite conductivity equations (2) and (3) that for practical cases the thermal conductivity of the cylinder has an insignificant effect on the stability analysis. This can be seen by considering the familiar criteria that a lumped (infinite k_1) analysis is appropriate if the Biot modulus is less than 0.1. The Biot number is defined as hd/k_1 where, in this case, h is a function of time, infinite at $t = 0$ and rapidly decreasing thereafter. The transient Biot number, then, can be expressed as $\text{Nu}(t)\cdot k^*$. Values of k^* for

Table 1 Values of the property ratios α and k^* for common conductors in air and water

	In Air		In Water	
Material	$\alpha \frac{(2\rho_2 c_2)}{\rho_1 c_1}$	$k^* \frac{(k_2)}{k_1}$	α	k^*
Aluminum	0.00097*	0.00013	3.4	0.0030
Brass	0.0072	0.00023	2.5	0.0055
Bronze	0.00079	0.00099	2.8	0.024
Constantan	0.00064	0.0011	2.3	0.027
Copper	0.00068	0.000067	2.4	0.0016
Platinum	0.00082	0.00036	2.9	0.0086
Steel				
0.5% C	0.00065	0.00048	2.3	0.011
1.0% C	0.00064	0.00060	2.3	0.014
1.5% C	0.00062	0.00071	2.2	0.017
Tungsten	0.00090	0.00016	3.2	0.0038
Nominal Ranges:	(0.0006 → 0.001)		(2.2 → 3.4)	
		(0.00007 → 0.001)		(0.002 → 0.03)

* All properties are at room temperature and pressure, values from reference [6].

various combinations of cylinder and medium materials are given in Table 1. It can be shown that for typical values of k^* of 0.01 → 0.001, the transient Biot modulus drops below 0.1 very quickly, substantially before the Ra_δ reaches 1100. The clear implication is that the infinite k_1 solutions are satisfactory at the time of stability delay. In the extreme and unlikely case where the conductivity of the medium exceeds that of the cylinder ($k^* > 1.0$), there would be a significant temperature drop across the cylinder with respect to that in the medium. However, the effect on the calculation of delay time is still minimal. This can be visualized by comparing two calculations, one a lumped analysis with no temperature variation across the cylinder, and the other the actual case. At the same instant of time the actual or finite k_1 case will have a lower wall temperature but the penetration of the normalized (T/T_w) temperature field will be deeper into the surrounding fluid. Since the calculation of Ra_δ is proportional to $(T_w - T_\infty)\delta^3$, the two effects tend to be self canceling.

It is of interest to consider the relationship of this work with the solutions of the boundary layer equations for natural convection problems in the literature. Analytical solutions for the vertical flat plate problem with both a step change in wall temperature and a step change in heat flux are available. In these cases the end of the conduction regime is related to the arrival of the leading edge effect. The form of this effect is a traveling singularity instigated by the impulsive boundary condition. The question arises, then, whether some analogous effect would be at work for the horizontal cylinder, since the streamwise boundary layer equations describing the situation are the same with the exception of a variable body force term. Experimental runs were attempted at high Grashof number to shed light on this question as the boundary layer assumptions are generally considered valid for $\mathrm{Gr} > 10^4$. This Grashof number is based on the assumption of an instantaneously applied wall temperature (or a constant wall heat flux, Gr*). In the experimental case, of course, the Gr number is a function of time, the wall temperature (or wall heat flux) is delayed at least a small amount by the heat capacity of the cylinder. It was observed that at values of input heat rate sufficient for the steady state Gr number to be greater than 10^4, stability delay tripped the flow to convection substantially before this value was reached, i.e., when the boundary layer equations were inapplicable. In the physical case this experience would appear to be valid, the stability hypothesis being a more appropriate simplification of the real flow situation at very short times than the boundary layer approximations.

Conclusions

1 The thermal stability theory for the onset of convection about a suddenly heated horizontal cylinder has been extended to include the cases of finite diameter cylinders with general heat transfer properties.

2 It has been shown that the heat capacity ratio of the cylinder and surrounding fluid has a dominant effect on the solution for the delay time while the thermal conductivity exerts only a negligible influence. The diameter effect is accounted for in the nondimensionalization of the heat rate and delay time.

3 Experimental data have been generated which, along with previously obtained data, demonstrate the applicability of the extended stability theory to predicting the onset of global convection under a wide range of conditions.

4 Some local fluid motion, or washing of the cylinder sides, was detected. This motion might promote early deviation of the cylinder temperature response from pure conduction prediction, but was shown to be of insufficient magnitude to disrupt the stability mechanism occurring in the fluid layer at the top of the cylinder.

Acknowledgment

This work was supported by the National Science Foundation through grant number ENG 75-14616.

References

1 Ostroumov, G. A., "Unsteady Heat Convection Near a Horizontal Cylinder," *Soviet Technical Physics,* Vol. 1, 1956, pp. 2627–2641.

2 Vest, C. M., and Lawson, M. L., "Onset of Convection Near a Suddenly Heated Horizontal Wire," *International Journal of Heat and Mass Transfer,* Vol. 15, 1972, pp. 1281–1283.

3 Parsons, J. R., and Mulligan, J. C., "Transient Free Convection From a Suddenly Heated Horizontal Wire," ASME JOURNAL OF HEAT TRANSFER, Vol. 100, 1978, pp. 423–428.

4 Low, A. R., "On the Criterion for Stability of a Layer of Viscous Fluid Heated from Below," *Proceedings of the Royal Society,* Series A, Vol. 125, 1929.

5 Carslaw, H. S., and Jaeger, J. C., *Conduction of Heat in Solids,* 2nd ed., Oxford University Press, London, 1959, pp. 341–347.

6 Rohsenow, W. M. and Hartnett, J. P., *Handbook of Heat Transfer,* McGraw-Hill, New York, 1973, pp. 2.23–2.85.

L. Iyican[1]
Graduate Student,
University of Houston,
Houston, TX 77004

Y. Bayazitoğlu
Associate Professor,
Rice University,
Houston, TX 77001
Assoc. Mem. ASME

L. C. Witte
Professor,
University of Houston,
Houston, TX 77004
Mem. ASME

An Analytical Study of Natural Convective Heat Transfer within a Trapezoidal Enclosure

The natural convection motion and the heat transfer within a trapezoidal enclosure with parallel cylindrical top and bottom walls at different temperatures and plane adiabatic sidewalls are studied. Two-dimensional natural convective fields for a range of Rayleigh numbers, up to 2.7 × 10^6, and enclosure tilt angles, 0 to 180 deg measured from vertical, are investigated. The Galerkin's method of solution is applied to nonlinear form of the momentum and energy equations to determine the velocity and temperature fields. The average and local Nusselt numbers are also presented.

Introduction

Natural convection problems in enclosures have been of interest for many years. A review of the literature reveals an overwhelming number of references on natural convection. However, almost all the work completed thus far is restricted to relatively simple geometries such as rectangular enclosures or cylindrical annuli.

The studies in the literature usually involve experimental and/or numerical techniques. Although the analytical methods based on spectral expansion techniques have been accepted as another powerful tool for thermoconvective flows, they have not been utilized to solve the fully nonlinear problem of natural convection in enclosures. Their application so far have been restricted to linear stability analysis of thermal flows, natural convection between parallel plates and infinite Prandtl number approximation.

In the absence of sufficient information on natural convection in irregular geometries, the extensive literature available on rectangular enclosures is the basic mainstay for this investigation. Hart [1, 2] presents extensive analytical and experimental study of flow stability in an inclined rectangular box. He determines the regions of different flow regimes in Ra-Inclination Angle plane. Arnold, et al. [3–5] investigate the effects of aspect ratio and inclination angle on the natural convection problem of a high Pr fluid in finite rectangular regions. Spradley and Churchill [6] present a numerical study of unsteady laminar thermal convection in compressible fluids at various reduced levels of gravity. Koutsoheras and Charters [7] show the effect of Ra, aspect ratio, and inclination angle on the heat transfer through an inclined air cell by the numerical solution of two-dimensional governing equations. Pepper and Harris [8, 9] obtain numerical solutions to two and three-dimensional natural convection in rectangular cavities by a strongly implicit procedure. Chan and Banerjee [10, 11] develop a numerical technique based on a primitive form of conservation equations to investigate three-dimensional natural convection in rectangular enclosures. Ozoe, et al. [12–14] present experimental and numerical results on natural convection in long square and rectangular channels at various tilt angles. They consider large variations in Pr and aspect ratio. The experimental work by Ozoe, et al. [15] involving three-dimensional photography is very illustrative in showing the transition between the flow modes due to natural convection in an inclined rectangular box. Ozoe, et al. [16–18] give a three-dimensional finite-difference method to solve the same problem. However, they limited their Ra range up to 8 × 10^3. Powe, et al. [19] present results of a finite-difference solution for natural convection within horizontal cylindrical annuli filled with air. An extensive experimental and numerical investigation of natural convection within horizontal annuli between concentric and eccentric cylinders is investigated by Kuehn and Goldstein [20, 21].

This work presents an analytical study to investigate two-dimensional natural convection in the trapezoidal enclosure with adiabatic sidewalls shown in Fig. 1. If the enclosure is fluid-filled and a temperature difference is maintained between the bottom and the top surfaces as shown, a buoyancy-driven convective field will develop. This leads to natural convective heat transfer across the groove from the hot bottom to the cold top surface. The situation is complicated by tilting the groove through an angle from vertical. In the complete absence of previous information on trapezoidal enclosures, the extensive data collected for rectangular enclosures can be used to make some qualitative predictions on the possible flow modes in trapezoidal enclosures. Such brief discussion, offered below, should be thought of as pure speculation from the results of rectangular geometry [1, 2], and is not an outcome of this study. At very low Rayleigh numbers, the fluid will be nearly stagnant and the heat transfer is by pure conduction through the fluid layer from the hot plate to the cold plate. The temperature distribution in this case will be that of two-dimensional steady-state heat conduction in the enclosure. This simplest flow mode is called the conduction regime and is present at all tilt angles. When the Rayleigh number exceeds a critical value, which is different for each tilt angle, a steady two-dimensional unicellular convection sets within the enclosure. Such a motion occurs first at an inclination angle of 90 deg (vertical), and its initiation is retarded as the inclination angle is changed from 90 to 180 deg or from 90 to 0 deg. The magnitude of this flow increases from 0 to 90 deg and starts declining after 90 deg, and it almost vanishes at 180 deg. As the Rayleigh number is increased, this two-dimensional flow gets even stronger.

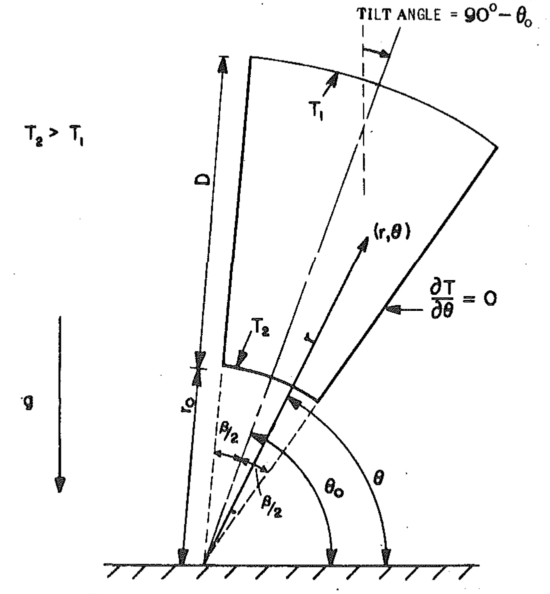

Fig. 1 Trapezoidal enclosure configuration

---

[1] Presently with Shell Development Company, Houston, TX.

Contributed by the Heat Transfer Division for publication in the JOURNAL OF HEAT TRANSFER. Manuscript received by the Heat Transfer Division October 9, 1979.

In this flow regime, the energy is mostly transported by the circular motion of the convection cell; therefore, it is called the convection regime. The upper limit of this flow regime largely depends on the tilt angle. From 90 to 180 deg, this flow regime is present for a good range of Rayleigh numbers; but as the tilt angle changes from 90 to 0 deg, a three-dimensional steady cellular motion in the form of longitudinal rolls starts appearing. The Rayleigh number required for initiation of such a flow is lowest at 0 tilt angle (horizontal position with the hotter plate at the bottom). In fact, at 0 tilt angle, the range of Rayleigh number for the occurrence of the two-dimensional cellular motion is so small that the direct change from the conduction regime to the three-dimensional cellular motion is possible. For a given Rayleigh number, the range of tilt angle around 0 deg in which the three-dimensional cells occur becomes smaller as the Prandtl number increases. For Pr = 0.7 (air), this range may be expected to change from 0 to 60–70 deg with the increasing Rayleigh number. In this tilt angle range, further increase in the Rayleigh number causes unsteadiness and finally transition to turbulence. For the rest of the tilt angles, the two-dimensional cellular motion is dominant for a large range of Rayleigh numbers. Around 90 deg at large Rayleigh numbers, multiple, stationary transverse cells may be expected to set in for a short range of Rayleigh numbers before the initiation of transverse travelling waves. However, for tilt angles greater than 90 deg (up to 180 deg) the two-dimensional cellular motion is expected to change to three-dimensional longitudinal rolls instead of two-dimensional transverse rolls [2]. Although it is not strictly relevant to the present problem, useful background can also be obtained from the literature on natural convection between two parallel plates, of which references [22] and [23] are representative of an extensive literature.

For a range of Ra and tilt angles, using Galerkin's method of solution, this paper presents the velocity and temperature fields in the trapezoidal enclosure of Fig. 1. Average and local Nusselt numbers were also calculated from the knowledge of velocity and temperature distributions. As related to the method of solution used here, Orszag [24, 25] gave an introduction to Galerkin flow approximations and to methods to implement them efficiently. He then compares the Galerkin method with finite difference methods and concludes that cut-off Fourier expansion methods require considerably less computer time and memory than the finite difference methods for the same accuracy. Catton, et al. [26] obtained a solution to the steady two-dimensional natural convective flow problem in an inclined rectangular slot by the Galerkin method. They studied 60 to 135 deg range of tilt angles and they used the infinite Pr number approximation which simplified the momentum equation by neglecting the nonlinear convective terms. Denny and Clever [27] compared the Galerkin and finite difference methods for solving highly non-linear thermal problems. They pointed out that in the Galerkin method, the wall gradients are as accurate as the internal field results in contrast to finite difference methods. Shaughnessy, et al. [28] explained the use of spectral expansions for solving nonlinear partial differential equations.

The present work has moderate Pr number, therefore, neither zero Pr nor infinite Pr simplifications are made and the Galerkin method is applied to nonlinear form of the momentum and energy equation. The results are presented up to 2.7×10^6 Ra number for the cylindrical trapezoidal enclosure of Fig. 1, tilt angles ranging from 0 to 180 deg.

Analysis

The configuration for the analytical model is shown in Fig. 1. The cross-sectional view of the model is a trapezoid of altitude D, with parallel cylindrical sides which are kept at constant temperatures T_1 and T_2 ($T_2 > T_1$). The nonparallel sidewalls are considered to be adiabatic. The centerline of the trapezoid makes an angle of θ_0 with the horizontal, and the length of the enclosure in the direction perpendicular to this trapezoid is long enough to eliminate any depth effects. The angle between the centerline of the trapezoid and the vertical is called the tilt angle.

Assuming the thermal and fluid properties to be constant, and neglecting the viscous dissipation, under steady-state conditions the mass, momentum, and energy balance equations with Boussinesq approximation [29] describing the natural convective flow in this enclosure can easily be obtained. The nondimensionalized form of these equations takes the following form.

$$\nabla \cdot \mathbf{V} = 0 \qquad (1a)$$

$$(\mathbf{V} \cdot \nabla)\mathbf{V} = -\nabla P + \nabla^2 \mathbf{V} + \mathrm{Gr} \cdot T(\mathbf{e}_r \sin\theta + \mathbf{e}_\theta \cos\theta) \qquad (1b)$$

$$(\mathbf{V} \cdot \nabla) T = \frac{1}{\mathrm{Pr}} \nabla^2 T \qquad (1c)$$

where $\mathbf{V} = \mathbf{e}_r u_r + \mathbf{e}_\theta u_\theta$ is the velocity vector, and the operators ∇ and ∇^2 are defined as

$$\nabla \equiv \mathbf{e}_r \frac{\partial}{\partial r} + \mathbf{e}_\theta \frac{1}{r}\frac{\partial}{\partial \theta}, \quad \nabla^2 \equiv \frac{1}{r}\frac{\partial}{\partial r}\left(r \frac{\partial}{\partial r}\right) + \frac{1}{r^2}\frac{\partial^2}{\partial \theta^2} \qquad (2)$$

Introducing the stream function, ψ, so that the continuity equation (1a) is identically satisfied, and upon taking the curl of equation (1b) and combining the resulting equation with the definition of stream function, the pressure terms in equation (1b) can be eliminated as

$$(\mathbf{V} \cdot \nabla)(\nabla^2 \psi) = \nabla^4 \psi + \mathrm{Gr}\left(\frac{\partial T}{\partial r}\cos\theta - \frac{1}{r}\frac{\partial T}{\partial \theta}\sin\theta\right) \qquad (3)$$

where $\nabla^4 = \nabla^2(\nabla^2)$ is the biharmonic operator, and ψ is defined as $u_r = -1/r\ \partial\psi/\partial\theta$ and $u_\theta = \partial\psi/\partial r$.

The boundary conditions of the problem described above take the following form

Nomenclature

a_n', a_{nm} = expansion coefficients
A_2 = area of inner cylindrical surface of trapezoid
b_n', b_{nm}, d_m' = expansion coefficients
D = altitude of trapezoid
e_m' = expansion coefficients
$\mathbf{e}_r$, $\mathbf{e}_\theta$ = unit vector in r and θ-directions
g = gravitational acceleration
Gr = Grashof number, $g\gamma\Delta T D^3/\nu^2$
k = thermal conductivity
l_{mn} = expansion coefficients
Nu = Nusselt number, $QD/(A_2 k \Delta T)$
$\overline{\mathrm{Nu}}$ = Nusselt number for base flow
Nu_y = Nu_θ, local nusselt number transformed into x-y plane
Nu_θ = local Nusselt number, $q_\theta D/(k\Delta T)$
P = dimensionless pressure, $(P - P_0)/[\rho(\nu/D)^2]$
P_0 = hydrostatic pressure
Pr = Prandtl number, ν/α

q_θ = heat flux per unit area from hot, inner cylindrical surface
Q = rate of heat flow
r = dimensionless distance in r-direction, r/D
r_1 = dimensionless radius of outer cylindrical surface, r_0/D
r_2 = dimensionless radius of inner cylindrical surface, $(r_0 + D)/D$
Ra = Rayleigh number, (Pr) (Gr)
T = dimensionless temperature, $(T - T_0)/(T_2 - T_1)$
$T_0 = (T_1 + T_2)/2$
T_1 = temperature of cold, upper cylindrical surface
T_2 = temperature of hot, bottom cylindrical surface
$\overline{T}$ = dimensionless base flow temperature
t = an arbitrary independent variable

u_r, u_θ = dimensionless velocities in r and θ-directions, $u/(\nu/D)^2$
V = dimensionless velocity vector, $\mathbf{V}/(\nu/D)^2$
α = thermal diffusivity
β = angle between sidewalls of trapezoid
γ = thermal coefficient of volume expansion
θ = angular coordinate measured from horizontal in counter-clockwise direction
θ_0 = angle between trapezoidal centerline and horizontal
$\theta_1 = \theta_0 - \beta/2$
$\theta_2 = \theta_0 + \beta/2$
ν = kinematic viscosity
ρ = density
ψ = stream function
$\bar{\psi}$ = stream function of base flow
ψ_n, ψ_n^*, ϕ, ξ = eigenfunctions

$$\psi = \frac{\partial\psi}{\partial r} = \frac{\partial\psi}{\partial\theta} = 0 \text{ at } r = r_1, r_2 \text{ and/or } \theta = \theta_1, \theta_2 \tag{4a}$$

$$T = T_1 \text{ at } r = r_1, \quad T = T_2 \text{ at } r = r_2 \tag{4b}$$

$$\frac{\partial T}{\partial\theta} = 0 \text{ at } \theta = \theta_1, \theta_2 \tag{4c}$$

Due to the nature of the cylindrical coordinate system the above governing equations are complicated to solve. Therefore, the following coordinate transformation as shown in Fig. 2 is utilized.

$$q = \ln r, \qquad s = \theta \tag{5}$$

Next, in order to change the intervals of both independent variables q and s to $(-\frac{1}{2}, \frac{1}{2})$, the coordinates q and s are transformed to x and y by the following linear transformation.

$$x = \frac{q - q_1}{q_2 - q_1} - \frac{1}{2}, \qquad y = \frac{s - s_1}{s_2 - s_1} - \frac{1}{2} \tag{6}$$

where $q_1 = \ln r_1$, $q_2 = \ln r_2$, $s_1 = \theta_1$, and $s_2 = \theta_2$.

The governing equations in the x-y plane are obtained by the substitution of the transformation relations (5) and (6) into the equations (1c) and (3) as

$$\begin{aligned} y_0 \frac{\partial\psi}{\partial y} &\left\{\left(2 - x_0 \frac{\partial}{\partial x}\right)\left(x_0^2 \frac{\partial^2}{\partial x^2} + y_0^2 \frac{\partial^2}{\partial y^2}\right) \psi\right\} \\ &+ x_0 \frac{\partial\psi}{\partial x} \left\{y_0 \frac{\partial}{\partial y} \left(x_0^2 \frac{\partial^2}{\partial x^2} + y_0^2 \frac{\partial^2}{\partial y^2}\right) \psi\right\} \\ = &\left(x_0^2 \frac{\partial^2}{\partial x^2} + y_0^2 \frac{\partial^2}{\partial y^2} + 4 - 4x_0 \frac{\partial}{\partial x}\right)\left(x_0^2 \frac{\partial^2}{\partial x^2} + y_0^2 \frac{\partial^2}{\partial y^2}\right) \psi \\ &+ \mathrm{Gr}(r_1 r_2)^{3/2} e^{(3x/x0)} \left\{y_0 \frac{\partial T}{\partial y} \sin\left(\frac{y}{y_0} + \theta_0\right)\right. \\ &\left. - x_0 \frac{\partial T}{\partial x} \cos\left(\frac{y}{y_0} + \theta_0\right)\right\} \end{aligned} \tag{7a}$$

$$x_0 y_0 \left(\frac{\partial\psi}{\partial x}\frac{\partial T}{\partial y} - \frac{\partial\psi}{\partial y}\frac{\partial T}{\partial x}\right) = \frac{1}{\mathrm{Pr}} \left(x_0^2 \frac{\partial^2}{\partial x^2} + y_0^2 \frac{\partial^2}{\partial y^2}\right) T \tag{7b}$$

where $x_0 = 1/\ln(r_2/r_1)$ and $y_0 = 1/\beta$, and β is the groove angle.

Similarly, the transformation of the boundary conditions (4) yields the following conditions in the x-y plane.

$$\psi = \frac{\partial\psi}{\partial x} = \frac{\partial\psi}{\partial y} = 0 \text{ at } x = \pm\tfrac{1}{2} \text{ or } y = \pm\tfrac{1}{2} \tag{8a}$$

$$T = \tfrac{1}{2} \text{ at } x = -\tfrac{1}{2}, \qquad T = -\tfrac{1}{2} \text{ at } x = \tfrac{1}{2} \tag{8b}$$

$$\frac{\partial T}{\partial y} = 0 \text{ at } y = \pm\tfrac{1}{2} \tag{8c}$$

Conduction Regime. Before attempting to solve the above governing equations a special case will be considered. For the small values of Gr, the convective terms will be neglected. This resulting flow is usually termed the *base flow*, which is the simplest possible flow, and the heat is transferred only by molecular conduction. The variables of this regime are indicated by overbars. The solution of the energy equation without the nonlinear convective terms simply becomes

$$\overline{T} = -x \tag{9}$$

and the momentum equation reduces to

$$\begin{aligned} \left\{x_0^4 \frac{\partial^4}{\partial x^4} + 2x_0^2 y_0^2 \frac{\partial^4}{\partial x^2 \partial y^2} + y_0^4 \frac{\partial^4}{\partial y^4}\right. \\ \left. + 4\left(1 - x_0 \frac{\partial}{\partial x}\right)\left(x_0^2 \frac{\partial^2}{\partial x^2} + y_0^2 \frac{\partial^2}{\partial y^2}\right)\right\} (\bar{\psi}/\mathrm{Gr}) \\ = e^{(3x/x_0)} \left(K_1 \cos\frac{y}{y_0} - K_2 \sin\frac{y}{y_0}\right) \end{aligned} \tag{10a}$$

with

$$\bar{\psi} = \frac{\partial\bar{\psi}}{\partial x} = \frac{\partial\bar{\psi}}{\partial y} = 0 \text{ at } x = \pm\tfrac{1}{2} \text{ or } y = \pm\tfrac{1}{2} \tag{10b}$$

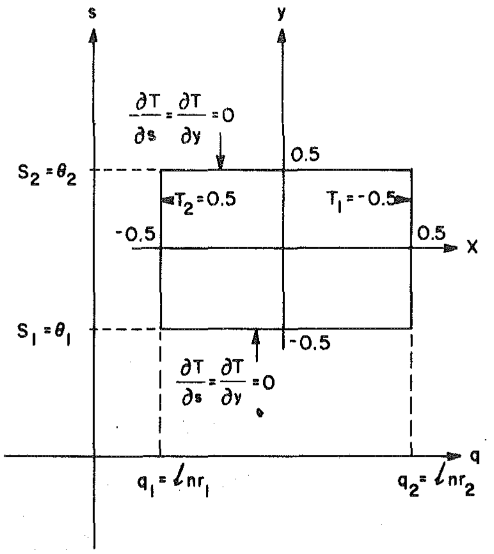

Fig. 2 Coordinate transformation

where $K_1 = x_0(r_1 r_2)^{3/2} \cos\theta_0$, $K_2 = x_0(r_1 r_2)^{3/2} \sin\theta_0$, and $\bar{\psi}$ is the stream function under base flow conditions.

Equation (10b) suggests that the ratio of the base flow stream function to the Grashof number, $\bar{\psi}/\mathrm{Gr}$, (and, thus, u_r/Gr and u_θ/Gr) is independent of Gr, provided, of course, that Gr is small enough for a base flow to exist. Equation (10a) cannot be solved by the method of separation of variables since it contains terms with cross differentiation. However, Galerkin's Method can be successfully applied to obtain the solution for $\bar{\psi}$. The base flow stream function can be expressed in a series expansion form as

$$\bar{\psi}(x, y) = \sum_{m=1}^{M} \sum_{n=1}^{N} \mathrm{l}_{nm} \bar{\psi}_n(x) \cdot \bar{\psi}_m^*(y) \tag{11}$$

where $\bar{\psi}_n$ and $\bar{\psi}_m^*$ are two complete orthogonal sets of functions in the intervals $-\frac{1}{2} \le x \le \frac{1}{2}$ and $-\frac{1}{2} \le y \le \frac{1}{2}$, respectively, and l_{nm} are the expansion coefficients to be determined.

Functions $\bar{\psi}_n$ and $\bar{\psi}_m^*$ should be chosen such that they will satisfy the proper boundary conditions for $\bar{\psi}$, equation (10b), in x and y directions, respectively. Therefore, the C and S functions [30, 31] are used as,

$$\bar{\psi}_i(t) = \bar{\psi}_i^*(t) = \begin{cases} C_i(t), & \text{for even } i \\ S_i(t), & \text{for odd } i \end{cases} \tag{12a}$$

where i can be n or m, and t can be x or y, and

$$C_i(t) = \frac{\cosh(\lambda_i t)}{\cosh(\lambda_i/2)} - \frac{\cos(\lambda_i t)}{\cos(\lambda_i/2)},$$

$$S_i(t) = \frac{\sinh(\mu_i t)}{\sinh(\mu_i/2)} - \frac{\sin(\mu_i t)}{\sin(\mu_i/2)} \tag{12b}$$

in which λ_i and μ_i ($i = 1, 2, 3, \ldots$) are the positive roots of the equations $\tanh(\lambda_i/2) + \tan(\lambda_i/2) = 0$ and $\tanh(\mu_i/2) - \tan(\mu_i/2) = 0$, respectively.

After the substitution of the expansion (11) into equation (10a), the resulting equation is multiplied by $\bar{\psi}_i(x)\bar{\psi}_j(y)$ and then it is doubled-integrated in the full domain of x and y to obtain $N \times M$ algebraic equations for the $N \times M$ unknowns. From these equations the expansion coefficients, l_{nm} and therefore the stream function are determined.

Once the base flow stream function is known, the velocity components can be calculated by

$$u_r = -\frac{1}{r}\frac{\partial\bar{\psi}}{\partial\theta} = -\frac{1}{r}\frac{\partial\bar{\psi}}{\partial s} = -\frac{1}{\beta}(r_1 r_2)^{-1/2} e^{(-x/x_0)} \frac{\partial\bar{\psi}}{\partial y} \tag{13a}$$

$$u_\theta = \frac{\partial\bar{\psi}}{\partial r} = \frac{1}{r}\frac{\partial\bar{\psi}}{\partial q} = \frac{(r_1 r_2)^{-1/2}}{\ln(r_2/r_1)} e^{(-x/x_0)} \frac{\partial\bar{\psi}}{\partial x}. \tag{13b}$$

Convection Regime. Obviously, in the convection regime, the temperature field cannot be determined without the knowledge of the velocity distribution in the enclosure. Therefore the governing equations must be solved simultaneously.

The temperature profile in the convective regime can be expressed as the sum of a conductive part and a convective part, as

$$T(x, y) = \overline{T}(x) + T_c(x, y) = -x + T_c(x, y) \qquad (14)$$

so that the substitution of equation (14) into equations (7*b*) and (8) removes the non-homogeneity on the temperature boundary conditions and adds a nonhomogeneous term to the homogeneous energy equation. Next, equation (14) is substituted into equation (7*a*) in order to change the variable T to T_c. Now, all the boundary conditions are homogeneous, Galerkin's method of solution can be applied by the following expansions for ψ and T_c,

$$\psi(x, y) = \sum_{m=1}^{M} \sum_{n=1}^{N} a_{nm}\psi_n(x) \cdot \psi_m(y),$$

$$T_c(x, y) = \sum_{m=1}^{M} \sum_{n=1}^{N} b_{nm}\phi_n(x) \cdot \zeta_m(y) \qquad (15)$$

where

$$\psi_i(t) = \begin{cases} C_i(t) \text{ for even } i, \\ S_i(t) \text{ for odd } i, \end{cases}$$

$$\phi_i(t) = \sin\{i\pi(t + 1/2)\}, \quad i = 1, 2, 3 \ldots,$$

$$\zeta_i(t) = \cos\{(i-1)\pi(t + 1/2)\}, \quad i = 1, 2, 3 \ldots$$

and functions C_i and S_i are given by equations (12*b*). Finally, the expansion forms of u_x and u_y can be obtained in the following form.

$$u_x(x, y) = \frac{\partial\psi}{\partial y} = \sum_{m=1}^{M} \sum_{n=1}^{N} a_{nm}\psi_n(x)\psi_m'(y),$$

$$u_y(x, y) = \frac{\partial\psi}{\partial x} = \sum_{m=1}^{M} \sum_{n=1}^{N} a_{nm}\psi_n'(x)\psi_m(y) \qquad (16)$$

Then the radial and angular velocity component, u_r and u_θ can be determined from equation (13) as

$$u_r = \frac{(r_1/r_2)^x}{(r_1r_2)^{1/2}} \cdot u_x, \quad u_\theta = -\frac{(r_1/r_2)^x}{(r_1r_2)^{1/2}\ln(r_2/r_1)} \cdot u_y \qquad (17)$$

where prime denotes the differentiation with respect to argument.

Evaluation of the Nusselt Number. Defining the Nusselt number, Nu, of the enclosure based on the altitude, D, the total heat transfer rate, Q, from the hot bottom of the enclosure, and the surface area of the bottom surface, A_2, gives $\mathrm{Nu} = QD/(kA_2\Delta T)$ which can be shown to be equal to

$$\mathrm{Nu} = \frac{1}{\beta}\int_{\theta_1}^{\theta_2} \left(\frac{\partial T}{\partial r}\right)_{r_1} d\theta \qquad (18a)$$

After substitution of the coordinate transformation, in the conduction regime, $T = \overline{T}(x) = -x$; the base flow normalized Nusselt number $\overline{\mathrm{Nu}}$, can be evaluated as,

$$\overline{\mathrm{Nu}} = \frac{1}{r_1 \ln(r_2/r_1)} \qquad (18b)$$

Next, we will define a local Nusselt number on the bottom of the grove as

$$\mathrm{Nu} = \frac{q_\theta D}{k\Delta T} \qquad (19a)$$

where $q_\theta = -k\,\Delta T/D(\partial T/\partial r)r_1$. Therefore, the local Nusselt Number transformed into the x-y coordinate system in terms of the temperature gradient becomes

$$\mathrm{Nu}_\theta = \mathrm{Nu}_y = -\frac{1}{r_1\ln(r_2/r_1)}\left(\frac{\partial T}{\partial x}\right)_{x=-1/2} \qquad (19b)$$

where $(\partial T/\partial x)_{x=-1/2}$ can be obtained from equations (14) and (15*b*) as

$$\left(\frac{\partial T}{\partial x}\right)_{x=-1/2} = -1 + \pi \sum_{m=1}^{M} \sum_{n=1}^{N} nb_{nm}\xi(y) \qquad (19c)$$

Finally, the relationship of the Nusselt number with the local Nusselt number can easily be demonstrated as

$$\mathrm{Nu} = \int_{-1/2}^{+1/2} \mathrm{Nu}_y dy \qquad (20)$$

Results and Discussions

For a given enclosure configuration, using Galerkin's method, the solutions in conduction regime can readily be obtained. For convection regime Galerkin's method results in the expansion coefficients of the stream function, ψ and of the temperature, T. The nonlinear set of algebraic equations in terms of these coefficients are numerically solved in an iterative fashion. The base flow stream function results of conduction regime are used as the initial guess values to calculate the velocities u_x and u_y of the convective regime. The iterative procedure is continued until the expansion coefficients converge. Using this value of the stream function, the temperature field is computed and the iterative procedure is continued until convergence of both the expansion coefficients of the stream function and the temperature field are obtained. Once the expansion coefficients are determined, the stream functions, the temperature distributions, the velocity components, the local Nusselt number distributions and the average Nusselt numbers are evaluated. The following numerical values were used in the computations; $r_0 = 1.866$, $D = 3$, $\beta = 30$ deg, $\mathrm{Pr} = 0.71$ (air).

Before presenting the flow patterns and temperature profiles in the trapezoidal enclosure, the coordinate positions on this enclosure are given in Fig. 3 for convenience. This figure can be used in conjunction with the rest of the figures given in this chapter to enhance clarification.

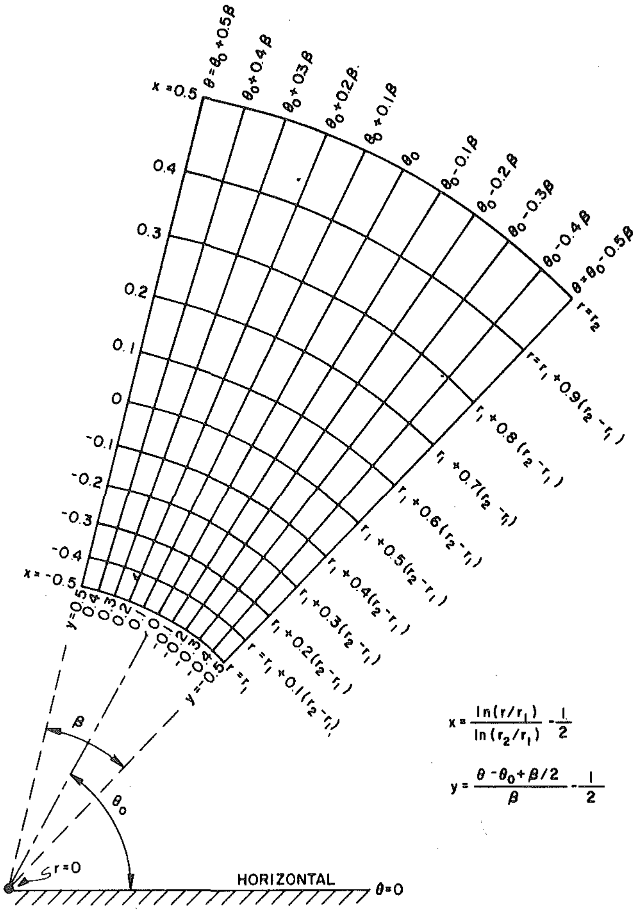

Fig. 3 Cylindrical and *x*-*y* coordinates shown simultaneously on the trapezoid

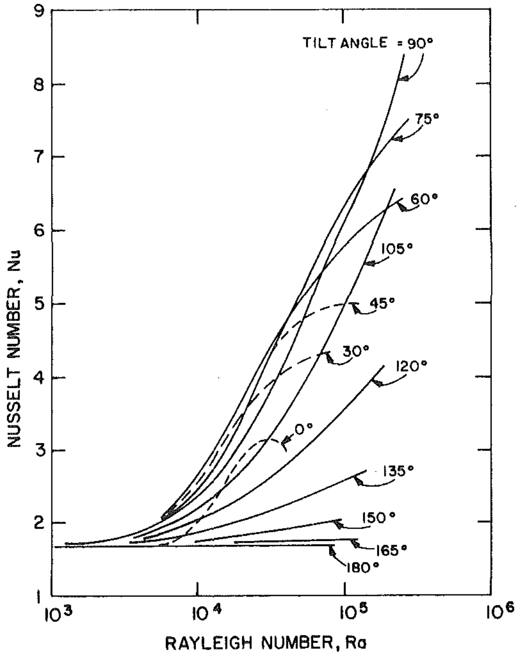

Fig. 4 Variation of Nusselt number with Rayleigh number at different tilt angles

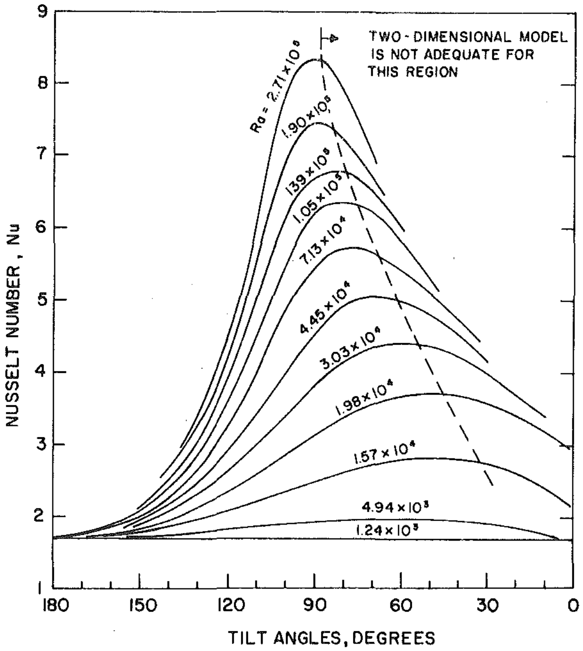

Fig. 5 Variation of Nusselt number with tilt angle at different Rayleigh numbers

The average Nusselt numbers calculated at different tilt angles for various Rayleigh number are given in two different forms in Figs. 4 and 5. Figure 3 is probably more illustrative in showing the region in which the analytical model is applicable. At a tilt angle of 180 deg, the hot plate is on top. Therefore, no convection is developed. As the tilt angle is decreased towards 90 deg, the two-dimensional natural convection composed of a single cell is initiated at a Rayleigh number above 10^3. This single cell convection is strongest in a region around a tilt angle of 90 deg, so that the Nusselt number shows a maximum value in this region. As the tilt angle further decreases towards 0 deg, this two-dimensional convection gets weaker and the Nusselt number shows a decline in this region. In a region between 0 to 90 deg, convective flow is expected to become three-dimensional. The experimental data available in literature on rectangular geometry shows that the value of the Nusselt number decreases as the tilt angle is decreased from 90 deg. At an angle between 0 and 90 deg, the Nusselt number goes through a minimum value and starts increasing as the tilt angle further decreases towards 0 deg. This phenomenon is known to be due to the change in the direction of convection cells. The two-dimensional transfer cells occurring at 90 deg tilt angle become oblique at the tilt angle where the Nusselt number shows a minimum and then become three-dimensional, longitudinal rolls at 0 deg tilt angle. The experimental results on trapezoidal geometries [32] show similar characteristics on Nu versus tilt angle curves. Therefore, in a region between 0 and 90 deg, convective flow is expected to become three-dimensional. At high Rayleigh numbers close to 0 deg tilt angle, iterations of the computer program did not converge to a solution. This is expected since the flow in this region is probably three-dimensional. In the region lying between the two-dimensional and three-dimensional flow regions, the two-dimensional solution may not be applicable because of the possible coexistence of the three-dimensional rolls which could not be simulated by the two-dimensional model. This region is excluded by a dashed line in Fig. 5. The position of this dashed line is not exact since the change from two to three dimensional motions is expected to be a gradual one. The convergence of the computer program at Rayleigh numbers above 10^5 slowed down, probably indicating a transition to another flow mode, since three-dimensional unsteady flow regimes are observed at high Ra in rectangular geometries.

Stream functions at various tilt angles and Rayleigh numbers are presented in Figs. 6 and 7. First, the stream patterns at the various Rayleigh numbers at an inclination of 90 deg are given to show the effect of Rayleigh number on flow. Then the stream patterns are given at various tilt angles to show the effect of inclination angle on flow.

The examination of the stream function in Figs. 6 and 7 shows the single-cellular nature of the two-dimensional flow existing in the Ra range considered. The value of the stream function increases towards the central portion of the slot and reaches a maximum there. At 90 deg tilt angle, this maximum value of the stream function changes from 1.7 at Ra = 4.9×10^3 to more than 12.0 at Ra = 2.71×10^5, indicating an almost ten-fold increase in the magnitude of the velocity component, u_r changes from about 7 to 65 while the maximum value of the angular velocity component, u_θ shows a drastic change from less than 5 to over 100 as Ra increases from 4.94×10^3 to 2.71×10^5. Therefore, the profound effect of Ra on the convective motion is evident. At Ra above 10^5, the waviness in the stream patterns increases and initiation of a multicellular structure in the middle portion of the slot is observed. The convergence of the computer program slowed in that region. It is suspected that the growth of this multicellular pattern may lead to either a three-dimensional or a time-dependent flow structure.

The examination of the flow patterns as a function of tilt angle in Fig. 7 shows that the geometrical shape of the cellular flow is almost symmetrical with respect to the centerline of the groove for 90 deg tilt angle. For tilt angles below and above that value, the cellular pattern gets tilted from the centerline of the slot. It is also observed that the strength of the convective flow falls sharply as the tilt angle changes from 90 to 180 deg. This is indicated by the sharp drop in the maximum value of the stream function.

Figures 8 and 9 show the effect of tilt angle and RA on temperature distribution in the slot. The sharp increase in the temperature gradients with increasing Ra at the tilt angle of 90 deg is observed. At Ra = 4.9×10^3, only small variations from the base flow temperature distribution are observed. However, temperature gradients close to the hot and cold plates get sharper as Ra increases, and at Ra = 2.17 $\times 10^5$ almost all temperature variations seem to be confined in narrow regions adjacent to the hot and cold plates with almost no temperature variations in between. This suggests the existence of relatively narrow thermal boundary layers on the hot and cold plates.

In Fig. 10 the horizontal lines represent the corresponding average Nusselt number for each local Nusselt number distribution curve. In each case, the local Nusselt number changes from a minimum at one sidewall to a maximum towards the other sidewall along the hot plate. The difference between those minimum and maximum values is large.

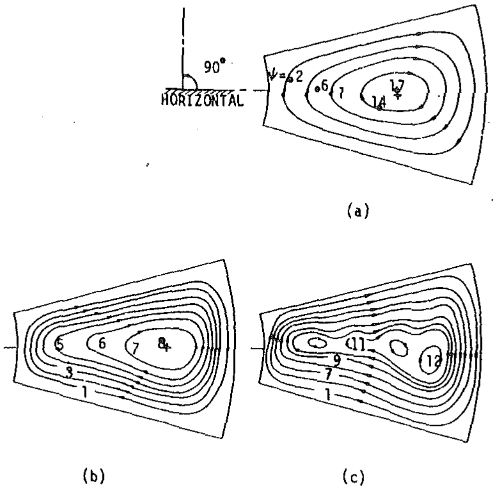

Fig. 6 Stream functions for various Rayleigh numbers at 90 deg tilt angle for Pr = 0.71. (*a*) Ra = 4.94 × 10³, (*b*) Ra = 7.13 × 10⁴, (*c*) Ra = 2.71 × 10⁵

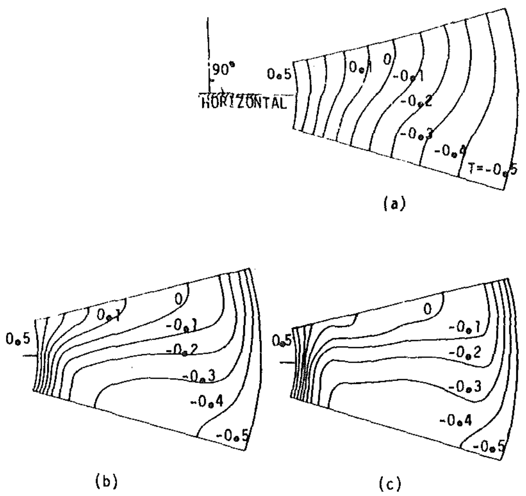

Fig. 8 Isotherms for various Rayleigh numbers at 90 deg tilt angle for Pr = 0.71. (*a*) Ra = 4.94 × 10³, (*b*) Ra = 7.13 × 10⁴, (*c*) Ra = 2.71 × 10⁵

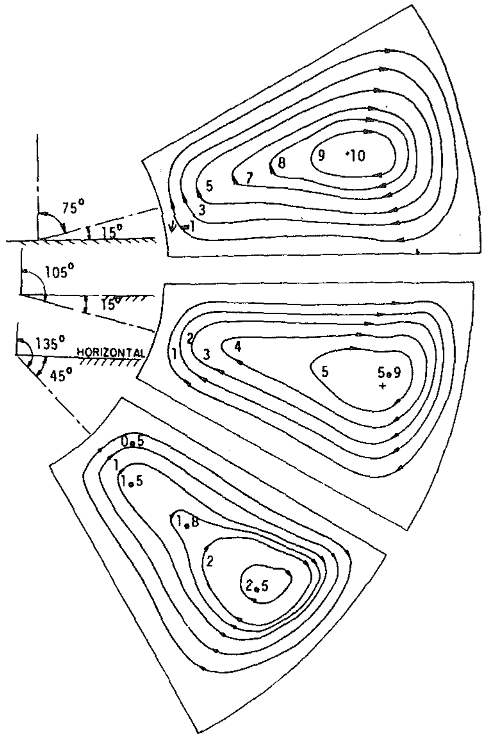

Fig. 7 Stream functions for various tilt angles for Pr = 0.71 and Ra = 7.13 × 10⁴

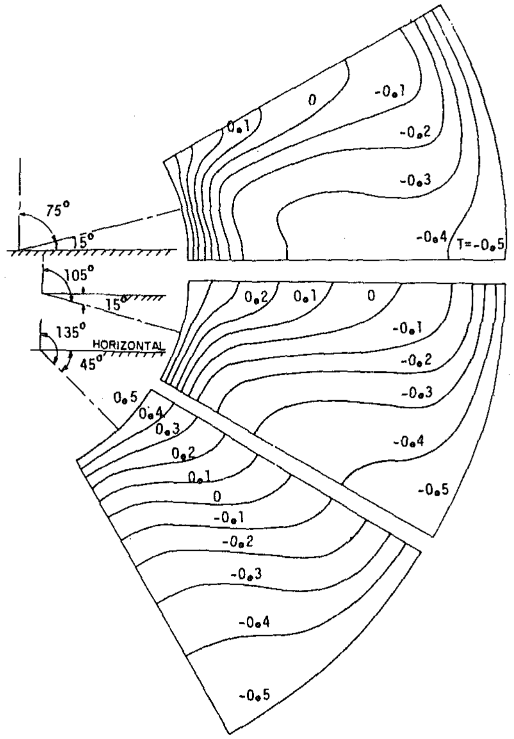

Fig. 9 Isotherms for various tilt angles for Pr = 0.71 and Ra = 7.13 × 10⁴

For example, at Ra = 7.13 × 10⁴ and tilt angle = 90 deg, the local Nusselt number changes from a minimum of 2 to a maximum of 7.5, with an average value of approximately 5.5.

In all computations presented in this work, the value of the index N used was 10, which corresponds to 100 terms in each of the expansions given in equations (15). The Nusselt numbers at $\mathrm{Ra} > 10^5$ indicated a difference of 1–3 percent as compared with the Nusselt numbers used with $N = 12$ (which increases the number of terms to 144 in each expansion). For smaller RA numbers, $\mathrm{Ra} < 10^5$, this difference decreases down to zero at $\mathrm{Ra} \cong 10^4$. In obtaining the results, the solution did not oscillate as N became large.

Concluding Remarks

The spectrum of flow modes due to natural convection in an enclosure may change from a state of no motion to the complicated turbulent flow. Flow instabilities lead to numerous other flow modes between these two extreme cases. The initiation, development and disappearance of each flow mode is largely affected by the variation of a large number of parameters, e.g., the geometry of the enclosure, the type of fluid in the enclosure, boundary conditions, the Rayleigh number, and inclination with respect to gravity. Due to the experimental and mathematical difficulties combined with the possibilities of large variations in various flow parameters and the flow modes, it is impossible to make a general analysis to cover the whole spectrum of flow modes in an enclosure with an arbitrary shape. Therefore, one must restrict oneself to a certain enclosure shape and to a certain range of flow parameters to be able to reduce the governing equations into a tractable form. In this work one such model is demonstrated. In spite of the relative simplicity of this model compared to real flow, the equations are still too complicated to be solved exactly. Therefore, approximate solution techniques must be applied in order to obtain any solution. The most commonly available approximate solution techniques are analytical methods using spectral expansions and various numerical techniques. In the solution of thermal convection problems, the numerical finite difference method is much more widely used than the Galerkin method, which is one of the most commonly

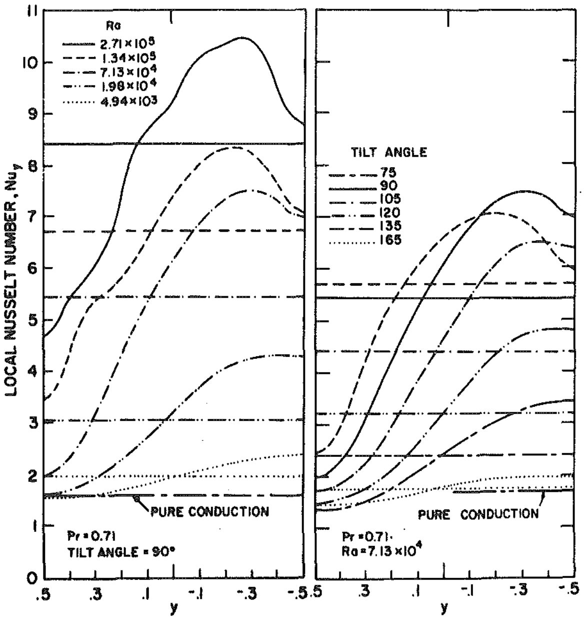

Fig. 10 Variation of local Nusselt number distribution with Rayleigh number (at tilt angle 90 deg) and with tilt angle (at Ra = 7.13×10^4) (Horizontal lines indicate the average value of the Nusselt number at the corresponding tilt angle and Rayleigh number.)

known spectral expansion methods. However, the limited literature on the comparison of these two methods indicates that neither of the methods is superior to the other one [24, 25, 27, 28]. The comparison of the Galerkin and the finite difference methods for the solution of highly nonlinear thermally-driven flows by Denny and Clever [27] indicates that "with increasing precision in the wall heat flux and/or shear, the computational costs for both methods become comparable; however, for errors in excess of 2–3 percent, the Galerkin method is more economical." The disadvantage of the Galerkin method seems to be the laborious preparation of the algebraic problem. However, the Galerkin method may be better suited for the determination of relatively sharp velocity and temperature gradients near the boundaries.

The two-dimensional analytical model used in this work was capable of handling the first two flow regimes occuring in the enclosure. Up to Rayleigh number of 10^3, a conduction-dominated regime prevails, and afterwards a two-dimensional unicellular convective regime takes place. This regime is dominant up to Rayleigh numbers more than 10^5 for tilt angles of 90 deg or greater. For lower tilt angles, however, the top limit of Rayleigh number where this regime is valid decreases towards 0 deg tilt angle and expected to be around 10^4 for 0 deg tilt angle. Above this limit three-dimensional effects are expected to be dominant.

The geometry considered in this work is a very close approximation to the geometry involved in the moderately concentrating trapezoidal solar collectors. The experimental results related to the natural convection heat transfer in the trapezoidal solar collectors are given in references [32] and [33]. The comparison of those experimental results with the results of the present investigation showed reasonable agreement [33].

Acknowledgment

The authors wish to acknowledge the National Science Foundation for support under Grant ENG 77-04122.

References

1 Hart, J. E., "Transition to a Wavy Vortex Regime in Convective Flow Between Inclined Plates," *Journal of Fluid Mechanics*, Vol. 48, 1971, pp. 265–271.

2 Hart, J. E., "Stability of the Flow in a Differentially Heated Inclined Box," *Journal of Fluid Mechanics*, Vol. 47, 1971, pp. 547–576.

3 Arnold, J. N., Bonaparte, P. N., Catton, I., and Edwards, D. K., "Experimental Investigation of Natural Convection in a Finite Rectangular Region Inclined at Various Angles from 0 to 180," *Proceedings of the 1974 Heat Transfer and Fluid Mechanics Institute*, Stanford University Press, 1974, pp. 321–329.

4 Arnold, J. N., Catton, I., and Edwards, D. K., "Experimental Investigation of Natural Convection in Inclined Rectangular Regions of Differing Aspect Ratios," ASME JOURNAL OF HEAT TRANSFER, Vol. 98, 1976, pp. 67–71.

5 Arnold, J. N., Edwards, D. K., and Wu, P. S., "Effect of Cell Size on Natural Convection in High L/D Tilted Rectangular cells Heated and Cooled on Opposite Faces," ASME Paper 78-WA/Ht-11.

6 Spradley, L. W., and Churchill, S. W., "Pressure-and Buoyancy-driven Thermal Convection in a Rectangular Enclosure," *Journal of Fluid Mechanics*, Vol. 70, 1975, pp. 705–720.

7 Koutsoheras, W., and Charters, W. W. S., "Natural Convection Phenomena in Inclined Cells with Finite Side-Walls—A Numerical Solution," *Solar Energy*, Vol. 19, 1977, pp. 433–438.

8 Pepper, D. W. and Harris, S. D., "Numerical Simulation of Natural Convection in Closed Containers by a Fully Implicit Method," *Journal of Fluids Engineering*, Vol. 99, 1977, pp. 649–656.

9 Pepper, D. W. and Harris, S. D., "Numerical Solution of Three-Dimensional Natural Convection by the Strongly Implicit Procedure," ASME Paper 78-WA/HT-10.

10 Chan, A. M. C., and Banerjee, S., "A Numerical Study of Three-Dimensional Roll Cells within Rigid Boundaries," ASME JOURNAL OF HEAT TRANSFER, Vol. 101, 1979, pp. 233–237.

11 Chan, A. M. C., and Banerjee, S., "Three-Dimensional Numerical Analysis of Transient Natural Convection in Rectangular Enclosures," ASME JOURNAL OF HEAT TRANSFER, Vol. 101, 1979, pp. 114–119.

12 Ozoe, H., Sayama, H., and Churchill, S. W., "Natural Convection in an Inclined Rectangular Channel at Various Aspect Ratios and Angles—Experimental Measurements," *International Journal of Heat and Mass Transfer*, Vol. 18, 1975, pp. 1425–1431.

13 Ozoe, H., Sayama, H., and Churchill, S. W., "Natural Convection in an Inclined Square Channel," *International Journal of Heat and Mass Transfer*, Vol. 17, 1974, pp. 401–406.

14 Ozoe, H., Yamamoto, K., and Churchill, S. W., "Natural Circulation in an Inclined Rectangular Channel Heated on One Side and Cooled on the Opposing Side," *International Journal of Heat and Mass Transfer*, 1974, pp. 1209–1217.

15 Ozoe, H., Sayama, H., and Churchill, S. W., "Natural Convection Patterns in a Long Inclined Rectangular Box Heated from Below. Part I. Three-Dimensional Photography," *International Journal of Heat and Mass Transfer*, Vol. 30, 1977, pp. 123–129.

16 Ozoe, H., Yamamoto, K., and Churchill, S. W., "Three-Dimensional Natural Convection in an Inclined Channel with a Square Cross-Section," *American Institute of Chemical Engineering Journal*, Vol. 25, 1979, pp. 709–716.

17 Ozoe, H., Yamamoto, K., Churchill, S. W., and Sayama, H., "Three-Dimensional Numerical Analysis of Laminar Natural Convection in a Confined Fluid Heated from Below," ASME JOURNAL OF HEAT TRANSFER, Vol. 98, 1976, pp. 202–207.

18 Ozoe, H., Yamamoto, K., and Sayama, H., "Natural Convection Patterns in a Long Inclined Rectangular Box Heated from Below: Part II. Three-Dimensional Numerical Results," *International Journal of Heat and Mass Transfer*, Vol. 20, 1977, pp. 131–139.

19 Powe, R. E., Carley, C. T., and Carruth, S. L., "A Numerical Solution for Natural Convection in Cylindrical Annuli," ASME JOURNAL OF HEAT TRANSFER, Vol. 93, 1971, pp. 210–220.

20 Kuehn, T. H., and Goldstein, R. J., "An Experimental and Theoretical Study of Natural Convection in the Annulus between Horizontal Concentric Cylinders," *Journal of Fluid Mechanics*, Vol. 74, 1976, pp. 695–719.

21 Kuehn, T. H., and Goldstein, R. J., "An Experimental Study of Natural Convection Heat Transfer in Concentric and Eccentric Horizontal Cylindrical Annuli," ASME JOURNAL OF HEAT TRANSFER, Vol. 100, 1978, pp. 635–640.

22 Hollands, K. G. T., Unny, T. E., Raithby, G. D., and Konicek, L., "Free Convective Heat Transfer Across Inclined Air Layers," ASME JOURNAL OF HEAT TRANSFER, Vol. 98, 1976, pp. 189–193.

23 Clever, R. M., and Busse, F. H., "Transition to Time Dependent Convection," *Journal of Fluid Mechanics*, Vol. 65, 1974, pp. 625–645.

24 Orszag, S. A., "Numerical Simulation of Incompressible Flows within Simple Boundaries: Accuracy," *Journal of Fluid Mechanics*, Vol. 49, 1971, pp. 75–112.

25 Orszag, S. A., "Numerical Simulations of Incompressible Flows within Simple Boundaries. I. Galerkin (Spectral) Representations," *Studies in Applied Mathematics*, Vol. 50, 1971, pp. 293–327.

26 Catton, I., Ayyaswamy, P. S., and Clever, R. M., "Natural Convection Flow in a Finite, Rectangular Slot Arbitrarily Oriented with Respect to the Gravity Vector," *International Journal of Heat and Mass Transfer*, Vol. 17, 1974, pp. 173–184.

27 Denny, V. E., and Clever, R. M., "Comparisons of Galerkin and Finite Difference Methods for Solving Highly Nonlinear Thermally Driven Flows," *Journal of Computational Physics*, Vol. 16, 1974, pp. 271–284.

28 Shaughnessy, E. J., Custer, J. R., and Douglass, R. W., "Partial Spectral Expansions for Problems in Thermal Conduction," ASME JOURNAL OF HEAT TRANSFER, Vol. 100, 1978, pp. 435–441.

29 Gray, D. D., and Giorgini, A., "The Validity of the Boussinesq Approx-

imation for Liquids and Gases," *International Journal of Heat and Mass Transfer,* Vol. 19, 1976, pp. 545–551.

30 Harris, D. L., and Reid, W. H., "On Orthogonal Functions Which Satisfy Four Boundary Conditions. Tables for Use in Fourier-Type Expansions." *Astrophysical Journal Supplements,* Ser. 3, 1958, pp. 429–452.

31 Chandrasekhar, S., *Hydrodynamic and Hydromagnetic Stability,* Oxford, Clarendon Press, 1961, pp. 634–643.

32 İyican, L., "Natural Convective Heat Transfer in Trapezoidal Enclosures," Ph.D. Dissertation, U. of Houston, Dec. 1979.

33 İyican, L., Witte, L. C., and Bayazitoğlu, Y., "An Experimental Study of Natural Convection in Trapezoidal Enclosures," ASME JOURNAL OF HEAT TRANSFER, (in press).

An Experimental Study of Natural Convection in Trapezoidal Enclosures

L. Iyican[1]
L. C. Witte
Department of Mechanical Engineering,
University of Houston,
Houston, TX 77004

Y. Bayazitoğlu
Department of Mechanical Engineering and
Materials Science,
Rice University,
Houston, TX 77001

Experimental data for natural convection of air in an inclined trapezoidal enclosure are reported for a Rayleigh number range of $\sim 2 \times 10^3$ *to* $\sim 5 \times 10^7$*. The small side of the trapezoid was electrically heated while the opposing large side was cooled to a uniform temperature. The effect of tilt angle from 0 to 90 deg (from horizontal) was investigated at 15 deg increments. Data were also obtained for 180 deg (hot surface facing down). A comparison of the data to an analysis using a two-dimensional circulation pattern showed reasonable agreement in the Rayleigh number-tilt angle range where two-dimensional circulation could be expected. The experimental data are correlated by an equation of the form,* $Nu = C\,Ra^n$*, over a wide Rayleigh number range. The data exhibit a local minimum in the Nusselt number-tilt angle curve between 90 and 0 deg in a manner similar to that observed in inclined rectangular channels.*

Introduction

Natural convection in inclined enclosures has received increased attention in recent years. A large number of papers on natural convection have been published, but little work has been devoted to unorthodox geometries which can arise in practical applications.

This paper describes a study of natural convection in trapezoidal enclosures; if the enclosure is fluid-filled and a temperature difference is maintained between the surfaces, a buoyancy-driven convective field will develop. This leads to natural convection heat transfer across the enclosure from the hot to the cold surface. The situation is further complicated by tilting the enclosure through an angle from the horizontal.

An important application on the trapezoidal groove geometry is to the so-called moderately concentrating solar collector. In this application, the trapezoidal geometry results when the absorbing surface and sidewalls are enclosed by the addition of a cover plate. The cover plate, which is at a lower temperature than the absorber, is used to suppress convection and radiation heat losses. The sidewalls are reflective surfaces and could contribute to the overall convective field in the groove.

Experiments were performed using an apparatus containing four trapezoidal grooves (see Fig. 1). Each groove consisted of an electrically-heated aluminum surface at the bottom, a water-cooled copper plate at the top, and two enclosing sidewalls. Two sidewall conditions were considered: aluminum sidewalls (with the capability of sidewall heating) to simulate high heat loss sidewalls, and balsa wood sidewalls with no heating to simulate low heat loss sidewalls.

A Rayleigh number range from $\sim 2 \times 10^3$ to $\sim 5 \times 10^7$ was provided by changing the pressure inside a pressure chamber from 0.068 to 10.2 atmospheres. Air was used for all experiments. Experiments were carried out at various tilt angles from 0 deg (horizontal) to 90 deg (vertical). A tilt angle of 180 deg (heated surface facing down) was also tested since this position is the most stable configuration, approximating a pure conduction case.

The measurements of temperature and of energy supplied to the groove were used to calculate the Nusselt number as a function of the Rayleigh number at different tilt angles for each sidewall condition.

A companion analysis of the heat transfer in a trapezoidal enclosure with adiabatic sidewalls was performed and is reported in detail in references [1, 2]. The model was based on a two-dimensional circulation pattern. Consequently, it is not applicable to the complete Nu-Ra-tilt angle range covered by our experiments. However, comparisons of the experiments with the analysis in regimes where the two-dimensional flow model is applicable are made.

Literature Review

A review of the literature reveals an overwhelming number of references. However, almost all the work completed thus far is restricted to relatively simple geometries such as rectangular or cylindrical enclosures. The literature for rectangular enclosures provides a body of data that relates closest to the trapezoidal geometry investigated in this study. To a lesser degree, the body of work available on natural convection in cylindrical annuli provides some insight.

An experimental investigation of convective heat transfer in liquids between two parallel plates at various inclination angles was described by Dropkin and Somerscales [3]. They covered a Ra range of 5×10^4 to 7×10^8 and a Pr range of 0.02 to 11,560. Their results were put into a power law form relating the variables Ra, Pr, and Nu. A constant of proportionality at different tilt angles was evaluated.

Hollands, et al. [4] measured heat transfer through inclined air layers of high aspect ratio, heated from below. They covered Ra up to 10^5 and inclination angles from 0 to 70 deg measured from horizontal.

Arnold, et al. [5, 6] measured heat transfer in a rectangular region with aspect ratios from 1 to 12. Ra up to 10^6 were covered. The variation of Nu with tilt angle showed a local minimum Nu between 70 and 30 deg. Nu is maximum at 0 deg tilt angle. By their explanation, the minimum is caused by a transition between a unicellular two-dimensional circulation near 90 deg to Benard-type instabilities near 0 deg tilt angle. Hart [7, 8] performed extensive analytical and experimental studies of flow regimes in an inclined box with basically the same conclusions as reported by Arnold.

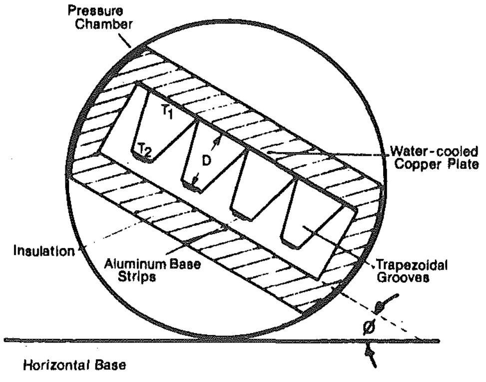

Fig. 1 *Cross-section of experimental apparatus*

---

[1] Present address: Shell Development Co., Houston, Texas 77001.

Contributed by the Heat Transfer Division for publication in the JOURNAL OF HEAT TRANSFER. Manuscript received by the Heat Transfer Division October 15, 1979.

Ozoe, et al. [9–15] report extensive experimental and numerical work related to rectangular geometries. In [9] they report a minimum in the Nu between 0 and 90 deg for low aspect ratios. The minimum is attributed to a change in the nature of the circulation pattern. In [10], they state that the preferred mode of convection in a square box at 90 deg tilt is a single two-dimensional roll with its axis along the long dimension. Three-dimensional photographs reported in [13] actually showed the transition between the flow modes as the tilt angle changes.

Natural convective motion and heat transfer have also been studied using visualization techniques. Brooks and Probert [16], Presner and Hsu [17], and Farhadieh and Tankin [18] studied high aspect ratio horizontal layers. Meyer, et al. [19] and Randall, et al. [20, 21] used interferometry to study convection across air in tilted enclosures. Grashof numbers up to 3×10^5 were achieved. Kuehn and Goldstein [22, 23] used Mach-Zehnder interferometry to determine temperature distributions and local heat transfer coefficients in cylindrical annuli. They used air and water. They found that eccentricity of the inner cylinder substantially alters the local and average heat transfer.

Flack, et al. [24, 25] have measured heat transfer in triangular enclosures. The enclosure consisted of a heated surface facing down at 45 deg adjacent to a cooled surface facing down at 45 deg; the enclosure was completed by a horizontal adiabatic surface connecting the two slanted walls. No tilting was performed. This situation is not amenable for comparison to our trapezoid data.

The papers cited in this section represent the types of observations which have been made in enclosed geometries. A much more extensive discussion of the literature is given by Iyican [1].

Experimental Apparatus

A cross-section of the apparatus is shown in Fig. 1. There are four trapezoidal grooves, each 61-cm long and enclosed by a 0.238-cm thick copper plate on top, a 0.051-cm thick aluminum plate at the bottom and two slanted sidewalls. The sidewalls were made of aluminum in one set of experiments and were replaced by balsa wood sidewalls for the second set of experiments. Figure 2 shows the details of the enclosures for the aluminum sidewalls.

The cover plate was kept at a uniform temperature by water flowing through a 1.27-cm o.d. copper tubing soldered to it. The heated surface was 1.91-cm wide and was insulated from the sidewalls with 0.318-cm wide fir wood strip at each side. The heated surfaces were heated individually by means of electrical heating tapes. These tapes were 1.27-cm wide and 61-cm long and were glued to the surfaces by a thermally-conductive, electrically-insulative glue.

Each heated plate and its heating element were glued into a groove cut into a long fir wood strip (see Fig. 2 for dimensions). The aluminum sidewalls were glued to each other at the top with silicone rubber and were fastened at the bottom to the wood strip.

The space between the two aluminum sidewalls and the fir wood strip connecting them was filled with a styrofoam piece shaped like a triangular prism. A styrofoam strip was glued with silicone rubber to the top of the sidewalls along the axial direction in order to separate the cover plate from the sidewalls and to prevent air leakage from one groove to the other. In the case of the wood sidewalls a triangular-shaped balsa wood piece was tightly fitted into the space between wood strips holding the absorber plate. The trapezoidal grooves were closed at both ends by 0.318-cm thick styrofoam inserts.

The apparatus was covered completely with 5.08-cm thick styrofoam blocks. The styrofoam at the sides was rounded to make the outside of the insulated apparatus fit easily into the pressure chamber.

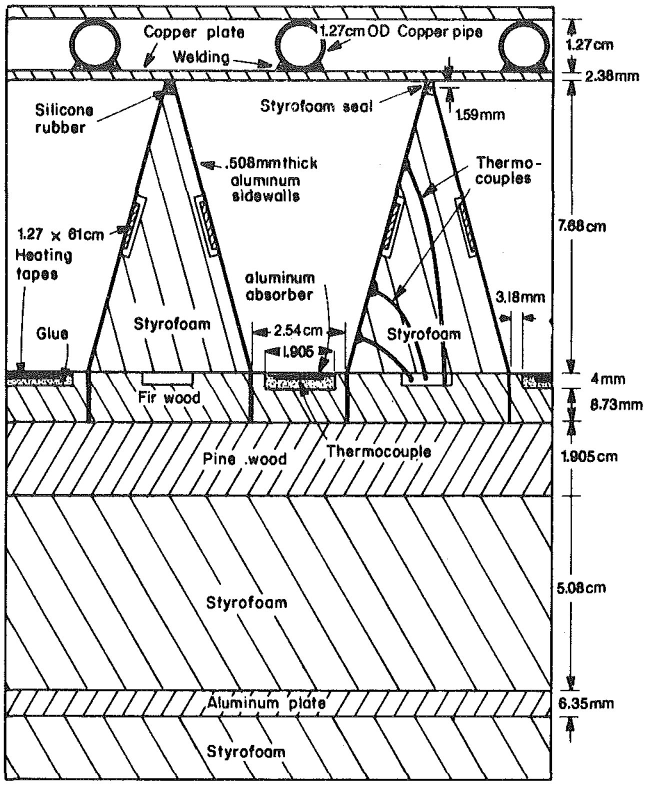

Fig. 2 Details of the trapezoidal enclosure with aluminum sidewalls

An electrical system was designed to supply power to each heated plate and each sidewall individually. This system consisted of a d-c power supply, a transistor control unit, a voltmeter, and an ammeter.

The pressure chamber assembly was a 1.524-m long, 45.7-cm o.d. steel pipe closed at one end by an endcap. At the other end a slip-on flange was welded to the pipe. An O-ring fitted into a groove cut in the outer face of the slip-on flange provided a pressure seal.

Components in the chamber held the apparatus in a fixed position and were used to mount the panels for the heating tape and thermocouple connectors. An air cylinder with 2000 psi air was connected to the vessel and provided the desired pressure. A vacuum pump was used to achieve pressures less than atmospheric.

The heated aluminum base strip does not extend fully across the base of the trapezoid. Chu, et al. [26] studied the effect of heater size and location on the heat transfer and circulation patterns in a long rectangular enclosure. In their study, the heater was placed on an insulated vertical wall and the opposite wall was cooled. The horizontal surfaces were either isothermal or adiabatic. For a square channel with a centrally-located heater the circulation is not increased significantly if the heater size is greater than 20 percent of the wall height. The heated surface in the trapezoid is centrally-located and covers 75 percent of the surface. Consequently no significant effect of heater size or location should be present.

Nomenclature

A = heat transfer area
B = trapezoid base width
C = coefficient in equation Nu = C Ra$^{.375}$
c_p = specific heat of air
D = height of trapezoidal groove
g = gravity acceleration
Gr = Grashof number
k = thermal conductivity of air
Nu = Nusselt number
Pr = Prandtl number
q = rate of heat transfer
Ra = Rayleigh number
Ra$_c$ = critical Rayleigh number
T_1 = temperature of the cooled plate
T_2 = temperature of the heated surface
β = trapezoid angle
ρ = density of air
μ = viscosity of air
γ = coefficient of thermal expansion, $1/T$
ϕ = tilt angle, measured from horizontal

Subscripts

t = total
c = conduction

Scope of Experiments

Experiments were performed by supplying a fixed amount of energy to the heating tapes and measuring the temperatures in the trapezoidal grooves for fixed values of the pressure and tilt angle. The two outer grooves were used as guard heaters, thus minimizing side effects. To insure that results were not influenced by end effects data from the mid-points of the two central grooves were used for analysis. These values were used along with the system dimensions and material properties to calculate a Nusselt number defined as

$$\mathrm{Nu}_t = \frac{q \cdot D}{A \cdot (T_2 - T_1) \cdot k} \qquad (1)$$

A corresponding Rayleigh number was also calculated,

$$\mathrm{Ra} = \frac{\rho^2 g \gamma C_p \, (T_2 - T_1)\, D^3}{\mu k} \qquad (2)$$

The Ra range was achieved primarily by varying the pressure, directly affecting the ρ^2-term in eq. (2). Pressure ranged from 0.068 to 10.2 atmospheres. Air was the working fluid throughout. In all experiments, the trapezoidal angle β was 30 deg, the base B was 2.54-cm and height D was 7.68-cm.

The heated base was varied from 35 to 66°C while the copper cover varied over only a very narrow range, 26 to 28°C. Tilt angles from 0 to 180 deg were covered.

For the system using aluminum sidewalls, 73 experiments were performed with ten of these being replication experiments at previously measured points. For the wood sidewalls, 109 experiments, including ten for replication, were undertaken. The replication test showed that reproducibility of 5 percent or better was achieved.

Data Reduction

Temperature measurements along the aluminum sidewalls showed very little variation with position, regardless of the tilt angle. The explanation for this behavior is that thermal barriers separated the aluminum from the hot and cold surfaces. Thus, the energy provided to the sidewall was quickly distributed over the sidewall and it assumed almost the average temperature between the hot and cold surfaces. Although not measured, approximately the same behavior would be expected for the wood sidewalls since they more closely approximate an adiabatic wall case. This behavior also prevailed for those cases where small amounts of sidewall heating were used.

The total energy supplied to the heating elements is transported to the copper plate by convection in the air, radiation exchange, and conduction up the sidewalls. Also there is small conduction loss through the insulating superstructure underlying the heating elements. Therefore, heat transfer due to radiation exchange and to conduction through the insulation must be subtracted from the total heat dissipated by the heating elements to obtain energy supplied from the absorber and sidewalls to the cover plate by conduction and convection.

Conduction losses were calculated from a one-dimensional modelling of the structure underlying the heating tapes. The symmetry of the system and the minimization of edge and end effects give adequate justification for this technique. Radiation transport from the

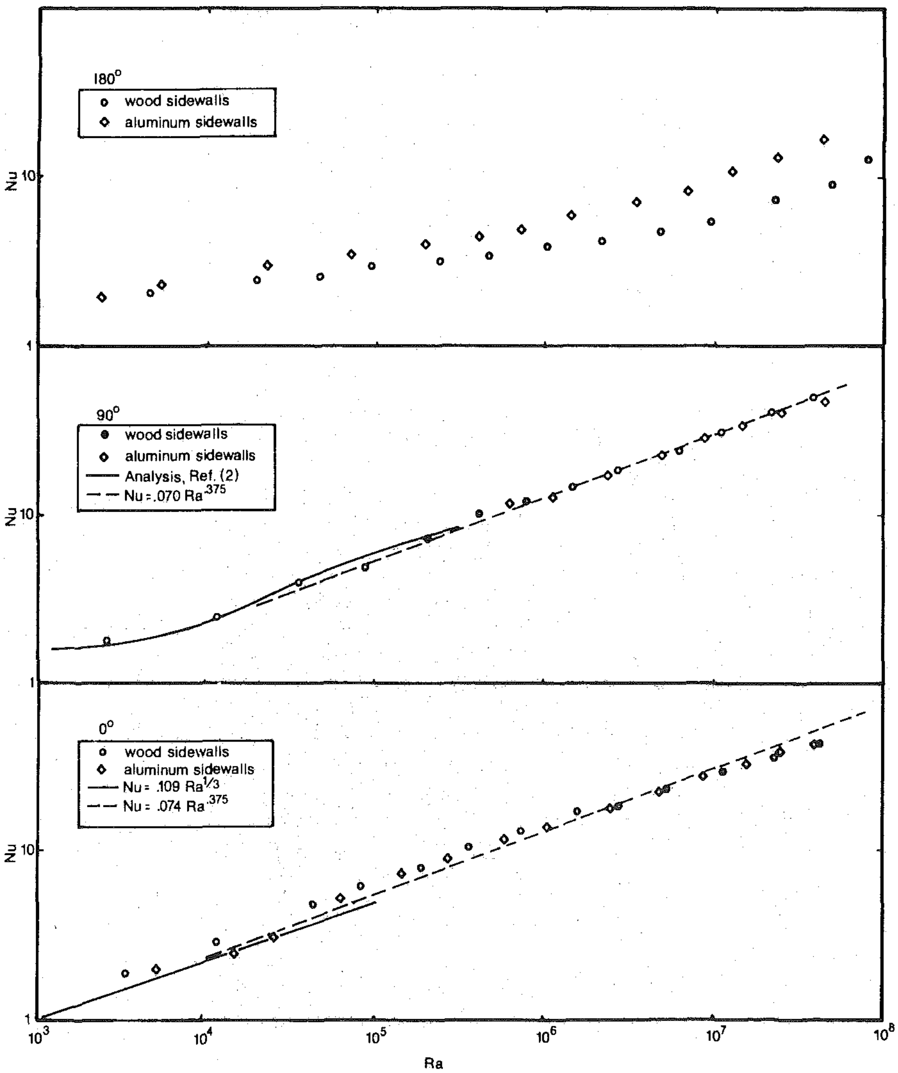

Fig. 3 Experimental data for 0, 90 and 180 deg tilt angles

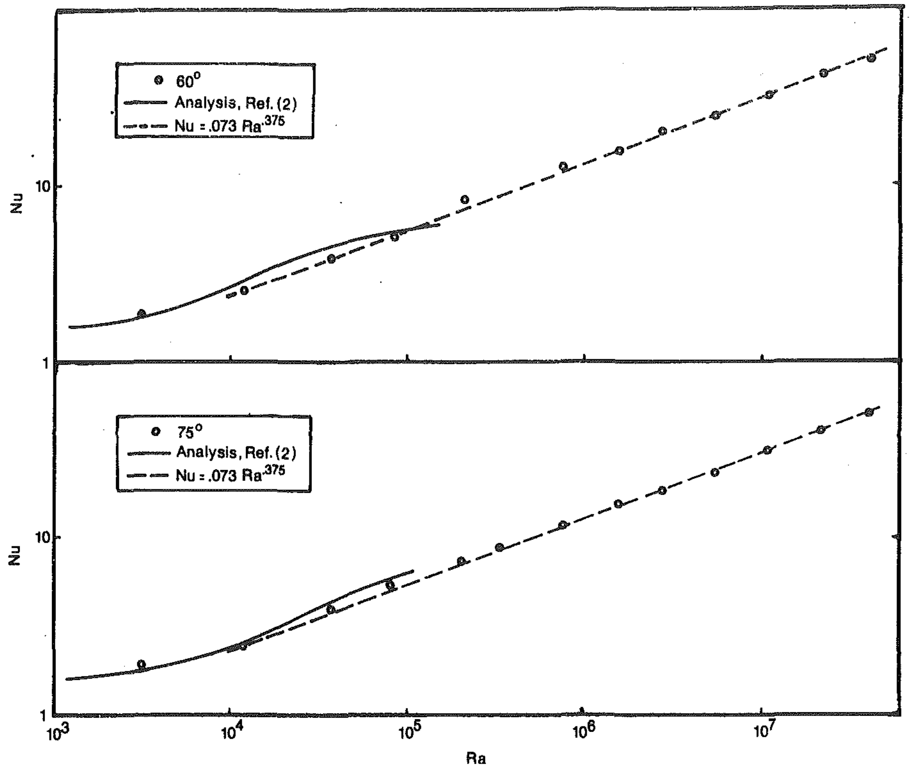

Fig. 4 Comparison of data for 60 and 75 deg to two-dimensional analysis. Correlating equations are also shown.

heated surface can be calculated from a surface radiation analysis for the enclosure. An analogous electrical circuit was set up and used to generate three algebraic equations, one of which yielded the net radiative transport from the hot absorber surface. The radiation loss varied from 2 to 6 percent of the energy supplied for wood sidewalls. For aluminum sidewalls, it ranged from 2 up to about 4 percent. The conduction loss through the back of the system ranged up to 3 percent for the wood sidewall system and up to about 4 percent for the aluminum sidewall case.

The separation of conduction along the sidewalls from the convection to the air is somewhat more complicated than the conduction or radiation loss terms. Basically, the technique is based on the fact that as Ra approaches Ra_c, the convective effect tends to disappear and the net transport is by conduction through the air and the sidewalls. Pure conduction across the air can be calculated; for perfectly-conducting sidewalls the Nu_c would be 1.0; for adiabatic sidewalls, $\mathrm{Nu}_c = 1.6$. The experimental data for the aluminum sidewalls case showed that Nu_t approaches ~32 for Ra less than $\sim 4 \times 10^3$ for all tilt angles. Therefore, to find the Nu due to convection from the heated surface to the air alone, a factor of 31 was subtracted from all data. Since the ΔT did not change appreciably over the entire Ra range for each sidewall material, the conductive effect remains approximately constant. A similar correction was performed for the wood sidewalls case.

An error estimate for the experimental data was carried out with the result that uncertainties of ± 10 percent would be the maximum expected for the Nu-Ra data points. The maximum uncertainty occurs at low Ra. Reference [1] contains the details of this error analysis.

Experimental Results

Figure 3 shows the data plotted as Nu versus Ra for 0, 90 and 180 deg which encompass the full range of tilt angles. These data show that the effect of sidewall material is essentially negligible for this geometry, except for 180 deg (hot surface facing down). Ideally, this case is one in which pure conduction occurs. However, end effects and possibly small deviations from horizontal along the groove cause weak convection to occur. Apparently the aluminum sidewalls promote these convection patterns more readily than the less conductive wood sidewalls. At other tilt angles differences in the two sets of data become negligible within the accuracy of the experiments.

As mentioned before, a two-dimensional heat transfer analysis was performed as a companion study to the experiments [2]. These calculations for $\phi = 90$ deg were stable up to Ra of about 2×10^5. A comparison of the analysis to the data for 90 deg shown in Fig. 3 shows good agreement for Ra up $\sim 2 \times 10^5$. Figure 4 shows the data for 60 and 75 deg along with the two-dimensional calculations for Ra up to about 10^5. The agreement between the two-dimensional model and experiments gets progressively worse as the tilt angle decreases. This is probably a reflection of the fact that the flow undergoes a transition from a two-dimensional to a three-dimensional flow pattern as the angle is decreased.

Figure 5 shows the complete set of data for wood sidewalls. Plotted in this way, the data show a minimum in Nu between 90 and 0 deg tilt angle. As Ra increases, the minimum moves closer to the 90 deg point. This phenomenon has been observed by several investigators. The data of Arnold, et al. [6] show this minimum occurring near the 90 deg point dependent upon the aspect ratio and Ra. Their data were limited to $\mathrm{Ra} \leq 10^6$ with $\mathrm{Pr} = 4.5$ (water) and 2000 (silicone oil). Hart [7, 8] has shown that the minimum point is moved toward 0 deg for increasing Pr. The three-dimensional photographs of Ozoe, et al. [13] in a long square channel illustrate the physics responsible for the minimum. A change in the basic nature of the flow regime between 0 and 90 deg occurs. At 0 deg, roll-cells with axes normal to the long axis of the channel are prevalent. At 90 deg, the flow is unicellular with the axis parallel to the long axis. Between 0 and 90 deg, the cells become oblique and finally undergo transition into a two-dimensional unicellular pattern at 90 deg. Ozoe's data were for glycerol ($\mathrm{Pr} = 2700$–3000) and $\mathrm{Ra} = 12{,}000$; they exhibit a minimum very near the 0 deg tilt angle. The trapezoid data for air in Fig. 5 show a minimum closer to 90 deg as the Ra increases. This behavior corresponds with the observations of Hart and Arnold.

Correlations suggested by Hollands [4] and Randall [21] which are for plane geometries of large aspect ratio do not correlate the trapezoid data well especially at higher Ra. The aspect ratio is defined by the ratio of the width of the two heat transfer surfaces to the spacing between the two surfaces. Using either of the lateral dimensions of the trapezoid, the aspect ratio for the trapezoid data would be less than unity. Figure 6 shows a comparison of the trapezoid data to Hollands correlation for 45 deg. The data of Randall [21] for 45 deg are also shown for comparison. The trapezoid data lie generally above both Holland's correlation and Randall's data and the trend at higher Ra is significantly different. Ozoe's data for inclined channels [11] indicate that Nu increases for smaller aspect ratio at a fixed Ra. This could account for the lack of agreement between the trapezoid data and the parallel plate data of Randall and Hollands.

For Ra above $\sim 10^4$, the trapezoid data are correlated reasonably well by a power law similar to that suggested by Ozoe, et al. [11]. Following the suggestion of Clever [27], they correlated their data for rectangular enclosures with an equation of the form, $Nu = C\,Ra^n$. For air in a rectangular enclosure they found that $Nu = 0.109\,Ra^{1/3}$ fit their data for 0 deg tilt angle. Figure 5 shows Ozoe's correlation compared to the trapezoid data for 0 deg. The form of the equation is adequate, but for $Ra \geq 10^4$, an exponent of 0.375 and different coefficients are required. These correlating equations are shown on Figs. 3 and 4 and Table 1 lists the coefficients for all of the trapezoid data from 0 to 90 deg.

This correlation provides excellent agreement for tilt angles above 45 deg. For smaller angles, the correlation tends to overpredict Nu at higher Ra.

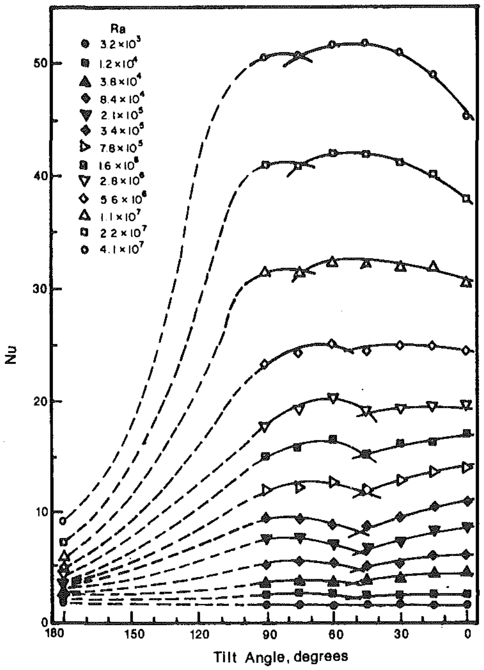

Fig. 5 Heat transfer data for wood sidewalls. Dashed lines indicate expected behavior between 180 and 90 deg.

Summary

Experimental data for air in trapezoidal enclosures exhibit a local minimum in the Nu-tilt angle curve between 90 and 0 deg; the angle where the minimum occurs is a function of Ra and moves toward 90 deg as the Ra increases. A comparison of the data to a two-dimensional analysis shows good agreement at 90 deg, but the agreement gets progressively worse as the angle is decreased toward 45 deg. This behavior is undoubtedly caused by a change from a two to a three-dimensional flow pattern as the angle is decreased. A similar effect has been observed in rectangular inclined channels.

The data are not correlated well by equations formulated for parallel plate enclosures of high aspect ratio by Hollands and Randall. However, the data are correlated reasonably well in the region $10^4 \leq Ra \leq 10^7$ by an equation of the form $Nu = C\,Ra^n$.

Acknowledgments

Funds from NSF Grant ENG 77-04122 were used to support this work. Incentive funding from the University of Houston Energy Laboratory is also appreciated.

References

1 Iyican, L., "Natural Convection Heat Transfer in Trapezoidal Enclosures," Ph.D. dissertation, University of Houston, Dec. 1979.

2 Iyican, L., Bayazitoglu, Y., and Witte, L. C., "An Analytical Study of Natural Convection Heat Transfer within a Trapezoidal Enclosure," ASME JOURNAL OF HEAT TRANSFER, in press.

3 Dropkin, D. J., and Somerscales, E., "Heat Transfer by Natural Convection in Liquids Confined by Two Parallel Plates which are Inclined at Various Angles with Respect to the Horizontal," ASME JOURNAL OF HEAT TRANSFER, Vol. 87, Feb., 1965, pp. 77–84.

4 Hollands, K. G. T., Unny, T. E., Raithby, G. D., and Konicek, L., "Free Convective Heat Transfer Across Inclined Air Layers," ASME JOURNAL OF HEAT TRANSFER, Vol. 98, 1976, pp. 189–193.

5 Arnold, J. N., Bonaparte, P. N., Catton, I., and Edwards, D. K., "Experimental Investigation of Natural Convection in a Finite Rectangular Region Inclined at Various Angles from 0° to 180°," *Proceedings of the 1974 Heat Transfer and Fluid Mechanics Institute,* Stanford Univ. Press, 1974, pp. 321–329.

6 Arnold, J. N., Catton, I., and Edwards, D. K., "Experimental Investigation of Natural Convection in Inclined Rectangular Regions of Differing Aspect Ratios," ASME JOURNAL OF HEAT TRANSFER, Vol. 98, Feb., 1976, pp. 67–71.

7 Hart, J. E., "Stability of the Flow in a Differentially Heated Inclined Box," *Journal of Fluid Mechanics,* Vol. 47, Pt. 3, 1971, pp. 547–576.

8 Hart, J. E., "Transition to a Wavy Vortex Regime in Convective Flow Between Inclined Plates," *Journal of Fluid Mechanics,* Vol. 48, Pt. 2, 1971, pp. 265–271.

9 Ozoe, H., Yamamoto, K., and Churchill, S. W., "Natural Circulation in

Table 1 Coefficients for the equation $Nu = C\,Ra^{0.375}$
$Ra \geq 10^4$

ϕ	0	15	30	45	60	75	90
C	0.074	0.076	0.076	0.073	0.073	0.073	0.070

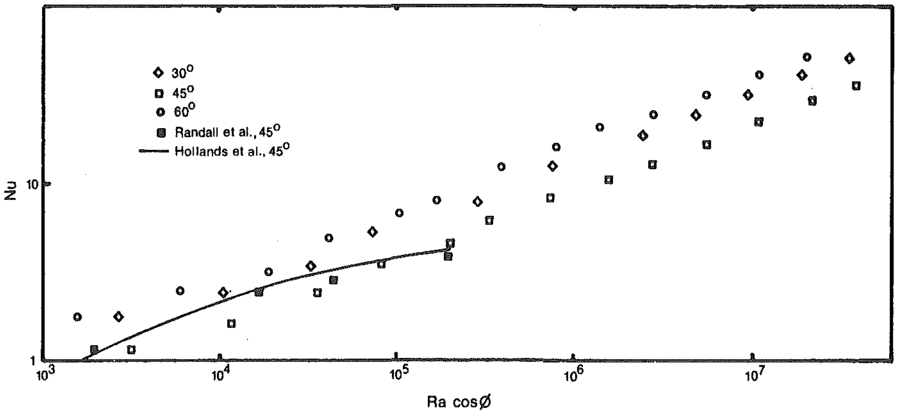

Fig. 6 Comparison of intermediate tilt angle data to the correlation of Hollands and to the data of Randall

an Inclined Rectangular Channel Heated on One Side and Cooled on The Opposing Side," *International Journal of Heat and Mass Transfer*, Vol. 17, 1974, pp. 1209–1217.

10 Ozoe, H., Sayama, H., and Churchill, S. W., "Natural Convection in an Inclined Square Channel," *International Journal of Heat Mass Transfer*, Vol. 17, 1974, pp. 401–406.

11 Ozoe, H., Sayama, H, and Churchill, S. W., "Natural Convection in an Inclined Rectangular Channel at Various Aspect Ratios and Angles—Experimental Measurements," *International Journal of Heat and Mass Trnasfer*, Vol. 18, No. 12, 1975, pp. 1425–1431.

12 Ozoe, H., Yamamoto, K., Churchill, S. W., and Sayama, H., "Three-Dimensional Numerical Analysis of Laminar Natural Convection in a Confined Fluid Heated from Below," ASME JOURNAL OF HEAT TRANSFER, Vol. 98, 1976, pp. 202–207.

13 Ozoe, H., Sayama, H., and Churchill, S. W., "Natural Convection Patterns in a Long Inclined Rectangular Box Heated from Below. Part I. Three-Dimensional Photography," *International Journal of Heat Mass Transfer*, Vol. 20, 1977, pp. 123–129.

14 Ozoe, H., Yamamoto, K., and Sayama, H., "Natural Convection Patterns in a Long Inclined Rectangular Box Heated from Below: Part II. Three-Dimensional Numerical Results," *International Journal of Heat Mass Transfer*, Vol. 20, 1977, pp. 131–139.

15 Ozoe, H., Yamamoto, K., and Churchill, S. W., "Three-Dimensional Natural Convection in an Inclined Channel with a Square Cross-Section," *American Institute of Chemical Engineering Journal*. Vol. 25, No. 4, July, 1979, pp. 709–716.

16 Brooks, R. C., and Probert, S. D., "Heat Transfer Between Parallel Walls: An Interferometric Investigation," *Journal of Mechanical Engineering Science*, Vol. 14, No. 2, 1972, pp. 107–127.

17 Presner, D. S., and Hsu, G. R., "Thermal Convection in Laterally Bounded Air Spaces," Department of Thermal and Environmental Engineering, School of Engineering Technology, Southern Illinois University, Carbondale, Ill., 1972.

18 Farhadieh, R., and Tankin, R. S., "Interferometric Study of Two-Dimensional Benard Convection Cells," *Journal of Fluid Mechanics*, Vol. 66, 1974, p. 739.

19 Meyer, B. A., El-Wakil, M. M., and Mitchell, J. W., "Natural Convection Heat Transfer in Small and Moderate Aspect Ratio Enclosures—An Application to Flat Plate Collectors," Unpublished Paper, Mechanical Engineering Dept., University of Wisconsin, Madison, Wisc.

20 Randall, K. R., El-Wakil, M. M., and Mitchell, J. W., "Natural Convection Characteristics of Flat Plate Collectors—Progress Report," Engineering Experiment Station, C00/2971-1, Apr. 1977.

21 Randall, K. R., Mitchell, J. W., and El-Wakil, M. M., "Natural Convection Heat Transfer Characteristics of Flat Plate Enclosures," ASME JOURNAL OF HEAT TRANSFER, Vol. 101, Feb., 1979, pp. 120–125.

22 Kuehn, T. H., and Goldstein, R. J., "An Experimental and Theoretical Study of Natural Convection in the Annulus between Horizontal Concentric Cylinders," *Journal of Fluid Mechanics*, Vol. 74, Pt. 4, 1979, pp. 695–719.

23 Kuehn, T. H., and Goldstein, R. J., "An Experimental Study of Natural Convection Heat Transfer in Concentric and Eccentric Horizontal Cylindrical Annuli," ASME JOURNAL OF HEAT TRANSFER, Vol. 100, Nov., 1978, pp. 635–640.

24 Flack, R. D., Konopnicki, T. T., and Rooke, J. H., "The Measurement of Natural Convective Heat Transfer in Triangular Enclosures," ASME Paper No. 78-WA/HT-9, Dec., 1978.

25 Flack, R. D., and Witt, C. L., "Velocity Measurements in Two Natural Convection Air Flows Using a Laser Velocimeter," ASME JOURNAL OF HEAT TRANSFER, Vol. 101, No. 2, 1979, pp. 256–260.

26 Chu, H. H-S., Churchill S. W., and Patterson, C. V. S., "The Effect of Heater Size, Location, Aspect Ratio, and Boundary Conditions on Two-Dimensional, Laminar, Natural Convection in Rectangular Channels," ASME JOURNAL OF HEAT TRANSFER, Vol. 98, No. 2, May, 1976, pp. 194–201.

27 Clever, R. M., "Finite Amplitude Longitudinal Convection Ratio in an Inclined Layer," ASME JOURNAL OF HEAT TRANSFER, Vol. 95, 1973, pp. 407–409.

E. Saatdjian
J. P. Caltagirone
Laboratoire d'Aérothermique du C.N.R.S.,
4ter, route des Gardes,
F 92190-MEUDON, France

Natural Convection in a Porous Layer under the Influence of an Exothermic Decomposition Reaction

A porous medium saturated with a gas is bounded by two impermeable planes. As the temperature of the lower side is increased, part of the porous matrix decomposes exothermically into gaseous products. A two dimensional model which couples the effects of this reaction to natural convection is solved numerically. At first, the reaction dominates the phenomena; the temperature and velocity components increase and a thermal front passes through the layer. As the reaction dies out due to a depletion of reactant, convective effects alone remain. Though this final state is well known, the density of the fluid is, here, allowed to vary and, furthermore, an ideal gas instead of an incompressible liquid is considered.

Introduction

For natural convection in a porous medium bounded by two isothermal planes, Lapwood [1] predicted the criteria for the onset of convection. The critical transition (conduction to convection) Rayleigh number derived ($4\pi^2$) has been verified experimentally by Katto and Masuoka [2]. Since then, numerous researchers [3, 4] have investigated the convective flow for Rayleigh numbers exceeding the critical value; unsteady flows have been confirmed experimentally for a critical Rayleigh number (240–280) depending on the type of porous medium and on the cell dimensions.

In general, the mathematical formulation is simplified by the Boussinesq approximation. The fluid density differences are neglected everywhere except in the buoyancy term of Darcy's law. This assumption is appealing for two reasons.

1 The fluid is considered to be incompressible in the continuity equation and, thus, a simple stream function can be introduced.

2 The density variations with pressure are also neglected in the equation of state. If, furthermore, the coefficient of thermal expansion is also assumed as constant, a linear state equation relating the density to the temperature only is obtained.

When the imposed temperature gradient is significant, the fluid physical properties can no longer be considered as constant. Liquids subject to an important temperature difference exhibit an enormous decrease in viscosity. For this reason, Kassoy and Zebib [5], Horne and O'Sullivan [6] and Straus and Schubert [7] consider the effects of variable viscosity on the stability of a porous layer.

Porous layers with internal heat generation are treated in [8]; however, when heat and mass transfer occur simultaneously, the phenomenon is less well known. Consider a porous medium bounded by two impermeable planes and saturated with a gas. The matrix consists of a mixture of fiberglass and a resin. As the matrix temperature is increased, the resin decomposes exothermically into gaseous products. Some pipe insulators behave in this way when the temperature of the hotside is quite high. Prud'homme and Caltagirone [9] have solved a similar problem though they neglect convection and consider the process to be one-dimensional.

In this paper, we propose a two-dimensional model which couples the effects of the decomposition reaction (heat generation and mass transfer) to natural convection. The resin density, fluid density, velocity components and temperature disturbances are obtained numerically using a finite difference scheme. The parameters introduced by the resin reaction (heat of reaction, order of reaction, initial resin concentration, etc.) play an important role in the evolution of the process. However, once the resin stock is depleted (partially or totally), convective effects alone subsist. This final state is also the focus of our attention. Though, as we mentioned, it has been widely investigated, the formulation used here has two basic differences. We consider the saturating fluid to be an ideal gas and we allow its density to vary everywhere.

Governing Equations

A plane porous matrix of thickness, ℓ, is bounded by two impermeable surfaces and initially at ambient temperature T_{amb}. At time $t' = 0$, the temperature of the lower surface ($y' = 0$) is increased to $T' = T_p$. The porous matrix is composed of a mixture of a nonreacting fiberglass and a resin which decomposes exothermically into gaseous products as the matrix temperature increases.

In order to simplify the equations, two main assumptions are made.

1 The matrix properties remain unchanged during the reaction. This assumption is valid because in most commercial applications the weight fraction of nonreacting fiberglass is quite high (>9/10).

2 The gaseous products and the fluid which initially filled the enclosed region are the same. In other words, we neglect diffusion between two different gases, the fluid properties correspond to those of a unique fluid.

The equations of the phenomena are

$$\frac{\partial \rho'_A}{\partial t'} = -k_0 \, \rho'^N_A \, e^{-Ea/RT'} \tag{1}$$

$$\epsilon \frac{\partial \rho'_B}{\partial t'} + \nabla \cdot \rho'_B \, \mathbf{V} = k_0 \, \rho'^N_A \, e^{-Ea/RT'} \tag{2}$$

$$\mathbf{V} = -\frac{K}{\mu} \left[\nabla P' - \rho'_B \, \mathbf{g}\right] \tag{3}$$

$$(\rho c)^* \frac{\partial T'}{\partial t} + (\rho c)_B \, \mathbf{V} \cdot \nabla T' = \lambda_0^* \, \nabla^2 T' + \Delta H_R k_0 \rho'^N_A \, e^{-Ea/RT'} \tag{4}$$

The resin decomposition reaction of order N is expressed in terms of the resin density ρ'_A. The resin is assumed to be stationary (it does not diffuse) and only one decomposition reaction is considered. For elementary reactions, the temperature dependent term is represented by Arrhenius' law [10].

Equation (2) is the fluid continuity equation with the production term in the right hand side. Darcy's law (3) is applicable for flow through porous media; the permeability K and the fluid viscosity μ are assumed to be constants. The energy equation (4) exhibits the heat generation term due to the exothermic reaction. The thermal conductivity of the porous medium λ_0^* and the heat of reaction ΔH_R are also assumed to be constants. The heat and mass production terms depend both on the resin density and on the temperature. Since the former is initially finite, a time will be reached when these terms will

---

Contributed by the Heat Transfer Division for publication in the JOURNAL OF HEAT TRANSFER. Manuscript received by the Heat Transfer Division May 16, 1980.

no longer influence the phenomenon.

The fluid equation of state is

$$P' = \frac{\rho'_A RT'}{M} \tag{5}$$

Equations (1–5) are rendered dimensionless with the following reference parameters: ρ_{A0} for the resin density, ρ_{B0} for the fluid density, $(\rho c)^* \ell^2/\lambda_0^*$ for time, $\lambda_0^*/(\rho c)_B \ell$ for velocity, T_{amb} for temperature, ℓ for length, and P_0 for pressure. Inserting the equation of state in Darcy's law, the dimensionless, two-dimensional system of equations becomes

$$\frac{\partial \rho_A}{\partial t} = -\sigma_1 \rho_A^N e^{\gamma[1-1/T]} \tag{6}$$

$$\epsilon \frac{\partial \rho_B}{\partial t} + \frac{(\rho c)^*}{(\rho c)_B}\left[u \frac{\partial \rho_B}{\partial x} + v \frac{\partial \rho_B}{\partial y} + \rho_B\left(\frac{\partial u}{\partial x} + \frac{\partial v}{\partial y}\right)\right] = \sigma_2 \rho_A^N e^{\gamma[1-1/T]} \tag{7}$$

$$u = -P_1\left[\rho_B \frac{\partial T}{\partial x} + T \frac{\partial \rho_B}{\partial x}\right] \tag{8a}$$

$$v = -P_1\left[\rho_B \frac{\partial T}{\partial y} + T \frac{\partial \rho_B}{\partial y}\right] - \text{RaGa}\, \rho_B \tag{8b}$$

$$\frac{\partial T}{\partial t} + u \frac{\partial T}{\partial x} + v \frac{\partial T}{\partial y} = \frac{\partial^2 T}{\partial x^2} + \frac{\partial^2 T}{\partial y^2} + \delta \rho_A^N e^{\gamma[1-1/T]} \tag{9}$$

Apart from $(\rho c)^*/(\rho c)_B$ and N, six dimensionless parameters appear in the equations.

$$\sigma_1 = \frac{k_0 \rho_{A0}^{N-1} (\rho c)^* \ell^2 e^{-\gamma}}{\lambda_0^*} \qquad \sigma_2 = \frac{\sigma_1 \rho_{A0}}{\rho_{B0}},$$

$$\gamma = \frac{Ea}{RT_{\text{amb}}}, \qquad \delta = \frac{\Delta H_R k_0 \rho_{A0}^N \ell^2 e^{-\gamma}}{\lambda_0^* T_{\text{amb}}},$$

$$P_1 = \frac{K(\rho c)_B P_0}{\mu \lambda_0^*}, \qquad \text{RaGa} = \frac{K(\rho c)_B \rho_{B0} g \ell}{\mu \lambda_0^*}$$

σ_1, σ_2, δ, and γ are introduced by the decomposition reaction; P_1 depends on the reference pressure, P_0; and RaGa is the Rayleigh number multiplied by the Gay-Lussac number. Since the pressure gradients are created by density differences (natural convection) the reference pressure P_0 is taken as $P_0 = \rho_{B0} g \ell$. Thus, P_1 and RaGa become equal. Notice that since $\beta = 1/T$, for an ideal gas, RaGa is equivalent to a local Rayleigh number.

The boundary and initial conditions in dimensionless form are

$$\rho_{A0} = 1; \quad \rho_B = 1 \quad \text{for} \quad t = 0$$

$$\frac{\partial T}{\partial x} = 0; \quad \frac{\partial \rho_B}{\partial x} = 0; \quad u = 0 \quad \text{for} \quad x = 0 \text{ and } x = 1 \tag{10}$$

$$T = \frac{T_p}{T_{\text{amb}}}; \quad v = 0 \quad \text{for} \quad y = 0$$

$$\frac{\partial T}{\partial y} = B_i\,[1 - T]; \quad v = 0 \quad \text{for} \quad y = 1$$

Equations (6–9) with conditions (10) are solved numerically.

Numerical Procedure

The system of partial differential equations in dimensionless form (6–9) is solved using finite differences, for basic reading we refer to [11].

The decomposition reaction and fluid continuity equations are both first order; because of its simplicity, an explicit scheme is used for both of them. The energy equation (9) is solved by the implicit alternating direction method. Obviously, the boundary and initial conditions are accounted for when applicable. Once the fluid density and temperature distributions are known, the velocity components u and v are calculated directly from (8a) and (8b).

For each time step, we assume that the fluid is in equilibrium with the resin and temperature distributions. Equation (7) and thus (8) are subject to iterations within each time step.

The calculations proceed in the following way: once the initial conditions are given, the resin density profile is calculated from (6). By iterating (7) and (8a, 8b) we obtain the fluid density and the velocity components. Finally, the temperatures are calculated from (9) and a new time step begins.

In all calculations, a grid of 17 × 17 is employed. The disadvantage of using an explicit scheme is that the time step has to be sufficiently small to assure convergence. For a convergence error on the fluid density of 10^{-4}, the time step size is 4×10^{-5} for (6) and (9) and 5×10^{-6} for (7).

The resin density, fluid density, horizontal and vertical velocity components and temperature distributions are thus obtained. With the aid of a tracer, isotherms and isochores (for both the fluid and the resin) are plotted. Though a stream function is not introduced, the velocity components are known and thus their magnitude and direction are traced at each grid point.

The porous matrix corresponds to a commercial insulating material of high porosity ($\epsilon > 0.95$). For simplicity we assume that $(\rho c)^* = (\rho c)_B$ and $\lambda_0^* = \lambda_B^*$. The initial temperature distribution $T = 1 + (T_p/T_{\text{amb}} - 1)(1 - y) + 0.1 \cos \pi \times \sin \pi y$ is used. In a later section we discuss the precision of the numerical scheme used here; whether the grid and the time steps are sufficiently fine or not.

Discussion

The transient behavior of both the temperature and resin concentration is shown in Figs. 1 and 2; the profiles are plotted at the same instants of time. The dimensionless parameters corresponding to both

Nomenclature

Bi = Biot number ($h\ell/\lambda_0^*$)
Ea = energy of activation (j/mole)
g = acceleration due to gravity (m/s^2)
Ga = Gay-Lussac number ($1/\beta\Delta T$)
h = heat transfer coefficient on the upper boundary (w/m^{2}K)
ΔH_R = heat of reaction (j/mole)
k_0 = frequency factor
K = permeability (m^2)
ℓ = thickness of the porous layer (m)
M = molecular weight of the fluid (kg/mole)
N = order of reaction
P = dimensionless pressure
P_0 = reference pressure (kg/ms^2)
P_1 = dimensionless parameter $\left(\frac{K(\rho c)_B P_0}{\mu \lambda_0^*}\right)$
R = universal gas constant (j/mole K)
Ra = Rayleigh number $\left(\frac{K(\rho c)_B \rho_{B0} g \ell \beta \Delta T}{\mu \lambda_0^*}\right)$
t = dimensionless time
T = dimensionless temperature
T_{amb} = ambient temperature (K)
T_p = lower surface temperature (K)
u, v = horizontal and vertical velocity components respectively (dimensionless)
x, y = horizontal and vertical coordinates respectively (dimensionless)
β = coefficient of thermal expansion (K^{-1})
γ = dimensionless parameter $\frac{Ea}{RT_{\text{amb}}}$
δ = dimensionless parameter $\frac{\Delta H_R k_0 \rho_{A0}^N \ell^2 e^{-\gamma}}{\lambda_0^* T_{\text{amb}}}$
ϵ = porosity
λ_0^* = thermal conductivity of the porous medium (w/m K)
μ = fluid viscosity (kg/ms)
ρ_A = dimensionless resin density
ρ_{A0} = reference resin density (kg/m^3)
ρ_B = dimensionless fluid density
ρ_{B0} = reference fluid density (kg/m^3)
$(\rho c)^*$ = heat capacity per unit volume of the porous medium (j/m^{3}K)
$(\rho c)_B$ = heat capacity per unit volume of fluid (j/m^3 K)
σ_1 = Dimensionless parameter $\frac{k_0 \rho_{A0}^{N-1} (\rho c)^* \ell^2 e^{-\gamma}}{\lambda_0^*}$
σ_2 = Dimensionless parameter $\frac{\sigma \rho_{A0}}{\rho_{B0}}$
primes denote real variables

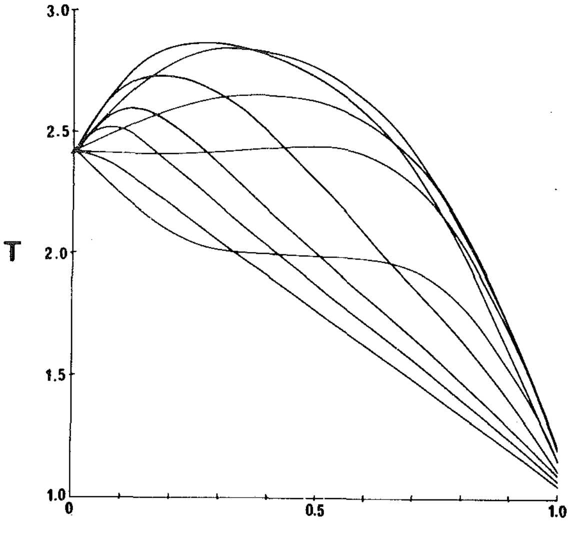

Fig. 1 Temperature distribution versus vertical direction for different values of *t*

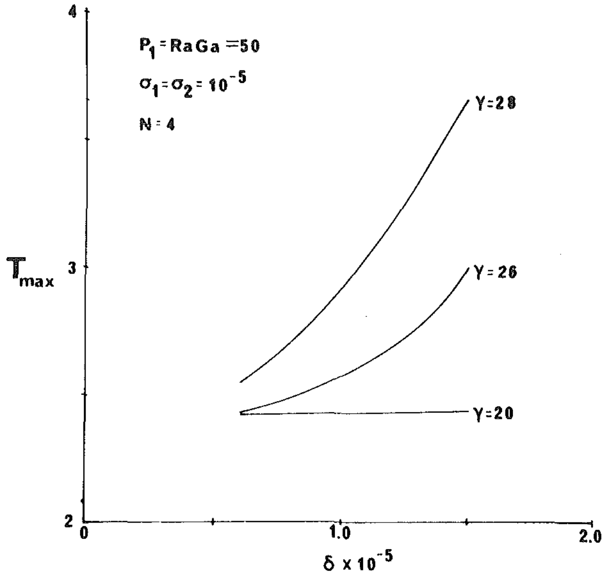

Fig. 3 Maximum temperature in the layer as a function of δ and γ

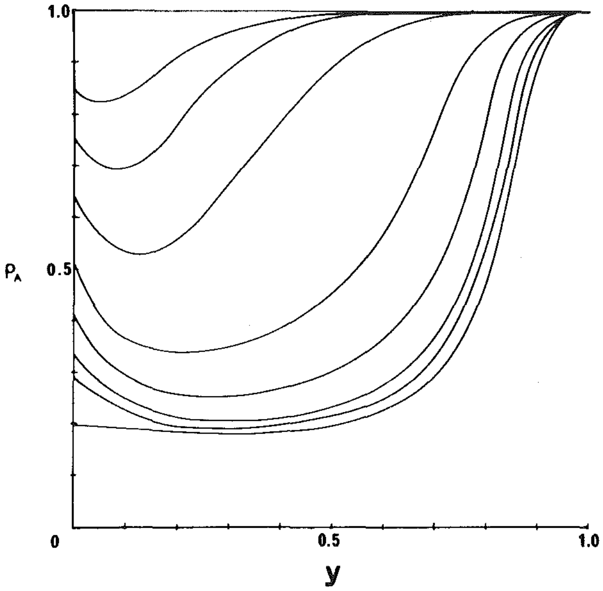

Fig. 2 Resin concentration versus vertical direction for different values of *t*

figures are $x = 0.5, \gamma = 28, N = 4, \mathrm{Bi} = 25, P_1 = \mathrm{Ra\,Ga} = 50, T_p/T_{\mathrm{amb}} = 2.42, \delta = \sigma_1 = \sigma_2 = 10^{-5}$. The figures show that the temperature profile is disturbed by the exothermic reaction and vice versa.

At first, the hotter lower surface ignites the decomposition reaction and the temperatures near this region become higher than the lower matrix temperature. This temperature increase is coupled with a decrease in the resin concentration (a minimum) since the resin decomposes fastest where the temperature is highest. Thus, a minimum resin concentration is located where the temperature is at maximum.

The thermal front then moves upward through the layer as a result of both conductive and convective transport and a similar process occurs. In the upper region, the temperature remains low since the Biot number is large. In the end, the resin concentration near the lower surface is too low for heat to be generated. At steady state, the familiar S-shaped temperature profile corresponding to unaltered natural convection is obtained. The minimum in the resin density also disappears, though after a longer time.

The maximum temperature in the layer and the rate of reaction are dependent on the magnitude of several parameters. As mentioned earlier, the values of the parameters correspond to those of a commercial insulating material. In some cases, a slight increase in just one parameter leads to an appreciable change in the profiles. The temperature profile is severely affected by both δ and γ which depend on the heat of reaction and the energy of activation, respectively. Figure 3 shows the maximum temperature in the layer for different values of both of these. All the parameters mentioned above remain the same. When γ is small, the resin decomposes very little for the considered values of δ. Thus, the temperature rarely exceeds the lower surface temperature and only convective effects influence the profiles. For $\gamma = 28$, an increase in δ is accompanied by a large increase in the maximum temperature in the layer.

In order to visualize the two-dimensional aspect of the phenomenon and the importance of convective transport, Figs. 4 and 5 show (from left to right) the isotherms, resin and fluid isochores and the velocity profile for P_1 = RaGa = 30 and for P_1 = RaGa = 100, respectively, at different stages of the evolution.

A critical transition conduction-convection RaGa number has been calculated by a linear stability analysis on the steady-state equations. The two coupled linear, ordinary differential equations with variable coefficients are solved by series. For $T_p/T_{\mathrm{amb}} = 2.42$, the critical RaGa number is 46. This implies (since $\beta = 1/T$ for an ideal gas) that the critical Ra number is equal to 38. The moderate density differences accounted for in all terms explain why this value is slightly lower than $4\pi^2$.

For P_1 = RaGa = 30, the isotherms, resin and fluid isochores and the velocity profile converge toward a pure conduction, motionless regime. The last row of Fig. 4 corresponds to the steady state; the dimensionless velocities are smaller than 0.01. The isotherms are horizontal lines, the phenomenon is thus one-dimensional.

When P_1 = RaGa = 100, the process is two-dimensional since the isotherms, resin, and fluid isochores vary with the horizontal axis. The velocity profile is arranged into a well-formed cell which is rotating clockwise.

The bottom row in Fig. 5 was traced at steady state when only convective effects remained. A comparison with previous work is useful.

For an incompressible fluid with constant physical properties and satisfying a linear state equation, the stream lines and the cell are symmetrical. When taking into account, for liquids, the temperature variation of the viscosity [5, 7] the cell is deformed downward. This is due to the fact that liquids move faster on the hot, low viscosity lower boundary where convection is concentrated.

From the steady-state profiles shown in Fig. 5, one can see that the cell is displaced towards the lower, right-hand side. In this region the vertical and horizontal temperature gradients (and thus the velocity components) are the highest. Since we have assumed that the fluid viscosity is constant, the nonsymmetry is caused by the terms $\mathbf{V}\cdot\nabla\rho_B$ in the continuity equation.

The cell lateral displacement is more pronounced here than in either [5] or [7]. In the former, the Boussinesq approximation is invoked while in the latter only the density variations in the vertical direction are considered. The lateral temperature gradient is much smaller—one-fifteenth to one-sixth as large—than its vertical counterpart and thus the procedure in [7] is justified.

The vertical displacement is less evident here than in [5, 7]. These authors deal with liquids whose viscosity variation is very important. Here, only the moderate density differences pull the cell downwards. It would be most interesting to examine the viscosity effects for gases. Unlike liquids, as the temperature of the gas increases, its viscosity also increases. This would tend to counter the effects caused by the decrease in density.

Error Analysis

By performing an overall heat and mass balance on the layer we can estimate the accuracy of the finite difference scheme. The error depends on the size of both the grid and the time steps; these were given previously.

The total amount of fluid in the layer is directly related to the total amount of resin that has reacted. At any time t^*, it can be shown that

$$\overline{\rho_B}\,(t = t^*) = \overline{\rho_B}\,(t = 0) + \frac{\sigma_2}{\sigma_1}\,[\overline{\rho_A}\,(t = 0) - \overline{\rho_A}\,(t = t^*)] \quad (11)$$

where $\overline{\rho_A}$ and $\overline{\rho_B}$ are the average resin and fluid densities. In all calculations, the conservation of mass is observed to within 99.3 percent.

The overall heat balance gives (in dimensionless form again)

$$\frac{d\overline{T}}{dt} = -\frac{\delta}{\sigma_1}\frac{d\overline{\rho_A}}{dt} - \left.\frac{dT}{dy}\right|_{y=0} - \mathrm{Bi}\,[T|_{y=1} - 1] \quad (12)$$

where $\overline{T}$ is the average temperature in the layer. To determine the heat input through the lower surface $dT/dy|_{y=0}$ a fourth order discretisation formula is used, all the other quantities of (12) are known directly. The calculated error is of less than 10 percent though it would have been lower if the precise value for $dT/dy|_{y=0}$ had been known.

Figure 6 shows $\overline{\rho_A}$ and $\overline{T}$ as a function of time. We can conclude from these results that the numerical parameters are adequate; a finer grid will give little additional precision while rendering the costs prohibitive.

Concluding Remarks

The problem considered couples the effects of two independent phenomena: convective movement and a chemical decomposition reaction. At the start of the evolution, the decomposition reaction perturbates the profiles while convective transport acts as a carrier. Then, due to a depletion of reactant, natural convection alone subsists. The numerical model used allows the fluid density to vary in all terms.

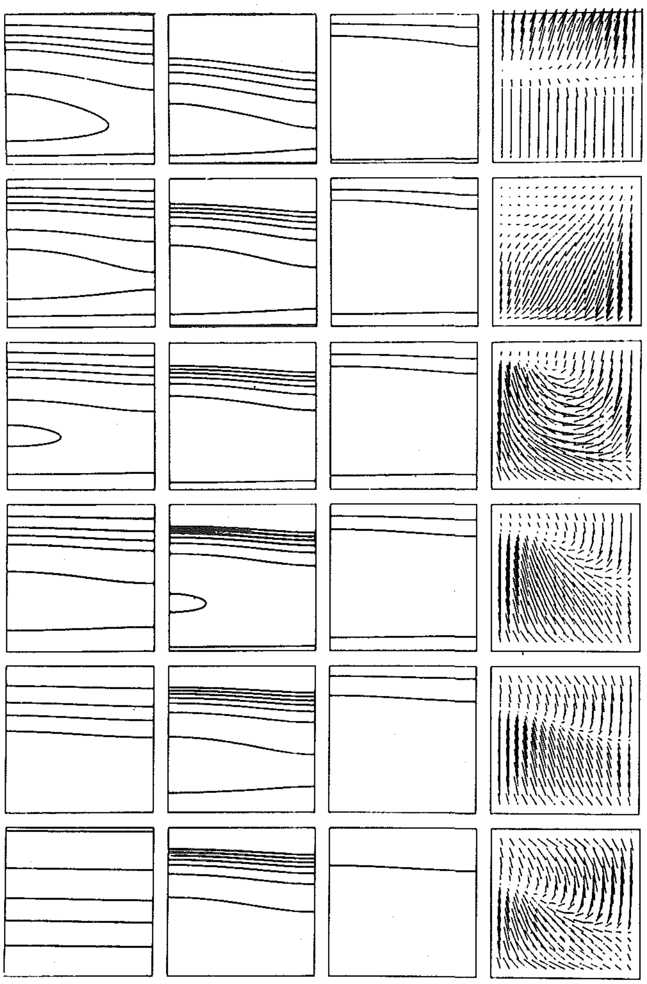

Fig. 4 **Different stages in the evolution of (from left to right) isotherms, resin isochores, fluid isochores, and the velocity profile for P_1 = RaGa = 30**

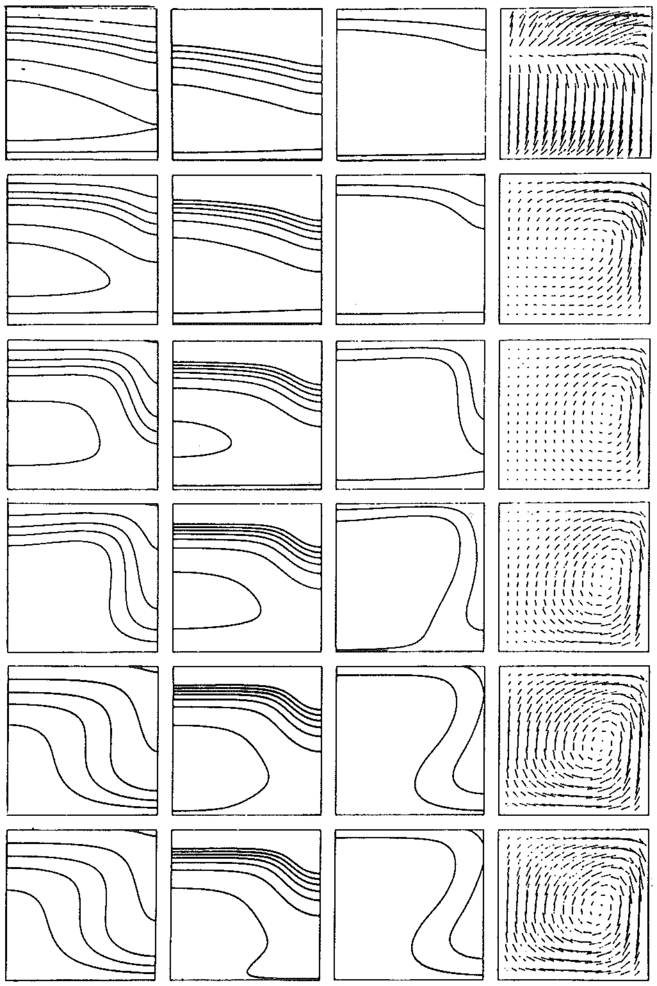

Fig. 5 **Different stages in the evolution of (from left to right) isotherms, resin isochores, fluid isochores, and the velocity profile for P_1 = RaGa = 100**

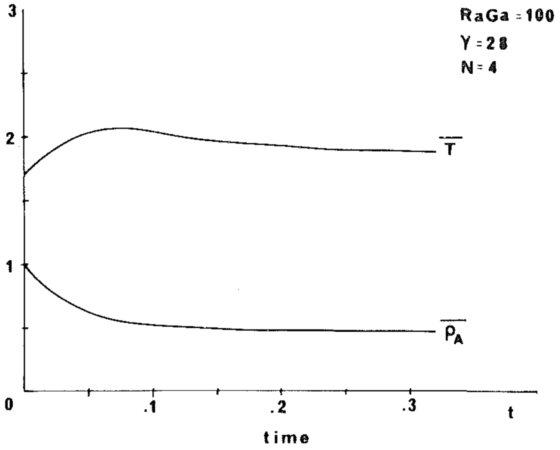

Fig. 6 The average resin concentration and the average temperature in the layer versus time ($\overline{\rho_A} = \int_0^1 \int_0^1 \rho_A(x, y, t)dxdy$ and $\overline{T} = \int_0^1 \int_0^1 T(x, y, t)$-*dxdy*

At steady state and for the moderate conditions considered, the results show that if the density differences are accounted for in all terms, the cell formed is asymmetrical. The stability criterion is modified slightly, the critical Rayleigh number as expected is lower than $4\pi^2$, the value obtained when invoking the Boussinesq approximation.

Acknowledgments

The authors wish to thank Professor J. J. Bernard for his useful comments and patience. Professor R. Prud'homme's guidance was most helpful.

References

1 Lapwood, E. R., "Convection of a Fluid in a Porous Medium," *Proceedings of the Cambridge Philosophy Society,* Vol. 44, 1948, pp. 508–521.

2 Katto, Y., and Masuoka, T., "Criterion for Onset of Convective Flow in a Fluid in a Porous Medium," *International Journal of Heat and Mass Transfer,* Vol. 10, 1967, pp. 297–309.

3 Caltagirone, J-P., "Thermoconvective Instabilities in a Horizontal Porous Layer," *Journal of Fluid Mechanics,* Vol. 72, 1975, pp. 269–287.

4 Straus, J. M., "Large Amplitude Convection in a Porous Media," *Journal of Fluid Mechanics,* Vol. 64, 1974, pp. 51–63.

5 Kassoy, D. R., and Zebib, A., "Variable Viscosity Effects on the Onset of Convection in a Porous Media," *Physics Fluids,* Vol. 18, 1975, pp. 1649–1651.

6 Horne, R. N., and O'Sullivan, M. J., "Convection in a Porous Medium Heated from Below: the Effect of Temperature Dependent Viscosity and Thermal Expansion Coefficient," ASME JOURNAL OF HEAT TRANSFER, Vol. 100, 1978, pp. 448–452.

7 Straus, J. M., and Schubert, G., "Thermal Convection of Water in a Porous Medium: Effects of Temperature and Pressure Dependent Thermodynamic and Transport Properties," *Journal Geophysical Research,* Vol. 82, 1977, pp. 325–333.

8 Hardee, H. C., and Nilson, R. H., "Natural Convection in a Porous Media with Heat Generation," *Nuclear Science and Engineering,* Vol. 63, 1977, pp. 119–132.

9 Caltagirone, J-P., and Prud'homme, R., "Transfert de Chaleur en Présence de Réactions Chimiques Exothermiques dans les Calorifuges de Fibres Minérales," Rapport Intérieur 18 du laboratoire d'Aérothermique du CNRS, 1977.

10 Levenspiel, O., *Chemical Reaction Engineering,* John Wiley and Sons, New York, 1972, p. 21.

11 Carnahan, B., Luther, H. A., and Wilkes, J. O., *Applied Numerical Methods,* John Wiley and Sons, New York, 1969.

J. N. Reddy[1]
Akio Satake
University of Oklahoma,
Norman, Okla. 73019

A Comparison of a Penalty Finite Element Model with the Stream Function-Vorticity Model of Natural Convection in Enclosures

This paper is concerned with a comparative study of the stream function-vorticity formulation and penalty function formulation of the two-dimensional equations governing natural convection in enclosures. The penalty function formulation presented herein is the only correct way of describing it for the problem at hand. The penalty-finite element model developed herein is novel with this work, and involves two velocities, temperature, and stream function as degrees of freedom at each node. The model includes, as a special case, the penalty-finite element model of natural convection in enclosures reported in the literature. Numerical results obtained using the two formulations are compared for several geometries, and boundary conditions, and the effects of Rayleigh number and Prandtl number on the flow and heat transfer are studied.

1 Introduction

Convection phenomena induced by body forces have been the subject of many theoretical and numerical investigations. As pointed out by Ostrach [1] convection problems can be classified into two major types: *external problems,* such as the flow around a heated rod or plate caused by existence of a temperature difference between the body and the fluid; and *internal* (*or confined*) *problems,* such as the flow in a fluid-filled cavity caused by the temperature differences between the walls of the cavity. Due to their important role in many engineering problems of practical interest, internal problems have received greater attention. These problems include: thermal insulation of buildings, Batchelor [2], heat transfer through double-glazed window, Elder [3] and Gill [4], cooling of electronic equipment, Pedersen [5], general circulation of planetary atmospheres, Hart [6], crystal growth from the melt, Carruthers [7], sterilization of canned foods, Hiddink, et al. [8], cooling fluids in channels surrounding a nuclear reactor core, Petuklov [9], convectively cooled underground electric cable systems, Chato and Abdulhadi [10], and many others.

For internal high Rayleigh number (i.e., Ra $> 10^3$) flows, the region exterior (i.e., core) to the boundary layer is influenced by the behavior of the surrounding boundary layer. This coupling of the boundary layer and the core region constitutes the main source of difficulty for obtaining analytical solutions to internal problems, forcing one to seek numerical solutions. In order to capture the boundary layer effects, one must use a small mesh near the walls. This requires the use of a nonuniform mesh in the interest of accuracy and computational efficiency (use of a nonuniform mesh is also necessitated by irregular configurations of enclosures). The inability of the finite difference methods to accurately describe irregular domains and permit the use of nonuniform, nonrectangular meshes, and the complexity involved in developing higher-order finite difference approximations have lead the researchers to consider the finite element method, which is known to have overcome the above mentioned shortcomings of the finite difference method. The feasibility of the finite element method to convection heat transfer in rectangular enclosures has been studied by Tabarrok and Lin [11] using the stream function-vorticity-temperature formulation, Gartling [12] using the pressure-velocity-temperature formulation, Heinrich, et al. [13, 14], and Reddy and Mamidi [15, 16] using penalty function methods. The penalty formulation described by Marshall, et al. [14] is completely ad hoc, and problem oriented.

In the present paper a correct way of formulating the problem by the penalty function method is described. The penalty formulation presented herein for natural convection in enclosures treats the incompressibility condition and stream function-velocity relations as constraints. Therefore, as a special case, the present model includes the penalty models described in [13–15]. Further, two formulations, namely, the stream function-vorticity formulation and a penalty function formulation are compared for relative accuracy and computational time. The present results are also compared with those of other investigators available in literature.

2 Governing Equations and Formulations

Under the standard assumption of convection heat transfer (i.e. Boussinesq approximation holds), the two-dimensional equations governing a Newtonian fluid in the presence of a temperature gradient (but in the absence of other body forces) can be written as,

conservation of mass:

$$\frac{\partial u}{\partial x} + \frac{\partial v}{\partial y} = 0 \tag{1}$$

conservation of linear momentum:

$$A(u) = -\frac{1}{\rho_0}\frac{\partial P}{\partial x} + \nu\left[2\frac{\partial^2 u}{\partial x^2} + \frac{\partial}{\partial y}\left(\frac{\partial u}{\partial y} + \frac{\partial v}{\partial x}\right)\right] - g\beta(T - T_0) \tag{2}$$

$$A(v) = -\frac{1}{\rho_0}\frac{\partial P}{\partial y} + \nu\left[2\frac{\partial^2 v}{\partial y^2} + \frac{\partial}{\partial x}\left(\frac{\partial u}{\partial y} + \frac{\partial v}{\partial x}\right)\right] \tag{3}$$

conservation of energy:

$$A(T) = \alpha\left(\frac{\partial^2 T}{\partial x^2} + \frac{\partial^2 T}{\partial y^2}\right) \tag{4}$$

where α is the thermal diffusivity,

$$\alpha = k/\rho_0 C_p, \; A = u\frac{\partial}{\partial x} + v\frac{\partial}{\partial y} \tag{5}$$

and x is taken positive downward (i.e., along the acceleration due to gravity). Here (u, v) are the components of velocity along (x, y)—directions; P is the pressure; T is the temperature (T_0 is the reference temperature); ρ_0 is the reference value of the density of the fluid; ν is the kinematic viscosity, β is the coefficient of thermal expansion; k is the thermal conductivity; C_p is the specific heat at constant pressure; and g is the acceleration due to gravity. To complete the description of the equations, equation (1–4) must be adjoined by

---

[1] Present address: Department of Engineering Science and Mechanics, Virginia Polytechnic Institute and State University, Blacksburg, VA.

Contributed by the Heat Transfer Division for publication in the JOURNAL OF HEAT TRANSFER. *Manuscript received by the Heat Transfer Division* September 7, 1979.

appropriate boundary conditions of the problem. We assume that the following general boundary conditions (of mixed type) are specified.

$$\alpha\left(\frac{\partial T}{\partial x}n_x + \frac{\partial T}{\partial y}n_y\right) = \hat{q} \text{ on } \partial\Omega_{1T},\ T = \hat{T} \text{ on } \partial\Omega_{2T} \qquad (6)$$

$$\left.\begin{aligned} t_x &\equiv \left(2\nu\frac{\partial u}{\partial x} - \overline{P}\right)n_x + \nu\left(\frac{\partial u}{\partial y} + \frac{\partial v}{\partial x}\right)n_y = \hat{t}_x \text{ on } \partial\Omega_{1u} \\ t_y &\equiv \nu\left(\frac{\partial u}{\partial y} + \frac{\partial v}{\partial x}\right)n_x + \left(2\nu\frac{\partial v}{\partial y} - \overline{P}\right)n_y = \hat{t}_y \text{ on } \partial\Omega_{1v} \end{aligned}\right\} \qquad (7)$$

$$u = \hat{u} \text{ on } \partial\Omega_{2u},\ v = \hat{v} \text{ on } \partial\Omega_{2v},\ \overline{P} = P/\rho_0 \qquad (8)$$

Here $n = (n_x, n_y)$ denotes the unit normal to the boundary $\partial\Omega$; and $\partial\Omega_1$ and $\partial\Omega_2$ denote disjoint (i.e., $\partial\Omega_1 \neq \partial\Omega_2$) portions of the total boundary $\partial\Omega$ of the bounded region Ω. That is,

$$\partial\Omega_{1u} + \partial\Omega_{2u} = \partial\Omega_{1v} + \partial\Omega_{2v} = \partial\Omega = \partial\Omega_{1T} + \partial\Omega_{2T} \qquad (9)$$

That is, $\partial\Omega_{1u}$ and $\partial\Omega_{1v}$ denote the portions of the boundary on which the tractions t_x and t_y, respectively, are specified; and $\partial\Omega_{2u}$ and $\partial\Omega_{2v}$ denote the portions on which the velocities are specified. Quantities with a carat (^) denote specified quantities on the appropriate boundary. Further, we use the following variables for the nondimensionalization. Let d denote the length of the enclosure (along y), ℓ the height (along x), and T_h and T_c the temperatures of the hot and cold walls, respectively.

The above equations in the primitive variables (u, v, p, T) are often replaced by equations in terms of the descriptive variables (ψ, ζ, T) for numerical approximations. The stream function ψ is introduced to satisfy the incompressibility condition (1). Define the stream function by

$$u = \frac{\partial\psi}{\partial y},\ v = -\frac{\partial\psi}{\partial x}, \qquad (10)$$

and the vorticity, ζ, by

$$\zeta = \frac{\partial v}{\partial x} - \frac{\partial u}{\partial y} = -\nabla^2\psi. \qquad (11)$$

Consequently, equations (1–4) reduce to

$$-\nabla^2\zeta = \mathrm{J}(\psi, \zeta) + g\beta\frac{\partial T}{\partial y}, \qquad (12)$$

$$-\nabla^2\psi = \zeta, \qquad (13)$$

$$\nabla^2 T = \frac{1}{\alpha}\mathrm{J}(\psi, T), \qquad (14)$$

where $\mathrm{J}(\cdot,\cdot)$ is the Jacobian,

$$\mathrm{J}(p, q) = \frac{\partial p}{\partial x}\frac{\partial q}{\partial y} - \frac{\partial p}{\partial y}\frac{\partial q}{\partial x} \qquad (15)$$

We now give two formulations, one based on the primitive variables equations (1–4), and the other based on the stream function and vorticity equations (12–14). It is convenient to recast these equations in terms of the normalized (i.e., nondimensionalized) variables. We use here two different normalizations ($i = 1, 2$).

$$\begin{gathered} x = x'd,\ y = y'd,\ u = u'U_i,\ v = v'U_i, \\ \theta = (T - T_c)/(T_h - T_c) \qquad (16) \\ P = P'U_i{}^2\rho_0,\ U_i = \alpha_i/d, \end{gathered}$$

where $\alpha_1 = \alpha$, and $\alpha_2 = \nu$, and the quantities with primes denote the nondimensional variables. For the sake of brevity, we shall omit the primes in the following.

Penalty Formulation. The penalty function concept of Courant [17] involves the reduction of variational problems which are posed as *conditional* extremum problems to variational problems without constraints by the introduction of a penalty functional associated with the constraints. The concept has been known for a long time, and at the present time many investigations are devoted to the exploitation of the concept of other situations, and applications to particular problems. Zienkiewicz [18], guided by the analogy between nearly incompressible elasticity and Stokes problem, suggested the application of the penalty method to viscous incompressible flow problems; in [13–15, 18] the incompressibility condition is treated as the constraint. Another modification is suggested recently by Reddy [16], who treated, in order to introduce the stream function into the primary calculations, the stream function-velocity relations along with the incompressibility condition as constraints. The formulation presented in [16] is the only correct way to describe the penalty formulation of natural convection in enclosures.

The penalty method seeks to satisfy the constraint conditions in a least squares sense. Applied to the problem at hand, i.e. find the solution (u, v, P, T) to equations (1–4) subject to the constraint conditions in (1) and (10), the penalty method seeks solutions to the variational problem,

$$\delta I(u, v, \psi, \theta) \equiv \delta I_0(u, v, \theta) + \delta G(u, v, \psi) = 0 \qquad (17)$$

where u, v, ψ, and θ are the nondimensional variables, and

$$\begin{aligned} \delta I_o(u, v, \psi, \theta) = \int_\Omega \bigg\{&[A(u) - \mathrm{PrRa}\theta]\delta u + \mathrm{Pr}\left[2\frac{\partial u}{\partial x}\frac{\partial \delta u}{\partial x}\right. \\ &\left. + 2\frac{\partial v}{\partial y}\frac{\partial \delta v}{\partial y} + \left(\frac{\partial u}{\partial y} + \frac{\partial v}{\partial x}\right)\left(\frac{\partial \delta u}{\partial y} + \frac{\partial \delta v}{\partial x}\right)\right] \\ &+ A(v)\delta v + A(\theta)\delta\theta + \frac{\partial\theta}{\partial x}\frac{\partial\delta\theta}{\partial x} + \frac{\partial\theta}{\partial y}\frac{\partial\delta\theta}{\partial y}\bigg\}\,dxdy \\ &- \int_{\partial\Omega_{1u}}\hat{t}_x\delta u\,ds - \int_{\partial\Omega_{1v}}\hat{t}_y\delta v\,ds - \int_{\partial\Omega_{1T}}\hat{q}\delta\theta\,ds \qquad (18) \end{aligned}$$

$$\begin{aligned} G(u, v, \psi) = \frac{\epsilon_1}{2}\int_\Omega\left(\frac{\partial u}{\partial x} + \frac{\partial v}{\partial y}\right)^2 dxdy \\ + \frac{\epsilon_2}{2}\int_\Omega\left\{\left(u - \frac{\partial\psi}{\partial y}\right)^2 + \left(v + \frac{\partial\psi}{\partial x}\right)^2\right\}dxdy \qquad (19) \end{aligned}$$

Here Pr is the Prandtl number, Ra is the Rayleigh number,

$$\mathrm{Pr} = \nu/\alpha,\ \mathrm{Ra} = g\beta d^3(T_h - T_c)/\nu\alpha, \qquad (20)$$

and ϵ_1 and ϵ_2 are the penalty parameters (for normalization $i = 1$).

Note that in the penalty method, the pressure does not appear. This is because the pressure is the Lagrange multiplier associated with the incompressibility constraint, which is satisfied only in a weak sense in the penalty method. However, the Lagrange multiplier can be computed in the penalty method by (see Polyak [19])

$$P_\epsilon = -\epsilon\left(\frac{\partial u_\epsilon}{\partial x} + \frac{\partial v_\epsilon}{\partial y}\right). \qquad (21)$$

Convergence of the solution $(u_\epsilon, v_\epsilon, P_\epsilon, \psi_\epsilon, \theta_\epsilon)$ of the penalty formulation to the true solution (as $\epsilon \to \infty$) can be proved (see [19–22]).

Stream Function-Vorticity Formulation. In terms of the nondimensional variables, equations (12–14) can be expressed as

$$\begin{gathered} -\nabla^2\zeta = b_i\mathrm{J}(\psi, \zeta) + c_i\frac{\partial\theta}{\partial y}, \\ -\nabla^2\psi = \zeta, \qquad (22) \\ -\nabla^2\theta = a_i\mathrm{J}(\psi, \theta). \end{gathered}$$

where (a_i, b_i, c_i) denote the coefficients for the two types of nondimensionalizations.

$$(a_1, b_1, c_1) = (1, 1/\mathrm{Pr}, \mathrm{Ra}),\ (a_2, b_2, c_2) = (\mathrm{Pr}, 1, \mathrm{Gr}). \qquad (23)$$

Here Gr denotes the Grashoff number, Gr = Ra/Pr. The variational formation of equations (22) indicate that either θ, ζ, and ψ be specified on portions of boundary or their normal derivatives be specified there. This presents a problem with regard to the vorticity ζ which is generally unknown on the boundary. It is now a common practice (see [11]) to approximate the boundary values of ζ using the second equation in (22). The Taylor series expansion is employed to express the stream function inside the domain in terms of its values on the boundary:

$$\psi_i = \psi_w + \left(\frac{\partial\psi}{\partial n}\right)\bigg|_w (\Delta n) + \frac{1}{2}\left(\frac{\partial^2\psi}{\partial n^2}\right)\bigg|_w (\Delta n)^2 + \dots, \qquad (24)$$

where $(\cdot)|w$ is the value at the wall of the enclosure, and Δn is the normal distance from the wall to a point (or node) i. Using $\zeta_w = -\partial^2\psi_w/\partial n^2$ and noting that ψ_w = constant = 0 along the solid wall of the enclosure, we obtain (omitting the higher order terms in equation (24)),

$$\zeta_w = -\frac{2\psi_i}{(\Delta n)^2}. \qquad (25)$$

The variational formulation of equations (22) is given by

$$\begin{aligned} B(\zeta, \bar{\zeta}) &= b_i J(\psi, \zeta; \bar{\zeta}) + c_i Q(\bar{\zeta}), \\ B(\psi, \bar{\psi}) &= R(\bar{\psi}), \qquad (26) \\ B(\theta, \bar{\theta}) &= a_i J(\psi, \theta; \bar{\theta}), \end{aligned}$$

where

$$\begin{aligned} B(p, q) &= \int_\Omega \left(\frac{\partial p}{\partial x}\frac{\partial q}{\partial x} + \frac{\partial p}{\partial y}\frac{\partial q}{\partial y}\right) dxdy, \\ J(p, q; f) &= \int_\Omega J(p, q) f\, dxdy, \qquad (27) \\ Q(\zeta) &= \int_\Omega \frac{\partial\theta}{\partial y}\zeta\, dxdy,\ R(\psi) = \int_\Omega \zeta\psi\, dxdy. \end{aligned}$$

Here we assumed that the boundary values of ψ, ζ, and θ are specified.

3 Finite-Element Formulations

Penalty-Finite Element Model. In the penalty method, we discretize the region occupied by the fluid into a finite set of subregions, called finite elements. We consider a typical finite element, Ω_e, and develop the finite element equations corresponding to the equations (17–19). We assume the following interpolation of the variables (u, v, ψ, θ) over the element Ω_e.

$$\begin{aligned} u &= \sum u_i N_i(x, y), \quad v = \sum v_i N_i(x, y), \\ \psi &= \sum \psi_i N_i(x, y), \quad \theta = \sum \theta_i N_i(x, y), \qquad (28) \end{aligned}$$

wherein $N_i(x, y)$ are the interpolation (or shape) functions, which depend on the type of element chosen; and u_i, v_i, ψ_i, and θ_i are the values of the functions (u, v, ψ, and θ) at the i-th node of the element. In the present paper a bilinear quadrilateral element (with four nodes) is used.

Since the variational formulation (17) is valid in Ω it is valid, in particular, in Ω_e with $\hat{t}_x$, $\hat{t}_y$ and $\hat{q}$ are *assumed*, for the moment, to be known on the element boundary. Substituting (28) into the element equation corresponding to (17), we obtain (collecting the coefficients of δu_i, δv_i, $\delta\psi_i$ and $\delta\theta_i$),

$$[K^e]\{\Delta^e\} = \{F^e\}, \quad [C^e]\{\theta^e\} = \{Q^e\}, \qquad (29)$$

wherev$_i$, $\delta\psi_i$ and $\delta\theta_i$),

$$[K^e]\{\Delta^e\} = \{F^e\}, \quad [C^e]\{\theta^e\} = \{Q^e\}, \qquad (29)$$

wherev$_i$, $\delta\psi_i$ and $\delta\theta_i$),

$$[K^e]\{\Delta^e\} = \{F^e\}, \quad [C^e]\{\theta^e\} = \{Q^e\}, \qquad (29)$$

wherev$_i$, $\delta\psi_i$ and $\delta\theta_i$),

$$[K^e]\{\Delta^e\} = \{F^e$$

$$C_{ij}{}^e = A_{ij} + S_{ij}{}^x + S_{ij}{}^y,\ A_{ij} = \int_{\Omega_e} N_i A(N_j)\, dxdy,\ [S] = [S^{00}],$$

$$S_{ij}{}^{\xi\eta} = \int_{\Omega_e} N_{i,\xi} N_{j,\eta} dxdy,\ (\xi, \eta = 0, x, y), \quad S_{ij}{}^{\xi\xi} = S_{ij}{}^{\xi}, \text{ etc.}$$

$$H_{ij}{}^x = A_{ij} + \Pr(2S_{ij}{}^x + S_{ij}{}^y),\ H_{ij}{}^y = A_{ij} + \Pr(2S_{ij}{}^y + S_{ij}{}^x), \qquad (30)$$

$$\{F^e\} = \{F_i{}^x, F_i{}^y\}^T, \quad \{\Delta^e\} = \{u_i, v_i, \psi_i\}^T, \quad \{\theta^e\} = \{\theta_i\}^T,$$

$$F_i{}^x = \Pr\mathrm{Ra} \int_{\Omega_e} \theta N_i\, dxdy + \int_{\partial\Omega_{1u}{}^e} \hat{t}_x N_i\, ds,$$

$$F_i{}^y = \int_{\partial\Omega_{1v}{}^e} \hat{t}_y N_i\, ds,\ Q_i{}^e = \int_{\partial\Omega_{1T}{}^e} \hat{q} N_i\, ds.$$

Note that the matrix [A] is computed assuming that u and v are known a priori, necessitating the use of an iterative procedure for the solution of the assembled equations. By setting ϵ_2 to zero, one obtains from equation (29), the penalty finite-element model presented in [13–15].

Stream Function-Vorticity Finite Element Model. Using interpolation of the form in equation (28) in equations (26), we obtain

$$\begin{aligned} [B^e - b_i J^e]\{\zeta^e\} &= \{F^{1e}\}, \\ [B^e]\{\psi^e\} &= \{F^{2e}\}, \qquad (31) \\ [B^e - a_i J^e]\{\theta^e\} &= \{0\}, \end{aligned}$$

where

$$\begin{aligned} B_{ij}{}^e &= B(N_i, N_j),\ J_{ij}{}^e = J(\psi, N_i; N_j), \\ F_j{}^{1e} &= c_i Q(N_j), \quad F_j{}^{2e} = R(N_j), \qquad (32) \end{aligned}$$

and $B(\cdot, \cdot)$, $J(\cdot, \cdot; \cdot)$, $Q(\cdot)$ and $R(\cdot)$ are given by equation (27).

Computational Procedure. The element equations in (29) and (31) are assembled in the usual manner to obtain the associated global matrices. However, these matrix equations are nonlinear and require iterative procedures. The following iterative procedure is employed in the present study. At the beginning of the first iteration the matrix coefficients are computed assuming that the velocity vector is zero. Then the temperature equation is solved for $[\theta]$. Using the computed temperature, the velocity and stream function equations are solved, completing one cycle of iteration. Using the velocity (and/or stream function) field obtained in the previous iteration, matrix coefficients for the next iteration are computed and the procedure is repeated until the Euclidean norm of the difference of the solutions at any two successive iterations becomes sufficiently small (say, $<10^{-4}$). In the present study we used, to accelerate the convergence, a weighted sum of the variables in computing the matrix coefficients for the next iteration. For example, at the end of rth iteration we have, $0 < \rho_1, \rho_2 < 1$,

$$\begin{aligned} \{u\}^* &= \rho_1\{u\}_r + (1 - \rho_1)\{u\}_{r-1}, \\ \{\theta\}^* &= \rho_2\{\theta\}_r + (1 - \rho_2)\{\theta\}_{r-1}. \end{aligned} \qquad (33)$$

One can transfer the nonlinear (convective) terms to the right side of the equation and assume that it is known from the previous iteration. This gives a constant coefficient matrix and saves computational time in recomputing the coefficient matrices during each iteration. However, this procedure is found to result in divergent solutions even for moderately high Rayleigh numbers.

The algebraic complexity and the nonlinear nature of the matrices in equation (30) forces one to use numerical integration to evaluate various matrix coefficients. Another reason which necessitates the use of numerical integration is the "reduced integration" required by the penalty method. To establish the existence and uniqueness of solutions, the penalty-finite-element approximations should satisfy the continuity and coercivity conditions of a generalized Lax-Milgram theorem (see Oden and Reddy [23]). These conditions are satisfied by the penalty finite-element approximations, provided the parameter appearing in the coercivity condition is independent of the mesh size. That is, the finite element chosen for the penalty method be such that this parameter does not depend on the mesh size. It is found that (see Zienkiewicz, et al. [24]) numerical integration of matrix coefficients associated with the penalty functional $G(u, v, \psi)$ with one less number of Gaussian points (in each direction) will ensure that the parameter is independent of the mesh size. Further study in this direction seems to be necessary.

Alternate but more direct explanation of this latter observation is also given here. The penalty-finite element equation (29) has the form $(\epsilon_1 = \epsilon_2 = \epsilon)$,

$$([K_1] + \epsilon[K_2])\{\Delta\} = \{F\}.$$

As ϵ is increased to a large value (in an attempt to satisfy the constraints more closely), the magnitude of $[K_1]$ in comparison to $\epsilon[K_2]$ becomes negligible in the computer, and we have

$$\epsilon[K_2]\{\Delta\} = \{F\}, \quad \text{or } [K_2]\{\Delta\} = \frac{1}{\epsilon}\{F\}. \tag{35}$$

This implies that as ϵ is made larger and larger only constraint equations are left (which results in a trivial solution since $\epsilon^{-1} \sim 0$), and the contributions of conservation of momentum and energy are lost. To circumvent this difficulty two things must be done. First, the magnitude of ϵ be such that the matrix $[K_1]$ is not negligibly small compared to $[K_2]$. Second, the matrix $[K_2]$ must be singular so that there are less number constraint equations than the number of unknowns. This can be achieved by using reduced integration on the elements of $[K_2]$. That is, the standard 2 × 2 Gauss rule must be used to evaluate the elements of $[K_1]$, whereas only 1 × 1 Gauss rule must be used to evaluate the elements of $[K_2]$. A value of $\epsilon_1 = \epsilon_2 = \epsilon = 10^8$ was used in all problems discussed here.

4 Numerical Results and Discussion

In any approximate method, physics of the problem plays a crucial role in constructing a reasonable approximation. The finite element method is no exception. For example, one needs to visualize, using physical arguments, possible flow and temperature patterns in an enclosure in order to lay a mesh that can reasonably approximate what is intuitively expected. In the case of high Rayleigh number flows in rectangular enclosures, boundary layer appears (due to the no-slip boundary condition) at the walls. Since the boundary layer influences the behavior of the core region, it must be modeled adequately by employing refined mesh at the walls. Another important consideration, when using an approximate method, is in the specification of the right boundary conditions of the problem at hand. In the penalty formulation, all physical boundary conditions can be handled without difficulty.

Here we compare the numerical results obtained by the penalty-finite element model and the stream function-vorticity finite element model for free convection in rectangular enclosures. The right and left vertical walls of the enclosure are maintained, respectively, at hot and cold ($\theta_c = -0.5$, $\theta_h = 0.5$) temperatures, and the top and bottom (horizontal) walls are either insulated or have specified temperature variations (see Fig. 1). The models are compared for relative accuracy and computational time. Since most of the previous investigators presented results in graphical form, it is not possible to compare the present results quantitatively. However, present results are compared for Nusselt numbers, vorticity and stream function values with those available in the literature.

First, the effect of the two normalizations mentioned earlier on the numerical convergence was studied. Normalization 1 ($i = 1$) was used in both models, while Normalization 2 ($i = 2$) was used only in the stream function-vorticity model. All of the calculations were carried in double precision on an IBM 370/158 computer. It was found that the use of Normalization 2 presents convergence problems for Ra > 10^4 and Pr < 1. The numerical procedure used there employed the constant coefficient matrix, treating $\{F^1\}$ in equation (31) as known from the previous iteration. The slow convergence (or divergence) is a direct result of this numerical procedure, which yields numerical solution proportional to c_2 (or inversely to the Prandtl number). Thus any error in $\partial\theta/\partial y$ is amplified in this procedure and leads to nonconvergent solution. Normalization 1 was found to give faster convergence, even for large Rayleigh numbers, for both formulations.

Next, penalty-finite element model with stream function included in the model (i.e., $\epsilon_2 \neq 0$) was compared with the penalty-finite element model without stream function (i.e., $\epsilon_2 = 0$). The model problem used was that of a square cavity with top and bottom walls insulated. A 12 × 12 mesh of linear elements (see Fig. 1) was used in both models. The vorticity was computed at the Gauss points in both models. The stream function in the second model ($\epsilon_2 = 0$) was calculated using equation (11), in which the velocities are known from the primary calculations. It was observed that the isotherms and streamlines (for Ra = 10^3, Pr = 10) obtained using the two models were virtually the same; however, the computational time and the value of ψ at the vorticity center differed: $\psi_{\max} = 1.1697$, cpu = 25 s/iteration for $\epsilon_2 \neq 0$, and $\psi_{\max} = 1.1689$, cpu 15 s/iteration for $\epsilon_2 = 0$. Therefore, the remaining problems were analyzed using the second model ($\epsilon_2 = 0$).

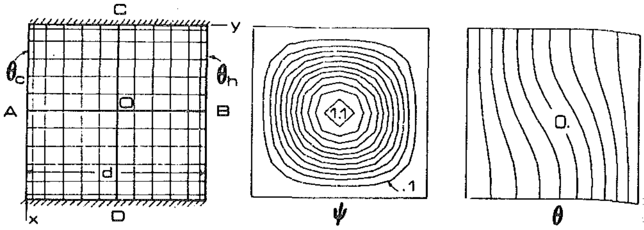

Fig. 1 Isotherms and streamlines obtained by the penalty-finite element model ($\epsilon_2 = 0$, Ra = 10^3, and Pr = 10)

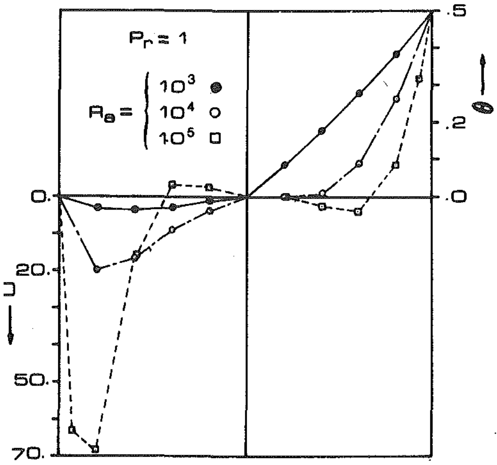

Fig. 2 Velocity and temperature distribution along the center lines of the enclosure

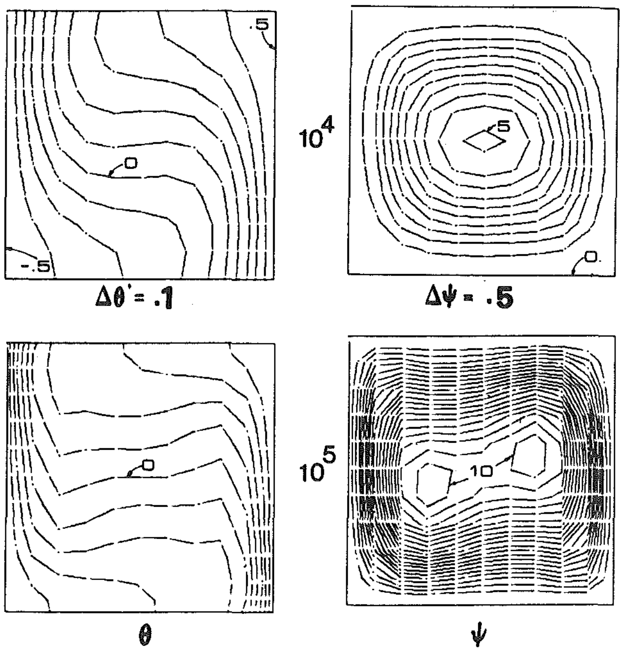

Fig. 3 Isotherms and stream lines obtained by the penalty-finite element model for Ra = 10,000 and 1,00,000 (Pr = 1)

The effect of the Rayleigh number (for fixed Prandtl number) on the velocity and temperature fields was investigated using the two formulations. Figure 2 shows the vertical component and the temperature along the (horizontal) center of the cavity. The results were obtained by the penalty-finite element model with a 10 × 10 uniform mesh for Ra = 10^3, 10^4, and 12 × 12 nonuniform mesh for Ra = 10^5, of linear elements. Figure 3 shows the isotherms and stream lines obtained by the penalty-finite element model for Ra = 10^4, and 10^5, and Pr = 1. The numerical results obtained by the stream function-vorticity finite element model, for Ra = 10^3 and 10^4, were found to be very close to those obtained by the penalty-finite element model and cannot be plotted distinctly on the present scale. Therefore, the results are compared in Table 1 for Ra = 10^3, 10^4, and Pr = 1. As can be seen from the table, the penalty-finite element model (PFEM) predicts values of the stream function lower than those predicted by the stream function-vorticity finite element model (SVFEM). However, the stream function-vorticity finite-element model did not give convergent results for these two Rayleigh numbers. Thus, the penalty formulation could be used to analyze higher Rayleigh number flows than those could be analyzed by the stream function-vorticity model. Figure 4 shows isotherms and stream lines obtained using the penalty-finite element model (with 12 × 12 nonuniform mesh) for Ra = 10^6, and Pr = 1.

Figures 3 and 4 show that isotherms tend to be vertical in the (thermal) boundary layer at vertical walls (i.e., vertically stratified) and they are horizontal in the core region. The vorticity and stream function values at the center of the enclosure obtained by both formulations are compared in Table 2 for various Rayleigh numbers and Prandtl numbers. Again, the results obtained using the penalty finite element model (also see [13]) are lower than those obtained using the stream function-vorticity model. However, the vorticity values in the penalty model were computed at the Gaussian points (which do not coincide with the vorticity center) and therefore would not be the same as those computed at the vorticity center.

The vorticity distribution along vertical cross-section of the enclosure is shown in Fig. 5 for Ra = 10^4. In the penalty-finite element model, the vorticity was computed from the velocity field at the Gaussian points. Note that the solutions obtained by both formulations are almost identical for Pr = 1; however, for small Prandtl numbers there seems to exist small differences in the solutions.

Table 3 shows a comparison of the Nusselt number computed by various investigators (for square enclosure, Ra = 1.47×10^4, Pr = 0.733). Note that the Nusselt number obtained by the penalty-finite element model is the lowest of all. In Table 4 the two finite-element formulations are compared for computational time (in cpu), number of iterations taken for convergence, and the Nusselt number. The penalty-finite element model requires only slightly more (because of the computation of ψ) time than the stream function-vorticity model; however, the number of iterations required is smaller in the former model.

Figure 6 shows the effect of Prandtl number on the temperature, stream function and vorticity (for Ra = 10^4). These solutions were obtained using the stream function-vorticity finite element model. Similar plots for the temperature and stream function were obtained by the penalty finite element model, but due to their close agreement with those obtained by the stream function-vorticity finite element model, they are not shown here. Different Prandtl numbers, for a fixed Rayleigh number, mean fluids with different (material) properties. For fluids with low Prandtl number (i.e., ratio of viscosity to thermal diffusivity), the stream lines and vorticity lines show symmetry about the center.

Figures 7–9 show the effect of the aspect ratio (height to width of the enclosure, $\gamma = \ell/d$) on the temperature and flow fields. All of the results were obtained by the penalty-finite element model. Figure 7 shows the isotherms and stream lines fora rectangular enclosure of aspect ratio 3. The Rayleigh number and Prandtl numbers are the same as those used by Hellums and Churchill [30]. Ra = 1.466×10^4, Pr = 0.733. The present results agree qualitatively with those of

Table 1 Comparison of the stream function and temperature values obtained by the penalty-finite element model (PFEM) and stream function-vorticity finite element models (SVFEM) (Pr = 1.0, Mesh: 10 × 10)

		Ra = 10^3		Ra = 10^4	
Quantity	x/y	PFEM	SVFEM	PFEM	SVFEM
Stream function at y = 0.5	0.0	0.0	0.0	0.0	0.0
	0.1	0.1566	0.2236	0.7067	0.9811
	0.2	0.5011	0.6094	2.2585	2.7201
	0.3	0.8410	0.9746	3.7707	4.3745
	0.4	1.0755	1.2228	4.7925	5.4913
	0.5	1.1581	1.3098	5.1474	5.8797
Temperature at x = 0.5	1.0	0.5	0.5	0.5	0.5
	0.9	0.3871	0.3851	0.2646	0.2514
	0.8	0.2777	0.2744	0.0883	0.0733
	0.7	0.1765	0.1734	0.0011	0.0006
	0.6	0.0851	0.0832	−0.0150	−0.011
	0.5	0.	0.	0.	0.

Table 3 Comparison of the Nusselt number obtained by various investigators (Ra = 1.47×10^4, Pr = 0.733)

Source		Nusselt number (Nu)*	Remarks
Present	PFEM	2.360	4-node rect. element (10 × 10 mesh)
	SVFEM	2.687	4-node rect. element (10 × 10 mesh)
Tabarrok and Lin [11]		2.695	3-node triangular element (10 × 10)
Catton, et al. [25]		2.71	Galerkin Method
Cormack, et al. [26]		2.64	21 × 21 FDM
		2.874	11 × 11 FDM
Wilkes, et al. [27]		2.516	21 × 21 FDM
Ozoe, et al. [28]		2.75	experiment

* Nusselt number is defined (in the present coordinates) by,

$$\text{average, Nu} = \int_0^1 \left.\frac{\partial\theta}{\partial y}\right|_{y=0} dx.$$

Table 2 Stream function and vorticity values at the center of the enclosure (10 × 10 mesh)

		Stream function (ψ)		Vorticity (ξ)	
Ra	Pr	PFEM	SVFEM	PFEM	SVFEM
	10^{-2}	1.1386	1.2636	−31.26	−33.36
	10^{-1}	1.1561	1.3041	−31.41	−34.44
10^3	1	1.1581 (1.18)*	1.3096	−31.31	−34.52
	10^1	1.1581	1.3098	−31.32	−34.52
	10^2	1.1581	1.3098	−31.32	−34.52
	10^{-2}	5.0128	5.4504	−96.32	−83.99
	10^{-1}	5.0403	5.5451	−101.5	−88.94
10^4	1	5.1474 (5.13)*	5.7823	−103.1	−99.78
	10^1	5.2016	5.8797	−106.9	−104.1
	10^2	5.2070	5.8892	−107.3	−104.5

* Values from reference [13], wherein a 4 × 4 mesh of the 9-node rectangular elements was used.

Table 4 Comparison of the Nusselt number, computational time and number of iterations required for convergence (n) for the penalty finite element model (PFEM1) and stream function vorticity finite element model (SVFEM)

		Penalty finite element			Stream function-vorticity		
Ra	Pr	$n^\dagger$	cpu	Nu	n	cpu	Nu
	10^{-2}	11	3.09	1.0992	18	2.55	1.2582
	10^{-1}	9	2.38	1.1558	16	2.36	1.1367
10^3	1	8	2.33	1.1666 (1.14)*	16	2.39	1.1387
	10	8	2.29	1.1666	15	2.34	1.1387
	10^2	8	2.25	1.1666	15	2.31	1.1387
	10^{-2}	20	5.26	1.9993	22	3.35	2.2004
	10^{-1}	20	5.33	2.0390	28	4.28	2.2600
10^4	1	16	4.26	2.1318 (2.49*)	26	4.05	2.3962
	10	17	4.33	2.1440	20	3.13	2.4144
	10^2	17	4.37	2.1442	20	3.12	2.4146

† convergence tolerance, 10^{-4}.

* values from reference [13], wherein a 4 × 4 mesh of nine-node rectangular elements was used.

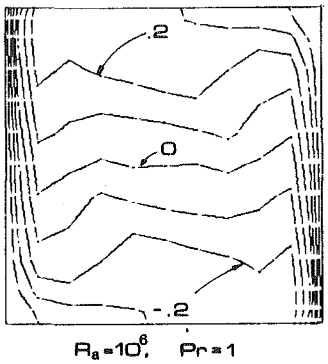

Fig. 4(*a*) Isotherms

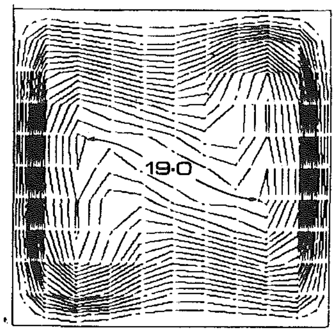

Fig. 4(*b*) Isostreams

Fig. 4 Isotherms and isostreams for Ra = 10^6, Pr = 1 by penalty formulation (mesh: 12 × 12)

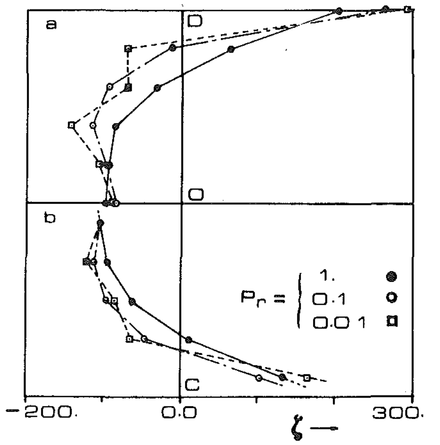

Fig. 5 Vorticity distribution along vertical cross section (Ra = 100,00, Mesh: 10 × 10) (*a*) stream function-vorticity model (SVFEM) (*b*) penalty FEM (PFEM)

Hellums and Churchill. Figure 8 shows similar results for a rectangular enclosure of aspect ratio 1.83, and with linear temperature distribution on the horizontal walls as indicated in the figure (Ra = 8,200, Pr = 2,450). This example is the same as that considered by Szekely and Todd [31], who have computed experimental and finite difference solutions. The plotted values of the steady-state isotherms seem to agree well with those of Szekely and Todd. In general, it was observed that for larger aspect ratios the numerical solutions converged faster. Finally, Fig. 9 shows similar results for an aspect ratio of 16, Ra = 10^5, and Pr = 1. This problem was studied experimentally by Elder [29] for slightly different Rayleigh number (Ra = 3 × 10^5). A symmetric (about the center) but nonuniform mesh of 24 × 14 was used. The isotherms and stream lines shown in Fig. 9(*a*) are those obtained at the end of 30 iterations, with the error (in the velocity field) between the last two iterations being less than 10^{-3}. Due to time limitation on the job card, the solution at the end of thirty iterations was stored on a tape using free format. The computation was initiated with the solution on the tape as the starting value for the 31st iteration. After 30 more (i.e., total 60) iterations, the error was found to be only slightly less than that computed at the end of the first 30 iterations, and computation was terminated plotting the isotherms and stream lines (see Fig. 9(*b*)). While the isotherms virtually remained unaltered, the

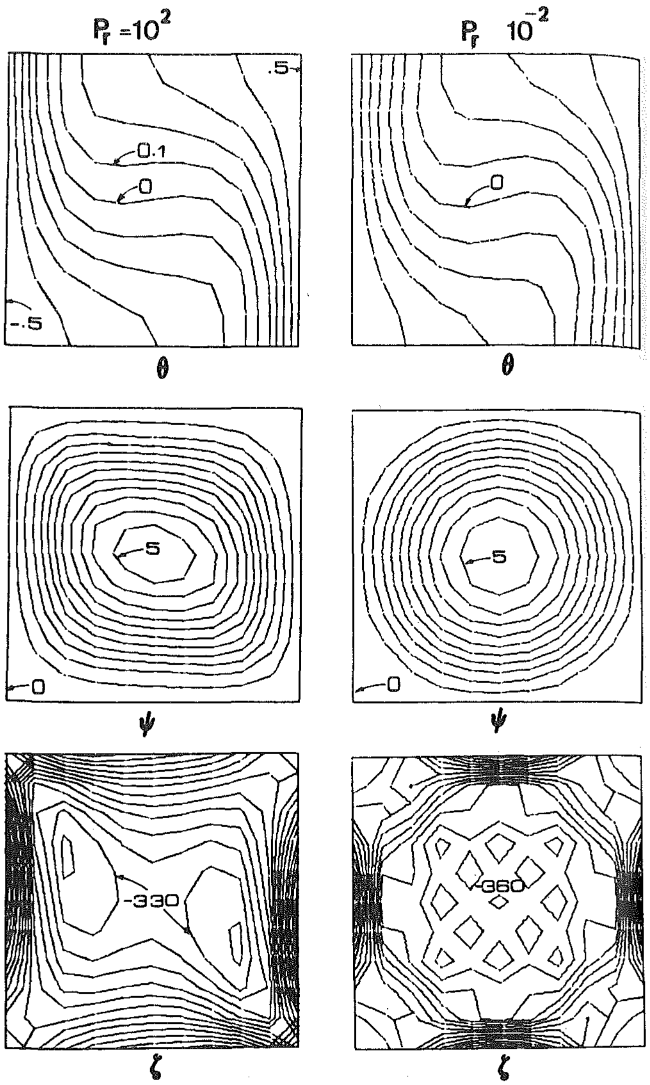

Fig. 6 Isotherms, isostreams, and equivorticity lines for various Prandtl numbers by stream function-vorticity formulation (Ra = 10^4)

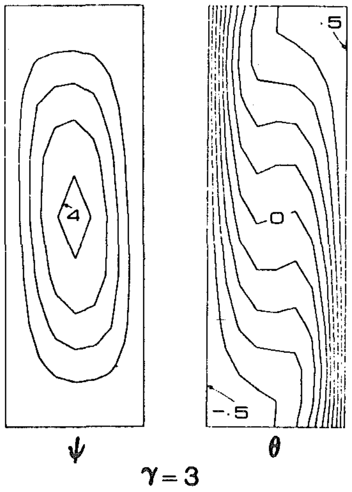

Fig. 7 Isotherms and stream lines for Ra = 14,660, Pr = 0.733

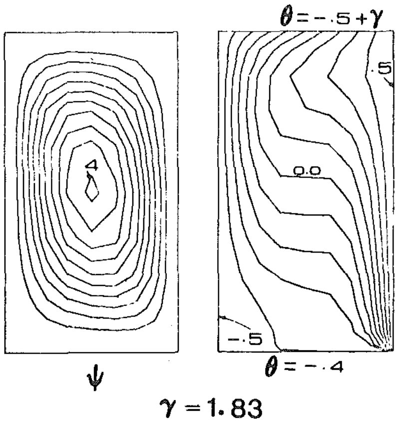

Fig. 8 Isotherms and stream lines for Ra = 8200, Pr = 2450

stream lines in the core region separated into small cells. Also, the stream lines in the boundary layer remained stratified vertically. The results in Fig. 9(*a*) seem to agree, qualitatively, well with those reported by Elder.

In closing we present numerical results for a nonrectangular enclosure (see Fig. 10). Figure 11 shows isotherms and stream lines for $\mathrm{Ra} = 10^4$ and 10^5, $\mathrm{Pr} = 1$. The top and bottom walls were assumed to be insulated. Since no results are available in the literature at this writing, comparison is not made. These results could serve as test cases for future numerical invvestigations.

5 Conclusions

Compared to the mixed finite element model of Gartling [12], the stream function-vorticity finite element model, and the penalty-finite element models seem to be computationally simpler. The mixed model, by formulation, results in a large system of (non-positive definite) equations. Without special consideration, results obtained for the pressure are often erroneous. The stream function-vorticity model suffers from the disadvantage that the boundary conditions on the vorticity be known a priori. De Vahl Davis [32] pointed out that computation of the boundary values of the vorticity from the stream function could result in up to 30 percent error. The results obtained by the penalty method are on the lower side of those obtained by the stream function-vorticity model. It is desirable to have experimental results in order to compare and make accuracy evaluation of the formulations. The stream function-vorticity model presents convergence problems for Rayleigh numbers higher than 10^4. In the penalty model, one is required to assess an optimal value of the penalty parameter. For very high Rayleigh numbers, the penalty parameter should be very large, and this in turn (coupled with word length in the computer) could cause the equations ill-conditioned.

In the present study, only moderate Rayleigh numbers were studied. For Rayleigh numbers higher than 10^6, say of the order 10^7–10^9, most traditional numerical schemes have computational difficulties (in terms of convergence and numerical stability). The so-called upwind differencing could prove to be very effective. In order to use the upwind differencing a logical procedure that can be automated on the computer must be thought out for the finite element method. This area seems to be open for additional research. Another area for which sufficient information is lacking is the free convection in nonrectangular (or irregular) and three-dimensional enclosures, In both cases, unsteady analyses need to be performed. Theoretical as well as numerical investigations into instabilities at high Rayleigh numbers (say, in the turbulent region) are definitely far from complete.

Acknowledgments

The results reported herein were obtained during an investigation supported by the Atmospheric Sciences Division of the National Science Foundation through Grant ATM77-23111. Their support is gratefully acknowledged.

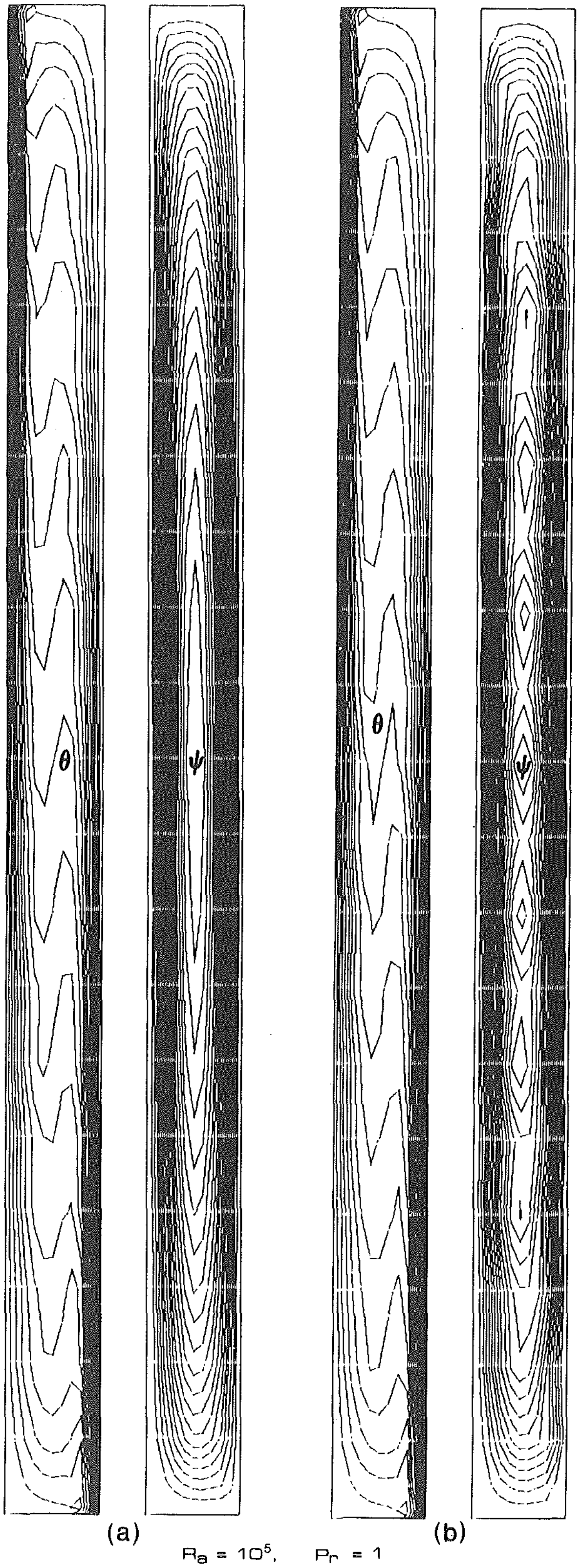

Fig. 9 Isotherms and streamlines for the vertical slot problem of Elder [29] ($\mathrm{Ra} = 10^5$, $\mathrm{Pr} = 1$, $\gamma = 16$, mesh = 24×14); (*a*) after 30 iterations, error $\simeq 10^{-3}$ (*b*) after 60 iterations, error $< 10^{-3}$.

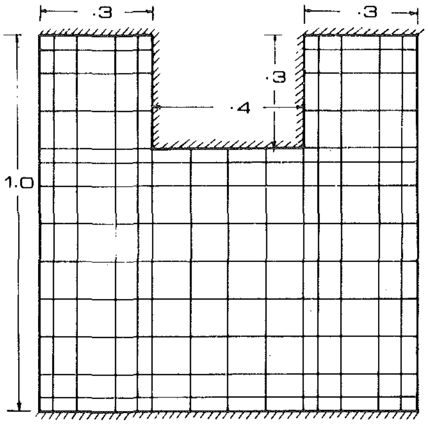

Fig. 10 Finite element mesh for nonrectangular cavity (14 × 13 nonuniform mesh)

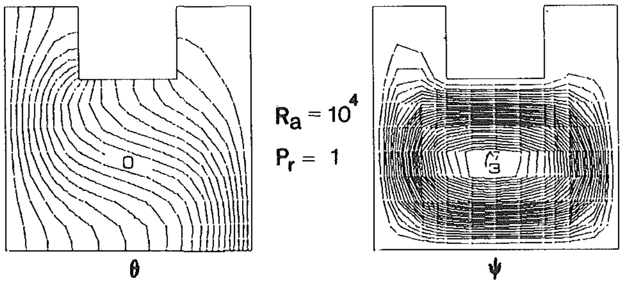

Fig. 11(*a*)

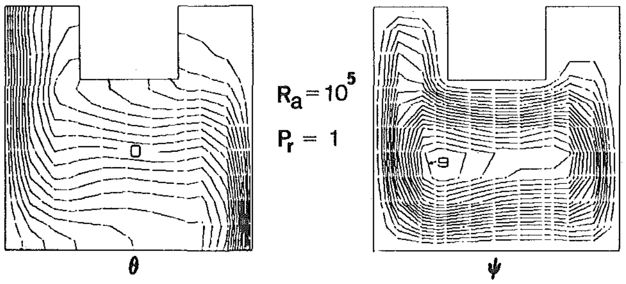

Fig. 11(*b*)

Fig. 11 Temperature and stream function for nonsquare enclosure by the penalty-finite element model (*a*) temperature and (*b*) stream function

References

1 Ostrach, S., "Natural Convection in Enclosures," *Advances in Heat Transfer*, Vol. 8, 1972, pp. 161–227.

2 Batchelor, G. K., "Heat Transfer by Free Convection Across a Closed Cavity Between Vertical Boundaries at Different Temperature," *Quarterly Journal Applied Mathematics*, Vol. 12, 1954, pp. 209–233.

3 Elder, J. W., "Numerical Experiments with Free Convection in a Vertical Slot," *Journal of Fluid Mechanics*, Vol. 24, 4, 1965, pp. 823–843.

4 Gill, A. E., "The Boundary Layer Regime for Convection in a Rectangular Cavity," *Journal of Fluid Mechanics*, Vol. 26, 3, 1966, pp. 515–536.

5 Pedersen, B. D., et al., "Development of a Compressed Gas-Insulated Transmission Line," I.E.E.E. Winter Power Meetirg, Paper 71 TP 193 PWR, 1971.

6 Hart, J. E., "Stability of Thin Non-Rotating Hadley Circulation," *Journal of Atmospheric Science* Vol 29, 1972, p. 687.

7 Carruthers, J. P., "Crystal Growth From the Melt," *Treatise on Solid State Chemistry*, Vol. 5, Plenum Press, 1975, p. 325.

8 Hiddink, J., et al., "Natural Convection Heating of Liquids in Closed Containers," *Applied Science Research*, Vol. 32, 1976, p. 217.

9 Petuklov, B. S., "Actual Problems of Heat Transfer in Nuclear Power Engineering," *International Seminar on Future Energy Production*, Hemisphere Publishing Corporation, Washington, D.C., 1976, pp. 151–163.

10 Chato, J. C., and Abdulhadi, R. S., "Flow and Heat Transfer in Convectively Cooled Underground Electric Cable Systems: Part 1—Velocity Distributions and Pressure Drop Correlations; Part 2—Temperature Distributions and Heat Transfer Correlations," ASME JOURNAL OF HEAT TRANSFER, Feb., 1978, pp. 30–40.

11 Tabarrok, B. and Lin, R. C., "Finite Element Anslysis of Free Convection Flows," *International Journal of Heat and Mass Transfer*, Vol. 20, 1977, p. 945.

12 Gartling, D. K., "Convective Heat Transfer Analysis by the Finite Element Method," *Computer Methods in Applied Mechanics and Engineering*, Vol. 12, 1977, pp. 365–382.

13 Heinrich, J. C., Marshall, R. S., and Zienkiewicz, O. C., "Penalty Function Solution of Coupled Convective and Conductive Heat Transfer," *International Conference on Numerical Methods in Laminar and Turbulent Flow*, Swansea, July 1978.

14 Marshall, R. S., Heinrich, J. C., and Zienkiewicz, O. C., "Natural Convection in a Square Enclosure by a Finite-Element Penalty Function Method Using Primitive Fluid Variables," *Numerical Heat Transfer*, Vol. 1, 1978, pp. 315–330.

15 Reddy, J. N., and Mamidi, D. R., "Penalty Velocity-Stream Function Finite Element Models for Free Convection Heat Transfer Problems," *Recent Advances in Engineering Science*, R. L. Sierakowski (ed.) University of Florida, Gainesville, 1978, pp. 381–386.

16 Reddy, J. N., "Penalty Finite Element Methods for the Solution of Advection and Free Convection Flows," *Finite Element Methods in Engineering*, A. P. Kabaila and V. A. Pulmano (eds.), The University of New South Wales, Sydney, Australia, 1979, pp. 583–598.

17 Courant, R., *Calculus of Variations and Supplementary Notes and Exercise*, revised and amended by J. Moser, New York University, 1956.

18 Zienkiewicz, O. C., "Constrained Variational Principles and Penalty Analysis Function Methods in Finite Elements," *Lecture Notes on Mathematics*, Springer-Verlag, Berlin, 1973.

19 Polya, B. T., "The Convergence Rate of the Penalty Function Method," *Zhurnal Vychislitel'noi Matematiki i Matematicheskoi Fiziki*, Vol, 11, 1971, pp. 3–11; English translation: U.S.S.R. *Computational Mathematics and Mathematical Physics*, Vol. 11, 1971, pp. 1–12.

20 Bercovier, M., "Perturbations of Mixed Variational Problems, Applications to Mixed Finite Element Methods," *R.A.I.R.O., Analyze Numerique/ Numerical Analysis*, Vol. 12, 1978, pp. 211–236.

21 Reddy, J. N., "On the Finite Element Method with Penalty for Incompressible Fluid Flow Problems," *The Mathematics of Finite Elements and Applications III*, Whiteman, J. R. (ed.), Academic Press, New York, 1979, pp. 227–235.

22 Reddy, J. N., "On the Mathematical Theory of Penalty-Finite Elements for Navier-Stokes Equations," *Proceedings of the Third International Conference Finite Elements in Flow Problems*, June 10–13, Banff, Alberta, Canada, 1980.

23 Oden, J. T. and Reddy, J. N., *An Introduction to the Mathematical Theory of Finite Elements*, Wiley-Interscience, New York, 1976.

24 Zienkiewicz, O. C., Taylor, R. L., and Too, J. M., "Reduced Integration Techniques in General Analysis of Plates and Shells," *Int. J. Numer. International Journal of Numerical Methods in Engineering*, Vol. 3, 1971, pp. 275–290.

25 Catton, Y., Ayyaswamy, P. S., and Clever, R. C., "Natural Convection Flow in a Finite Rectangular Slot Arbitrarily Oriented with Respect to the Gravity Vector," *International Journal of Heat and Mass Transfer*, Vol. 17, 1974, pp. 173–184.

26 Cormach, P. E., Lead, L. G., and Seinfeld, J. H., "Natural Convection in a Shallow Cavity with Differentially Heated End Walls, Part 2, Numerical Solutions," *Journal of Fluid Mechanics*, Vol. 65, 1974, pp. 231–246.

27 Wilkes, J. O., and Churchill, S. W., "The Finite Difference Computation of Natural Convection in a Rectangular Enclosure," *American Institute of Chemical Engineers.*, Vol. 12, 1966, pp. 161–166.

28 Ozoe, H., Sayan, H., and Churchill, S. W., "Natural Convection in an Inclined Rectangular Channel of Various Aspect Ratios and Angles—Experimental Measurements," *International Journal of Heat and Mass Transfer*, Vol. 18, 1975, pp. 1425–1431.

29 Elder, J. W., "Laminar Free Convection in a Vertical Slot," *Journal of Fluid Mechanics*, Vol. 23, 1965, pp. 77–98.

30 Hellums, J. D. and Churchill, S. W., "Transient and Steady State, Free and Natural Convection, Numerical Solutions," *AIChE Journal*, Vol. 8, 1962, pp. 690–695.

31 Szekely, J., and Todd, M. R., "Natural Convection in a Rectangular Cavity Transient Behavior and Two Phase Systems in Laminar Flow," *International Journal of Heat and Mass Transfer*, Vol. 14, 1971, pp. 467–482.

32 De Vahl Davis, G., "Laminar Natural Convection in an Enclosed Rectangular Cavity," *International Journal of Heat and Mass Transfer*, 1968, Vol. 11, pp. 1675–1693.

L. S. Yao
F. F. Chen

Department of Mechanical
and Industrial Engineering,
University of Illinois at Urbana-Champaign,
Urbana, IL 61801

Effects of Natural Convection in the Melted Region Around a Heated Horizontal Cylinder

Two heat transfer modes are involved in the process of melting around a heated horizontal cylinder: conduction and convection. The magnitude of convection is proportional to the Rayleigh number based on the width of the melted region. The importance of natural convection increases with time. For a short period after the beginning of melting, heat transfer is dominated by conduction. A regular perturbation solution is presented to demonstrate the increasing effect of natural convection on the melting process.

1 Introduction

Phase-change problems such as melting and freezing have been extensively studied for the last century due to their wide applications. A comprehensive review of previous works concerning the natural convection effect can be found in [1–2]. Recently, the development of thermal storage systems require further study of the problem. The thermal storage systems usually contain horizontal pipes through which a hot fluid flows. The thermal energy is transferred from the pipes to the surrounding thermal storage materials and stored there. It is desirable to select thermal storage materials of low melting temperature to take advantage of their large latent heat during the process of changing phase. Currently, the available latent heat systems employ a containerized PCM-a la the thermal 81 tubes. In this paper, we concentrate on the natural-convection effects on the melting process for a single tube. With the improved knowledge about the effects of natural convection, the response time of the system may be improved by altering the design.

An idealized model to simulate the thermal storage unit consists of a hot horizontal cylinder embedded in an infinite solid. Traditionally, the phase-change problem in this kind of geometry is solved with the assumption that the energy is transferred by conduction alone. Therefore, the melting front is axisymmetric and the analysis can be simplified to problems of one-dimensional and unsteady conduction. However, two recent experiments [1, 2] clearly show that the melting front is by no means axisymmetric. It propagates faster upward than downward. Natural convection plays an increasingly important role in the process of transferring energy. The effects of natural convection on the phase-change process is the topic studied in the paper.

The difficulty associated with the phase-change problems is that the boundary between two phases moves and is not known a priori. A gap function is introduced to immobilize the melting front in the transformed coordinate. The domain of the melted region becomes a unit circle. This removes the complication of an asymmetric moving boundary. The effects of the moving boundary are modeled into the governing equations whose forms, although manageable, become rather complicated.

The general formulation of the mathematical model is presented in the second section. It is demonstrated that the importance of the natural convection depends on the Rayleigh number evaluated on the characteristic width of the melted region. At the beginning of the melting process, conduction is the dominant energy transfer mode. The importance of natural convection gradually increases as the melted region grows. Eventually, the natural convection develops into a turbulent motion. In this paper, we concentrate on the short-time solution where conduction is the dominant energy transfer mode, and natural convection is treated as a perturbed quantity.

The regular perturbation series are developed in the second section and the solutions are outlined in Section 3. In Section 4 the numerical results are presented and discussed.

2 Analysis

The physical model considered is an infinitely long circular cylinder of radius a horizontally embedded in an infinite solid material (Fig. 1). The temperature of the solid is held at the melting temperature, T_m, originally. The surface temperature of the hot cylinder is kept at a constant temperature, say $T_i > T_m$, when the melting begins. The position of the melting front is denoted by $R(\psi,t)$ which is not axisymmetric due to natural convection. The variation of density through phase change which is the most commonly adopted assumption in the theoretical study of phase-change problems is not considered here. The buoyancy force induced by the density stratification is, however, included by using what is known as the Boussinesq approximation.

The equations governing the stream function and the temperature in cylindrical polar coordinates are

$$\frac{\partial}{\partial \bar{t}}(\nabla^2 \bar{f}) + \frac{1}{\bar{r}}\bar{\mathrm{J}}(\bar{f}, \nabla^2 \bar{f}) = \beta g\left[\sin\psi \frac{\partial T}{\partial \bar{r}} + \frac{\cos\psi}{\bar{r}}\frac{\partial T}{\partial \psi}\right] + \nu\nabla^2 \bar{f} \tag{1a}$$

$$\frac{\partial T}{\partial \bar{t}} + \frac{1}{\bar{r}}\bar{\mathrm{J}}(\partial f, T) = \alpha\nabla^2 T \tag{1b}$$

where $\bar{r}$ and ψ denote the radial and the azimuthal coordinates, $\bar{t}$ is the time. ν is the kinematic viscosity, α is the thermal diffusivity, β is the thermal expansion coefficient, and g is the gravitational acceleration. T represents temperature and $\bar{f}$ is the stream function which is related to the velocities by

$$\bar{u} = -\frac{1}{\bar{r}}\frac{\partial \bar{f}}{\partial \psi}; \quad \bar{v} = \frac{\partial \bar{f}}{\partial \bar{r}} \tag{2}$$

where $\bar{u}$ is the radial velocity and $\bar{v}$ is the azimuthal velocity. Γ^2 is the Laplace operator in cylindrical polar coordinates and is

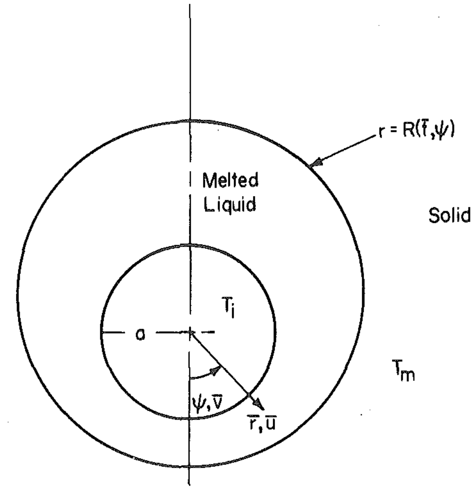

Fig. 1 Physical model and coordinates

Contributed by the Heat Transfer Division for publication in the JOURNAL OF HEAT TRANSFER. Manuscript received by the Heat Transfer Division January 10, 1980

$$\nabla^2 = \frac{\partial^2}{\partial \bar{r}^2} + \frac{1}{\bar{r}}\frac{\partial}{\partial \bar{r}} + \frac{1}{\bar{r}^2}\frac{\partial^2}{\partial \psi^2} \tag{3a}$$

and $\bar{J}$ is the Jacobian defined as

$$\bar{J}(\bar{f}, \nabla^2\bar{f}) = \frac{\partial \bar{f}}{\partial \bar{r}} \cdot \frac{\partial}{\partial \psi}\nabla^2\bar{f} - \frac{\partial \bar{f}}{\partial \psi} \cdot \frac{\partial}{\partial \bar{r}}\nabla^2\bar{f} \tag{3b}$$

The moving melting front presents some difficulties in the analysis of the melting problem. A dimensionless gap width of the melted liquid,

$$B(\beta, t) = [R(\psi, t) - a]/a, \tag{4}$$

is introduced. With the help of equation (4), the dimensionless variables are introduced.

$$f = \bar{f}/\alpha \quad \text{(stream function)}, \tag{5a}$$

$$r = [(\bar{r} - a)/(aB)] \quad \text{(radial-coordinate transformation)} \tag{5b}$$

$$t = \bar{t}/(a^2/\alpha\epsilon) \quad \text{(time)} \tag{5c}$$

$$\epsilon = C(T_i - T_m)/L\left(\frac{\rho_l}{\rho_s}\right) \quad \text{(Stefan number)} \tag{5d}$$

$$\theta = (T - T_m)/(T_i - T_m) \quad \text{(temperature)} \tag{5e}$$

where C is the specific heat and L is the latent heat.

Substitution of equations (5) into equations (1) give the dimensionless governing equations. They are

$$\Pr \cdot \left[\epsilon \cdot B \cdot \left(\frac{\partial}{\partial t} - \frac{r\dot{B}}{B}\frac{\partial}{\partial r}\right) \cdot \nabla_1{}^2 f + \frac{1}{r + 1/B} \cdot \mathrm{J}(f, \nabla_1{}^2 f)\right]$$
$$= \mathrm{Ra}\left[\sin\psi \cdot \frac{\partial\theta}{\partial r} + \frac{\cos\psi}{r + 1/\mathrm{B}} \cdot \left(\frac{\partial\theta}{\partial\psi} - \frac{rB'}{B}\frac{\partial\theta}{\partial r}\right)\right] + B \cdot \nabla_1{}^4 f, \tag{6a}$$

$$\epsilon \cdot B \cdot \left(\frac{\partial\theta}{\partial t} - \frac{r\dot{B}}{B}\frac{\partial\theta}{\partial r}\right) + \frac{1}{r + 1/B} \cdot \mathrm{J}(f, \theta) = B \cdot \nabla_1{}^2 f, \tag{6b}$$

where

$$\Pr = \nu/\alpha \quad \text{(Prandtl number)} \tag{7a}$$

$$\mathrm{Ra} = \frac{\beta g(T_i - T_m)a^3}{\nu\alpha} \text{(Rayleigh number)} \tag{7b}$$

$$\nabla_1{}^2 = \frac{1}{B^2}\left[\frac{\partial^2}{\partial r^2} + \frac{1}{r + 1/B}\frac{\partial}{\partial r} + \frac{1}{(r + 1/B)^2}\left(\frac{\partial}{\partial\psi} - \frac{rB'}{B}\frac{\partial}{\partial r}\right)^2\right] \tag{7c}$$

and

$$\mathrm{J}(f, \nabla_1{}^2 f) = \frac{1}{B}\left[\frac{\partial f}{\partial r} \cdot \left(\frac{\partial}{\partial\psi} - \frac{rB'}{B}\frac{\partial}{\partial r}\right)(\nabla_1{}^2 f)\right.$$
$$\left. - \frac{\partial}{\partial r}(\nabla_1{}^2 f) \cdot \left(\frac{\partial}{\partial\psi} - \frac{rB'}{B}\frac{\partial}{\partial r}\right) f\right] \tag{7d}$$

In equations (6) and (7), the superscripted dot denotes the derivative with respect to t, and the prime with respect to ψ. The terms which contain $\dot{B}$ represent the convection due to the moving melting front; B' introduces the convective effects due to the asymmetric development of the melting front. It should be pointed out that the radial-coordinate transformation, equation (5b), immobilizes the moving boundary and transforms the undetermined asymmetric geometry into a unit circle. The convective effects introduced by the moving boundary are modeled into the governing equations. A similar transformation [4] has been used to study the natural convection in the melted region around a heated vertical cylinder. A time-dependence of the melting front has been dismissed from the transformation. This results in a simpler set of the governing equations which is suitable for small Stefan numbers.

Equation (6) shows that the buoyancy forces are proportional to Ra which is evaluated at the radius of the inner cylinder. However, equations (7) show that $\nabla_1{}^2 f \sim 1/B^2$ and $\mathrm{J} \sim 1/B^3$. This indicates that the magnitude of buoyancy forces are actually depending on $\mathrm{Ra}_B = \mathrm{Ra} \cdot B^3$. In other words, the importance of the natural convection increases with the amount of the melted liquid. Since the value of B is small at the beginning of the melting process, conduction is the dominant heat transfer mode. As the melting front propagates, the natural convection gradually becomes the dominant heat transfer mode. Eventually, the natural convection develops into a turbulent motion.

In this paper, we concentrate on the short-time solution where natural convection is weak and can be treated as a perturbed quantity and conduction is the dominant heat transfer mode. Also, we assume that the Stefan number is small. This is a desirable characteristic in selecting thermal storage materials. For small Stefan numbers, the melting front moves slowly and a quasi-steady approximation can be justified. With these two assumptions in mind, the regular perturbation series can be expressed

$$\theta = [\theta_{00} + \epsilon\theta_{01} + \ldots] + \mathrm{Ra}\cos\psi[\theta_{10} + \epsilon\theta_{11} + \ldots]$$
$$+ \mathrm{Ra}^2\cos 2\psi[\theta_{20} + \epsilon\theta_{21} + \ldots] + \ldots, \tag{9a}$$

$$f = \mathrm{Ra}\sin\psi[f_{10} + \epsilon f_{11} + \ldots]$$
$$+ \mathrm{Ra}^2\sin 2\psi(f_{20} + \epsilon f_{21} + \ldots) + \ldots \tag{9b}$$

where all the expansion functions depend only on r. Since the asymmetry of the melted region is determined by the asymmetric distribution of heat flux induced by natural convection, the gap width can also be expanded into a power series of Ra and ϵ, such as

$$B = B_{00} + \epsilon \cdot B_{01} + \ldots] + \mathrm{Ra} \cdot \cos \cdot \psi[B_{10} + \epsilon \cdot B_{11} + \ldots]$$
$$+ \mathrm{Ra}^2 \cdot \cos(2\psi)[B_{20} + \epsilon \cdot B_{21} + \ldots] + \ldots, \tag{9c}$$

where all the Bs depend only on t. It should be emphasized here that the perturbation series are not limited by the value of Ra; instead, they are limited by the value of $\mathrm{Ra} \cdot B^3$. Therefore, the value of Ra only partially determines how long the perturbation series are valid since the value of B increases with time. The upper limit of $\mathrm{Ra} \cdot B^3$ for which the series solution can be applied will be discussed in the last section.

The governing equations of θ's and f's can be obtained by substituting equations (9) into equations (6) and collecting the terms of equal order ϵ and Ra. They are listed below.

Ra°:

$$\epsilon^{\circ}: \frac{\partial^2\theta_{00}}{\partial r^2} + \frac{1}{r + 1/B_{00}}\frac{\partial\theta_{00}}{\partial r} = 0 \tag{10}$$

$$\epsilon: \frac{\partial^2\theta_{01}}{\partial r^2} + \frac{1}{r + 1/B_{00}} \cdot \frac{\partial\theta_{01}}{\partial r}$$
$$= \left[r \cdot B_{00}\dot{B}_{00} + \frac{B_{01}}{(1 + B_{00} \cdot r)^2}\right]\frac{\partial\theta_{00}}{\partial r} + \dot{B}_{00} \cdot B_{00}{}^2\frac{\partial\theta_{00}}{\partial B_{00}} \tag{11}$$

Ra:

Nomenclature

A_i = constants
a = radius of the hot cylinder
B = gap function, equation (4)
f = stream function
g = gravitational acceleration
k = thermal conductivity
Pr = Prandtl number
r = radial coordinate
R = contour of the melted region
Ra = Rayleigh number
$\mathrm{Ra}_B = \mathrm{Ra} \cdot B^3$
T = temperature
θ = dimensionless temperature, equation (5e)
ν = kinematic viscosity
α = thermal diffusivity
β = thermal expansion coefficient
ψ = azimuthal coordinate
ρ = density

Superscripts

— = dimensional quantity
′ = derivative with respect to ψ
· = derivative with respect to t

Subscripts

i = inner cylinder
m = melting front
number = indication of the expansion order

$$\epsilon^\circ: \nabla_2^4 f_{10} + B_{00}^2 \frac{\partial\theta_{00}}{\partial r} = 0, \qquad (12a)$$

$$\nabla_2^2\theta_{10} = \left(\frac{B_{10}}{B_{00}} + \frac{f_{10}}{1 + B_{00}\cdot r}\right)\cdot\frac{\partial\theta_{00}}{\partial r}, \qquad (12b)$$

where

$$\nabla_2^2 = \frac{\partial^2}{\partial r^2} + \frac{1}{r + 1/B_{00}}\cdot\frac{\partial}{\partial r}\frac{1}{(x + 1/B_{00})^2}. \qquad (13)$$

The higher-order equations can be obtained similarly; however, the complexity increases very fast.

Equations (10–14) depend on B's. In the process of solving equations (10–13), the gap functions B_{00}, B_{01}, B_{10}, etc., have to be determined in order to complete the solution. The equations governing the gap functions can be obtained from the principle of energy conservation along the melting front, the boundary between two phases. It is

$$-k_l(\partial T/\partial\bar{r})_{\bar{r}=R} = \rho_s L(dR/d\bar{t}), \qquad (14)$$

where k is the thermal conductivity and ρ is the density. The subscripts l and s distinguish the liquid and the solid phases. In terms of the dimensionless variables, equations (14) become

$$(dB^2/dt) = -2(\partial\theta/\partial r)_{r=1} \qquad (15)$$

Substitution of equation (9c) into equation (15) and collection of the terms of equal order ϵ and Ra result in
Ra°:

$$\epsilon^\circ: B_{00}\dot{B}_{00} = \frac{\partial\theta_{00}}{\partial r}_{r=1} \qquad (16)$$

$$\epsilon: B_{00}\dot{B}_{01} = \left[-\frac{\partial\theta_{01}}{\partial r} + \frac{B_{01}}{B_{00}}\cdot\frac{\partial\theta_{00}}{\partial r}\right]_{r=1} \qquad (17)$$

Ra:

$$\epsilon^\circ: B_{00}\dot{x}_{10} = \left[\frac{\partial\theta_{10}}{\partial r} + \frac{B_{10}}{B_{00}}\cdot\frac{\partial\theta_{00}}{\partial r}\right]_{r=1} \qquad (18)$$

3 Solution

The boundary conditions required to solve the above equations are

$$(1)\ r = 0: \theta = 1, \text{(constant temperature)} \qquad (19a)$$

$$f = (\partial f/\partial r) = 0, \text{(no-slip condition)} \qquad (19b)$$

$$(2)\ r = 1: \theta = 0, \text{(melting temperature)} \qquad (19c)$$

$$f = (\partial f/\partial r) = 0 \qquad (19d)$$

The initial condition for the melting front is

$$t = 0, B = 0. \qquad (20)$$

Physically, equation (20) can be interpreted to imply that no liquid region exists before the surface temperature of the inner cylinder is suddenly raised from $\theta = 0$ to $\theta = 1$.

The solutions of equations (10–12) which satisfy the conditions (19–20) are listed below.
Ra°:

$$\epsilon^\circ: \theta_{00} = 1 - A_1\cdot\ln(1 + B_{00}\cdot r), \qquad (21a)$$

where

$$A_1 = 1/\ln(1 + B_{00}); \qquad (21b)$$

$$\epsilon: \theta_{01} = A_2\cdot\ln\left(r + \frac{1}{B_{00}}\right) + A_3 + C_{01}(r) \qquad (22)$$

where

$$C_{01}(r) = \frac{A_1\cdot B_{01}}{B_{00}^2(r + 1/B_{00})}$$
$$+ A_1^2\, B\, B_{00}^3\cdot\left\{0.25\cdot A_1\cdot B_{00}^2\cdot\frac{(r + 1/B_{00})^2}{1 + B_{00}}\cdot[\ln(1 + B_{00}\cdot r) - 1]\right.$$
$$\left.+ 0.25\cdot(r + 1/B_{00})^2 - (1 + 1/B_{00})\cdot(r + 1/B_{00})\right\} \qquad (23a)$$

$$A_2 = [C_{01}(0) - C_{01}(1)]/\ln(1 + B_{00}) \qquad (23b)$$

$$A_3 = A_2\cdot\ln B_{00} - {}_{01}(0) \qquad (23c)$$

Ra:

$$\epsilon^\circ: f_{10} = A_1\cdot B_{00}\left\{\frac{1}{16}\cdot(r + 1/B_{00})^3\cdot[\ln(r + 1/B_{00}) - 1.25 + A_4]\right.$$
$$+ 0.25\cdot A_5\cdot(r + 1/B_{00})\cdot 2\cdot\ln(r + 1/B_{00}) - 1]$$
$$\left.+ A_6\cdot(r + 1/B_{00}) + \frac{A_7}{r + 1/B_{00}}\right\} \qquad (24)$$

$$\theta_{10} = -\frac{A_1}{A_{10}}\cdot\frac{B_{10}\cdot(1 + B_{00})}{B_{00}} + A_{11}\left(r + \frac{1}{B_{00}}\right)$$
$$+ \frac{A_{12}}{r + \dfrac{1}{B_{00}}} + C_{10}(r) \qquad (25)$$

where

$$C_{10}(r) = A_1^2\cdot B_{00}^2\cdot\left\{\frac{1}{128}\cdot(r + 1/B_{00})^3\cdot[\ln(r + 1/B_{00}) - 2 + A_4]\right.$$
$$+ \frac{1}{8}\cdot A_5\cdot(r + 1/B_{00})[\ln^2(r + 1/B_{00}) - 21n(r + 1/B_{00}) + 1]$$
$$+ \frac{1}{8}\cdot A_6\cdot(r + 1/B_{00})[21n(r + 1/B_{00}) - 1] - 0.5A_7]$$
$$\left.\cdot\ln(r + 1/B_{00})/(r + 1/B_{00})\right\}, \qquad (26a)$$

and

$$A_4 = (1 + \ln B_{00}) - [4\cdot A_5\cdot B_{00}^2(1 + B_{00})^2]/A_{10},$$

$$A_5 = \{A_8\cdot A_9 - 4\cdot(1 + B_{00})^2\cdot[A_9 - A_{10}\cdot(1 + B_{00})^2]$$
$$\cdot\ln(1 + B_{00})\}/\{16\cdot B_{00}^2\cdot[A_9\cdot\ln(1 + B_{00}) - A_{10}^2]\},$$

$$A_6 = \frac{A_8}{A_{10}} + \frac{A_4}{A_{10}}\cdot[\ln(1 + B_{00}) + A_{10}\cdot\ln B_{00}],$$

$$A_7 = (A_5\cdot A_8\cdot A_{10} - A_8^2)/[A_9\cdot\ln(1 + B_{00})], \qquad (26b)$$

$$A_8 = 0.25\cdot(1 + B_{00})^2\cdot\ln(1 + B_{00})]/B_{00}^2$$

$$A_9 = (1 + B_{00})^4 - 1,$$

$$A_{10} = (1 + B_{00})^2 - 1,$$

$$A_{11} = \frac{B_{00}}{A_{10}}[B_{10}A_1 - (1 + B_{00})C_{10}(1) + C_{10}(0)]$$

$$A_{12} = \frac{(1 + B_{00})}{B_{00}A_{10}}[B_{10}A_1 + C_{10}(1) - (1 + B_{00})C_{10}(0)]$$

The solutions of higher orders can be obtained by following a similar procedure. The extension is straight-forward; however, the algebra becomes very complex and tedious. The computer method may be the appropriate approach to obtain the series. It should, however, be remembered that the expansion procedure is restricted to small Rayleigh numbers and Stefan numbers. Inclusion of the terms of higher orders may be able to extend the applicable domain of the series solution; but the extended series are still limited by the method of solution. For the longtime solution, large Ra_B, a direct numerical solution may be more appropriate. Therefore, only the solutions up to the first-order of ϵ or Ra are presented here. They are sufficient to predict the beginning process of the phase change in thermal storage where neither an experimental measurement nor a numerical solution can easily achieve the desirable accuracy.

Equations (23–26) show that the solution is independent of the Prandtl number, at least up to the first order of ϵ and Ra. It should, however, be noticed that the selected scalings, equations (5), which nondimensionalize the equations, implicitly impose a restriction on the Prandtl number. The formulation is for Prandtl numbers which are not too small. For very small Prandtl number such as liquid metals, the inertia forces, equation (6*a*), may not be small, and the diffusion may be controlled by the kinematic viscosity instead of the thermal diffusivity. The case of very small Prandtl number can be safely ruled out from the selection of material for thermal storage and is, therefore, not considered in this paper.

The corresponding gap functions are

$$4t = 1 + (1 + B_{00})^2[2 \ln (1 + B_{00}) - 1] \tag{27a}$$

$$B_{01} = \exp\left[\int_0^t G_1(B_{00})dt\right]\left\{\int_0^t G_2(B_{00}) \times \exp\left[-\int_0^t G_1(B_{00})dt\right]dt\right\} \tag{27b}$$

$$B_{10} = \exp\left[\int_0^t G_1(B_{00})dt\right]\left\{\int_0^t G_3(B_{00}) \exp\left[-\int_0^t G_1(B_{00})dt\right]dt\right\} \tag{27c}$$

where

$$G_1 = (-1/B_{00}{}^2)(\partial\theta_{00}/\partial r)|r = 1 \tag{28a}$$

$$G_2 = (-1/B_{00})(\partial\theta_{01}/\partial r)|r = 1 \tag{28b}$$

$$G_3 = (-1/B_{00})(\partial\theta_{10}/\partial r)|r = 1 \tag{28c}$$

Equations (27*b*) and (27*c*) are at best, difficult to integrate closed-form therefore, they are numerically integrated. Their numerical values of B's are presented in the following section.

4 Results and Discussion

The propagation of the melting front can be described from equation (9*c*) after the values of B_{00}, B_{01}, B_{10}, etc., are calculated. Since the regular perturbation solution with the quasi-steady approximation is valid only for small Ra·B^3 and ϵ, we only present the solutions up to the first order of Ra or ϵ. The values of B_{00}, B_{01}, and B_{10} are shown in Fig. 2. B_{00} represents the location of the melting front due to the heat conduction. The gradient of B_{00} with respect to time gradually levels off when the melting front moves away from the inner cylinder. B_{01} is the first-order unsteady effect. Its values are negative. This implies that the zeroth-order quasi-steady solution tends to overpredict the propagation rate of the melting front.

B_{10} is the first-order effect due to natural convection. Its values are also negative. Physically, B_{10} shows that natural convection sends a hot fluid upward along the surface of the hot cylinder. The liquid is cooled along the melting front and flows toward the bottom of the annulus region. Consequently, there is more solid being melted above the inner cylinder than below it. The gradient of B_{10} with respect to time increases with time. This shows that the effect of natural convection is unimportant at the beginning of the melting, even though in theory, natural convection exists as soon as some solid is melted. Its importance increases proportional to the third power of the width, B, of the melted region. At the beginning of the melting process, the magnitude of natural convection is too small to be measured accurately (see Bathelt, et al.). A comparison of the gradient of B_{00} and B_{10} with respect to time clearly shows the role that natural convection plays in the melting process. Since the gradient of B_{10} becomes steeper and that of B_{00} less steep as the size of the melted region grows, the natural convection eventually becomes the dominant heat transfer mode in the melting process.

The valid range of the series solution depends on Ra_B. For a larger Ra, the series solution can be applied up to a smaller B. The exact value of Ra_B for which the series solution may be applied can be determined from a numerical solution (longtime solution) which is, unfortunately, unavailable at present. However, the maximum value of Ra_B for which the melting front continuously propagates at $\psi = 0$ can be easily obtained from the numerical values of the B's. For Ra = 500, the resolidification, which is physically unrealistic, starts about $\text{Ra}_B = 2020$. For Ra = 1000, it starts at 2165 and for Ra = 5000, it is 2600. It can be concluded that the series solution becomes unrealistic about Ra·B^3 = 2000.

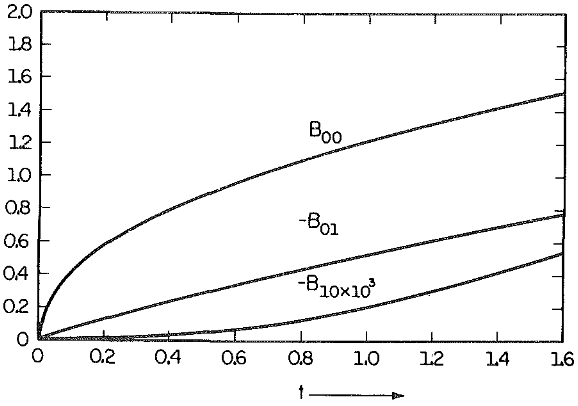

Fig. 2 Melting front

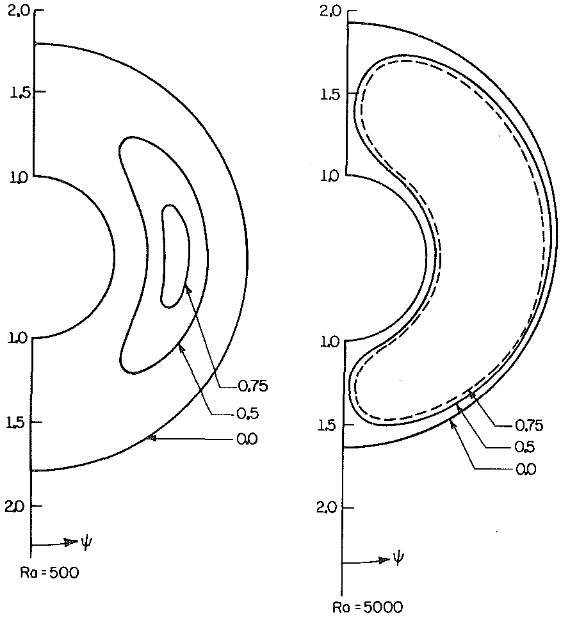

Fig. 3 Streamlines in the asymmetric melted liquid region (ϵ = 0.1, t = 0.392)

Two plots of the shape and the streamlines of the melted-liquid region are given in Fig. 3 for Ra = 500, and 5000, respectively. The case of larger Ra represents the higher temperature of the hot cylinder and results in a more eccentric melted-liquid region. It should be noted that the solutions of 0(Ra°) do not only represent the heat conduction in a concentric geometry. As soon as the actual shape of the melted-liquid region is determined, a significant part of the conduction effect in the eccentric melted-liquid region is included in the solution of 0(Ra°) through the transformation of radial coordinate, equation (5*b*). This is similar to the case of heat transfer in eccentric annuli. A detailed discussion on the properties of that series solution, such as fast convergence with respect to the eccentric effect can be found in [3].

Three profiles of dimensionless radial velocity ($\psi = 0°$), derived from equations (2*a*) and (24) are given in Fig. 4 for t = 0.45, 1.04, and 1.55. For example, the maximum $|\bar{u}a/\alpha|$ at t = 1.55 is 0.5×10^{-2}. Similarly, the azimuthal velocity ($\psi = 90°$) is plotted in Fig. 5.

The azimuthal shear, $\tau_{r\psi}$, can be derived from the stream function and is

$$(a^2/\mu\alpha)\tau_{r\psi} = (1/B^2)(\partial^2 f/\partial r^2) = (\text{Ra} \sin \psi)/(B_{00} + \epsilon B_{01} + \text{Ra} \cos \psi\, B_{10}) f_{10,rr} + \ldots \tag{29}$$

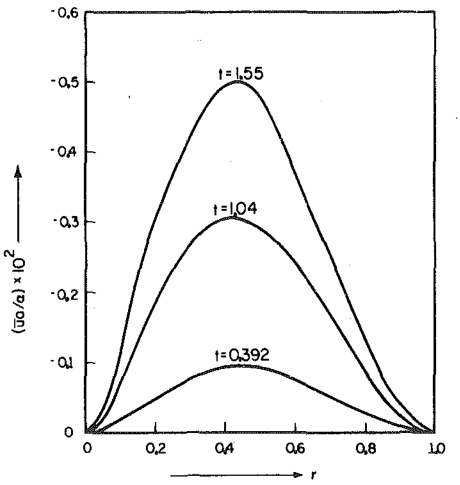

Fig. 4 Radial velocity (Ra = 500, ϵ = 0.1, and ψ = 0 deg)

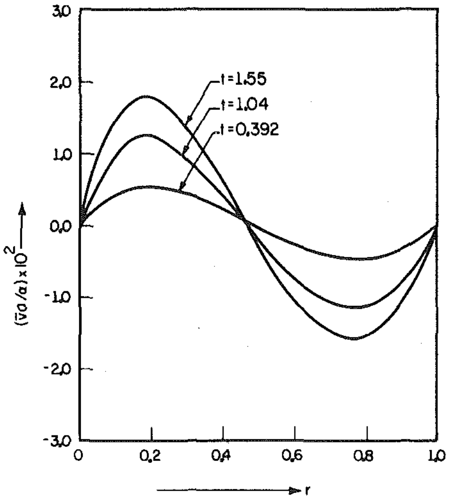

Fig. 5 Azimuthal velocity (Ra = 500, ϵ = 0.1, and ψ = 90 deg)

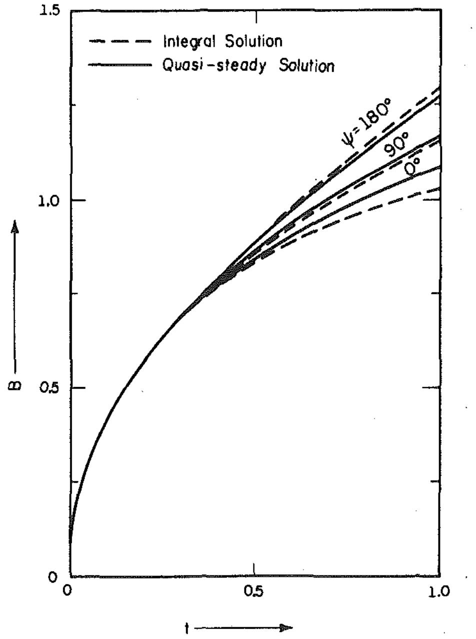

Fig. 7 Comparison of B predicted by the quasi-steady solution and the integral solution

where μ is the viscosity of the melted liquid and the subscript denotes the derivative. The value of $f_{10,rr}$ along the surface of the inner cylinder, $r = 0$, and that of the outer cylinder, $r = 1$, can be calculated from equation (24). The shear along the surface of the inner cylinder is larger.

Typical temperature distribution along $\psi = 0°$ C when Ra = 500 and 0.1 is plotted in Fig. 6 for $t = 0.392$, 1.04, and 1.55, respectively. the amplitude of the natural convection increases with time; the temperature profile becomes more curved. The surface temperature gradient increases along the lower half surface of the inner cylinder due to the ever increasing local impinging flow. On the contrary, the temperature gradient along the lower half of the melting front decreases due to the local inverse stagnation point flow. This is the reason why the melting front propagates slower in the downward direction. The temperature distribution along $\psi = 180$ deg is exactly opposite to that along $\psi = 0$ deg. This is the reason why the melting front propagates faster upwardly.

Heat transfer rate, q, can be estimated from the temperature distribution, equations (9a, 23a, 24a), and (26a). It is

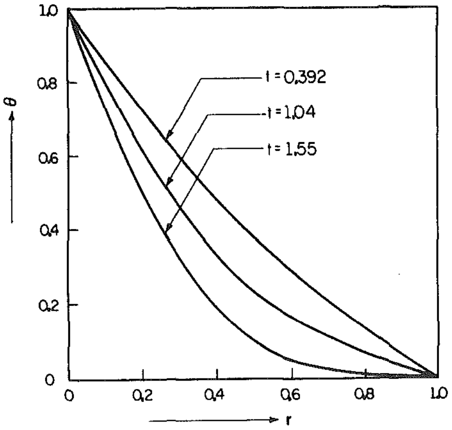

Fig. 6 Temperature distribution (Ra = 500, ϵ = 0.1, and ψ = 0 deg)

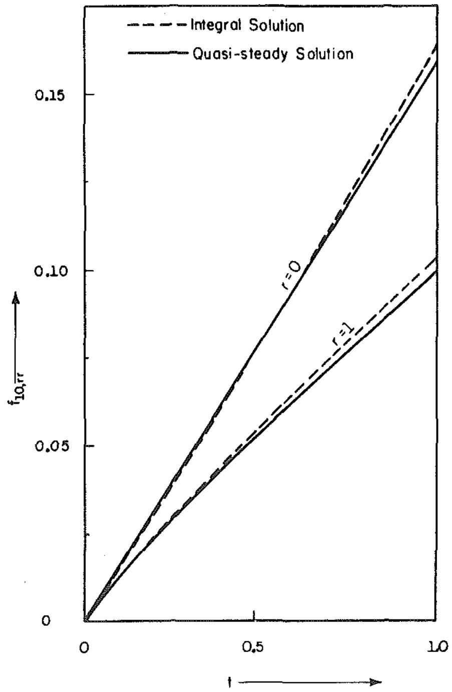

Fig. 8 Comparsion of f_{10rr} predicted by the quasi-steady solution and the integral solution

$$(q \cdot a)/[k(T_i - T_m)] = -(1/B)(\partial\theta/\partial r) = -[\theta_{00,r} + \epsilon\theta_{01,r} + \mathrm{Ra}\cos\psi\,\theta_{10,r} + \ldots]/ \times [B_{00} + \epsilon B_{01} + \mathrm{Ra}\cos\psi B_{10} + \ldots] \quad (30)$$

where k is the thermal conductivity of the melted liquid and the subscript, r, denotes the derivative with respect to r. The values of $\theta_{00,r}$, $\theta_{01,r}$, and $\theta_{10,r}$ along the surfaces of the inner cylinder and the melted front can be easily evaluated from equations (21a, 22), and (25).

The perturbation solution presented above is limited to small Ra_B and ϵ. For a heat-conduction problem it has been proved that the quasi-steady approximation can provide a fairly accurate prediction when ϵ is smaller than 0.1. Since there is no rigorous solution available to compare with, the upper limit that the quasi-steady solution can be applied cannot be determined now. However, the comparison of the quasi-steady solution with the approximate integral solution [5] seems to confirm that $\epsilon = 0.1$ is also the reasonable upper limit. Figure 7 shows the predicted location of the melting front by two different approximate methods. The agreement for $t < 0.5$ is extremely satisfactory. The difference increases but is bounded by 5 percent up to $t = 1$. The comparison of hear stress, $f_{10,rr}$ is very well as shown in Fig. 8. Since the integral solution is limited for small Ra_B's, no rigorous conclusion can be made on the limitation of Ra_B for the regular perturbation solution besides what has been discussed in the text. It is worthy to re-emphasize again the solution can only be applied before the natural convection becomes one of the dominant heat transfer modes. This is why the solution is labeled short-time solution. A direct numerical solution of equation (6) is needed if one is interested in the development of the melting porocess for a longer period where the natural convection becomes dominant.

References

1 Bathlet, A. G., Viskanta, R., and Leidenfrost, W., "An Experimental Investigation of Natural Convection in the Melted Region around a Heated Horizontal Cylinder," *Journal of Fluid Mechanics*, Vol. 90, pt. 2, 1979, pp. 227–239.

2 Sparrow, E. M., Schmidt, R. R., and Ramsey, J. W., "Experiments on the Role of Natural Convection in the Melting of Solids," ASME JOURNAL OF HEAT TRANSFER, Vol. 100, 1978, pp. 11–16.

3 Yao, L. S., "Analysis of Heat Transfer in Slightly Eccentric Annuli," to appear in the ASME JOURNAL OF HEAT TRANSFER, Vol. 99, 1977, pp. 520–526.

4 Sparrow, E. M., Patankar, S. V., and Ramadhyani, S., "Analysis of Melting in the Presence of Natural Convection in the Melted Region," ASME JOURNAL OF HEAT TRANSFER, Vol. 99, 1977, pp. 520–526.

5 Yao, L. S., and Cherney, W., "Transient Phase-Change around a Horizontal Cylinder," 19th ASME/AIChE National Heat Transfer Conf., Orlando, Fla., July 27–30, 1980, Paper No. 80-HT-78.

M. G. O'Callaghan
E. G. Cravalho
Massachusetts Institute of Technology, Cambridge, Mass.

C. E. Huggins
Blood Bank and Transfusion Service, Massachusetts General Hospital, Boston, Mass. 02114

Instability of the Planar Freeze Front During Solidification of an Aqueous Binary Solution

A model describing the heat transfer, solute redistribution, and interface stability during the planar solidification of an aqueous binary solution has been developed. The temperature field was calculated using a modified Kármán-Pohlhausen integral technique. With this technique, the averaged heat conduction equation was solved with the full set of boundary conditions using an assumed spatial variation of the temperature profile. The concentration field was solved for analytically. The stability of the planar freezing morphology was determined using the Mullins-Sekerka stability criterion, in which the time variation of a sinusoidal perturbation of the planar interface was calculated. Application of this criterion to the freezing of saline indicates that for any practical freezing rate the planar interface was unstable. This represents an indictment of the planar freezing model and indicates the tendency for aqueous solutions to freeze dendritically.

Introduction

For a quantitative understanding of the solidification of an impure aqueous solution, the solid-liquid interface morphology as well as the temperature and concentration fields must be determined. The planar interface has been the assumed morphology in many previous investigations in this area because it represents the simplest possible interface morphology. However, the thermodynamic stability of this freezing geometry is an issue that has been completely ignored in most cases and implicitly assumed in others. If instability of the planar interface is indicated, the interface will experience a transition to a more complicated morphology, representing an indictment of the planar interface assumption.

In this paper, the thermodynamic stability of the planar interface will be analyzed during the freezing of a slab of an aqueous binary solution. The Mullins-Sekerka stability criterion [1–3] will be used in this analysis to provide quantitative stability information as a function of the thermal and diffusional conditions imposed on the interface. Calculation of the required temperature and concentration profiles will be accomplished using the Kármán-Pohlhausen integral technique [4,5]. The analysis will be applied to the freezing of an NaCl – H_2O solution.

Transport Equations and Boundary Conditions

The planar freezing geometry is shown schematically in Fig. 1. Heat is extracted at constant flux rate from the plane at $x = 0$. The region $0 \le x \le s$ is occupied by ice and the region $s < x \le \ell$ is occupied by a liquid solution. The solid-liquid interface is located at $x = s(t)$ and the plane $x = \ell$ is a plane of symmetry representing the center of a planar slab of thickness 2ℓ. The field is infinite in extent in the vertical direction and in the direction normal to the paper.

The differential equations of energy and mass transport have been derived repeatedly for this system [6,7], and are given by

$$\alpha_j \frac{\partial^2 T_j}{\partial x} = \frac{\partial T_j}{\partial t} \qquad (1)$$

and

$$D \frac{\partial^2 C}{\partial x^2} = \frac{\partial C}{\partial t} \qquad (2)$$

for heat and solute diffusion respectively, where $j = s,\ell$ refers to the solid and liquid regions. The mass transport equation may be more conveniently represented by transforming to a coordinate system that is moving with the solid-liquid interface. Using the transformation

$$x' = x - Rt \qquad (3)$$

we can write equation (2) as

$$D \frac{\partial^2 C}{\partial x'^2} + R \frac{\partial C}{\partial x'} = \frac{\partial C}{\partial t} \qquad (4)$$

where R is the pseudo-steady interface velocity. The coordinate x' is measured away from the interface, so at $x' = 0, x = R \cdot t = s(t)$.

The boundary and initial conditions for the temperature and concentration fields are summarized in Table 1. In the freezing of most aqueous solutions, solute molecules are excluded completely from the advancing solid [8]. This condition is expressed mathematically by setting the absolute particle velocity to zero in the moving coordinate system to give

$$D \frac{\partial C}{\partial x'} (x' = \text{o}, t) + RC\,(x' = \text{o}, t) = 0 \qquad (5)$$

Since R, D and C are positive for all x', the concentration gradient must be negative at the interface.

The temperature profiles described by equation (1) for $j = s,\ell$ must match at the interface. Then

$$T_s(x = s,t) = T_\ell(x = s,t) = T_i. \qquad (6)$$

If we assume that the solid phase and the liquid solution just adjacent to it are essentially in thermal equilibrium, the interface solute concentration will determine the interface temperature from the locus of two-phase equilibrium states. This locus may be approximated by a power series of the form

$$T_i = a' + b'C_i + c'C_i^2 + d'C_i^3 \qquad (7)$$

The rate of advance of the solid-liquid interface is controlled by the removal of the latent heat of fusion. Conservation of energy applied to a control volume centered on the interface gives

$$K_s \frac{\partial T_s}{\partial x}(x = s,t) - K_\ell \frac{\partial T_\ell}{\partial x}(x = s,t) = \rho_s L \frac{ds}{dt} \qquad (8)$$

The left-hand side of equation (8) represents the net heat flux out of the control volume as calculated by the Fourier conduction law, which is equated to the rate of liberation of the heat of fusion.

The entire freezing field is assumed to be initially in a state of uniform cooling. That is

$$\frac{\partial T}{\partial t}(x,t = 0) = \text{constant} \qquad (9)$$

Using this condition in equation (1) with $j = \ell$, we obtain

$$T_\ell(x,t = 0) = T_i(C_o) - \frac{H}{K_\ell}x + \frac{H}{2K_\ell \ell}x^2 \qquad (10)$$

Equation (10) shows that an initially parabolic temperature distri-

---

Contributed by the Heat Transfer Divison for publication in the JOURNAL OF HEAT TRANSFER. Manuscript received by the Heat Transfer Division October 31, 1979.

Table 1 Summary of differential equations, initial and boundary conditions

	Solid Region	Liquid Region
heat transfer equations	$\alpha_s \frac{\partial^2 T_s}{\partial x^2} = \frac{\partial T_s}{\partial t}$	$\alpha_\ell \frac{\partial^2 T_\ell}{\partial x^2} = \frac{\partial T_\ell}{\partial t}$
mass transfer equations	$C = 0$	$D \frac{\partial^2 C}{\partial x'^2} + R \frac{\partial C}{\partial x'} = \frac{\partial C}{\partial t}$
boundary conditions	$K_s \frac{\partial T_s}{\partial x} (x = o,t) = -H$	$\frac{\partial T_\ell}{\partial x} (x = \ell,t) = 0$
	$T_s(x = s,t) = T_i(C_i)$	$T_\ell(x = s,t) = T_i(C_i)$
	---	$\frac{\partial C}{\partial x'} (x = \ell,t) = 0$
interface conditions	$K_s \frac{\partial T_s}{\partial x} (x = s,t) - K_\ell \frac{\partial T_\ell}{\partial x} (x = s,t) = \rho_s L \frac{ds}{dt}$	
	$D \frac{\partial C}{\partial x'} (x' = o,t) + RC\,(x' = o,t) = 0$	
	$T_i(C_i) = a' + b'C_i + c'C_i{}^2 + d'C_i{}^3$	
initial conditions	---	$C(x',t = o) = C_o$
	$T_s(x,t = o) = T_i(C_o)$	$T_\ell(x,t = o) = T_i(C_o) - \frac{H}{K_\ell}x + \frac{H}{2K_\ell \ell}x^2$
	$s(t = o) = 0$	

bution exists in the field and is a function of the imposed heat flux and the initial freezing temperature. The quantity $T_i(C_o)$ represents the freezing temperature at the initial solute concentration.

Kármán-Pohlhausen Heat Balance Integral

The heat conduction problem involving the change of phase of a binary alloy is nonlinear primarily because of the moving boundary condition and because of the interface temperature depression from the build-up of solute. One of the most useful techniques for solution of this type of problem is the heat balance integral developed originally by Pohlhausen [4] and Kármán [5] and modified by Goodman [9–11] and O'Callaghan [6], [12]. The method consists of assuming the spatial form of the temperature distribution (usually a power series) and solving an averaged form of the heat conduction equation, called the heat balance integral. The problem is reduced by this method to one of solving ordinary differential equations in time only. The assumed form of the temperature profiles is

$$T_s = a_s + b_s x + c_s x^2 \tag{11}$$

and

$$T_\ell = a_\ell + b_\ell x + c_\ell x^2. \tag{12}$$

With the boundary conditions listed in Table 1, these expressions become

$$T_s = T_i + \frac{H(s - x)}{K_s} - c_s(s^2 - x^2) \tag{13}$$

and

$$T_\ell = T_i + 2c_\ell \ell(s - x) - c_\ell(s^2 - x^2), \tag{14}$$

where c_s, c_ℓ and s are functions of time.

Consider two control volumes, fixed with respect to the laboratory reference frame, one containing the solid and the other containing the liquid. Conservation of energy for the control volumes becomes

$$H + K_s \frac{\partial T_s}{\partial x} (x = s,t) = \frac{K_s}{\alpha_s} \int_o^s \frac{\partial T_s(x,t)}{\partial t} dx \tag{15}$$

$$-K_\ell \frac{\partial T_\ell}{\partial x} (x = s,t) = \frac{K_\ell}{\alpha_\ell} \int_s^\ell \frac{\partial T_\ell\,(x,t)}{\partial t} dx \tag{16}$$

for the solid and liquid regions, respectively. These expressions represent the averaged energy equations discussed above. Using equations (13) and (14) in equations (15) and (16), we obtain after manipulation

Nomenclature

a = temperature constant (K)
a' = constant in freezing point equation (K)
b = linear temperature coefficient (K/m)
b' = linear coefficient in freezing point equation (K – m^3/mole)
c = parabolic temperature coefficient (K/m^2)
c' = quadratic coefficient in freezing point equation (K – m^6/mole^2)
C = concentration (moles/m^3)
d' = cubic coefficient in freezing point equation (K – m^9/mole^3)
D = diffusion coefficient of solute in solvent (m^2/s)
g = normalized thermal gradient at the interface (K/m)
G_c = concentration gradient at the interface (mole/m^4)
H = heat flux at $x = 0$ (W/m^2)
K = thermal conductivity (W/m – K)
ℓ = half width of slab (m)
L = latent heat of fusion (N – m/kg)
m = liquidus slope (K – m^3/mole)
R = interface speed (m/s)
s = interface position (m)
t = time (s)
T = temperature (K)
x = spatial coordinate (m)
x' = moving spatial coordinate (m)
α = thermal diffusivity (m^2/s)
ρ = density (g/m^3)

Subscripts

i = interface
ℓ = liquid region
o = initial condition
s = solid region

$$2\alpha_s c_s s = s\frac{dT_i}{dt} + \left(\frac{Hs}{K_s} - 2c_s s^2\right)\frac{ds}{dt} - \frac{2s^3}{3}\frac{dc_s}{dt} \tag{17}$$

and

$$2\alpha_\ell c_\ell(\ell - s) = (\ell - s)\frac{dT_i}{dt} + 2c_\ell(\ell - s)^2\frac{ds}{dt} - \frac{2(\ell - s)^3}{3}\frac{dc_\ell}{dt} \tag{18}$$

Finally, equations (13) and (14) are used in the moving boundary condition, equation (8), to obtain

$$\rho_s L\frac{ds}{dt} = -H + 2K_s c_s s + 2K_\ell c_\ell\,(\ell - s) \tag{19}$$

These are three ordinary differential equations in the four unknowns c_s, c_ℓ, s and T_i.

Interface Concentration and Temperature

If we assume that the characteristic length of the concentration profile is much less than the length of the liquid region $(\ell - s)$, then the slope of the profile will decrease to zero far from the plane of symmetry $(x = \ell)$. In this case the concentration boundary condition at $x = \ell$ listed in Table 1 will be equivalent to

$$C \to C_0 \text{ as } x' \to \infty \quad \text{for all } t. \tag{20}$$

The reader should note that equation (20) is not valid as the liquid layer becomes small (i.e. as $s \to \ell$). However, it will be shown that the planar interface becomes unstable long before the liquid layer becomes thin.

Equation (4) together with equations (5) and (20) has been solved by Smith, et al. [13] by the LaPlace Transform method. The interface concentration is given by

$$\frac{C_i - C_0}{C_0} = \operatorname{erf}\psi + 2\psi^2(1 + \operatorname{erf}\psi) + \frac{2\psi}{\sqrt{\pi}}e^{-\psi^2} \tag{21}$$

where $\psi = \frac{R}{2}\sqrt{\frac{t}{D}}$.

Since equilibrium has been assumed between solid and liquid at the interface, the interface temperature may be specified by equation (7) using the interface concentration as expressed by equation (21). To obtain an expression for dT_i/dt, the chain rule is used to give

$$\frac{dT_i}{dt} = \frac{dC_i}{dt}\frac{dT_i}{dC_i} \tag{22}$$

Using equation (21) we have

$$\frac{dT_i}{dt} = \frac{C_0 R^2}{2D}\left\{\frac{e^{-\psi}}{\psi\sqrt{\pi}} + (1 + \operatorname{erf}\psi)\right\}\{b'2c'C_i + 3d'C_i^2\}. \tag{23}$$

Stability of the Planar Interface

The original experimental study of the breakdown of a planar freeze front was done by Rutter and Chalmers [14]. They proposed a qualitative criterion which predicted instability whenever growth conditions produced a layer of constitutionally supercooled liquid. This theory was subsequently quantified by Tiller, et al. [15]. Unfortunately, the theoretical basis for the constitutional supercooling criterion is uncertain.

The recent theoretical analysis by Mullins and Sekerka [1–3] has become the definitive work on the stability of the planar interface. Their approach was to calculate the time dependence of the amplitude of a sinusoidal perturbation of infinitesimal initial amplitude introduced into the shape of the plane. Since an arbitrary infinitesimal perturbation may be reduced to sinusoidal Fourier components, and since all of the relevant equations are linear, the development of the perturbation is simply a superposition of the development of its components. Therefore, the interface is unstable if any sinusoidal wave grows and stable if none grows.

For the case of aqueous binary solutions where solute is completely rejected from the solid phase, the Mullins-Sekerka stability criterion is given by

$$(g_\ell + g_s) - mG_c > 0 \tag{24}$$

where

$$g_j = \frac{K_j}{K_s + K_\ell}\frac{dT_j}{dx}(x = s,t) \tag{25}$$

$$G_c = \frac{dC}{dx'}\,(x' = 0) \tag{26}$$

and

$$m = \frac{dT_i}{dC_i} = b' + 2c'C_i + 3d'C_i \tag{27}$$

The first term in the criterion arises from thermal gradients, is positive since g_ℓ, $g_s > 0$ and thus favors stability. The second term, representing the effect of solute accumulation on the equilibrium melting temperature is always negative since m and G_c always have the same sign, and favors instability. Overall instability of the interface occurs if there are *any* conditions for which the magnitude of the second term exceeds that of the first term, otherwise stability prevails.

The temperature gradients in the liquid and the solid are given by equations (13) and (14) together with the results of the simulations of equations (17–19) and (23). Making these substitutions, we have

$$g_s = \frac{K_s}{K_s + K_\ell}\left(2c_s s - \frac{H}{K_s}\right) \tag{28}$$

and

$$g_\ell = \frac{K_\ell}{K_s + K_\ell}\,(-2c_\ell(\ell - s)) \tag{29}$$

The concentration gradient is given by the interface boundary condition, equation (5),

$$G_c = \frac{R}{D}C_i. \tag{30}$$

where C_i is given in equation (21).

Results and Discussion

Equations (17–20) were simultaneously integrated using a fourth order Runge-Kutta integration routine to obtain c_s, c_ℓ, s and T_i as functions of time. The physical properties used in the simulation are those of an aqueous sodium chloride solution and are listed in Table 2. The free field concentration C_0, was assumed to be 145 moles/m^3 while several values of heat flux at $x = 0$ were used ranging from -300 to -15000 (W/m^2).

Table 2 Material properties for sodium chloride-water solution

Quantity	Symbol	Value
density of solid	ρ_s	912 kg/m^3
density of liquid	ρ_ℓ	998 kg/m^3
thermal conductivity of solid	K_s	$2.21\,\frac{\mathrm{N-m}}{\mathrm{s-m-K}}$
thermal conductivity of liquid	K_ℓ	$0.588\,\frac{\mathrm{N-m}}{\mathrm{s-m-k}}$
thermal diffusivity of solid	α_s	$1.26 \times 10^{-6}\,\frac{\mathrm{m}^2}{\mathrm{s}}$
thermal diffusivity of liquid	α_ℓ	$0.133 \times 10^{-6}\,\frac{\mathrm{m}^2}{\mathrm{s}}$
length of freezing field	ℓ	5×10^{-3} m
latent heat of fusion	L	$0.334\,\frac{\mathrm{MN-m}}{\mathrm{kg}}$
diffusion coefficient of NaCl in water	D	$1.29 \times 10^{-9}\,\frac{\mathrm{m}^2}{\mathrm{s}}$

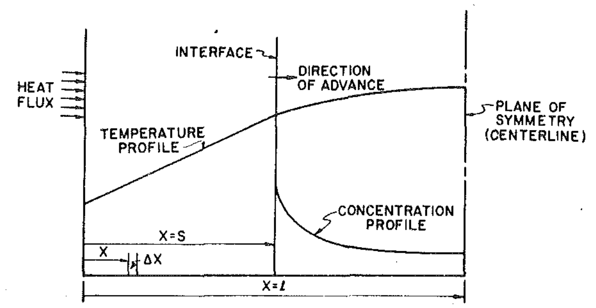

Fig. 1 Planar freezing geometry with representative temperature and concentration profiles

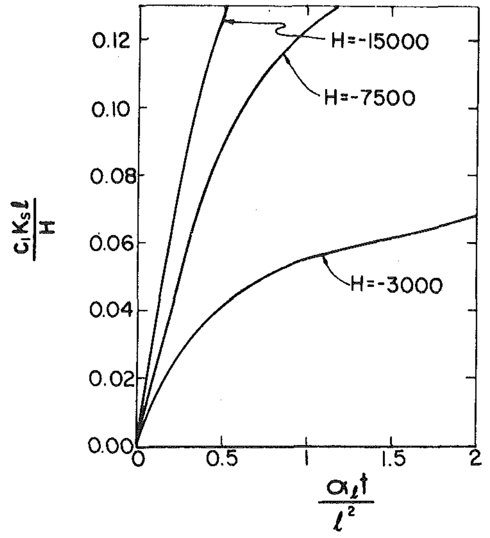

Fig. 2 Variation of the solid phase curvature parameter with time as a function of heat flux (W/m²)

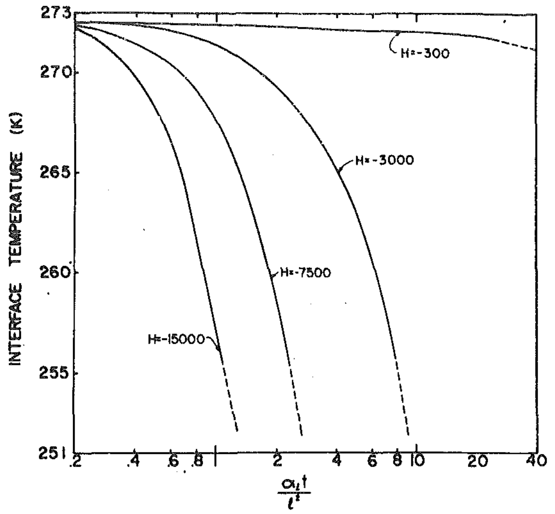

Fig. 3 Interface temperature profiles as a function of heat flux (W/m²). The dotted lines indicate the estimated extension of the curves beyond the simulation time.

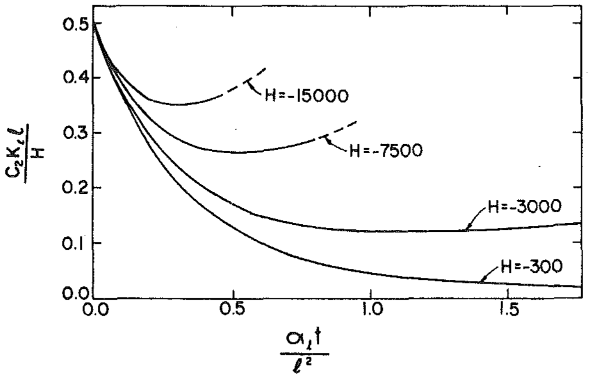

Fig. 4 Variation of liquid phase curvature parameter with time as a function of heat flux (W/m²)

As shown by equations (11) and (12), c_s and c_ℓ are the quadratic coefficients in the temperature profiles, and represent their spatial curvature. The coefficients also directly reflect the importance of thermal mass, since the profiles would have no curvature if the respective thermal mass, was zero. The dynamic variation of c_s is shown in Fig. 2. When the solidification process has just begun, the curvature in the solid region temperature profile should be small since there is little thermal mass. The liberation of the latent heat of fusion at $x = s$ requires a large heat flux in the solid and magnifies the importance of the growing thermal mass.

The depression of the interface temperature with time is shown in Fig. 3. Initially, the interface temperature is relatively constant, reflecting the slow rate of advance of the interface and the weak dependence of interface temperature on concentration at low solute levels. As the interface speed increases, the rate of solute build-up follows, and the dependence of interface temperature on concentration becomes stronger. These effects together produce a very rapid depression of the interface temperature. The sharp rise in the curvature of the solid region temperature profile (see Fig. 2) is due to this depression of the interface temperature and to the growing effect of thermal mass.

The liquid phase curvature parameter is plotted against time in Fig. 4. The initial decrease is due to the "flattening" of the temperature profile in the unfrozen liquid. During this phase, the interface temperature is relatively constant and the thermal energy remaining in the liquid is rapidly being removed. As the interface temperature is depressed, the temperature curvature in the liquid must increase slightly to maintain zero temperature gradient at $x = \ell$.

Interface position as a function of time is shown in Fig. 5. Except for a brief transient, the interface speed is constant, validating the pseudo-steady assumption made in solving the mass transfer problem. By far, the largest thermal load in the system is the liberation of the latent heat of fusion, so that sensible temperature changes in either the solid or the liquid region are energetically negligible.

The Mullins-Sekerka stability criterion may be evaluated by substituting the numerical values of c_s, c_ℓ, and s into equation (24) together with equations (7, 13) and (28–30). The results are plotted in Fig. 6. Since the interface initially has zero velocity, equations (23) and (30) indicate that it is also stable. However, when an appreciable interface velocity is attained, the stability function exceeds zero indicating that the planar interface is unstable.

Experiments on transparent organic liquids [16] show that as a planar interface becomes unstable, it initially becomes gently undulatory, as illustrated in Fig. 7. These perturbations or bumps are exposed to constitutionally supercooled liquid and tend to grow faster than the basal plane. The accelerated growth liberates additional heat which decreases the supercooling. Growth of the perturbations will continue until the supercooling has entirely vanished, resulting in stable, fully developed dendrites.

Conclusions

The stability of the planar freezing geometry was found to depend on the rate of freezing and the transport and thermodynamic properties of the particular solute under consideration.

The primary destabilizing factor in freezing aqueous systems is the complete rejection of solute from the solid phase, which produces a severe concentration gradient at the interface. Metals which form alloy solids exhibit a similar phenomenon; but the effect is less important since solute is incorporated into the solid material. Enhanced diffusion of the solute away from the interface would delay the onset of instability, but the maximum effect of this enhancement is limited. The stability analysis presented in this paper represents a "most

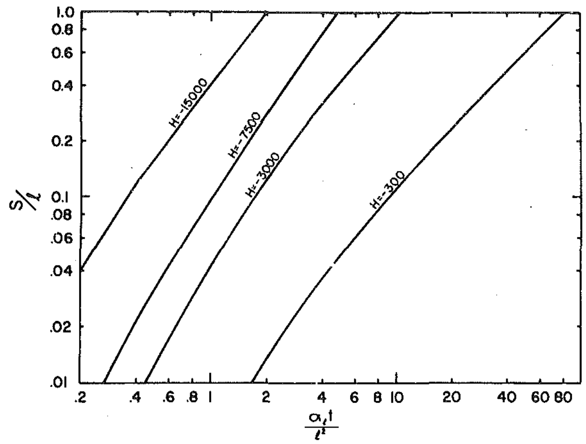

Fig. 5 Nondimensional interface position as a function of time

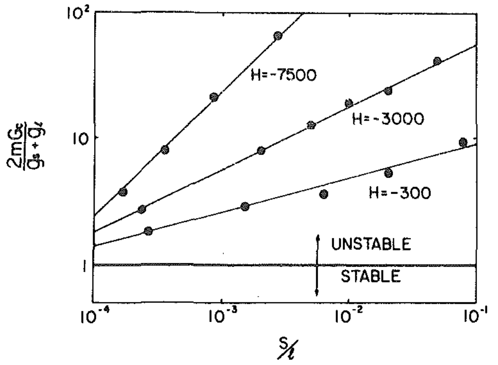

Fig. 6 Mullins-Sekerka stability function [1, 2] as a function of interface position. Solutions frozen under these conditions exhibit unstable planar interfaces.

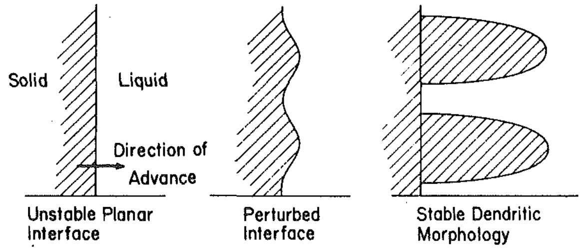

Fig. 7 Development of the stable dendritic morphology from a perturbed unstable planar interface

stable" aqueous system since the NaCl – H_8O diffusion coefficient is very large. Using a solute with a lower diffusion coefficient would make the interface substantially less stable.

The depression of the freezing temperature at the interface increases the heat flux in the liquid and therefore represents a stabilizing influence. A solute with a more severe freezing point depression curve would tend to have more stable planar morphology. However, from the severe instability shown in Fig. 6, it may be concluded that the effect of freezing point depression is negligible compared to the build-up of solute at the interface.

References

1 Mullins, W. W., and Sekerka, R. F., "Morphological Stability of a Particle Growing by Diffusion or Heat Flow," *Journal of Applied Physics,* Vol. 31, p. 323, 1963.

2 Mullins, W. W., and Sekerka, R. F., "Stability of a Planar Interface During Solidification of a Dilute Binary Alloy," *Journal of Applied Physics,* Vol. 35, p. 126, 1963.

3 Sekerka, R. F., "A Stability Function for Explicit Evaluation of the Mullins-Sekerka Interface Stability Criterion," *Journal of Applied Physics,* Vol. 36, p. 461, 1965.

4 Pohlhausen, K., "Zur naherungsweisen Integration der Differential gleichung der laminaren," *Zeitschrift fuer Angewandte Mathematik und Mechani,* Vol. 1, p. 252, 1921.

5 von Karman, T., "Uber laminare und terbulente Reibung," *Zeitschrift fuer Angewandte Mathematik und Mechani,* Vol. 1, p. 233, 1921.

6 O'Callaghan, M. G., "An Analysis of the Heat and Mass Transport During the Freezing of Biomaterials," Ph.D. Thesis, Department of Mechanical Engineering, Massachusetts Institute of Technology, Cambridge, Mass., Oct. 1978.

7 Rohsenow, W. M., Choi, H. Y., *Heat, Mass and Momentum Transfer,* Prentice-Hall, New Jersey, 1961.

8 Fabuss, B. M., *Thermodynamic Properties of Saline Water,* U.S. Office of Saline Water, Saline Water Research and Development Progress Report No. 136, July, 1965.

9 Goodman, T. R., "The Heat Balance Integral and Its Application to Problems Involving Change of Phase," ASME JOURNAL OF HEAT TRANSFER, Vol. 80, p. 335, 1958.

10 Goodman, T. R., "Application of Integral Methods to Transient Nonlinear Heat Transfer," *Advances in Heat Transfer,* Vol. 1, Irvine, T. F. and Hartnett, J. P., eds. 1964, p. 51.

11 Goodman, T. R., "The Heat Balance Integral-Further Considerations and Refinements," ASME JOURNAL OF HEAT TRANSFER, Vol. 83, p. 83, 1961.

12 O'Callaghan, M. G., Cravalho, E. G., and Huggins, C. E., "Instability of the Planar Interface During the Freezing of Biomaterials," *Cryobiology,* Vol. 15, p. 704, 1978 (abstract).

13 Smith, V. G., Tiller, W. A. and Rutter, J. W., "A Mathematical Analysis of Solute Redistribution During Freezing," *Canadian Journal of Physics,* Vol. 33, p. 723, 1956.

14 Rutter, J. W., and Chalmers, B., "Solute Redistribution during Planar Solidification," *Canadian Journal of Physics,* Vol. 31, p. 15, 1953.

15 Tiller, W. A., Rutter, J. W. Jackson, K. A. and Chalmers, B., "The Redistribution of Solute Atoms During the Solidification of Metals," *Acta Metallurgica,* Vol. 1, p. 428, 1953.

16 Flemings, M. C., *Solidification Processing,* McGraw-Hill, New York, 1974.

Shi-chune Yao
Associate Professor,
Mem. ASME

Anil Rane
Graduate Student.

Department of Mechanical Engineering,
Carnegie-Mellon University,
Pittsburgh, PA 15213

Heat Transfer of Laminar Mist Flow in Tubes

Convective heat transfer of laminar mist flow is analyzed for constant wall temperature and constant heat flux conditions, respectively. The diminishing of droplet size, the increasing of vapor velocity, and the dilution of droplet density along the tube are considered in the present study. Calculations are performed from the inlet of thermal entrance region to the final fully developed single phase flow of vapor at the far downstream. Nondimensional parameters influencing mist flow heat transfer are revealed and discussed. Fundamental heat transfer behavior of mist flow is studied and the results appear as an extension of our present understanding of single phase flow heat transfer.

Introduction

The heat transfer of single phase flow in tubes has been studied extensively [1]. However, the heat transfer of droplet flow in tubes has not been analyzed adequately in the past due to its complicated nature. Droplet flow heat transfer usually occurs at high void fraction and finds wide application in process and energy industries. The vapor is superheated by the hot wall; however, the droplets are generally at the saturation condition. Since the two phase mixture is at thermally nonequilibrium state, the droplets evaporate and generate saturated vapor into the stream.

Limited analytical work has been performed for droplet flow heat transfer. Since the void fraction of droplet flow is high, a general approach was proposed to consider the vapor phase energy balance by regarding the effect of droplets as equivalent heat sink distributed in the vapor. Sun, et al. [2], calculated fully developed laminar droplet flow heat transfer by assuming a zero axial temperature gradient of the vapor. Dix and Andersen [3] further analyzed this result for parabolic velocity profile. The application of these fully developed heat transfer results to the entire length of tube is questionable, because the behavior of entrance region is unknown for droplet flow. Therefore, Yao [4] investigated the convective heat transfer of laminar droplet flow in thermal entrance region of circular tubes considering constant droplet number density and constant droplet size near the tube entrance.

In the special case of low pressure systems, the vapor density is much lower than the liquid density and the latent heat of evaporation is very high. The evaporation of droplets will generate vapor but with insignificant change in droplet size. Therefore, the heat sink effect of the droplets declines along the tube length mainly due to the dilution of droplet number density. This problem of laminar droplet flow heat transfer in tubes at low system pressure with constant droplet size and varying droplet number density has been studied by Rane and Yao [5].

At high system pressures, or in a very long heated tube, the droplet size will diminish substantially in the tube. Eventually all the droplets evaporate and disappear from the stream. Therefore, the droplet flow heat transfer becomes an extrance problem with the fully developed heat transfer equal to that of pure vapor flow, where all the droplets evaporate completely. The diminishing of droplet size is especially pronounced if a mist flow is considered because of the large surface-to-volume ratio of the very small droplets. The objective of this paper is to study the heat transfer behavior of laminar flow at these kinds of realistic conditions.

Model

In droplet flow, heat transfer occurs between wall and vapor, wall and droplet, vapor and droplet, in addition to the thermal radiation. In this study, post dry-out condition is analyzed, where the wall temperature is higher than the Leidenfrost temperature of the droplets. It is generally known that at pool film boiling, the conductive heat transfer between the liquid and wall is insignificant as compared to the vapor convective heat transfer [6]. More specifically, McCanthy (Kendall) [7] observed that the droplet-wall contact heat transfer is negligible when the wall temperature is above the Leidenfrost temperature. Therefore, the direct conductive heat transfer during wall and droplet contacts can be neglected in this study.

For many liquids, the Leidenfrost temperature is not very high so that the contribution of thermal radiation can be neglected at the post dry-out conditions. Using an order of magnitude analysis [4], the radiative heat transfer can be neglected with respect to the convective heat transfer if

$$\frac{r_0(T_w - T_s)}{2\epsilon_\ell \sigma (T_w{}^4 - T_s{}^4)} \gg 1 \tag{1}$$

By neglecting the droplet-wall contact heat transfer and the thermal radiation, only the wall to vapor and vapor to droplet heat transfer will be considered in the analysis.

For simplicity, at the inlet of thermal entrance, all the droplets are assumed to have the same size. At laminar flow, droplets may move radially due to the presence of radial temperature or velocity gradients [8]. A droplet will be pushed away from the wall due to its nonuniform evaporation near the wall. A rotating droplet will move either toward or away from the wall depending on the relative velocity between the droplet and surrounding vapor. These radial mixings make each droplet evaporate at approximately the same rate. Therefore, the size of droplets is uniform at any tube cross section but varies along the tube.

In this paper, the thermal entrance heat transfer of droplet flow is studied. It is known that the vapor velocity profiles are parabolic at both the inlet of this region and at its fully developed condition of single phase flow where all droplets evaporate completely. At the middle part of thermal entrance the vapor velocity may deviate from parabolic profile with a steeper gradient at the hot wall due to the stronger evaporation of droplets locally. In order to justify the assumption of parabolic velocity profile for the whole region, a calculation was performed for comparison by using a bi-linear velocity profile with the gradient at the wall twice the value of the parabolic profile. The result of this comparison shows local heat transfer at the middle part of the thermal entrance with only 7 percent difference. Therefore it was decided that detailed calculation using coupled mass, momentum, and energy equations considering refined local velocity profiles will not be performed in the present study.

Additional conditions can be assumed to further simplify the model. As discussed in reference [9], when the flow quality is higher than 0.5, the momentum of small droplets gives negligible influence to the vapor velocity profile. When the chemical composition of the vapor and the droplet are identical, mass transfer due to concentration difference does not occur. When droplet size is assumed to be small, for example considering the mist, the drag of vapor dominates the motion of the droplets. As shown in the Appendix, the heat transfer between a droplet and vapor will be determined by conduction due to the low droplet Reynolds number at this condition.

Contributed by The Heat Transfer Division for publication in the JOURNAL OF HEAT TRANSFER. Manuscript received by the Heat Transfer Division September 19, 1979.

Practically, the vapor temperature increases along the tube, therefore, the vapor properties vary along the stream. The gas heat transfer at laminar thermal entrance with variation of physical properties has been studied by Worsoe-Schmidt and Leppert [10] for constant wall flux and constant wall temperature conditions using implicit finite difference scheme. Slight variations of Nusselt numbers from the result of constant-property condition are observed; however, the difference is much less in magnitude than the variation of mist flow Nusselt numbers due to droplet heat sink effect, as illustrated in the later part of this paper. Therefore, constant vapor properties is assumed in this study as a first approach.

In summary, the important assumptions used in the present analysis are

1 negligible droplet-wall contact heat transfer
2 negligible thermal radiative heat transfer,
3 uniform droplet size at tube inlet, droplet size varying axially,
4 high flow quality (>0.5), constant fluid properties, and parabolic velocity profile, and
5 conductive heat transfer between vapor and the small droplets.

The schematic of droplet flow heat transfer is shown in Fig. 1.

Studies have been performed for the droplet flow heat transfer with abundant experimental data available. However, most of these experiments did not report important information in detail such that these data can not be used to validate our analysis. For example, the droplet size spectrum is seldom measured. Some studies contain droplet size information [11, 12]; but these tests are for turbulent flow. As a result, there is no appropriate experimental data on laminar droplet flow heat transfer which is complete enough for us to compare with the results of the present analysis.

Formulation

The presence of droplets in the superheated vapor behave as heat sinks. Heat is transferred from the superheated vapor to the saturated droplets, and the subsequently generated vapor is heated up to the vapor stream temperature. The equivalent heat sink per unit volume becomes

$$n\pi d^2 h_d (T - T_s) + n\pi d^2 h_d (T - T_s) C_p (T - T_s)/h_{fg} \qquad (2)$$

where the h_d is the heat transfer coefficient from superheated vapor to a saturated droplet. It has been reported that the evaporation at the droplet surface will reduce the heat transfer coefficient as compared to an equivalent nonevaporating droplet or solid sphere [13]. The relationship is

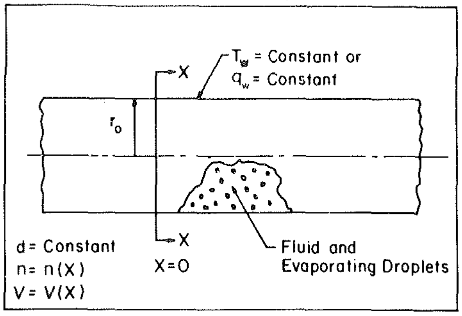

Fig. 1 Schematic of mist flow heat transfer in tubes

$$h_d = h_p/(1 + C_p(T - T_s)/h_{fg}) \qquad (3)$$

where h_p is the heat trasnfer coefficient of a solid sphere which is not at evaporating condition. Combining (2) and (3) the heat sink term can be represented in a simple form as

$$n\pi d^2 h_p (T - T_s) \qquad (4)$$

In this study, the heat transfer in thermal entrance region of a tube is considered. With the heat sink described in equation (4) and the parabolic velocity profile, the energy equation for the vapor phase can be written as

$$2\rho_v C_p V\left(1 - \left(\frac{r}{r_0}\right)^2\right)\frac{\partial T}{\partial x} = \frac{k}{r}\frac{\partial}{\partial r}\left(r\frac{\partial T}{\partial r}\right) - n\pi d^2 h_p (T - T_s) \qquad (5)$$

The initial condition and boundary conditions are

$$T = T_s \text{ at } x = 0 \qquad (6)$$

$$\frac{\partial T}{\partial r} = 0 \text{ at } r = 0 \qquad (7)$$

and

$$T = T_w \text{ at } r = r_0 \qquad (8)$$

for constant wall temperature condition, or

$$k\frac{\partial T}{\partial r} = q_w \text{ at } r = r_0 \qquad (9)$$

for constant wall heat flux condition. In this equation the mean vapor velocity V will vary along the stream due to the vapor generation from droplets.

Nomenclature

A = liquid loading parameter, defined in equation (34)
C = wall superheat parameter defined in equations (36, 37)
C_p = specific heat of vapor
d_0 = droplet diameter at thermal entrance
d = droplet diameter or differential notation
D = nondimensional droplet parameter, defined in equation (19)
Fr = Fraude number defined in equation (A-14)
h_{fg} = latent heat of evaporation
h_d = heat transfer coefficient for evaporating droplets defined in equation (3)
h_p = heat transfer coefficient of nonevaporating droplet or sphere
k = thermal conductivity of vapor
n = droplet number density
n_0 = droplet number density at thermal entrance
Nu_x = local Nusselt number defined by equations (40, 41)
Pr = Prandtl number of vapor
q_w = heat flux at the wall
R = nondimensional radial position (r/r_0)
Re = Reynolds number for vapor based on tube diameter and mean vapor velocity at thermal entrance
Re_d = droplet Reynolds number based on droplet size and its velocity relative to vapor
Re′ = Reynolds number defined in equation (A-13)
r = radial position
r_0 = radius of circular tube
S = heat sink parameter defined in equation (35)
t = time
T = temperature of vapor
T_m = bulk mean temperature of vapor
T_s = saturation temperature
T_w = wall temperature
U = mean droplet velocity
V = mean vapor velocity
V_0 = mean vapor velocity at the inlet of thermal entrance
x = axial position in thermal entrance region
X = nondimensional axial position
θ = nondimensional vapor temperature
θ_m = nondimensional bulk mean temperature
ϵ_ℓ = droplet emissivity
σ = Stefan-Boltzmann Constant for thermal radiation
ρ_ℓ = liquid density
ρ_v = vapor density
λ = the parameter defined in equation (A-10)
μ = dynamic viscosity of vapor
β = reciprocal time constant defined in equation (A-5)
α_0 = void fraction of vapor at thermal entrance
ν = kinematic viscosity of vapor

At steady-state, the number of droplets passing through any tube cross-section is equal to the value at the tube inlet. Hence, the local mean vapor velocity can be related to the local droplet number density by assuming same velocity for droplets and vapor. That gives

$$Vn = V_0 n_0 \tag{10}$$

The variation of droplet number density can be related to the change of droplet size as

$$\rho_\ell n \pi d^2 \frac{1}{2} dd = -\rho_v \frac{dV}{V} \tag{11}$$

$$= -\rho_v \frac{dn}{n} \tag{12}$$

with the initial condition

$$n = n_0 \text{ when } d = d_0 \tag{13}$$

at the inlet of tube. Therefore the droplet density is presented in terms of droplet size as

$$\frac{1}{n} = \frac{1}{n_0} + \frac{\pi}{6} \left\{\frac{\rho_l}{\rho_v}\right\} \{d_0^3 - d^3\} \tag{14}$$

Finally, the change of droplet size can be related to the evaporation of the droplet by assuming the droplets travel at the same velocity as the vapor. That is

$$\pi d^2 h_d (T_m - T_s) = -\frac{1}{2} \rho_\ell h_{fg} \pi d^2 \frac{dd}{dt} \tag{15}$$

$$= -\frac{1}{2} \rho_\ell h_{fg} \pi d^2 \frac{dd}{dx} V \tag{16}$$

with the initial condition

$$d = d_0 \text{ at } x = 0 \tag{17}$$

where T_m is used for the heat transfer to an averaged droplet. Approximation was made here that the droplet velocity is very close to the vapor velocity when droplets are small. The bulk mean temperature is defined as

$$T_m = \frac{4}{r_0^2} \int_0^{r_0} T \left(1 - \left(\frac{r}{r_0}\right)^2\right) r dr \tag{18}$$

With equations (10, 14) and (16), equation (5) is able to consider the variations of mean vapor velocity and droplet density along the tube length. This set of equations can be nondimensionalized and presented in terms of

$$D = (d/d_0) \tag{19}$$

$$R = (r/r_0) \tag{20}$$

$$X = (x/r_0)/(\text{Re Pr}), \text{ and} \tag{21}$$

$$\theta = (T - T_s)/(T_w - T_s) \tag{22}$$

for constant wall temperature condition, or

$$\theta = k(T - T_s)/(q_w r_0) \tag{23}$$

for constant wall heat flux condition,
where

$$\text{Re} = 2\rho_v V_0 r_0 / \mu \tag{24}$$

and

$$\text{Pr} = \mu C_p / k. \tag{25}$$

The resulting energy equation for vapor is

$$[1 + A(1 - D^3)][1 - R^2] \frac{\partial \theta}{\partial X} = \frac{1}{R} \frac{\partial}{\partial R}\left(R \frac{\partial \theta}{\partial R}\right) - S \left(\frac{D}{(1 + A(1 - D^3))}\right) \theta \tag{26}$$

with initial and boundary conditions

$$\theta = 0 \text{ at } X = 0 \tag{27}$$

$$\frac{\partial \theta}{\partial R} = 0 \text{ at } R = 0 \tag{28}$$

and

$$\theta = 1 \text{ (constant } T_w\text{) at } R = 1 \tag{29}$$

or

$$\frac{\partial \theta}{\partial R} = 1 \text{ (constant } q_w\text{) at } R = 1 \tag{30}$$

where the nondimensional droplet size D is determined from equations (16) and (3)

$$D(1 + A(1 - D^3)) \frac{dD}{dX} = -\frac{2}{3} \frac{S}{A} \left(\frac{\theta_m}{C^{-1} + \theta_m}\right) \tag{31}$$

with initial condition

$$D = 1 \text{ at } X = 0 \tag{32}$$

The bulk mean temperature of vapor is defined as

$$\theta_m = 4 \int_0^1 \theta (1 - R^2) R dR \tag{33}$$

In these governing equations, three important nondimensional parameters which influence the mist flow heat transfer are identified. They are the liquid loading parameter

$$A = \frac{\pi}{6} (n_0 d_0^3) \frac{\rho_\ell}{\rho_v} \tag{34}$$

the heat sink parameter

$$S = n_0 \pi d_0^2 h_{p0} r_0^2 / k \tag{35}$$

and the wall superheat parameter which is

$$C = C_p (T_w - T_s) / h_{fg} \tag{36}$$

for constant wall temperature conditions, and

$$C = C_p q_w r_0 / k h_{fg} \tag{37}$$

for constant wall heat flux conditions. All these parameters are based upon the inlet condition of the mist flow.

Calculations

Finite difference method is used to solve equations (26–33) numerically. Marching technique is employed with a modified form of semi-implicite method. Gauss elimination method is used to solve the matrix. All the variables are in double precision to reduce truncation error. Axial increment of X is set to 0.0001. The radial increment of R is selected as 0.025. The local Nusselt number obtained from single phase calculations (i.e., $S = 0.00$) are compared with the solution of Graetz problem [14] with satisfactory agreement showing the difference within 0.5 percent in all the range of study.

Results and Discussion

The liquid loading parameter A can be related to the local void fraction of the two phase flow as

$$A = \frac{\rho_\ell}{\rho_v} (1 - \alpha) \tag{38}$$

With this, the heat sink parameter S can be arranged in the form of

$$S = 6A \left(\frac{\rho_v}{\rho_\ell}\right) \left(\frac{h_p d_0}{k}\right) \left(\frac{r_0^2}{d_0^2}\right) \tag{39}$$

where the $h_p d_0 / k$ is the droplet Nusselt number with respect to the vapor. In mist flow this Nusselt number is close to 2.0 as shown in the Appendix. Therefore, for a given liquid loading A, the value of S is inversely proportional to the surface area of a droplet. In other words, the heat sink parameter S denotes the degree of dispersion of the liquid in the mist flow.

Constant Wall Temperature. Due to the evaporation of the droplets, the vapor velocity increases along the tube. Figure 2 shows the variation of vapor velocity with the axial locations. The stronger the heat sink effect the faster the droplets evaporate, and therefore the more the vapor velocity increases along the tube. Eventually, all the droplets are evaporated and the flow becomes single phase vapor flow. The final vapor velocity is dependent upon the initial liquid loading A as indicated in Fig. 2. For example, the maximum liquid loading considered in this study is 1.0. The corresponding final single phase vapor Reynolds number becomes twice its inlet value when all the liquid is evaporated.

The local Nusselt number of mist flow is defined as

$$\mathrm{Nu}_x = \frac{q_w 2r_0}{(T_w - T_m)k} = \frac{2}{1-\theta_m}\left.\frac{\partial\theta}{\partial R}\right|_{R=1} \tag{40}$$

which are presented as a function of X in Fig. 3 for S equals 15 and 100, and in Fig. 4 for S equals 60 and 200 with the liquid loading as a parameter.

Figures 3 and 4 indicate that the magnitude of Nusselt number is sensitive to the variation of the heat sink parameter S. Large value of S means strong heat sink and gives high heat transfer rate from the wall. For the extreme condition of single phase vapor flow, the heat sink parameter S equals zero. The present calculations give the same single phase results as obtained by Kays [1]. At far downstream of any droplet flow, all the droplets are evaporated completely at the location indicated by the dashed line in Figs. 3 and 4. Beyond this point, the flow is single phase; however, it will take additional distance to develop its temperature profile fully. Eventually, the fully developed Nusselt number for laminar single phase flow, 3.66, is reached. This means that the mist flow heat transfer is essentially a generalized entrance phenomenon of vapor flow heat transfer.

In equation (35), when the value of heat sink parameter S is fixed the total surface area of droplets is fixed. Then the equation (39) indicates that at the given value of S, a large value of A implies the droplet size is large in the stream. As indicated in Figs. 3 and 4, the mist flow with a same value of S but large value of A travels far before all the droplets are completely evaporated. On the other hand, for a given liquid loading parameter A, a small value of S implies large droplets which travel far before they are evaporated completely.

The mean vapor temperature increases along the axial direction. The variation of the non-dimensional mean vapor temperature θ_m is shown in Fig. 5 for S equals 15 and 100, and in Fig. 6 for S equals 60 and 200. When the value of heat sink parameter S is high, the thermal shielding effect of the droplets to the heat transfer from wall is strong. Hence, the mean vapor temperature increases at a slow rate along the tube. Eventually, all the droplets disappear far downstream. The bulk mean vapor temperature approaches the wall temperature asymptotically in all the cases.

With the Nu_x and θ_m known, the wall heat flux can be evaluated from equation (40) where the $(T_w - T_s)$ can be evaluated from $(T_w - T_m)(1 - \theta_m)$.

Constant Heat Flux. The local Nusselt number for mist flow at constant wall heat flux condition is defined as

$$\mathrm{Nu}_x = \frac{q_w 2r_0}{(T_w - T_m)k} = \frac{2}{\theta_w - \theta_m}, \tag{41}$$

where the θ is defined in equation (23). The Nu_x is presented in Fig.

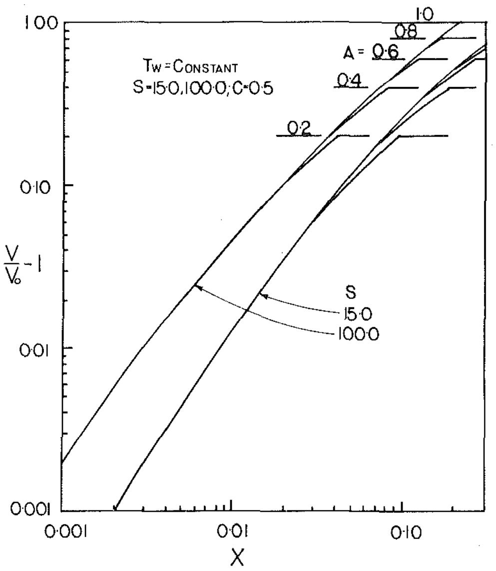

Fig. 2 **The variation of mean vapor velocity with axial locations at constant wall temperature conditions**

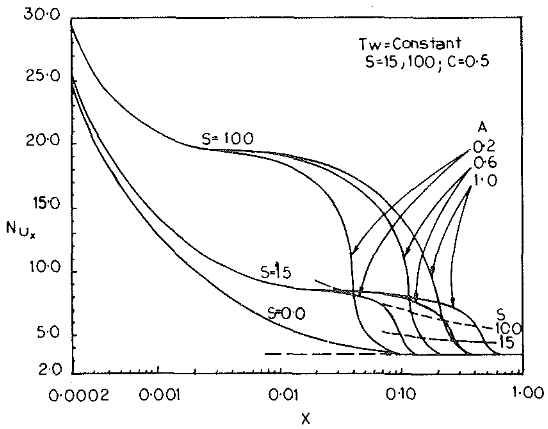

Fig. 3 **The variation of local Nusselt number with axial locations for S = 15, 100 at constant wall temperatures**

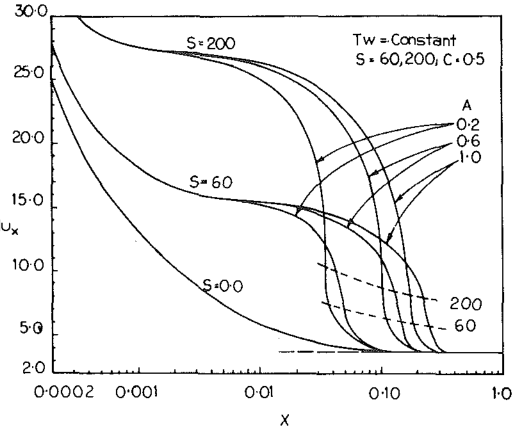

Fig. 4 **The variation of local Nusselt number with axial locations for S = 60, 200 at constant wall temperature**

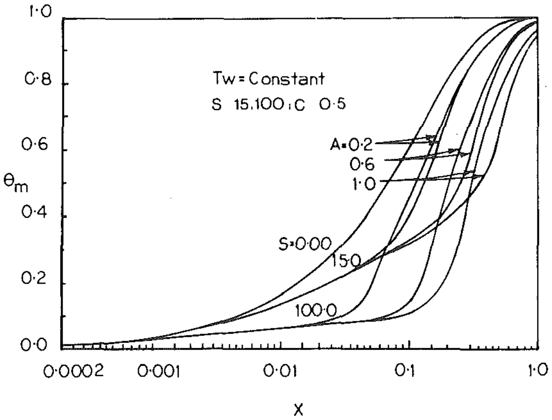

Fig. 5 **The variation of mean vapor temperature with axial locations for S = 15, 100 at constant wall temperature**

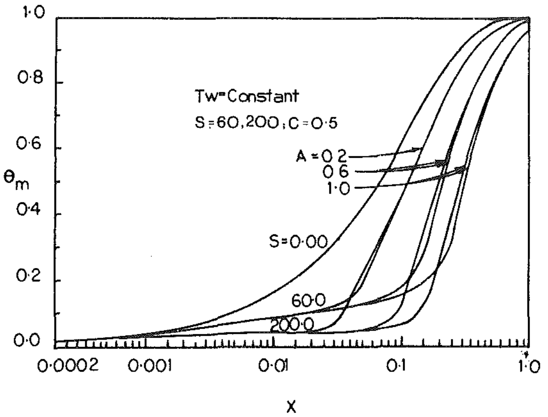

Fig. 6 The variation of mean vapor temperature with axial locations for $S = 60, 200$ at constant wall temperature

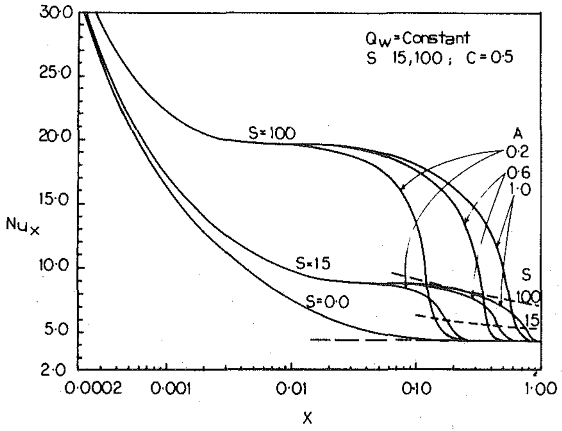

Fig. 7 The variation of local Nusselt number with axial locations for $S = 15, 100$ at constant wall fluxes

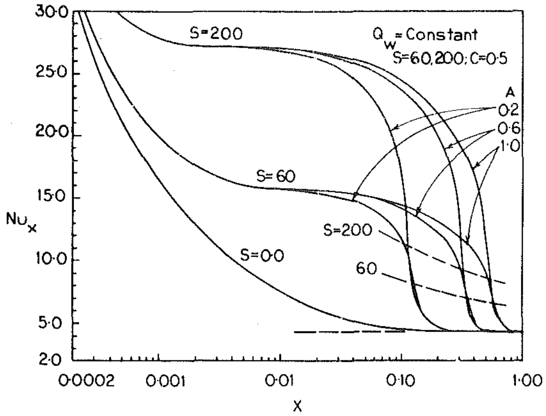

Fig. 8 The variation of local Nusselt number with axial locations for $S = 60, 200$ at constant wall fluxes

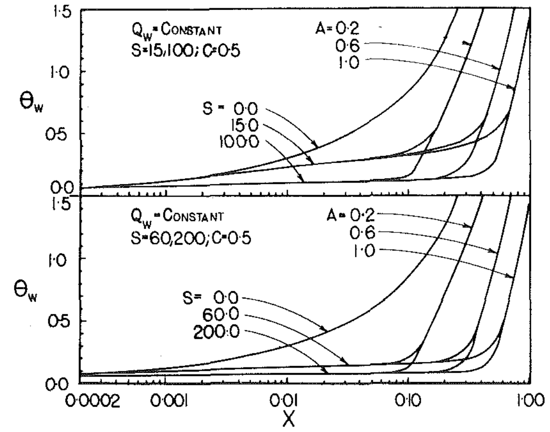

Fig. 9 The variation of wall temperature with axial locations at constant heat flux conditions

7 as a function of X for S equals 15 and 100, and in Fig. 8 for S equals 60 and 200. Generally, the same trend of variation as that of Figs. 3 and 4 are observed. However, the Nusselt number for constant flux case is always higher than the Nusselt number for constant wall temperature case at the same inlet condition. Similarly, the mist flow eventually changes into single phase vapor flow with a fully developed Nusselt number 4.36, which agrees well with the result of single phase laminar flow. Like the constant wall temperature condition, when the S value is fixed the mist flow travels far for large values of A, which means the same total droplet surface area but large droplet size in the flow.

For the same liquid loading parameter A, the flow with larger droplets will have smaller S due to the less number of droplets. The larger droplets contain more liquid and therefore tend to take a longer distance to evaporate completely. On the other hand, this flow with large droplets will have less capability to cool the vapor. Subsequently, higher mean vapor temperature will be observed, which tend to evaporate the droplets faster. At constant wall temperature conditions, the increase of mean vapor temperature has a limit which is the wall temperature. However, in constant wall heat flux condition the mean vapor temperature may increase, bascially, without bound. The location where all the droplets evaporate completely is determined based on these two competing effects.

For constant heat flux condition the variation of wall temperature along the axial location X is shown in Fig. 9 for various S values. It indicates that the smaller the value of S, the faster the wall temperature increases. After all the droplets disappear, the wall temperature increases very rapidly like the single phase vapor heat transfer.

The effect of wall superheat parameter C on the local Nusselt number Nu_x is shown in Fig. 10. The dashed curves are for constant wall heat flux condition and the solid curves are for constant wall temperature condition. It appears from the figure that for high values of C the droplets evaporate fast and the local heat transfer reduces quickly along the stream.

Finally, the variation of normalized droplet diameter D, along the axial location X, is shown in Fig. 11 for S equals 15 and 100 at constant heat flux condition. Generally, the droplet size reduces at a very fast rate when its size is getting smaller. This is because the surface to volume ratio of a droplet increases rapidly as its size reduces. It is also interesting to compare the curves with same A but different S. The curve of smaller S shows slower reduction of the normalized droplet size.

Conclusion

The laminar mist flow heat transfer in tubes is strongly dependent upon the liquid loading parameter A, the heat sink parameter S, and the super-heat parameter C. In the present study, the fundamental heat transfer beahavior of laminar mist flow at constant wall temperature and constant wall flux conditions is revealed. The classical laminar vapor flow heat transfer turns out to be a special case of the laminar mist flow heat transfer phenomenon.

References

1 Kays, W. M., *Convective Heat and Mass Transfer*, McGraw-Hill, 1966.

2 Sun, K. H., Gonzalez-Santalo J. M., and Tien, C. L., "Calculations of Combined Radiation and Convective Heat Transfer in Rod Bundles Under Emergency Cooling Conditions," ASME JOURNAL OF HEAT TRANSFER, Vol. 98, 1976, pp. 414–420.

3 Dix, G. E. and Andersen, J. G. M., "Spray Cooling Heat Transfer for a BWR Fuel Bundle," *Thermal and Hydraulic Aspects of Nuclear Reactor Safety*, Vol. 1, *Light Water Reactor*, Edited by O. C. Jones and S. G. Bankoff, ASME, 1977, p. 236.

4 Yao, S. C., "Convective Heat Transfer of Laminar Droplet Flow in Thermal Entrance Region of Circular Tubes," ASME JOURNAL OF HEAT TRANSFER, Vol. 101, No. 3, 1979, pp. 480–483.

5 Rane, A. and Yao, S. C., "Heat Transfer of Evaporating Droplet Flow in Low Pressure Systems," ASME Paper No. 79-WA/HT-10.

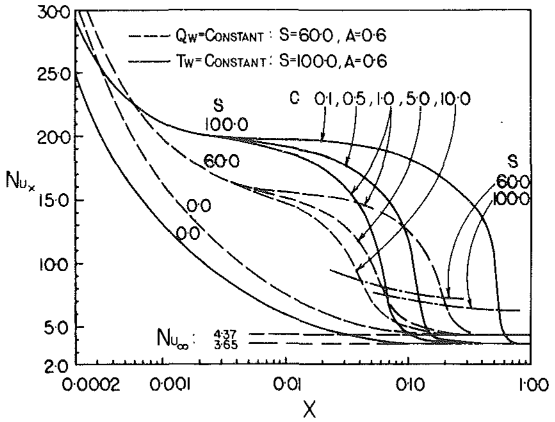

Fig. 10 The variation of local Nusselt number with superheat parameter *C*

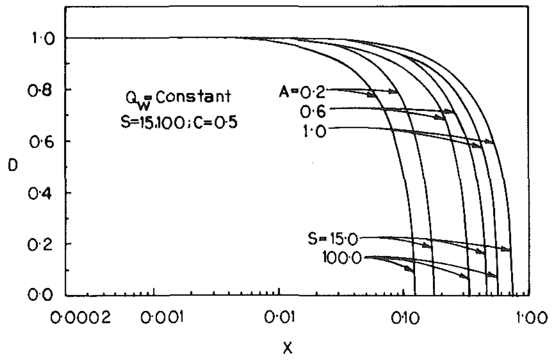

Fig. 11 The variation of droplet diameter with axial locations at constant heat flux conditions

6 Yao, S. C. and Henry, R. E., "An Investigation of the Minimum Film Boiling Temperature on Horizontal Surfaces," ASME JOURNAL OF HEAT TRANSFER, Vol. 100, 1978, pp. 260–267.

7 Kendall, G. E., "Heat Transfer to Impacting Drops and Post Critical Heat Flux Dispersed Flow," Ph.D. Thesis, MIT, 1978.

8 Ganic, E. N. and Rohsenow, W. M., "On the Mechanism of Liquid Drop Deposition in Two-Phase Flow," ASME JOURNAL OF HEAT TRANSFER, Vol. 101, 1979, pp. 288–294.

9 Tien, C. L., "Heat Transfer by Turbulent Flowing Fluid-Solid Mixture in a Pipe," ASME JOURNAL OF HEAT TRANSFER, May 1961, pp. 183–188.

10 Worsoe-Schmidt, P. M. and Leppert, G., "Heat Transfer and Friction for Laminar Flow of Gas in a Circular Tube at High Heating Rate," *International Journal of Heat Mass Transfer,* Vol. 8, 1965, pp. 1281–1301.

11 Forslund, R. P. and W. M. Rohsenow, "Dispersed Flow Film Boiling," ASME JOURNAL OF HEAT TRANSFER, Nov. 1968, pp. 399–407.

12 Koizumi, Y. and Ueda, T., "Post Dryout Heat Transfer to R-113 Upward Flow in a Vertical Tube," *International Journal of Heat Mass Transfer,* Vol. 22, 1979, pp. 669–678.

13 Yuen, M. C. and Chen, L. W., "Heat Transfer Measurements of Evaporating Liquid Droplets," *International Journal of Heat Mass Transfer,* Vol. 21, 1978, pp. 537–542.

14 Lipkis, R., discussion of "Numerical Solutions for Laminar-Flow Heat Transfer in Circular Tubes," by W. Kays, Trans. ASME, Nov. 1955, p. 1272.

15 Ranz, W. and Marshall, Jr., W., "Evaporation From Drops," *Chemical Engineering Progress,* Vol. 48, 1952, pp. 141–146, 137–180.

16 Habib, I. S., "The Interaction of a Hot Gas Flow and a Cold Spray in Channels," ASME JOURNAL OF HEAT TRANSFER, Vol. 98, 1976, pp. 421–426.

APPENDIX

The Heat Transfer Coefficient of Mist Droplets

The convective heat transfer coefficient of droplets in mist flow is [15]

$$\frac{h_p d}{k} = 2.0 + 0.6\mathrm{Re}_d^{1/2}\mathrm{Pr}^{1/3} \qquad \text{(A-1)}$$

Since the size of the droplet is small, equation (A-1) may be approximated by

$$\frac{h_p d}{k} = 2.0 \qquad \text{(A-2)}$$

The criterion for the validity of this simplification in an upflowing accelerating mist flow is derived in this Appendix.

Equation (A-2) is accurate if the second term at the right side of (A-1) is much smaller than the first term. Since the Pr of most vapor is close to 1, that gives

$$\mathrm{Re}_d = \frac{\rho_v (V-U)d}{\mu} \ll \frac{100}{9} \qquad \text{(A-3)}$$

The Re_d is evaluated from the relative velocity between the droplet and vapor which can be described by the motion equation of droplet. As indicated in (A-3), only the limiting condition is of concern; the droplet size at inlet can be used as a characteristic representation in the motion equation. That gives

$$\frac{dU}{dt} = \beta(U - V) - g \qquad \text{(A-4)}$$

where

$$\beta = 18\mu/\rho_\ell d_0^2 \qquad \text{(A-5)}$$

is derived from Stokes drag for small droplets at small Re_d. Equation (A-4) is for vertical upward mist flow with very low vapor density. Equation (A-4) can be written in terms of the relative velocity $(U - V)$ by adding the term dV/dt to both sides of the equation.

$$\frac{d}{dt}(V - U) = -\alpha(V - U) + g + \frac{dV}{dt} \qquad \text{(A-6)}$$

The maximum of the relative velocity happens when $d(V - U)/dt$ equals zero. Setting equation (A-6) to zero, the maximum relative velocity can be evaluated in terms of dV/dt which is to be found. Therefore, the criterion (A-3) becomes

$$\frac{dg}{\nu\alpha} + \frac{d}{\nu\alpha}\frac{dV}{dt} \ll \frac{100}{9} \qquad \text{(A-7)}$$

where dV/dt is to be evaluated.

The vapor velocity V can be related to the droplet size in the evaporating mist flow. From equations (10) and(14) the vapor velocity is

$$\frac{V}{V_0} = 1 + A(1 - D^3) \qquad \text{(A-8)}$$

where the nondimensional droplet size D varies along with time, which can be evaluated from the energy balance of a droplet. That gives [5]

$$D^2 = 1 - 2\lambda t/d_0^2 \qquad \text{(A-9)}$$

where

$$\lambda = \left(\frac{k}{\rho C_p}\right)\frac{C}{1 + 0.5C} \qquad \text{(A-10)}$$

Equation (A-9) is in a similar form to the parabolic profile. The same assumption found in reference [16] is used in the derivation. From equations (A-8) and (A-10), we obtain

$$\frac{dV}{dt} = 3ADV_0\frac{\lambda}{d_0^2} \qquad \text{(A-11)}$$

Substituting equation (A-11) into equation (A-7) with the approximation using d_0 for d at the location of maximum relative velocity, the criterion for the validity of equation (A-2) becomes

$$\left(\frac{\mathrm{Re}'}{\mathrm{Fr}}\right)\left(\frac{\rho_\ell}{\rho_v}\right) + \left(\frac{\mathrm{Re}'}{\mathrm{Pr}}\right)\left(\frac{3AC}{1 + 0.5C}\right) \ll 200 \qquad \text{(A-12)}$$

where

$$\mathrm{Re}' = V_0 d_0/\nu \qquad \text{(A-13)}$$

$$\mathrm{Fr} = V_0^2/g d_0 \qquad \text{(A-14)}$$

For example, the upward water-vapor mist flow with $A = 1, C = 0.3$, $V_0 = 2$ m/s at atmospheric conditions with droplet size 100 μm is well within the range of validity of the equation (A-12).

Liquid-Liquid Direct-Contact Heat Transfer in a Spray Column

L. L. Moresco
Project Scientist,
Combustion Power Company, Inc.,
Menlo Park, Calif.

E. Marschall
Professor,
Department of Mechanical and Environmental
Engineering,
University of California,
Santa Barbara, Calif.

A computer-aided measuring technique was used for a study of direct-contact liquid-liquid heat transfer. Measurements of local mean and bulk temperatures of dispersed phase, continuous phase, and interface allow determination of the local heat transfer coefficients on both sides of the interface. Obtained results are either presented in terms of Nusselt number correlations or are discussed qualitatively.

Introduction

Numerous extensive reviews of experimental and theoretical investigations of direct-contact liquid-liquid heat transfer were published over the past years, most notably by Sideman and Shabtai [1], Sideman [2], Kehat and Sideman [3], Ferrarini [4], Hupfauf [5], and recently by Bühler [6]. From these and other publications it is quite apparent that the mechanism of direct-contact heat transfer has not been satisfactorily explored. For instance, none of the reported research has been directed toward the determination of the local heat transfer coefficients on both sides of the liquid-liquid interface, be it through a rigorous analysis with realistic boundary conditions or a carefully designed experiment. Theoretical approaches continue to rely on constraints which on one hand facilitate the analysis, and on the other hand limit their usefulness to qualitative results. Experimental studies of direct-contact heat transfer turn out to be rather involved since they require exact temperature measurements in both phases, including the liquid-liquid interface.

Recently, Moresco and Marschall [7] presented a computer-aided experimental technique which allows determination of the temperature fields in a direct-contact heat exchanger. Details of this measuring technique can be found in reference [7, 8]; thus only the general approach need be discussed here. This technique was used to determine the local temperature of the continuous flow, the dispersed flow, and the liquid-liquid interface in a vertical, counterflow spray-column. With the temperature distributions known, local heat transfer coefficients were determined and correlated.

Experimental Procedure and Data Processing

Temperature measurements were carried out with the help of a commercially available thermocouple made from 0.025 mm dia alumel and chromel wire. The junction of the thermocouple was measured to have a diameter of 0.0584 mm. This thermocouple is supported by a glass cylinder as shown in Fig. 1. The outer diameter of the glass cylinder is approximately 0.2 mm. The probe can be moved vertically and locked in any desired position within the column. Continuous phase and dispersed phase flow freely in a random fashion over the thermocouple junction. High speed movies revealed that as the dispersed phase drops are pierced by the probe, the liquid-liquid interface is not significantly disturbed as long as the probe is aligned with the drop flow direction. Thermo voltages were recorded every 0.65 10^{-3} s, converted to temperatures, and stored for further processing in a micro-computer.

Figure 2 shows a recording of temperatures as a dispersed liquid drop passes over the thermocouple probe. This recording was obtained in an experiment in which hot water streamed from top to bottom of the column as continuous phase while cold oil flowed upward in uniform droplets as the dispersed phase. The black dots represent the recorded thermocouple temperatures. The major task now is to correct the temperature readings for the time response of the thermocouple and to determine in which phase the measurements were taken. This is achieved through use of a computer code which is based on the following assumptions: At the liquid-liquid interface, both phases have the same temperature; the heat flux across the liquid-liquid interface is continuous; and the time constant of the thermocouple takes on a different value in the continuous and dispersed phase, mainly because of the different physical properties in both phases. First a search program is invoked which, based on these assumptions, locates the liquid-liquid interfaces. Then a lumped-capacity analysis of the thermocouple in contact with each fluid is used to determine the respective fluid temperatures in terms of thermocouple temperature history and the particular time constants. The correct fluid temperatures are presented in Fig. 2 as crosses. Also shown are the locations of the liquid-liquid interface. Since the drop velocity is known, the distance between the two interface locations can be

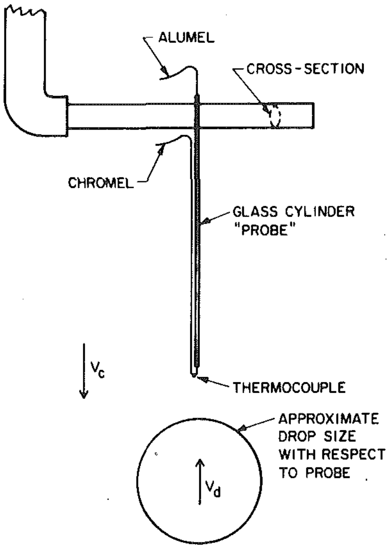

Fig. 1 Schematic of thermocouple probe

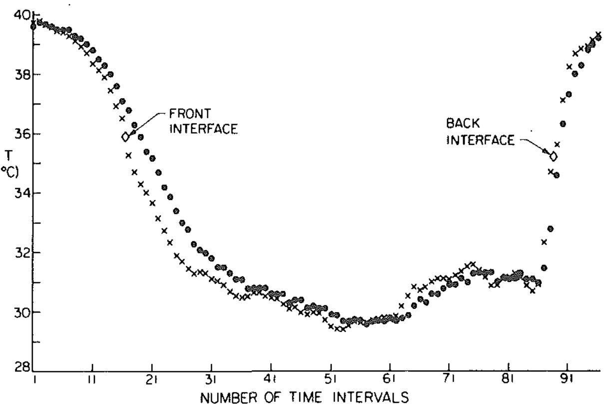

Fig. 2 Continuous and dispersed flow temperature variations at a fixed location

---

Contributed by the Heat Transfer Division for publication in the JOURNAL OF HEAT TRANSFER. Manuscript received by the Heat Transfer Division December 13, 1979.

evaluated. Assuming a spherical drop shape and a cylindrically symmetric temperature profile with respect to the vertical drop axis, the distance between the two interface locations determines where the thermocouple enters, moves across, and leaves the drop. Fifty to 100 such temperature histories obtained at a fixed location in the column are sufficient to determine the local bulk temperature of the continuous phase and the local mean temperature of the dispersed phase, as well as the local mean liquid-liquid interface temperature. All temperature calculations were carried out with developed computer codes. Figure 3 shows for the same experiment the measured local water bulk temperature T_c, mean interface temperature T_i, and mean oil temperature T_d versus the column length. In addition to the discussed measurements, flowrates, inlet and outlet temperatures, drop size and velocity, and hold-up were also determined.

Heat Transfer Calculations

Once the temperatures of the continuous phase, the interface, and the dispersed phase along the column are found, as shown in Fig. 3, the local internal mean heat transfer coefficient h_d is found from the energy balance.

$$m_d c_{pd} \frac{dT_d}{dt} - h_d A (T_i - T_d) = 0 \tag{1}$$

In equation (1) m_d is the mass of a single droplet of dispersed phase and c_{pd} is the specific heat of the dispersed phase. The derivative of the dispersed phase temperature T_d with respect to time t is calculated from

$$\frac{dT_d}{dt} = \frac{dT_d}{dz} v_{d/T}$$

where $v_{d/T}$ is the velocity of the dispersed phase droplet with respect to the column and z is a coordinate aligned with the column axis. The derivative dT_d/dz is obtained from a third order spline fit of the local mean dispersed phase temperature T_d over the column length, A is the surface area of a droplet, T_i and T_d are the local mean interface temperature and dispersed phase temperatures, respectively.

For the external heat transfer coefficient h_c, an energy balance yields

$$m_d c_{pd} \frac{dT_d}{dt} - h_c A (T_c - T_i) = 0 \tag{2}$$

In this equation T_c is the local continuous phase bulk temperature, while T_i is again the local interface temperature.

Once the two heat transfer coefficients h_c and h_d are known, an overall local heat transfer coefficient h_0 is derived from

$$\frac{1}{h_0} = \frac{1}{h_c} + \frac{1}{h_d}$$

Local Nusselt numbers for the internal and external heat transfer coefficients are calculated from

$$\mathrm{Nu}_d = \frac{h_d D}{k_d} \tag{3}$$

and

$$\mathrm{Nu}_c = \frac{h_c D}{k_c} \tag{4}$$

for the dispersed phase and continuous phase, respectively. Reynolds numbers for continuous and dispersed phase are obtained from the definitions

$$\mathrm{Re}_c = \frac{v_r D}{\nu_c}, \tag{5}$$

and

$$\mathrm{Re}_d = \frac{v_r D}{\nu_d} \tag{6}$$

where v_r is the relative velocity of the droplets with respect to the continuous phase, D is the drop diameter, and ν is the kinematic viscosity of the two fluids, respectively.

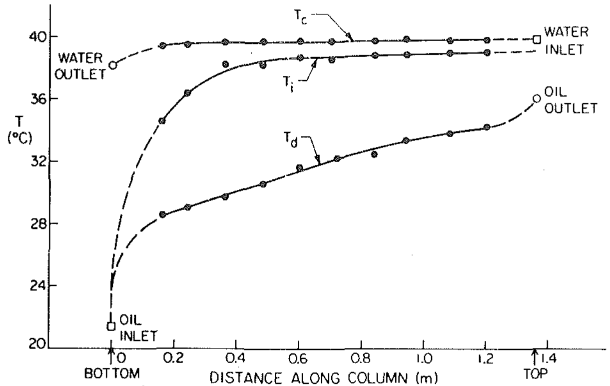

Fig. 3 **Local bulk water temperature, local mean interface temperature, and local mean dispersed flow temperature versus column length**

In the region near the nozzle for dispersed inlet flow (from zero to about 16 cm from the nozzle), in which temperature probe data were not recorded due to the rapid variation of drop shape, a conservative estimate of the average heat transfer coefficient was made. Assuming that the temperature of the dispersed phase and the interface decreases linearly from its values at the position 16 centimeters from the nozzle down to the inlet dispersed phase inlet temperature and the continuous phase temperature decreases linearly down to the continuous phase exit temperature, equations (1) and (2) were solved for h_c and h_d, and corresponding average Nusselt numbers were calculated for this region of the column.

Experiments were carried out in an Elgin type spray column with an inner diameter of 0.05 m and an effective length of 1.20 m. Distilled water served as the continuous phase fluid, while Amsco odorless mineral spirits were used as dispersed phase fluid. All physical properties of the oil, with the exception of the thermal conductivity, were measured over the temperature range of interest. The thermal conductivity was obtained from the literature. Water inlet temperatures were varied between 300 and 370K, and water flow rates ranged from $0.17 * 10^{-2}$ kg/s to $0.3 * 10^{-2}$ kg/s. Dispersed phase hold-up ranged from 0.7 to 1.5 percent, while drop diameter took on values from 0.007 to 0.01 m. For a given set of inlet temperatures and flow rates, variation in drop diameter could not be noticed.

Results

It seems to be appropriate to discuss first the general behavior of the local heat transfer coefficients in terms of relevant parameters. Not surprisingly, the coefficients h_c and h_d are relatively constant along the column except for a minor increase near the coalescence region for the droplets and a dramatically higher value for h_d near the

Nomenclature

A = droplet surface area
c_{pd} = specific heat of dispersed phase
D = drop diameter
h_c = external heat transfer coefficient
h_d = internal heat transfer coefficient
k_c = thermal conductivity of continuous phase
k_d = thermal conductivity of dispersed phase
m_d = mass of single droplet
Nu_c = continuous phase Nusselt number
Nu_d = dispersed phase Nusselt number
Pe_d = dispersed phase Peclet number
Re_c = continuous phase Reynolds number
Re_d = dispersed phase Reynolds number
t = time
T_c = continuous phase bulk temperature
T_d = dispersed phase mean temperature
T_i = interface mean temperature
$v_{d/T}$ = drop velocity relative to column
v_r = drop velocity relative to continuous phase
z = coordinate
μ_i = dispersed phase viscosity
μ_0 = continuous phase viscosity
ν_c = continuous phase kinematic viscosity
ν_d = dispersed phase kinematic viscosity

dispersed phase nozzle. Due to the low thermal conductivity of the dispersed fluid (oil), the inverse of the internal heat transfer coefficient $1/h_d$ is the major governing resistance to overall heat exchange.

Experimental results for the internal Nusselt numbers are shown in Fig. 4. Measured Nusselt numbers are consistently 15 percent higher than Nusselt number predictions obtained with the popular Handlos and Baron [9] equation

$$\mathrm{Nu}_d = \frac{0.00375\,\mathrm{Pe}_d}{(1+\mu_i/\mu_0)} \tag{7}$$

Equation (7) was postulated for heat or mass transfer based on assumed circular internal circulation patterns and other assumptions not supported by experimental evidence. A stepwise regression analysis of experimental data obtained in this study was performed and the following Nusselt number relationship was found to represent the experimental results well.

$$\mathrm{Nu}_d = 0.0178\,\mathrm{Re}_d{}^{0.95}\,\mathrm{Pr}_d{}^{0.22} \tag{8}$$

Outside fluid properties enter this equation indirectly through the relative velocity between continuous and dispersed phase used in the Reynolds number.

External heat transfer coefficients h_c plotted versus the continuous phase Reynolds number are presented in Fig. 5. The data points in this figure are mean column values of the local heat transfer coefficients. Peclet number variations were small for a particular experiment and the values of h_c varied within less than ± 10 percent. Results show Nusselt numbers to be considerably smaller than the values formerly predicted analytically, using assumed flowfields for the circulating droplets, as for instance, reported in reference [10, 11]. The Nusselt numbers are also considerably smaller than the ones predicted by Ferrarini [4] which were used in the recent investigations by Hupfauf [5] and Bühler [6]. Interestingly enough, the Nusselt numbers obtained in this study are also much smaller than those which can be predicted with the Ranz and Marshall equation [12]. Even though this equation was originally obtained for droplets evaporating in air, it is consistently recommended for prediction of heat transfer rates from solid spheres to a surrounding fluid. Heat transfer from a solid sphere to a moving fluid has frequently been assumed to be a limiting case of heat transfer from a droplet moving in a fluid. The results of this study do not support this assumption.

It should be pointed out that all formerly reported equations for external Nusselt numbers or external heat transfer coefficients were obtained either through analysis containing frequently unwarranted assumptions, or through mass transfer experiments with dissolving drops which clearly are not realistic substitutes for heat transfer experiments, or by assuming internal heat transfer coefficients and then forcing the external heat transfer coefficients to take on such values that internal and external heat transfer coefficients match experimentally obtained overall heat transfer coefficients. The only exception to the just described procedures is apparently the one used by Pierce [13]. Pierce found in his experimental work that external Nusselt numbers for liquid mercury drops fell below those for solid spheres. The range of data obtained by Pierce as well as the Ranz and Marshall equation are also shown in Fig. 5. While there is no obvious explanation why the Nusselt numbers found in this study are below the Nusselt numbers obtained from the Ranz and Marshall equation, it is interesting to note that Pierce's study which is the only other experimental study aside from this one in which external heat transfer coefficients were determined directly, yielded Nusselt numbers of the same order.

The external Nusselt numbers were correlated by a stepwise regression routine and the following relationship was established.

$$\mathrm{Nu}_c = 0.156\,\mathrm{Re}_c{}^{0.5}\,\mathrm{Pr}_c{}^{0.5} \tag{9}$$

A rough estimation of the average heat transfer coefficients near the dispersed phase entrance nozzle following the procedure outlined previously revealed that not only are these heat transfer coefficients higher than those along the major portion of the column, but the internal heat transfer coefficients have become so large as compared to the external heat transfer coefficient, that the major resistance to heat transfer is now found to lie in the continuous phase. This result seems to indicate that the heat transfer mechanism near the dispersed phase entrance region is governed by different phenomena than in the rest of the column. High speed films taken show dramatic accelerations take place during drop release which certainly should have an influence on the heat transfer mechanism.

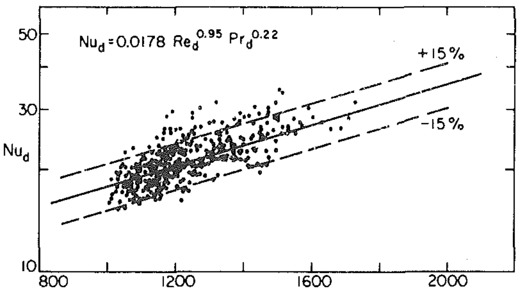

Fig. 4 Internal Nusselt number correlation

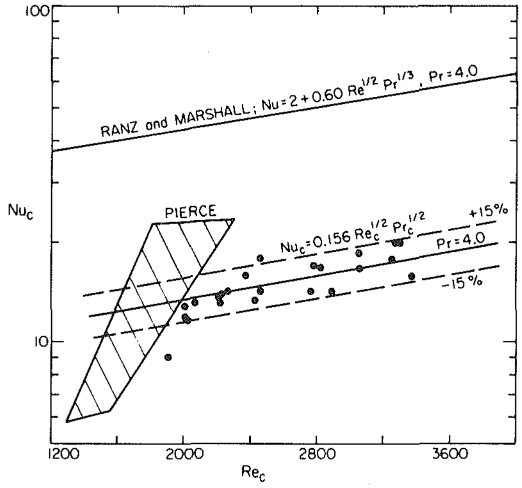

Fig. 5 External Nusselt number correlation

Conclusion

A refined, computer-aided measuring technique allowed determination of local temperatures of continuous phase, dispersed phase, and interface in a liquid-liquid direct-contact heat exchanger. A complete set of these temperatures has never been measured before. Based on the obtained temperature profiles, local heat transfer coefficients at both sides of the liquid-liquid interface were calculated. The experiments were carried out with oil as the dispersed phase, while pure water served as continuous phase. The following conclusions below can be drawn from the experimental results.

The internal heat transfer coefficient for a rising drop in a continuous phase can be predicted reasonably well with the Handlos and Baron [9] equation, except for regions in which entrance and exit effects play a dominant role. For conditions chosen in this study, the correlation

$$\mathrm{Nu}_d = 0.0178\,\mathrm{Re}_d{}^{0.95}\,\mathrm{Pr}_d{}^{0.22} \tag{10}$$

is a better representation for the internal heat transfer coefficients.

During drop formation and release, the internal heat transfer coefficients are very much higher than predicted by equation (7). In fact, during this process, the major resistance to heat transfer is found in the continuous and not, as usually assumed, in the dispersed phase.

External heat transfer coefficients (in the continuous phase) have significantly lower values than the values obtained in previous endeavors. Since in previous investigations the liquid-liquid interface temperature has never been measured, reported results had to be based on assumptions which, according to this study are not realistic. For the range investigated, external heat transfer coefficients are well represented by

$$Nu_c = 0.156\, Re_c^{0.5}\, Pr_c^{0.5} \qquad (11)$$

Acknowledgments

Support through NSF Grant No. Eng. 76-15068 is acknowledged.

References

1 Sideman, S., and Shabtai, H., "Direct-Contact Heat Transfer Between a Single Drop and an Immiscible Liquid Medium," *The Canadian Journal of Chemical Engineering,* Vol. 42, 1964, pp. 107–117.

2 Sideman, S., "Direct-Contact Heat Transfer Between Immiscible Liquids," *Recent Advances in Chemical Engineering,* Vol. 6, 1966, pp. 207–286.

3 Kehat, E., and Sideman, S., "Heat Transfer by Direct Liquid-Liquid Contact," *Recent Advances in Liquid-Liquid Extraction,* Chapter 13, Pergamon Press, 1971.

4 Ferrarini, R., "Die Berechnung der Strömung und des Wärmeaustausches in flüssig-flüssig Sprühkolonnen," Diss. No. 4650, ETH Zürich, Switzerland, 1972.

5 Hupfauf, A., "Lokaler Wärmeübergang und Rückvermischung in flüssig-flüssig Sprühkolonnen," Diss. ETH 5093, ETH Zürich, Switzerland, 1973.

6 Bühler, B. S., "Hydrodynamik und Wärme-austausch in einem Flüssig-Flüssig Sprühturm," Diss. No. 6027, ETH Zürich, Switzerland, 1977.

7 Moresco, L. L., and Marschall, E., "Temperature Measurements in a Liquid-Liquid Direct-Contact Heat Exchanger," *AIChE Symposium Series,* No. 189, Vol. 75, 1979, pp. 266–272.

8 Moresco, L. L., "The Effect of Dissolved Solids on Direct-Contact Heat Transfer," Doctoral Thesis, UCSB, 1979.

9 Handlos, A. E., and Baron, T., "Mass and Heat Transfer from Drops in Liquid-Liquid Extraction," *AIChE Journal,* Vol. 3, No. 1, 1957, pp. 127–135.

10. Baussinesque, M., "Calcul du pouvoir refroidissant des courants fluides," *Chimie et Physique Americaine,* Vol. 29, 1913, pp. 364–372.

11. Acrivos, A., and Taylor, T. D., "Heat and Mass Transfer from Single Spheres in Stokes Flow," *The Physics of Fluids,* Vol. 5, No. 4, 1962, pp. 387–394.

12. Ranz, W. E., and Marshall, W. R., cited by: Bird, Stewart, Lightfoot, *Transport Phenomena,* Wiley, New York, 1960, page 409.

13. Pierce, R. D., Dwyer, O. E., and Martin, J. J., "Heat Transfer and Fluid Dynamics in Mercury-Water Spray Columns," *AIChE Journal,* Vol. 5, No. 2, 1959, pp. 257–262.

A Mechanistic Model for Countercurrent Steam-Water Flow

A. Segev
R. P. Collier
Battelle Columbus Laboratories,
Columbus, Ohio 43201

A one-dimensional model has been developed to describe the flow behavior of a liquid film draining down a heated wall, in the presence of countercurrent vapor flow. The effects of nonequilibrium void generation at the walls and condensation of countercurrent vapor on the penetrating liquid film interface, as well as on the bypassed liquid, have been considered. The momentum exchange is described by a correlation, assumed to apply at the entrance region, where the amount of liquid film flow is limited by the net vapor upflow. Theoretical predictions were compared with over 600 test results, obtained in $^1/_{15}$- and $^2/_{15}$-scale models of a PWR downcomer, over a wide range of test parameters. The comparisons exhibit a fairly good agreement.

Introduction

During a postulated loss-of-coolant accident (LOCA) due to a break in a cold leg of a large pressurized water reactor (PWR), emergency core cooling (ECC) water would be injected into the primary system piping to provide cooling for the reactor core. Depressurization during the blowdown phase of the LOCA would result in core steam flow in the reverse direction down through the core and up the downcomer annulus. This upward steam flow has the potential to retard or even prevent the penetration of the injected ECC fluid to the lower plenum. In addition, steam generated on the heated walls of the pressure vessel and core barrel may also cause a delay in the penetration of ECC fluid to the lower plenum. Bypass of ECC fluid to the broken cold leg would delay refilling of the lower plenum and consequently delay the reflooding and cooling of the reactor core.

Extensive experimental studies of downcomer behavior have been conducted at Battelle Columbus Laboratories (BCL) [1,2] and at Creare [3,4] in PWR models of different scales. A schematic sketch of a reactor scale model is shown in Fig. 1. ECC is injected into three cold legs at a fixed rate, $W_{\ell in}$, and enters the downcomer as a horizontal jet which impacts the core barrel, distributes over it, and changes its flow direction. It may flow downward and/or it may be bypassed around the upper downcomer annulus and out the break. Visual observations indicate that the penetration phenomenon is very chaotic in nature, involving both thermal effects (such as hot wall quenching, vapor generation, and condensation) and hydrodynamic effects (such as surface wave development, instabilities leading to "bridging" and plug flow, entrainment, and turbulent mixing). Because of these complications, purely theoretical approaches often face numerous difficulties, and the use of empirical models is necessary.

Semi-empirical correlations have been constructed by several investigators using numerical best fits to test data. These correlations include functional dependencies based on physical reasoning where possible. In general, the confidence with which we can use these semi-empirical correlations to extrapolate to conditions not tested is a function of the degree of physical basis supporting the model.

In the models developed by Block, et al. [5] at Creare, and Carbiener, et al. [6] at BCL, the momentum balance between the gas and the liquid is established by the empirical Wallis flooding correlation [7]. Overall condensation is described in terms of an empirical parameter which reflects the degree of nonequilibrium. The condensation parameter as well as the two arbitrary parameters in Wallis correlation are determined from numerical best fits to steam-water penetration data.

A comprehensive statistical analysis of data trends has been performed by Beckner, et al. [8]. A new correlation form has been suggested which includes five free parameters evaluated for each geometry. The comparison between experimental data and prediction exhibited very good agreement.

Alb and Chambré [9] developed a different type of correlation, based on dimensional analysis. It was given in terms of Froude numbers based on superficial velocities of steam and water, and also included five free parameters determined from data taken in Battelle's $^1/_{15}$- and $^2/_{15}$-scale models. Here also, a very good fit was obtained.

A time dependent, multi-dimensional formulation has been developed for the computer program K-TIF [10] which utilizes empirical functional dependencies to describe mean transport and interaction processes between the countercurrent streams of vapor and liquid.

In an attempt to understand the effects of condensation, heated walls, and countercurrent flow on the ECC penetration and downcomer dynamics we have developed a physical model based on the simple flow pattern of a liquid film draining down a heated wall, assuming that a one-dimensional presentation of this flow configuration represents the average chaotic phenomenon which occurs in the downcomer.

Model

Figure 2 is a sketch of the geometry considered. Subcooled liquid with temperature $T_{\ell in}$ is injected at a rate of $W_{\ell in}$ into the downcomer. In the downcomer entrance region, momentum exchange occurs between the liquid and the upward flowing vapor, resulting in a liquid flow partitioning; some liquid flows down the superheated walls as a film, with mass flow rate $W_{\ell i}$. The remainder, $W_{\ell in} - W_{\ell i}$, is bypassed and flows toward the break. Vapor is generated by subcooled boiling as the liquid film drains down the walls. At small distances from the entrance, the vapor generated remains as discrete bubbles attached to the surface while growing and collapsing. In this region the fraction of wall heat flux used in the formation of net vapor is insignificant. At a specific distance from the entrance, the bubble diameter is large enough so that it detaches from, or slides along, the heated surface. New bubbles are rapidly created at these active sites, and significant void is produced. The point at which void is first formed under the nonequilibrium conditions is denoted by z_0, and

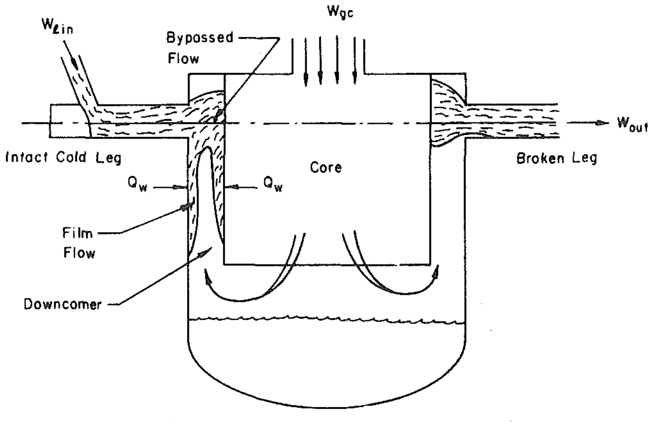

Fig. 1 Schematic sketch of a reactor scale model

Contributed by the Heat Transfer Division for publication in the JOURNAL OF HEAT TRANSFER. Manuscript received by the Heat Transfer Division October 31, 1979.

the mixed mean liquid temperature at that point is T_0. (In Fig. 2, we describe the extreme case in which the vapor generated at the wall is contained in the liquid film as a bubbly layer. Actually, bubbles may leave the liquid film at any location along the wall.)

The vapor produced at the hot walls and/or vapor introduced at the bottom of the annulus (reverse core steam) flows upward, establishing a countercurrent flow. Mass transfer in the system, in the form of condensation (at the vapor-liquid film interface and on the bypassed liquid) and vaporization (at the heated walls), affects the momentum exchange between the two phases, which in turn influences the overall system behavior. Depending on the mass exchange phenomena which take place along the film, two film regions may be observed: (1) when $z_0 \leq z \leq L$, convection, wall vapor production, and condensation at the countercurrent vapor-liquid interface are involved simultaneously; (2) when $0 \leq z \leq z_0$, only convection and condensation are involved.

In developing the conservation equations we consider a well mixed turbulent liquid film for which the velocity and temperature profiles may be assumed to be uniform normal to the wall. Any waves and instabilities which may be present due to the vapor upflow are neglected. We also assume that the pressure in the downcomer is constant and that the vapor is at the saturation temperature. For the general case which involves forced convection, vapor generation and countercurrent condensation, the change in liquid flow rate (W_ℓ) is equal to the net mass exchange of vapor condensed at the film interface (W_c) and vapor generated at the wall (W_{gw}).

$$dW_\ell = dW_c - dW_{gw} \tag{1}$$

The liquid and vapor energy equations are given respectively by

$$\begin{aligned}(W_\ell + dW_c - dW_{gw})C_p(T - T_0 + dT) + dW_{gw}C_p(T_s - T_0)\\ = W_\ell C_p(T - T_0) + [h_{fg} + C_p(T_s - T_0)]dW_c + P_h q_\ell dz,\end{aligned} \tag{2}$$

$$h_{fg}dW_{gw} = P_h q_g dz, \tag{3}$$

where q_ℓ is the quenching heat flux (the heat transferred to the liquid which raises its enthalpy), q_g is the boiling heat flux (heat supplied to generate void), C_p is the liquid specific heat, and P_h is the heated perimeter.

By combining equations (2) and (3) we get the mixture energy equation

$$C_p W_\ell dT = P_h q_w dz + [h_{fg} + C_p(T_s - T)]\,(dW_c - dW_{gw}), \tag{4}$$

where q_w is the wall heat flux, given by

$$q_w = q_\ell + q_g. \tag{5}$$

Equation (4) can also be written as

$$-d\,\{W_\ell[h_{fg} + C_p(T_s - T)]\} = P_h q_w dz. \tag{6}$$

Substituting equations (3) and (5) into equation (4) and assuming that $h_{fg} \gg C_p(T_s - T)$ we get

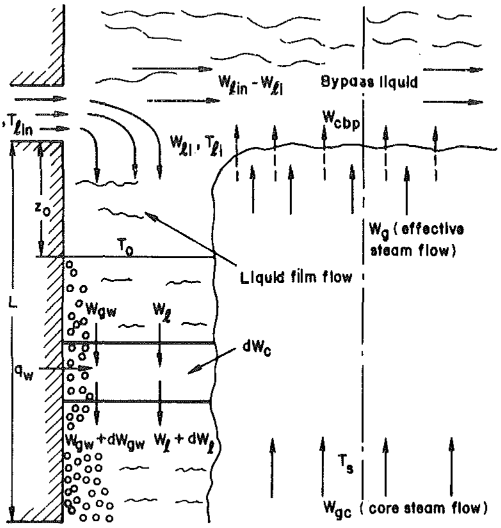

Fig. 2 Schematic sketch of a falling liquid film in countercurrent flow

$$C_p W_\ell \frac{dT}{dz} = P_h q_\ell + h_{fg}\frac{dW_c}{dz}. \tag{7}$$

The temperature profile may now be evaluated according to equation (7) if wall heat flux partitioning, the condensation distribution, and the local liquid film flow rate are known. At present, most of these parameters are unknown in countercurrent flows, suggesting the use of certain approximations and assumptions. Two special cases may be examined.

No Condensation. When no countercurrent condensation occurs along the film, the energy transport processes are similar to those described in several papers [11, 12] dealing with the determination of the void fraction distribution in a heated tube. Equation (7) is then simplified to

$$\frac{dT}{dz} = \frac{P_h q_\ell}{C_p W_\ell}, \tag{8}$$

and can be integrated in the same way as it was done in reference [11] to yield

$$\frac{T - T_s}{T_0 - T_s} = \exp\left(-\frac{z - z_0}{\ell}\right), \tag{9}$$

where ℓ is the significant boiling length (difference between the length which is required to heat the bulk liquid up to saturation when no evaporation takes place, and z_0) given by

$$\ell = \frac{W_{\ell 0} C_p (T_s - T_0)}{P_h q_w}. \tag{10}$$

The point z_0 is determined from

Nomenclature

A = annulus cross section
C = parameter
C_a = average circumference
C_p = specific heat of liquid
f, f_1 = parameters
g = gravitational acceleration
h = heat transfer coefficient
h_{fg} = heat of vaporization
$J_x{}^*$ = dimensionless volumetric flux of phase x
$J_{cbp}{}^*$ = dimensionless volumetric flux of steam condensed on bypassed liquid
$J_{gb}{}^*$ = dimensionless volumetric flux of core steam at complete bypass point
$J_{\ell p}{}^*$ = dimensionless volumetric flux of penetrating liquid

L = length of core barrel
ℓ = significant boiling length
m = parameter
P = pressure
P_h = heated perimeter
Q, Q_1, Q_2 = heat transfer rates
Q^* = dimensionless heat transfer rate
q = heat flux
S = gap thickness
T = temperature
T_s = saturation temperature
W = mass flow rate
W_{gw} = vapor generation rate
z = distance
Γ = mass flow rate per unit width

λ = parameter
μ = viscosity
ρ = density

Subscripts

c = condensation
g = vapor
gc = core steam
ℓ = liquid
ℓi = film inlet
ℓin = inlet of cold leg
o = point of net vaporization
t = total
tm = net mass exchange on liquid film
w = wall

$$z_0 = \frac{W_{\ell i} C_p (T_0 - T_{\ell i})}{P_h q_w}. \qquad (11)$$

Equation (9) describes the temperature profile assumed by Zuber, et al. [12] which was shown to be adequate for void fraction calculation in tubes. Correlations which predict the temperature at the net vapor generation point (T_0) for flows in a tube are available in the literature [13,14].

Adiabatic Wall. When $q_w = q_\ell = 0$, equations (1–3) reduce to the case of condensation on subcooled liquid flowing on an adiabatic wall, solved by Linehan, et al. [15] and Liu, et al. [16]. The integration of equation (7) in this case results in the following temperature profile.

$$T(z) = T_{\ell i} + \frac{h_{fg}}{C_p} \ln \frac{W_\ell(z)}{W_{\ell i}}. \qquad (12)$$

Net Mass Exchange. In addition to the special cases studied, valuable information may be obtained by evaluating the net mass exchange along the wall. To do so, equation (6) is integrated along the film, taking into account the different mass exchange processes in each film region.

$0 \leq z \leq z_0$. In this region no vapor is generated at the walls and the only mass exchange is due to countercurrent condensation of upflow steam. The integration of equation (6) from $z = 0$ to z_0 subject to the boundary conditions

$$\begin{aligned} z &= 0,\ W_\ell = W_{\ell i},\ T = T_{\ell i}, \\ z &= z_0,\ W_\ell = W_{\ell 0},\ T = T_0, \end{aligned} \qquad (13)$$

results in a relationship between $W_{\ell 0}$ and $W_{\ell i}$,

$$W_{\ell 0} = \frac{W_{\ell i}[h_{fg} + C_p(T_s - T_{\ell i})] - Q_1}{h_{fg} + C_p(T_s - T_0)}, \qquad (14)$$

where

$$Q_1 = \int_0^{z_0} P_h q_w dz. \qquad (15)$$

$z_0 \leq z \leq L$. In this region the integration of equation (6) from z_0 to z yields

$$W_\ell(z) = \frac{W_{\ell 0}[h_{fg} + C_p(T_s - T_0)] - Q_2(z)}{h_{fg} + C_p(T_s - T)}, \qquad (16)$$

where $Q_2(z)$ is the wall heat transfer rate given by

$$Q_2(z) = \int_{z_0}^{z} P_h q_w dz. \qquad (17)$$

The total net mass exchange along the film (W_{tm}) is described by

$$W_{tm} = W_{\ell i} - W_\ell(L), \qquad (18)$$

or

$$W_{tm} = \frac{Q - W_{\ell i} C_p [T(L) - T_{\ell i}]}{h_{fg} + C_p[T_s - T(L)]}, \qquad (19)$$

where

$$Q \equiv Q_1 + Q_2(L) = \int_0^L P_h q_w dz. \qquad (20)$$

The amount of vapor generated is given by

$$W_{gwt}(z) = \frac{Q_2(z) - W_{\ell 0} C_p (T - T_0)}{h_{fg} + C_p(T_s - T)} + \int_{z_0}^{z} dW_c, \qquad (21)$$

where

$$W_{gwt}(z) = \int_{z_0}^{z} dW_{gw}. \qquad (22)$$

Momentum Exchange

The amount of heat removed by the liquid, and consequently the amount of condensation and vaporization along the liquid film, is dependent on the inlet liquid flow rate, $W_{\ell i}$, which in turn is limited by the momentum exchange between the two countercurrent streams. This limiting mechanism is not well defined as it may result from a combination of interfacial shear, turbulent mixing, entrainment, or surface instabilities. Two major techniques may be used to overcome this problem. One technique assumes an empirical functional form for the interfacial momentum exchange and solves numerically the multidimensional two-phase momentum equations [10]. A simpler and less expensive method, which is global in nature and consequently generally more limited in its application, uses "flooding" correlations to describe the net result of the total momentum exchange between the phases. At present, we use the latter approach, utilizing the well-known Wallis correlation [7]

$$J_{gi}{*}^{1/2} + m J_{\ell i}{*}^{1/2} = C, \qquad (23)$$

where m and C are empirically determined parameters and J_g* and $J_\ell*$ are dimensionless volumetric fluxes of the upflow vapor and downflow liquid, respectively, at the entrance region, where liquid hold-up is assumed to occur.

The relation between the dimensionless flux of phase x and the mass flow rate is given by

$$J_x* = \frac{W_x}{A[\rho_x g C_a (\rho_\ell - \rho_g)]^{1/2}}, \qquad (24)$$

where A is the annulus cross section and C_a is the average annulus circumference. The choice of C_a as the characteristic dimension is based on experimental studies with distorted gap size which have shown that the data do not collapse when the hydraulic diameter is used as a characteristic dimension. Better agreement was obtained when C_a was utilized in the definition of J_x*.

The Wallis correlation is considered as a hydrodynamic limiting relationship in which the upward flowing gas at the entrance region controls the liquid flow partitioning between film flow ($J_{\ell i}*$) and flow being bypassed ($J_{\ell \text{in}}* - J_{\ell i}*$). The coefficients m and C are assumed to be independent of thermal conditions and constant for a specific geometry, and so, they can be determined from air-water experiments. This correlation can also be applied to flows which involve mass exchange, such as steam-water flows, by considering $J_{gi}*$ to be the effective gas flux for momentum exchange. In other words, $J_{gi}*$ is assumed to be the net steam flux at the entrance region, consisting of steam from the simulated core ($J_{gc}*$) and the net mass exchange in the system.

When applying the one-dimensional analysis to ECC penetration in PWR scaled models, the mass exchange is not limited only to condensation and/or vaporization along the liquid film. As shown in Fig. 2, additional mass exchange occurs on the liquid which is being bypassed. This mass exchange component is denoted by the nondimensional parameter $J_{cbp}*$. Thus, the resultant expression for $J_{gi}*$ is

$$J_{gi}* = J_{gc}* + J_{tm}* - J_{cbp}*. \qquad (25)$$

Rewriting equation (19) in terms of the dimensionless volumetric flux and substituting into equation (25) we get

$$J_{gi}* = J_{gc}* - f\lambda J_{\ell i}* - J_{cbp}* + Q*, \qquad (26)$$

where

$$Q* = \frac{Q}{A[\rho_g g C_a (\rho_\ell - \rho_g)]^{1/2} h_{fg}}, \qquad (27)$$

$$\lambda = \frac{C_p(T_s - T_{\ell i})}{h_{fg}} \left(\frac{\rho_\ell}{\rho_g}\right)^{1/2}, \text{ and} \qquad (28)$$

$$f = \frac{T(L) - T_{\ell i}}{T_s - T_{\ell i}}. \qquad (29)$$

The dimensionless parameters λ and f represent condensation potential and the efficiency of heat transferred to the liquid from the hot walls and/or from condensation, respectively.

In an analogy to the condensation process on the liquid film we assume the following form for steam condensation on the liquid being bypassed

$$J_{cbp}^* = f_1\lambda(J_{\ell \mathrm{in}}^* - J_{\ell i}^*), \qquad (30)$$

where f_1 is a parameter representing the efficiency of steam condensation on the bypassed liquid. Substituting equations (26) and (30) into equation (23) we get

$$[J_{gc}^* - (f - f_1)\lambda J_{\ell i}^* - f_1\lambda J_{\ell \mathrm{in}}^* + Q^*]^{1/2} + mJ_{\ell i}^{*1/2} = C, \qquad (31)$$

which is an implicit equation for $J_{\ell i}^*$ from which the liquid penetration flux can be obtained.

As shown in equation (29), the value for the parameter f may be obtained via the temperature $T(L)$. However, at the present time it is difficult to determine this temperature analytically when simultaneous vaporization and condensation are involved except for the two special cases discussed previously. In the case of an adiabatic wall, f represents the condensation efficiency and from equation (12) we find that

$$f = \frac{h_{fg}}{C_p(T_s - T_{\ell i})}\ell n\,\frac{W_\ell(L)}{W_{\ell i}}. \qquad (32)$$

An alternative form for f was derived by Liu, et al. [16] using a heat transfer coefficient formulation for vapor condensation on a countercurrent liquid film with adiabatic wall.

$$f = 1 - \exp\left(-\frac{hL}{C_p\Gamma}\right), \qquad (33)$$

where Γ is the film mass flow rate per unit width and h is the heat transfer coefficient.

When no condensation is present it can be shown that f assumes a slightly different form than given in equation (29). In this special case we find that

$$f = \frac{T(L) - T_0}{T_s - T_{\ell i}}, \qquad (34)$$

or with the use of equation (13)

$$f = \left[1 - \exp\left(-\frac{L - z_0}{\ell}\right)\right]\left(\frac{T_s - T_0}{T_s - T_{\ell i}}\right), \qquad (35)$$

were f represents the effectiveness of energy convection. When $f = 0$, $T(L) = T_0$ (equation (34)) and $dT/dz = 0$. Equation (8) indicates that for this case $q_\ell = 0$, which means that when $f = 0$ all the wall heat flux is transferred as a boiling component to generate vapor. When q_ℓ becomes very large ℓ becomes very small (equation (10)) and T_0 approaches $T_{\ell i}$. Consequently, as shown by equation (35), f approaches 1.

Delivery Time Delay

At the early stage of penetration, the walls are maintained at a high temperature, causing a delay in liquid delivery. In the absence of counterflow, it is known that the quenching liquid front velocity is controlled by thermal conduction within the walls. When counterflow of vapor (core vapor and/or wall generated vapor) is present, a reduction of inlet liquid film flow rate may occur. In this case, the quenching process is hydrodynamically controlled. The end of quenching and subsequently, the delivery time delay, are determined when the quenching liquid front reaches the bottom of the channel and penetration commences, i.e., when $W_\ell(L) = 0^+$. From equation (16), with the use of equation (14), the approximate inlet liquid film flow rate which results in $W_\ell(L) = 0^+$ is given in a dimensionless form by

$$J_{\ell i}^* = \left(\frac{\rho_g}{\rho_\ell}\right)^{1/2} Q^*. \qquad (36)$$

Substituting this condition into equation (31), we get an implicit equation for Q^*, which represents the wall heat transfer rate required to sustain a sufficiently large vapor production to result in zero penetration.

The time at which the transient wall heat transfer rate (assumed to be conduction limited in reference [17]) is equal to the calculated Q^* is the delivery delay time.

Results

Equation (31) was solved and compared with experimental data for adiabatic walls. It was solved for J_{gc}^*, assuming the liquid penetration flux as an independent parameter, and for $J_{\ell p}^*$, assuming J_{gc}^* to be the independent parameter. A limited comparison was also obtained between calculated and experimental delivery time delay. These results will be presented in a future communication.

As shown in equation (33), the value for f could be evaluated if the condensing heat transfer coefficient is known and is uniform along the film. Unfortunately, no such data on countercurrent condensation are currently available in the literature. Thus, the heat transfer coefficient correlation obtained by Lee, et al. [18] for a cocurrent steam-water flow in a rectangular channel is used. Modified for an annulus geometry we get

$$f = 1 - \exp\left[-0.0074\left(\frac{\mu_\ell}{\mu_g}\right)^{1/3}\left(\frac{\rho_g}{\rho_\ell}\right)^{1/6}\frac{L}{S}\,\frac{J_{gc}^{*1/3}}{J_{\ell i}^{*0.29}}\right], \qquad (37)$$

were S is the annulus gap size.

The condensation on the bypassed liquid is determined by considering the situation near the complete bypass point ($J_{\ell i}^* = 0$). At this point the only mass exchange in the system is on the liquid being bypassed, and from equation (31) we find that

$$f_1 = \frac{J_{gb}^* - C^2}{\lambda J_{\ell \mathrm{in}}^*}, \qquad (38)$$

where J_{gb}^* is the steam flux necessary to cause complete bypass, determined for a specific geometry from data correlation [19].

The steady steam flux (J_{gc}^*) necessary to bypass a given amount of liquid was calculated from Equation (31) and is compared in Figs. 3 and 4 to the experimentally measured values obtained in 1/15- and 2/15-scale models. In Fig. 3, we used Creare's data obtained in their 1/15-scale model with a deep plenum and scaled gap with various liquid temperatures [3]. The data include "uncontrolled pressure" runs (i.e., the pressure in the lower plenum increases with increasing steam flow) and runs in which the valves on the broken cold leg were partially closed resulting in an increase of lower plenum pressure. The agreement shown in Fig. 3 is fairly good.

Relatively good agreement is also exhibited when theoretical predictions are compared with experimental data obtained in Battelle's 1/15- [1] and 2/15-scale [2] models. As an example, see Fig. 4.

From the calculations it was determined that liquid penetration depends strongly on the externally supplied steam flow rate (J_{gc}^*) and liquid subcooling, and to a lesser extent on pressure and liquid injection rate. The effects of subcooling and pressure on the liquid penetration rate at a specific J_{gc}^* are accounted for mainly through

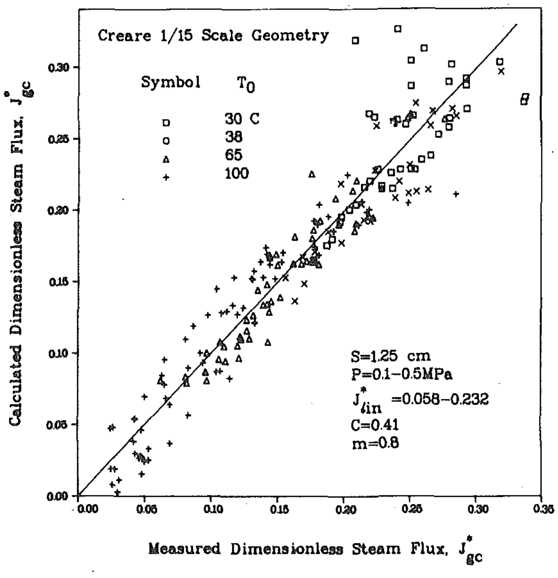

Fig. 3 Comparison between calculated and experimental J_{gc}^* for Creare's 1/15-scale model

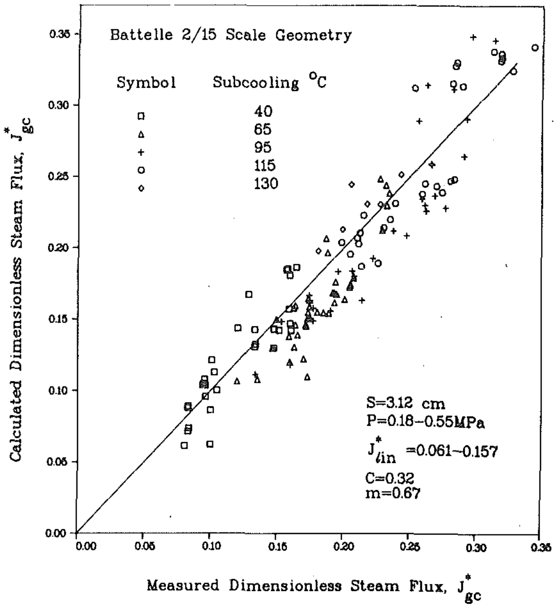

Fig 4 Comparison between calculated and experimental J_{gc}* for Batelle's 2/15-scale model

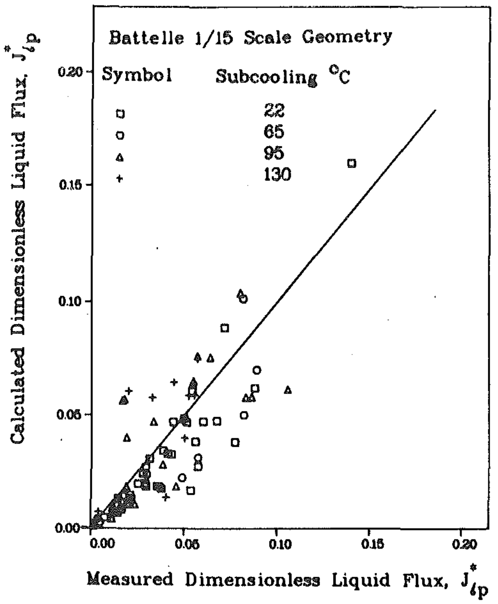

Fig. 5 Comparison between calculated and experimental $J_{\ell p}$* for Batelle's 1/15-scale model

the condensation potential, λ, so when λ increases the liquid penetration rate increases. Liquid injection rate was shown to affect the amount of steam condensation on the bypassed liquid, thus for a specific J_{gc}* an increase in the liquid injection flow rate results in an increase in liquid penetration rate. However, the injection rate effect diminishes when the liquid is saturated, since no condensation occurs; it is similar to an air-water system. The consistently good agreement exhibited suggests that for the range of liquid temperatures and vessel pressures tested the condensation effect and its dependence on scale, subcooling, and pressure are well modeled by the analysis.

Equation (31) was also solved for $J_{\ell i}$*, from which the penetrating liquid flux, $J_{\ell p}$*, was calculated and compared to experimental values. The comparison in Fig. 5 shows that the agreement is not as good as that shown in Figs. 3 and 4. This results primarily from the shape of the experimental penetration curves which indicate that a relatively small change in steam flow results in a relatively large change in liquid penetration rate. This sensitivity is the reason for the difficulties encountered in evaluating theoretical models by performing comparisons with data in terms of penetrating liquid flux.

Discussion

The main objective of the present paper has been to establish a general solution for liquid penetration in countercurrent flow, involving condensation and vaporization, to simulate ECC penetration. This was done by developing a mechanistic model based on a one-dimensional film flow configuration, with the assumption that it represents the average behavior of the chaotic phenomenon observed in the downcomer. The solution is based on standard mass and energy conservation principles, coupled with an empirical correlation which represents the momentum exchange. As shown, even for the simple case of falling film, a general solution can not be obtained unless more information on mass and momentum exchange in countercurrent flow is available. However, by using certain physical approximations the comparisons with experiments show consistently good agreement over a wide range of test conditions.

The mechanistic approach adopted here is different from the "best estimate analysis" utilized in references [5] and [6] which is a semi-empirical, lumped parameter system approach. The mechanistic model results in a more detailed description of flow behavior and mass exchange processes, identifying two condensation components: condensation on the penetrating liquid film in countercurrent flow, and condensation on the bypassed liquid, which is essentially condensation on a turbulent liquid ring.

As in the best estimate analysis we also use a correlation representing the net effect of momentum exchange. At present we have used the Wallis correlation although it was shown [20] that flooding of air-water flows in 1/15- and 2/15-scale models of PWR's is not scaled well by the J* parameters. However, when the Wallis correlation is applied separately to data in each scaled model and separate best fit values for m and C are used, fairly good agreement is obtained. As long as the Wallis equation is used only as a correlation with no scaling application, the parameters m and C play no significant role and we can use it, as any other correlation, for our purpose. Thus, the different values for m and C which were used in the present analysis were evaluated for each geometry for air-water or steam-saturated water experiments. As far as scaling is concerned it appears that the Wallis correlation can be applied when the dependence of m and C on scale is evaluated.

The condensation on the liquid film was described by using a heat transfer coefficient developed for cocurrent flow in a horizontal channel, as no data on countercurrent condensation were readily available in the literature. The good agreement obtained here for a countercurrent flow in an annulus suggests that the condensation mass flow does not depend strongly on geometry and/or vapor flow direction, for the range of flow rates discussed. This unexpected indication awaits experimental verification. We have tried to use the same correlation to describe the condensation component on the liquid being bypassed. However, the agreement obtained was poor. This was expected as the flow configuration of the falling film is different from the configuration of the bypassed liquid. Thus, we have determined the condensation on the liquid being bypassed by assuming that the condensation efficiency is constant for a given geometry and flow conditions and is equal to the efficiency at the complete bypass point.

We recognize that in applying this idealized one-dimensional model to the three-dimensional phenomena actually occurring even in the small scale models we have ignored several phenomena observed to be of importance at specific conditions, namely, periodic delivery of slugs of water, sweepout of liquid from the lower plenum by the core steam, flooding and voiding of lower plenum liquid, and boiling on the lower plenum hot walls.

In spite of the obvious limitations, the model developed provides a useful tool for examining the effects of the major variables on liquid penetration in a countercurrent flow situation. The physical insights obtained will serve as a basis for modifying and improving existing correlations used for scaling ECC bypass phenomena.

Acknowledgment

This research was sponsored by the U. S. Nuclear Regulatory Commission under Contract NRC-04-76-293-04.

References

1 Cudnik, R. A., et al. "Reactor Safety Program Applications and Coordination, Task 1—Steam-Water Mixing Program and System Hydrodynamics," Quarterly Report, Jan.–Mar. 1976, BMI-NUREG-1949 (June, 1976). Available from National Technical Information Service (NTIS), Springfield, VA 22161.

2 Cudnik, R. A., et al., "Topical Report on Baseline Plenum Filling Behavior in a $^2/_{15}$-Scale Model of a Four-Loop Pressurized Water Reactor," NUREG/CR-0069, BMI-1997 (Apr. 1978). Available from National Technical Information Service (NTIS), Springfield VA 22161.

3 Crowley, C. J., Block, J. A., and Cary, C. N., "Downcomer Effects in a $^1/_{15}$-Scale PWR Geometry—Experimental Data Report," NUREG-0281, Creare TN-242 (Feb. 1977). Available from National Technical Information Service (NTIS), Springfield, VA 22161.

4 Rothe, P. H., Crowley, C. J., and Block, J. A., "Progress on ECC Bypass Scaling," Quarterly Progress Report, Oct.–Dec. 1977, NUREG/CR-0048, Creare TN-272 (Mar. 1978). Available from National Technical Information Service (NTIS), Springfield, VA 22161.

5 Block, J. A., et al., "Analysis of ECC Delivery," Topical Report Creare TN-231 (Apr. 1976). Available from National Technical Information Service (NTIS), Springfield, VA 22161.

6 Carbiener, W. A., et al., "Steam-Water Mixing and System Hydrodynamics Program Task 4," Quarterly Progress Report, Oct.–Dec. 1977, NUREG/CR-0034, BMI-1993 (March, 1978). Available from National Technical Information Service (NTIS), Springfield, VA 22161.

7 Wallis, G. B., *One-Dimensional Two-Phase Flow,* McGraw-Hill New York, 1969.

8 Beckner, W. D., Reyes, Jr., J. N., and Anderson, R., "Analysis of ECC Bypass Data," NUREG-0583, USNRC July 1979.

9 Alb, G. P., and Chambré, P. L., "Correlations for the Penetration of ECC Water in a Model of a PWR Downcomer Annulus," *Nuclear Engineering and Design,* Vol. 53, 1979, p. 237.

10 Amsden, A. A., and Harlow, F. H., "K-TIF: A Two-Fluid Computer Program for Downcomer Flow Dynamics," LASL Report, LA-NUREG-6994 (Jan. 1978). Available from National Technical Information Service (NTIS), Springfield, VA 22161.

11 Ahmad, S. Y., "Axial Distribution of Bulk Temperature and Void Fraction in a Heated Channel with Inlet Subcooling," JOURNAL OF HEAT TRANSFER, Vol. 92, 1970, p. 595.

12 Zuber, N., Staub, F. W., and Bijwaard, G., "Vapor Void Fraction in Subcooled Boiling and in Saturated Boiling Systems," *Proceedings, Third International Heat Transfer Conference,* Chicago, Vol. V., 1966 p. 24.

13 Collier, J. C., *Convective Boiling and Condensation,* McGraw-Hill, London, 1972.

14 Saha, P., and Zuber, N., "Point of Net Vapor Generation and Vapor Void Fraction in Subcooled Boiling," Paper No. B4 7, in *Proceedings, Fifth International Heat Transfer Conference,* Vol. IV, Tokyo, Japan (1974).

15 Linehan, J. H., Petrick, M., and El-Wakil, M. M., "The Condensation of a Saturated Vapor on a Subcooled Film During Stratified Flow," *AIChE Progress Symposium Series,* Vol. 66, No. 102, 1970, p. 11.

16 Liu, J. S. K., Collier, R. P., and Cudnik, R. A., "Flooding of Countercurrent Steam-Water Flow in an Annulus," in *Topics in Two-Phase Heat Transfer and Flow* S. G. Bankoff, ed., ASME, New York, Dec. 1978.

17 Block, J. A., and Wallis, G. B., "Heat Transfer and Fluid Flow Limited by Flooding," *AIChE Symposium Series,* Vol. 74, No. 174, 1978 p. 73.

18 Lee, L., et al. "Local Condensation Rates in Horizontal Cocurrent Steam-Water Flow," *Nonequilibrium Interfacial Transport Processes,* J. C. Chen and S. G. Bankoff, eds., ASME, New York, 1979 pp. 79–83.

19 Collier, R. P., et al., "Status Report on ECC Penetration Scaling Research," NUREG/CR-0651, BMI-2019 (Feb. 1979). Available from National Technical Information Service (NTIS), Springfield, VA 22161.

20 Dworak, J. A., Segev, A., and Collier, R. P., "Scaling Air-Water Flooding in PWR Geometries," *Transaction of the American Nuclear Society,* Vol. 33, 1979, p. 973.

B. L. Bhatt
Asst. Professor.

G. L. Wedekind
Professor.
Mem. ASME

Oakland University
Rochester, Mich. 48063

A Self-Sustained Oscillatory Flow Phenomenon in Two-Phase Condensing Flow Systems

This paper presents the results of an experimental and theoretical investigation of an unstable flow phenomenon that leads to sustained limit-cycle type of oscillations of large amplitude, and which under certain conditions, can involve flow reversals. This unstable behavior normally exists for conditions of low outlet throttling. Upstream compressible volume and downstream inertia appear to be the dominant energy storage mechanisms for the self-sustained oscillations. A linearized analysis based on the system mean void fraction model successfully predicts the experimentally observed stability boundary.

Introduction

Two-phase condensing flow phenomena occur in a variety of industrial applications including reheat and reboiler systems associated with nuclear or conventional power plants, ocean thermal energy conversion, space power generation, solar energy conversion, vapor compression refrigeration and chemical processing.

Fluctuations in two-phase condensing flows, like those observed by Soliman and Berenson [1], have been attributed to local liquid film instabilities in the early stages of the condenser. These instabilities, or waves within the liquid film at the liquid vapor interface, propagate downstream into the semi-annular/stratified flow regime and on into the slug flow regime in the later portions of the condensing flow process. All of these local flow fluctuations, inherent in two-phase flow, contribute to stochastic fluctuations in the outlet flowrate of subcooled liquid. It is significant to note that the amplitudes of these fluctuations may be on the order of magnitude of 5 to 30 percent of the mean value.

During the present investigation, it was observed that under certain operating conditions, particularly with low outlet throttling, these random fluctuations in the outlet flowrate give way to a well-developed sinusoidal oscillation or instability. In fact, the random fluctuations are quite likely the triggering mechanism for this type of system instability. A typical characteristic of this instability is that the outlet liquid flowrate experiences flow oscillations which tend to grow in amplitude up to a certain limit, and then settle down to a sustained oscillatory mode of fixed amplitude. The amplitude of these oscillations can be substantially greater than the mean flowrate, thereby introducing flow reversals in the outlet flowrate.

This type of reversing flow oscillation represents a violent flow process, and thus is not a desirable situation from the standpoint of system design and control. Experimental data representing such a limit cycle type of oscillations are depicted in Fig 1. The initiation, growth and the final limit cycle behavior of these oscillations are quite apparent.

However, since the instability is oscillatory, it is natural to question whether it is related to the density wave or pressure drop-flowrate instabilities encountered in evaporating flows. There are a number of indicators which would eliminate it from being a density wave instability. First and most important, the basic physics which exist in the typical evaporating flow system, experiencing density wave oscillations [2], are not present in a condensing flow system. This is also confirmed in reference [3]. Another indicator is that the frequency of the condensing flow oscillations is strongly dependent upon the volume of vapor upstream of the two-phase region, whereas the frequency for density wave oscillations is normally related to the fluid transport time through the evaporator.

There are, however, some similarities between the observed condensing flow oscillatory instability, and the pressure drop-flowrate instabilities [4] encountered in evaporating flows. The similarities are that the fluid inertia and compressibility form important energy storage mechanisms for both cases. Although there are differences in the two-phase pressure drop-flowrate behavior, the major difference lies in the contribution of transient flow surge characteristics [5] which exist for condensing but not for evaporating flow systems. Therefore, the unstable flow oscillations to be investigated appear to be unique to condensing flow systems.

As already mentioned, the objectives of this paper are to present the results of a study aimed at determining the principal physical mechanisms responsible for the occurrence of the above-mentioned sustained oscillatory behavior, and to formulate a theoretical model which adequately describes these mechanisms. A linearized analysis will then be used to establish a criterion for the onset of the observed unstable flow phenomenon. These theoretical results will be verified by direct comparison with the experimental observations. Also, a comparison will be made between the theoretical and experimentally observed frequencies of oscillations for various operating conditions. Finally, the system of non-linear governing equations will be solved numerically in an effort to establish the fact that the theoretical model predicts the existence of a type of *limit cycle.*

Discussion of Physical Mechanisms Responsible for Oscillations

Before going into the analytical details of the problem under consideration, it seems appropriate to discuss the possible physical mechanisms responsible for the limit cycle oscillations depicted in Fig. 1.

Referring to the schematic of the flow system depicted in Fig. 2, assume that the condenser is initially operating under what is conventionally referred to as steady-state conditions. Also, assume that the system inlet and outlet pressures, p_i and p_0 respectively, remain constant, and that flow resistances of the system are concentrated at the system inlet and outlet. Next, initially assume that an inherent fluctuation or a disturbance in the two-phase region causes a slight increase in the system pressure, p, which is assumed to be uniform over the two-phase and the upstream vapor region. This action has two primary implications. First it may tend to reduce the flowrate coming into the system from the high pressure reservoir. The magnitude of this effect will of course depend upon the extent of throttling or the magnitude of the flow resistance that exists across the upstream throttling valve.[1] Second, the slight pressure increase in the system will tend to cause the outlet flowrate of the subcooled liquid to increase. Again the magnitude of this increase depends upon the extent of throttling, or the magnitude of the flow resistance across the

Contributed by the Heat Transfer Division for publication in the JOURNAL OF HEAT TRANSFER. Manuscript received by the Heat Transfer Division January 4, 1980.

---

[1] Under certain conditions the flow may be "choked." In that case, there will not be any flow change across the upstream throttling valve.

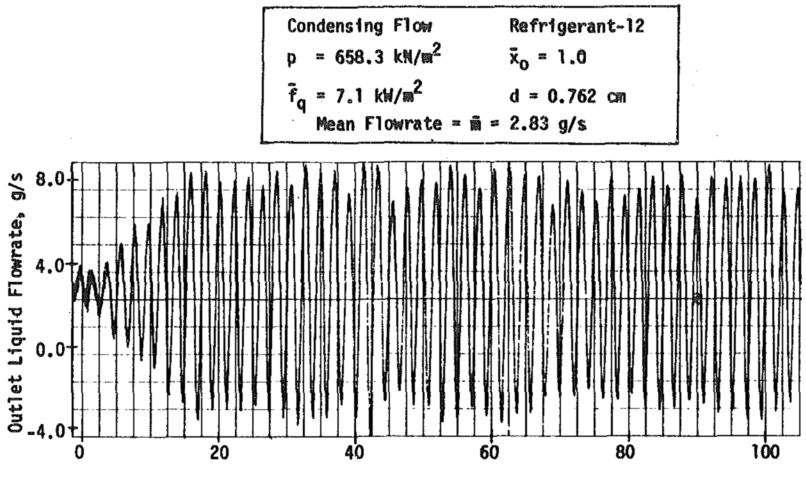

Fig. 1 Transient and sustained flow oscillations in outlet flowrate of subcooled liquid

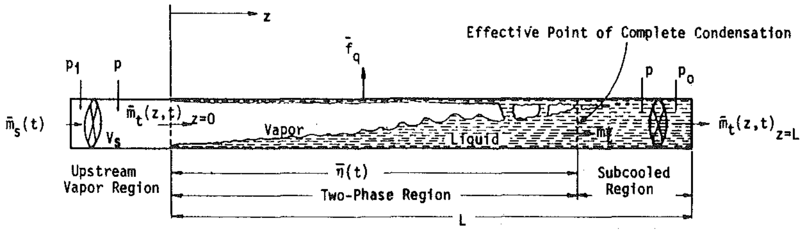

Fig. 2 Schematic of horizontal condensing flow system with upstream vapor region, upstream throttling, and downstream throttling

downstream throttling valve. A secondary effect of the system pressure increase is that there is a momentary increase in the vapor storage due to a slight density increase due to compressibility.

The increase in the liquid flowrate will cause the effective point of complete condensation to move downstream, thus increasing the heat transfer surface area available for condensation. The inertia of the liquid, primarily in the subcooled liquid region but also in the two-phase region, will tend to cause the increased outlet liquid flowrate

Nomenclature

A_t = total cross-sectional area of tube, m^2
$a_0{}^* - a_3{}^*$ = coefficients in equation (20)
$b_0{}^*$ = coefficient in equation (20)
c = (c$_i$ + c$_o$), equation (18)
c_i = intercept on pressure drop axis, equation (14), KN/m^2
c_0 = constant in equation (15), KN/m^2
f_q = local heat flux, W/m^2
$\bar{f}_q$ = spatially averaged heat flux, W/m^2
h = enthalpy of saturated liquid, J/Kg
h' = enthalpy of saturated vapor, J/Kg
k_i, k_o = inlet and exit orifice coefficients, $\Delta p/\rho_a{}'v^2$ and $\Delta p/\rho v^2$, respectively
$k_i{}^*$ = linearized valve resistance at inlet, $2(k_i/\rho_a{}'A_t{}^2)\bar{m}$, KN·s/m^2·g
$k_o{}^*$ = linearized valve resistances at outlet, $2(k_o/\rho A_t{}^2)\bar{m}$, KN·s/m^2·g
L = total length of the condenser plus the length of piping between the outlet of condenser and inlet of the liquid receiver, m
$L_0 = (L - \bar{\eta})$, m
$\bar{m}$ = steady-state mean flowrate through the system, g/s
$\bar{m}_L(t) = \bar{m}_t(z, t)_{z=L}$, g/s
$\bar{m}_s(t)$ = total mass flowrate at inlet of upstream compressible volume, g/s
$m_t(z,t)$ = local instantaneous total mass flowrate of fluid, g/s
$\bar{m}_t{}^*$ = instantaneous nonfluctuating total mass flowrate of fluid leaving two-phase region relative to moving boundary of the two-phase region, g/s
N_c, N_i = dimensionless numbers, equation (31)
N_0 = dimensionless number, equation (30)
P = inside perimeter of tube, m
p = spatial mean system pressure, KN/m^2
p_i = pressure upstream of inlet throttling valve, KN/m^2
p_o = pressure downstream of outlet throttling valve, KN/m^2
S = Laplace variable, s^{-1}
T_o = temperature of subcooled liquid at the outlet, °C
t = time, s
t^* = dimensionless time
V_s = volume of vapor upstream of two-phase region, m^3
$V' = (V_s + A_t\bar{\alpha}_s\bar{\eta})$, m^3
ω_n = natural angular frequency, radians/s
$\omega_n{}^*$ = dimensionless natural angular frequency
$\bar{x}$ = nonfluctuating flow quality
$\bar{x}_0$ = nonfluctuating flow quality at $z = 0$
z = spatial co-ordinate in the axial direction, m
$\bar{\alpha}_a$ = area mean void fraction (nonfluctuating)
$\bar{\alpha}_s$ = system mean void fraction (nonfluctuating)
$\gamma = \dfrac{d\rho'}{dp}$, equation (7), g/m·KN
$\bar{\eta}$ = steady-state position of the effective point of complete condensation, m, equation (13) $\bar{\eta}(t)$ = nonfluctuating effective point of complete condensation, m
ρ = density of saturated liquid, Kg/m^3
ρ' = density of saturated vapor, Kg/m^3
$\rho_a{}'$ = density of saturated vapor at the average pressure across the upstream throttle valve, Kg/m^3
τ_c = time constant of condensing flow system, s

Note: Unless otherwise indicated, barred (-) symbol of quantities generally refer to nonfluctuating quantities in reference to random fluctuations. Also, thermodynamic properties are assumed to be nonfluctuating. However, in order to simplify the notation, no bar (-) has been indicated on these quantities.

to be maintained a little longer than what it would be without the inertia, so that the effective point of complete condensation will move further downstream than normal. As a result of the additional downstream motion of the effective point of complete condensation, the overall heat transfer area available for condensation will increase further, which in turn causes a larger increase in the condensation rate. Since the initial increase in the system pressure earlier would have caused a reduction in the inlet vapor flowrate from the high pressure reservoir, the condensation rate would temporarily be greater than the inlet vapor flowrate. This would result in a depressurization within the two-phase region, and hence within the upstream vapor volume as well.

The system depressurization will cause a reversal of the previously described phenomenon and the entire process will be repeated in a cyclical manner.

If conditions are right, it is possible that the initiated oscillations will grow in magnitude, becoming either unbounded or converge to a type of limit cycle. An unstable linear system would yield unbounded flow oscillations, but non-linear effects such as the downstream throttling would be responsible for limiting the amplitude of the oscillations.

If the above discussion is accurate, then it is apparent that the condenser heat transfer, liquid-vapor density ratio, vapor compressibility, downstream liquid inertia, upstream vapor volume, and upstream and downstream throttling would seem to be the dominant physical parameters responsible for the oscillatory behavior of the condensing flow system. Clearly the various processes that seem to be operating to produce the observed oscillatory phenomenon must be taking place at proper times and phase shifts such that energy is supplied to the system at the right time and phase to overcome the various damping or viscous effects, otherwise the large oscillations could not be sustained.

In concluding this section, it should be pointed out that the above qualitative discussion is intended for the particular unstable flow phenomenon which is under consideration in this study, which may be only one of many possible flow instabilities encountered in condensing flow systems. For instance, in parallel multi-tube condensers used in reheat systems associated with nuclear power plants, one of the reviewers of this paper indicated that condensation in the outlet header might drive the system unstable; thus the exit vapor volume, not considered in the present work, would be an important parameter.

Model for Unstable Flow Phenomenon

In view of the principal physical mechanisms responsible for the unstable flow phenomenon discussed in the previous section, it becomes necessary to couple the effects of the upstream vapor volume, downstream liquid inertia, and upstream and downstream throttling with the two-phase region. Figure 2 represents a schematic for such a flow system.

In the formulation of the model for predicting the onset of the unstable flow phenomenon, the concept of a system mean void fraction [5, 6] will be utilized to describe the primary physical mechanisms involved in the two-phase region. The nonfluctuating system mean void fraction, $\bar{\alpha}_s$, is expressed as

$$\bar{\alpha}_s(t) = \frac{1}{\bar{\eta}(t)} \int_{z=0}^{\bar{\eta}(t)} \bar{\alpha}_a(z, t) dz \qquad (1)$$

where $\bar{\alpha}_a(z, t)$ is the local area mean void fraction.

Together with the concept of a system mean void fraction, the model will be formulated around the conservation of mass and energy principles applied to the various regions in the condenser. Both the effects of compressibility of vapor and the inertia of liquid will be incorporated into the formulation. Since it is proposed to study the onset of unstable flow phenomenon in the absence of any externally forced flow changes, care will have to be taken such that the system is allowed to close on itself and be responsive to any feedback effects.

Two-Phase Region. The condensing flow system model for this region will be formulated around the following simplifications.

1 The system mean void fraction is assumed to be invariant with time.

2 The random fluctuations due to the stochastic nature of the two-phase flow process are assumed not to influence the deterministic transients.

3 Viscous dissipation, longitudinal heat conduction and changes in kinetic energy are neglected.

4 The specific enthalpies and the density of the liquid are assumed to be the saturated properties, independent of both axial position and time, and evaluated at the time averaged mean system pressure.

5 The density of the vapor phase is assumed to be a function of mean system pressure, which is allowed to vary with time.

6 The spatially averaged heat flux, for the entire two-phase region, is assumed to be independent of time.

Conservation of Mass and Energy. The conservation of mass principle, simultaneously applied to the liquid and vapor in the two-phase region can be expressed as

$$\frac{d}{dt} \int_{z=0}^{\bar{\eta}(t)} [\rho(1 - \bar{\alpha}_a) + \rho' \bar{\alpha}_a] A_t dz = m_t(z, t)_{z=0} - \overline{m}_t^* \qquad (2)$$

The conservation of energy principle simultaneously applied to the liquid and vapor in the two-phase region can be expressed as

$$\frac{d}{dt} \int_{z=0}^{\bar{\eta}(t)} [\rho h(1 - \bar{\alpha}_a) + \rho' h' \bar{\alpha}_a] A_t dz$$
$$= - \int_{z=0}^{\bar{\eta}(t)} f_q P \, dz + \{[h(1 - \bar{x}) + h' \bar{x}] m_t(z, t)\}_{z=0} - h \overline{m}_t^* \qquad (3)$$

The enthalpy rather than the internal energy is involved as a consequence of the flow work at the inlet and outlet, and, as a consequence of the boundary work which exists because the system boundary is moving with time. It is also assumed that slight changes in the system energy, due to changes in the system pressure, are small in comparison to each one of the individual terms on the right-hand side of the above equation.

Combined Conservation of Mass and Energy. Equations (2) and (3) along with equation (1), assumptions (1, 4) and (5), and an inlet flow quality of unity, yield after rearrangement

$$A_t \rho' (h' - h) \bar{\alpha}_s \frac{d\bar{\eta}(t)}{dt} + A_t (h' - h) \bar{\alpha}_s \bar{\eta}(t) \frac{d\rho'}{dt}$$
$$= -\bar{f}_q P \bar{\eta}(t) + (h' - h) \overline{m}_t(z, t)_{z=0} \qquad (4)$$

This equation, in the absence of compressibility effects, reduces to equation (7) of reference [5], which is the incompressible form of the governing differential equation for the effective point of complete condensation.

Upstream Vapor Region. The upstream vapor region, as depicted in Fig. 2, represents the volume of vapor upstream of the two-phase region and downstream of the throttling valve. For simplicity, this vapor is assumed to be saturated and at the mean condenser pressure, p. Also, it is assumed to occupy a constant volume, V_s, throughout which the density, ρ', is uniform but time varying. These assumptions also imply that any pressure drop in this vapor region is negligible, except across the inlet throttling valve.

Conservation of Mass. The conservation of mass principle when applied to the upstream vapor region yields

$$V_s \frac{d\rho'}{dt} = \overline{m}_s(t) - \overline{m}_t(z, t)_{z=0} \qquad (5)$$

Pressure Drop Across the Inlet Throttling Valve. The vapor flows into the upstream vapor region from a vapor source[2] after flowing across a throttling valve (see Fig. 2). Therefore, the pressure drop across the valve can be expressed as[3]

---

[2] In the present work the vapor source is the high pressure reservoir (see Fig. 3 of reference [5]).

[3] Assuming that the flow is not choked.

$$p_i - p(t) = \frac{k_i}{\rho_a' A_t^2}\overline{m}_s^2(t) \tag{6}$$

where p_i is invariant with time.

Compressibility of Vapor. For small changes in the mean condenser pressure, p, the vapor density ρ' can be related to it by the equation of state

$$\frac{d\rho'}{dt} = \gamma\frac{dp}{dt} \tag{7}$$

Subcooled Liquid Region. With reference again to Fig. 2, the subcooled liquid region is represented by $\overline{\eta}(t) < z \leq L$. For simplicity, it will be assumed that the density of liquid in the subcooled region is the same as that of saturated liquid.

Conservation of Mass. Applying the conservation of mass principle to the subcooled region yields

$$-\rho A_t\frac{d\overline{\eta}(t)}{dt} = \overline{m}_t^* - \overline{m}_L(t) \tag{8}$$

Pressure Drop in the Subcooled Liquid Region. Both viscous and inertia effects are assumed to exist in the subcooled liquid region at the condenser outlet. The total pressure drop can be expressed as the sum of the viscous pressure drop and the inertia pressure drop. Therefore,

$$p(t) - p_o = \frac{k_o}{\rho A_t^2}\overline{m}_L^2(t) + \left\{\frac{L - \overline{\eta}(t)}{A_t}\right\}\frac{d\overline{m}_{L(t)}}{dt} \tag{9}$$

where the outlet pressure, p_o, is invariant with time. A detailed derivation of equation (9) which is based upon the application of the momentum principle is given in reference [8].

Combined Condenser Flow System Equations. The governing differential equations for each one of the regions can now be combined. Equation (2), together with assumptions (1, 4) and (5), and equations (5) and (8) can be combined to yield the conservation of mass equation for the whole condenser; thus

$$\overline{m}_L(t) = \overline{m}_s(t) + (\rho - \rho')A_t\overline{\alpha}_s\frac{d\overline{\eta}(t)}{dt} - \{V_s + A_t\overline{\alpha}_s\overline{\eta}(t)\}\frac{d\rho'}{dt} \tag{10}$$

Also, substituting equation (5) into equation (4) leads to

$$\frac{d\overline{\eta}(t)}{dt} + \frac{1}{\tau_c}\overline{\eta}(t) = \frac{\overline{m}_s(t)}{\rho'\overline{\alpha}_s A_t} - \left\{\frac{V_s + A_t\overline{\alpha}_s\overline{\eta}(t)}{A_t\overline{\alpha}_s\rho'}\right\}\frac{d\rho'}{dt} \tag{11}$$

where τ_c is the condenser system time constant [5] given by

$$\tau_c = \frac{A_t\overline{\alpha}_s\rho'(h' - h)}{\overline{f}_q P} \tag{12}$$

Simplification and Linearization of the Governing Equations. The objective of the formulation being developed here is to predict the onset of the particular condensing flow system instability under consideration. This can be done first by linearizing the system of equations that were derived in the last section, and then combining them in an effort to get a single differential equation governing the outlet flowrate of subcooled liquid. The resulting differential equation can then be investigated for the conditions leading to the onset of instabilities. In keeping with these objectives, the following simplifications will be introduced into the governing equations.

1 In addition to the various thermodynamic properties that were considered time invariant, the density ρ' of vapor, wherever it appears in the coefficient of derivative terms, will be assumed to be time invariant and evaluated at the spatial and time averaged system pressure.

2 The effective point of complete condensation, $\overline{\eta}(t)$, which appears in the coefficient of the derivative $(d\rho'/dt)$ as well as in the coefficient of $(d\overline{m}_L/dt)$ in equation (9) will be assumed to be constant and evaluated at its mean position, $\overline{\eta}$, where

$$\overline{\eta} = \frac{1}{2}\{[\overline{\eta}(t)]_{\max} + [\overline{\eta}(t)]_{\min}\} \tag{13}$$

3 The nonlinear flow resistances both at the inlet to the vapor region and at the outlet of the subcooled liquid region will be linearized, by assuming constant local slopes, k_i^* and k_o^*, respectively, of the single phase, steady state pressure drop versus flowrate curve at the operating point. Therefore, equations (6) and (9), together with simplification 2 above can be written as

$$p_i - p(t) = k_i^*\overline{m}_s(t) + c_i \tag{14}$$

and

$$p(t) - p_o = k_o^*\overline{m}_{L(t)} + c_o + \frac{L_o}{A_t}\frac{d\overline{m}_{L(t)}}{dt} \tag{15}$$

where k_i^* and k_o^* are given by

$$k_i^* = \frac{2k_i}{\rho_a' A_t^2}\overline{m}; \quad k_0^* = \frac{2k_o}{\rho A_t^2}\overline{m} \tag{16}$$

Using the above simplifications, it is now possible to obtain a linearized system of equations. Differentiating equation (15) with respect to time and substituting into equation (7) yields

$$\frac{d\rho'}{dt} = \gamma\left\{k_o^*\frac{d\overline{m}_{L(t)}}{dt} + \frac{L_o}{A_t}\frac{d^2 m_{L(t)}}{dt^2}\right\} \tag{17}$$

Equations (14) and (15) can be combined to yield

$$(p_i - p_o) = k_i^*\overline{m}_s(t) + k_o^*\overline{m}_L(t) + \frac{L_o}{A_t}\frac{d\overline{m}_{L(t)}}{dt} + c \tag{18}$$

where $c = (c_i + c_o)$ will be assumed to be a constant, since the objective here is to predict the onset of an unstable flow phenomenon to a slight disturbance about the mean operating flowrate.

$$\text{Also, } (p_i - p_o) = \text{constant} \tag{19}$$

The linearized form of equations (10) and (11) with equations (17–19) form a complete set of linear equations. They can be combined to yield a single differential equation governing the outlet liquid flowrate. This can be achieved once $\overline{m}_s(t)$ and $\overline{\eta}(t)$ are eliminated from the above set of linear equations. The resulting differential equation will be of third order. However, if one also resorts to nondimensionalization, the resulting differential equation becomes

$$a_0^*\frac{d^3 m_L^*}{dt^{*3}} + a_1^*\frac{d^2 m_L^*}{dt^{*2}} + a_2^*\frac{dm_L^*}{dt^*} + a_3^* m_L^* = b_0^* \tag{20}$$

where $m_L^* = [\overline{m}_L(t)/\overline{m}]$; $t^* = (t/\tau_c)(\rho'/\rho)$ and the various coefficients are given by the following equations.

$$a_0^* = (\rho'/\rho)^2\left(\frac{V'\gamma L_0}{A_t\tau_c^2}\right) \tag{21}$$

$$a_1^* = \left(\frac{\rho'}{\rho}\right)\left(\frac{1}{\tau_c}\right)\left[\frac{k_o^*}{k_i^*} + V'\gamma k_o^*\right] + \left(\frac{\rho'}{\rho}\right)^2\frac{1}{\tau_c^2}\left[\frac{V'\gamma L_o}{A_t}\right] \tag{22}$$

$$a_2^* = \left[\frac{k_o^*}{k_i^*} + \frac{\rho'}{\rho}\right] + \left(\frac{\rho'}{\rho}\right)\frac{1}{\tau_c}\left[\frac{L_o}{A_t k_i^*} + V'\gamma k_o^*\right] \tag{23}$$

$$a_3^* = \left[\frac{k_o^*}{k_i^*} + 1.0\right] \tag{24}$$

and

$$b_0^* = \frac{(p_i - p_o) - c}{\overline{m}k_i^*} \tag{25}$$

Prediction of the Onset of Unstable Flow Phenomenon. An examination of equation (20) indicates that for a fixed pressure drop, $(p_i - p_o)$, across the condensing flow system, the forcing function is a constant. The response of the dependent variable in the equation to any momentary disturbance could either decay with time or grow and become unbounded. In between these two limits the system could, if the values of the parameters are just right, go into an oscillatory mode.

To investigate the conditions for marginal stability, a Laplace transform of equation (20) yields the characteristic equation in the Laplace variable 'S', which is of third order and is given by

$$a_0^*S^3 + a_1^*S^2 + a_2^*S + a_3^* = 0 \tag{26}$$

An examination of the roots of the above characteristic equation will give the criterion for the stability of the system [7]. An application of the Routh criterion [7] to equation (26) yields

$$a_1^* a_2^* - a_0^* a_3^* \geq 0 \text{ for stability} \tag{27}$$

Specifically, the equality sign in the above equation yields the condition for marginal stability. Under that condition the associated dimensionless frequency is given by

$$\omega_n^{*2} = \frac{a_3^*}{a_1^*} = \frac{a_2^*}{a_o^*} \tag{28}$$

where the dimensionless and dimensional natural frequencies of the system are related by

$$\omega_n^{*2} = \left(\frac{\rho}{\rho'}\right)^2 \tau_c^2 \omega_n^2 \tag{29}$$

Equations (21–24) can be substituted into equations (27) and (28) to obtain the condition for marginal stability and the associated frequency, respectively, in terms of the various system parameters. However, for the conditions obtainable in the experimental program of this current study, an examination of the various coefficients given by equations (21–24) revealed that in the coefficient a_2^*, the last two terms on the right-hand side of equation (23) were negligible in comparison to the first two terms. Also, for low outlet throttling and reasonably high throttling at inlet, the ratio $(k_o^*/k_i^*) \ll 1.0$. Therefore it can be neglected in equation (24) expressing the coefficient a_3^*. All of the terms in equation (22) were found to be of the same order of magnitude; therefore they are all retained. With the above-mentioned approximations applied to various coefficients, the criterion for the stability of the condensing flow system can be expressed as

$$\{N_c + N_i\} \geq N_0 \tag{30}$$

where

$$N_c = \left(\frac{\tau_c}{V'\gamma k_i^*}\right); \quad N_i = \left(\frac{A_t k_o^* \tau_c}{L_0}\right) \tag{31}$$

and

$$N_0 = \left\{\frac{1}{(\rho/\rho')(k_o^*/k_i^*) + 1} - (\rho'/\rho)\right\} \tag{32}$$

The associated natural frequency for the marginal stability is given by

$$\omega_n = \left\{\left[\frac{k_o^*}{k_i^*} + \frac{\rho'}{\rho}\right]\left[\frac{A_t}{V'\gamma L_0}\right]\right\}^{1/2} \tag{33}$$

Experimental Observations

The objective of the experimental program was to verify the stability criterion developed in the previous section.

Experimental Apparatus. The experimental apparatus involved in this study, except for a few modifications, is the same as described in reference [5]. The basic elements of this experimental apparatus are a high pressure reservoir, a tube in tube type horizontal condenser, and a low pressure reservoir. Vapor is generated in the high pressure reservoir. A regulating valve located at the outlet of this reservoir controls the flow rate of vapor that is supplied to the tube side of the condenser. The subcooled liquid at the outlet of the condenser is then collected and stored in the low pressure reservoir. A throttling valve was located between the outlet of the condenser and the inlet to the low pressure reservoir. Since one of the objectives of the overall experimental program involved a visual observation of the dynamic characteristics of two-phase condensing flow, the present tests were carried out on an all-glass concentric-tube condenser test section.

The other modifications in the experimental schematic shown in Fig. 3 of reference [5] involved removal of the liquid turbine flowmeters and check valves at the downstream end of the condenser. This was done to minimize the flow resistance in the subcooled liquid region and to concentrate the remaining flow resistance at the regulating valve before entering the low pressure reservoir. For certain operating conditions described later in this section, when it was necessary to increase the flow resistance in the subcooled liquid region, it was achieved by throttling the flow at this regulating valve. The valve coefficient of this regulating valve, for various angular positions of opening, was obtained by carefully conducted tests using single phase liquid freon-12.

There was also a provision for varying the length of the piping between the outlet of the condenser and the inlet of the low pressure reservoir. This made it possible to vary the outlet liquid inertia effects. To study the effects due to the upstream compressible volume, provision was made for introducing known compressible volumes into the piping between the high pressure reservoir and the inlet of the two-phase region. These compressible volumes were electrically heated to prevent condensation of vapor inside them. Further details about the experimental apparatus are given in reference [8].

Procedure for Taking Data. The experimental procedure that was followed for verifying the stability criterion developed earlier consisted of establishing obtainable operating conditions which represent a suitable point within the unstable domain of Fig. 3. System instability was indicated by the initiation, growth and the subsequent self-sustained limit cycle oscillations. The next step involved introducing a change in the operating conditions which would make the system go stable. System stability was indicated by a vanishing of the sustained oscillatory behavior and the reappearance of the inherent random fluctuations.

Theoretically, it is possible to establish unstable operation and the subsequent means of stabilizing the system by varying any one or more parameters represented in equation (30). However, it is easy to recognize that the variation of some of the parameters is not conveniently realizable in actual practice. Therefore, a test procedure was devised which made it possible to verify the stability criterion in a reasonably convenient manner.

The procedure consisted of keeping the outlet throttling valve completely open, and slowly varying the inlet vapor flowrate while simultaneously monitoring the pressure drop across the outlet flow resistance, the inlet vapor flowrate, the pressure in the upstream compressible volume and the pressure at inlet to the two-phase region. The initial operating point was then set such that the instability was clearly established. After operating for a while in this mode, the downstream throttling valve in the subcooled liquid region was gradually closed. As the flow resistance increased, it eventually resulted in a gradual attenuation in the amplitude of the self-sustained

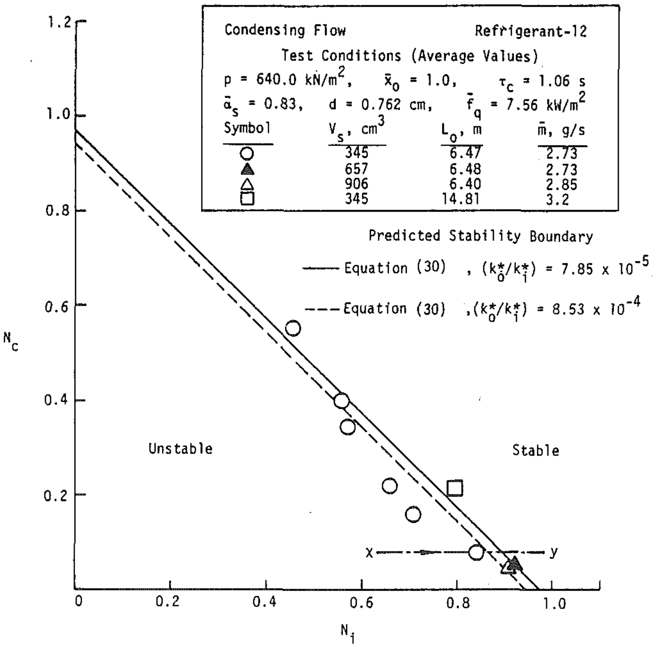

Fig. 3 Comparison of experimental and theoretical stability boundaries. (The data points represent the conditions at which the sustained oscillatory behavior was suppressed and the system reverted back to random fluctuations.)

oscillations until a further increase in resistance would suppress the sustained oscillatory behavior, causing the oscillations to revert back to typical inherent random fluctuations. This final position of the outlet throttling valve was recorded making it possible to determine a quantitative value for the flow resistance from the calibration curve obtained earlier. The operating conditions at which the instability disappeared were used to locate a position on the stability plot of Fig. 3. An estimate of the experimental uncertainty of the data is of the order of ±10 percent. The initial operating conditions for each of the data points shown on the figure were established by varying the inlet throttling between the high pressure reservoir and the upstream vapor volume, the volume of the upstream vapor region and the liquid inertia length.

It is important to point out that after the transition from unstable to stable operation had been achieved by increasing the throttling at the outlet, the throttling was gradually decreased until the instability reappeared. However, as might be expected, the onset of the instability did not appear at the same valve setting where the system had been stabilized earlier, but had to be opened further before the system became unstable. This indicated a type of hysteresis effect. However, if the system was externally disturbed with the system operating at the stability boundary, the unstable oscillatory behavior returned. A quick change in the inlet vapor flowrate followed by returning it to its original value was employed as the external disturbance.

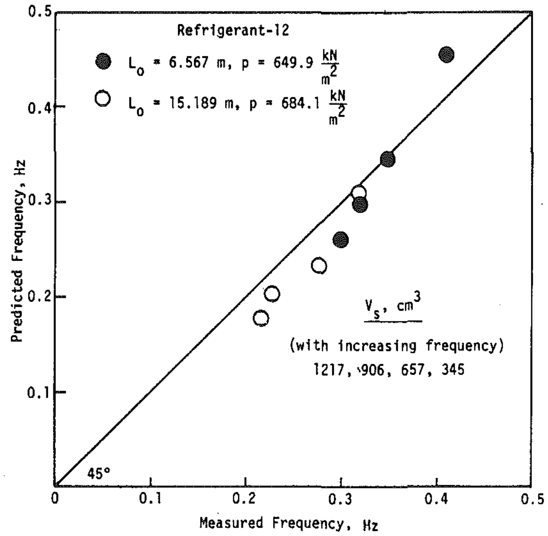

Fig. 4 Comparison of measured and predicted frequency of self-sustained oscillations

Comparison of Theoretical Results with Experimental Data. The experimental data indicating the onset of unstable flow phenomenon or the transition between the unstable and stable operation is shown by the data points in Fig. 3. Also plotted on the same graph is the simplified stability criterion given by equation (30). This is shown by the solid straight line that represents the boundary between the stable and unstable domains. The intercept 'N_o' on the abscissa and the ordinate in Fig. 3 is a function of the liquid/vapor density ratio of the fluid and the ratio of the outlet to the inlet throttling, as represented by the right-hand side of equation (30). For each experimental data point, the value of this intercept will change slightly which shifts the stability boundary a little. For the ranges of density ratio and the ratio of outlet and inlet throttling involved in the experimental data presented here, the shift in the value of 'N_o' is very small; the entire range of values is covered by the zone between the dashed and the solid line.

A comparison of the experimental data and theoretical stability boundary indicates reasonable agreement, especially if the uncertainty in pinpointing the exact position at which the system becomes stable is incorporated into the experimental data. This agreement lends considerable confidence that the physical mechanisms included in the stability model are indeed the principal physical mechanisms governing the particular condensing flow system instability presented in this paper.

Another important check on the capability of the proposed model to predict the observed phenomenon is through the comparison of the predicted frequency at the marginal stability conditions with the

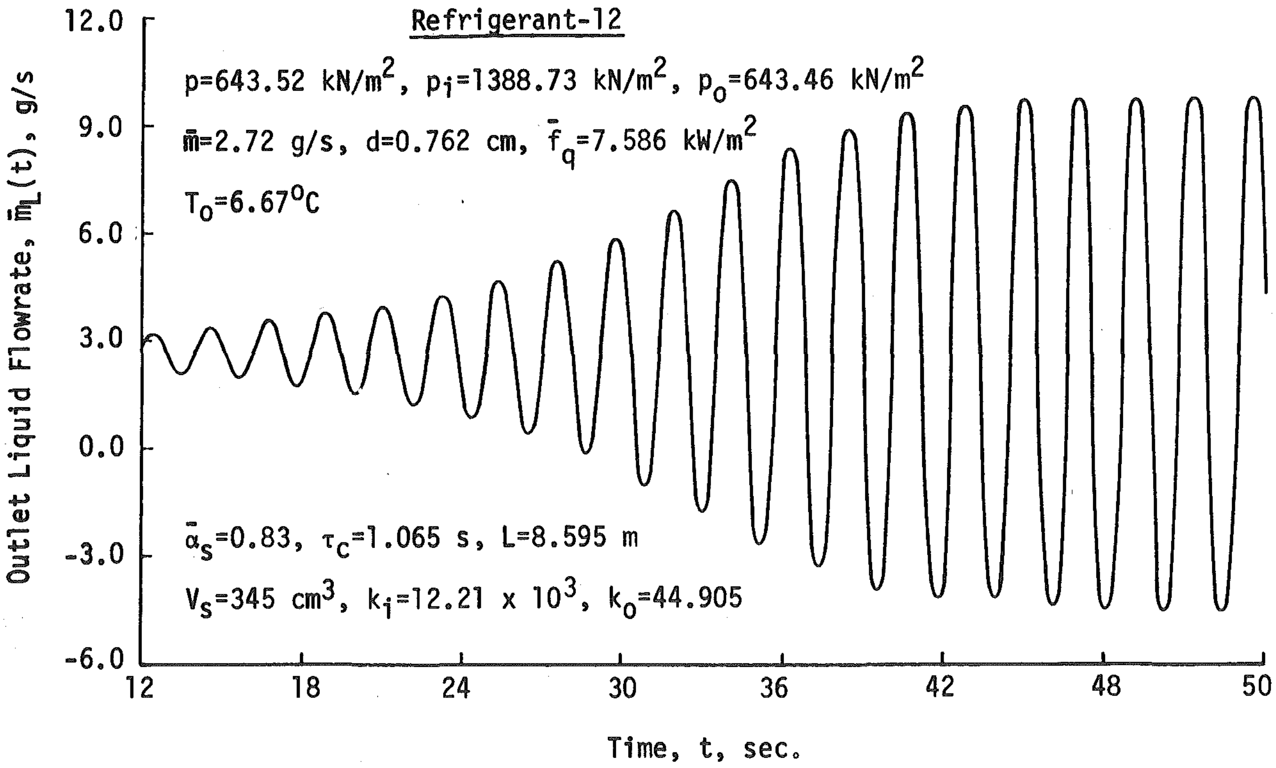

Fig. 5 Predicted response of system mean void fraction model with nonlinearities

frequency of the self-sustained oscillations obtained experimentally. Such a comparison is shown in Fig. 4. Again, the agreement between the predicted and experimental values is quite good. An examination of the expression for the frequency, ω_n, given by equation (33), indicates the presence of the important physical parameters which formed the basis of the analysis presented in the previous section, further confirming the validity of the present model.

Nonlinear Analysis

The linearized analysis presented earlier yields the criterion for the stability of the condensing flow system for the specific instability that is under investigation in this paper. However, it cannot give any amplitude information or growth behavior of the oscillations including the existence of a limit-cycle. This information can be obtained only if the system of nonlinear equations are solved without any linearizing assumptions. Specifically the system of nonlinear equations represented by equations (5–7, 9–11) and (19) need to be solved simultaneously. A digital computer simulation program which enables a user to simulate a system in the same manner as used by analog computer programmers, together with a fourth order Runge-Kutta integration technique, was used to solve the above set. For further details see *reference* [8].

The numerical results of solving the system of equations clearly indicated the existence of a type of limit cycle within the unstable domain of Fig. 3. A typical numerical solution corresponding to the point 'x' in Fig. 3 is shown in Fig. 5. The existence of a limit cycle is clearly discernible and is similar to that obtained experimentally. The peak-to-peak amplitude of the oscillations shown in Fig. 5 (+9.98 to −4.69 g/s) compared fairly well with the experimentally obtained limit cycle oscillations (+6.95 to −1.36 g/s) for the same conditions. When the initial conditions on these numerical solutions were altered to impart a sizable value to the initial derivative of outlet flowrate the resulting limit cycle was again similar to the one shown in Fig. 5. The only difference was that the time required to reach the limit was considerably reduced. It might be useful to note that the limit cycle frequency may not necessarily be the same as the small signal oscillation frequency. The fact that it is indicates that the nonlinearity is "soft;" it is just strong enough to stabilize the oscillation at amplitudes large relative to the steady state. Also, it seems that there is a little more damping in the system than has been accounted for in the model. A possible source could be a finite, transient two-phase pressure drop, which has not been included in the present model.

When the value of the outlet flow resistance was increased, the operating conditions shifted from the position 'x' on the stability plot of Fig. 3 to the point designated by 'y'. Since this latter position is in the stable domain, the numerical solution to the nonlinear equations for this condition showed a decaying oscillatory response.

Summary and Conclusions

The studies presented in this paper were primarily concerned with an experimental and theoretical investigation of an unstable condensing flow phonomenon that leads to a sustained limit-cycle type of oscillations of large amplitude, which under certain conditions can involve flow reversals. This unstable behavior normally existed for conditions of low outlet throttling.

Several physical mechanisms for the occurrence of this type of instability were established. They are the condenser heat transfer, vapor-liquid density ratio, downstream inertia, upstream vapor compressibility, upstream vapor volume, and downstream and upstream flow resistances. A particular interaction between these physical quantities leads to the unstable behavior. A linearized analysis based on the system mean void fraction model successfully predicted the experimentally observed stability boundary. The results were presented in the form of a two-dimensional stability plot.

Upstream compressible volume and downstream inertia appear to be the dominant energy storage mechanisms for the self-sustained limit cycle oscillations. The major transient characteristics of these experimentally observed oscillations were predicted by the system mean void fraction model with nonlinear elements.

Acknowledgments

The authors would like to acknowledge the National Science Foundation Engineering Division, Mechanical Sciences and Engineering Section, Heat Transfer Program for its part in the support of this research under Grants GK-35884 and ENG-7823982. The Oakland University Research Committee is also acknowledged for its equipment support during the experimental phase of this research.

References

1 Soliman, M., and Berenson, P. J., "Flow Stability and Gravitational Effect in Condenser Tubes," *Proceedings of the Fourth International Heat Transfer Conference*, Paris, France, Vol. VI, 1970, paper No. Cs 1.8.

2 Stenning, A. H., and Veziroglu, T. N., "Flow Oscillation Modes in Forced-Convection Boiling," *Proceedings of 1965 Heat Transfer and Fluid Mechanics Institute*, Stanford University Press, 1965, pp. 301–316.

3 "The Design and Performance Analysis of Compact Heat Exchangers," Vol. 1, Northern Research and Engineering Corporation, p. 204, 1965.

4 Maulbetsch, J. S., and Griffith, P., "System-Induced Instabilities in Forced Convection Flows with Subcooled Boiling," *Proceedings of the Third International Heat Transfer Conference*, August 1966, pp. 247–257.

5 Wedekind, G. L., and Bhatt, B. L., "An Experimental and Theoretical Investigation into Thermally Governed Transient Flow Surges in Two-Phase Condensing Flow," *Proceedings of the Two-Phase Flow and Heat Transfer Symposium-Workshop*, Fort Lauderdale, Fla., Oct. 1976. Also, ASME JOURNAL OF HEAT TRANSFER, Vol. 99, No. 4, Nov. 1977, pp. 561–567.

6 Wedekind, G. L., Bhatt, B. L., and Beck, B. T., "A System Mean Void Fraction Model for Predicting Various Transient Phenomena Associated with Two-Phase Evaporating and Condensing Flows," *Proceedings of the NATO Advanced Study Institute on Two-Phase Flows and Heat Transfer*, Istanbul, Turkey, Aug. 1976. Also, *International Journal of Multiphase Flow*, Vol. 4, 1978, pp. 97–114.

7 Porter, B., *Stability Criteria for Linear Dynamical Systems*, Academic Press, New York, 1968.

8 Bhatt, B. L., "An Experimental and Theoretical Study of Various Transient and Oscillatory Flow Phenomena in Two-Phase Condensing Flow Systems," Ph.D. Thesis, School of Engineering, Oakland University, Rochester, Mich., 1978.

S. Chongrungreong
Chulalongkorn University,
Bangkok, Thailand

H. J. Sauer, Jr.
University of Missouri-Rolla,
Rolla, MO 65401

Nucleate Boiling Performance of Refrigerants and Refrigerant-Oil Mixtures

Current and previous studies by the authors and others have shown shown that the carry-over of oil in refrigeration systems can have a significant influence on the boiling performance in the evaporator of refrigeration systems. This investigation was conducted primarily to develop a general correlation equation for predicting the heat transfer coefficient for refrigerants and refrigerant-oil mixtures under pool boiling conditions. Experimental results were obtained to establish the validity of the correlation equation.

Introduction

Many water chillers of the centrifugal type have evaporators utilizing a flooded mode of operation whereby the water is circulated through the tubes and refrigerant evaporates on the shell side of the tubes. Many of the refrigerants in common use today are miscible in lubricant oil. As a result, for systems with oil-lubricated compressors, some amount of oil is transported through the system. The fluid boiling on the outside of the tubes in the evaporator is a refrigerant-oil mixture.

Boiling heat transfer has been studied utilizing many techniques. These studies have indicated that several variables are important in nucleate boiling such as pressure, fluid properties, surface condition, boiling temperature, type and amount of impurities, and others. Experimental observations have shown that changes in magnitude of these properties and conditions significantly affect pool boiling heat transfer.

The effect of oil in refrigerants on pool boiling heat flux was investigated by Stephan [1] and Dougherty and Sauer [2]. The results demonstrated that the boiling temperature of the oil-refrigerant mixture is higher than that for the pure refrigerant at the same pressure. In the current study, saturation temperature at the higher oil concentration was 2°C above that for the pure refrigerant. Other thermodynamic properties of the refrigerant are significantly changed by the addition of oil. Both viscosity and surface tension are increased when oil goes into solution with the refrigerant. As a result of these and very possibly other changes, the boiling heat transfer characteristics of refrigerant-oil mixtures are significantly different from the boiling performance of the pure refrigerant. Therefore, a refrigerant-oil mixture could possibly either increase or decrease heat transfer performance as a result of the influence oil has on the thermophysical properties of the refrigerant. The refrigerants completely miscible in oil, such as R-12 and R-11, generally have shown decreased heat transfer performance with increasing percentage of oil in the mixture. The only aberation in this rather systematic reduction occurs at oil concentrations of 3 percent or less. In some cases, the foaming action of the oil may actually increase the heat transfer coefficient as oil concentration goes from 0 to 3 percent. For oil below 3 percent by weight in the mixture, this change should be small enough that design or performance calculations based on oil-free heat transfer data can be made without serious errors.

Many papers have been published dealing with the boiling of mixtures and no attempt has been made herein to provide a review of other than the most directly pertinent articles.

Existing Predictive Equations

As a result of the lack of complete understanding of the nucleate boiling mechanism and the surface and geometric effects on nucleate boiling, reliable generalized correlations have not yet been found. Table 1 provides a listing of some of the existing, commonly used, correlations for pool nucleate boiling of single component fluids. When comparisons are made with available experimental data on the boiling of refrigerants, each of these predictive equations leaves something to be desired.

Development of Correlation

The principal assumptions made in the present study are

1 The system contains only pure, air-free, refrigerant or oil-refrigerant mixture. The properties of the liquid are taken as the properties of the pure refrigerant or of the oil-refrigerant mixture only.

2 The main heat transfer resistance is concentrated in a thin liquid layer, adjacent to the heating surface, in which turbulence is caused by the rapid formation of vapor bubbles; therefore, the height of the liquid in the container is not an independent variable.

3 The mixture of oil and pure refrigerant is an ideal solution because no chemical reaction occurs during mixing and the mixture is homogeneous.

As listed in the previous sections, attempts have been made by various investigators to correlate pool boiling heat transfer data. The boiling mechanism is so complicated that a pure analytical expression for the heat transfer, derived from basic theoretical relations, has not yet been obtained. A semiempirical method employing dimensional analysis proved to be the most satisfactory approach. This method required the proper selection of all variables that affect the nucleate boiling performance.

Nucleate boiling starts when the temperature of the surface exceeds the saturation temperature by a few degrees. Adjacent to the surface a thin layer of superheated liquid is formed in which bubbles nucleate and grow from some preferred spots on the surface. It has been found previously that in nucleate boiling at low heat flux density, both the temperature of the surface and the heat transfer rate vary over the heated area. The values which are usually reported are average values.

The most important variable for derivation of nucleate boiling heat transfer correlation may be taken as the heat flux (Q/A) and the average temperature difference between the surface and the liquid. These two variables are related by the defining equation for the heat transfer coefficient, that is $h = Q/A\Delta T$. By the assumption that the main heat transfer resistance is concentrated in a thin liquid layer adjacent to the heating surface in which turbulence is caused by the rapid formation of vapor bubbles, the height of the liquid in the container is not a primary variable, but the liquid properties should be the controlled variables. However, for a large flooded evaporator there may be a significant "submergence effect" resulting from the liquid head on the refrigerant evaporation process. For example, with R-11, a 2 ft column of liquid generates a static pressure of 1.33 psi and an increase in boiling point, some 5°C higher than at the liquid sur-

---

Contributed by the Heat Transfer Division and presented at the 18th AIChE/ASME National Heat Transfer Conference, San Diego, California, August 6–8, 1979. Revised manuscript received by the Heat Transfer Division January 10, 1980. Paper No. 79-HT-79.

Table 1 Predictive equations for nucleate pool boiling of single component fluids

A. McNeilly [3]: $$\frac{hD}{k_L} = 0.225 \left[\frac{DQ/A}{h_{fg}\mu_L}\right]^{0.69} \left[\frac{PD}{\sigma}\right]^{0.31} \left[\frac{\rho_L - \rho_V}{\rho_V}\right]^{0.33} \left[\frac{\mu_L C_L}{k_L}\right]^{0.69} \qquad (1)$$

B. Rohsenow [4]: $$\frac{C_L \Delta T}{h_{fg}} = C_{sf} \left[\frac{Q/A}{\mu_L h_{fg}} \left(\frac{g_0 \sigma}{g(\rho_L - \rho_V)}\right)^{0.5}\right]^{0.33} \left(\frac{C_L \mu_L}{k_L}\right) \qquad (2)$$

C. Gilmour [5]: $$\left(\frac{h}{C_L G}\right) \left(\frac{C_L \mu}{k_L}\right)^{0.6} \left(\frac{\sigma \rho_L}{p^2}\right)^{0.425} = \frac{\Phi}{(DG/\mu_L)^{0.3}} \qquad (3)$$

D. Kutateladze [6]: $$\frac{h}{k_L} \left(\frac{g_0 \sigma}{g(\rho_L - \rho_V)}\right)^{0.5} = 7. \times 10^{-4} \left[\frac{Q/A}{\alpha_L \rho_V h_{fg}} \left(\frac{g_0 \sigma}{g(\rho_L - \rho_V)}\right)^{0.5}\right]^{0.7} \left[\frac{P}{\sigma} \left(\frac{g_0 \sigma}{g(\rho_L - \rho_V)}\right)^{0.5}\right]^{0.7} \left[\frac{C_L \mu_L}{k_L}\right]^{-0.35} \qquad (4)$$

E. Borishanskiy-Minchenko [7]: $$\frac{h}{k_L} \left(\frac{\sigma}{g(\rho_L - \rho_V)}\right)^{0.5} = 8.7 \times 10^{-4} \left[\frac{Q/A}{\alpha_L \rho_V h_{fg}} \left(\frac{\sigma}{g(\rho_L - \rho_V)}\right)^{0.5}\right]^{0.7} \left[\frac{P}{\sigma} \left(\frac{\sigma}{g(\rho_L - \rho_V)}\right)^{0.5}\right]^{0.7} \qquad (5)$$

F. Forster-Zuber [8]: $$\frac{Q/A}{\Delta T k_L} \left[\frac{\Delta T C_L \rho_L \sqrt{\pi \alpha_L}}{h_{fg} \rho_V} \left(\frac{2\sigma}{\Delta P}\right)^{0.5} \left(\frac{\rho_L}{\Delta P}\right)^{0.25}\right] = 0.0015 \left[\frac{\rho_L}{\mu_L} \left(\frac{\Delta T C_L \rho_L \sqrt{\pi \alpha_L}}{h_{fg} \rho_V}\right)^{0.2}\right]^{0.62} \left[\frac{\mu_L C_L}{k_L}\right]^{0.33} \qquad (6)$$

G. Mikic-Rohsenow [9]: $$\frac{Q/A}{\mu_L h_{fg}} \left(\frac{\sigma g_0}{g(\rho_L - \rho_V)}\right)^{0.5} = B(\phi \Delta T)^{m+1} \qquad (7)$$

where $$\phi^{m+1} = \frac{{k_L}^{0.5} {\rho_L}^{2.125} {C_L}^{2.375} {h_{fg}}^{(m-2.875)} {\rho_V}^{(m-1.875)}}{\mu_L (\rho_L - \rho_V)^{1.125} \sigma^{(m-1.375)} {T_L}^{(m-1.875)}}$$

H. Levy [10]: $$Q/A = \frac{1}{B_L} \frac{k_L C_L {\rho_L}^2}{\sigma T_L (\rho_L - \rho_V)} (\Delta T)^3 \qquad (8)$$

I. Forster-Grief [11]: $$Q/A = 4.3 \times 10^{-5} \frac{\alpha_L C_L \rho_L (T - 459.67)}{\sigma^{0.5} (h_{fg} \rho_V)^{1.5}} [C_L\ (T - 459.67) \alpha^{0.5}]^{0.25} \left(\frac{\rho_L}{\mu_L}\right)^{0.625} \left(\frac{\mu_L C_L}{k_L}\right)^{0.33} (\Delta P)^2 \qquad (9)$$

face. For R-12 the increase would be less than 1°C. In operating systems, this submergence effect is significantly reduced since the boiling refrigerant is full of bubbles and therefore at some density less than for liquid alone. The liquid properties that are the importance variables in nucleate boiling heat transfer are all dependent upon the boiling temperature and boiling pressure. In nucleate boiling, bubbles are created by the expansion of entrapped refrigerant vapor. Therefore, the vapor density of the refrigerant ρ_V and density of the liquid mixture ρ_L are other variables. The degree of turbulence, caused by the bubble formation, is considered to depend on the liquid viscosity μ_L and the diameter of bubbles departing from the surface depends on specific heat, heat flux, thermal conductivity of the liquid, liquid density, vapor density, latent heat of vaporization, thermal diffusivity and the time needed for a bubble to reach the break-away diameter. But the time needed for a bubble to reach this diameter depends on the heat flux (i.e., as heat flux increases, the time decreases). At higher heat flux the surface tension is not an important variable in forming a bubble. As reported by Leppert and Pitts [14], several investigators found that bubble growth is limited by the rate of heat diffusion to the interface, and that "the effects of liquid inertia and surface tension are small and can be neglected." Therefore, surface tension has not been included in the derivation of the equations.

Based on the correlation of the model with experimental data, the most important variable needed to extend the results to mixtures proved the volume fraction of pure liquid refrigerant ϕ_f. It is defined as $\phi_f = V_f/(V_f + V_o)$ where V_f = volume of pure refrigerant; V_o = volume of pure liquid oil. This variable is used to account for the quantities of pure refrigerant in contact with the heating surface when compared with the total refrigerant-oil mixture. Now one can conclude that the heat transfer coefficient depends on Q/A or ΔT, h_{fg}, μ_L, C_L, k_L, ρ_V, ρ_L, T_L, P, and ϕ_f. These variables are then assumed to be related by

$$h = \alpha [X_1]^{a_1} [X_2]^{a_2} [X_3]^{a_3} \ldots [X_n]^{a_n} \qquad (10)$$

The X's can be dimensional groups or dimensionless groups, such as Q/A, $\mu_L C_L/k_L$, etc.

The constants of equation (10) can be determined by changing the equation into the multiple linear regression model as

$$Y = A_0 + \sum_{j=1}^{k} A_j X_j \qquad (11)$$

The coefficients of equation (11) can be determined by using the least-squares technique. This technique is used for deriving a model that "best fits" a set of experimental data. This means that the error function which relates the differences between the model and the data is minimized. The error function to be minimized is the sum of the squares of the differences between each data point and the value predicted by the model.

Nomenclature

A = area
B = proportionality constant in Mikic-Rohsenow equation, dimensionless
B_L = proportionality constant in Levy equation, dimensionless
C = specific heat
C_{sf} = proportionality constant in Rohsenow equation, dimensionless
D = characteristic dimension of heated surface
D_d = diameter of a bubble departing from a horizontal surface
g = earth's gravitational acceleration
g_0 = conversion factor (gravitational constant)
G = mass velocity of liquid, defined for Gilmour equation as $\frac{V}{A}\frac{\rho_L}{\rho_V}$
h = heat transfer coefficient
h_{fg} = latent heat of vaporization
k = thermal conductivity
m = numerical exponent in Mikic-Rohsenow equation, dimensionless
P = pressure
Q = heat transfer rate
q = heat flux density
t = time
T = temperature
T_L = saturation temperature of boiling liquid
ΔT = temperature difference between test surface and bulk liquid, $T_w - T_L$
v = vapor rate
W = weight fraction
α = thermal diffusivity
μ = viscosity
ν = kinematic viscosity
ϕ = function defined in Mikic-Rohsenow equation
ϕ_f = volume fraction of pure refrigerant
Φ = proportionality constant of Gilmour equation, dimensionless
ρ_L = saturated liquid density
ρ_V = saturated vapor density
σ = surface tension

Subscripts

f = fluid
L = liquid
m = mixture
o = oil
V = vapor
w = wall

The resulting equation, developed using experimental data from both this and other investigations [1, 2, 12], proposed for use in predicting the boiling heat transfer coefficient of refrigerant-oil mixtures, is

$$h = 0.05253 \left[\frac{(Q/A)D}{Lh_{fg}}\right]^{0.569} \left[\frac{\mu_L C_L}{k_L}\right]^{0.395} \times [P]^{1.695} \left[\frac{D}{0.01588}\right]^{-0.444} \left[\phi_f \frac{\rho_L}{\rho_V}\right]^{1.579} \quad (12)$$

where h = heat transfer coefficient, $W/m^2 - K$, Q = heat transfer rate, W, A = surface area, m^2, D = characteristic dimension of heated surface, m, μ_L = viscosity of saturated liquid, g/m − s, h_{fg} = latent heat of vaporization, W − s/g, c_L = specific heat of liquid, k_L = thermal conductivity of liquid, W/m − K, P = pressure, atmospheres, ϕ = volume fraction of pure refrigerant, dimensionless, ρ_L = liquid density, g/cm^3, and ρ_V = vapor density, g/cm^3.

Experimental Investigation

The experimental equipment used in this investigation consisted principally of five basic systems: (1) boiling/condensing vessel system, (2) test fluid and cylindrical test element, (3) power supply, (4) auxiliary refrigeration unit for condenser, and (5) instrumentation and control system. Figure 1 shows schematically the arrangement of the various components. The experimental apparatus has been designed and constructed earlier by Dougherty and Sauer [2]. Tests were conducted with type L commercial copper tubing having outside diameters of 0.625, 0.875, and 1.125 inches. Heat transfer results were obtained at pressures of 1 and 2 atmospheres; and with refrigerant-oil compositions of 0, 5, and 10 percent oil by weight. These oils were all paraffin base, but with different viscosities. The corresponding designations and viscosities are shown in Table 2. Data were taken with three types of refrigeration oil. The refrigerant was R-11.

The oil-refrigerant mixtures were prepared on a weight basis by weighing pre-calculated amounts of each pure component to give the required weight percent for the mixture. The volume fraction, ϕ_f, was determined from the weight percents by

$$\phi_f = \frac{W_f/\rho_f}{\dfrac{W_f}{\rho_f} + \dfrac{W_o}{\rho_o}}.$$

Results

Figures 2 and 3 present typical results of heat transfer coefficient versus heat flux density for oil-free refrigerant-11 in comparison with the results of Stephan [1], Rohsenow [4], Forster and Zuber [8], McNeilly [3], Gilmour [5], Borishanskiy and Minchenko [7], Kutateladze [6], Dougherty and Sauer [2], and the proposed predictive equation.

As can be seen from both figures, the current experimental results fall within the range of the various predictive equations. Of these equations, the proposed predictive equation appears to agree best with the experimental data of Dougherty and Sauer and of Stephan. No predictive equations were proposed by these investigations for comparison.

Figure 4 indicates that the present predictive curve agrees very well with Stephan's data. Refrigerant-12 data fall close to the predictive line for pressures of 1 atmosphere, 2 atmospheres and 3 atmospheres. Equation (12) can predict Stephan's data [12] with errors smaller than 16 percent.

Figures 5–9 show the effect of oil concentration and pressure on R-11 boiling. It can be seen that when oil concentration increases the heat transfer coefficient decreases for all three types of oil (3GS, 4GS, and 5GS). These results are in good agreement with those obtained by Stephan [1], Dougherty and Sauer [2], and Chaddock [13] for oil concentrations higher than 3 percent. It was also noted that heat transfer coefficient increases with increasing saturation pressure.

The proposed equation (12) agrees very well with the current data for R-11 as well as with Stephan's data for oil-free refrigerants, R-11, R-12, R-13, R-21, R-22, R-113, R-114, and ammonia, with errors

Table 2 Viscosities of refrigerant oils

oil designation	viscosity
3GS	155 SUS/38°C
4GS	290 SUS/38°C
5GS	515 SUS/38°C

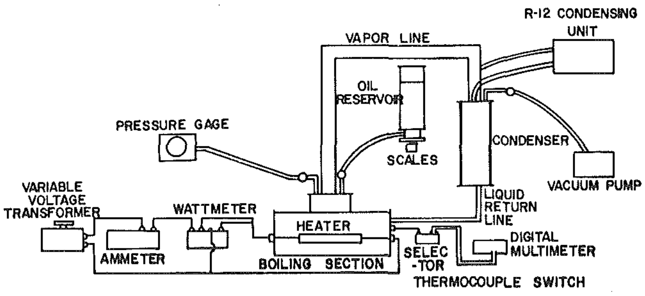

Fig. 1 Schematic of apparatus

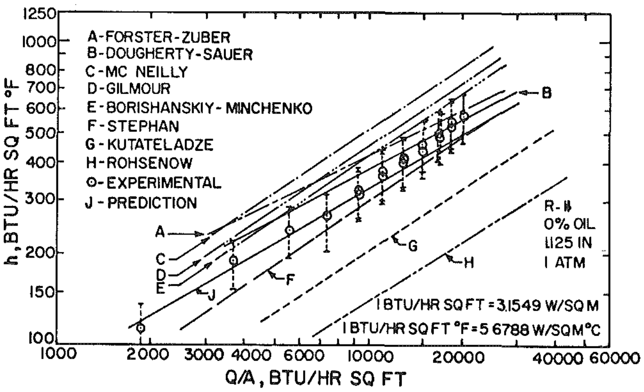

Fig. 2 Comparison of several boiling correlations with experimental data for $1\frac{1}{8}$ in. o.d. tubing

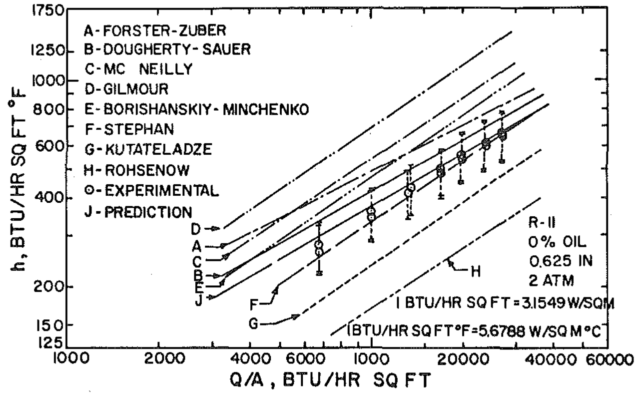

Fig. 3 Comparison of several boiling correlations with experimental data for $\frac{5}{8}$ in. o.d. tubing

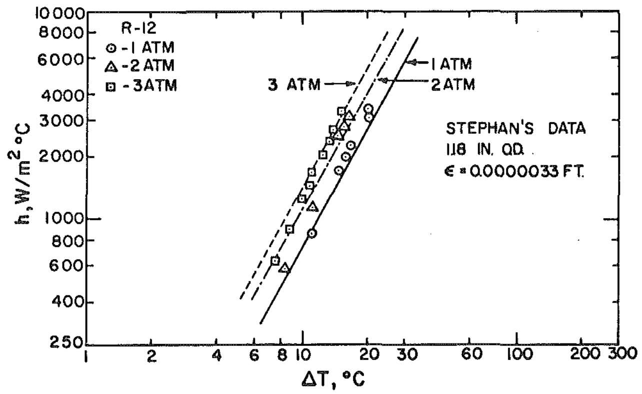

Fig. 4 Comparison of Stephan's [12] data with proposed correlation

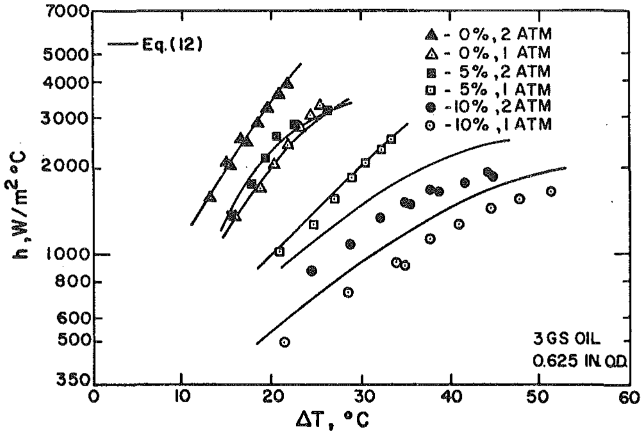

Fig. 5 Comparison of experimental data with proposed correlation for R-11 and 3GS oil boiling from $^5/_8$ in. o.d. tubing

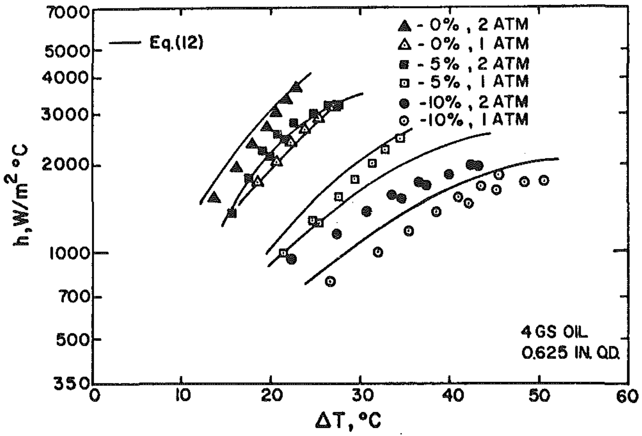

Fig. 6 Comparison of experimental data with proposed correlation for R-11 and 4GS oil boiling from $^5/_8$ in. o.d. tubing

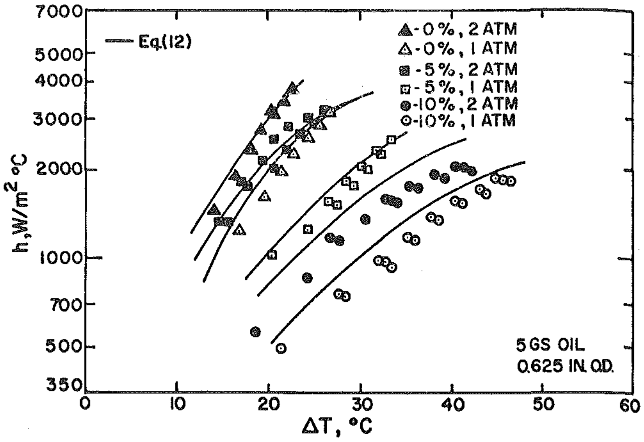

Fig. 7 Comparison of experimental data with proposed correlation for R-11 and 5GS oil boiling from $^5/_8$ in. o.d. tubing

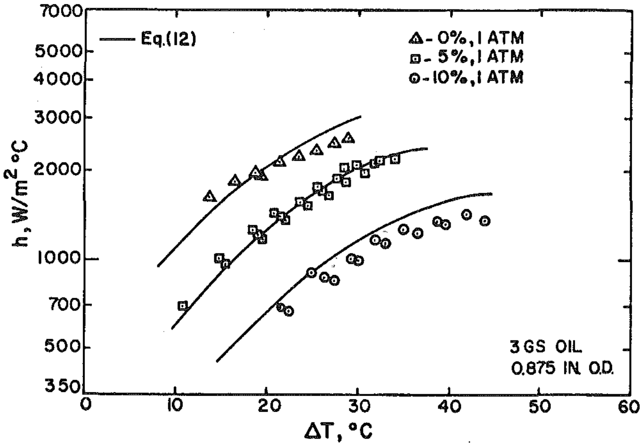

Fig. 8 Comparison of experimental data with proposed correlation for R-11 and 3GS oil boiling from $^7/_8$ in. o.d. tubing

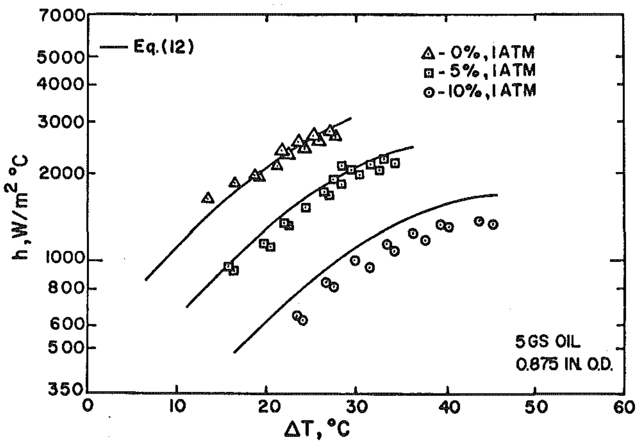

Fig. 9 Comparison of experimental data with proposed correlation for R-11 and 5GS oil boiling from $^7/_8$ in. o.d. tubing

smaller than 16 percent except for ammonia where disagreement was as high as 33 percent.

However, since property data for refrigerant-oil mixtures is extremely limited, a simpler equation was also developed which correlates the heat transfer coefficient with only three variables; Q/A, ϕ_f, and P:

$$h = 6.17[Q/A]^{0.55}[\phi_f]^{3.65}P^{0.24} \tag{13}$$

where h = heat transfer coefficient, W/m^{2}K, Q = heat transfer rate, W, A = surface area, m^2, ϕ_f = volume fraction of pure refrigerant, dimensionless, P = boiling pressure, atmospheres.

Equations (12) and (13) agree qualitatively with the experimental data: (1) h increases as P increases; (2) h decreases as μ increases; (3) h increases as Q/A increases; (4) h slightly increases as D increases; and (5) h increases as ϕ_f increases.

Although surface roughness does not affect the boiling performance and should be included in this equation, there were not sufficient data for inclusion of this parameter of this time.

Quantitatively, equation (12) agrees with the current data as follows: (1) For Refrigerant R-11 with 0 percent oil, the maximum error is less than 17.7 percent; (2) for Refrigerant R-11 with 5 percent oil, the maximum error is less than 33 percent; (3) for Refrigerant R-11 with 10 percent oil the maximum error increases to 43 percent—probably due to inaccuracies in predictive properties of the mixture. The simpler equation (13) actually yields better agreement at the high oil concentration (maximum error of 25 percent at 10 percent oil). This is believed due to lack of accurate property information for the mixture with high oil concentration.

Conclusions and Recommendations

In general, the nucleate boiling heat transfer coefficient increases with increasing pressure, but decreases with increasing oil concentration. For oil concentrations of 5 percent or greater, the heat transfer coefficient always decreases with increasing oil content, and for large oil concentrations (10 percent), the heat transfer coefficient is greatly reduced when compared with oil-free refrigerant. Experimental results also show that the heat transfer coefficient h decreases with increasing viscosity of oil. The data for oil-free refrigerant R-11 agree very well with Stephan's data [12] and Dougherty-Sauer's [11], with the error being smaller than the uncertainty due to the instrumentation (19 percent).

Equation (12) is recommended for prediction of boiling performance of refrigerant-oil mixtures *when one knows* the fluid properties, the diameters of tubes, Q/A and ϕ_f. This equation agrees very well with existing data for the refrigerants.

Equation (13) can also be used to predict the heat transfer coefficient. This equation requires only that Q/A, pressure and the volume fraction of refrigerant or percent of oil be known.

More accurate fluid properties of mixtures, such as viscosity, density, thermal conductivity, and specific heat are needed before accurate prediction of thermal performance can be made.

It should be noted that the results presented in this paper are for single, plain tubes. Heat transfer in typical flooded refrigerant evaporators is affected not only by nucleation but also by the connection of the upward flow of vapor through the tube bundle. Furthermore, since many present day R-11 evaporators used finned tubes, experimental work with such surfaces is continuing.

References

1 Stephan, K., "Influence of Oil on Heat Transfer of Boiling of Freon 12 and Freon 22," XI International Congress of Refrigeration, I.I.R. Bulletin No. 3, 1963.

2 Dougherty, R. L., and Sauer, Jr., H. J., "Nucleate Pool Boiling of Refrigerant-Oil Mixtures from Tubes," *ASHRAE Transactions,* Vol. 80, 1975.

3 McNeilly, M. J., *Journal of the Imperial College of Chemical Engineering,* Vol. 7, p. 18, 1953.

4 Rohsenow, W. M., "A Method of Correlating Heat Transfer for Surface Boiling of Liquids," *Trans. ASME,* Vol. 73, 1951.

5 Gilmour, C. H., "Nucleate Boiling—A Correlation," *Chemical Engineering Progress,* Vol. 54, Oct. 1958, pp. 77–79.

6 Kutateladze, S. S., *Fundamentals of Heat Transfer,* Academic Press, New York, 1963, p. 362.

7 Borishanskiy, V. M., and Minchenko, F. P., *Fundamentals of Heat Transfer,* Academic Press, New York, 1963, p. 362.

8 Forster, H. K., and Zuber, N., "Dynamics of Vapor Bubbles and Boiling Heat Transfer," *AIChE Journal,* Vol. 1, Dec. 1955, pp. 531–535.

9 Mikic, B. B., and Rohsenow, W. M., "A New Correlation of Pool-Boiling Data Including the Effect of Heating Surface Characteristics," ASME JOURNAL OF HEAT TRANSFER, May 1969, pp. 245–250.

10 Levy, S., "Generalized Correlation of Boiling Heat Transfer," ASME JOURNAL OF HEAT TRANSFER, Feb. 1969, pp. 37–42.

11 Forster, K. E., and Grief, R., "Heat Transfer to a Boiling Liquid, Mechanisms and Correlations," ASME JOURNAL OF HEAT TRANSFER, Vol. 81, 1959, p. 43.

12 Stephan, K., "The Computation of Heat Transfer to Boiling Refrigerants," *Kaltechnik,* Vol. 15, 1963.

13 Chaddock, J. B., "Influence of Oil on Refrigerant Evaporator Performance," *ASHRAE Transactions,* Vol. 82, 1976.

14 Leppert, G., and Pitts, C. C., "Boiling," *Advances in Heat Transfer,* Edited by T. F. Irvine and J. P. Hartnett, Vol. 1, p. 218, Academic Press, New York, 1964.

D. K. Edwards
School of Engineering and Applied Science,
University of California,
Los Angeles, Calif.

Anisotropic Conduction and Surface Radiation around a Hollow Cylinder

An analytical expression is developed for the temperature distribution in the wall of a hollow cylinder radiantly heated externally in a circumferentially nonuniform manner. The solution includes two-dimensional anisotropic conduction within the wall, external radiation absorption and emission, and internal radiation heat transfer. Sample results are presented for a graphite-reinforced boom exposed to solar heating in space.

Introduction

The hollow cylinder and sphere are geometries for which exact solutions of the diffuse-walled enclosure problem are known [1]. It is of interest to know how simultaneous wall conduction and radiation affect the heat flux or temperature distribution in hollow cylinders or spheres. The hollow cylinder is particularly interesting, because space vehicle booms are often hollow cylinders made of carbon-reinforced plastics. When such booms, sometimes of the order of 10 m in length, are exposed to solar heating from one side they may bow considerably unless circumferential wall conduction and internal radiation maintains minimal temperature differences across them. Such booms are often fabricated with fiber reinforcements running along surfaces of constant radius and separated in the radial direction. Since graphite reinforcement fibers are highly conducting, the boom walls conduct anisotropically, offering some resistance to conduction in the radial direction even though the wall thickness is small compared to the circumference. The radial resistance tends to make the cylinder wall somewhat more nonisothermal.

Charnes and Raynor [2] and Nichols [3] considered the thin-walled cylinder with wall conduction, external radiation, and rotation but with no internal heat exchange. Nichols [3] and Hrycak [4] treated the sphere, with allowance for internal radiation. Sparrow and Krowech [5] considered the cylinder with external radiation, spike heat input at bases of connecting fins, and internal convection into an opaque fluid. Hrycak and Helgans [6] considered internal radiation and conduction for hollow thin walled cylinders of beryllium copper and accordingly neglected radial resistance to conduction. They formulated the internal radiation in terms of the black body radiosity σT^4 and so obtained a result valid only for perfectly black interior walls. The problem considered here is for two-dimensional conduction and internal radiation including interreflections from a nonblack wall.

Formulation

The heat conduction equation for an anisotropic medium whose principal directions coincide with those of the cylindrical coordinate system is

$$0 = \frac{1}{r}\frac{\partial}{\partial r}\left(rk_r\frac{\partial T}{\partial r}\right) + \frac{1}{r}\frac{\partial}{\partial \theta}\left(\frac{k_\theta \partial T}{r\partial \theta}\right) + \frac{\partial}{\partial z}\left(k_z\frac{\partial T}{\partial z}\right) \tag{1}$$

Due to a high absorption coefficient, that is, a radiation mean free path very short compared to the thickness δ of the cylinder wall, the radiative transfer is considered to be a surface phenomenon affecting only the boundary condition on equation (1). On the exterior, at $r = R + \delta/2$ where R is the mean radius as shown in Fig. 1, the boundary condition is

$$-k_r\frac{\partial T}{\partial r} = \epsilon_e\sigma T^4 - \alpha_e q_e^- \tag{2}$$

where q_e^- is the external irradiation. On the interior, at $r = R\text{-}\delta/2$,

$$+k_r\frac{\partial T}{\partial r} = \epsilon_i\sigma T^4 - \alpha_i q_i^- \tag{3}$$

A reasonably general provision for the externally absorbed radiation $\alpha_e q_e^-$ is taken in the form of a Fourier series

$$G^* = \alpha_e q_e^-/\epsilon_e\sigma T_0^4 = 1 + \sum_{n=1}^{\infty} a_n \cos n\theta \tag{4}$$

where the coefficients a_n are found from

$$a_n = \frac{2}{\pi}\int_0^\pi \frac{\alpha_e q_e^-}{\epsilon_e\sigma T_0^4}\cos n\theta\, d\theta - \frac{2}{\pi}\int_0^\pi \cos n\theta\, d\theta \tag{5}$$

and σT_0^4 is defined by requiring $a_0 = 0$, so that

$$\sigma T_0^4 = \frac{1}{\pi\epsilon_e}\int_0^\pi \alpha_e q_e^-\, d\theta \tag{6}$$

Equation (4) provides for any physically realistic symmetrical external heating. For example, if the external heating is provided by solar irradiation $G_s \cos\beta \cos\theta$ over the half cylinder $-\pi/2 < \theta < \pi/2$ by rays inclined at angle $\pi/2\text{-}\beta$ from the cylinder axis and if the solar absorptivity α_s is not a function of angle of incidence, there is found

$$\sigma T_0^4 = \frac{\alpha_s}{\epsilon_e}\frac{G_s \cos\beta}{\pi} \tag{6a}$$

and

$$a_1 = \pi/2, \quad a_{2k} = \frac{2(-1)^{k+1}}{(2k)^2 - 1}, \quad a_{2k+1} = 0, \tag{5a}$$

for $k = 1,2,3, \ldots$

The internal radiation is formulated using radiosity-irradiation equations for a diffuse enclosure with internally averaged total emissivity/absorptivity ϵ_i. The radiosity is

$$q^+(\theta) = \epsilon_i\sigma T^4 + (1 - \epsilon_i)q^-(\theta) \tag{7}$$

The irradiation is the shape-factor-kernel-weighted average of the radiosity [1] as depicted in Fig. 1.

$$q^-(\theta) = \int_{-\pi}^{\theta} q^+(\theta')\frac{1}{4}\sin\left(\frac{\theta - \theta'}{2}\right)d\theta' + \int_{\theta}^{\pi} q^+(\theta')\frac{1}{4}\sin\left(\frac{\theta' - \theta}{2}\right)d\theta' \tag{8}$$

Linearization is made by writing

$$q^+(\theta) = \sigma T_0^4[1 + 4\epsilon_i T^* + (1 - \epsilon_i)q^*] \tag{9}$$

$$q^-(\theta) = \sigma T_0^4[1 + q^*] \tag{10}$$

where q^* is the dimensionless irradiation

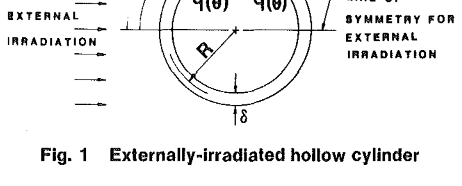

Fig. 1 Externally-irradiated hollow cylinder

Contributed by the Heat Transfer Division for publication in the JOURNAL OF HEAT TRANSFER. Manuscript received by the Heat Transfer Division March 3, 1980.

$$q^*(\theta) = \int_{-\pi}^{+\pi} [4\epsilon_i T^*(\theta') + (1 - \epsilon_i)q^*(\theta')] \frac{1}{4} \sin \frac{|\theta - \theta'|}{2} d\theta' \quad (11)$$

and

$$T^*(\theta,\eta) = (T - T_0)/T_0 \quad (12)$$

The net internal heat flux, the right hand side of equation (3), becomes

$$q_i = \epsilon_i \sigma T_0{}^4 [4T^* - q^*] \quad (13)$$

The quantity $T^*(\theta,\eta)$ is defined in equation (12). In equations (9, 11), and (13) the quantity $T^*(\theta)$ is understood to be evaluated at the inside wall, $T^*(\theta,\eta = 0)$.

Equation (1) is simplified for $\delta/R \ll 1$ as follows. Let $y = r - (R - \delta/2)$ so that the derivatives with respect to r are in terms of y. Then assume that the remaining r terms may be approximated by the constant value of R. Let a dimensionless radial coordinate be

$$\eta = (k_\theta/k_r)^{1/2} y/R \quad (14)$$

Consider the case of a long cylinder where $\partial T/\partial z \doteq 0$. Then equation (1) becomes

$$0 = \frac{\partial^2 T^*}{\partial \eta^2} + \frac{\partial^2 T^*}{\partial \theta^2} \quad (15)$$

subject to

$$(k^*/\eta_e) \frac{\partial T^*}{\partial \eta} = G^* - 1 - 4T^*, \eta = \eta_e \quad (16)$$

and

$$(k^*/\eta_e) \frac{\partial T^*}{\partial \eta} = \frac{\epsilon_i}{\epsilon_e} [4T^* - q^*], \eta = 0 \quad (17)$$

where

$$k^* = \frac{k_\theta \delta}{R^2 \epsilon_e \sigma T_0{}^3}, \eta_e = (k_\theta/k_r)^{1/2} \delta/R \quad (18a,b)$$

Equations (11) and (15) with equations (16, 17), and (4) and the symmetry conditions, $\partial T^*/\partial \theta = 0$ at $\theta = 0,\pi$, formulate the problem.

Series Solution

A series solution to equation (15) follows from separation of variables

$$T^*(\theta,\eta) = \sum_{n=1}^{\infty} [b_n \cosh n\eta + c_n \sinh n\eta] \cos n\theta \quad (19)$$

It clearly satisfies the circumferential symmetry conditions at $\theta = 0$ and π, and it remains to satisfy the radial conditions. The linear combination of cos $n\theta$ terms of $T^*(\theta,0)$ gives rise to a similar result for q^* [7],

$$q^*(\theta) = \sum_{n=1}^{\infty} d_n \cos n\theta \quad (20)$$

where from equation (11)

$$d_n = \frac{4\epsilon_i S_n}{1 - (1 - \epsilon_i)S_n} \quad (21)$$

where

$$S_n = \frac{1}{\cos n\theta} \int_{-\pi}^{+\pi} \frac{1}{4} \sin \frac{|\theta - \theta'|}{2} \cos n\theta' d\theta' = \frac{-1}{(4n^2 - 1)} \quad (22)$$

Hence to satisfy equations (17) and (16) one writes

$$c_n = \frac{\epsilon_i}{\epsilon_0} \frac{\eta_e}{k^*} \frac{1}{n} e_n b_n \quad (23)$$

and

$$b_n = \frac{a_n}{4 \cosh n\eta_e + \dfrac{\epsilon_i}{\epsilon_0} e_n \left[1 + 4 \dfrac{\eta_e}{nk^*} \sinh n\eta_e\right] + \dfrac{nk^*}{\eta_e} \sinh n\eta_e} \quad (24)$$

where

$$e_n = \frac{4(1 - S_n)}{1 - (1 - \epsilon_i)S_n} \quad (25)$$

Discussion

The problem is now completely solved, subject to the simplifications made: (1) symmetrical external irradiation, (2) small δ/R, but, due to anisotrophy, not necessarily small $(k_\theta/k_r)^{1/2}\delta/R$, (3) linearized radiation, and (4) diffuse gray interior wall. For a given external irradiation and surface finish, equation (6) is used to find T_0, and equation (5) fixes the set of a_n coefficients. Then equation (24) fixes b_n; equations (22, 23), and (25) fix c_n; and equation (19) gives T^*. Dimensional values of T follow from equation (12).

For external heating of the form $\alpha_s G_s \cos \beta \cos \theta$, on the half cylinder, where α_s and G_s are not functions of θ, the maximum temperature occurs at $\theta = 0, y = \delta$, and the minimum occurs at $\theta = \pi, y = \delta$. For such an external condition the difference between the temperatures at $\theta = 0$ and $\theta = \pi$ is $2b_1T_0$, on the inside of the cylinder. To minimize this temperature difference for a fixed value of T_0, one wants a large ϵ_i, a small ϵ_e, a large k_θ and δ, and a small R. Equation (6a) shows that, to have a small ϵ_e for a fixed T_0, α_s needs to be small too; i.e., a fixed α_s/ϵ_e must be maintained. Thus the designer may use aluminized tape to achieve a low ϵ_e and add white dots or stripes to adjust α_s/ϵ_e.

The fin approximation $T(\theta,y) \doteq T(\theta)$ may be invoked when sinh η_t/η_e and cosh η_e are very nearly unity. The first-order result for $\Delta T = T_{\max} - T_{\min}$ is that the result taking account of radial resistance equals the result obtained from neglecting it times a correction factor

Nomenclature

a_n = external flux coefficients, equation (5)
b_n = temperature distribution coefficients, equation (19)
c_n = temperature distribution coefficients, equation (19)
d_n = internal radiation coefficients, equations (20, 21)
e_n = internal net flux coefficients, equation (25)
G_s = solar irradiation, W/m^2
k = thermal conductivity, W/m K
n = integer 1,2,3, . . .
q = heat flux, W/m^2
q^+ = radiosity, equation (7), W/m^2
q^- = irradiation, equation (8), W/m^2
r = radial coordinate, m
R = mean radius of cylinder, m
S_n = radiation integral, equation (22)
T = temperature, K
y = distance from inner surface of wall, m
z = axial coordinate, m
α = Absorptivity
β = Angle from normal to z-axis
δ = Wall thickness, m
ϵ = Emissivity
η = Dimensionless y-coordinate, equation (14)
θ = Angle from line of symmetry for external radiation
π = 3.141592 . . .
σ = Stefan-Boltzmann constant, approximately 5.67 × 10^{-8} W/m^2 K^4

Subscripts

e = external
i = internal
n = nth term
0 = zeroth term
r = radial
$r.r.$ = radial resistance
s = solar
θ = Circumferential

Superscripts

* = dimensionless quantity
+ = away from wall
− = toward wall

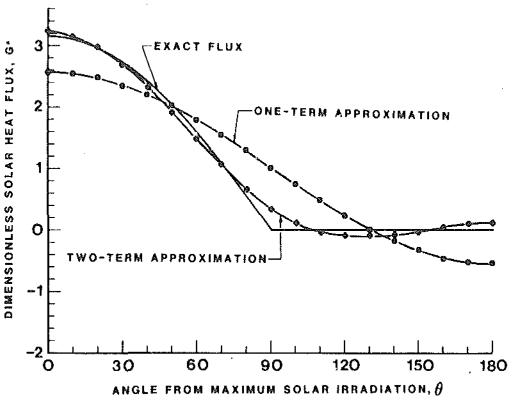

Fig. 2 Series representation of dimensionless solar heat flux

$$\Delta T_{\text{with } r.r.} = \Delta T_{\text{no } r.r.} \left[1 + \left(\frac{16}{4-\epsilon_i}\right)\left(\frac{\delta \epsilon_i \sigma T_0{}^4}{k_r T_0}\right)\right] \qquad (26)$$

Figure 2 gives insight into why only two terms need be carried for most practical calculations. The two-term representation of an $\alpha_s G_s$ $\cos\beta \cos\theta$ external source is seen to be close to the exact curve. Figure 3 shows $T(\theta, \eta = 0)$ as indicated by just the first term and by the first two terms of equation (19) for a sample case: $R = 40$ mm, $\delta = 0.50$ mm, $G_s = 1382$ W/m^2, $\beta = 0$, $\alpha_s = 0.94$, $\epsilon_e = \epsilon_i = 0.90$, $k_\theta = 50$ W/m K, and $k_r = 0.50$ W/m K. The addition of the second term raises the predicted temperature of both the $\theta = 0$ and $\theta = \pi$ points and maintains the fixed temperature difference $2b_1T_0$. Addition of higher-than-second-order terms gives a result which cannot be distinguished from the two-term approximation graphed in Fig. 3.

It is clear that, since the radiation is linearized, an external convective cooling in a terrestrial situation can be readily accommodated. If a convective cooling term $h(T - T_e)$ is added to the right hand side of equation (2), it can be incorporated into the present solution by the following changes: (1) Replace ϵ_e wherever it appeared by

$$\epsilon_e' = \epsilon_e + hT_0/4\sigma T_0{}^4 \qquad (27)$$

(2) Replace equation (5) with

$$a_n = \frac{2}{\pi}\int_0^\pi \frac{\alpha_e q_e{}^- + h(T_e - T_0) + hT_0/4}{\epsilon_e' \sigma T_0{}^4} \cos n\theta d\theta - \frac{2}{\pi}\int_0^\pi \cos n\theta d\theta \qquad (28)$$

(3) Replace equation (6) with

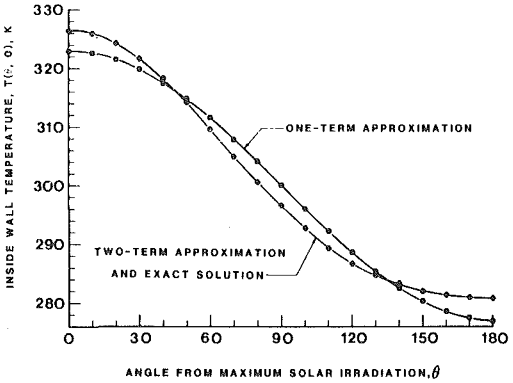

Fig. 3 Temperature distribution on inside surface of wall $\eta_e = 0.125$, $\epsilon_e = \epsilon_i = 0.90$, $T_0 = 300$ K

$$\epsilon_e \sigma T_0{}^4 + h(T_0 - T_e) = \frac{1}{\pi}\int_0^\pi \alpha_e q_e{}^- d\theta \qquad (29)$$

This transcendental equation requires numerical solution to find temperature T_0.

Acknowledgment

The space boom deflection problem was brought to the authors' attention by Mr. J. T. Bevans of TRW Systems. After the analysis reported was made, Mr. T. Ishimoto kindly pointed out the prior work of Hrycak and Helgans.

References

1 Sparrow, E. M., and Cess, R. D., *Radiation Heat Transfer*, Hemisphere/McGraw Hill, New York, 1978, pp. 113–116.
2 Charnes, A., and Raynor, S., "Solar Heating of a Rotating Cylindrical Space Vehicle," *ARS Journal*, Vol. 30, pp. 479–484, 1960.
3 Nichols, L. D., "Surface Temperature Distribution on Thin-Walled Bodies Subjected to Solar Radiation in Interplanetary Space," NASA TN D-584, 1961.
4 Hrycak, P., "Influence of Conduction on Spacecraft Skin Temperatures," *AIAA Journal*, Vol. 1, pp. 2619–2621, 1963.
5 Sparrow, E. M., and Krowech, R. J., "Circumferential Variations of Bore Heat Flux on Outside Surface Temperature for a Solar Collector Tube," ASME JOURNAL OF HEAT TRANSFER, Vol. 99, pp. 360–366, 1977.
6 Hrycak, P., and Helgans, Jr., R. E., "Equilibrium Temperatures of Long Thin-Walled Cylinders in Space," *Chemical Engineering Process Symposium Series*, Vol. 61, pp. 172–179, 1968.
7 Edwards, D. K., and Sun, W. M., "Effect of Wall Radiation on Thermal Instability in a Vertical Cylinder," *International Journal of Heat Mass Transfer*, Vol. 14, pp. 15–19, 1971.

T. R. Wagner
F. P. Incropera
W. G. Houf

Heat Transfer Laboratory,
School of Mechanical Engineering,
Purdue University,
West Lafayette, IN 47907

Visible Radiation Transfer in a Black Ink Suspension

Measurements of the directional and spatial distribution of the radiation intensity have been made for an irradiated India ink suspension, and the results have been used to determine radiation fluxes associated with the forward and backward directions. The inherent radiative properties of the ink have also been measured and used with appropriate theories (the discrete ordinate and three-flux methods) to predict the radiation field within the suspension. For the prescribed laboratory conditions, the radiation is concentrated within a cone of half angle $\theta \approx 0.85$ *rad throughout the suspension, and for this region good agreement is obtained between the intensity measurements and predictions based on the discrete ordinate method. Good agreement is also obtained between radiation fluxes measured for the forward direction and predictions based on both the discrete ordinate and three-flux methods. Agreement between the predicted and measured intensities for* $\theta \gtrsim 0.85$ *rad, as well as agreement between predicted and measured radiation fluxes for the backward direction, is less satisfactory. Differences are attributed to uncertainties in the radiation intensity and phase function measurements.*

Introduction

The problem of visible radiation transfer in liquids is relevant to natural water bodies and to liquid layers used for the collection of solar energy. This transfer strongly influences thermal structure and photosynthetic activity in natural water impoundments [1], as well as the performance of solar ponds [2, 3] and absorbing liquid solar collectors [4–6]. The problem typically involves one-dimensional transfer in a planar, scattering-absorbing suspension. The incident radiation, which may be composed of diffuse and collimated components, experiences Fresnel reflection and refraction at an air-liquid interface, absorption and anisotropic scattering within the liquid, and reflection at the bottom surface.

Interest in the foregoing problem has stimulated efforts to develop detailed procedures for predicting the radiation field in aqueous suspensions [3, 7–10]. These procedures treat one-dimensional transfer in a plane-parallel system and, accounting for anisotropic scattering and surface reflection and refraction effects, may be used to predict radiation intensities and fluxes at any point within the suspension. In recent years, properties required for implementation of the solution methods (the extinction coefficient, the scattering albedo, and the scattering phase function) have been measured for a variety of aqueous suspensions [11–14].

To develop confidence in the use of available theories and radiation property data for predicting solar radiation transfer in liquid suspensions, it is necessary to compare predictions based on such results with radiation field measurements made under controlled laboratory conditions. The objective of this study has been to make such comparisons for a representative aqueous suspension. Because it is presumed to be spectrally nonselective and is receiving consideration as a working fluid for absorbing liquid solar collectors [4], an India ink suspension was chosen for consideration. Detailed measurements have been made of the radiation field in an irradiated suspension, and the results have been compared with predictions based on the use of established theories with radiative properties measured for the ink.

Experimental Procedures

A schematic of the system used for the radiation measurements is shown in Fig. 1. A 294 L plexiglass tank (0.61 m deep and 0.56 by 0.86 m on the sides) was used as a container for the India ink suspension, which was prepared by mixing 10 mL of Higgins 813 Eternal Ink, a commercially available black drawing ink, with 290 L of tap water. The ink is a suspension of carbon black particles, having effective diameters from 0.02 to 0.06 μm, in an aqueous solution of shellac, gums and preservatives. Monochromatic radiation measurements were made by submerging a fiber optic probe in the culture. The probe was constructed of stainless steel tubing (1.9 mm o.d., 1.1 mm i.d.) in which a 1 mm monofilament plastic fiber was inserted. The probe tip was capped with a brass barrel guide having a 0.33 mm aperture and a glass cover. The aperture was separated from the tip by a distance of 11 mm, and the half angle of view of the probe was determined to be 0.058 rad (3.3 deg). The probe was supported by a traversing mechanism which permitted travel in each of the three rectangular coordinates, as well as rotation about a horizontal axis. All probe and traverser components were painted with Nextel velvet black to minimize reflections.

The light source for the experiments consisted of an overhead bank of twelve 150 W flood lamps, arranged 4 by 3 on approximately 0.21 m centers. A large, fused opal (diffusing) glass plate was suspended approximately 1.5 m below the lamps, and white paper sheets were used to form vertical side walls between the lamps and the tank. The sheets minimized light loss and promoted a more uniform distribution of radiation incident on the diffusing glass. A small rectangular section was cut from the glass to permit insertion of the probe traversing mechanism.

The directional distribution of the radiation incident on the suspension was measured by using the fiber optic probe, and the results are shown in Fig. 2. The deviation from isotropic conditions is small (less than 10 percent) for $\theta^* \lesssim 0.7$ rad (40 deg), but becomes significant for larger values of the incident angle, at which the intensity of the incident radiation decreases sharply to zero. The probe was also used to map the variation in the normal intensity ($\theta^* = 0$) over a horizontal plane just above the air interface, and the standard deviation of the measurements was found to be less than 10 percent over a central region which occupied approximately 60 percent of the total surface area of the suspension.

Three different boundaries are pertinent to radiation transfer in the suspension and include the air interface, the tank sides, and the tank bottom. The air interface and the bottom are natural boundaries which characterize many applications, while the tank sides represent an unnatural boundary which could affect the assumption of one-dimensional radiation transfer in the suspension. With an index of refraction of 1.49 for the plexiglass, the water-plexiglass-air interface is completely reflectant to all radiation which is incident on the side walls at angles $\theta \leq 42$ deg. Accordingly, because it is refracted into a cone of half angle $\theta \leq 48.6$ deg, most of the irradiation which is transmitted by the air interface and reaches the sidewalls without having been scattered will be reflected back into the suspension. However, because optical depths associated with the suspension are large and all measurements are made along a vertical line at the center

---

Contributed by the Heat Transfer Division for publication in the JOURNAL OF HEAT TRANSFER. Manuscript received by the Heat Transfer Division November 8, 1979.

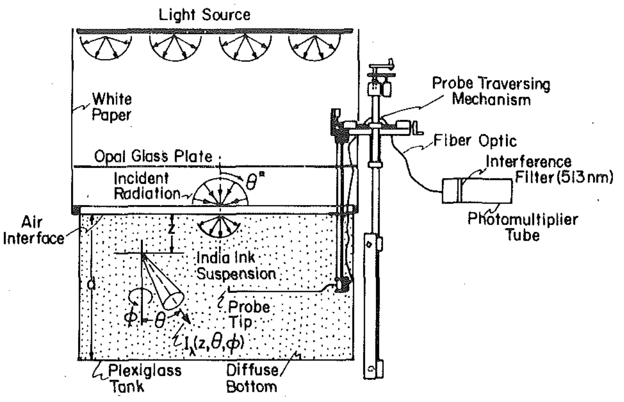

Fig. 1 India ink suspension and measurement system

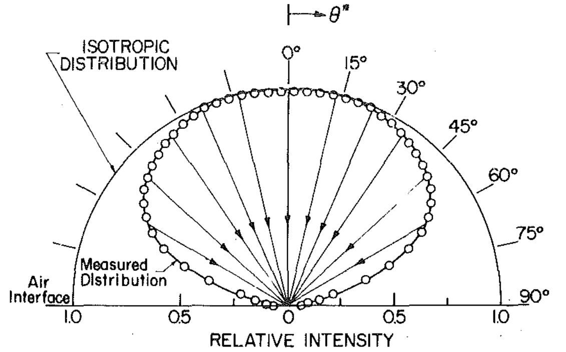

Fig. 2 Actual and isotropic distributions of the radiation incident at the air interface of the suspension

of the tank, it is still reasonable to neglect two and three-dimensional effects resulting from this reflection.

The bottom boundary was controlled through the use of two plexiglass sheets, which were coated with Nextel velvet optical paints. One surface was coated with a diffusely reflecting white paint of reflectance $\rho_d = 0.91$, and the other surface was coated with a black paint of reflectance $\rho_d \approx 0$ [15]. The air interface is optically smooth and, in addition to providing for refraction of all incident radiation into a cone of half angle $\theta = 48.6$ deg (0.85 rad), it provides for the reflection of upwelling radiation incident from the suspension.

Radiation measurements were made at 6 depths in the suspension, and for each depth a total of 51 measurements were made in an angular scan of the probe from $\theta = 0$ rad (probe tip facing upward) to $\theta = \pi$ rad (probe tip facing downward) in increments of 0.0628 rad (3.6 deg). The first depth, z_0, corresponds to a location just below the air-water interface ($z_0 = 6.4$ mm), for which radiation intensities are large and are primarily associated with the forward direction ($0 \leq \theta < \pi/2$ rad). The forward flux at this location, which may be expressed as

$$F_{f,\lambda}(z_0) = \int_0^{2\pi} \int_0^{\pi/2} I_\lambda(z_0, \theta) \cos\theta \sin\theta d\theta d\phi \qquad (1)$$

has been used as a reference condition for normalization of all other fluxes. Accordingly, the normalized flux at any location corresponds to

$$\overline{F}_\lambda(z) = \frac{\int_0^{2\pi} \int_{\theta_1}^{\theta_2} I_\lambda(z, \theta) \cos\theta \sin\theta d\theta d\phi}{\int_0^{2\pi} \int_0^{\pi/2} I_\lambda(z_0, \theta) \cos\theta \sin\theta d\theta d\phi} \qquad (2)$$

where the values of θ_1 and θ_2 depend upon whether one is interested in the forward flux ($\theta_1 = 0, \theta_2 = \pi/2$), the backward flux ($\theta_1 = \pi/2, \theta_2 = \pi$), or the net flux ($\theta_1 = 0, \theta_2 = \pi$). Equation (2) is evaluated from the measurements of this study by assuming the azimuthal dependence of the radiation field to be negligible and by assuming the measured intensity $I_\lambda(z, \theta)$ to be constant over the angle between measurements (0.0628 rad). The normalized flux may then be expressed as

$$\overline{F}_\lambda(z) = \frac{\sum_{i=n_1}^{n_2} [I_\lambda(z, \theta_{i-1}) + I_\lambda(z, \theta_i)][\sin^2(\theta_i) - \sin^2(\theta_{i-1})]}{\sum_{i=1}^{25} [I_\lambda(z_0, \theta_{i-1}) + I_\lambda(z_0, \theta_i)][\sin^2(\theta_i) - \sin^2(\theta_{i-1})]} \qquad (3)$$

where summing from $n_1 = 1$ to $n_2 = 25$ would give the forward flux, from $n_1 = 26$ to $n_2 = 51$ would give the backward flux, and from $n_1 = 1$ to $n_2 = 51$ would give the net flux.

A measure of the spectral intensity of the radiation was obtained from the output of the fiber optic probe, which was rendered monochromatic by passing it through a 513 nm interference filter (Special Optics 9-2103-5145) having an 8 nm bandwidth. The monochromatic radiation was transmitted to a photomultiplier tube (EMI 9558Q), and the resulting signal was transferred to a variable gain current-to-voltage amplifier (Keithley, Model 18000). The output was then averaged over a 10 s interval by using a Matrix (Model 1605) voltage-to-frequency converter with a Data Precision (Model S740) frequency counter. The averaged signal, P, which was recorded using a line printer, is related to the intensity of the radiation intercepted by the probe by an expression of the form

$$P = \alpha \int_{A_p} \int_{\Omega_p} I_\lambda g(\Omega) \mu d\Omega dA \qquad (4)$$

where α is a proportionality constant determined by the sensitivity of the photomultiplier tube and the characteristics of the signal processing system, A_p is the exposed area of the probe, Ω_p is the probe solid angle of view and $g(\Omega)$ is a function accounting for the angular sensitivity of the probe. Neglecting the variation of I_λ over the probe field of view, it follows that, to a good approximation,

$$P = \left[\alpha \int_{A_p} \int_{\Omega_p} g(\Omega) \mu d\Omega dA\right] I_\lambda \qquad (5)$$

where the term in brackets depends on the characteristics of the probe tip design, the photomultiplier tube and the signal processing system.

Nomenclature

d = depth of the suspension, m
F = radiative flux, W/m^2
$\overline{F}$ = normalized flux
F_1, F_2, F_3 = fluxes associated with regions 1 ($0 \leq \theta < \theta_{\text{crit}}$), 2($\theta_{\text{crit}} \leq \theta < \pi/2$) and 3($\pi/2 \leq \theta \leq \pi$) of the three-flux method, W/m^2
F_b = backward or upwelling ($\pi/2 \leq \theta \leq \pi$) flux, W/m^2
F_f = forward or downwelling ($0 \leq \theta < \pi/2$) flux, W/m^2
F_n = net ($0 \leq \theta \leq \pi$) flux, W/m^2
I = intensity, W/m^2-sr
$\overline{I}$ = normalized intensity
p = phase function
z = vertical coordinate (measured from the air-water interface), m
z_0 = location of measurements closest to air-water interface, 6.4 mm
β = extinction coefficient, m^{-1}
θ = polar angle, rad
θ_{crit} = critical angle for internal reflection, rad
κ = absorption coefficient, m^{-1}
μ = cosθ
σ = scattering coefficient, m^{-1}
ρ = reflectance
τ = optical depth
ϕ = azimuthal angle
ω = scattering albedo

Subscripts

b = backward direction
d = bottom condition
f = forward direction
n = net
λ = spectral
1, 2, 3 = regions of the three-flux method

Superscripts

* = incident radiation at the air interface

Accordingly, since all radiation results of this study are normalized, the intensity may be equated to the recorded signal P.

Experimental errors associated with the radiation measurements may be attributed to long term drift in the light source and the photomultiplier tube, as well as suspension settling and sidewall reflection effects. The cumulative error resulting from these effects is small for measurements made in the central portion of the forward direction, where signals are large, but is likely to be significant for measurements associated with the sideward and backward directions, where signals are considerably weaker.

Theoretical Methods

The radiation field within a planar, scattering-absorbing medium is determined by the equation of transfer, which may be expressed as

$$\mu \frac{dI_\lambda}{d\tau_\lambda} = -I_\lambda(\tau_\lambda, \mu, \phi) + \frac{\omega_\lambda}{4\pi} \int_0^{2\pi} \int_{-1}^{+1} p_\lambda(\mu', \phi' \rightarrow \mu, \phi) I_\lambda (\tau_\lambda, \mu', \phi') d\mu' d\phi' \quad (6)$$

The dependent variable is the spectral intensity, $I_\lambda(\tau_\lambda, \mu, \phi)$, of the radiation at the optical depth $\tau_\lambda = \beta_\lambda z$ and in the direction of μ and ϕ. The radiative properties of the medium required to solve equation (6) include the extinction coefficient, β_λ, the scattering albedo, ω_λ, and the scattering phase function, p_λ.

Two methods have been used to solve equation (6), and in both cases the incident radiation was assumed to be uniform and to experience Fresnel reflection and refraction at the air interface, as well as diffuse reflection at the bottom. In the three-flux method of solution [10], the radiation field is separated into three isotropic components associated with the following regions: Region 1 ($0 \leq \theta < \theta_{\text{crit}}$), Region 2 ($\theta_{\text{crit}} \leq \theta < \pi/2$), and Region 3 ($\pi/2 \leq \theta \leq \pi$). The critical angle, θ_{crit}, is the angle of total internal reflection at the air interface and may be computed from knowledge of the change in the index of refraction associated with the interface. For an air-water interface, $\theta_{\text{crit}} = 48.6$ deg (0.85 rad). Previous measurements [18] have indicated that a large fraction of the downward propagating radiation in a diffusely irradiated aqueous suspension is concentrated in Region 1. The three-flux method may be used to determine the variation with optical depth of the radiation fluxes associated with the three regions (F_1, F_2, F_3), from which the forward flux ($F_f = F_1 + F_2$), the backward flux ($F_b = F_3$), and the net flux ($F_n = F_1 + F_2 - F_3$) may be determined.

In the more detailed method of discrete ordinates [9, 10], the radiation field is divided into a finite number of directions (ordinates), and a discrete intensity is assigned to each direction. Twenty-four ordinates were used in this study, and the method allowed for determining the directional distribution of the radiation, as well as the forward, backward and net radiation fluxes, as a function of optical depth. Two solutions were obtained using this method. In one case the directional distribution of the incident radiation was assumed to be isotropic, while in the other case the actual (measured) distribution was used (Fig. 2).

The radiative properties required for implementation of the theoretical methods were obtained from measurements performed on a small sample extracted from the India ink suspension. Procedures previously applied to other suspensions [14] were used to measure the extinction coefficient, β_λ, the absorption coefficient, κ_λ, and the phase function, p_λ, at $\lambda = 513$ nm. The scattering albedo, $\omega_\lambda = \sigma_\lambda/\beta_\lambda$, was then inferred from knowledge of the scattering coefficient, $\sigma_\lambda = \beta_\lambda - \kappa_\lambda$.

Values of $\beta_\lambda = 6.78$ m^{-1} and $\omega_\lambda = 0.15$ were obtained for the sample *of this study (a 0.00345 percent aqueous suspension of India ink), with* the value of β_λ providing an overall optical depth of $\tau_{\lambda,d} = \beta_\lambda d = 4.0$ for the suspension. By comparison, the extinction coefficient and *albedo associated with clear, natural waters at the same wavelength* are $\beta_\lambda \approx 0.4$ m^{-1} and $\omega_\lambda \approx 0.5$ [11]. The comparatively low value of the albedo for the ink suspension may be attributed to the strong effect which the carbon black particles have on radiation absorption. It has been found that, for ink concentrations in the range from approximately 0.0025 to 0.0125 percent, the albedo of the suspension is consistently low and decreases with increasing concentration [16]. This result suggests that the contribution of absorption to extinction becomes more important with increasing concentration.

The phase function distribution obtained for the sample of this study is shown in Fig. 3. The data were fit with a cubic spline approximation and were then shifted upward to satisfy the phase function normalization requirement. The directional distribution of p_λ implies that scattering is primarily in the forward direction, although the distribution is less sharply forward peaked than results obtained for other aqueous suspensions [14].

The accuracy of the extinction coefficient and phase function measurement procedures has been tested by comparing measurements obtained for 2 μm diameter latex spheres with predictions based on the Mie theory [17]. The agreement between results was within approximately ±10 percent for the extinction coefficient and ±25 percent for the phase function, and the discrepancies were attributed to the effects of multiple scattering on the measurements. Due to the low signals associated with phase function measurements

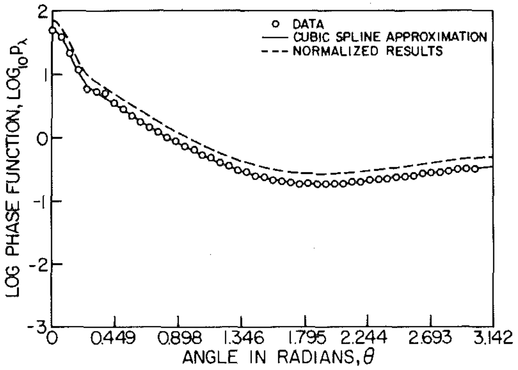

Fig. 3 Log$_{10}$ of the phase function for the India ink

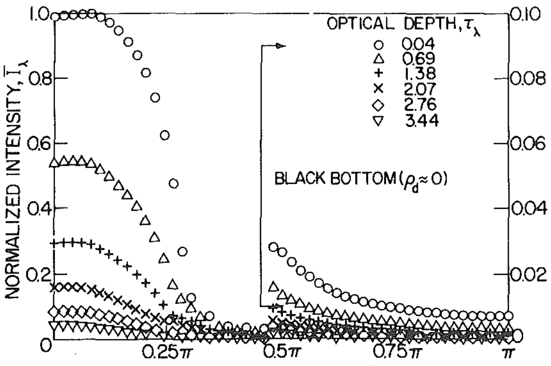

Fig. 4 Directional distribution of the normalized radiation intensity for the India ink suspension with a black bottom

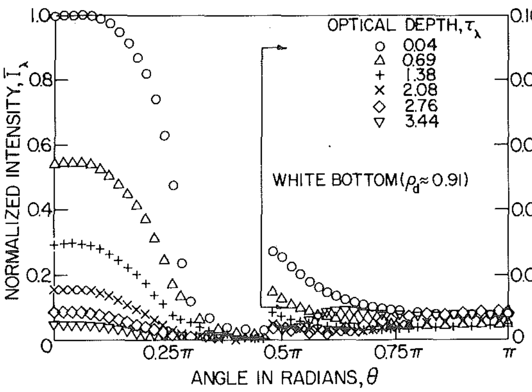

Fig. 5 Directional distribution of the normalized radiation intensity for the India ink suspension with a white bottom

in the backward direction, however, the existence of uncertainties exceeding ±25 percent would not be unreasonable.

Results

Radiation intensity measurements made for the India ink suspension are plotted in Figs. 4 and 5 for the black and white bottom conditions, respectively. The data have been normalized with respect to the maximum intensity at z_0, and a ten-fold scale expansion has been used for the upwelling ($\theta > \pi/2$) intensities. For both bottom conditions the directional distribution of the radiation within the suspension is concentrated within a cone of half angle $\theta \approx 0.27\ \pi$ rad, which corresponds to the critical angle into which all incident radiation is refracted at the air interface. A small amount of radiation appears in the region $0.27\ \pi$ rad $< \theta \leq 0.5\ \pi$ rad and is due primarily to the scattering of radiation from within the cone. For all values of the angle θ associated with the forward direction, absorption acts to diminish the radiation intensity with increasing optical depth, while scattering acts to redistribute the radiation from smaller to larger values of θ. The net effect is one of promoting a more uniform (isotropic) directional distribution of the downwelling radiation with increasing τ_λ. However, the existence of a phase function which is highly forward peaked precludes the effect from becoming significant until large values of τ_λ are reached.

The results of Figs. 4 and 5 also indicate that, for both bottom conditions, the intensity of the downwelling ($\theta < \pi/2$) radiation decays rapidly, and in virtually the same manner, with increasing τ. However, a small amount of radiation does reach the bottom, creating slightly different conditions for the upwelling radiation. For the white bottom, reflection contributes to upwelling intensities which exceed those associated with the black bottom for the lower half ($\tau_\lambda \gtrsim 2$) of the suspension and which do not decrease monotonically with increasing τ_λ. For the black bottom, the only contribution to the upwelling radiation is made by the scattering of downwelling radiation, and the intensity of the upwelling radiation decays monotonically to zero with increasing τ_λ. These effects are revealed more clearly in Fig. 6, where intensity is plotted as a function of optical depth for 11 different angles ranging from 0 to π rad in increments of $\pi/10$ rad. For each angle the intensity is normalized with respect to the value at z_0 for that angle. For the black bottom, the intensity is strongly attenuated, irrespective of angle, while for the white bottom, the intensity of the upwelling radiation in the lower half of the suspension is affected by the bottom reflection process. The effect would become more pronounced with decreasing $\tau_{\lambda,d}$.

Comparisons may be made between the radiation measurements and predictions based upon the discrete ordinate and three-flux methods. Factors which may contribute to discrepancies between the experimental and theoretical results include: (1) departure of the directional distribution of the laboratory irradiation from the distribution used in the analysis, (2) experimental errors associated with the radiation intensity measurements, and (3) experimental uncertainties associated with the radiative property measurements.

Comparisons of the radiation intensity measurements with predictions based on the discrete ordinate method are made in Fig. 7 for the black bottom condition. To standardize the comparisons and to consider the effects of both attenuation and redistribution of the radiation, the experimental and theoretical results are normalized with respect to the intensity corresponding to $z = z_0$ and $\theta = 0$ rad. Predictions have been made for the actual directional distribution of the incident radiation, as well as for an isotropic distribution, which is often assumed in theoretical treatments of the problem (Fig. 2).

Over the entire range of optical depths, the agreement between the data and predictions based on the isotropic distribution (solid curves) is good for the central portion of the forward hemisphere. The data are, however, consistently overpredicted for that portion of the forward direction ranging from $\theta \approx 0.15\ \pi$ rad to $\theta \approx 0.3\ \pi$ rad. This discrepancy may be attributed to the fact that the measured directional distribution of the irradiation (Fig. 2) is characterized by a significant departure from isotropy at an incident angle of $\theta^* \approx 40$ deg ($0.22\ \pi$ rad). Assuming an index of refraction of 1.333 for the aqueous suspension, this angle corresponds to a refracted angle of $\theta \approx 29$ deg ($0.16\ \pi$ rad) in the suspension. Hence, for the assumed isotropic distribution, the angle at which the discrete ordinate method begins to overpredict the measured intensities corresponds to the angle at which the directional distribution of the incident radiation experiences a significant departure from isotropy. This interpretation is supported by comparing the data with predictions based on the measured directional distribution of the incident radiation (dashed curves). In this case there is far better agreement between the results for that portion of the forward hemisphere corresponding to $\theta \lesssim 0.3\ \pi$ rad.

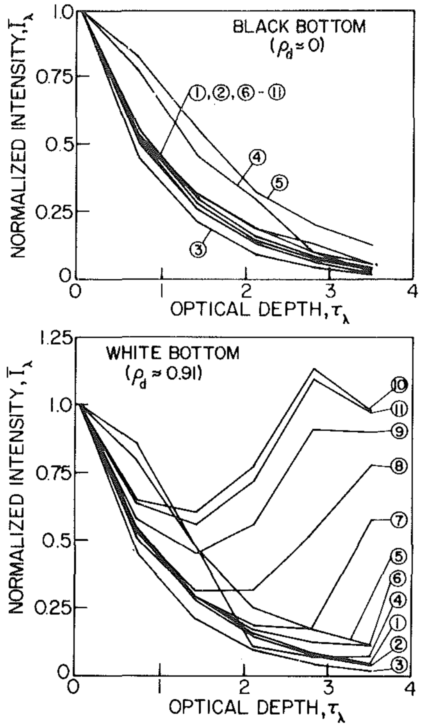

Fig. 6 Variation of the normalized radiation intensity with optical depth for 11 angles ranging from $\theta = 0$ rad (Case 1) to $\theta = \pi$ rad (Case 11) in increments of $\pi/10$ rad

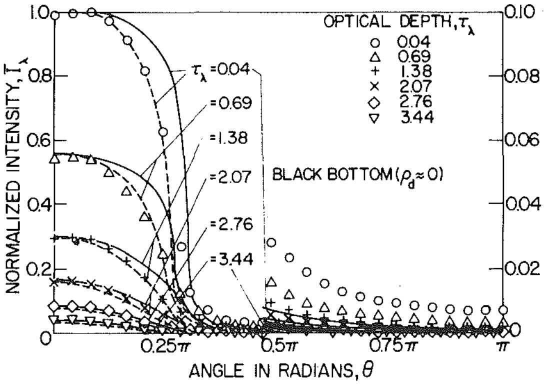

Fig. 7 Comparison of measured radiation intensities with predictions based on the discrete ordinate method (dashed curve computed from actual directional distribution of irradiation; solid curve computed from isotropic approximation)

For portions of the forward direction corresponding to $0.3\ \pi$ rad $\lesssim \theta \leq 0.5\ \pi$ rad and for the entire backward direction ($\theta > 0.5\ \pi$ rad), the data are underpredicted by the discrete ordinate method for both directional distributions of the irradiation. In this case differences are likely due to uncertainties associated with the radiation intensity and phase function measurements, both of which become large with increasing values of θ. Since the suspension opacity is large and since the trends also characterize the white bottom condition, it is unlikely that the discrepancies can be attributed to uncertainties in predicting bottom reflection effects. Note that, for the backward direction, there is negligible difference between the predictions based on the two directional distributions.

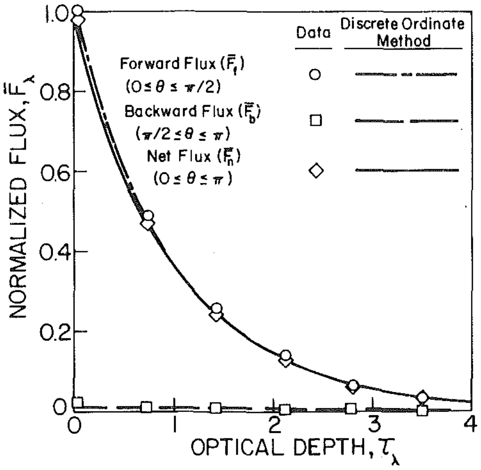

Fig. 8 Comparison of measured forward, backward and net fluxes with predictions based on the discrete ordinate method (black bottom)

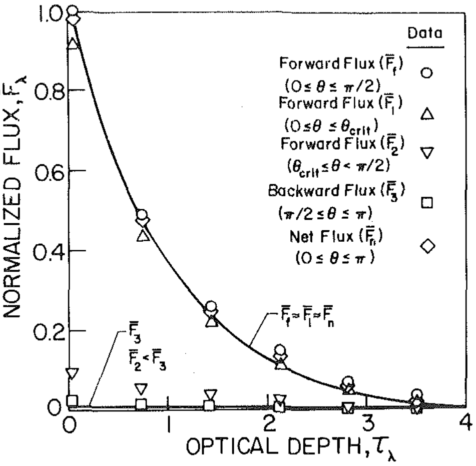

Fig. 9 Comparison of measured fluxes with predictions based on the three-flux method (black bottom)

Comparisons between predictions and measurements may also be made in terms of radiation fluxes computed from equations (2) and (3). Such a comparison is made in Fig. 8, where all fluxes are normalized with respect to the forward flux at z_0. Note that, once normalized, there is negligible difference between predictions based on the actual directional distribution of the irradiation and the assumed isotropic distribution. The agreement between the theoretical and experimental results is excellent throughout the suspension, and it is evident that the inability to accurately predict intensities associated with the backward direction (Fig. 7) has little effect on the accuracy of the predicted forward and net fluxes.

A comparison of the experimental results with predictions based on the three-flux method is made in Fig. 9. Five fluxes are considered and include the combined forward flux, the Region 1 and Region 2 components of the forward flux, the backward flux and the net flux. Although the theoretical method underpredicts the Region 2 forward flux and the backward flux, there is good agreement between results for the complete forward flux, $\bar{F}_f$, and the net flux, $\bar{F}_n$, throughout the suspension.

Summary

Radiation field measurements have been made in a suspension of India ink which is characterized by a large extinction coefficient, $\beta_\lambda = 6.78\ \text{m}^{-1}$, a scattering albedo of $\omega_\lambda = 0.15$ and a scattering phase function which is strongly peaked in the forward direction. The overall optical depth of the suspension is $\tau_{\lambda,d} = 4$, and the suspension has been irradiated across an air interface. The directional distribution of the incident radiation was nearly isotropic up to an angle of $\theta^* \approx 40$ deg (0.70 rad), but was characterized by a significant reduction of the intensity with increasing angle beyond 40 deg. The radiation measurements have been compared with predictions based on the discrete ordinate and three-flux methods, and the key conclusions of the study are as follows.

1 The directional distribution of the measured radiation just below the interface is concentrated within a cone of half angle $\theta \approx 48.6$ deg (0.85 rad) about the nadir, and most of the radiation which is not absorbed remains within this cone throughout the suspension. Some of the radiation is scattered from the cone into the backward direction, but due to the existence of a highly forward peaked phase function, all radiation intensities associated with this direction are less than 3 percent of the maximum intensity associated with the forward direction.

2 The effects of bottom reflection are small, but discernable, for the conditions of this study. In the lower half of the suspension, intensities associated with the backward direction are larger for a white (highly reflecting) bottom than for a black bottom. Differences would become more pronounced with decreasing optical depth, $\tau_{\lambda,d}$.

3 The directional distribution of the radiation intensity within the suspension is well predicted by the discrete ordinate method for $\theta \lesssim 48.6$ deg (0.85 rad), when the measured directional distribution of the irradiation is used for the predictions. If the irradiation is assumed to be isotropic, however, the data are significantly overpredicted for the region 29 deg (0.50 rad) $\lesssim \theta \lesssim 48.6$ deg (0.85 rad). Irrespective of the directional distribution of the irradiation used for the discrete ordinate calculations, the data are underpredicted for $\theta \gtrsim 48.6$ deg. The discrepancy is attributed to uncertainties in the radiation intensity and phase function measurements associated with this region.

4 Good agreement is obtained between the data and predictions of the forward and net radiation fluxes for both the discrete ordinate and three-flux methods.

Acknowledgments

This work was supported by the National Science Foundation under grant ENG 77-22143.

References

1 Dake, J. M. K., and Harleman, D. R. F., "Thermal Stratification in Lakes: Analytical and Laboratory Studies," *Water Resources Research*, Vol. 5, No. 2, 1969, pp. 488–495.

2 Rabl, A., and Nielsen, C. E., "Solar Ponds for Space Heating," *Solar Energy*, Vol. 17, No. 1, 1975, pp. 1–12.

3 Viskanta, R., and Toor, J. S., "Absorption of Solar Radiation in Ponds," *Solar Energy*, Vol. 21, No. 1, 1978, pp. 17–25.

4 Minardi, J. E., and Chuang, H. N., "Performance of Black Liquid Solar Collector," *Solar Energy*, Vol. 17, No. 3, 1975, pp. 179–183.

5 Trentleman, J., and Wojciechowski, P. H., "Performance Analysis of a Black Liquid Absorbing Collector," *Proceedings of The Annual Meeting American Section International Solar Energy Society*, Vol. 1, 1977, pp. 21–25.

6 Landstrom, D. K., Stickford, G. H., Talbert, S. G., and Hess, R. E., "Development of a Low-Temperature, Low-Cost, Solar Collector Using a Black-Liquid Concept," *Proceedings of The Annual Meeting American Section International Solar Energy Society*, Vol. 2, 1978, pp. 228–233.

7 Viskanta, R., and Toor, J. S., "Radiative Transfer in Waters," *Water Resources Research*, Vol. 8, No. 3, 1972, pp. 595–608.

8 Viskanta, R., and Toor, J. S., "Effect of Multiple Scattering on Radiant Energy Transfer in Waters," *Journal Geophysics Research*, Vol. 78, No. 18, 1973, pp. 3538–3551.

9 Daniel, K. J., Laurendeau, N. M., and Incropera, F. P., "Prediction of Radiation Absorption and Scattering in Turbid Water Bodies," ASME JOURNAL OF HEAT TRANSFER, Vol. 101, No. 1, 1979, pp. 63–67.

10 Incropera, F. P., and Houf, W. G., "A Three-Flux Method for Predicting Radiative Transfer in Aqueous Suspensions," ASME JOURNAL OF HEAT TRANSFER, Vol. 101, No. 3, 1979, pp. 496–501.

11 Tyler, J. E., Smith, R. C., and Wilson, W. H., "Predicted Optical Properties for Clear Natural Water," *Journal Optical Society America*, Vol. 62, No. 1, 1972, pp. 83–91.

12 Hale, G. M., and Querry, M. R., "Optical Constants of Water in the 200 nm to 200 μm Wavelength Region," *Applied Optics*, Vol. 12, No. 3, 1973, pp. 555–563.

13 Privoznik, K. G., Daniel, K. J., and Incropera, F. P., "Absorption, Extinction and Phase Function Measurements for Algal Suspensions of Chlorella Pyrenoidosa," *Journal Quantitative Spectroscopy and Radiative Transfer*, Vol. 20, 1978, pp. 345–352.

14 Incropera, F. P., and Privoznik, K. G., "Radiative Property Measure-

ments for Selected Water Suspensions," *Water Resources Research*, Vol. 15, No. 1, 1979, pp. 85–89.

15 Touloukian, Y. S., DeWitt, D. P., and Hernicz, R. S., "Thermal Radiative Properties: Coatings," *Thermophysical Properties of Matter*, Vol. 9, IFI/Plenum, New York, 1972.

16 Wagner, T. R., "Measurements of Visible Radiation Transfer in a Black Dye Suspension under Laboratory Conditions," Ms Thesis, School of Mechanical Engineering, Purdue University, W. Lafayette, Ind., 1979.

17 Daniel, K. J., Laurendeau, N. M., and Incropera, F. P., "Optical Property Measurements for Suspensions of Unicellular Algae," Paper No. 78-HT-14, AIAA-ASME Thermophysics and Heat Transfer Conf., Palo Alto, 1978.

18 Daniel, K. J., Laurendeau, N. M., and Incropera, F. P., "Comparison of Predictions with Measurements for Radiative Transfer in an Algal Suspension," *International Journal of Heat Mass Transfer*, Vol. 21, 1978, pp. 1379–1384.

M. N. Özişik[1]
Institut für Verfahrens-und Kältetechnik,
ETH-Zentrum,
CH-8044 Zürich, Switzerland

W. H. Sutton
Department of Mechanical and Aerospace
Engineering, North Carolina State University,
Raleigh, N.C. 27650

A Source Function Expansion in Radiative Transfer

The radiative heat transfer problem for an isotropically scattering slab with specularly reflecting boundaries is reduced to the solution of a set of algebraic equations by expanding the source function in Legendre polynomials in the space variable in the integral form of the equation of radiative transfer. The lowest order S-1 analysis requires very little computer time for calculations, is easy to apply and yields results which are sufficiently accurate. For an absorbing, emitting, isotropically scattering medium with small and intermediate optical thickness (i.e., $\tau = 2$), which is of great interest in engineering applications, and for which the P-1 and P-3 solutions of the P-N method are not sufficiently accurate, the S-1 solution yields highly accurate results. In the case of a slab with diffusely reflecting boundaries, the problem is split up into a set of simpler problems each of which is solved with the source function expansion technique as a special case of the general problem considered.

Introduction

The solutions of one-dimensional, linear transport equation in neutron transport theory have been reported in the literature by various highly interrelated methods utilizing a suitable expansion in the space variable [1–6] or by the application of the integral transform technique [7–9]. Recently, some radiative heat transfer problems have been solved by the application of Fourier transform technique [10–12]. In all of these methods of analysis, the integral form of the transport equation is reduced to the solution of a set of algebraic equations. The advantage of expansion in the space variable lies in the fact that the convergence of the solution is fast, thus, even the lower order solutions yield results which are sufficiently accurate for most applications.

In the present investigation, a Legendre polynomial expansion in the space variable is applied to the source function and the integral form of the equation of radiative transfer is transformed into a set of algebraic equations. The resulting system of equations for this case is identical to those obtainable by the Fourier transform technique; but, the Legendre polynominal expansion is a more general approach for the solution of such problems. The reason for this is that the Legendre polynomial expansion is a simple, straightforward method, involves none of the very complicated and lengthy analysis that is needed in the Fourier transform technique and can be applied for more general situations.

Analysis

Consideration is given to radiative heat transfer in an absorbing, emitting, isotropically scattering slab of optical thickness $2a$, and bounded by specularly reflecting surfaces. The mathematical formulation of the problem is given by

$$\mu \frac{\partial I(x,\mu)}{\partial x} + I(x,\mu) = S(x), \text{ in } |x| \le a,\ |\mu| \le 1 \tag{1a}$$

$$I(-a,\mu) = c_1 + b_1 I(-a,-\mu),\ \mu > 0 \tag{1b}$$

$$I(a,-\mu) = c_2 + b_2 I(a,\mu),\ \mu > 0 \tag{1c}$$

where the *source function*, $S(x)$, is defined as

$$S(x) = (1-\omega)H(x) + \frac{\omega}{2}\int_{-1}^{1} I(x,\mu')d\mu' \tag{1d}$$

Here x is the optical variable, μ is the cosine of the angle between the positive x direction and the direction of the beam, $I(x,\mu)$ is the radiation intensity, b_1 and b_2 are the specular reflectives of the boundaries, c_1 and c_2 represent the emission of radiation from the boundaries, $H(x)$ is the emission of radiation from the medium, and ω is the single scattering albedo.

The radiative transfer problem defined by equations (1) can be transformed into an integral equation for the source function, $S(x)$, by the procedure described in reference [13]. We find

$$\begin{aligned} S(x) = {} & (1-\omega)H(x) + \frac{\omega}{2}[c_1E_{2,b}(a+x) \\ & + c_2b_1E_{2,b}(3a+x) + c_2E_{2,b}(a-x) + c_1b_2E_{2,b}(3a-x)] \\ & + \frac{\omega}{2}b_1b_2\int_{-a}^{a}\{E_{1,b}[4a+(x-y)] + E_{1,b}[4a-(x-y)]\}S(y)dy \\ & + \frac{\omega}{2}\int_{-a}^{a}\{b_1E_{1,b}[2a+(x-y)] + b_2E_{1,b}[2a-(x-y)]\}S(-y)dy \\ & + \frac{\omega}{2}\int_{-a}^{a}E_1(|x-y|)S(y)dy \end{aligned} \tag{2a}$$

where we defined the following modified exponential integral functions, $E_{k,b}(x)$,

$$E_{k,b}(x) = \int_0^1 \frac{e^{-x/\mu}}{1-b_1b_2e^{-4a/\mu}}\mu^{k-2}d\mu \tag{2b}$$

for $k = 1$ or 2, $x > 0$. We note that for b_1 or b_2 equal to zero, the $E_{1,b}(x)$ and $E_{2,b}(x)$ functions reduce to the usual exponential integral functions $E_1(x)$ and $E_2(x)$, respectively.

The source function $S(x)$ is expanded in terms of the Legendre polynomials $P_n(x/a)$ as

$$S(x) = \sum_{n=0}^{\infty}\left(\frac{n+\frac{1}{2}}{a}\right)M_nP_n\left(\frac{x}{a}\right) \text{ in } |x| \le a \tag{3}$$

The expansion coefficients M_n are determined by utilizing the orthogonality property of the Legendre polynomials. We find

$$\begin{aligned} M_n = {} & (1-\omega)\int_{-a}^{a}P_n\left(\frac{x}{a}\right)H(x)dx + \frac{\omega}{2}\int_{-a}^{a}P_n\left(\frac{x}{a}\right)[c_1E_{2,b}(a+x) \\ & + c_2b_1E_{2,b}(3a+x) + c_2E_{2,b}(a-x) + c_1b_2E_{2,b}(3a-x)]dx \\ & + \frac{\omega}{2a}(-1)^n\sum_{m=0}^{\infty}(-1)^m\left(m+\frac{1}{2}\right)M_m\int_{-a}^{a}\int_{-a}^{a}P_n\left(\frac{x}{a}\right)P_m\left(\frac{y}{a}\right) \\ & \cdot\{b_1b_2[E_{1,b}(4a-x+y) + E_{1,b}(4a-y+x)] + E_1(|x-y|)\}dxdy \\ & + \frac{\omega}{2a}(-1)^n\sum_{m=0}^{\infty}\left(m+\frac{1}{2}\right)M_m\int_{-a}^{a}\int_{-a}^{a}P_n\left(\frac{x}{a}\right)P_m\left(\frac{y}{a}\right) \\ & \cdot[b_1E_{1,b}(2a+y-x) + b_2E_{1,b}(2a-y+x)]dxdy, \end{aligned} \tag{4}$$

where $n = 0, 1, 2, 3, \ldots.$

Here we note that equations (4) obtainable by the Fourier transform technique after an elaborate and lengthy manipulation as described

---

[1] Permanent Address: Department of Mechanical and Aerospace Engineering, North Carolina State University, Raleigh, N.C., 27650.

Contributed by the Heat Transfer Division for publication in the JOURNAL OF HEAT TRANSFER. Manuscript received by the Heat Transfer Division February 4, 1980.

in the reference [12], are derived here with a simple and straightforward Legendre polynomial expansion.

Equations (3) and (4) form the complete solution of the problem for the determination of the source function. That is, the system (4) provides an infinite set of algebraic equations for the determination of the expansion coefficients, M_n. In practice, the system is terminated after a finite number of terms, N. Once the expansion coefficients, M_n, are known from the solution of the system (4), the source function, $S(x)$, is determined according to equation (3). Knowing the source function, various physical quantities of interest, such as the radiation intensity, the radiative heat flux, the reflectivity or the transmissivity of the slab are readily determined from their definitions.

The coefficients in the system of equations (4) involve single and double integrals containing a product of $P_n(x/a)$ and $E_{k,b}(x)$ functions as the integrand. For the cases of b_1 or b_2 equal to zero, these integrals are evaluated analytically for low orders of N and listed in the Appendix. For the general case and higher values of N, the integrals are evaluated here numerically using a 20 point gaussian quadrature.

The principal advantage of the method in reducing the radiation problem to the solution of a set of algebraic equations given by the system (4) is that even for the very low order solutions (i.e., low values of N), very accurate results are obtainable for the radiative heat flux.

Consider, for example, the radiation problem (1) for $c_1 = 1$, $b_1 = c_2 = H(x) = 0$. Clearly, this particular case corresponds to a physical situation in which the boundary at $x = a$ of the slab is transparent and irradiated by an isotropic radiation of unit intensity, the boundary at $x = a$ has a specular reflectivity b_2, while contribution of the emission terms $H(x)$ and c_2 from the medium and the wall at $x = a$ are considered negligible.

For the case of $N = 1$, for example, equation (3) for the source function reduces to

$$S(x) = \frac{1}{2a}\left(M_0 + 3M_1\frac{x}{a}\right) \tag{5}$$

where the equations for the determination of the coefficients M_0 and M_1 are obtained from equations (4) as

$$\begin{aligned} M_0 = {} & \frac{\omega}{2}\int_{-a}^{a}[E_2(a+x) + b_2E_2(3a-x)]dx \\ & + \frac{\omega}{4a}\left\{M_0\int_{-a}^{a}\int_{-a}^{a}E_1(|x-y|)dxdy + 3M_1 \right. \\ & \left. \times \int_{-a}^{a}\int_{-a}^{a}\frac{y}{a}E_1(|x-y|)dxdy\right\} \\ & + b_2\frac{\omega}{4a}\left\{M_0\int_{-a}^{a}\int_{-a}^{a}E_1(2a-y+x)dxdy \right. \\ & \left. + 3M_1\int_{-a}^{a}\int_{-a}^{a}\frac{y}{a}E_1(2a-y+x)dxdy\right\} \end{aligned} \tag{6}$$

and

$$\begin{aligned} M_1 = {} & \frac{\omega}{2}\int_{-a}^{a}\frac{x}{a}[E_2(a+x) + b_2E_2(3a-x)]dx \\ & + \frac{\omega}{4a}\left\{M_0\int_{-a}^{a}\int_{-a}^{a}\frac{x}{a}E_1(|x-y|)dxdy \right. \\ & \left. + 3M_1\int_{-a}^{a}\int_{-a}^{a}\frac{x}{a}\frac{y}{a}E_1(|x-y|)dxdy\right\} \\ & - b_2\frac{\omega}{4a}\left\{M_0\int_{-a}^{a}\int_{-a}^{a}\frac{x}{a}E_1(2a-y+x)dxdy \right. \\ & \left. + 3M_1\int_{-a}^{a}\int_{-a}^{a}\frac{x}{a}\frac{y}{a}E_1(2a-y+x)dxdy\right\} \end{aligned} \tag{7}$$

The analytic expressions for various integrals appearing in equations (6) and (7), derived from references [14–16] are listed in the Appendix.

The equations for higher order solutions can be obtained from equations (3) and (4) in a similar manner.

The net radiative heat flux $q^r(x)$ anywhere in the medium is determined from

$$q^r(x) = [q^+(x) - q^-(x)] \tag{8a}$$

where

$$q^+(x) = 2\pi\int_0^1 I(x, \mu')\mu'd\mu' \tag{8b}$$

$$q^-(x) = 2\pi\int_0^1 I(x, -\mu')\mu'd\mu' \tag{8c}$$

and the forward and backward radiation intensities $I(x, \mu)$ and $I(x, -\mu)$, respectively, are related to the source function in accordance with the expressions given in reference [13]; hence, they are known when the source function is known.

The hemispherical reflectivity, R, and the transmissivity, Γ, of the slab for $b_1 = 0$ are determined from

$$R = \frac{q^-(-a)}{\pi c_1} \text{ and } \Gamma = \frac{q^r(a)}{\pi c_1} = (1 - b_2)\frac{q^+(a)}{\pi c_1} \tag{9}$$

Simplification for Diffuse Reflection

When the boundaries of the slab are diffusely emitting and diffusely reflecting surfaces, the problem (1) takes the form

$$\mu\frac{\partial I(x, \mu)}{\partial x} + I(x, \mu) = S(x), \text{ in } |x| \le a,\ |\mu| \le 1 \tag{10a}$$

$$I(-a, \mu) = c_1 + 2d_1K_1,\ \mu > 0 \tag{10b}$$

$$I(a, -\mu) = c_2 + 2d_2K_2,\ \mu > 0 \tag{10c}$$

where

$$K_1 = \int_0^1 I(-a, -\mu')\mu'd\mu' \tag{11a}$$

$$K_2 = \int_0^1 I(a,\mu')\mu'd\mu' \tag{11b}$$

$$S(x) = (1 - \omega)H(x) + \frac{\omega}{2}\int_{-1}^{1} I(x, \mu')d\mu' \tag{11c}$$

and d_1 and d_2 are the diffuse reflectivities of the boundary surfaces at $x = -a$ and $x = a$, respectively. The problem (10) can be split up into simpler problems such that each of the simpler problems become a special case of the problem (1); hence, the solution of the problem (10) can be obtained by the method described previously.

The radiation intensity $I(x, \mu)$ of the problem (10) is taken as,

$$\begin{aligned} I(x, \mu) = {} & I_0(x, \mu) + (c_1 + 2d_1K_1)I_1(x, \mu) \\ & + (c_22d_1K_2)I_2(x, \mu) \end{aligned} \tag{12}$$

where $I_0(x, \mu)$, $I_1(x, \mu)$ and $I_2(x, \mu)$ are the solutions of the following three simpler problems

Nomenclature

a = one-half of the optical thickness of the slab

b_1, b_2 = specular reflectivity of the front and back boundaries, respectively

c_1, c_2 = radiation emitted at the boundaries

d_1, d_2 = twice the value of diffuse reflectivity of the front and back boundaries, respectively

$E_n(x)$ = exponential integral function of order n

$H(x)$ = intensity of radiation emitted by the medium

$I(x, \mu)$ = radiation intensity

$P_n(x)$ = the Legendre polynomial of order n

$q^r(x)$ = net radiative heat flux

$q^+(x)$, $q^-(x)$ = forward and backward half-range fluxes respectively

R = hemispherical reflectivity of the slab

$S(x)$ = the source function

x = the optical variable

Γ = transmissivity of the slab

μ = direction cosine

ω = single scattering albedo

Table 1 The accuracy of the S-1 analysis in determining the hemispherical reflectivity and transmissivity of a slab from the solution of problem 1 for $c_1 = 1$, $b_1 = c_2 = H(x) = 0$, $b_2 = 0.5$.

		Hemispherical Reflectivity*			Hemispherical Transmissivity*		
ω	Method	$2a = 0.5$	$2a = 1$	$2a = 2$	$2a = 0.5$	$2a = 1$	$2a = 2$
0.1	S-1	0.1344	0.0539	0.0248	0.2308	0.1170	0.0332
	Exact	0.1344	0.0539	0.0248	0.2307	0.1169	0.0332
0.2	S-1	0.1619	0.0808	0.0497	0.2412	0.1256	0.0370
	Exact	0.1619	0.0808	0.0498	0.2412	0.1256	0.0372
0.3	S-1	0.1925	0.1116	0.0784	0.2529	0.1358	0.0419
	Exact	0.1926	0.1117	0.0786	0.2529	0.1359	0.0420
0.4	S-1	0.2270	0.1474	0.1120	0.2662	0.1481	0.0482
	Exact	0.2271	0.1475	0.1122	0.2663	0.1483	0.0486
0.5	S-1	0.2661	0.1897	0.1524	0.2814	0.1632	0.0566
	Exact	0.2664	0.1898	0.1526	0.2816	0.1635	0.0573
0.6	S-1	0.3110	0.2407	0.2023	0.2991	0.1822	0.0687
	Exact	0.3115	0.2408	0.2021	0.2993	0.1827	0.0697
0.7	S-1	0.3630	0.3036	0.2666	0.3197	0.2065	0.0862
	Exact	0.3638	0.3039	0.2657	0.3202	0.2075	0.0880
0.8	S-1	0.4240	0.3837	0.3541	0.3442	0.2386	0.1136
	Exact	0.4253	0.3846	0.3527	0.3450	0.2405	0.1172
0.9	S-1	0.4968	0.4899	0.4837	0.3736	0.2828	0.1601
	Exact	0.4988	0.4929	0.4838	0.3748	0.2868	0.1689

* Exact results from reference [13]

$$\mu \frac{\partial I_0(x,\mu)}{\partial x} + I_0(x,\mu) = S_0(x), \text{ in } |x| \le a, |\mu| \le 1 \qquad (13a)$$

$$I_0(-a,\mu) = 0, \mu > 0 \qquad (13b)$$

$$I_0(a,-\mu) = 0, \mu > 0 \qquad (13c)$$

where

$$S_0(x) = (1-\omega)H(x) + \frac{\omega}{2}\int_{-1}^{1} I_0(x,\mu')d\mu' \qquad (13d)$$

and

$$\mu \frac{\partial I_1(x,\mu)}{\partial x} + I_1(x,\mu) = S_1(x), \text{ in } |x| \le a, |\mu| \le 1 \qquad (14a)$$

$$I_1(-a,\mu) = 1, \mu > 0 \qquad (14b)$$

$$I_1(a,-\mu) = 0, \mu > 0 \qquad (14c)$$

where

$$S_1(x) = \frac{\omega}{2}\int_{-1}^{1} I_1(x,\mu')d\mu' \qquad (14d)$$

and

$$\mu \frac{\partial I_2(x,\mu)}{\partial x} + I_2(x,\mu) = S_2(x), \text{ in } |x| \le a, |\mu| \le 1 \qquad (15a)$$

$$I_2(-a,\mu) = 0, \mu > 0 \qquad (15b)$$

$$I_2(a,\mu) = 1, \mu > 0 \qquad (15c)$$

where

$$S_2(x) = \frac{\omega}{2}\int_{-1}^{1} I_2(x,\mu')d\mu' \qquad (15d)$$

Clearly, equations (13–15) are special cases of problem (1); hence, they can readily be solved with the approach described previously. However, to determine $I(x, \mu)$ from relation (12), we need to know the coefficients K_1 and K_2. These coefficients are readily determined by utilizing the solutions $I_i(x, \mu)$, ($i = 0, 1, 2$) of the above simpler problems as now described. From equation (12) we write

$$I(-a,-\mu) = I_0(-a,-\mu) + (c_1 + 2d_1K_1)I_1(-a,-\mu) + (c_2 + 2d_2K_2)I_2(-a,-\mu) \qquad (16a)$$

$$I(a,\mu) = I_0(a,\mu) + c_1 2d_1K_1I_1(a,\mu) + (c_2 + 2d_2K_2)I_2(a,\mu) \qquad (16b)$$

Equations (16) are operated on by the operator $\int_0^1 \mu d\mu$ and the definitions of K_1 and K_2 are utilized. We respectively obtain

$$K_1 = Q_0(-a) + (c_1 + 2d_1K_1)Q_1(-a) + (c_2 + 2d_2K_2)Q_2(-a) \qquad (17a)$$

$$K_2 = Q_0(a) + (c_1 + 2d_1K_1)Q_1(a) + (c_2 2d_2K_2)Q_2(a) \qquad (17b)$$

where we defined

$$Q_i(\mp a) = \int_0^1 \mu I_i(\mp a, \mp\mu)d\mu, \; i = 0, 1 \text{ or } 2 \qquad (17c)$$

Here, $Q_i(\mp a)$'s are known quantities since $I_i(\mp a, \mp\mu)$ are available from the solutions of the simpler problems (13–15). Then, equations (17a) and (17b) provide two independent relations for the determination of the coefficients K_1 and K_2 which completes the analysis of the diffuse problem (10).

Results and Discussion

To illustrate the accuracy of the lowest order S-1 solution, we consider the problem of specularly reflecting boundaries defined by equation (1) for the following special case.

$$c_1 = 1, b_1 = c_2 = H(x) = 0.$$

The physical significance of this particular situation was discussed previously. For this particular case, we list in Table 1 the hemispherical reflectivity and transmissivity of the slab determined with the S-1 solution together with the exact results for the optical thicknesses $2a = 0.5, 1, 2$, when the specular reflectivity of the boundary at $x = a$ is $b_2 = 0.5$.

As further illustration of the accuracy of the S-1 analysis, we consider the auxiliary problem given by equation (13) for an internal energy source of strength $H(x) = 1$. We choose this particular case because the exact solution is available for certain cases. We list in Table 2 the results obtained with the S-1 solution for the half-range flux, $q_0^+(a)$,

$$q_0^*(a) = 2\pi \int_0^1 I_0(a,\mu)\mu d\mu$$

and because of symmetry we have $|q_0^+(a)| = |q_0^-(-a)|$.

Over the range of parameters considered in this paper, the lowest order S-1 solution yields results which are sufficiently close to the exact solutions. In order to provide a numerical comparison between the S-1 solution and the P-1 and P-3 results, we consider the hemispherical reflectivity given in Table 1 for the case of optical thickness $2a = 2$. For low values of ω, say $\omega = 0.1$, the hemispherical reflectivity is 0.0248 with S-1; negative, hence meaningless, with P-1; 0.0073 with P-3; and 0.0248 with the exact analysis. For high values of ω, say $\omega = 0.9$, the hemispherical reflectivity is 0.4837 with S-1; 0.4690 with P-1; 0.4821 with P-3; and 0.4838 with the exact analysis.

The usefulness of the present S-1 solution lies in the range of small

Table 2 The S-1 analysis in the determination of exit flux $q_0^+(a)$ from the solution of equations (13) for $H(x) = 1$ and optical thickness $2a = 1$

ω	$q_0^+(a) = 2\pi \int_0^1 I_0(a,\mu)\mu d\mu$ $S-1$	Exact*
0	2.4524	2.4523
0.1	2.3504	2.3472
0.2	2.2344	2.2290
0.3	2.1009	2.0955
0.4	1.9460	1.9391
0.5	1.7639	1.7565
0.6	1.5468	1.5399
0.7	1.2835	1.2778
0.8	0.9575	0.9538
0.9	0.5434	0.5421

Calculated using the singular eigenfunction expansion technique from the analysis given in reference [13], pp. 421–428.

and intermediate optical thicknesses, which is of great interest in engineering applications and for which P-1 and P-3 solutions are not sufficiently accurate. Only for large optical thicknesses and $\omega \to 1$, the P-1 and P-3 approximations yield sufficiently accurate results.

For a scattering medium, the advantage of the present method over the P-N method is in the treatment of the boundary conditions. In the P-N method, the boundary conditions are approximated by using the so-called Marshak's or Mark's boundary conditions. In the present method they are represented exactly, except for the approximation associated with the expansion of the source function.

The present method can be extended to composite media consisting of parallel layers of slabs, anisotropic scattering and to other geometries such as the spherical symmetry. The extension to more than one dimensional problems is also possible.

Furthermore, the S-1 analysis is very simple and requires very little computer time for the calculation (i.e., the entire results for Table 1 were run in three jobs for a total of 7.8 run time including CPU and I/O on the IBM 370/165). There appeared to be no significant increase in computer time for computation for larger optical thicknesses. However, the S-3 solution requires slightly more computing time since the number of terms to be evaluated is increased.

Acknowledgment

One of the authors, M. Necati Özişik, gratefully acknowledges the hospitality extended to him by the Institut für Verfahrens-und Kältetechnik, ETH-Zentrum, Zürich, Switzerland during his stay.

References

1 Asaoka, T., "Space-Angle Energy-Time Dependent Neutron Transport in a Homogeneous Slab by the J_N Method, "*Nuclear Science Engineering*, Vol. *34*, 1968, p. 122.

2 Carlvik, I., "Monoenergetic Critical Parameters and Decoy Constants for Small Homogeneous Spheres and Thin Homogeneous Slabs," *Nuclear Science Engineering*, Vol. *31*, 1968, p. 295.

3 Kschwenolt, H., "Application of the J_N Method in Neutron Transport in Slabs and Spheres," *Nuclear Science Engineering*, Vol. *36*, 1969, p. 447.

4 Asaoka, T., and Benanni, E. C., "The J_N Method for Transport Problems in a Multiregion Slab with Anisotropic Scattering," *Transfer American Nuclear Society*, Vol. *12*, 1969.

5 Kschwendt, H., "Legendre Expansion and Integral Equations of Displacement Type, "*Journal Comparative Physics*, Vol. *5*, 1970, p. 84.

6 Stepanek, J., and Ligou, J., "A Solution of the Coupled Integral and Differential Form of the Transport Equation Using a Legendre Polynomials Source Density Approximation in Angle and Space for Slab Geometry, "*4th International Conference on Reactor Shielding*, Paris, Oct. 9–13, 1972.

7 Boffi, V. C., and Premuda, F., "Two Group Neutron Transport Theory for a Finite Critical Slab," *Nuclear Science Engineering*, Vol. *38*, 1969, p. 205.

8 Hembd, H., "The Integral Transform Method for Neutron Transport Problems," *Nuclear Science Engineering*, Vol. *40*, 1970, p. 224.

9 Boffi, V. C., Molinari, V. G., Premuda, F., and Trombetti, T., "Convergence of the Integral Transform Method for the Solution of Monoenergetic Neutron Transport Equation," *Camitato Nazionale Energia Nucleare*, Rome, Report No. RJ/FI(72), 1972, p. 31.

10 Boffi, V. C., Santarelli, F., and Stramigioli, C., "Rigorous Constructive Solutions in Radiative Heat Transfer," *Journal of Quantitive Spectroscopy and Radiative Transfer*, Vol. *18*, 1977, p. 189.

11 Boffi, V. C., and Spiga, G., "Integral Theory of Radiative Transfer with Anisotropic Scattering and General Boundary Conditions," *Journal of Mathematical Physics*, Vol. *18*, 1977, p. 2448.

12 Sutton, W. H., and Özisik, M. N., "A Fourier Transform Solution for Radiative Transfer in a Slab with Isotropic Scattering and Boundary Reflection," *Journal of Quantitive Spectroscopy and Radiative Transfer*, Vol. *22*, 1979, p. 22.

13 Özisik, M. N., *Radiative Transfer*, John Wiley and Sons, New York, 1973.

14 Van de Hulst, H. C., "Scattering in Planetary Atmosphere," *Astrophysics Journal*, Vol. *107*, 1948, p. 220.

15 Chandrasekhar, S., *Radiative Transfer*, Dover Publications, New York, 1960.

16 Le Caine, J., "A Table of Integrals Involving the Functions $E_n(x)$, "*National Research Council of Canada*, Report No. MT-131, 1948.

APPENDIX

Analytic Expressions for the Integrals in Equations (6) and (7)

$$\int_{-a}^{a} E_2(a+y)dy = \int_{-a}^{a} E_2(a-y)dy = \frac{1}{2} - E_3(2a) \quad \text{(A-1)}$$

$$\int_{-a}^{a} E_2(3a+y)dy = \int_{-a}^{a} E_2(3a-y)dy = E_3(2a) - E_3(4a) \quad \text{(A-2)}$$

$$\int_{-a}^{a} \frac{y}{a} E_2(a+y)dy = -\frac{1}{2} + E_3(2a) + 2aE_2(2a) + \frac{4}{3}a^2E_1(2a) - \frac{e^{-2a}}{3a}(2a^2+2a+1) + \frac{1}{6a} \quad \text{(A-3)}$$

$$\int_{-a}^{a} \frac{y}{a} E_2(a-y)dy = -\int_{-a}^{a} \frac{y}{a} E_2(a+y)dy \quad \text{(A-4)}$$

$$\int_{-a}^{a}\int_{-a}^{a} E_1(|x-y|)dxdy = 4a - 1 + \frac{1}{2}E_3(2a) \quad \text{(A-5)}$$

$$\int_{-a}^{a}\int_{-a}^{a} \frac{y}{a} E_1(|x-y|)dxdy = \int_{-a}^{a}\int_{-a}^{a} \frac{x}{a} E_1(|x-y|)dxdy = 0 \quad \text{(A-6)}$$

$$\int_{-a}^{a}\int_{-a}^{a} \frac{x}{a}\cdot\frac{y}{a}\cdot E_1(|x-y|)dxdy = \frac{4a}{3} - 1 + \frac{1}{2a^2} - \frac{e^{-2a}}{6a^2}[4a^3+6a^2+6a+3) + \frac{4}{3}a^2E_1(2a) + \frac{8}{3}aE_2(2a) + 2E_3(2a) \quad \text{(A-7)}$$

$$\int_{-a}^{a}\int_{-a}^{a} E_1(2a-y+x)dxdy = \frac{1}{2} - 2E_3(2a) + E_3(4a) \quad \text{(A-8)}$$

The expressions (A-1) through (A-4) are obtained by the manipulation of the relations given in reference [16]; the remaining expressions (A-5) through (A-8) are derived.

J. Higenyi[1]
Graduate Student.

Y. Bayazitoğlu
Assistant Professor,
Assoc. Mem. ASME

Mechanical Engineering Department,
Rice University,
Houston, TX 77001

Differential Approximation of Radiative Heat Transfer in a Gray Medium

Axially Symmetric Radiation Field

The differential approximation is used to analyze an axially symmetric radiation field for a gray medium within a finite, cylindrical enclosure. The medium emits, absorbs, and isotropically scatters radiant energy and is subject to a specified heat generation. Numerical solutions are obtained for the radiative heat flux and emissive power distributions. It is found that the accuracy of the differential approximation is of the same order for the axially symmetric and one-dimensional problems.

1 Introduction

The basis for analyzing a radiation field in a medium which absorbs, emits, and scatters radiant energy is the radiation transport equation [1–6]. It is an integral-differential equation in the spectral intensity of radiation and is usually subject to boundary conditions represented in an integral form. Methods for solving the transport equation include the Monte Carlo technique [7–8], the zone method [9–10] and exact solutions [11–12]. All these solution methods are either very difficult or computationally expensive, even when the simplification of a gray medium is introduced. In order to simplify the analysis, one has to resort to approximate methods of solution. Because of its general nature and simplicity, the differential approximation has been applied in analyzing a radiation field [1–7].

One form of the differential approximation commonly used in cylindrical geometries is the spherical harmonics method (the P_N approximation) [2–6]. For pure radiation, one-dimensional problems have been solved by the P_1 approximation [6, 7, 13, 14] and by the modified first order approximations [15–18]. The modified approximations compare favorably with the Monte Carlo method [19] but their extension to coupled radiation exchanges or multidimensional problems is too involved. The accuracy of the P_1 approximation for the one-dimensional geometries [20–24] and for multidimensional cartesian geometry [25] has been studied. But the accuracy of P_1 approximation has not been assessed for a multi-dimensional cylindrical geometry. Hence, the objective of this paper is to determine the accuracy of P_1 approximation for an axially symmetric radiation field. The approximate solutions will be compared with the exact solutions of Dua and Cheng [26].

2 Analysis

In this section, we consider a gray medium which absorbs, emits, and isotropically scatters radiant energy within a finite, cylindrical enclosure [20]. Assuming local thermodynamic equilibrium and a steady-state condition, the governing transport equation is given by [6, 7, 27].

$$l_r \frac{\partial \psi}{\partial r} - \frac{l_\theta}{r}\left(\frac{\partial \psi}{\partial \phi} - \frac{\partial \psi}{\partial \theta}\right) + l_z \frac{\partial \psi}{\partial z} + (\alpha + \sigma)\psi = \alpha \Phi + \frac{\sigma}{4\pi}\int_\Omega \psi d\Omega \quad (1)$$

where ψ and Φ are the dimensionless intensity and Planck function, respectively. If equation (1) is multiplied by powers (zeroth and first) of l_r, l_z and l_θ individually and integrated over a solid angle of 4π, one obtains

$$\frac{1}{r}\frac{\partial}{\partial s_i}(h_i \psi_{s_i}) = \alpha(4\pi\Phi - \psi_0) \quad (2)$$

$$\frac{1}{r}\frac{\partial}{\partial s_i}(h_j \psi_{s_i s_j}) + \frac{1}{r}(\delta_{rs_i} + \delta_{\theta s_i})\psi_{rs_i} - \frac{1}{r}(\psi_0 - \psi_{zz})\delta_{rs_i} = -(\alpha + \sigma)\psi_{s_i} \quad (3)$$

where

$$\psi_0 = \int_\Omega \psi d\Omega,\ \psi_{s_i} = \int_\Omega \psi l_{s_i} d\Omega, \psi_{s_i s_j} = \int_\Omega \psi l_{s_i} l_{s_j} d\Omega \quad (4)$$

and

$$i,j = 1, 2, 3; h_1 = h_3 = r; h_2 = 1; s_1 = r; s_2 = \theta; s_3 = z$$

In the P_1 approximation, the second order moments $\psi_{s_i s_j}$ are given by [7]

$$\psi_{s_i s_j} = \frac{1}{3}\psi_0 \delta_{ij} \quad (5)$$

Substitution of equation (5) into equation (3) for ψ_r and ψ_z leads to

$$\psi_r = -\frac{1}{3(\alpha + \sigma)}\frac{\partial \psi_0}{\partial r},\ \psi_z = -\frac{1}{3(\alpha + \sigma)}\frac{\partial \psi_0}{\partial z} \quad (6)$$

For an axially symmetric radiation field $\partial/\partial\theta = 0$; hence, combining equations (2) and (6) one obtains

$$\frac{\partial^2 \psi_0}{\partial \tau^2} + \frac{1}{\tau}\frac{\partial \psi_0}{\partial \tau} + \frac{\partial^2 \psi_0}{\partial \eta^2} = -3(1 - \lambda)(4\pi\Phi - \psi_0) \quad (7)$$

$$\psi_r = -\frac{1}{3}\frac{\partial \psi_0}{\partial \tau},\ \psi_z = -\frac{1}{3}\frac{\partial \psi_0}{\partial \eta} \quad (8)$$

where $\tau = (\alpha + \sigma)r$, $\eta = (\alpha + \sigma)z$ and $\lambda = \sigma/(\alpha + \sigma)$. For pure radiation conservation of energy gives

$$U = 4\pi\Phi - \psi_0 = S/\alpha I^* \quad (9)$$

where S and U are the heat source and dimensionless heat source, respectively.

Equation (7) is usually subject to boundary conditions of the form.

$$\psi_0 \pm E_i \frac{\partial \psi_0}{\partial x} = 4\pi\Phi_{w,i} \quad (10)$$

$$E_i = 2(2 - \epsilon_{wi})/3\epsilon_{wi},\ x = \tau, \eta;\ i = 1, 2 \quad (11)$$

where the minus sign is used for the lower boundary and plus sign for the upper boundary.

2.1 Medium Emissive Power Specified. If the emissive powers of the medium and boundary surfaces are specified, equation (7) and its associated boundary conditions in equation (10) is solved numerically. To enable comparison with the exact solution [27], the medium emissive power was assumed to be uniform. Furthermore, all surface

---

[1] Presently with the Faculty of Technology, Makerere University, Kampala, Uganda.

Contributed by the Heat Transfer Division for publication in the JOURNAL OF HEAT TRANSFER. Manuscript received by the Heat Transfer Division September 13, 1979.

emissive powers were also uniform at the same level as that of medium emissive power. Numerical results obtained by a finite difference method for non-scattering medium are shown in Figs. 1–4.

2.2 Medium Subject to Heat Generation. The thermal conditions specified below are typical of those applied in combustion furnace problems. We let the medium be subject to a variable heat generation which is a function of axial coordinate z only. The lateral surfaces are diffuse emitters and reflectors, while the plane end surfaces are radiatively adiabatic. Substituting equation (9) into equation (7) leads to

$$\frac{\partial^2\psi_0}{\partial\tau^2}+\frac{1}{\tau}\frac{\partial\psi_0}{\partial\tau}+\frac{\partial^2\psi_0}{\partial\eta^2}=3(\lambda-1)U(\eta) \qquad (12)$$

subject to boundary conditions

$$\psi_0 \pm E_i\frac{\partial\psi_0}{\partial\tau}=4\pi\Phi_{w,i} \text{ at } r_1 \text{ or } r_2$$

$$\text{and } \frac{\partial\psi_0}{\partial\eta}\pm H_i\psi_0=0 \text{ at } \eta=0 \text{ or } \eta_2 \qquad (13)$$

where the plus sign is used for the upper boundary. From equations (12) and (13) the solution may be obtained numerically or analytically. The latter form as obtained by superposition and separation of variables is presented in the Appendix.

3 Results and Discussion

3.1 An Isotropic, Homogeneous Radiation Field. The radiative quantities displayed in Figs. 1–4 are due to medium emission. All surfaces are black and maintained at zero temperatures while the medium is isothermal. These are part of the thermal conditions which constitute an isotropic, homogeneous radiation field. Figures 1 and 2 show the averaged intensity and radial heat flux along the centerline $(r,0)$ for a hollow cylindrical enclosure. Similar quantities are shown in Figs. 3(a) and 3(b) in the case of a concentric, cylindrical enclosure. The averaged intensity and the axial heat flux along the outer surface (R,z) are displayed in Figs. 4(a) and 4(b), respectively.

The problem whose solution is shown graphically in Figs. 1–4 does not have a practical application. However, the solutions can be used to assess the accuracy of the differential approximation. For the purpose of comparison, results of Dua and Cheng [26] are included; they were obtained by numerical integration of a closed form exact solution. It is observed that the magnitude of the error depends on the optical thickness, location, geometry of the enclosure, and whether the quantity desired is the heat flux or the averaged intensity. The maximum percent errors range between 10 and 35. In general, large errors occur in a medium which is optically thin. For example, when $\tau_0 = 0.1$, the percent error is about 35 for the averaged intensity in a hollow cylinder at points $(0,0)$ and (R,L) and about 30 at a point near midway between the inner and outer surfaces of a concentric cylinder. The percent errors in the radial heat fluxes at points $(R,0)$ and $(r_1,0)$ and the axial heat flux at (R,L) for the same optical thickness (0.1) are about 10, 30 and 35, respectively. In the medium with an optical thickness of 5.0, the maximum percent error is about 10 and occurs in the averaged intensity at a point (R,L). Smaller errors in the optically thick media are expected since the diffusion or P_1 approximation adequately model the actual behavior of the medium.

The percent errors cited above are of the same order of magnitude as that observed for one-dimensional problems [20, 21]. A similar result was reached for multidimensional problems in cartesian geometry. If one is dealing with pure radiation problems, such errors may not be acceptable and exact solutions need be sought. However, it must be remembered that exact solutions are difficult and tedious; the solutions used for comparison were obtained under special conditions which greatly simplify the exact form solution approach. For other thermal conditions, the simplicity of the differential approximation may be a desirable advantage. It has been shown that higher approximations greatly improve results as compared to the P_1 approximation [20, 21]. From the solutions shown in Fig. 1–4, it is conceivable that higher approximations would result in greater improvements for axially asymmetric problems.

3.2 Radiating Medium Subjected to a Heat Source. The physical problem considered in this section involves a radiating medium within finite hollow and finite concentric cylindrical enclosures. All boundary surfaces are black and maintained at zero temperatures. Results for a uniform heat source are shown in Figs. 5–6.

Figure 5 shows the emissive power distribution along the center line $(r,0)$ in a hollow cylindrical medium. The emissive power distributions along the centerline $(r,0)$ of a concentric cylinder are displayed in Fig. 6 for a radius ratio, r_1/r_2, of 0.1. A general feature is observed from Figs. 5–6. It is seen that the emissive power distributions are almost uniform and the heat fluxes vary almost linearly when the medium is optically thin ($\tau_0 = 0.1$). In an optically thick medium ($\tau_0 = 5.0$), the emissive power varies more rapidly near the cold walls than within the medium resulting in a non-linear variation in the heat flux. This is explained by the fact that in an optically thick medium, the influence of the cold wall is felt almost equally throughout the medium.

For the purpose of comparison, solutions of one-dimensional problem are included in Fig. 5. These results can be calculated from a closed form exact solution [21]. It is observed that the emissive power along the centerline $(r,0)$ increases when the length of the cylinder is increased. This is to be expected, as increasing the length results in more available thermal energy for absorption. It is also seen that an axially symmetric problem cannot be approximated by a one-dimensional problem because the effect of length on the emissive power is not negligible at all three representative optical depths (0.1, 1.0 and 5.0).

3.3 Medium under Radiative Equilibrium. Figure 7 shows the emissive power distribution along the centerline $(r,0)$ for a concentric cylindrical medium under radiative equilibrium. All surfaces except surface (r_1,z) were maintained at zero temperatures and there was no internal heat generation. It is observed that the effect of decreasing the radius ratio, r_1/r_2, is to lower the emissive power. This is so because the enclosed medium sees more of the cold outer surface than the inner surface. A decrease in the radius ratio exposes more of the medium to the cold outer surface resulting in low emissive power.

4 Conclusions

The problem of determining radiative transport in an axially symmetric cylindrical enclosure has been carried out by use of P_1 approximation. Thermal conditions considered include an isothermal medium, a specified heat generation and radiative equilibrium. The

Nomenclature

B, B_w = medium and wall emissive powers, respectively
E_i = defined in equation (11).
H_1, H_2 = coefficients each 3/2.
I = intensity of radiation
I^* = reference intensity.
I_n = modified Bessel function of first kind and order n.
K_n = modified Bessel function of second kind and order n.
L = half length of the cylinder.
Q = net radiant heat flux.
r = coordinate variable
R = radius of a hollow cylinder.
S = heat generation per unit volume
U = defined in equation (2).
z = axial coordinate variable.
α = volumetric absorption coefficient.
ϵ_w = surface emissivity.
$\eta = (\alpha + \sigma)z$.
$\lambda = \sigma/(\alpha + \sigma)$.
σ = volumetric scattering coefficient.
$\tau = (\alpha + \sigma)r$.
$\tau_0 = (\alpha + \sigma)R$ or $(\alpha + \sigma)(r_2 - r_1)$.
Φ, Φ_w = dimensionless Planck functions, $B/\pi I^*$ and $B_w/\pi I^*$.
ψ_0 = average integrated intensity, dimensionless.
ψ_r, ψ_z = radiant heat fluxes in r and z-direction, dimensionless.

Subscripts

r = radial direction
z = axial direction
1, 2 = lower and upper boundary layers

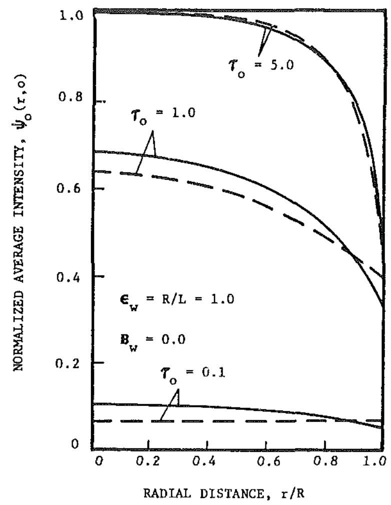

Fig. 1 Average intensity along (*r*, 0) in an isothermal hollow cylindrical medium. —— exact [26], - - - P_1 approximation

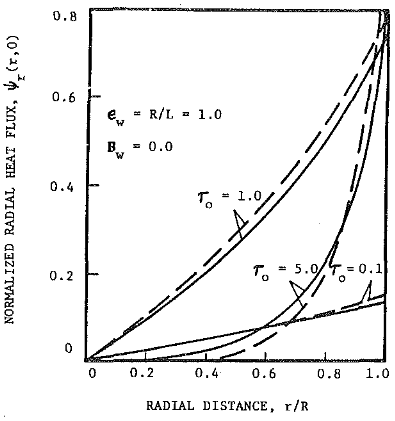

Fig. 2 Radial heat flux along (*r*, 0) in an isothermal hollow cylindrical medium. —— exact [26] - - - P_1 approximation

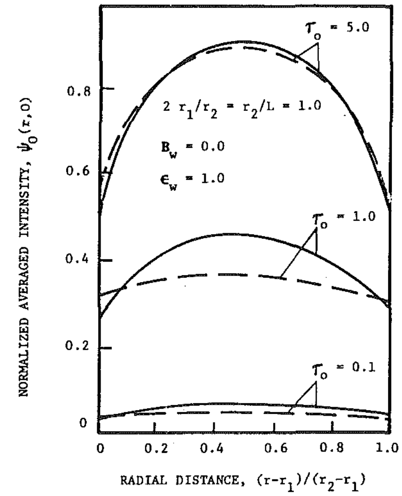

Fig. 3(*a*) Average intensity along (*r*, 0) in an isothermal, concentric, cylindrical medium. —— exact [26], - - - P_1 approximation

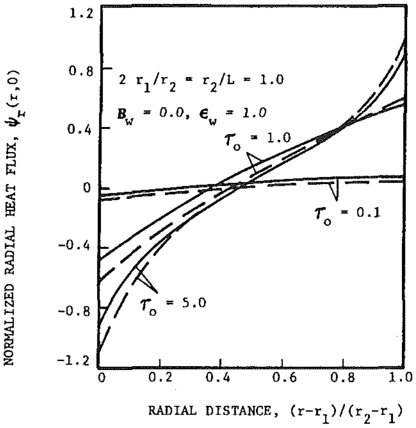

Fig. 3(*b*) Radial heat flux along (*r*, 0) in an isothermal concentric, cylindrical medium. —— exact [26], - - - P_1 approximation

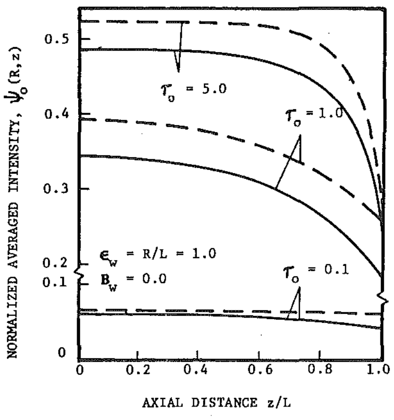

Fig. 4(*a*) Average intensity along (*R*, *z*) in an isothermal hollow cylindrical medium. —— exact [26], - - - P_1 approximation

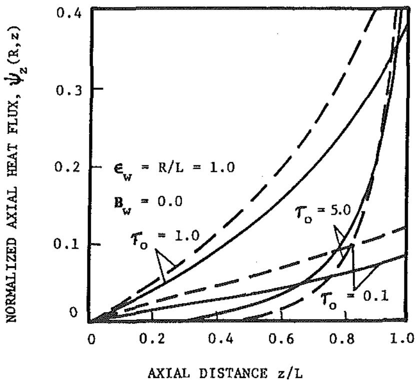

Fig. 4(*b*) Axial heat flux along (*R*, *z*) in an isothermal hollow cylindrical medium. —— exact [26], - - - P_1 approximation

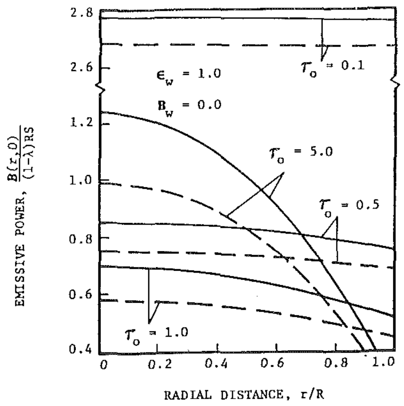

Fig. 5 Emissive power along (r, 0) in a hollow cylinder with a uniform heat source. —— infinite cylinder, exact. - - - finite cylinder, $R/L = 1.0$

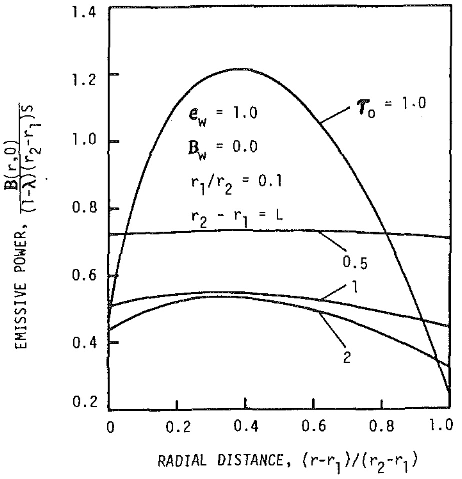

Fig. 6 Emissive power along (r, 0) in a finite concentric cylinder with a uniform heat source

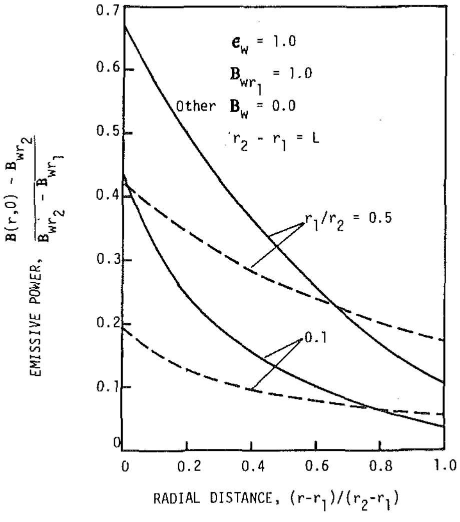

Fig. 7 Emissive power along (r, 0) in a finite concentric cylindrical medium under radiative equilibrium. —— $\tau_0 = 2.$ - - - $\tau_0 = 0.5$

results for an isothermal medium show that the accuracy of P_1 approximation, relative to the exact solutions, is of the same order for the axially symmetric and one-dimensional problems. This conclusion established a motivation for using higher order approximations in multidimensional problems [20, 24].

Acknowledgment

This work was supported in part by the National Science Foundation under Grant ENG 78-27611.

References

1 Chandrasekhar, S., *Radiative Transfer*, Dover, New York, 1960.

2 Davison, B., *Neutron Transport Theory*, Oxford University Press, London, 1958.

3 Kourganoff, V., *Basic Methods in Transport Problems*, Dover, New York, 1963.

4 Sampson, D. H., *Radiative Contributions to Energy and Momentum Transport in a Gas*, Interscience, New York, 1965.

5 Viskanta, R., "Radiative Transfer, and Interaction of Convection with Radiation Heat Transfer," in *Advances in Heat Transfer*, edited by T. F. Irvine, and J. P. Hartnett, Academic Press, New York, 1966.

6 Özisik, N. M., *Radiative Transfer*, John Wiley and Sons, New York, 1973.

7 Siegel, R., and Howell, J. R., *Thermal Radiation Heat Transfer*, McGraw-Hill, New York, 1972.

8 Steward, F. R., and Cannon, P., "The Calculation of Radiative Heat Flux in a Cylindrical Furnace using the Monte Carlo Method, "*International Journal of Heat and Mass Transfer*, Vol. 14, 1969, pp. 245–261.

9 Hottel, H. C., and Sarofim, A. A., *Radiative Transfer*, McGraw-Hill, New York, 1967.

10 Einstein, T. H., "Radiant Heat Transfer to Absorbing Gases Enclosed in a Circular Pipe with Conduction, Gas Flow and Internal Heat Generation," NASA TR R-156, 1963.

11 Heaslet, M. A., and Warming, R. F., "Theoretical Predictions of Radiative Transfer in a Homogeneous Cylindrical Medium," *Journal of Quantitative Spectroscopy and Radiative Transfer*, Vol. 6, 1966, pp. 751–774.

12 Desoto, S., "Coupled Radiation, Conduction and Convection in Entrance Flow," *International Journal of Heat and Mass Transfer*, Vol. 11, 1975, pp. 245–259.

13 Shorin, S. N., "Heat Exchange by Radiation in the Presence of an Absorbing Medium," *Engineer's Digest*, Vol. 12, 1951, pp. 324–328.

14 Deissler, R. G., "Diffusion Approximation for Thermal Radiation in Gases with Jump Boundary Conditions," ASME JOURNAL OF HEAT TRANSFER, Vol. 86C, 1964, pp. 240–246.

15 Chou, Y. S., and Tien, C. L., "A Modified Moment Method for Radiative Transfer in Non-Planar Systems," *Journal of Quantitative Spectroscopy and Radiative Transfer*, Vol. 8, 1968, pp. 919–933.

16 Modest, M. F., and Stevens, D. S., "Two-Dimensional Radiative Equilibrium of a Gray Medium Between Concentric Cylinders," *Journal of Quantitative Spectroscopy and Radiative Transfer*, Vol. 19, 1978, pp. 353–365.

17 Olfe, D. B., "Application of the Modified Differential Approximation to Radiative Transfer in a Gray Medium between Concentric Cylinders and Spheres," *Journal of Quantitative Spectroscopy and Radiative Transfer*, Vol. 8, 1968, pp. 899–907.

18 Yuen, W. W., and Tien, C. L., "Approximate Solutions of Radiative Transfer in One-Dimensional Non-Planar Systems," *Journal of Quantitative Spectroscopy and Radiative Transfer*, Vol. 19, 1978, pp. 533–549.

19 Perlmutter, M., and Howell, J. R., "Radiant Transfer through a Gray Gas Between Concentric Cylinders using Monte Carlo," ASME JOURNAL OF HEAT TRANSFER, Vol. 86C, 1966, pp. 169–179.

20 Bayazitoğlu, Y., and Higenyi, J., "Higher-Order Differential Equations of Radiative Transfer: P_3 Approximation," *American Institute of Aeronautics and Astronautics Journal*, Vol. 17, 1979, pp. 424–431.

21 Higenyi, J. K., "Higher Order Differential Approximation of Radiative Energy Transfer in a Cylindrical Gray Medium," Ph.D. Thesis, Rice University, Texas, 1980.

22 Selcuk, N., and Siddall, R. G., "Two Flux Spherical Harmonics Modelling of Two-Dimensional Radiative Heat Transfer in Furnaces," *International Journal of Heat and Mass Transfer*, Vol. 19, 1976, pp. 313–321.

23 Lowke, J. J., and Capriotti, E. R., "Calculation of Temperature Profiles of High Pressure Electric Arcs using the Diffusion Approximation," *Journal of Quantitative Spectroscopy and Radiative Transfer*, Vol. 9, 1969, pp. 207–231.

24 Higenyi, J., and Bayazitoğlu, Y., "Radiative Transfer of Energy of a Gray Medium in a Cylindrical Enclosure with Heat Generation," *American Institute of Aeronautics and Astronautics Journal*, Vol. 18, 1980, (in press)

25 Cheng, P. "Exact Solutions and Differential Approximation for Multi-Dimensional Radiative Transfer in Cartesian Coordinate Configurations," *Progress in Astronautics and Aeronautics*, Vol. 31, 1972, pp. 269–308.

26 Dua, S.-Sham, and Cheng, P., "Multi-Dimensional Radiative Heat Transfer in Non-Isothermal Cylindrical Media with Non-Isothermal Walls," *International Journal of Heat and Mass Transfer*, Vol. 18, 1975, pp. 245–259.

27 Uesugi, A., and Tsujita, J., "Diffuse Reflection of a Searchlight Beam by Slab, Cylindrical and Spherical Media," *Astronomical Society of Japan Publications*, Vol. 21, 1969, pp. 370–383.

APPENDIX

An analytical solution to equation (12) subject to boundary conditions in equations (13) takes the form [21]

$$\psi_0 = \psi_{01} + \psi_{02} + f(\eta) \tag{A1}$$

Here the function $f(\eta)$ accounts for the nonhomogeneity in the differential equation due to the heat generation, while ψ_{01} and ψ_{02} account for the influence of the inner and outer radial bounday emissive power. They are explicitly given by

$$f(\eta) = 3(\lambda - 1) \int \left\{ \int U(\xi) d\xi \right\} d\eta,$$

$$\times \left\{ \begin{matrix} \dfrac{df}{d\eta} - H_1 f = 0, \text{ at } \eta = \eta_1 \\ \dfrac{df}{d\eta} + H_2 f = 0, \text{ at } \eta = \eta_2 \end{matrix} \right\} \tag{A2}$$

$$\psi_{01} = \sum_{m=1}^{\infty} A_{m,1}[I_0(\gamma_m \tau) + J_m(E_2, \tau_2) K_0(\gamma_m \tau)] Z_m(\eta) \tag{A3}$$

$$\psi_{02} = \sum_{m=1}^{\infty} A_{m,2}[I_0(\gamma_m \tau) + J_m(E_1, \tau_1) K_0(\gamma_m \tau)] Z_m(\eta) \tag{A4}$$

where $A_{m,i} = \dfrac{1}{R_i N_m} \displaystyle\int_0^{\eta_2} Z_m(\eta) g_i(\eta) d\eta$, $J_m(E_i, \tau_i)$

$$= \frac{E_i \gamma_m I_1(\gamma_m \tau_i) + I_0(\gamma_m \tau_i)}{E_i \gamma_m K_1(\gamma_m \tau_i) - K_0(\gamma_m \tau_i)}$$

$$Z_m = \gamma_m \cos \gamma_m \eta + H_1 \sin \gamma_m \eta, \quad \tan \gamma_m \eta_2 = \frac{\gamma_m (H_1 + H_2)}{\gamma_m{}^2 - H_1 H_2}$$

$$N_m = \frac{1}{2} \left[(\gamma_m{}^2 + H_1{}^2) \left(\eta_2 + \frac{H_2}{\gamma_m{}^2 + H_2{}^2} \right) + H_1 \right],$$

$$g_i(\eta) = 4\pi \Phi_{w,i} - f(\eta)$$

$$R_i = I_0(\gamma_m \tau_i) + J_m(E_n, \tau_n) K_0(\gamma_m \tau_i) + E_i \gamma_m [I_1(\gamma_m \tau_i) - J_m(E_n, \tau_n) K_1(\gamma_m \tau_i)]$$

for $i = 1, 2$ and $n = 3 - i$.

Note that for a hollow cylinder, one lets $A_{m,1}$ and $J_m(E_1, \tau_1)$ equal to zero. Furthermore, symmetry about $z = 0$ plane requires H_1 to be identically zero. The medium Planck function Φ and heat fluxes ψ_r and ψ_z are obtained from equation (A1) using equations (8).

C. N. Liu[1]
T. M. Shih
Department of Mechanical Engineering,
University of Maryland,
College Park, MD 20742

Laminar, Mixed-Convection, Boundary-Layer, Nongray-Radiative, Diffusion Flames

The two-dimensional, laminar, mixed-mode convection (free and forced), boundary-layer, radiative, diffusion flame has been analytically investigated with special attention directed toward the nongray nature of the combustion products. The solution procedures include Shvab-Zeldovich approximation and von Mises transformation for the physical transport equations and the finite difference method for the computation of the transformed equations. The local radiative fluxes for nongray, gray and radiatively-ideal gases are prescribed in detail. Twelve parameters that govern the flame characteristics have been identified. Setting appropriate parameters to zero yields several limiting solutions which are compared with the reported results. In addition to extensive results of distributions in the field variables and fluxes, the ratio of the radiation loss to the combustion energy evolved was computed and a radiatively-ideal gas having behaviors similar to the nongray gases was identified.

1 Introduction

The classical problem of a laminar boundary-layer flame has been extensively investigated for the past two decades [1–9]. Unfortunately, since such a combustion system usually generates radiatively participating products, such as the soot, water vapor and carbon dioxide, the physical phenomena remain incompletely understood due to the nongray nature of the medium. In many studies, the gaseous radiation therefore was assumed to be negligible and the complexity of the gaseous radiation was avoided. In the present analysis, it is attempted to extend these previous analyses to a more realistic system in which the convection, radiation, mass transfer and the combustion coexist.

When the gaseous absorption coefficients which are dependent on the wave length, temperature and partial pressures are considered, the complexity of the problem is greatly increased. Tien reviewed the application of the total band absorptances for carbon dioxide and water vapor to problems of this type in the infrared range [10]. This application, however, is restricted to isothermal and homogeneous systems. For nonisothermal and inhomogeneous systems, a certain scaling method is also needed for the computation of the total band absorptances [11–14]. In these scaling methods, the detailed information about the distributions of temperature and partial pressures must be known and the computation becomes very tedious. It has been found [6] that only peak values of the partial pressures and temperatures need to be used in calculating the intensities. Due to its simplicity, this peak-value scaling technique was adopted here.

In addition to the absorbing-emitting gases, soot plays an important role in the radiative emission. The absorption coefficient of soot was theoretically derived using Mie theory [15]. Its spectral dependence was simplified to a simple function of the wavelength with good agreement with the experimental data [16–18]. Based on these results, a model of gray soot was further proposed [5]. In the present study, the gray model was used.

Although the nongray characteristics of gases were intensively studied, these analyses have not been widely applied to combustion systems such as boundary-layer radiative flames. Reference [7] appears to be the only work in which the similarity method was used to examine a nongray radiative stagnation flame. In the present paper, the mixed-convection, combustion, mass transfer and nongray radiation are simultaneously considered. In addition to obtaining the detailed distributions of field variables and their fluxes, we attempted to seek for a radiatively-ideal gas (having constant absorption coefficient) which yields similar local radiative flux as the nongray medium. Finally, the ratio of the radiative output to the heat of combustion, which is an important parameter to the fire-safety researchers, was also obtained for the plexiglass burning.

2 Governing Equations

The continuity, momentum, enthalpy, and species equations describing a steady, two-dimensional, nongray-radiative, boundary-layer flame can be respectively written as

$$\frac{\partial \rho u}{\partial x} + \frac{\partial \rho v}{\partial y} = 0 \tag{1a}$$

$$\rho u \frac{\partial u}{\partial x} + \rho v \frac{\partial u}{\partial y} = \frac{\partial}{\partial y}\left(\mu \frac{\partial u}{\partial y}\right) + g(\rho_\infty - \rho) \tag{1b}$$

$$\rho u \frac{\partial h}{\partial x} + \rho v \frac{\partial h}{\partial y} = \frac{\partial}{\partial y}\left(\frac{k}{C_p}\frac{\partial h}{\partial y}\right) + \dot{q}_c''' + \dot{q}_r''' \tag{1c}$$

$$\rho u \frac{\partial Y_i}{\partial x} + \rho v \frac{\partial Y_i}{\partial y} = \frac{\partial}{\partial y}\left(\rho D \frac{\partial Y_i}{\partial y}\right) + \dot{m}_i''' \tag{1d}$$

where $h \equiv \int_{T_\infty}^{T} C_p dT$ and $\dot{q}_c'''$ and $\dot{m}_i'''$ are volumetric combustion heat and mass generation rates respectively, $\dot{q}_r'''$ the gradient of the radiative flux and Y_i the mass fraction of species such as the fuel, oxygen, water vapor and carbon dioxide. The boundary conditions for the flame over a vertically pyrolyzing fuel slab as shown in Fig. 1

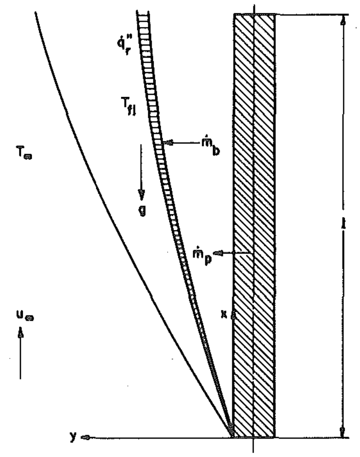

Fig. 1 System schematic of a two-dimensional, steady-state, laminar, nongray-radiative, boundary-layer flame adjacent to a pyrolyzing fuel slab

---

[1] Presently at IBM, General Products Division, San Jose, CA. 95193.

Contributed by the Heat Transfer Division for publication in the JOURNAL OF HEAT TRANSFER. Manuscript received by the Heat Transfer Division November 8, 1979.

are

$$u = 0,\ h = h_w,\ Y_f = Y_{fw},\ v = -D\frac{\partial Y_f}{\partial y}\Big/(1 - Y_{fw}) \text{ at } y = 0 \qquad (2a)$$

$$u = u_\infty,\ h = 0,\ Y_{\rm ox} = Y_{\rm ox\infty} \text{ at } y \to \infty \qquad (2b)$$

It is noteworthy that the energy balance at the pyrolyzing wall

$$\frac{k}{C_p}\frac{\partial h}{\partial y}\Big|_0 - \dot q_{rw}'' = \dot m_p'' L + \text{conduction into the solid} \qquad (3)$$

should not be considered as one of the boundary conditions in equation (2a). This is because equation (3) is used to provide the information of the heat conduction into the solid. If this information is not of interest to us as in the present analysis, equation (3) is just a redundant boundary condition.

Since $\dot q_c'''$ is a complicated unknown function of several field variables, it is customary to introduce the Shvab-Zeldovich variables to eliminate $\dot q_c'''$ [1 ~ 4, 7, 9]. The two assumptions associated with this approach are that the Lewis number for all species is equal to unity and that a single-step global chemical reaction takes place stoichiometrically. For laminar flames, we can further propose that the reaction zone is so thin like a sheet that the reactants do not coexist. Therefore, the computed Shvab-Zeldovich variable solutions can be used to recover the primitive variables.

After the Shvab-Zeldovich transformation of equations (1c, 1d) and further normalization, we derive

$$\rho u\frac{\partial J_1}{\partial x} + \rho v\frac{\partial J_1}{\partial y} = \frac{\partial}{\partial y}\left(\frac{k}{C_p}\frac{\partial J_1}{\partial y}\right) + \frac{1}{Q_p Y_{\rm ox\infty} - h_w}\frac{\partial \dot q_r''}{\partial y} \qquad (4a)$$

$$\rho u\frac{\partial J_2}{\partial x} + \rho v\frac{\partial J_2}{\partial y} = \frac{\partial}{\partial y}\left(\rho D\frac{\partial J_2}{\partial y}\right) \qquad (4b)$$

subject to the transformed boundary conditions

$$J_1 = J_2 = 1, \text{ at } y = 0 \qquad (5a)$$

$$J_1 = J_2 = 0, \text{ at } y \to \infty \qquad (5b)$$

where J_1 and J_2 are defined in the Nomenclature. For nonradiative flames, i.e., $\dot q_r'' = 0$, J_1 and J_2 are identical. The last boundary condition in equation (2a) must be transformed accordingly into

$$v(0) = \frac{Y_{fw} + Y_{\rm ox\infty}\nu_f M_f/\nu_{\rm ox}M_{\rm ox}}{1 - Y_{fw}}\left(-D\frac{\partial J_2}{\partial y}\right)_{y=0} \qquad (6)$$

Equations (1a, 1b) remain unchanged except that the buoyancy term in equation (1b) now takes a new form

Table 1 Four wavelength-dependent components of the local radiative flux

Symbol	Mathematical Expression	Physical Representation
$Q_{\rm I}$	$2\varepsilon_w\int_0^\infty e_{b\lambda}(T_w)E_3(\kappa_\lambda)d\lambda$	wall emission after being attenuated by the medium existing along the path 0 → y
$Q_{\rm II}$	$4(1 - \varepsilon_w)\int_0^\infty E_3(\kappa_\lambda)\int_0^{\kappa_{\delta\lambda}} e_{b\lambda}(t)E_2(t)dt\ d\lambda$	reflective flux of the boundary-layer radiation arriving at the wall, being reflected by the wall and attenuated by the medium existing along the path 0 → y
$Q_{\rm III}$	$2\int_0^\infty\int_0^{\kappa_\lambda} e_{b\lambda}(t)E_2(\kappa_\lambda - t)dt\ d\lambda$	emission of the medium in the region from the wall to the location y
$Q_{\rm IV}$	$2\int_0^\infty\int_{\kappa_\lambda}^{\kappa_{\delta\lambda}} e_{b\lambda}(t)E_2(t - \kappa_\lambda)dt\ d\lambda$	emission of the medium in the region from the location y to the boundary-layer edge δ

Nomenclature

a = absorption coefficient, m^{-1}
A_i = total band absorptance for the ith band, μm^{-1}. peak value when overbarred.
B = mass transfer number, $(\beta_w - \beta_\infty)/(\beta_T - \beta_w)$
D_3 = third Damköhler number, $Q_p Y_{\rm ox\infty}/h_w$
$E_n(t)$ = exponential integral of order n
e = emissive power, cal/m^2-s
$f = \nu_f M_f/\nu_{\rm ox}M_{\rm ox}$
f_v = volumetric fraction of soot
F_v = maximum of f_v
Gr = Grashof number, $g(T_w - T_\infty) \times \ell^3/\nu_\infty{}^2 T_\infty$
J_1 = normalized Shvab-Zeldovich variable, $(\gamma - \gamma_\infty)/(\gamma_w - \gamma_\infty)$
J_2 = normalized Shvab-Zeldovich variable, $(\beta - \beta_\infty)/(\beta_w - \beta_\infty)$
ℓ = length of the fuel slab, m
L = effective heat of pyrolysis, cal/kg
$\dot m''$ = local mass flux, kg/m^2-s
M = molecular weight, kg
Pr = Prandtl number, ν/α
Q_p = heat of reaction per kg of oxygen, cal/kg
$\dot q_r''$ = local radiation flux, cal/m^2-s
r = mass consumption number, $(Y_{\rm ox\infty}/Y_{fw}) \times (\nu_f M_f/\nu_{\rm ox}M_{\rm ox})$
Re = Reynolds number, $u_\infty\ell/\nu_\infty$
u = x-direction velocity, m/s
v = y-direction velocity, m/s
$\alpha = k/\rho C_p$, m^2/s
β = Shvab-Zelodvich variable, $Y_f/\nu_f M_f - Y_{\rm ox}/\nu_{\rm ox}M_{\rm ox}$
$\beta_T = 1/\nu_f M_f$, kg^{-1}
γ = Shvab-Zeldovich variable, $-h/Q_p\nu_{\rm ox}M_{\rm ox} - Y_{\rm ox}/\nu_{\rm ox}M_{\rm ox}$
δ = boundary-layer thickness, m
$\theta_r = T_\infty/T_w$
$\kappa(y)$ = optical thickness, $\int_0^y a(z)dz$
ν = kinematic viscosity, m^2/s, or stoichiometric coefficient
ξ = radiation-convection number, $\sigma T_w{}^4/\rho_\infty u_\infty h_w$
$\phi = m/n$ for a fuel $C_mH_nO_j$
χ = ratio of the total radiation output to the total chemical energy evolved
ω = wave number, μm^{-1}

Subscripts

ad = adiabatic
b = fuel burning or black body
C = carbon dioxide
f = fuel
g = gas
$f\ell$ = flame sheet
N = nitrogen
ox = oxygen
p = pyrolyzing or combustion products
r = radiation
s = soot
u = upstream
w = wall of the pyrolyzing fuel
wa = water

Superscripts

— = normalized on ℓ for lengths, u_∞ for velocities, $\rho_\infty u_\infty$ for mass fluxes, $\sigma T_w{}^4$ for radiative fluxes and T_w for temperatures

$$g(\rho_\infty/\rho - 1) = g(1/\theta_r - 1)[D_3 - J_1(D_3 - 1)],\ y \le y_{f\ell}$$
$$= g(1/\theta_r - 1)\,[D_3(1 + r)J_2/r - (D_3 - 1)J_1],\ y > y_{f\ell} \qquad (7)$$

The radiative flux $\dot{q}_r''$ shown in equation (4a) will be specified in detail in the following sections.

3 Local Radiative Flux

According to the approximation of isotropic media, the local radiative flux can be expressed [15, 19] as

$$\dot{q}_r''(x, y) = Q_{\rm I} + Q_{\rm II} + Q_{\rm III} - Q_{\rm IV} \qquad (8)$$

The mathematical expressions and the physical meanings of the four components are listed in Table 1. It is desirable to eliminate their wave-length dependence by introducing the total band absorptance for carbon dioxide and water vapor. We will present briefly such a procedure for $Q_{\rm I}$ and simply list the final result for $Q_{\rm II}$, $Q_{\rm III}$ and $Q_{\rm IV}$ in Table 2.

The computation of the exponential integrals contained in the expressions is cumbersome. Since $E_2(t)$ and $E_3(t)$ can be closely approximated as exp $(-2t)$ and $\frac{1}{2}$ exp $(-2t)$, respectively, [20], $Q_{\rm I}$ is simplified into

$$Q_I = Q_{Ia} + Q_{Ib} \qquad (9)$$

where

$$Q_{Ia} = \epsilon_w \int_0^\infty e_{b\lambda}(T_w) \exp\left[-2\int_0^y a_{\lambda s}(z)dz\right] d\lambda \qquad (10a)$$

and

$$Q_{Ib} = -\epsilon_w \int_0^\infty e_{b\lambda}(T_w) \exp\left[-2\int_0^\infty a_{\lambda s}(z)dz\right] \times\left\{1 - \exp\left[-2\int_0^y a_{\lambda g}(z)dz\right]\right\} d\lambda \qquad (10b)$$

The spectral absorption coefficient of soot, $a_{\lambda s}$, was shown [17, 18] to be proportional to f_v/λ, where f_v is the volumetric fraction of soot in the mixture. In the present analysis, f_v is assumed as a linear function of y, i.e., $F_v y/y_{f\ell}$, in the region between the pyrolyzing wall and the reaction zone and is assumed to vanish elsewhere. With this assumption, $a_{\lambda s}$ can be expressed as $a_{\lambda s} = Gy/\lambda$ where $G \equiv 5.52\, F_v/y_{f\ell}$. Alternatively, using the gray soot approximation [5] and choosing the complex index of refraction to be 2 for the real part and 1 for the imaginary part, we can obtain a further simplified expression for the gray absorption coefficient of soot as

$$a_s = 3.6GTy/C_2 \qquad (11)$$

where C_2 is the Planck second constant (1.44×10^{-2} m K). Using equation (11), we can reduce equation (10a) to

$$Q_{Ia} = \epsilon_w \sigma T_w{}^4 \exp\left[-500\,G\int_0^y zT(z)dz\right] \qquad (12)$$

Table 2 Eight wavelength-independent components of the local radiative flux. The overbar denotes peak values. C_1 and C_2 are Planck constants.

Component	Mathematical Expression
Q_{Ia}	$\epsilon_w \sigma T_w{}^4 \exp\left[-500G\int_o^y zT(z)dz\right]$
Q_{Ib}	$-\epsilon_w \sum_{i=1}^{9} e_{b\omega_i}(T_w) \exp\left(-\omega_i G y^2\right) \bar{A}_i(2y)/\omega_i{}^2$
Q_{IIa}	$48(1-\epsilon_w)C_1 G\int_o^\delta z/\left[C_2/T(z) + G\left(y^2 + z^2\right)\right]^5 dz$
Q_{IIb}	$\sum_{i=1}^{9}\int_o^\delta \frac{e_{b\omega_i}(T)}{\omega_i{}^2}\frac{d}{dz}\left\{\exp\left[-\omega_i G\left(y^2 + z^2\right)\right]\right\} \bar{A}_i(2y + 2z)dz\ (1 - \epsilon_w)$
Q_{IIIa}	$48C_1 G\int_o^y z/\left[C_2/T(z) + G\left(y^2 - z^2\right)\right]^5 dz$
Q_{IIIb}	$-\sum_{i=1}^{9}\int_o^y \frac{e_{b\omega_i}(T)}{\omega_i{}^2}\frac{d}{dz}\left\{\exp\left[-\omega_i G\left(y^2 - z^2\right)\right]\right\} \bar{A}_i(2y - 2z)dz$
Q_{IVa}	$48C_1 G\int_y^\delta z/\left[C_2/T(z) + G\left(z^2 - y^2\right)\right]^5 dz$
Q_{IVb}	$\sum_{i=1}^{9}\int_y^\delta \frac{e_{b\omega_i}(T)}{\omega_i{}^2}\frac{d}{dz}\left\{\exp\left[-\omega_i G\left(z^2 - y^2\right)\right]\right\} \bar{A}_i(2z - 2y)dz$

The total band absorptance for the ith band is defined as

$$A_i(y) = \int_0^\infty \left[1 - \exp\left(-\int_0^y a_{\lambda g}(z)dz\right)\right] d\omega \qquad (13)$$

where ω is the wave number. Substitution of equations (11, 13) into equation (10b) yields

$$Q_{Ib} = \epsilon_w - \sum_{i=1}^{9} e_{b\omega_i}(T_w) \exp\left(-\omega_i G y^2\right) \bar{A}_i(2y)/\omega_i{}^2 \qquad (14)$$

where the nine bands are at $15\mu (i = 1)$, 10.4μ, 9.4μ, 4.3μ and 2.7μ for CO_2 and $6.3\mu (i = 6)$, 2.7μ, 1.87μ and 1.38μ for H_2O. The total band absorptance can be expressed in terms of the band parameters [16, 17] as

$$\bar{A}(t_1, t_2) = c_3 \ell n\left\{t_1 f_2(t_2)\left[\frac{t_1 + 2}{t_1 + 2f_2(t_2)}\right] + 1\right\} \qquad (15)$$

where

$$t_1 = (c_1/c_3)\rho y,\ t_2 = (c_2{}^2/4c_1c_3)\,[(P_N + bP_i)/P]^n \qquad (16)$$

and $f_2(t_2) = 2.94\,[1 - \exp(-2.6t_2)]$. The parameters c_1, c_2, c_3, b and n were specified in reference [21]. Similar derivations can be carried out for $Q_{\rm II}$, $Q_{\rm III}$ and $Q_{\rm IV}$. Their final mathematical expressions are listed in Table 2.

4 Gray gas Approximation

The computation of $q_r''(x, y)$ shown in equation (8) is very time-consuming. One way of simplifying the computation is to introduce the Planck mean absorption coefficient defined as $\int_0^\infty e_{b\lambda} a_\lambda d\lambda/\sigma T^4$. Based on the exponential wide-band model, the Planck mean absorption coefficient has been calculated and plotted versus the temperature [10]. For computational convenience desired in the present analysis, those graphical results $a_{\rm C}/P_{\rm C}$ and a_{wa}/P_{wa} are empirically fitted by some simple explicit functions of the temperature [20]. These functions are free of λ dependence, therefore $\dot{q}_r''(x, y)$ can be reduced to

$$\begin{aligned}\dot{q}_r''(y) = {} & \epsilon_w \sigma T_w{}^4 \exp\left[-2\int_0^y a(z)dz\right] \\ & + 2(1 - \epsilon_w)\exp\left[-2\int_0^y a(z)\,dz\right]\int_0^\delta \sigma T^4(y)\exp \\ & \times\left[-2\int_0^y a(z)dz\right] a(y)\,dy \\ & + 2\int_0^y \sigma T^4(z)\exp\left[-2\int_z^y a(t)dt\right] a(z)dz \\ & - 2\int_y^\delta \sigma T^4(z)\exp\left[-2\int_y^z a(t)dt\right] a(z)dz \qquad (17)\end{aligned}$$

where $a = a_s + P_{\rm C}a_{\rm C} + P_{wa}a_{wa}$ and a_s is given in equation (11). Using equations (17), the computation time is reduced to ~2 percent of that required by nongray formula.

5 Radiatively-Ideal Gas Approximation

In the present analysis, the radiatively-ideal gas is defined as the gas that has a constant absorption coefficient. There are three merits in studying the behavior of such an ideal gas: (1) The combustion system complexed by the radiative participation of real gases can be easily analyzed; (2) Ten dimensionless parameters can be identified and (3) The possibility of searching for a radiatively-ideal gas which exhibits similar behavior as the real gas can be examined. Therefore, with the constancy of the absorption coefficient, equation (17) can be further reduced to

$$\dot{q}_r''(x, y) = 2\epsilon_w e_{bw} E_3(\kappa) + 4(1 - \epsilon_w) E_3(\kappa) \int_0^{\kappa_\delta} e_b(t) E_2(t) dt$$

$$+ 2 \int_0^{\kappa} e_b(t) E_2(\kappa - t) dt - 2 \int_{\kappa}^{\kappa_\delta} e_b(t) E_2(t - \kappa) dt \quad (18)$$

Equations (8, 17, 18) are the expressions for the local radiative flux with the fact that equation (8) has the least simplicity whereas equation (18) has the least accuracy.

6 Recovery of Physical Quantities

It is desirable to recover the physical quantities from the solutions J_1 and J_2. Through straightforward algebra and use of definitions, the following expressions can be derived.

$$\left.\begin{aligned} h/h_w &= D_3 - J_1(D_3 - 1) \\ Y_f/Y_{fw} &= (1 + r)J_2 - r \end{aligned}\right\} y \le y_{f\ell} \quad (19a)$$

$$\left.\begin{aligned} h/h_w &= D_3(1 + r)J_2/r - (D_3 - 1)J_1 \\ Y_{\text{ox}}/Y_{\text{ox}\infty} &= 1 - (1 + r)J_2/r \end{aligned}\right\} y > y_{f\ell} \quad (19b)$$

where $y_{f\ell}$ is determined by the assumption that Y_f and Y_{ox} vanish simultaneously at the flame sheet; i.e.,

$$J_2(y_{f\ell}) = r/(1 + r) \quad (20)$$

Since the mass burning rate is equal to the diffusion rate of the fuel vapor into the reaction zone, we obtain

$$\dot{m}_b'' = -\rho D \left.\frac{\partial Y_f}{\partial y}\right|_{y=y_{f\ell}} = -\rho D Y_{fw}(1 + r) \left.\frac{\partial J_2}{\partial y}\right|_{y=y_{f\ell}} \quad (21)$$

Equation (21) becomes very useful when we desire to find the ratio of the radiative output to the heat of combustion χ.

The flame temperature can be derived from the enthalpy expression in equation (19a) or in equation (19b) as

$$T_{f\ell} = [D_3 - J_1(y_{f\ell})(D_3 - 1)](T_w - T_\infty) + T_\infty \quad (22)$$

The mass fractions of the species are also needed to calculate the partial pressures of radiatively participating gases. Nitrogen is an inert gas and therefore its normalized mass fraction, $(Y_N - Y_{N\infty})/(Y_{Nw} - Y_{N\infty})$, satisfies the J_2 transport equation if Y_{NW} is assumed constant. Consequently,

$$Y_N(x, y) = J_2(x, y)(Y_{Nw} - Y_{N\infty}) + Y_{N\infty} \quad (23)$$

where $Y_{N\infty} = 1 - Y_{\text{ox}\infty}$. With the fact that the sum of Y_{fw}, Y_{Nw} and Y_{pw} equals unity and the assumption that the mass ratio of nitrogen to the combustion products (mainly CO_2 and H_2O) at the reaction zone is equal to that at the wall, it can be shown that

$$Y_{Nw} = \frac{7\nu_N(1 - Y_{fw})}{7\nu_N + 11\nu_C + 4.5\nu_{wa}} \quad (24)$$

where

$$\nu_N = \nu_{\text{ox}} M_{\text{ox}}(1 - Y_{\text{ox}\infty})/M_N Y_{\text{ox}\infty} \quad (25)$$

Once $Y_N(x, y)$ is computed from equations (24, 25), the assumption that the fuel and oxygen do not coexist yields

$$Y_p = 1 - Y_f - Y_N \text{ when } y \le y_{f\ell} \quad (26a)$$

$$Y_p = 1 - Y_{ox} - Y_N \text{ when } y > y_{f\ell} \quad (26b)$$

With the further assumption $Y_C/Y_{wa} = M_C\nu_C/M_{wa}\nu_{wa}$, we deduce

$$Y_C/Y_p = 22\nu_C/(22\nu_C + 9\nu_{wa}),\ Y_{wa}/Y_p = 9\nu_{wa}/(22\nu_C + 9\nu_{wa}) \quad (27a, b)$$

Equations (23–27) are the procedures of recovering the species mass fractions from $J_2(x, y)$. Consider, for example, a combustion system having methane as the fuel and the atmospheric air ($Y_{\text{ox}\infty} = 0.23$) as the oxident with $r = 0.2$. Let $J_2(x, y)$ arbitrarily be 0.5. Since this value is larger than $r/(1 + r)$, the corresponding y location is smaller than $y_{f\ell}$ and equation (26a) should be used. The final results are listed in Table 3.

If equations (1b, 4a, 4b, 6, 8) are nondimensionalized, i.e., the coordinates x and y are normalized on ℓ, velocities u and v on u_∞, radiative flux $\dot{q}_r''$ on σT_w^4 and the temperature on T_w, all the governing parameters listed in Table 4 will appear. Each of these twelve parameters is associated with a certain physical phenomenon. Only the mass transfer number deserves additional attention. It originates from the mass balance at the interface for inert systems [22] and is defined as $(Y_w - Y_\infty)/(1 - Y_w)$, where Y denotes the mass fraction of a certain species. In combustion systems, Y should be replaced by the Shvab-Zeldovich variable β since β satisfies a source-free transport equation, and not Y. When the heat conduction into the solid is negligible and the flame is assumed nonradiative, B can be shown from equation (3) to be equal to $(Q_p Y_{\text{ox}\infty} - h_w)/L$ which has been widely used in the analysis of nonradiative flames.

The present system can be readily reduced to several limiting cases by setting appropriate parameters to zero. The inert flow [23] can be generated by setting D_3 to zero. At Re = 0 or Gr = 0, the system becomes a pure free-convection flame [2, 3] or a pure forced-convection flame [1], respectively. At $\kappa_\ell = 0$ and $\epsilon_w = 0$, the flame becomes nonradiative [9]. For nongray systems, two additional parameters ϕ and F_v are needed.

7 Assumptions and Computational Accuracy

In the present analysis, the following assumptions have been made to simplify the solution procedure: (1) $\partial\dot{q}_r''/\partial y \gg \partial\dot{q}_r''/\partial x$ so that a marching finite difference method [24, 25] can be used. (2) The temperature and the fuel mass fraction are constant along the pyrolyzing wall. (3) The soot distribution is linear in y and $y \le y_{f\ell}$ and is zero if $y > y_{f\ell}$ so that the complexity of the reaction kinetics is avoided. (4) The radiative flux is linearized in J_1 as

$$\dot{q}_r'' \approx S_1 + S_2 J_1 \quad (28)$$

where

$$S_1 \equiv \dot{q}''_{r,u} - \left.\frac{\partial \dot{q}''_{r,u}}{\partial J_1}\right|_{J_{1,u}} \text{ and } S_2 \equiv \left.\frac{\partial \dot{q}''_{r,u}}{\partial J_1}\right|_{J_{1,u}} \quad (29)$$

Since no experimental data are available for comparison, the accuracy of the numerical result is tested using the following three indirect methods. First, the solutions $J_1(\bar{x}, \bar{y})$, $J_2(\bar{x}, \bar{y})$ and $u(\bar{x}, \bar{y})$ are functions of the 12 parameters only. If the ambient conditions and the fuel properties are varied such that the 12 parameters remain unchanged, these solutions should remain unchanged. Table 5 lists the input data of two typical computations so selected to yield the corresponding parametric values. The solutions $J_1(\bar{x}, \bar{y})$, $J_2(\bar{x}, \bar{y})$ and $\bar{u}(\bar{x}, \bar{y})$ of these two computations have been found identical. The second method is to check the balance of fuel vapor throughout the boundary layer. Since part of the pyrolyzate from the wall is consumed in the reaction zone, the unburned fuel is convected downstream into the wake. For a system having $B = 1.75$, $D_3 = 1.5$, $\text{Gr} = 4.88 \times 10^8$, Pr

Table 3 Typical values of species mass fractions

Variable	ν_N	$Y_{f\,w}$	$Y_{N\,w}$	Y_N	Y_f	Y_p	Y_c	Y_{wa}
Equation from which the value is calculated	Eq. (25)	Definition of r	Eq. (24)	Eq. (23)	Eq. (19a)	Eq. (26a)	Eq. (27a)	Eq. (27b)
value	7.652	0.288	0.518	0.644	0.115	0.241	0.133	0.108

$= 0.73$, $r = 0.20$, $\mathrm{Re} = 1.33 \times 10^4$, $\epsilon_w = 0.5$, $\theta_r = 0.4167$, $\kappa_\ell = 1.0$ and $\xi = 2.36 \times 10^{-2}$, the pyrolysis rate over the entire fuel slab is 1.943×10^{-3} kg/s, the combustion rate over the entire reaction zone is 6.514×10^{-4} kg/s and the unburned pyrolyzate flow rate at $x = \ell$ is 1.311×10^{-3} kg/s. Therefore, the balance of the fuel species is found within ± 1 percent error. The third method is to compare the present results with those reported in the literature only for limiting cases. These three methods thus partially tested the computational accuracy of the present result.

8 Results and Discussion

All the results presented here were computed using the parametric values chosen as: $\mathrm{Re} = 1.33 \times 10^4$, $\mathrm{Gr} = 4.88 \times 10^8$, $\mathrm{Pr} = 0.73$, $B = 1.75$, $\xi = 2.36 \times 10^{-2}$, $\epsilon_w = 0.5$, $\theta_r = 0.417$, $\kappa_\ell = 1.0$, $r = 0.2$, $D_3 = 5.596$, $\phi = 0.625$ and $F_v = 2.5 \times 10^{-6}$ unless specified otherwise. For radiatively-ideal gas, ϕ and F_v do not enter the problem. For gray and nongray gases, the optical thickness κ_ℓ is a complicated function of the wave length, temperature and species partial pressures. More comprehensive results are presented in reference [20].

Table 4 Definitions and related phenomena of 12 parameters. The last two are for gray and nongray systems only.

Parameter	Name	Definition	Related Phenomenon
Re	Reynolds Number	$\dfrac{u_\infty \ell}{\nu_\infty}$	forced convection
Gr	Grashof Number	$\dfrac{g(T_w - T_\infty)\ell^3}{\nu_\infty^2 T_\infty}$	free convection
Pr	Prandtl Number	ν/α	energy transport
B	Mass Transfer Number	$\dfrac{\beta_w - \beta_\infty}{\beta_T - \beta_w}$	mass transfer
ξ	Radiation-Convection Number	$\dfrac{\sigma T_w^4}{\rho_\infty u_\infty h_w}$	radiation and convection
ϵ_w	Wall Emissivity	—	wall radiation
θ_r	Temperature Ratio	T_∞/T_w	wall radiation
κ_ℓ	Optical Thickness	$a\ell$	gaseous radiation (for radiatively-ideal gas only)
r	Mass Consumption Number	$\dfrac{Y_{ox\infty}\nu_f M_f}{Y_{fw}\nu_{ox} M_{ox}}$	combustion
D_3	Third Damköhler Number	$\dfrac{Q_p Y_{ox\infty}}{h_w}$	combustion
F_v	Max. Soot Volum. Fraction	—	soot emission
ϕ	Ratio of C atoms to H atoms	m/n for $C_m H_n O_j$	nongray gaseous radiation

Table 5 Input data for two typical computations in which the parametric values remain the same

Variable	Computation #1	Computation #2	Parameter	Parametric Value
u_∞(m/sec)	1	2	Re	1.33×10^4
ν_∞(m^2/sec)	1.5×10^{-5}	1.2×10^{-4}	Gr	4.88×10^8
ℓ (m)	0.2	0.8	Pr	0.73
T_w($^\circ$K)	720	856	B	1.75
T_∞($^\circ$K)	300	357	ξ	2.36×10^{-2}
$Y_{ox\infty}$	0.230	0.274	ϵ_w	0.5
Y_{fw}	0.593	0.593	θ_r	0.417
$\nu_f M_f/\nu_{ox} M_{ox}$	0.516	0.516	κ_ℓ	1.0
Q_p(cal/kg)	3.16×10^6	3.16×10^6	r	0.2
k_∞(cal/m sec $^\circ$K)	7.54×10^{-3}	5.07×10^{-2}	D_3	5.596
C_p(cal/kg $^\circ$K)	310	310	F_v	2.5×10^{-6}
ϵ_w	0.5	0.5	ϕ	0.625
a(m^{-1})	5	1.25		
F_v	2.5×10^{-6}	2.5×10^{-6}		
fuel	$C_5H_8O_2$	$C_5H_8O_2$		

Figure 2 shows the distribution of the local radiative flux computed using the exponential wide-band model for nine bands and three principal bands, respectively. The three principal bands are at 4.3μ for CO_2 and 6.3μ and 2.7μ for H_2O. Based on several numerical experiments, the contribution of these three-band radiations to the total nine-band gaseous radiations is found to be approximately 90 percent. The computation time per streamwise step, however, is drastically reduced from 55 s for the nine-band computation to 16 s for the three-band computation. Therefore, in the present analysis, the three-band approximation with the result multiplied by a correction factor of 1.1 has been used.

Figure 3 shows the profiles of the local radiative flux computed using the gray gas model at $\bar{x} = 0.22$ parameterized in F_v. The flux

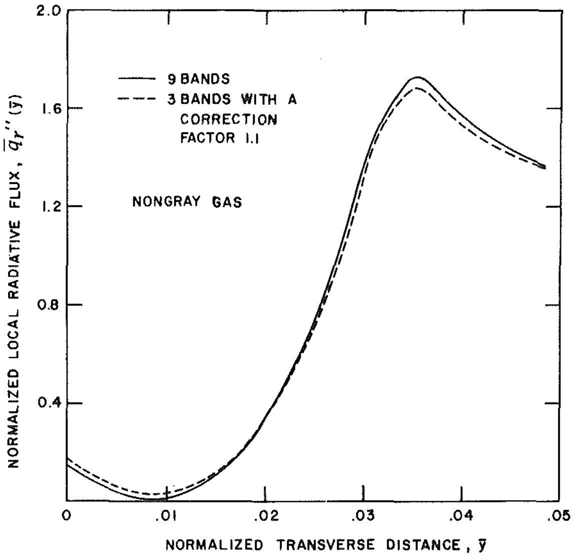

Fig. 2 Comparison of the local radiative flux computed using the nine-band model and the three-band approximation (with a correction factor 1.1)

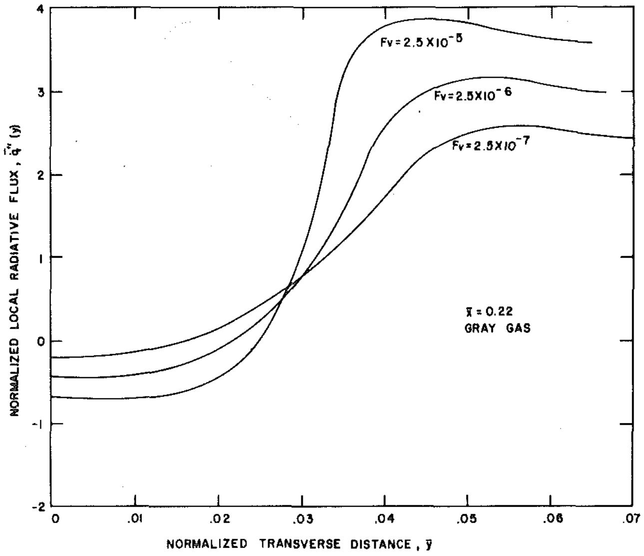

Fig. 3 $\overline{q_r''}$ versus $\bar{y}$ at $\bar{x} = 0.22$ parameterized in F_v for gray gases, $\phi = 0.625$

enhanced by the emission of hot soot and gases gradually increases along the optical path. It finally reaches a maximum value near the reaction zone ($\bar{y} \approx 0.05$) and then, being attenuated by the colder gases, starts to decrease. The effect of F_v on the radiative flux is such that, at large values of F_v, the *absolute* values of the radiative flux become large. This is becaue, for sootier flames, more soot emission is lost to the surroundings as well as to the wall.

In Fig. 4, some results obtained using the exponential wide-band model, the gray-gas approximation and the radiatively-ideal gas approximation are compared. Figure 4(*a*) presents the flame temperature as a function of $\bar{x}$. It can be seen that the deviation of the flame temperatures obtained by the three models is less than 5 percent. It is also interesting to compare these values with the theoretical adiabatic flame temperature. Let us consider that masses including $\nu_{ox}M_{ox}$ of oxygen at T_∞, $\nu_N M_N$ of nitrogen at T_∞ and $\nu_f M_f$ of fuel at T_w react in an adiabatic control volume to generate the heat of reaction $Q_p \nu_{ox} M_{ox}$ and the combustion products including $\nu_C M_C$ of CO_2, $\nu_{wa} M_{wa}$ of H_2O and $\nu_N M_N$ of N_2 at $T_{f\ell}$. By the first law of thermodynamics, it can be shown that

$$\frac{T_{f\ell,\mathrm{ad}} - T_\infty}{T_w - T_\infty} = \frac{fY_{ox\infty} + D_3}{Y_{ox\infty}\,(11\nu_C/8\nu_{ox} + 9\nu_{wa}/16\nu_{ox} - 1) + 1} \tag{30}$$

With substitution of $f = 0.516$, $Y_{ox\infty} = 0.23$, $D_3 = 5.596$, $\nu_C = 5$, $\nu_{ox} = 6$ and $\nu_{wa} = 4$, $T_{f\ell,\mathrm{ad}}$ is found to be 2443 K, or $\overline{T}_{f\ell,\mathrm{ad}} = 3.393$. Since the present system loses its energy by convection and radiation, the actual flame temperatures appear much lower than this theoretical adiabatic value. Figure 4(*b*) shows the pyrolysis flux and the flame stand-off distance versus $\bar{x}$. Again, the results obtained by the three models agree well with one another. Therefore, we can tentatively state that it seems possible to find a radiatively-ideal gas which has a constant absorption coefficient and exhibits similar flame characteristics as the nongray gases.

In Fig. 5, the flame temperature and the radiation loss computed using the gray gas model are plotted versus $\bar{x}$ for various values of ϕ. From this figure, we can evaluate the total radiation loss from the system, i.e., $\int_0^\ell \overline{\dot{q}_{r\infty}''}\,dx$. The influence of ϕ on $\overline{T_{f\ell}}$ and $\overline{\dot{q}_{r\infty}''}$ should also be noted. At larger values of ϕ, more CO_2 is produced and the effective emittance of the gas becomes larger; therefore, the radiation loss increases and the flame temperature drops. For the chemical reaction such as

$$C_mH_nO_j + \nu_{ox}O_2 + \nu_N N_2 \rightarrow mCO_2 + \frac{n}{2}H_2O + \nu_N N_2 \tag{31}$$

it is interesting to note that f can be expressed in terms of ϕ as

$$f = \nu_f M_f/\nu_{ox}M_{ox} = [12\phi + 1 + 16(j/n)]/[32\phi + 8 - 16(j/n)] \tag{32}$$

In cases of the hydrocarbon-fuel burning ($j = 0$), equation (32) reduces to

$$f = (12\phi + 1)/(32\phi + 8) \tag{33}$$

Equation (33) dictates that, for $0 < \phi < \infty$, values of f be chosen between $1/8$ and $3/8$. Since the mass consumption number r is defined as $fY_{ox\infty}/Y_{fw}$, care must be taken not to violate equations (32, 33) when the value of r is assigned.

In Fig. 6, the pyrolysis flux of the radiatively-ideal gas is shown as a function of $\bar{x}$ parameterized in Re. Since $\overline{\dot{m}_p''}$ is normalized on $\rho_\infty u_\infty$,

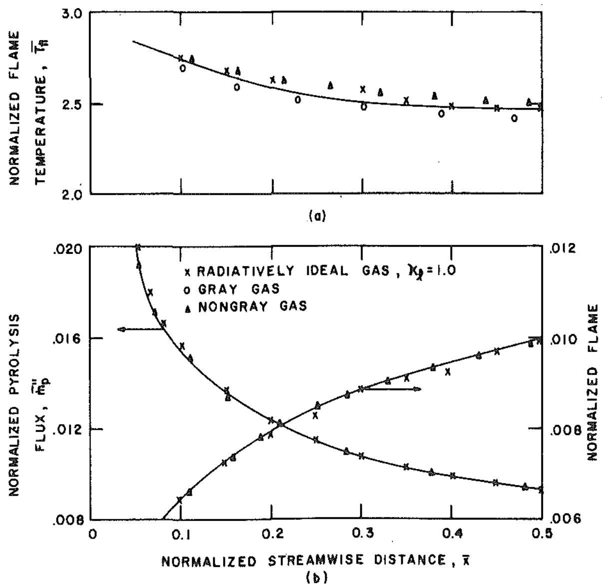

Fig. 4 Comparison of the flame temperature, pyrolysis flux and the flame stand-off distance computed using the three-band nongray gas model, gray gas model and the radiatively-ideal-gas approximation

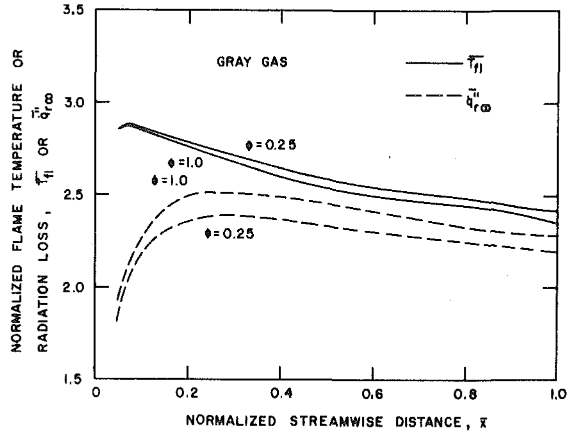

Fig. 5 $\overline{\dot{q}_{r\infty}''}$ **and** $\overline{T_{f\ell}}$ **versus** $\bar{x}$ **parameterized in** ϕ **for gray gases**

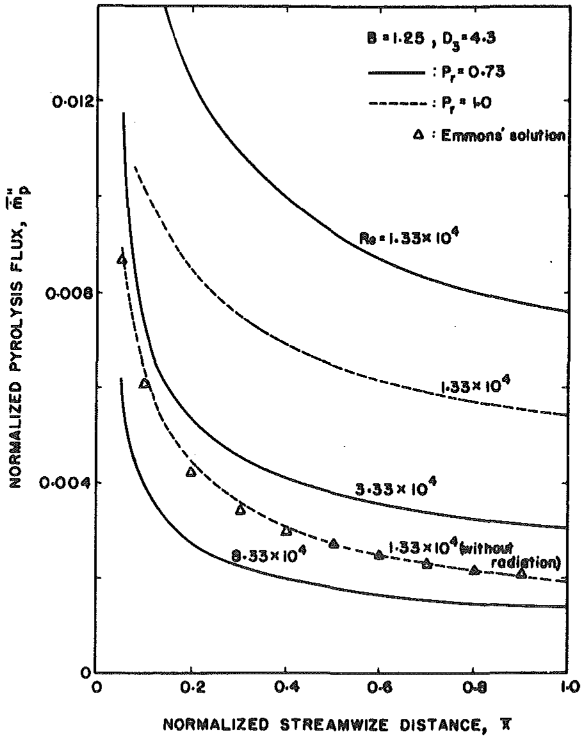

Fig. 6 Pyrolysis flux versus $\bar{x}$ **parameterized in Re for radiatively-ideal gases**

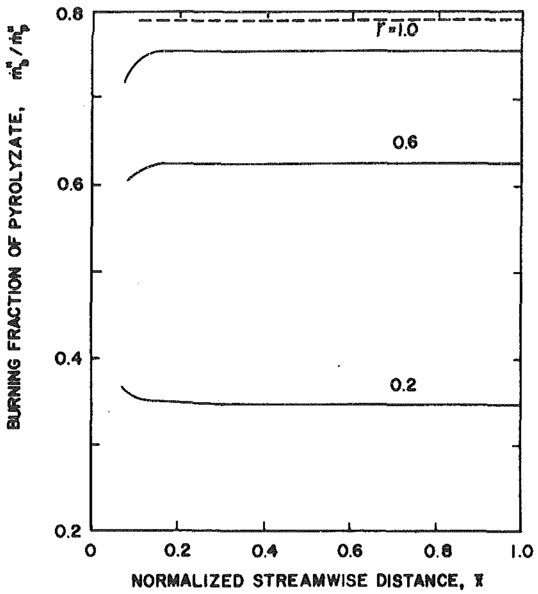

Fig. 7 $\dot{m}_b''/\dot{m}_p''$ versus $\bar{x}$ parameterized in r for radiatively-ideal gases

care should be taken when the effect of Re on $\overline{\dot{m}_p''}$ is examined. It is not difficult to show that the dimensional quantity, $\dot{m}_p''$, actually increases as u_∞ increases. Furthermore, Emmons' solution [1] for Gr $= 0$, $\kappa_\ell = 0$, $\epsilon_w = 0$ and Pr $= 1$ is plotted for comparison. It agrees well with the nonradiative result obtained from the present analysis. These two nonradiative results are shown much lower than the radiative counterpart. The reason lies in the fact that the radiative feedback, in addition to the convective heat transfer, enhances the pyrolysis.

The burned fraction of pyrolyzate $\dot{m}_b''/\dot{m}_p''$ is plotted versus $\bar{x}$ in Fig. 7 for various values of r. The trend that these fractions remain fairly constant along x suggests that $\dot{m}_p''$ and $\dot{m}_b''$ both decrease in a similar fashion with increasing x. Furthermore, for larger values of r, more abundant oxygen is available for reaction with the fuel vapor, and therefore more fuel vapor is burned. The result at $r = 1.0$ for the nonradiative case ($\kappa_\ell = 0$ and $\epsilon_w = 0$) is also drawn as the dashed line for comparison [4]. This burned fraction is overpredicted by ~5 percent of the present result probably due to omission of the radiative feedback which enhances the pyrolysis. From this figure and Figs. 5 and 6, the ratio of the total radiation output to the total chemical energy evolved can be evaluated as

$$\chi = \int_0^\ell \dot{q}_{r\infty}''dx \Big/ \int_0^\ell \dot{m}_b'' Q_p (\nu_{\rm ox} M_{\rm ox}/\nu_f M_f) dx$$

$$= 1.68 \times 10^{-3}/4.42 \times 10^{-3} = 38 \text{ percent}$$

The values of χ for sets of various parametric values can also be obtained using the present analysis. This information is particularly valuable to fire-safety researchers.

9 Conclusion

The laminar, two-dimensional, boundary-layer flame was analyzed with special attention directed to the nongray gaseous radiation. Based on the computed result of the local radiative flux, it was judged that the three-band approximation (4.3μ for CO_2, 6.3μ and 2.7μ for H_2O) yielded a solution close to that obtained by the nine-band model (Fig. 2). Without loss of accuracy, the three-band approximation saved considerable amount of computation time. Using the Planck mean absorption coefficient, we find that the gray-gas model provides even simpler computation procedures with satisfactory accuracy (Fig. 4). In this model, however, the absorption coefficient remains to be a function of the medium temperature. The simplest model having a radiatively-ideal gas was thus proposed. To find a constant value of the absorption coefficient which best describes the nongray nature, we conducted several numerical experiments. For $k_\ell = 1.0$, we found that the solution of the radiatively ideal system agrees with that of the present nongray system (Fig. 4). This agreement suggests that, in the future, the complicated nongray systems may not have to be investigated directly if an empirical relation such as $k_\ell = f(\text{Re, Gr, Pr}, B, \xi, \epsilon_w, \theta_r, r, D_3, F_v, \phi)$ can be obtained. Finally, the quantity χ for the system shown in Fig. 1 has been analytically obtained. This analytical value can be compared with the experimental result if available.

References

1 Emmons, H. W., "The Film Combustion of Liquid Fuel," *Zeitschrift fuer Angewandt Mathematik und Mechanik,* Vol. 36, 1956, pp. 60–71.

2 Kosdon, F. J., Williams, F. A., and Buman, C., "Combustion of Vertical Cellulosic Cylinders in Air," Twelfth Symposium (International) on Combustion, The Combustion Institute, 1969, pp. 253–264.

3 Kim, J. S., deRis, J., and Krosser, F. W., "Laminar Free-Convection Burning of Fuel Surface," Thirteenth Symposium (International) on Combustion, The Combustion Institute, 1971, pp. 949–961.

4 Pagni, P. J., and Shih, T. M., "Excess Pyrolyzate," Sixteenth Symposium (International) on Combustion, The Combustion Institute, 1976, pp. 1329–1343.

5 Yuen, W. W., and Tien, C. L., "A Simple Calculation Scheme for the Luminous Flame Emissivity," Sixteenth Symposium (International) on Combustion, The Combustion Institute, 1976, pp. 1481–1487.

6 Buckius, R. D., and Tien, C. L., "Infrared Flame Radiation," International Journal of Heat and Mass Transfer, Vol. 20, 1977, pp. 93–106.

7 Negrelli, D. E., Lloyd, J. R., and Novotny, J. L., "A Theoretical and Experimental Study of Radiation-Convection Interaction in a Diffusion Flame," ASME JOURNAL OF HEAT TRANSFER, Vol. 99, 1977, pp. 212–220.

8 Modak, A. T., "Thermal Radiation from Pool Fires," *Combustion and Flame,* Vol. 29, 1977, pp. 177–192.

9 Shih, T. M., and Pagni, P. J., "Laminar Mixed-Mode, Forced and Free, Diffusion Flames," ASME JOURNAL OF HEAT TRANSFER," Vol. 100, 1978, pp. 253–259.

10 Tien, C. L., "Thermal Radiation Properties of Gases," *Advances in Heat Transfer,* Vol. 5, Academic Press, New York, 1968, pp. 253–324.

11 Chan, S. H., and Tien, C. L., "Total Band Absorptance of Non-Isothermal Infrared-Radiating Gases," *Journal of Quantative Spectroscopy and Radiative Transfer,* Vol. 9, 1969, pp. 1261–1271.

12 Chan, S. H., and Tien, C. L., "Infrared Radiative Heat Transfer in Non-gray Non-isothermal Gases," *International Journal of Heat and Mass Transfer,* Vol. 14, 1971, pp. 19–26.

13 Edwards, D. K., and Balakrishnan, A., "Slab Band Absorptance for Molecular Gas Radiation," *Journal of Quantative Spectrostrophy and Radiative Transfer,* Vol. 12, 1972, pp. 1379–1387.

14 Edwards, D. K., and Balakrishnan, A., "Self-Absorption of Radiation in Turbulent Molecular Gases," *Combustion and Flame,* Vol. 20, 1973, pp. 401–417.

15 Siegel, R., and Howell, J. R., *Thermal Radiation Heat Transfer,* McGraw-Hill, 1972, p. 680.

16 McAdam, W. H., *Heat Transmission,* McGraw-Hill, 1953.

17 Howarth, C. R., Foster, P. J., and Thring, M. W., "The Effect of Temperature on Extinction of Radiation by Soot Particles," Third International Heat Transfer Conference, AIChE, New York, Vol. 5, 1966, pp. 122–128.

18 Dalzell, W. H., and Sarofim, A. F., "Optical Constants of Soot and Their Applications to Heat Flux Calculations," ASME JOURNAL OF HEAT TRANSFER, Vol. 91, 1969, pp. 100–104.

19 Sparrow, E. M., and Cess, R. D., *Radiation Heat Transfer,* Augmented Edition, Hemisphere, 1978.

20 Liu, C. N., "Two-Dimensional, Laminar, Mixed (Forced and Free) Convection, Radiative, Diffusion Flames," Ph.D. dissertation, Department of Mechanical Engineering, University of Maryland, College Park, MD., 1979.

21 Edwards, D. K., Glassen, L. K., Hauser, W. C. and Tuchscher, J. S., "Radiation Heat Transfer in Nonisothermal Nongray Gases," ASME JOURNAL OF HEAT TRANSFER, Vol. 89, 1967, pp. 219–229.

22 Kays, W. M., *Convective Heat and Mass Transfer,* McGraw-Hill, 1966, p. 321.

23 Lloyd, J. R., and Sparrow, E. M., "Combined Forced and Free Convection Flow on Vertical Surfaces," *International Journal of Heat Mass Transfer,* Vol. 13, 1970, pp. 434–438.

24 Patankar, S. V., and Spalding, D. B., *Heat and Mass Transfer in Boundary Layers,* 2nd ed., Morgan-Grampian, West Wickham, 1970.

25 Spalding, D. B., "A General Computer Program For Two-Dimensional Boundary Layer Problems," Report No. HTS/73/48, Department of Mechanical Engineering, Imperial College of Science and Technology, 1973.

G. Miller
Associate Professor.

V. Zakkay
Chairman.

Department of Applied Science,
New York University,
26-36 Stuyvesant Street,
New York, N. Y. 10003

Experiments on Heat Exchanger Solidity for Coal-Fired Fluidized Bed Applications

The efficient extraction of a high-temperature working fluid from a coal-fired fluidized bed combustor depends, to a great extent, on the design of the immersed heat exchanger. Of special importance is the solidity of the cooling tubes immersed in the bed. The interaction between increasing solidity and the consequent degradation of proper fluidization and circulation is being studied at the New York University fluidized bed combustion facility. In a preliminary set of experiments it was found that under certain conditions, the solidity of heat exchanger in the bed may be significantly increased, giving designers an additional variable parameter.

Introduction

The combined cycle process, utilizing coal burnt in a pressurized fluidized bed combustor may make a significant impact in the next decade as an efficient, clean, cost effective producer of large quantities of electricity. A number of industrial concerns are presently undertaking research and development efforts investigating various techniques to produce electricity in such pressurized vessels. At present, atmospheric pressure units are in the early stages of utilization for both industrial and utility applications.

The optimization of the performance of a coal-fired fluidized bed combustor is possible only if a thorough comprehension of the extremely complex flow patterns, and the parameters which can significantly effect such patterns, exists. For the past four years, New York University has been studying such flow patterns in two, 1 ft dia fluidized bed combustors (one, a gas fired and the other a coal fired unit) with a view toward establishing criteria to aid the designer of such vessels, particularly in establishing the heat exchanger configurations which optimize performance. A comprehensive description of the one-foot-diameter gas fired facility can be found in reference [1]. Previous research has attempted to quantify the effects on heat transfer of such parameters as flow profile at the distributor plate, bed pressure, the ratio of settled bed height to bed diameter, and heat exchanger geometry (vertical bundles, horizontal bundles, finned and unfinned tubing). The results of these investigations can be found in references [1–5]. The following summarizes the major results utilizing bed particles of 1 mm or larger.

1 Preferential flow distribution at the distributor plate can significantly improve the overall heat transfer in a shallow bed.

2 The effect of pressurizing a fluidized bed can for some geometries, result in as much as a 75 percent increase in heat transfer, for both long and short low solidity heat exchangers in deep or shallow beds.

3 The utilization of external vertical fins on vertical heat exchanger tubes has a minimum impact on heat transfer; in fact, at elevated pressure the reduction in heat transfer coefficient is so severe that only a small increase in heat extraction is found.

4 Heat exchanger configurations in deep beds (where the ratio of settled bed height to bed diameter is large) may experience highly nonuniform local heat transfer coefficients as a function of bed height. A low heat transfer coefficient at the bottom section of the bed, resulting from poor circulating of particles, may then be followed by an optimum heat transfer coefficient in the middle of the bed which may then be followed by a region of low heat transfer at the top of the bed. Thus, the overall performance of long heat exchangers in deep beds may be somewhat below expectation. In addition, problems associated with improper fluidization near the grid may arise, in particular, the possibility of local hot spots near coal injection points, leading to higher NO_x levels and tube fouling.

In the investigations performed with the gas fired combustor, utilizing methane eliminated the problems associated with coal combustion. Working at reduced bed temperatures (on the order of 300°C) simplifies data acquisition. Heat transfer results miss the radiative component (15–25 percent of the total) but otherwise the effect of bed temperature is not significant (see Fig. 1) for *large* particles. Of course, for small particles (significantly less than 1 mm in mean diameter), the effect of temperature on heat transfer has been observed to be pronounced in a number of studies.

There is some controversy with respect to the reasons for the increase in heat transfer coefficient with pressure utilizing large particles. A number of studies (e.g., [6–10]) have attributed the pressure effect to an increase in the convective heat transfer component. The previous results of the NYU program have indicated that for the operating conditions studied, the increased convective heat transfer could not explain the large increase in overall heat transfer. At the same time it was noted that bed expansion decreased substantially with pressure (for a given mass flow rate) indicating a significant suppression of the slugging tendency and a reduction in the bubbling phase.

The heat transfer model proposed by Glicksman and Decker (reference [12]) indicates that the effect of bed expansion can be of prime significance, and they scale the Nusselt number by the bed void fraction. They note that, while at high Reynolds number the heat transfer rate increases with gas density (and thus with pressure) through the effect on the convective component, at low Reynolds number, the heat transfer is influenced by gas density (or pressure) mainly by the effect on bed expansion (since conduction is independent of gas density). For the studies described here, the Reynolds number is usually on the order of tens to hundreds and, thus, the effect of bed expansion is extremely significant and, in some cases, predominant. Therefore, we have concluded that in our experiments, the increase in heat transfer with pressure, was due to a large extent to the suppression of slugs and bubbles since a large percentage of the heat transfer was conductive.

Rationale for the Study

A parameter which greatly affects the heat that is extracted from a coal fired fluidized bed is heat exchanger solidity (for a vertical configuration, defined as the ratio of heat exchanger cross section to boiler cross section area). A greater solidity can increase the working fluid (water or air) temperature or mass flow rate if the heat transfer coefficient can be maintained, or it can decrease the height of the heat exchanger bundle. On the other hand, increasing solidity will, eventually, impede circulation, thus decreasing the heat transfer coefficient significantly.

Contributed by the Gas Turbine Division and presented at the Gas Turbine Conference and Exhibit and Solar Energy Conference, San Diego, Calif., March 12–15, 1979 of THE AMERICAN SOCIETY OF MECHANICAL ENGINEERS. Manuscript received by the Heat Transfer Division October 29, 1979. Paper No. 79-GT-78.

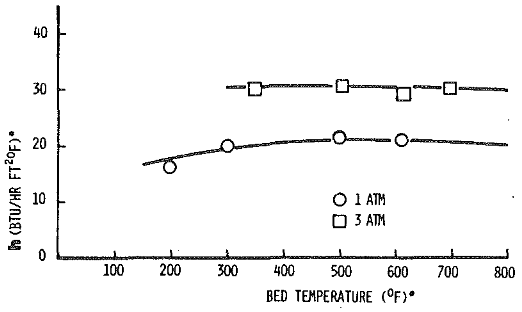

Fig. 1 Effect of bed temperature on overall heat transfer coefficient with large bed particles

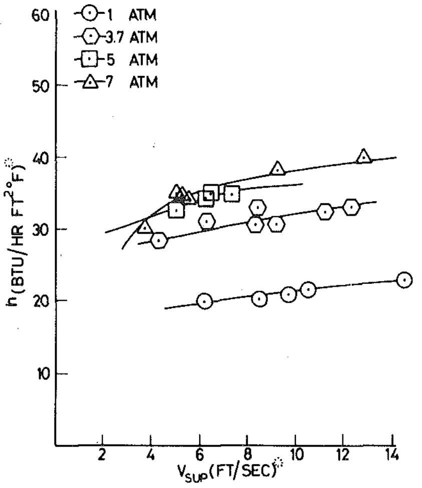

Fig. 2 Overall heat transfer coefficients for different operating pressures in shallow bed with 8 percent solidity of heat exchanger. 1 Btu/hr-ft²-deg f = 5.68 W/m²c, 1 ft/s = 0.3048 m/s

It has thus been the practice of most designers to design fluidized bed combustors with a low overall heat exchanger solidity, thus insuring an adequate level of fluidization. When a horizontal configuration is used, such as the design used in the British studies [11], the cross-section solidity is large (between 20 and 40 percent), but the volumetric solidity (the ratio of heat exchange volume to bed volume) becomes the important parameter, since there can be significant spaces between horizontal bundles. The British configuration yields a volumetric solidity of less than 10 percent, somewhat in line with solidities envisioned by designers utilizing vertical configurations; although the recent experiments of Curtiss Wright [13] have been conducted at somewhat higher solidities.

While the solidity of the heat exchanger to be utilized is an important parameter, there has been little research of a systematic nature to assess how solidity effects the heat transfer coefficient, all other parameters remaining the same. It was, therefore, decided that such a study would be conducted in the N.Y.U. gas fired combustor described in reference [1]. The initial results of this investigation are reported in the next sections. In the final section, conclusions based on these results are presented.

The Experimental Program

The basic heat exchanger configuration which has been utilized to study the effect of increasing solidity on heat transfer is a 6.2 ft (1.89 m) 2.38 in. (6.05 cm) o. d. vertical U-tube mounted so that the legs of the pipe are 6 in. (15.25 cm) above the distributor plate (where the air enters from below). This configuration represents a solidity of 8 percent. Overall and local heat transfer data were recorded as a function of bed pressure, settled bed depth (depth of bed prior to fluidization), and superficial velocity, utilizing water as the working fluid. By mounting a second U-tube in the bed and rerunning the entire matrix of experiments, the effect of doubling the solidity (to 16 percent) on overall heat transfer coefficient has been determined. Four levels of bed pressure (1, 3.7, 5, 7) atm and two bed depths 27 in. (0.68 m) and 55 in. (1.4 m) have been tested for a range of superficial velocities. The 27 in. (0.68 m) bed will be referred to as the shallow bed, the 55 in. (1.4 m) bed, the deep bed, in what follows. The particles in the bed were limestone with average initial diameters in the 1400–2000 mm. range. It is emphasized here that what follows are initial results of the investigation. Additional data needed for a complete quantitative analysis is in the process of being produced.

Results of the Study

Figure 2 presents heat transfer coefficients as a function of bed pressure for the shallow bed at 8 percent solidity (one U-tube). The increased heat transfer with pressure has been established, as stated previously, to be mainly due to the suppression of bubble growth or slug development with pressure in the Reynolds number range studied. Figure 3 presents the data for the deep bed at 8 percent solidity. In Fig. 4, the variation in local heat transfer with height for the shallow and deep beds at atmospheric conditions is presented. These data were determined utilizing thermocouples mounted inside the tube along its height. The causes and effects of these different distributions in shallow and deep beds have been discussed previously [4, 5] and have led to conclusion (4) of the Introduction.

Figures 5 and 6 present the effects of pressure on heat transfer in a shallow and deep bed with the solidity increased to 16 percent (by an addition of a second U-tube mounted perpendicular to the first one). The favorable effect of pressure on heat transfer is still present.

Figures 7 and 8 compare the two solidities at atmospheric conditions in a shallow and deep bed. It can be seen that the heat transfer coefficient may be slightly greater at 16 percent than at 8 percent at atmospheric conditions, even though one would expect flow circulation to be impeded somewhat at such a high solidity. The effect of increased solidity may have a favorable effect by causing bubble and slug suppression. Thus, the 16 percent solidity case may indicate a higher heat transfer coefficient. This is in line with the tests at the National Coal Board [11]. The British investigators reported little increase in heat transfer coefficient with pressure. This may be due to the fact that their horizontal tube bundles have extremely high local solidity (30 to 40 percent) which suppress bubble growth and inhibit slug development. Therefore, their data at atmospheric conditions indicate high heat transfer coefficients since even the atmospheric tests are probably in a smaller bed expansion regime. Our atmospheric data at 16 percent seem to support this conclusion.

Figures 9 to 14 present comparisons of the 8 and 16 percent solidity data at elevated pressures in the shallow and deep beds. It can be seen that at elevated pressures, the heat transfer coefficients are the same at the two solidities. Data from tests utilizing local probes (such as that presented in Fig. 4) indicate that the fluid mechanics and flow circulation in the bed at elevated pressure for the two heat exchanger configurations is very much the same, and thus the problems associated with poor fluidization expected at high solidity are not present when the solidity is increased to 16 percent.

Summary and Conclusions

Initial results of a test program to assess the effect of heat exchanger solidity on heat transfer in a coal fired fluidized bed indicates that the rule of thumb criterion of keeping the solidity below 10 percent in order to keep a good level of fluidization in a bed using large particles is too conservative. In fact, at atmospheric conditions, the heat transfer coefficient may be greater at higher solidities since the higher density of the heat exchanger tubes can lead to decreased bed expansion.

Additional testing must be carried out to determine at what level of solidity, degradation of performance will begin to occur. At the same time, though, the indication that a 16 percent solidity can achieve the same overall heat transfer coefficient as the 8 percent case is significant. If a designer must have a certain fixed flue-gas temperature so that the mass flow of *clean* working fluid is fixed, doubling the solidity would alleviate the problems of vibration and stress present for long heat exchangers (for pressurized applications), since the heat exchanger length could be halved. On the other hand, if the flue gas

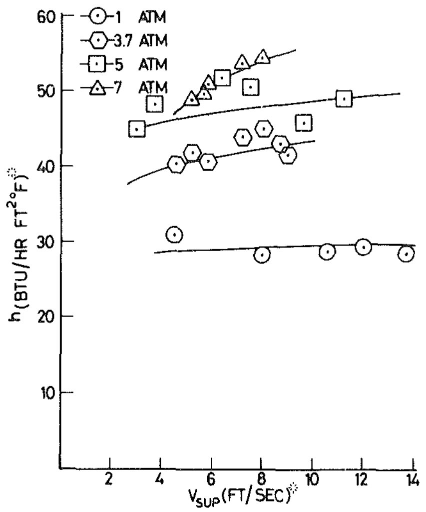

Fig. 3 Overall heat transfer coefficients for different operating pressures in a deep bed with 8 percent solidity of heat exchanger

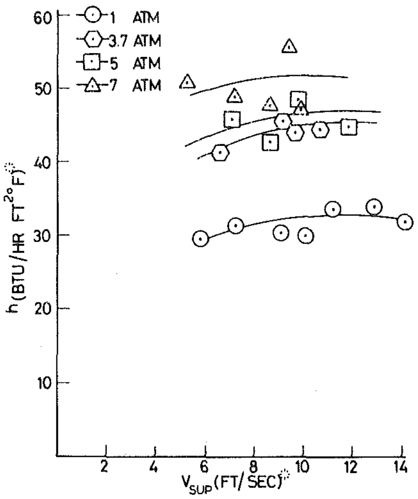

Fig. 6 Overall heat transfer coefficients for different operating pressures in a deep bed with 16 percent solidity of heat exchanger

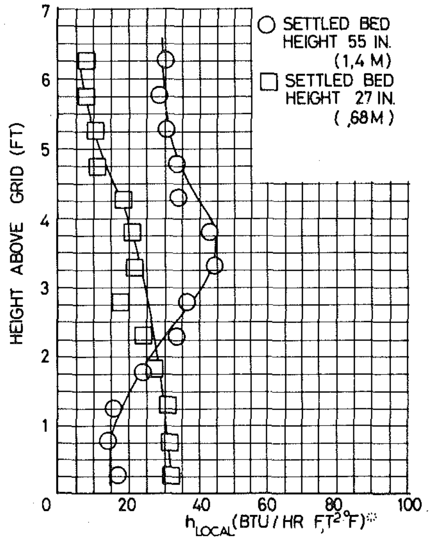

Fig. 4 Local heat transfer distribution for shallow and deep beds at atmospheric pressure (V_{sup} = 3.5 m/s) with 8 percent solidity of heat exchanger

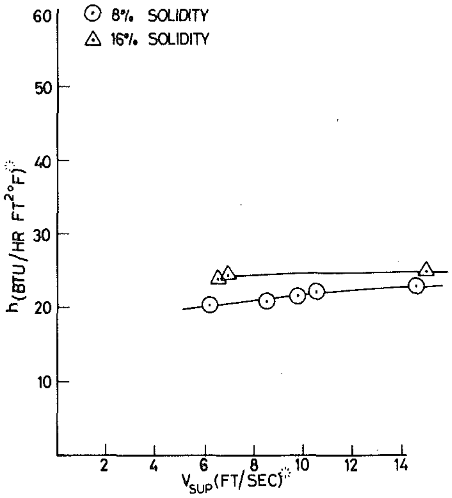

Fig. 7 Comparison of overall heat transfer coefficients for 8 and 16 percent solidities in a shallow bed at one atmosphere

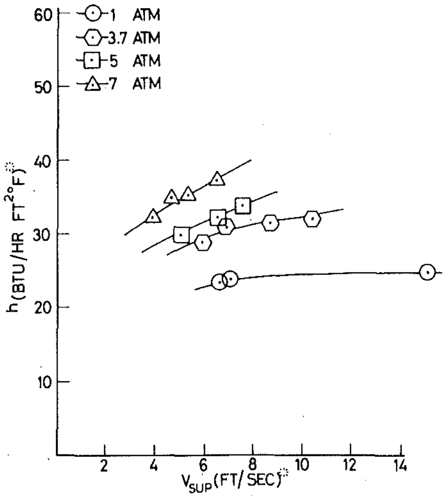

Fig. 5 Overall heat transfer coefficients for different operating pressures in shallow bed with 16 percent solidity of heat exchanger

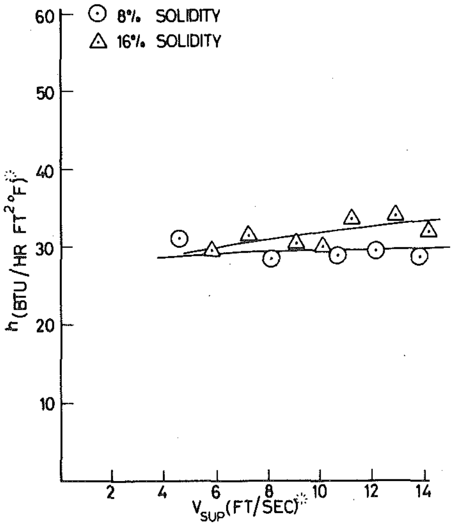

Fig. 8 Comparison of overall heat transfer coefficients for 8 and 16 percent solidities in a deep bed at one atmosphere

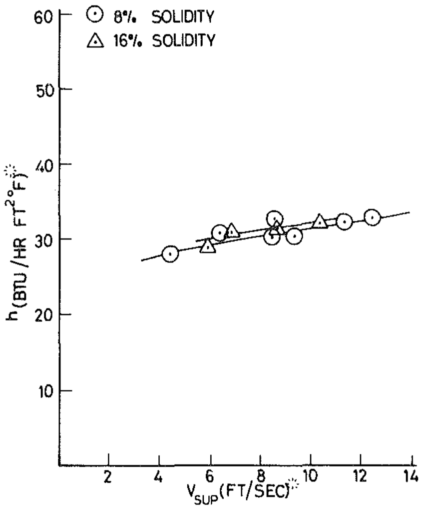

Fig. 9 Comparison of overall heat transfer coefficients for 8 and 16 percent solidities in a shallow bed at 3.7 atm

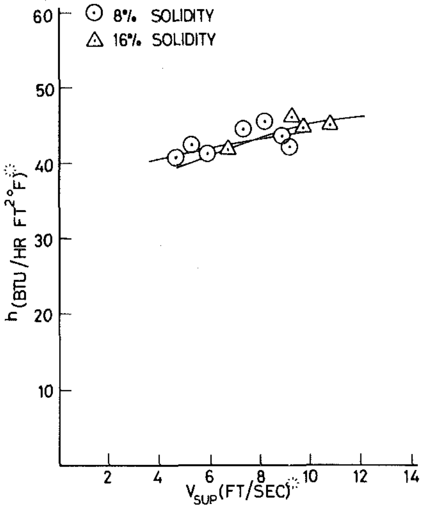

Fig. 10 Comparison of overall heat transfer coefficients for 8 and 16 percent solidities in a deep bed at 3.7 atm

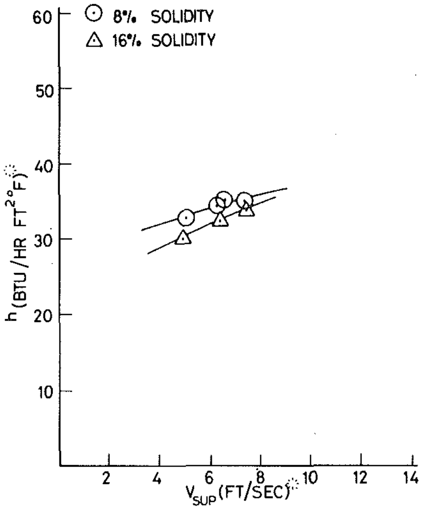

Fig. 11 Comparison of overall heat transfer coefficients for 8 and 16 percent solidities in a shallow bed at 5 atm

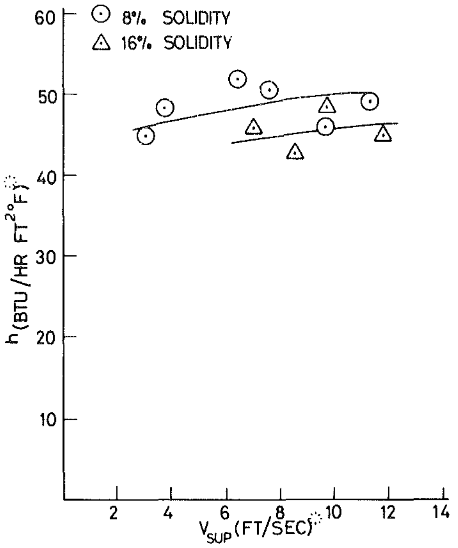

Fig. 12 Comparison of overall heat transfer coefficients for 8 and 16 percent solidities in a deep bed at 5 atm

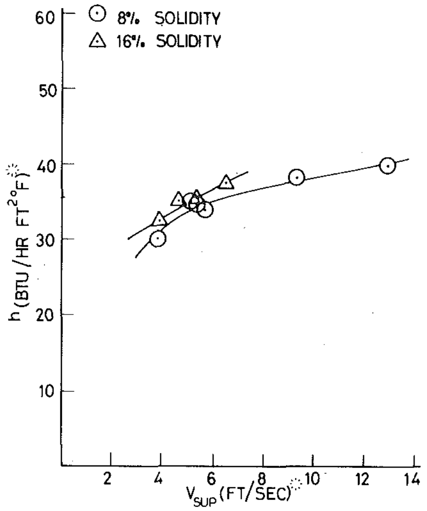

Fig. 13 Comparison of overall heat transfer coefficients for 8 and 16 percent solidities in a shallow bed at 7 atm

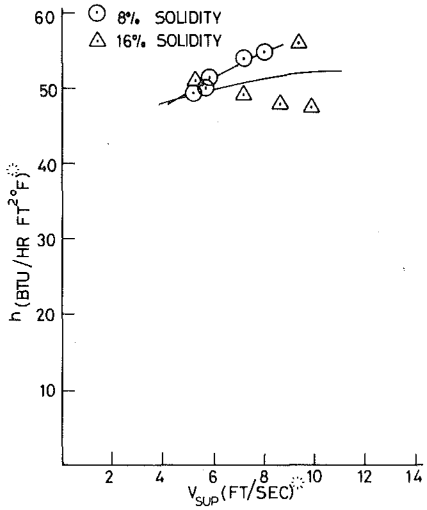

Fig. 14 Comparison of overall heat transfer coefficients for 8 and 16 percent solidities in a deep bed at 7 atm

temperature is not a fixed parameter, doubling the solidity indicates that twice the mass flow of *clean* working fluid could be extracted (or if the clean working fluid is air, an equivalent mass flow could be extracted at a much higher temperature).

As a matter of fact, the coal (and air) feed rate can be increased if a higher solidity is used, yielding a higher clean working fluid flow rate for a given exhaust temperature. Thus the designer can use solidity as a variable parameter increasing his flexibility with respect to design.

Once the optimum level of solidity of heat exchanger in the bed is determined for a given bed configuration, one can address the question of solidity variation with height. Suppose, for example, that a 20 percent solidity is determined as the level above which degradation in heat transfer occurs. It may well be possible that at intermediate or upper levels of deep beds, the solidity can be increased significantly above 20 percent for deep beds since, for deep beds, flow circulation, one to two bed diameters above the distributor plate, is of better quality. Thus, heat exchanger staging, where the solidity increases with height, might be an effective means of improving performance.

It must be emphasized that the results presented here were for only two solidities and gathered in a one foot diameter facility (at reduced temperature). While we feel that the effect of increased solidity on heat transfer is qualitatively as shown herein, quantitatively, the effects may be somewhat altered in a larger unit. Obviously, in a larger coal-fired bed the changes in fluid mechanics will yield changes in heat transfer levels, especially since the effect of bed diameter on bed expansion may be significant. New York University plans to begin construction of a 3 ft dia coal-fired pressurized vessel in the near future to ascertain such effects of scale.

Acknowledgments

This research was sponsored by the Department of Energy under Contract EF-75-C-01-2256.

References

1 Zakkay, V., Miller, G., and Brentan, A., "Heat Transfer Characteristics in a Fluidized Bed Packed With Heat Exchangers," presented at the 1977 Fall Meeting of the Catalytic Combustion-Fluidized Bed Combustion (Western Section, Stanford, Calif.) Oct. 17–18, 1977, NYU/DAS 77-17.

2 Zakkay, V., Miller, G., and Kiviat, G., "Heat Transfer Characteristics of Shallow and Deep Fluidized Beds Packed With Heat Exchangers," presented at the Miami International Conference on Alternative Energy Sources in Miami Beach, Fla., Dec. 5–7, 1977, NYU/DAS 77-24.

3 Miller, G., Zakkay, V., and Kiviat, G., "The Effects of Finned Tubing on Fluidized Bed Performance," presented at the Fifth International Conference on Fluidized Bed Combustion, sponsored by the Mitre Corporation, Dec. 12–14, 1977, NYU/DAS 77-29.

4 Miller, G., Zakkay, V., and Rosen, S., "Performance Characteristics of Deep Fluidized Beds and the Effects on Heat Exchanger Design," presented at the 71st Annual Miami Meeting of American Institute of Chemical Engineering; published by AIChE in *Chemical Engineering Progress*, Vol. 5, 1979, NYU Rpt. No. NYU/DAS 78-09.

5 Zakkay, V., and Miller, G., "Advanced Heat Exchanger Configurations for Coal-Fired Fluidized Beds," published in the ASME Proceedings, presented at the Winter Annual Meeting, San Francisco, Calif., Dec. 10–15, 1978, Paper No. 78-WA/HT-40, NYU/DAS 78-10.

6 Denloye, A. O., and Botterill, J. S. M., "Bed to Surface Heat Transfer in A Fluidized Bed of Large Particles," *Powder Technology*, Vol. 19, 1978, p. 197.

7 Canada, G. S., and McLaughlin, M. H., "Large Particle Fluidization and Heat Transfer at High Pressures," 70th Annual AIChE Meeting, 1977.

8 Cranfield, R. R., "Solid Mixing in Fluidized Beds of Large Particles," 70th Annual AIChE Meeting, 1977.

9 George, A. H., Catipovic, N. M., and Welty, J. R., "An Analytical Study of Heat Transfer to a Horizontal Cylinder in a Large Particle Fluidized Bed," ASME Paper No. 79-HT-78, 1979.

10 Adams, R. L., and Welty, J. R., "A Gas Convective Model of Heat Transfer In Large Particle Fluidized Beds," *AIChE Journal*, Vol. 25, No. 3, 1979, p. 395.

11 Hoy, H. R., and Roberts, A. G., "Further Experiments on the Pilot-Scale Pressurized Combustor at Leatherhead, England" in *Proceedings of the Fluidized Bed Combustion Technology Exchange Workshop*, Vol. 2, Apr. 13–15, 1977, NTIS No. Conf. -77-447.

12 Glicksman, L. R., and Decker, N., "Heat Transfer in Fluidized Beds With Large Particles," submitted to *Chemical Engineering Science*, 1980.

13 Moskowitz, S., Weth, G., and Leon, A., "Pressurized Fluidized Bed Pilot Electric Plant—A Technology Status," ASME Paper No. 79-GT-193, 1979.

Heat and Mass Transfer in Fixed Beds at Low Reynolds Numbers

L. R. Glicksman
F. M. Joos

Department of Mechanical Engineering,
Massachusetts Institute of Technology,
Cambridge, Mass. 02139

In a fixed or fluidized bed at low particle Reynolds numbers, the overall or effective Sherwood and Nusselt number has been found by many investigators to be much less than unity. The limiting value of the particle Sherwood or Nusselt number based on local concentration or temperature differences is shown to be equal to or greater than unity. An analytical model was established using realistic packed bed geometries to allow for diffusion in the flow direction, channeling due to nonuniformities in bed voidage and different particle sizes, and inaccuracies in the experimental measurements. The predicted values of the effective Sherwood and Nusselt numbers are found to agree closely with experimental measurements for gases and liquids. Diffusion is shown to be the primary mechanism for the fall-off in the effective bed characteristics.

Introduction

Since the pioneering work more than three decades ago of Gamson, et al. [1] on evaporation of water from celite spheres into air, a large number of investigators have studied mass and heat transfer from particles to surrounding fluids in fixed and fluidized beds. A number of different experimental techniques have been used for gases and liquids; a majority of the experiments were done under steady-state conditions. Correlations and review of the experimental data are found in a number of reviews such as references [2–6]. For particle Reynolds numbers greater than 50 the trend of the Sherwood number and Nusselt number has been more or less well established. The Sherwood number is consistently higher than that given by the Ranz-Marshall equation for a single sphere in an infinite media [7]. This is also true for the Nusselt number.

At low particle Reynolds numbers experimental results have been controversial. Early experiments on packed beds indicated that the calculated Sherwood number approached zero as the Reynolds number became very small. Moreover, the results of many investigators varied by an order of magnitude with recent results by Hsiung and Thodos [8] achieving higher Sh values at low Re. Nevertheless, recent data still indicate a decrease in the Sherwood number as the Reynolds number is reduced toward zero. Mass transfer experiments between particles and liquids are less definitive; in general, most of the data for liquids yield a Sherwood number which tends to fall at small Reynolds numbers. Heat transfer experiments at low particle Reynolds numbers have also tended to show the same kinds of behavior; the results for the heat transfer tests are further complicated because of conduction between adjacent particles. Much of the variation in the experimental data is due to the use of the effective Sherwood number based on the overall bed behavior. The effective Sherwood number is, in general, different from the particle Sherwood number which is based on local mass transfer rates and concentration differences. The former will be influenced by bed nonuniformities and backmixing or diffusion in the flow direction.

Many investigators have attempted to explain the behavior of particle mass transfer in fixed and fluidized beds at low Reynolds numbers. Some authors have constructed models to show the effective Sherwood number falls at low Reynolds numbers while the particle Sherwood number remains constant. The two mechanisms most commonly used to explain the deviation are nonuniform flow channeling in the bed or diffusion in the flow directions. No paper to date has considered both of these mechanisms together.

Recently a model formulated by Nelson and Galloway [9] has received considerable attention. The individual particle Sherwood number predicted from penetration theory was found to approach zero for low values of Reynolds numbers. However, penetration theory is not appropriate at the low Reynolds numbers [10] and, as Schlünder [11] points out, the boundary conditions which Nelson and Galloway use are incorrect. Rowe [12] observed that penetration theories do not predict the correct trend of the Sherwood number with changes in voidage. Its experimental confirmation was unsuccessfully attempted by Koloini, et al. [13]. In a later section Nelson and Galloway's work will be considered in detail.

In references [14–19] various mechanisms are examined to explain the low Reynolds number result.

An attempt will be made to include all of the important mechanisms into a single model for the mass transfer in a bed. Particular care will be used to distinguish between the effective Sherwood numbers for overall bed performance and the local or particle Sherwood number for mass transfer from an individual particle to the surrounding fluid. Results will be given using parameters which are representative of realistic bed geometries.

Proper Order of Magnitude of the Particle Sherwood and Nusselt Numbers

The local heat transfer or mass transfer coefficients for the individual particles when all particles in the bed are active is defined as the heat or mass flux per unit area from the particle to the surrounding fluid divided by the local characteristic driving potential difference. For heat transfer this driving potential difference is the surface temperature less the bulk temperature of the fluid in the flow channel adjacent to the surface. An analogous concentration difference is appropriate for mass transfer. At low Reynolds numbers the mechanism for the transfer of mass or heat from the surface is diffusion. The lower limit for the transfer coefficients must be

$$h \geq k_f/\delta_{\max},\ k \geq D/\delta_{\max} \qquad (1\text{–}2)$$

where $\delta_{\max}$ is half the average interstitial distance between neighboring particles. Then,

$$\mathrm{Sh}_p(\mathrm{Nu}_p) \geq d_p/\delta_{\max} \qquad (3)$$

This expression is also true for laminar flow through ducts. As the voidage of the bed increases, the lower limit given by equation (3) is too conservative. As the voidage approaches unity the right-hand side of equation (3) approaches a value of 2.0. Similarly, the Ranz-Marshall correlation should represent the lower limit for (Nu_p) and (Sh_p).

Prediction of Effective Sherwood Number

We are still left with the divergence between the particle Sherwood and Nusselt numbers, which should approach values greater than or equal to unity at small Reynolds numbers, and the various experimental results which indicate that the effective Sh and Nu approach values one or more orders of magnitude below unity. The former is defined as

$$\mathrm{Sh}_p = \frac{N d_p}{D[C_s - C_B]} \qquad (4)$$

Contributed by the Heat Transfer Division for publication in THE JOURNAL OF HEAT TRANSER. Manuscript received by the Heat Transfer Division January 15, 1980.

The effective Sherwood number for a large bed cannot be defined as easily. If fluid flows through the bed in steady one-dimensional plug flow, and there is no diffusion or backmixing in the flow direction, the concentration of the fluid leaving the bed, C_e can be expressed as

$$\frac{C_e - C_s}{C_i - C_s} = \exp\left[-\frac{\mathrm{Sh}_E A D}{d_p u A_{cs}}\right] \tag{5}$$

Most of the experimental measurements of Sh are found by measuring the exit, entrance and surface concentrations for the bed and deriving the value of Sh_E. However, Sh_E is only equal to Sh_p when all of the assumptions needed for the derivation of equation (5) hold true. When these conditions do not hold, Sh_E and Sh_p will differ and the accuracy with which Sh_p can be derived from experimental data depends on how closely the true physical conditions of the experiment are accounted for.

In the balance of this paper, we will examine low Reynolds number flow through a fixed bed which has a geometry typical of that used in experimental investigations. Conditions will be identified which tend to cause Sh_E to deviate from Sh_p.

First we will examine the consequences of nonuniform voidage or particle size across the bed surface. The voidage near the walls of a packed bed is considerably larger than in the rest of the bed [20]. Figure 1 illustrates the results of a simplified model for the voidage variation across the bed cross section for a constant voidage in the flow direction. The ratio of the superficial velocities for the two regions was found by applying Ergun's equation to each region. The Reynolds number is based on conditions in the majority of the bed, which has a voidage of 0.4. Typically the region of the bed near the walls has a voidage of 0.7 or greater. Since the resistance of the bed wall and radial mixing between regions of different voidage are not included, the results shown in Fig. 1 should be taken only as an upper limit for the velocity ratio between the two regions. If the bed was made of particles of two different sizes and the particles were segregated within the bed, the flow through these regions would be different. However, if particles in one section of the bed had twice the diameter of those in the other section, the velocity ratio at low Reynolds numbers is less than twenty percent of that for voidage variations as shown in Fig. 1 with local voidage of 0.7 and 0.4, respectively.

A second major parameter which may influence Sh_E is the axial diffusion through the bed. As the Reynolds number is reduced, axial diffusion becomes progressively more important in comparison to convective energy or mass transport.

Packed Bed Model

A model of a packed bed will be set up using a reasonable value for the individual particle Nusselt and Sherwood numbers, i.e., near unity at low Reynolds numbers. The effects of voidage variation, diameter variation, and axial diffusion will first be presented individually and then the effects will be combined.

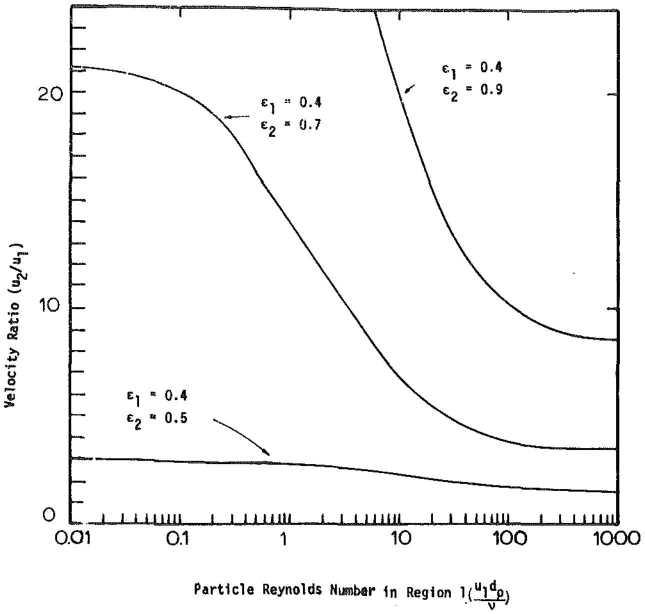

Fig. 1 The velocity ratio between two regions of different voidages with the same applied pressure difference

For the overall solution, the bed will be assumed to consist of two regions each with a constant fraction of the bed cross section, a_1, and a_2, for all heights (see Fig. 2). Each region has different but uniform voidage ϵ_1 and ϵ_2 and particle size $d_{p,1}$ and $d_{p,2}$, respectively. The average superficial velocity $\overline{u}$ is known.

The equation governing the mass transfer with axial diffusion is, for each of the separate regions of the bed

$$\epsilon_j D_{e,j} \frac{d^2 C_j}{dz^2} - u_j \frac{dC_j}{dz} - \frac{6(1-\epsilon_j)}{d_{p,j}} \chi k_j (C_j - C_s) = 0 \tag{6}$$

Boundary conditions for both regions are: At $z = 0$, the bed entrance, there is no net solute flux; and at $z = L$, the bed exit, the axial concentration gradient is zero. Lateral diffusion between the two regions of the bed is neglected.

The solute concentrations are found separately for the two regions and then combined to obtain the mass average exit concentration C_e for the entire cross section.

Nomenclature

A = total surface area of active particles in the packed bed (m^2)
A_{cs} = cross-sectional area of packed bed (m^2)
a = fraction of cross section for region of the bed with respect to the total bed cross section
C = solute concentration in the fluid (moles/m^3)
C_B = bulk concentration of fluid in the neighborhood of a particle (moles/m^3)
C_i, C_e = inlet and exit solute concentrations in the fluid for the packed bed model (moles/m^3)
C_s = concentration of the solute in the fluid at a particle's surface (moles/m^3)
D = molecular diffusion coefficient (m^2/s)
D_e = effective axial diffusion coefficient (m^2/s)
d_p = particle diameter (m)
h = heat transfer coefficient (W/m^{2}K)
k = mass transfer coefficient (m/s)
k_f, k_s = conductivities of fluid and particle (W/mK)
L = height of the packed bed (m)
N = mass transfer per unit particle surface area (moles/m^{2}s)
Nu = Nusselt number hd_p/k_f
Pr = Prandtl Number $\nu c_p/k_f$
Re_p = particle Reynolds number = ud_p/ν
Sc = Schmidt number = ν/D
Sh_p = individual particle Sherwood number defined by equation (4)
Sh_E = effective particle Sherwood number in a packed bed defined by equation (5)
t = time variable (s)
T = surface renewal period (s)
u = superficial velocity (m/s)
z = vertical length variable (m)
α = defined by equation (7b)
β = defined by equation (7c)
γ = defined by equation (7d)
δ = thickness of the fluid shell surrounding the particle (m)
ϵ = void fraction of a region in the bed
μ = dynamic viscosity (kg/ms)
ν = kinematic viscosity (m^2/s)
σ = standard deviation of measured concentrations
χ = fraction of active particles in the bed

Superscripts

$-$ = average value throughout the bed

Subscripts

j = j'th region of the packed bed (=1,2)
1,2 = regions 1 and 2 of the packed bed model

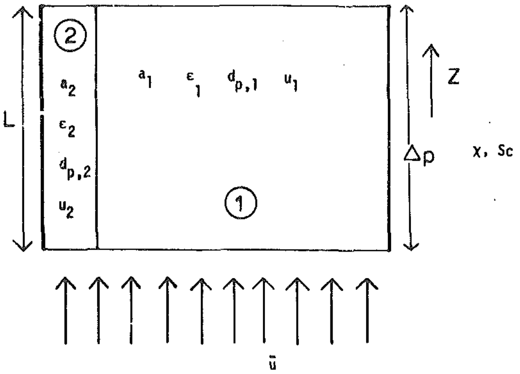

Fig. 2 Model of a packed bed

$$\frac{C_e}{C_s} = 1 - \frac{4\overline{d_p}}{\overline{\mathrm{Re}_p}} \sum_{j=1}^{2} \frac{a_j \alpha_j \,\mathrm{Re}_{p,j} \exp(\gamma_j)}{d_{p,j}[(\alpha_j + 1)^2 - (\alpha_j - 1)^2 \exp(-\beta_j)]} \tag{7a}$$

with

$$\alpha_j = \sqrt{1 + 24\chi(1 - \epsilon_j)\,\frac{k_j D_{e,j} \epsilon_j}{u_j{}^2 d_{p,j}}} \tag{7b}$$

$$\beta_j = \frac{u_j L}{\epsilon_j D_{e,j}}\,\alpha_j \tag{7c}$$

$$\gamma_j = \frac{u_j L}{2\epsilon_j D_{e,j}}\,(1 - \alpha_j) \tag{7d}$$

Fluid velocities through the two different regions are determined by assuming an equal pressure drop for each region for a fixed total flow rate. Ergun's relationship [21] was used for the pressure drop.

The effective diffusion coefficients, $D_{e,j}$, were found from use of de Ligny's [22] correlation for the Peclet number for axial mass diffusion for spherical particles (tortuosity was taken as 1/0.7). The effective thermal diffusivity was taken from Votruba, et al. [23] (with their recommended stagnant thermal conductivity and the coefficient $C_3 = 5.1$). The particle Sherwood and Nusselt numbers were taken from the Ranz-Marshall correlation [7]. Possibly a more realistic case would be to require that the inlet concentration to the two regions be the same, i.e., $C_1(0) = C_2(0)$. For the range of values of the parameters used, it was found that the inclusion of this condition has an inconsequential effect on the Sherwood numbers.

In the next section effective Sherwood numbers will be predicted for beds with typical dimensions. The choice of the values for the parameters was solely based on the criterion that the parameters have reasonable values, typical of those used in experiments reported in the literature or used in practice, particularly those of fixed beds with gas flowing through them.

Results

The influence of channeling and backmixing was determined for each case considered by solution of equation (7). Values of Sh_E defined by equation (5) will be presented as a function of the average Reynolds number $\overline{\mathrm{Re}_p} = (\bar{u}\,\overline{d_p}/\nu)$, average void fraction $\bar{\epsilon}$, average particle diameter $\overline{d_p}$ and the Schmidt number Sc.

$$\mathrm{Sh}_E = \frac{\overline{\mathrm{Re}_p}\mathrm{Sc}}{6(1 - \bar{\epsilon})\chi}\,\frac{\overline{d_p}}{L}\,\ell\mathrm{n}\,\frac{C_s}{C_s - C_e} \tag{8}$$

where $A/A_{cs} \equiv 6(1 - \bar{\epsilon})\chi\, L/\overline{d_p}$ and the inlet concentration C_i is assumed negligible.

1 **Axial Diffusion.** To distinguish the effect of diffusion in the direction of flow from others we will first assume the entire bed has a uniform voidage, $\epsilon_1 = \epsilon_2$ in equation (7).

Figure 3 compares the value of Sh_E and Sh_p with axial diffusion present. Note that as the Reynolds number decreases, the influence of axial diffusion increases and the effective value of the Sherwood number decreases rapidly. Care must be exercised in using the Peclet number correlation appropriate to the case at hand. Note that the bed used in this example is only five particles deep, thus the use of a continuum representation of the phenomena, implied by equation (6), is approximate at best. However, this approximation should give the correct order of magnitude of the various processes, adequate for the present work.

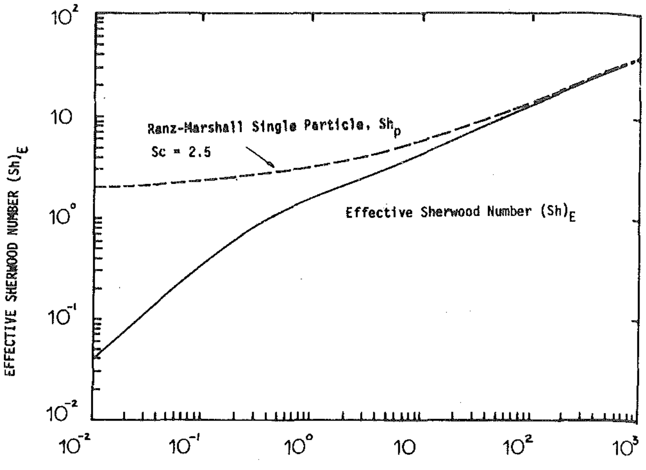

Fig. 3 Effective Sherwood number. Effect of axial diffusion. Bed conditions: $a_1 = 0.95$, $a_2 = 0.05$, $L = 5d_p$, $\epsilon = 0.4$, Sc = 2.5, $\chi = 1.0$

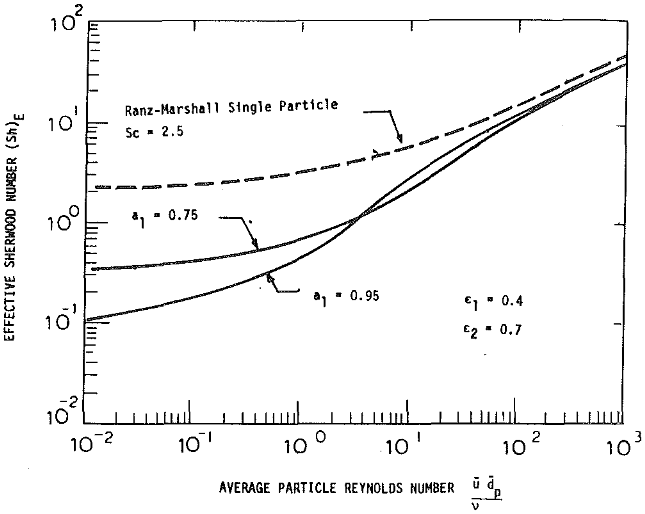

Fig. 4 Effective Sherwood number. Effect of channeling due to voidage variations across the bed cross section. Bed conditions, $L = 5d_p$, Sc = 2.5, $\chi = 1.0$

2 **Channeling—Voidage Variation.** In actuality, the voidage near the wall of a bed is higher than in the rest of the bed. Initial results were obtained omitting axial diffusion to more clearly illustrate the influence of channeling. For these cases, equation (6) can be simplified by setting D_e to zero. The solution for each area of uniform voidage becomes equation (5), with Sh_E replaced by Sh_p and using the properties of each area. Fig. 4 shows the results for the effective Sherwood number of the bed given by equation (8), where the exit concentration is the mass averaged concentration over the exit area of the bed. The average Reynolds number is used. As the area of high voidage decreases, the effective Sherwood number decreases. Since the results shown in Fig. 4 were derived using velocity ratios based on negligible wall friction and lateral mixing, these results represent the extreme lower limit for the effective Sherwood number due to voidage variations. In general, voidage variations will cause Sh_E to differ from Sh_p by one order of magnitude or less.

3 **Channeling—Particle Size Variation.** Since diameter

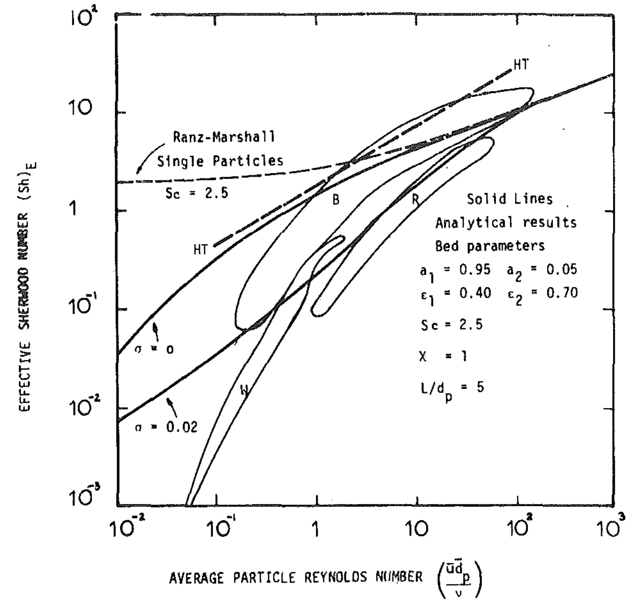

Fig. 5 Effective Sherwood number. Comparison of experimental results with analytical values including axial diffusion and channeling due to voidage variations. Effect of bias in Sh_E if experimental measurements of C_e greater than C_s are omitted. Analytical results when the standard deviation of measurements is two percent and zero. Experimental results from: *B*-[28], *R*-[29], *W*-[30], *HT*-[8]

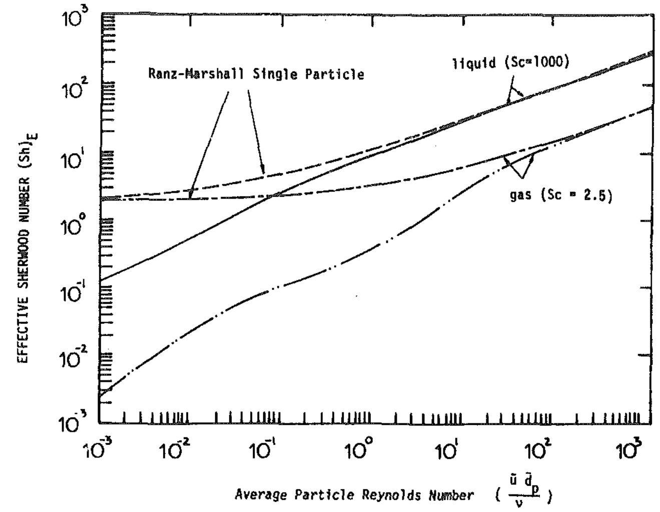

Fig. 6 Effective Sherwood number for gas and liquid systems including axial diffusion and channeling due to voidage variations. Bed conditions, $a_1 = 0.95$, $a_2 = 0.05$, $L = 5d_p$, $\epsilon_1 = 0.4$, $\epsilon_2 = 0.7$, $\chi = 1$

variations yield far less channeling than voidage variations, the former will have much smaller influence on Sh_E. For a diameter ratio of two, Sh_E falls to approximately 0.5 at low Reynolds numbers. Thus, channeling due to voidage variation should have a stronger influence than channeling due to particle size variation.

4 Combined Effects. The effective Sherwood number considering both axial diffusion and channeling due to voidage variations is shown in Fig. 5. The results are very close to those due to axial diffusion alone. At low Reynolds numbers, axial diffusion begins to dominate over convective effects and the influence of velocity variations across the bed cross section are diminished. Also shown in Fig. 5 are experimental values reported by various investigators. Although the theoretical results agree with some of the measured values for the effective Sherwood number, other investigators report still lower values of Sh_E.

5 Experimental Error. Figure 5 includes results for Sh_E when the possibility of experimental error is included. At low Reynolds numbers, the difference between the exit concentration of the fluid, C_e, and the saturation concentration of the fluid at the particle surface C_s becomes very small, approaching in magnitude the standard deviation of the experimental measurement, σ. Because of the complexity of experimental preparation many of the results were taken on experiments using a modest number of samples. As the difference between C_e and C_s approaches σ, some measurements of C_e will exceed C_s. Investigators would have been tempted to exclude these experimental results as erroneous. This would distort the random distribution and bias the mean of the measured exit concentration. The error between the biased mean exit concentration and the actual exit concentration would be,

$$C_{e,\text{meas.}} - C_e = -\sqrt{\left(\frac{2}{\pi}\right)}\,\frac{\exp\left[-\frac{1}{2}\left(\frac{1-C_e/C_s}{\sigma}\right)^2\right]}{\text{erfc}\left[-\frac{1-C_e/C_s}{\sqrt{2}\,\sigma}\right]} \qquad (9)$$

Figure 5 shows the error due to biasing the mean exit concentration.

For liquids in packed beds where the Schmidt number is much higher, the deviation between Sh_E and Sh_p due to axial diffusion and channeling appear at much lower $\overline{Re}_p$ [24, 25]. This is seen in Fig. 6. All bed parameters are as usual except that the Schmidt number is increased to 1000.

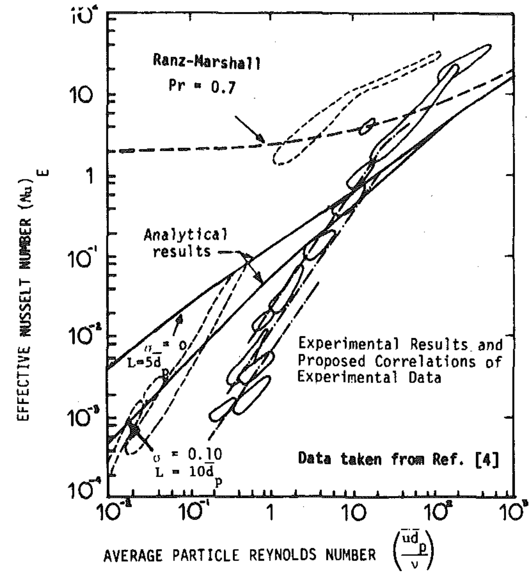

Fig. 7 Effective Nusselt number for gases and liquids in packed beds including axial conduction and channeling due to voidage variations. Bed conditions, $a_1 = 0.95$, $a_2 = 0.05$, $\epsilon_1 = 0.4$, $\epsilon_2 = 0.7$, $L = 5d_p$ and 10 d_p, Pr = 0.7, k_s/k_f = 1000, d_p = 1 mm

In heat transfer experiments an additional phenomenon is the particle-to-particle conduction. Figure 7 shows the predicted values of the Nusselt number when axial conduction and channeling are present in comparison with experimental results. Because of the large effective conductivity the effective Nusselt number has a larger decrease at small Reynolds numbers than does the effective Sherwood number.

In fluidized beds axial diffusion and channeling effects will also be present. Near the minimum fluidizing velocity, the entire fluidized bed acts like a packed bed with a somewhat larger voidage. If the two-phase hypothesis is accepted [4, 27], as the velocity is increased above minimum fluidization the dense phase remains at the minimum fluidization voidage. The axial diffusion in the dense phase should be identical to diffusion in a packed bed. The bubbles in a fluidized bed lead to a large amount of gas bypassing which causes channeling errors much more severe than those found in a packed bed. Thus, the difference between Sh_E and Sh_p in a fluidized bed should be equal to, or greater than, the difference found in a packed bed. This has been borne out by experimental results as shown in Fig. 8 taken from [2].

Penetration Theory Results

Nelson and Galloway attempt to explain the decrease in Sh_E at low Reynolds number as due to the decrease in Sh_p as Re_p is decreased. They apply the penetration theory to a particle surrounded by a spherical shell of fluid of radius $(d_p/2 + \delta)$. Besides the typical penetration theory boundary conditions (constant surface concentration, C_s, constant initial fluid concentration C_0), the authors assume that the outer boundary of the fluid shell is impermeable. They define the particle Sherwood number as

$$\mathrm{Sh}_p = \frac{\overline{N} d_p}{D(C_s - C_0)} \tag{10}$$

where $\overline{N}$ is the mass transfer rate per unit area of particle surface averaged over the period T that the fluid surface is renewed. In the paper, T is taken to be inversely proportional to Re_p. At low values of the Reynolds number, T increases, the fluid in the shell approaches saturation, and the mass transfer rate becomes small. The driving force in equation (10) is based on the initial concentration difference and it is invariant with time. Thus for low Reynolds numbers the Sherwood number based on equation (10) always goes to zero.

We have resolved the identical problem with a Sherwood number defined using the time averaged mass transfer rate and a time averaged driving potential, i.e., the difference between the surface concentration and the *time averaged* concentration at the outer shell of the fluid over the same time T.

$$\mathrm{Sh}_p = \frac{\overline{N} d_p}{D\left[C_s - C\left(\frac{d_p}{2} + \delta, t\right)\right]} \tag{11}$$

The solution is given in reference [27]. The results are shown on Fig. 9 for different values of the bed voidage. At low Reynolds numbers the Sherwood number, defined by equation (11), approaches a constant, finite value. The limiting value of Sh_p increases with decreasing voidage in agreement with experiments and contrary to the original results of Nelson and Galloway.

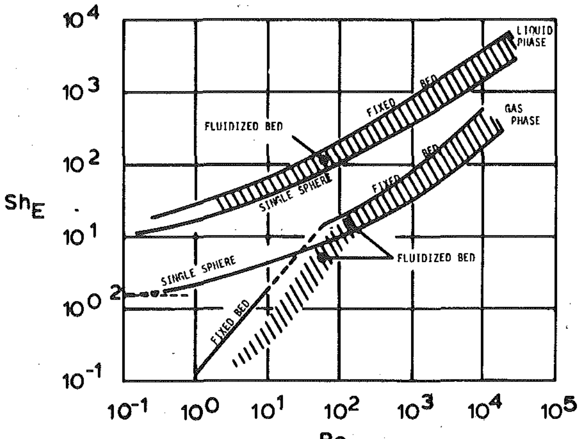

Fig. 8 Fluid-solid mass transfer in fixed and fluidized beds, from [2]

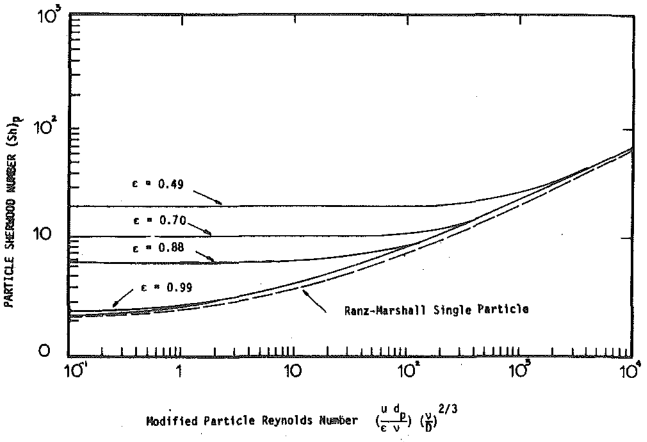

Fig. 9 Results from penetration theory where the particle Sherwood number is defined by time-averaged concentrations

Conclusion

At low Reynolds numbers the particle Nusselt and Sherwood numbers based on local temperature or concentration differences approach a value equal to or greater than unity. Results from penetration theory do not contradict these conclusions when the Sherwood number is properly defined.

When the overall heat or mass transfer performance of a fixed or fluidized bed is to be determined at low Reynolds numbers, a careful consideration of channeling and axial diffusion must be included. The overall or effective Sherwood and Nusselt number for the bed will be well below the values for individual particles. The decrease is primarily due to diffusion in the flow direction. Since the particles increase the overall thermal conductivity of beds with gas flows, the effective Nusselt number will be reduced more than the effective Sherwood number at low Reynolds numbers.

Channeling due to variations in voidage or particle size has a more modest influence on the effective Sherwood and Nusselt numbers of fixed beds. In shallow fluidized beds or spouting beds where appreciable gas bypassing of the dense phase can occur, channeling may be more important.

Error in the reduction of experimental data which introduces bias may be responsible for part of the observed decrease in the effective Sherwood and Nusselt numbers.

References

1 Gamson, B. W., Thodos, G., and Hougen, O. A., *Transactions of the American Institute of Chemical Engineers*, Vol. 39, 1943, p. 1.

2 Upadhyay, S. N., and Tripathi, G. J. *Scientific and Industrial Research*, Vol. 34, 1975, p. 10.

3 Colquhoun-Lee, I., and Stepanek, J., *Chemical Engineer*, London, No. 282, Vol. 108 Feb. 1974, p. 108.

4 Kunii D., and Levenspiel, O., *Fluidization Engineering*, J. Wiley and Sons, 1969.

5 Gupta, S. M., Chaube, R. B., and Upadhyay, S. N., *Chemical Engineering Science*, Vol. 29, 1974, p. 839.

6 Karabelas, A. J., Wegener, T. H., and Hanratty, T. J., *Chemical Engineering Science*, Vol. 26, 1971, p. 1581.

7 Ranz, W. E., and Marshall, W. R., *Chemical Engineering Progress*, Vol. 48, 1952, p. 173.

8 Hsiung, T. H., and Thodos, G., *International Journal of Heat and Mass Transfer*, Vol. 20, 1977, p. 331.

9 Nelson, P. A., and Galloway, T. R., *Chemical Engineering Science*, Vol. 30, 1, 1975.

10 Schlichting, H., *Boundary Layer Theory*, 6th Edition, McGraw-Hill, 1968.

11 Schlünder, E. U., *Chemical Engineering Science*, Vol. 32, 1977, p. 845.

12 Rowe, P. N., *Chemical Engineering Science*, Vol. 30, 1975, p. 7.

13 Koloini, T, Sopčič, M., and Žumer, M., *Chemical Engineering Science*, Vol. 32, 1977, p. 637.

14 Carberry, J. J., *AIChE Journal*, Vol. 6, 1960, p. 460.

15 Zabrodsky, S. S., *International Journal Heat and Mass Transfer*, Vol. 6, 1963, p. 23.

16 Rowe, P. N., *International Journal Heat and Mass Transfer*, Vol. 6, 1963, p. 989.

17 Gelperin, N. I., and Einstein, V. G., *Fluidization*, J. F. Davidson and D. Harrison, Editors, Academic Press, 1971, p. 471.

18 Kunii, D. and Suzuki, M., *International Journal of Heat and Mass Transfer*, Vol. 10 1967, p. 845.

19 Sørenson, J. P., and Stewart, W. E., *Chemical Engineering Science*, Vol. 29, 1974, p. 811.

20 Pillai, K. K., *Chemical Engineering Science*, Vol. 32, 1977, p. 59.

21 Ergun, S., *Chemical Engineering Progress*, Vol. 48, 1952, p. 89.

22 de Ligny, C. L., *Chemical Engineering Science*, Vol. 25, 1970, p. 1177.

23 Votruba, J., Hlavacek, V., and Marek, M., *Chemical Engineering Science*, Vol. 27, 1972, p. 1845.

24 Coeret, F., *Electrochim Acta*, Vol. 21, 1976, p. 185.

25 Mandelbaum, J. A., and Böhm, U., *Chemical Engineering Science*, Vol. 28, 1973, p. 569.

26 Davidson, J. F. and Harrison, D., *Fluidized Particles*, Cambridge University Press, Cambridge, 1963.

27 Joos, F. M., SM in ME Thesis, MIT, Feb. 1978.

28 Bar Ilan, M. and Resnick, W., *Industrial Engineering Chemistry*, Vol. 49, 1957, p. 313.

29 Resnick W. and White, R. R., *Chemical Engineering Progress*, Vol. 45, 1949, p. 377.

30 Wakao, N. and Tanisho, S., *Chemical Engineering Science*, Vol. 29, 1974, p. 1991.

31 Richardson, J. F. and Szekely, J., *Transactions of the Institute of Chemical Engineers*, Vol. 39, 1961, p. 212.

S. C. Huang
Y. P. Chang
Department of Mechanical Engineering,
State University of New York at Buffalo,
Buffalo, NY 14260

Heat Conduction in Unsteady, Periodic, and Steady States in Laminated Composites[1]

This paper provides analytical solutions for heat conduction in composites of infinite, semi-infinite, and finite laminates in unsteady, periodic, and steady states. For compactness and generality, Green's functions are used. The method of analysis applies for composites of any number of layers, but only solutions for two material composites are presented in this paper. Some calculated results of an example in steady and periodic states are shown and discussed.

1 Introduction

The analytical study on multidimensional heat conduction in composite regions has been of great interest in recent years due to the increasing usage of laminated and fiber reinforced materials. Most analyses reported in literature were made for two-dimensional heat flow in binary composites according to an approximate mathematical model [1–5]. By integrating the two differential equations with respect to the spatial variable normal to the laminates, they were reduced to two one-dimensional differential equations coupled by an "interaction term." Explicit expressions of "mixture" conductivity and specific heat were obtained. Using the mixture properties, the heterogeneous problem was reduced to one of a homogeneous material. This approach is usually called *mixture,* or *continuum,* or *continuum-mixture* theory.

Horvay and his associates [6–7] investigated the periodic solution of two-dimensional heat conduction in semi-infinite composites of two and three layers, with insulated broad-faces of the composite and temperature prescribed at the end as a harmonic function of time. To obtain an exact solution, they treated the problem as one of eigenfunctions with complex eigenvalues. Many interesting techniques were employed for the evaluation of the complex eigenvalues. Since the calculation of complex eigenvalues is usually quite complicated, the calculation of the temperature distribution in each laminate will require considerable efforts. Nevertheless, the complex eigenvalue approach does provide many interesting results, such as the steep changes of temperature in the proximity of the interface at high-frequency excitation and phase lag of temperature waves. Based upon their investigations, Horvay, et al. made a thorough discussion on the range of validity of the continuum-mixture theory [7].

This paper presents exact solutions in unsteady, periodic, and steady states for three and two-dimensional heat conduction in composites of infinite, semi-infinite, and finite laminates with or without contact resistance at interfaces. Concentrated or distributed, instantaneous or continuous, heat sources or sinks are considered in each laminate. Boundary conditions on the two broad faces of the composite can be of the first, the second or the third kind, or the combination of them. Boundary conditions on other surfaces, if any, are either of the first or the second kind or their combinations. The material of each laminate is isotropic and homogeneous with constant thermo-physical properties.

The purpose of this paper is to show that most composite-region problems can be solved exactly without the use of special mathematical techniques. Only two-layered composites are considered in this paper, though the method applies to any number of layers. However, for composites of a large number of layers, it is more convenient to use fundamental Green's functions [8, 9].

2 Formulation of Problems and Green's Functions

Consider first the heat conduction in unsteady state in a composite of two laminates: one in the region $(x, -y_1 < y < 0, z)$ called region 1 and the other in $(x, 0 < y < y_2, z)$ called region 2. Quantities in the two regions are distinguished by subscripts 1 and 2. The differential equations to be solved are

$$k_i \nabla^2 T_i - \rho_i c_i \frac{\partial T_i}{\partial t} = -q_i{}'''(x, y, z, t) + k_i \mu_i{}^2 T_i \qquad (2.1)$$

where $i = 1, 2$; ∇^2 is the Laplacian operator; and terms in the righthand side represent the rate of heat generation per unit volume, which is a linear function of temperature; subject to the initial and boundary conditions,

$$T_i = F_i(x, y, z) \qquad t = 0 \qquad (2.2)$$

$$k_1 \frac{\partial T_1}{\partial y} - h_1 T_1 = f_1(x, z, t) \qquad y = -y_1 \qquad (2.3)$$

$$k_2 \frac{\partial T_2}{\partial y} + h_2 T_2 = f_2(x, z, t) \qquad y = y_2 \qquad (2.4)$$

and the matching conditions at the interface

$$\left.\begin{aligned} k_1 \frac{\partial T_1}{\partial y} &= k_2 \frac{\partial T_2}{\partial y} && (2.5) \\ k_2 \frac{\partial T_2}{\partial y} &= h_c (T_2 - T_1) && (2.6) \end{aligned}\right\} \; y = 0$$

For the infinite laminate, in order to obtain unique solutions for all cases in steady and unsteady states, we impose the condition that

$$T_i = 0 \qquad |x|, |z| \to \infty \qquad (2.7)$$

and for semi-infinite or finite laminate, boundary conditions at surfaces other than $y = -y_1$ and $y = y_2$ is to be of the first or second kind, i.e., either the temperature or the heat flux is prescribed; for instance, in the case of semi-infinite laminates,

$$T_i = g_i(y, z, t) \qquad x = 0 \qquad (2.8)$$

or

$$-k_i \frac{\partial T_i}{\partial x} = q_i{}''(y, z, t) \qquad x = 0 \qquad (2.9)$$

together with condition (2.7) for $|z| \to \infty$, and $x \to \infty$. All prescribed functions are assumed to be bounded or absolutely integrable within each domain in question.

If $q_i{}'''$, f_i, g_i and $q_i{}''$ involve periodical functions of time, for in-

---

[1] This study was supported in part by the National Science Foundation ENG 76-83367.

Contributed by The Heat Transfer Division for publication in the JOURNAL OF HEAT TRANSFER. Manuscript received by The Heat Transfer Division September 14, 1979.

stance,

$$q_i''' = q_{0i}'''(x, y, z) \cos (w_1 t - \epsilon_1) \tag{2.10}$$

$$g_i = g_{0i}(y, z) \cos (w_2 t - \epsilon_2) \tag{2.11}$$

the solution of the unsteady-state problem will, in general, consist of steady-state, periodic-state, transient and nontransient solutions. If we are only interested in the periodic solution, we just drop the initial condition (2.2) and all nonperiodical prescribed data.

In steady state, we just drop the time-derivative term in (2.1), the initial condition (2.2) and the time-dependence of all the prescribed data.

If the heat generation in the laminate involves concentrated heat sources, for instance, continuous point sources at (x_{1i}, y_{1i}, z_{1i}) and instantaneous point sources at $(x_{2i}, y_{2i}, z_{2i}, t_2)$, we just replace q_i''' in (2.1) by

$$\begin{aligned} &q_i'''(x, y, z, t) + q_1\delta(x - x_{1i})\delta(y - y_{1i})\delta(z - z_{1i}) \\ &\qquad + Q_2\delta(x - x_{2i})\delta(y - y_{2i})\delta(z - z_{2i})\delta(t - t_2) \end{aligned} \tag{2.12}$$

We now wish to express the general solution for each state in terms of the Green's function which can be determined once and for all. The Green's function associated with the unsteady-state problem is to satisfy the differential equations

$$\begin{aligned} &k_i(\nabla^2 G_{ij} - \mu_i{}^2 G_{ij}) - \rho_i c_i \frac{\partial G_{ij}}{\partial t} \\ &\qquad = -\rho_i c_i \delta(x - x')\delta(y - y')\delta(z - z')\delta(t - t')\delta_{ij} \end{aligned} \tag{2.13}$$

where the subscript $j = 1, 2$ and denotes the region where the prescribed data (i.e., sources) reside. The solution of (2.13) is subject to the initial, boundary, and matching conditions for the infinite laminate.

$$G_{ij} = 0 \qquad t = t' \tag{2.14}$$

$$k_1' \frac{\partial G_{1j}}{\partial y} - h_1 G_{1j} = 0 \qquad y = -y_1 \tag{2.15}$$

$$k_2' \frac{\partial G_{2j}}{\partial y} + h_2 G_{2j} = 0 \qquad y = y_2 \tag{2.16}$$

$$\left.\begin{aligned} k_1 \frac{\partial G_{1j}}{\partial y} &= k_2 \frac{\partial G_{2j}}{\partial y} && (2.17) \\ k_2 \frac{\partial G_{2j}}{\partial y} &= h_c(G_{2j} - G_{1j}) && (2.18) \end{aligned}\right\} \quad y = 0$$

$$G_{ij} = 0 \qquad |x|, |z| \to \infty \tag{2.19}$$

For the semi-infinite laminate, the boundary condition at $x = 0$ to be satisfied is

$$G_{ij} = 0 \quad \text{or} \quad \frac{\partial G_{ij}}{\partial x} = 0 \qquad x = 0 \tag{2.20}$$

and for finite laminate, besides (2.20) additional boundary conditions are:

$$\begin{aligned} &G_{ij} = 0 \quad \text{or} \quad \frac{\partial G_{ij}}{\partial x} = 0 \qquad x = \ell_1 \\ &G_{ij} = 0 \quad \text{or} \quad \frac{\partial G_{ij}}{\partial z} = 0 \qquad z = 0, \ell_3 \end{aligned} \tag{2.21}$$

For periodic state, we drop $\delta(t - t')$ from (2.13) and initial conditions (2.14). In steady state, we replace $\rho_i c_i$ in the righthand side of (2.13) with k_i and drop the term $\rho_i c_i \partial G_{ij}/\partial t$ from (2.13) in addition to the modifications already made for periodic state.

3 Green's Functions and General Solutions in Unsteady State

Consider first the case of the infinite laminate, $(|x| < \infty, -y_1 < y < y_2, |z| < \infty)$. Since $|x| < \infty$ and $|z| < \infty$, and $G_{ij} = 0$ for $|x|, |z| \to \infty$, we may rewrite (2.13) in polar coordinates and seek the solution in the form [10]

$$G_{ij} = \frac{1}{2\pi} \sum_{n=1}^{\infty} \int_0^{\infty} \frac{1}{N_n} Y_i(\xi_{in} y)\, Y_j(\xi_{jn} y') J_0(\xi R) e^{-\lambda_n{}^2 (t - t')} \xi d\xi \tag{3.1}$$

where N_n is the norm of eigenfunction Y_i to be determined later; and

$$R^2 = (x - x')^2 + (z - z')^2 \tag{3.2}$$

$$\xi_{in}{}^2 = \frac{\lambda_n{}^2}{\alpha_i} - (\xi^2 + \mu_i{}^2) \tag{3.3}$$

We recall that $i = 1, 2$ denotes regions for field points while $j = 1, 2$ denotes regions for source points. We note also that (3.1) has already satisfied condition (2.19) and also (2.14–2.18) if $Y_i(\xi_{in} y)$ satisfies the following set of equations.

$$(k_i Y_i')' + (\rho_i c_i \lambda_n{}^2 - \xi^2 - \mu_i{}^2) Y_i = 0 \tag{3.4}$$

$$k_1' Y_1' - h_1 Y_1 = 0 \qquad y = -y_1 \tag{3.5}$$

$$k_2' Y_2' + h_2 Y_2 = 0 \qquad y = y_2 \tag{3.6}$$

$$\left.\begin{aligned} k_1 Y_1' &= k_2 Y_2' && (3.7) \\ k_2 Y_2' &= h_c(Y_2 - Y_1) && (3.8) \end{aligned}\right\} \quad y = 0$$

Obviously (3.4–3.6) is of the Sturm-Liouville system possessing eigenfunction solutions orthogonal with respect to the weight function $\rho_i c_i$ while (3.7) and (3.8) behave as internal constraints.

By the usual procedure of obtaining eigenfunctions, the solution of (3.4) for Y_1 and Y_2 satisfying (3.5–3.7) is obtained as:

$$Y_1 = \frac{\sin \xi_{1n} y}{k_1 \xi_{1n}} - \frac{k_1' \xi_{1n} + h_1 \tan \xi_{1n} y_1}{k_1 \xi_{1n}(k_1' \xi_{1n} \tan \xi_{1n} y_1 - h_1)} \cos \xi_{1n} y \tag{3.9}$$

$$Y_2 = \frac{\sin \xi_{2n} y}{k_2 \xi_{2n}} + \frac{k_2' \xi_{2n} + h_2 \tan \xi_{2n} y_2}{k_2 \xi_{2n}(k_2' \xi_{2n} \tan \xi_{2n} y_2 - h_2)} \cos \xi_{2n} y \tag{3.10}$$

Substituting (3.9) and (3.10) into (3.8), we obtain the eigenvalue equation

$$\sum_{i=1}^{2} \frac{k_i' \xi_{in} + h_i \tan \xi_{in} y_i}{k_i \xi_{in}(k_i' \xi_{in} \tan \xi_{in} y_i - h_i)} = \frac{1}{h_c} \tag{3.11}$$

Nomenclature

A = amplitude, defined in (6.6) and (6.7)
c = heat capacity
f = defined in (2.3) and (2.4)
F = defined in (2.2)
h = heat transfer coefficient
h_c = thermal contact conductance, defined in (2.6)
g = defined in (2.8)
Im = imaginary part
J_0 = Bessel function of the first kind of order zero
k, k' = thermal conductivity
q'' = heat flux
q''' = rate of heat generation per unit volume
q_1 = rate of heat generation
Q_2 = amount of heat generated instantaneously
R = defined in (3.2)
Re = real part
t = time
T = temperature
T = temperature
x, y, z = rectangular coordinates
$\bar{x}, \bar{y} = x/y_1, y/y_1$
y_1, y_2 = thickness for regions 1 and 2, respectively
$\bar{y}_2 = y_2/y_1$
Y' = differentiation of Y with respect to y
α = thermal diffusivity
δ = Dirac delta function
δ_{ij} = Kronecker delta function (1 for $i = j$, 0 for $i \neq j$)
ϵ = phase lag
μ = constant, defined in (2.1)
$\xi = \xi/y_1$
ρ = density
$\sigma = k_2/k_1$
ω = angular frequency
$\bar{\omega}_1, \bar{\omega}_2 = \omega y_1{}^2/\alpha_1, \omega y_1{}^2/\alpha_2$

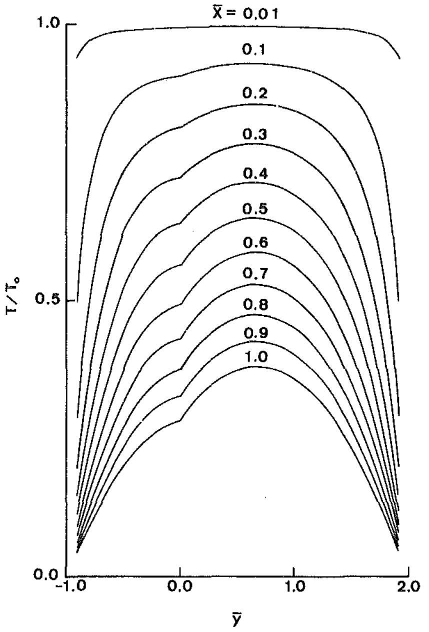

Fig. 1(*a*) **Temperature distribution in steady state, $\sigma = 0.1114$**

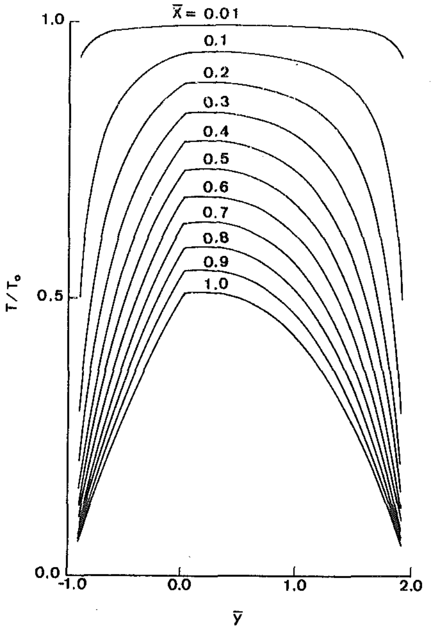

Fig. 1(*b*) **Temperature distribution in steady state, $\sigma = 8.9774$**

It can be easily shown, if we take the norm as

$$N_n = \int_{-y_1}^{0} \rho_1 c_1 Y_1^2 dy + \int_0^{y_2} \rho_2 c_2 Y_2^2 dy$$
$$= \frac{1}{2} \sum_{i=1}^{2} \frac{\rho_i c_i}{k_i^2 \xi_{in}^2} \left[\frac{(k_i'^2 \xi_{in}^2 + h_i^2) y_i + k_i' h_i}{(k_i' \xi_{in} \sin \xi_{in} y_i - h_i \cos \xi_{in} y_i)^2} + \frac{k_i' \xi_{in} \cos \xi_{in} y_i + h_i \sin \xi_{in} y_i}{\xi_{in} (k_i' \xi_{in} \sin \xi_{in} y_i - h_i \cos \xi_{in} y_i)} \right] \quad (3.12)$$

then the eigenfunctions are orthonormal [9].

For the semi-infinite laminate ($x > 0, -y_1 < y < y_2, |z| < \infty$) with boundary condition at $x = 0$ of the first or the second kind, we apply the simple reflection of image to obtain

$$G_{ij} = \frac{1}{2\pi} \sum_{n=1}^{\infty} \int_0^{\infty} \frac{1}{N_n} Y_i(\xi_{in} y) Y_j(\xi_{jn} y') \times [J_0(\xi R) \mp J_0(\xi R_1)] e^{-\lambda_n^2 (t-t')} \xi d\xi \quad (3.13)$$

where the $-$ and $+$ signs are for boundary conditions of the first and second kinds, respectively; R has been defined in (3.2) and

$$R_1^2 = (x + x')^2 + (z - z')^2 \quad (3.14)$$

For the finite laminate ($0 < x < \ell_1, -y_1 < y < y_2, 0 < z < \ell_3$) with boundary conditions at $x = 0, \ell_1$ and $z = 0, \ell_3$ all of the first kind, or all of the second kind, or the combination of the first and second, we can obtain G_{ij} by the fully eigenfunction expansion; for instance, if they are all of the first kind, we have

$$G_{ij} = \frac{4}{l_1 l_3} \sum_{m=1}^{\infty} \sum_{n=1}^{\infty} \sum_{p=1}^{\infty} \frac{1}{N_n} Y_i(\xi_{imnp} y)\, Y_j(\xi_{jmnp} y') \sin \frac{m\pi x}{\ell_1} \sin \frac{m\pi x'}{\ell_1} \sin \frac{p\pi z}{\ell_3} \sin \frac{p\pi z'}{\ell_3} e^{-\lambda_{mnp}^2 (t-t')} \quad (3.15)$$

where

$$\xi_{imnp}^2 = \frac{\lambda_{mnp}^2}{\alpha_i} - \left(\frac{m\pi}{\ell_1}\right)^2 - \left(\frac{p\pi}{\ell_3}\right)^2 - \mu_i^2 \quad (3.16)$$

If the two layers are perfectly contacted, we just set $h_c = \infty$ in (3.11) to evaluate the eigenvalues λ_n.

With Green's functions known, the solutions of the above problems can be readily written down by Green's formula. For instance, in the case of the semi-infinite laminate with temperature prescribed at $x = 0$, we obtain

$$T_i = \int_{-\infty}^{\infty} \int_0^{\infty} \left[\int_{-y_1}^{0} F_1(x', y', z') G_{i1}(x, y, z, t | x', y', z', 0) dy' + \int_0^{y_2} F_2(x', y', z') G_{i2}(x, y, z, t | x', y', z', 0) dy' \right] dx' dz'$$
$$+ \int_0^t \int_{-\infty}^{\infty} \int_0^{\infty} \left[\frac{1}{\rho_1 c_1} \int_{-y_1}^{0} q_1'''(x', y', z', t') \times G_{i1}(x, y, z, t | x', y', z', t') dy' + \frac{1}{\rho_2 c_2} \int_0^{y_2} q_2'''(x', y', z', t') \times G_{i2}(x, y, z, t | x', y', z', t') dy' \right] dx' dz' dt'$$
$$+ \int_0^t \int_{-\infty}^{\infty} \int_0^{\infty} \left[\frac{\alpha_1}{h_1} f_1(x', z', t') \frac{\partial}{\partial y'} G_{i1}(x, y, z, t | x', -y_1, z', t') - \frac{\alpha_2}{h_2} f_2(x', z', t') \frac{\partial}{\partial y'} G_{i2}(x, y, z, t | x', y_2, z', t') \right] dx' dz' dt'$$
$$+ \int_0^t \int_{-\infty}^{\infty} \left[\alpha_1 \int_{-y_1}^{0} g_1(y', z', t') \frac{\partial}{\partial x'} G_{i1}(x, y, z, t | 0, y', z', t') dy' + \alpha_2 \int_0^{y_2} g_2(y', z', t') \frac{\partial}{\partial x'} G_{i2}(x, y, z, t | 0, y', z', t') dy' \right] dz' dt' \quad (3.17)$$

If there are concentrated heat sources in the laminate, such as (2.12), we just replace q_i''' in (3.17) as given by (2.12).

4 Green's Functions and General Solutions in Periodic and Steady State

Consider first the case of the infinite laminate with heat generation involving periodic functions as typified in (2.10). To obtain the periodical solutions which are convenient in computation, we had better use periodic Green's functions. Let ω_p, where $p = 1, 2, 3, \ldots$, denote the frequency of p harmonics and $G_{ij,p}$ the Green's function associated with ω_p. We seek the solution of (2.13) for the present case in the form

$$G_{ij,p} = \frac{1}{2\pi} e^{\sqrt{-1}(\omega_p t - \epsilon_p)} \int_0^{\infty} Y_{ij}(y | y'; \xi_{ip}) J_0(\xi R) \xi d\xi \quad (4.1)$$

where R was defined in (3.2) and Y_{ij} satisfies,

$$Y_{ij}'' - \xi_{ip}^2 Y_{ij} = -\delta(y - y') \delta_{ij} \qquad -y_1 < y < y_2 \quad (4.2)$$

$$k_1' Y_{1j}' - h_1 Y_{1j} = 0 \qquad y = -y_1 \quad (4.3)$$

$$k_2' Y_{2j}' + h_2 Y_{2j} = 0 \qquad y = y_2 \tag{4.4}$$

$$\left.\begin{aligned} k_1 Y_{1j}' &= k_2 Y_{2j}' \quad (4.5)\\ k_2 Y'_{2j} &= h_c (Y_{2j} - Y_{1j}) \quad (4.6)\end{aligned}\right\} \; y = 0$$

$$\xi_{ip}{}^2 = \xi^2 + \mu_i{}^2 + \sqrt{-1}\,\frac{\omega_p}{\alpha_i} \tag{4.7}$$

The solution of (4.2) satisfying (4.3–4.6) can be found by the usual way. For $y < y'$ we obtain

$$Y_{11} = \frac{(\Delta_2 \cosh \xi_{1p} y + \Delta_1 \sinh \xi_{1p} y)[k_1 \xi_{1p} (k_2 \xi_{2_p} \Delta_3 + h_c \Delta_4) \cosh \xi_{1p} y' - h_c k_2 \xi_{2p} \Delta_3 \sinh \xi_{1p} y']}{\xi_{1p} \Delta} \tag{4.8}$$

$$Y_{22} = \frac{[k_2 \xi_{2p} (k_1 \xi_{1p} \Delta_1 + h_c \Delta_2) \cosh \xi_{2p} y + h_c k_1 \xi_{1p} \Delta_1 \sinh \xi_{2p} y](\Delta_4 \cosh \xi_{2p} y' - \Delta_3 \sinh \xi_{2p} y')}{\xi_{2p} \Delta} \tag{4.9}$$

$$Y_{12} = \frac{h_c k_2 (\Delta_2 \cosh \xi_{1p} y + \Delta_1 \sinh \xi_{1p} y)(\Delta_4 \cosh \xi_{2p} y' - \Delta_3 \sinh \xi_{2p} y')}{\Delta} \tag{4.10}$$

$$Y_{21} = \frac{h_c k_1 (\Delta_4 \cosh \xi_{2p} y - \Delta_3 \sinh \xi_{2p} y)(\Delta_2 \cosh \xi_{1p} y' + \Delta_1 \sinh \xi_{1p} y')}{\Delta} \tag{4.11}$$

where

$$\Delta_1 = k_1' \xi_{1p} \sinh \xi_{1p} y_1 + h_1 \cosh \xi_{1p} y_1$$

$$\Delta_2 = k_1' \xi_{1p} \cosh \xi_{1p} y_1 + h_1 \sinh \xi_{1p} y_1$$

$$\Delta_3 = k_2' \xi_{2p} \sinh \xi_{2p} y_2 + h_2 \cosh \xi_{2p} y_2$$

$$\Delta_4 = k_2' \xi_{2p} \cosh \xi_{2p} y_2 + h_2 \sinh \xi_{2p} y_2 \tag{4.12}$$

$$\Delta = h_c k_1 \xi_{1p} \Delta_1 \Delta_4 + k_2 \xi_{2p} \Delta_3 (k_1 \xi_{1p} \Delta_1 + h_c \Delta_2) \tag{4.13}$$

For $y > y'$, we just interchange y and y' in (4.8–4.9).

For the semi-infinite laminate, we obtain

$$G_{ij,p} = \frac{1}{2\pi} e^{\sqrt{-1}(\omega_p t - \epsilon_p)} \int_0^\infty Y_{ij}(y|y'; \xi_{ip}) \times [J_0(\xi R) \mp J_0(\xi R_1)]\xi d\xi \tag{4.14}$$

where R_1 was defined in (3.14); the minus and plus signs are for the boundary conditions at $x = 0$ of the first and second kinds, respectively. For the rectangular composite with boundary conditions of the first kind at each end of the composite, we obtain

$$G_{ij,p} = \frac{4}{\ell_1 \ell_3} e^{\sqrt{-1}(\omega_p t - \epsilon_p)} \sum_{m=1}^\infty \sum_{n=1}^\infty Y_{ij}(y|y'; \xi_{imnp}) \times \sin \frac{m\pi x}{\ell_1} \sin \frac{m\pi x'}{\ell_1} \sin \frac{n\pi z}{\ell_3} \sin \frac{n\pi z'}{\ell_3} \tag{4.15}$$

where

$$\xi_{imnp}{}^2 = \xi^2 + \mu_i{}^2 + \left(\frac{m\pi}{\ell_1}\right)^2 + \left(\frac{n\pi}{\ell_3}\right)^2 + \sqrt{-1}\,\frac{w_p}{\alpha_i} \tag{4.16}$$

For steady state, the Green's functions $G_{ij}(x, y, z|x', y', z')$ for infinite, semi-infinite and finite laminates can be obtained in the forms as (4.1, 4.14) and (4.15) by setting $\omega_p = \epsilon_p = 0$.

With the periodic Green's functions known, the periodic solution for a specific problem can be again readily obtained by Green's formula. For instance, in the case of the semi-infinite composite with the prescribed data

$$q_1''' = q_{01}'''(x, y, z) \cos(\omega_1 t - \epsilon_1) \qquad -y_1 < y < 0 \quad 0 < x < \infty \quad |z| < \infty \tag{4.17}$$

$$g_2 = g_{02}(y, z) \sin(\omega_2 t - \epsilon_2) \quad 0 < y < y_2 \quad x = 0 \quad |z| < \infty \tag{4.18}$$

the periodic solutions in regions $i = 1, 2$ are

$$T_i = \int_{-\infty}^\infty \int_{-y_1}^0 \int_0^\infty q_{01}'''(x', y', z') \times \mathrm{Re}[G_{i1,1}(x, y, z|x', y', z'; \omega_1 t)]dx'dy'dz' + \int_{-\infty}^\infty \int_0^{y_2} g_{02}(y', z')\mathrm{Im}\left[\frac{\partial}{\partial x'} G_{i2,2}(x, y, z|0, y', z'; \omega_2 t)\right] dy'dz' \tag{4.19}$$

The steady-state solution can also be readily written down by using the Green's formula. For instance, if the heat generation and boundary condition are (4.17) and (4.18) with $\cos(\omega_1 t - \epsilon_1)$ and $\sin(\omega_2 t - \epsilon_2)$ deleted, then we replace $G_{ij,p}(x, y, z|x', y', z'; \omega_p t)$ in (4.19) by $G_{ij}(x, y, z|x', y', z')$ to give the steady-state solutions T_1 and T_2. Note that for steady state the imaginary part notation Im drops and Re is no longer needed.

5 Green's Functions for Two-Dimensional Unsteady, Periodic and Steady States

If all the prescribed data are independent of z, then the problems that have been considered in preceding sections become two-dimensional. The two-dimensional Green's functions can be obtained by the same methods as those shown in Sections 3 and 4, or by integrating the three-dimensional Green's functions with respect to z over $(-\infty, \infty)$: for unsteady state,

$$G_{ij} = \frac{1}{\pi} \sum_{n=1}^\infty \int_0^\infty \frac{1}{N_n} Y_i(\xi_{in} y) Y_j(\xi_{jn} y') \cos \xi (x - x') e^{-\lambda_n{}^2 (t-t')} d\xi \qquad |x| < \infty \tag{5.1}$$

$$G_{ij} = \frac{2}{\pi} \sum_{n=1}^\infty \int_0^\infty \frac{1}{N_n} Y_i(\xi_{in} y) Y_j(\xi_{jn} y') \sin \xi x \sin \xi x' e^{-\lambda_n{}^2 (t-t')} d\xi \qquad x > 0 \tag{5.2}$$

$$G_{ij} = \frac{2}{\ell_1} \sum_{m=1}^\infty \sum_{n=1}^\infty \frac{1}{N_n}\, y\,(\xi_{imn} y)\, Y_j\,(\xi_{jmn} y') \times \sin \frac{m\pi x}{\ell_1} \sin \frac{m\pi x'}{\ell_1} e^{-\lambda_n{}^2 (t-t')}; \; 0 < x < \ell_1 \tag{5.3}$$

where

$$\xi_{in}{}^2 = \frac{\lambda_n{}^2}{\alpha_i} - (\xi^2 + \mu_i{}^2); \quad \xi_{imn}{}^2 = \frac{\lambda_{mn}{}^2}{\alpha_i} - \left(\frac{m\pi}{\ell_1}\right)^2 - \mu_i{}^2 \tag{5.4}$$

and for periodic state,

$$G_{ij,p} = \frac{1}{\pi} e^{\sqrt{-1}(w_p t - \epsilon_p)} \int_0^\infty Y_{ij}(y|y'; \xi_{ip}) \times \cos \xi (x - x') d\xi \qquad |x| < \infty \tag{5.5}$$

$$G_{ij,p} = \frac{2}{\pi} e^{\sqrt{-1}(w_p t - \epsilon_p)} \int_0^\infty Y_{ij}(y|y'; \xi_{ip}) \times \sin \xi x \sin \xi x' d\xi \qquad x > 0 \tag{5.6}$$

$$G_{ij,p} = \frac{2}{\ell_1} e^{\sqrt{-1}(w_p t - \epsilon_p)} \sum_{m=1}^\infty Y_{ij}(y|y'; \xi_{imp}) \times \sin \frac{m\pi x}{\ell_1} \sin \frac{m\pi x'}{\ell_1} \qquad 0 < x < \ell_1 \tag{5.7}$$

where

$$\xi_{ip}{}^2 = \xi^2 + \mu_i{}^2 + \sqrt{-1}\,\frac{\omega_p}{\alpha_i};$$

$$\xi_{imp}{}^2 = \left(\frac{m\pi}{\ell_1}\right)^2 + \mu_i{}^2 + \sqrt{-1}\,\frac{\omega_p}{\alpha_i} \tag{5.8}$$

All the functions Y's are those found in the last two sections. For

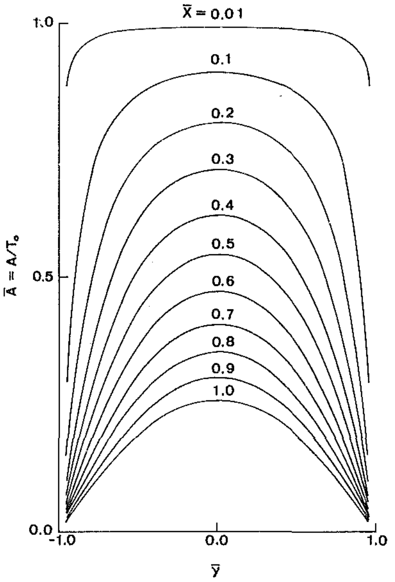

Fig. 2(*a*) Amplitudes of temperature in periodic state, $\bar{\omega}_1 = 1.0, \bar{\omega}_2 = 0.1043$, $\sigma = 8.9774$

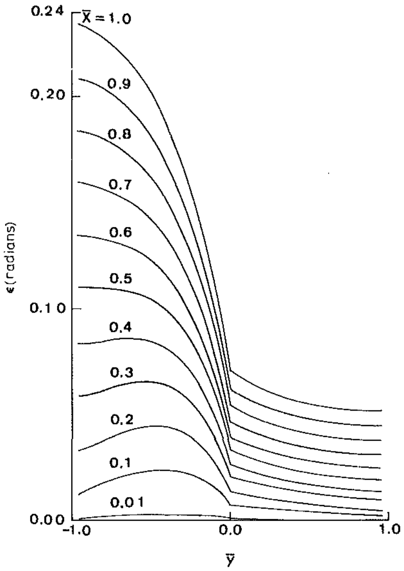

Fig. 2(*b*) Phase lags of temperature in periodic state, $\bar{\omega}_1 = 1.0, \bar{\omega}_2 = 0.1043$, $\sigma = 8.9774$

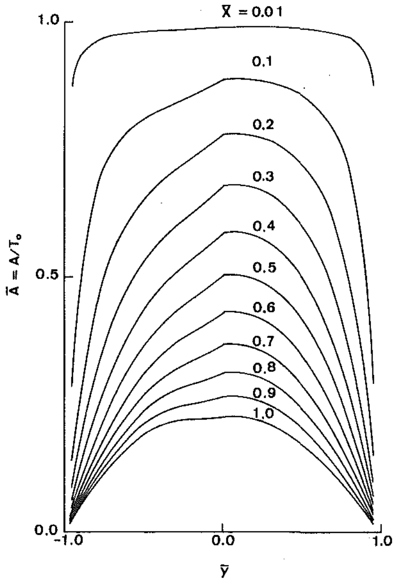

Fig. 3(*a*) Amplitudes of temperature in periodic state, $\bar{\omega}_1 = 10.0, \bar{\omega}_2 = 1.043$, $\sigma = 8.9774$

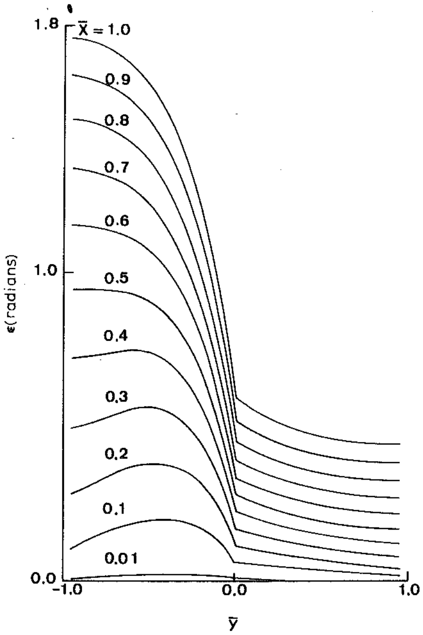

Fig. 3(*b*) Phase lags of temperature in periodic state, $\bar{\omega}_1 = 10.0, \bar{\omega}_2 = 1.043$, $\sigma = 8.9774$

steady state, we just delete the subscript p of $G_{ij,p}$ and $\exp\,[\sqrt{-1}(\omega_p t - \epsilon_p)]$ from (5.5–5.7).

6 Calculated Example for Steady and Periodic States

Consider a composite of two semi-infinite layers without contact resistance, without heat generation in the media and with the following boundary conditions

$$\begin{array}{ll} T_1 = T_2 = T_0 \cos \omega t & x = 0 \\ T_1 = T_2 = 0 & x \to \infty \\ T_1 = 0 & y = -y_1 \\ T_2 = 0 & y = y_2 \end{array} \qquad (6.1)$$

and matching conditions

$$\left.\begin{array}{l} T_1 = T_2 \\ k_1 \dfrac{\partial T_1}{\partial y} = k_2 \dfrac{\partial T_2}{\partial y} \end{array}\right\} y = 0 \qquad (6.2)$$

Clearly, this is a two-dimensional problem. Since steady and periodic solutions of composite-region problems usually are of more interest than transient solutions [6–7], we present here some calculated results of the periodic solution while the steady-state solution is only a special case for $\omega = 0$. Setting h_1, h_2 and $h_c = \infty$ in (4.8–4.11), substituting the resulted Y_{ij} (for the present case, $p = 1$ and is deleted) into (5.6) and applying G_{ij} to (4.19) we obtain

$$\frac{T_1}{T_0} = \frac{2}{\pi}\,\mathrm{Re}\left\{e^{\sqrt{-1}\omega t}\int_0^\infty \sin\bar{\xi}\bar{x}\left[\frac{1}{\bar{\xi}_1{}^2} - \frac{\{\bar{\xi}_1 \sinh\bar{\xi}_2\bar{y}_2 \cosh\bar{\xi}_1\bar{y} + \sigma\bar{\xi}_2\cosh\bar{\xi}_2\bar{y}_2[\sinh\bar{\xi}_1(1+\bar{y}) - \sinh\bar{\xi}_1\bar{y}]\}/\bar{\xi}_1{}^2 - \sigma(\cosh\bar{\xi}_2\bar{y}_2 - 1)\sinh\bar{\xi}_1(\bar{y}+1)/\bar{\xi}_2}{(\bar{\xi}_1\sinh\bar{\xi}_2\bar{y}_2\cosh\bar{\xi}_1 + \sigma\bar{\xi}_2\cosh\bar{\xi}_2\bar{y}_2\sinh\bar{\xi}_1)}\right]\bar{\xi}d\bar{\xi}\right\} \qquad (6.3)$$

$$\frac{T_2}{T_0} = \frac{2}{\pi}\,\mathrm{Re}\left\{e^{\sqrt{-1}\omega t}\int_0^\infty \sin\bar{\xi}\bar{x}\left[\frac{1}{\bar{\xi}_2{}^2} - \frac{\{\bar{\xi}_1 \cosh\bar{\xi}_1[\sinh\bar{\xi}_2\bar{y} + \sinh\bar{\xi}_2(\bar{y}_2 - \bar{y})] + \sigma\bar{\xi}_2\sinh\bar{\xi}_1\cosh\bar{\xi}_2\bar{y}\}/\bar{\xi}_2{}^2 - (\cosh\bar{\xi}_1 - 1)\sinh\bar{\xi}_2(\bar{y}_2 - \bar{y})/\bar{\xi}_1}{(\bar{\xi}_1\sinh\bar{\xi}_2\bar{y}_2\cosh\bar{\xi}_1 + \sigma\bar{\xi}_2\cosh\bar{\xi}_2\bar{y}_2\sinh\bar{\xi}_1)}\right]\bar{\xi}d\bar{\xi}\right\} \qquad (6.4)$$

where all the quantities have been nondimensionalized, and

$$\bar{\xi}_1{}^2 = \bar{\xi}^2 + \sqrt{-1}\ \bar{\omega}_1; \quad \bar{\xi}_2{}^2 = \bar{\xi}^2 + \sqrt{-1}\ \bar{\omega}_2 \qquad (6.5)$$

If we set $\bar{\omega}_1 = \bar{\omega}_2 = 0$, (6.3) and (6.4) yield the temperature distributions in steady state. In the study of periodic solution, the most important quantities are the amplitude and phase lag of temperature waves. Therefore (6.3) and (6.4) can be rewritten in the form

$$\frac{T_1}{T_0} = \bar{A}_1 \cos(\omega t - \epsilon_1) \qquad (6.6)$$

$$\frac{T_2}{T_0} = \bar{A}_2 \cos(\omega t - \epsilon_2) \qquad (6.7)$$

Some calculated results from (6.3) and (6.4) arranged in forms of (6.6) and (6.7) for a composite of copper and steel laminates are shown in Figs. 1(*a*)–4(*b*). Figures 1(*a*) and 1(*b*) show the temperature distributions in steady state for $y_2 = 2y_1$, $\sigma = 0.1114$ (region 1 is copper and region 2 steel) and $\sigma = 8.9774$ (region 1 is steel and region 2 copper). When the thickness of copper is two times that of steel, the edge of a temperature plateau occurs at the interface, resulting in a little heat flow from copper to steel. On the other hand, when the steel is twice the thickness of copper, heat flows from steel to copper at a significant rate. Consequently, the former gives rise to higher temperature inside the composite and steeper temperature gradients at surfaces $y = -y_1$ and $y = y_2$. For $y_1 = y_2$, i.e., equal thickness of laminates, (6.3) and (6.4) reduce to

$$\frac{T_1}{T_0} = \frac{T_2}{T_0} = 1 - \frac{2}{\pi}\int_0^\infty \frac{\sin\bar{\xi}\bar{x}\cosh\bar{\xi}\bar{y}}{\bar{\xi}\cosh\bar{\xi}}\,d\bar{\xi} \qquad (6.8)$$

It follows that temperature profiles in the composite is symmetrical with respect to the interface and is independent of laminate materials.

Amplitudes and phase lags of temperature waves are shown in Figs. 2(*a*)–4(*b*) for $y_1 = y_2$, $y_2 = 2y_1$, $\sigma = 8.9774$ and various values of $\bar{\omega}_1$ and $\bar{\omega}_2$. For $\bar{\omega}_1 = 1$ and $\bar{\omega}_2 = 0.1043$, amplitude profiles are almost the same as temperature distribution in steady state and phase lags are small, particularly in the laminate of copper, as displayed in Figs. 2(*a*) and 2(*b*). These results can be anticipated in view of (6.5), since the effect of $\bar{\omega}_i$ is small in comparison with that of $\bar{\xi}$ which varies from 0 to ∞. In the case of $\bar{\omega}_1 = 10$ and $\bar{\omega}_2 = 1.043$, the amplitude profiles in region 2 (copper) are similar to temperature profiles in steady state but not those in region 1 (steel), as is clearly seen in Fig. 3(*a*). There is an inflection point of each amplitude curve near the interface in region 1 (steel); i.e., the temperature increases at a fast rate as the interface is approached. Phase lags in Fig. 3(*b*) are much larger than those in Fig. 2(*b*). However, the ratio of phase lags, ϵ_1/ϵ_2, do not differ significantly from that in Figs. 2(*b*) and 3(*b*), because $\bar{\omega}_1/\bar{\omega}_2$ remains unchanged.

In Figs. 4(*a*) and 4(*b*) are illustrated the amplitude profiles and phase lags for $\bar{\omega}_1 = 1000$ and $\bar{\omega}_2 = 104.3$. The striking nature of these curves is that a very steep gradient takes place in both sides of the interface (Fig. 4(*a*)). Both the amplitude and the phase lag for a given value of x are essentially constant in each laminate except near the surfaces of the composite and its interface. The increase of thickness of copper laminate extends the flat part of each curve. The amplitude and phase lag for a given value of x undergo practically no change of magnitude.

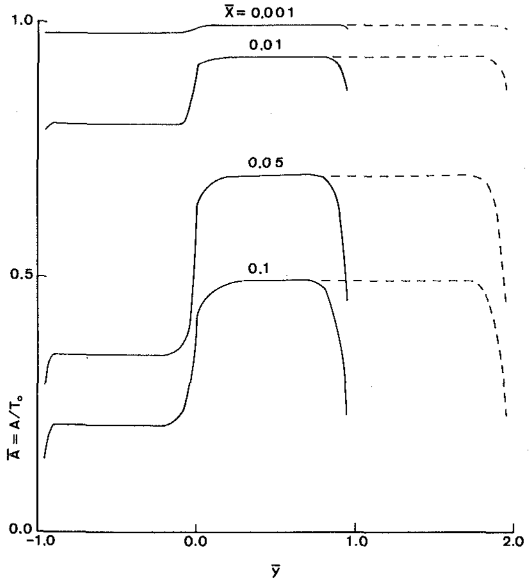

Fig. 4(*a*) **Amplitudes of temperature in periodic state, $\bar{\omega}_1 = 1000.0$, $\bar{\omega}_2 = 104.3$, $\sigma = 8.9774$. Solid lines are for $\bar{y}_2 = 1.0$ and dotted lines are for $\bar{y}_2 = 2.0$, coincided with solid lines for $\bar{y} < 1.0$.**

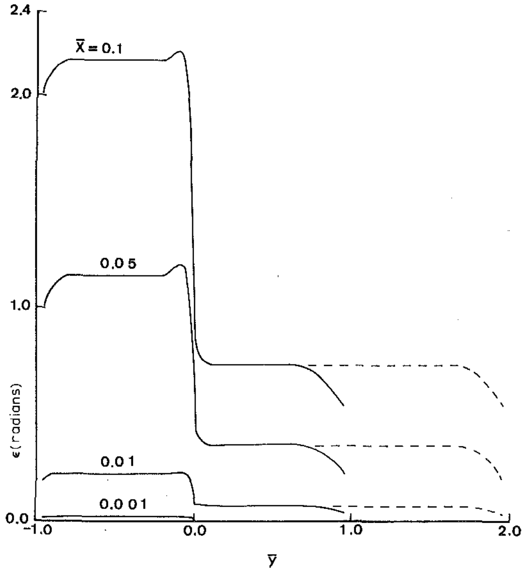

Fig. 4(*b*) **Phase lags of temperature in periodic state, $\bar{\omega}_1 = 1000.0$, $\bar{\omega}_2 = 104.3$, $\sigma = 8.9774$. Solid lines are for $\bar{y}_2 = 1.0$ and dotted lines are for $\bar{y}_2 = 2.0$, coincided with solid lines for $\bar{y} < 1.0$.**

From the calculated results on frequency response of temperature waves, we may divide the harmonic excitation at surface $x = 0$ into three classes: low frequency for $\bar{\omega}_{\max} < 1.0$, moderate frequency for $1 < \bar{\omega}_{\max} < 10$, and high frequency for $\bar{\omega}_{\max} > 10$. In the case of low frequency with $\bar{\omega}_{\max} \leq 1.0$, the temperature distribution in periodic state may be calculated with good approximation by

$$T(\text{periodic}) = T(\text{steady}) \cos \omega t \tag{6.9}$$

which may be called quasi-steady-state solution.

7 Concluding Remarks

As mentioned earlier, the continuum-mixture theory has been widely used in the analysis of multi-dimensional heat conduction in composite regions, because of its simplicity and the possibility of obtaining the *mixture* thermal conductivity and specific heat. It gives good results for $\bar{\omega} < 1$. In this case, the quasi-steady-state solution (6.9) also serves well. For $\bar{\omega} > 1$, the phase lag in the steel laminate is quite significant and therefore in the definition of mixture thermal properties, frequency should be taken into account. The sudden change of temperature gradient at the interface cannot be found by the continuum-mixture theory for $\bar{\omega} > 1$.

An alternative form of (4.14) for $G_{ij,p}$ can be found by using eigenfunctions $Y_i(\xi_{i\lambda p} y)$ which is given in the same form as (3.9) and (3.10), except that ξ_{in} is replaced by $\xi_{i\lambda p}$ defined by

$$\xi_{i\lambda p}{}^2 = \xi_\lambda{}^2 - \mu_i{}^2 - \sqrt{-1}\ \frac{\omega_p}{\alpha_i} \tag{7.1}$$

where we have used subscript λ to emphasize that the eigenvalues are complex. By using eigenfunctions $Y_i(\xi_{i\lambda p} y)$, the periodic Green's function and hence the temperature field will involve complex eigenvalues. That was the approach followed in [6] where, however, the temperature distribution was not reported because of the difficulty in computation.

Exact solutions obtained in this paper can be calculated without difficulty. For infinite and semi-infinite composites, the well known techniques in the numerical calculation of Fourier integral and Fourier transforms are to be employed [11, 12]. Exact solutions for composites of cylindrical layers can be treated by the same way.

References

1 Weng, M. T., and Koh, S. L., "A Continuum Theory of Heat Conduction in Laminates," *Proceedings of the 2nd SMIRT Conference*, Berlin, 1973, L1/5.

2 Ben-Amoz, M., "On Heat Conduction in Laminated Composites", *International Journal of Engineering Science*, Vol. 12, 1974, p. 633.

3 Nayfeh, A. H., "A Continuum Mixture Theory of Heat Conduction in Laminated Composites," *Journal of Applied Mechanics*, Vol. 97, 1975, p. 399.

4 Maewal, A., Bache, T. C., and Hegemier, G. A., "A Continuum Model for Diffusion in Laminated Composite Media," ASME JOURNAL OF HEAT TRANSFER, Vol. 98, 1976, p. 133.

5 Maewal, A., Gurtman, G. A., and Hegemier, G. A., "A Mixture Theory for Quasi-One-Dimensional Diffusion in Fiber-Reinforced Composites," ASME JOURNAL OF HEAT TRANSFER, Vol. 100, 1978, p. 128.

6 Horvay, G., Mani, R., Veluswami, M. A., and Zinsmeister, G. E., "Transient Heat Conduction in Laminated Composites," ASME JOURNAL OF HEAT TRANSFER, Vol. 95, 1973, p. 309.

7 Horvay, G., Gold, B., and Kaczenski, E. S., "Longitudinal Heat Propagation in Three-Phase Laminated Composites at High Exciting Frequencies," ASME JOURNAL OF HEAT TRANSFER, Vol. 100, 1978, p. 281.

8 Chang, Y. P., Kang, C. S., and Chen, D. J., "The Use of Fundamental Green's Function for the Solution of Heat Conduction in Anisotropic Media," *International Journal of Heat Mass Transfer*, Vol. 16, 1973, p. 1905.

9 Kang, C. S., and Chang, Y. P., "Effects of Change of Phase on Temperature Distribution Due to a Moving Heat Source," ASME *Journal of Engineering Materials and Technology*, Vol. 94, 1975, p. 39.

10 Chang, Y. P., "Heat Conduction in Isotropic and Anisotropic Media at Rest and in Motion," Lecture Notes, Dept. Mech. Eng., SUNY at Buffalo, to be published as a text.

11 Tranter, C. J., *Integral Transforms in Mathematical Physics*, John Wiley, New York, 1966.

12 Ditkin, V. A., and Prudnikov, A. P., *Integral Transforms and Operational Calculus*, Pergamon Press, New York, 1965.

Terukazu Ota
Assistant Professor.

Nobuhiko Kon
Technical Assistant.

Department of Mechanical Engineering,
Akita University,
Akita 010, Japan

Turbulent Transfer of Momentum and Heat in a Separated and Reattached Flow over a Blunt Flat Plate

Turbulent shear stress and heat flux were measured with a hot-wire anemometer in the separated, reattached, and redeveloped regions of a two-dimensional incompressible air flow over a flat plate of finite thickness having blunt leading edge. The characteristic features of the turbulent heat flux are found to be nearly equal to those of the turbulent shear stress in the separated and reattached flow regions. However, in the turbulent boundary layer downstream from the reattachment point, the development of turbulent heat flux appears to be much quicker than that of turbulent shear stress. Eddy diffusivities of momentum and heat are evaluated and then the turbulent Prandtl number is estimated in the thermal layer downstream of reattachment. These results are compared with the available previous data.

Introduction

Prediction of heat transfer in the separated, reattached, and redeveloped regions of incompressible or subsonic flow has been recognized to be very important in relation to various engineering aspects, and there have been many papers on a wide variety of flow configurations. Examples include downward or upward surface steps, abrupt circular channel expansions or contractions including an orifice induced separation, and roughness elements attached to a plane wall. They have been cited in a review paper by Fletcher, et al. [1] and also in papers by the present authors [2–4]. Furthermore, some studies were recently published by Sparrow, et al. [5, 6].

In spite of many works conducted for the heat or mass transfer behaviors in the separated, reattached, and redeveloped flow, there has been little information on the characteristics of the turbulent temperature fluctuation or the turbulent heat flux in such complicated flows. Accordingly, the detailed mechanism of heat transfer is considered to be still unclear. Recently Seki, et al. [7] measured the turbulent heat flux distributions in the separated, reattached, and redeveloped flow over a double backward facing step. In addition to the limited data on the turbulent heat flux noted above, there have been few studies of the eddy diffusivities of momentum and heat and the turbulent Prandtl number, which plays an important role in theoretical analyses of the heat transfer in the turbulent thermal layer [8, 9].

The purpose of the present study is to measure the turbulent shear stress and heat flux distributions in the separated, reattached, and redeveloped regions of a two-dimensional incompressible air flow over a blunt flat plate. The differences in their characteristic features and their mutual correlations are discussed. Moreover, in the turbulent thermal boundary layer downstream of reattachment, the eddy diffusivities of momentum and heat are evaluated and the turbulent Prandtl number is estimated with them. The flow configuration investigated is the same as that in previous works [2, 10] and is schematically shown in Fig. 1 along with the coordinate system employed. The flow separates at the leading edge of the plate and then reattaches to the plate surface at about four plate thicknesses downstream from the leading edge in the Reynolds number range studied. Subsequently turbulent flow and thermal boundary layers develop in the streamwise direction. Heat transfer coefficient attains a maximum at the reattachment point and afterward decreases monotonically with the longitudinal distance. Heating of the plate begins at the corner, point 0 in Fig. 1, so that the starting point of heating coincides with the separation point. Kottke, et al. [11, 12] recently measured the mass transfer on a flow configuration similar to the present one. The velocity and mass density fields, however, were not investigated in their studies.

Experimental Apparatus and Technique

The experiments were conducted in a wind tunnel which was the same as that in the earlier heat transfer study [2]. Two test plates were examined. One of them, the same as that used in reference [2] (20 mm thick, 100 mm wide and 400 mm long), with which the greater part of the experimental data were obtained. This plate will hereafter be called Plate I. Some additional measurements were made with another plate (22 mm thick, 100 mm wide and 550 mm long). It was the same as that used in reference [4]; it shows the nose shape effects on heat transfer behavior in the separated, reattached, and redeveloped flow over blunt flat plates, and will be called Plate II. The leading edges of the plates are cut at an angle of 90 deg in order that the flow always separates there. Detailed descriptions of the plates and the wind tunnel are omitted here. Heating of the plate was made by conducting electric current to a stainless steel sheet of 0.05 mm thick stuck to both sides of the plate; and the experiments were conducted under the condition of constant heat flux. Time mean values of temperature and velocity were measured with a temperature probe of 0.07 mm copper-constantan thermocouple and a constant temperature hot-wire anemometer along with a linearizing circuit, respectively. The single wire probe was made of tungsten wire of 0.005 mm dia and 1 mm long. It was calibrated in the upstream uniform flow and was mounted at 90 deg to the flow direction in the plane parallel to the plate surface.

In the measurements of the turbulent shear stress and heat flux, the anemometer was operated without the linearizer and the hot-wire was rotated in the x-y plane. The geometrical arrangement of hot-wire

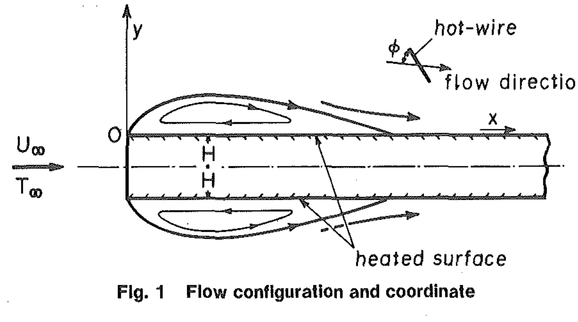

Fig. 1 Flow configuration and coordinate

Contributed by the Heat Transfer Division for publication in the JOURNAL OF HEAT TRANSFER. Manuscript received by the Heat Transfer Division July 27, 1979.

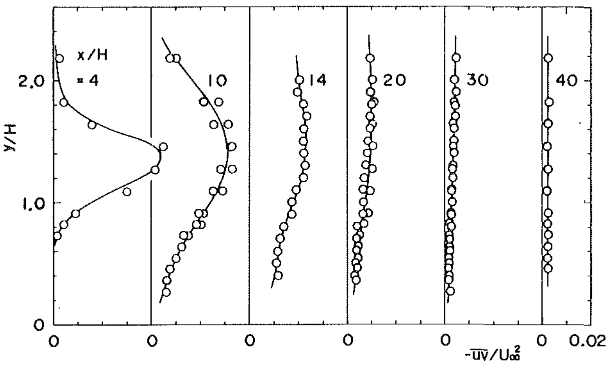

Fig. 2 Turbulent shear stress distribution

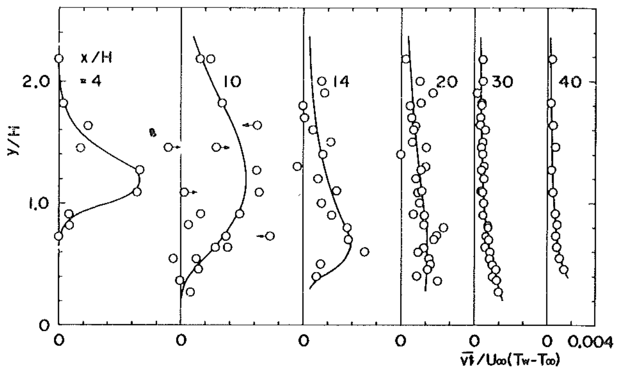

Fig. 3 Turbulent heat flux distribution

is included in Fig. 1. The inclination angles to the mean streamline were selected to be 60 and 120 deg, except in the vicinity of the plate surface where the angles were changed because of obstruction from the supporting system of the hot-wire. The prong and support of the hot-wire were aligned in the x-y plane in order to reduce their disturbance to the flow.

The analysis of the turbulent shear stress and heat flux from mean and rms fluctuating voltage readings of the anemometer was based on Kramers' formula [13] as follows: In a turbulent thermal boundary layer, the temperature fluctuation exists along with the velocity fluctuation. When measurements are conducted at two inclination angles of hot-wire to the flow direction ϕ and π-ϕ, the following equation is easily derived from Kramers' formula.

$$\Delta\overline{e^2} = \frac{1}{4} f^2 \cot\varphi \frac{\overline{uv}}{U^2} - \frac{1}{2} f \cot\varphi \frac{\overline{vt}}{U(T_{hw} - T)} \quad (1)$$

where $f = (1 - E_0^2/E^2)$, $\Delta\overline{e^2} = (\overline{e^2}/E^2)_\phi - (\overline{e^2}/E^2)_{\pi-\phi}$; E and e are mean and fluctuating voltages of the anemometer, respectively; and E_0 denotes the value of E at zero velocity; and T_{hw} is the hot-wire temperature. First, the turbulent shear stress is measured without heating the wall (in such a situation, the second term on the righthand side of equation (1) drops out). Secondly, the measurement is continued under conditions created by heating the wall and keeping the hot-wire temperature equal to that in the first step. Then the turbulent heat flux can be estimated from equation (1) based on the assumption that the turbulent shear stress may not be affected by heating the wall. That is, they are determined from

$$\frac{\overline{uv}}{U^2} = 4 \tan\varphi \frac{(\Delta\overline{e^2})_c}{f_c{}^2} \quad (2)$$

$$\frac{\overline{vt}}{U(T_{hw} - T)} = \frac{2 \tan\varphi}{f_h} \left\{ \frac{f_h{}^2}{f_c{}^2} (\Delta\overline{e^2})_c - (\Delta\overline{e^2})_h \right\} \quad (3)$$

where the subscripts c and h correspond to nonheating and heating conditions, respectively. More descriptions of the present method may be found in another paper by the present authors [14]. In the measurements, two steps mentioned above were reversed, since about 1½ hr were needed to reach a steady state in the second step, and, on the other hand, only about 20 min were required to attain steady state after termination of heating. Several methods can be considered to solve equation (1) for $\overline{uv}$ and $\overline{vt}$. The present method may appear unusual. However, it is simple and requires only one channel of hot-wire anemometer though the time required is relatively long.

In a previous heat transfer study [2], the Reynolds number formed with the upstream uniform flow velocity and half the plate thickness Re = $U_\infty H/\nu$ was varied from about 3000 to 18,000, and the heat transfer characteristics were found to be generally independent of the Reynolds number. Accordingly, the present experiments were conducted at a constant free stream velocity U_∞ = 18.8 m/s and the corresponding Reynolds number, Re = 12000. The heat flux per unit area and unit time q was about 1.7 kW/m^2 which was so low as to make effects of the temperature variation in the thermal layer upon the turbulent shear stress small. The measured range of streamwise distance are from x/H = 12 to 36. Note that these experiments were made with Plate I.

Some additional measurements were conducted with Plate II in order to extend the longitudinal distance so as to include the separated and reattached regions and also to confirm the repeatability and reliability of the data. The experimental conditions were U_∞ = 18.0 m/s, Re= 13600 and q = 2.5 kW/m^2. The cross sections tested are x/H = 4, 10, 20, 30 and 40. The nose shapes of these two plates are, however, not exactly equal to each other and the heat transfer features are a little different in the immediate neighborhood of the leading edge. The reattachment length for Plate II is about 9H [4], which is larger than 8H [2] for Plate I. It results in a difference of the turbulent shear stress and heat flux distributions at the same streamwise location as found in the following results. In spite of such differences, general characteristics of the heat transfer and the turbulent shear stress and heat flux are in good agreement for the two plates.

Experimental Results and Discussion

The present study directed its attention to the turbulent heat flux and shear stress in the turbulent thermal layer, which was found to be much thinner than the flow boundary layer in the reattached and redeveloped flow regions downstream of the reattachment point [2].

Figures 2 and 3 show the distributions of the turbulent shear stress and heat flux at several cross sections including the separated, reattached, and redeveloped flow regions. The results at x/H = 10, which is very close to the reattachment point, include the data obtained by repeating the measurements twice with Plate II. Those at x/H = 20 and 30 are the data measured with both Plates I and II.

The uncertainty of the present data depends, first of all, upon Kramers' formula on which the analysis of data is based. It was found in the preliminary experiments that its accuracy was very satisfactory in the present experimental range of velocity.

Nomenclature

$2H$ = plate thickness
Prt = turbulent Prandtl number
q = heat flux per unit area and unit time
Re = Reynolds number, $U_\infty H/\nu$
t = turbulent temperature fluctuation
T = mean temperature
T_w = wall temperature
T_∞ = temperature at upstream uniform flow
T_* = friction temperature
u, v = turbulent fluctuating velocities along and normal to mean streamline
U = mean velocity
U_m = free stream velocity outside boundary layer
U_∞ = velocity at upstream uniform flow
U_* = friction velocity
x = streamwise distance from leading edge along plate surface
y = distance normal to plate
δ_d = displacement thickness
δ_m = momentum thickness
δ_t = nominal thermal boundary layer thickness
δ_T = thermal boundary layer thickness
ϵ_h, ϵ_m = turbulent diffusivities of heat and momentum
κ = thermal diffusivity of air
ν = kinematic viscosity of air

The accuracy of nondimensional turbulent shear stress $-\overline{uv}/U_\infty{}^2$ determined from equation (2) is affected by the shift of mean voltage readings of the anemometer due to the variation of room temperature and due to the contamination of the hot-wire during the experiments, the precision of the linearizing circuit of the anemometer which was used for the measurements of mean velocity profile, and the exactness of the inclination angle of hot-wire to the mean flow direction. The uncertainty of $-\overline{uv}/U_\infty{}^2$ shown in Fig. 2 by considering these affecting factors is estimated to be about ±11 percent though the accuracy of Kramers' formula is not included.

On the other hand, the uncertainty of the turbulent heat flux $\overline{vt}$ calculated from equation (3) may be affected by the exactness of the hot-wire temperature and also the shift of room temperature, in addition to several factors described above in connection with that of turbulent shear stress. The uncertainty of $\overline{vt}/U_\infty(T_w - T_\infty)$, shown in Fig. 3, is estimated to be nearly ±18 percent by appraising minutely all the factors pointed out. However, as can be seen in equation (3), the turbulent heat flux is obtained by taking the difference between two readings of $\Delta\overline{e^2}$ which are nearly equal. Therefore, small reading errors may produce large errors in the value of $\overline{vt}$. Finally the uncertainty of $\overline{vt}/U_\infty(T_w - T_\infty)$ may become larger than ±20 percent when the reading error is included.

It is to be noticed here that equation (1) is derived from Kramers' formula under the assumption that the turbulent fluctuating velocity and temperature are very small compared with the corresponding mean values; that is, $\sqrt{\overline{u^2}}/U \ll 1$, $\sqrt{\overline{v^2}}/U \ll 1$, and $\sqrt{\overline{t^2}}/(T_{hw} - T) \ll 1$. Only their first order terms are considered in the evolution form of Kramers' formula. Therefore, the effects of the nonlinear terms ignored in the present study become large near the wall where the local turbulence intensities are high and the uncertainties of the present results increase. In the experiments, however, the measurements were not conducted close to the wall because of the obstruction from the supporting system of the hot-wire.

Especially in the neighborhood of the reattachment point, the local mean velocity is very low and the turbulent fluctuating velocity is high. It may result in the large nonlinear effects on the data. In addition to it, the unsteadiness of the flow and temperature fields therein is very severe and the reading error of the output voltage of the anemometer inevitably rises. Considering these factors in the reattached flow region, the uncertainty of $-\overline{uv}/U_\infty{}^2$ may be higher than about ±30 percent, and that of $\overline{vt}/U_\infty(T_w - T_\infty)$ may be of an order of ±50 percent. The large scatter and uncertainty of the data, especially, of $\overline{vt}/U_\infty(T_w - T_\infty)$ are found in Fig. 3, as expected from the discussions noted above. Flow visualization studies conducted with a free surface water channel made clear the flow in the separated and reattached flow regions, though the Reynolds number was of an order of 2000. Several large vortices of complicated form are produced in the separated flow region, their breakdown occurs quite frequently, and the randomly fluctuating fluid violently washes out the wall near the reattachment point.

The present results of the turbulent shear stress are generally in good agreement with the earlier data for the same flow configuration [15]. Nondimensional turbulent shear stress $-\overline{uv}/U_\infty{}^2$ shows a peak value of about 0.04 on the separated shear layer at $x/H = 4$. It is interesting to notice that the positions of peak at $x/H = 10$ and 14, which are close to the reattachment point, are nearly equal to that at $x/H = 4$. It suggests that an inner part of the separated shear layer may approach the reattachment point as the time-averaged separated streamline.

On the other hand, as far as the turbulent heat flux is concerned, its characteristic behavior appears to be similar to that of the turbulent shear stress in the separated and reattached flow regions, though there exists a large scatter therein as described above. Nondimensional turbulent heat flux $\overline{vt}/U_\infty(T_w - T_\infty)$ reaches its maximum value of an order of 0.006 in such flow regions. However in the turbulent boundary layer developing downstream from the reattachment point, its general feature seems to be quite different from that of the turbulent shear stress. The difference is easily understood from the results shown in Figs. 4 and 5, which represent streamwise variations of the turbulent shear stress and heat flux in the boundary layer downstream from the reattachment point. δ_d and δ_T in the figures denote the displacement and thermal boundary layer thicknesses, respectively, defined as

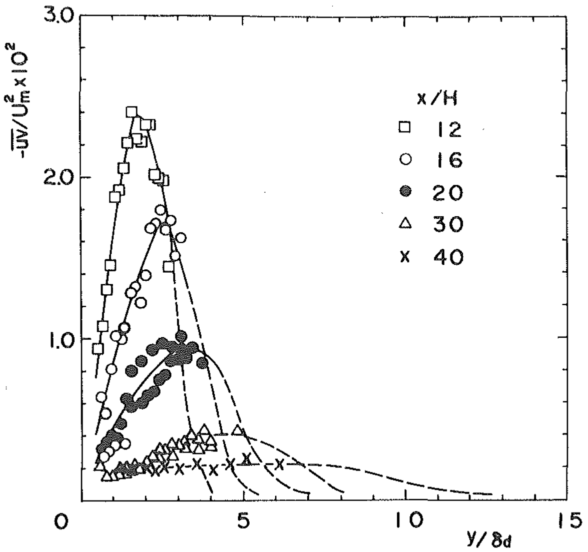

Fig. 4 **Streamwise variation of turbulent shear stress in redeveloped flow region**

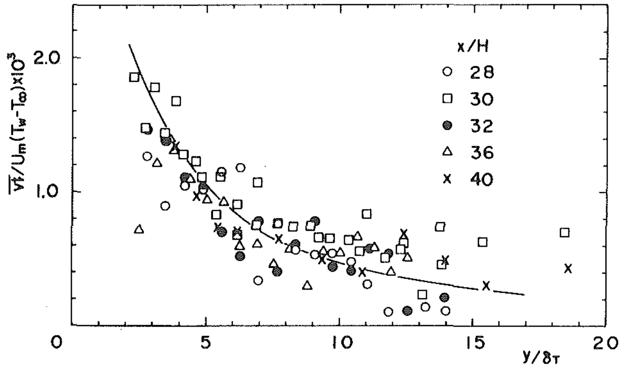

Fig. 5 **Streamwise variation of turbulent heat flux in redeveloped flow region**

$$\delta_d = \int_0^\infty (1 - U/U_m)dy \tag{4}$$

$$\delta_T = \int_0^\infty (T - T_\infty)/(T_w - T_\infty)dy \tag{5}$$

where U_m is the free stream velocity outside the boundary layer. Dotted lines in Fig. 4 exhibit average lines of the previous data of reference [15] for the same flow configuration as in the present study, since the present experiments are limited in the thermal layer. Some scatter found in the data at $x/H = 20$ and 30 in Fig. 4 may be due to the fact that the leading edges of Plates I and II are not exactly equal to each other. The reattachment length for Plate II is a little longer than for Plate I [4]. It causes higher values for the former than the latter as mentioned previously.

To the far downstream cross section, the turbulent shear stress attains its maximum at a point away from the wall and then decreases as getting farther away from the wall. The streamwise distance examined is not enough to reach a state where the turbulent shear stress decreases monotonically with the wall distance as found in the normal boundary layer without separation and reattachment over a plane wall [16]. The data at $x/H = 30$ and 40 are nearly equal to each other in the neighborhood of the wall but are quite different far from there. That is, the viscosity of fluid heavily affects the turbulent shear stress and promotes its diffusion in the vicinity of the wall. However, that effect decreases rapidly with the wall distance and the effects of the separation and reattachment upon the turbulent velocity fluctuation field remain far downstream in the outer layer.

On the other hand, the turbulent heat flux distribution shows no essential variation in shape at cross sections downstream from the reattachment point, as can be seen in Fig. 5, though somewhat large data scatter exists, especially at cross sections relatively close to the reattachment point. The turbulent heat flux decreases monotonically from the immediate neighborhood of the wall to the outer part of the thermal layer. An average line roughly estimated is included in Fig. 5. In the downstream of reattachment, the turbulent velocity fluctuation is still violent and it may promote strongly the diffusion of heat. The result is that the temperature distribution needs only a distance of about six plate thicknesses from the leading edge to reach a similar state and, on the other hand, the velocity profile requires about 15 plate thicknesses to become nearly similar in shape [17]. It may be inferred from these descriptions that the development of the turbulent fluctuating temperature field is much quicker than that of the turbulent fluctuating velocity field.

Described in Fig. 6 is the correlation between the turbulent heat flux and shear stress at several cross sections. Data scatter is not small. However, in general, the large value of $-\overline{uv}/U_\infty{}^2$ accompanies the small value of $\overline{vt}/U_\infty(T_w - T_\infty)$ and it results in negative slope of the correlation, though the outer part of the thermal layer may be excluded where both of them are small. Such a feature of the correlation between $-\overline{uv}$ and $\overline{vt}$ may be peculiar to flows accompanying the separation and reattachment, in which the turbulent shear stress reaches its maximum far away from the wall as previously shown in Fig. 4. The present streamwise distance examined is not enough to attain a state where the turbulent heat flux increases with the turbulent shear stress, as can be detected in the results of Johnson [18] for a turbulent boundary layer without separation and reattachment over a flat plate.

The eddy diffusivities of momentum and heat are very important in estimating degrees of the transfers of momentum and heat by the turbulent fluctuation, respectively. The turbulent Prandtl number is defined as their ratio and it plays an extremely important role in analyzing the turbulent heat transfer, since in many of the proposed turbulence models, its value is assumed to be constant or to be a known function of several factors [8, 9, 19]. They are defined respectively as follows.

$$\epsilon_m = -\overline{uv}/(\partial U/\partial y) \tag{6}$$

$$\epsilon_h = -\overline{vt}/(\partial T/\partial y) \tag{7}$$

$$\mathrm{Pr}t = \epsilon_m/\epsilon_h \tag{8}$$

It may be difficult to estimate them with reasonable reliability under the data scatter of the turbulent heat flux as found in Figs. 3 and 5. However, they are very important in understanding the detailed heat transfer mechanism and also in analyzing theoretically the turbulent heat transfer as noted above. Moreover, there have been few studies of them, especially in complicated flows such as treated in the present study. The authors tried to estimate them in consideration of these situations.

In the turbulent boundary layer developing downstream from the reattachment point, neither the velocity profile nor the temperature profile may be expressed by a simple power law. Therefore the only way to estimate gradients of velocity and temperature in equations (6) and (7) is graphical. It may produce a large uncertainty of velocity and temperature gradients. Furthermore data scatters of the turbulent shear stress and heat flux are not necessarily small as mentioned above. Consequently, relatively large data scatters are produced in ϵ_m, ϵ_h and Prt as found in the following results.

Representative examples of the turbulent diffusivity of heat are shown in Fig. 7 in nondimensional form of ϵ_h/κ where κ is the thermal diffusivity of air. Following statements can be extracted that in the neighborhood of the wall, ϵ_h increases roughly linearly with the wall distance and its gradient decreases to the downstream, and that in the outer part of the thermal layer, ϵ_h may be regarded to be about constant. This characteristic behavior of ϵ_h resembles that of ϵ_m far downstream from the reattachment point, though the outer layer may be excluded where ϵ_m seems to decrease with the wall distance [15].

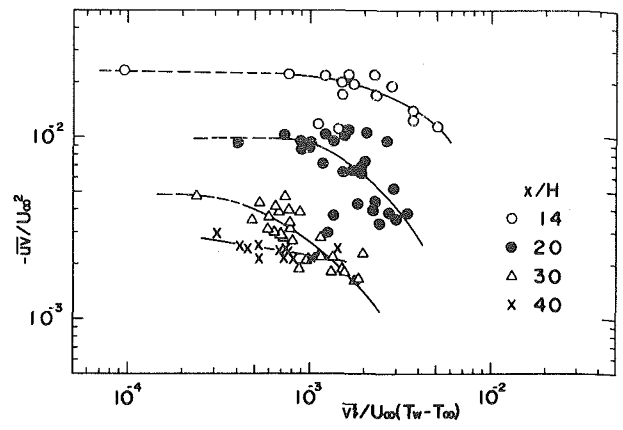

Fig. 6 Correlation of turbulent heat flux and shear stress

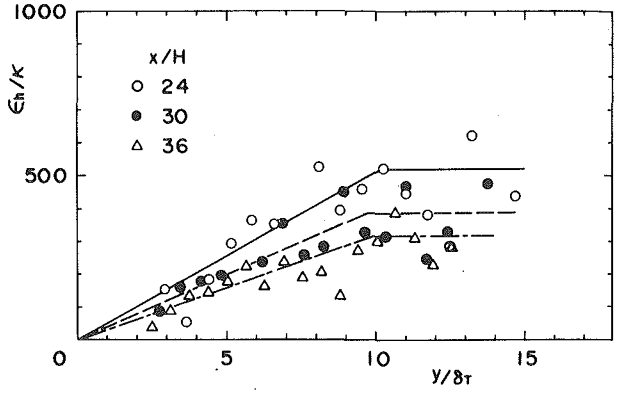

Fig. 7 Distribution of eddy diffusivity of heat

Shown in Fig. 8 is the correlation between ϵ_h and ϵ_m. Included in the figure is a line of $\epsilon_h = \epsilon_m$; that is, Prt = 1. As can be seen, the greater part of the data exists in the region of $\epsilon_m > \epsilon_h$. It suggests that the turbulent Prandtl number may be larger than unity at most of the measured points. Note that some data points showing large divergence from others are excluded from Figs. 7 and 8 for clearness.

There have been many prediction formulae of the turbulent Prandtl number in the turbulent thermal boundary layer. They are referred to in a review paper by Reynolds [19]. On the other hand, as pointed by Blom [20], the previous data of Prt are mostly evaluated by solving the boundary layer momentum and energy equations with the experimental values of the wall shear stress, the wall heat flux, and the velocity and temperature profiles; for example, see a work by Simpson, et al. [21]. There have been few data of Prt determined directly from the measured values of the turbulent shear stress and heat flux in the thermal layer over the plane wall.

Typical examples of the turbulent Prandtl number distribution in the thermal layer are exhibited in Fig. 9 along with previous data for the flow over a flat plate at zero pressure gradient [18, 20, 22, 23]. These data, except Johnson's, were read from a paper by Antonia, et al. [22]. Experimental conditions of Johnson [18], Blom [20] and Antonia are nearly equal to each other; that is, the wall temperature or the wall heat flux are changed discontinuously at a position where the boundary layer is presumed to reach a fully developed state. Fulachier's study appears to be done under a somewhat different situation; that is, the thermal layer also reaches a fully developed state [22]. δ_t in the figure is the nominal thermal boundary layer thickness defined as the distance from the wall to a point of $(T - T_\infty)/(T_w - T_\infty) = 0.01$. Scatter of the present data is not small but its degree is not much different from that of Johnson. Included in the figure is an average line of the present data at two cross sections x/H = 30 and 36 for clearness.

In general, the present value of Prt seems to be nearly equal to unity in the vicinity of the wall and to increase as the wall distance increases. Such behavior can be detected in Antonia's results but is somewhat different from those of Johnson and Blom. Fulachier's data exhibit

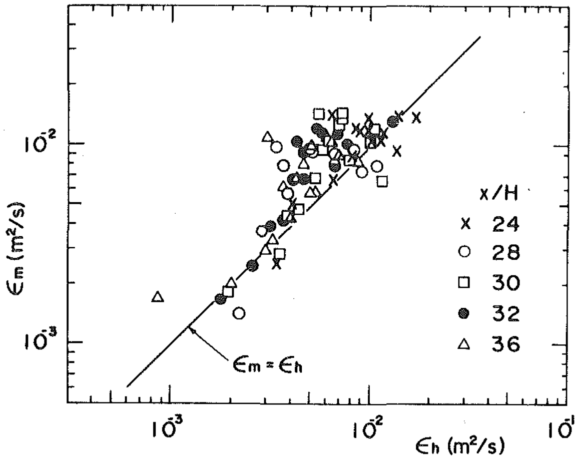

Fig. 8 Correlation of eddy diffusivities of heat and momentum

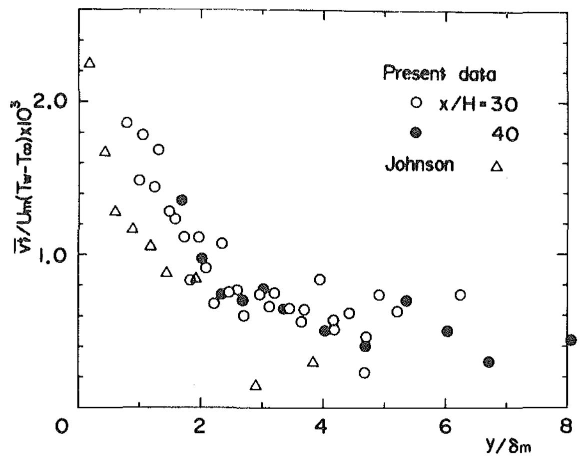

Fig. 10 Comparison of turbulent heat flux distribution

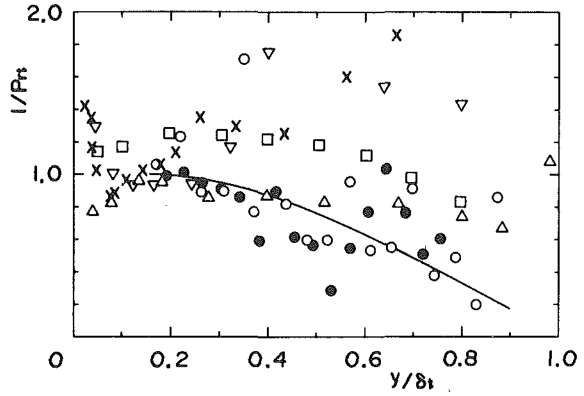

Fig. 9 Comparison of turbulent Prandtl number, present data, *x/H*: ○, 30; ●, 36; ▽, Johnson; ×, Blom; □, Fulachier; △, Antonia, et al.

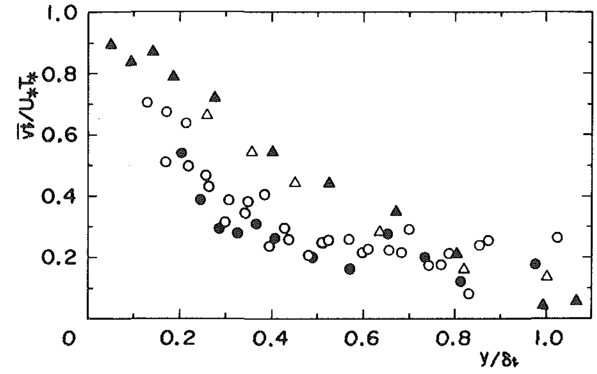

Fig. 11 Comparison of turbulent heat flux distribution, present data, *x/H*: ○, 30; ●, 40; Antonia, et al., x/δ_0: △, 5.7; ▲, 42.9

a trend rather similar to Antonia's. In the present study, the turbulent Prandtl numbers are estimated also at other cross sections. Their characteristic feature appears, in essence, not to be different from the data shown in Fig. 9. Some existing prediction formulae of Prt express it as a function of nondimensional eddy diffusivity of momentum ϵ_m/ν. In the present study, the authors tried to describe Prt as a function of ϵ_m/ν but successful results were not obtained.

The present results of the turbulent heat flux distribution are compared with the data by Johnson [18] and Antonia, et al. [22] in Figs. 10 and 11. In Johnson's study the wall temperature was changed discontinuously, and, on the other hand, the wall heat flux was changed in Antonia's work. All the results including the present ones show qualitatively the same trend; namely, the turbulent heat flux decreases monotonically as the distance from the wall increases. The present data are higher than those of Johnson as shown in Fig. 10 where δ_m is the momentum thickness defined as

$$\delta_m = \int_0^\infty (U/U_m)(1 - U/U_m)dy \tag{9}$$

On the other hand, Antonia's results are higher than the present ones as shown in Fig. 11, in which U_* and T_* denote the friction velocity and temperature defined as,

$$U_* = \sqrt{\tau_w/\rho} \text{ and } T_* = q/\rho C_p U_* \tag{10}$$

In equation (10), τ_w is the skin friction, ρ the density of air and C_p the specific heat at constant pressure. δ_0 in Antonia's data is the nominal boundary layer thickness at the upstream edge of heated section. Figures 10 and 11 show that the present turbulent heat flux at cross sections far downstream from reattachment is nearly equal to that in the turbulent boundary layer without separation and reattachment over the plane wall both in its shape and magnitude. It may be concluded that the violent mixing of the turbulent fluctuation downstream of reattachment produces the rapid diffusion of heat and results in the quick development of the turbulent fluctuating temperature field as compared with the turbulent fluctuating velocity field, as described previously.

Blom made his measurements under conditions similar to Johnson's. However, his data exhibit a peculiarity; that is, in the neighborhood of the wall, there exists a region where the turbulent heat flux varies little with the wall distance and its value is much larger than Johnson's (say about $\overline{vt}/U_\infty(T_w - T_\infty) = 0.0023$). The present results of the turbulent heat flux are also compared with the data by Seki, et al. [7] for a double backward facing step which accompanies the separation and reattachment of flow. However, the former is quite a bit higher than the latter. That is, the present data in the form of $\overline{vt}/U_\infty(T_w - T_\infty)$ are of the order of 0.002 to 0.003 at $x/H = 16$ but those of Seki, et al. are at most 0.0005 at $x/H = 15.3$ where H is the step height. Their flow configuration is different from the present one. The difference of the reattachment lengths may cause such discrepancy but its detail is not clear to the present authors at present.

Concluding Remarks

The turbulent heat flux along with the turbulent shear stress was measured in the separated, reattached, and redeveloped regions of a two-dimensional incompressible air flow over a blunt flat plate. It is found from the results that the characteristic features of the turbulent heat flux are nearly equal to those of the turbulent shear stress in the separated and reattached flow regions but are quite different in the redeveloped flow region. In the turbulent boundary layer developing downstream from the reattachment point, the development of the turbulent heat flux appears to be much quicker than that of the turbulent shear stress. The profile of the former, in essence, becomes nearly similar at about 15 plate thicknesses downstream from the leading edge though the data scatter is not small. On the other hand, the present streamwise distance is not enough to attain a state where the turbulent shear stress profile becomes similar.

Eddy diffusivities of momentum and heat are estimated and then the turbulent Prandtl number is evaluated in the thermal layer downstream of reattachment. Eddy diffusivity of heat appears to increase about linearly with the distance from the plate surface in the neighborhood of the wall and to be regarded as nearly constant in the outer layer. At the greater part of the measured points, the eddy diffusivity of momentum seems to be larger than that of heat. In consequence, the turbulent Prandtl number, in general, is greater than unity. It is nearly equal to unity near the wall and then increases with the wall distance. Thus the behavior of the turbulent Prandtl number is similar to that of Antonia, et al. for the turbulent boundary layer over the flat plate at zero pressure gradient.

The present turbulent heat flux distributions at the downstream cross sections far from the reattachment point are compared with the previous results for the turbulent thermal boundary layer over the flat plate. They show a very similar trend, that the turbulent heat flux decreases monotonically with the wall distance, though a quantitative difference of the data can be detected. It is found that there exists a large scatter of the turbulent heat flux in the reattached flow region. It may not be easy to obtain reliable data in such a complicated and randomly fluctuating flow region but the measuring method should be improved.

Acknowledgments

The authors express their thanks to M. Narita, Y. Matsumoto and C. Nara for their assistance in the experiments. Referees are also acknowledged for their comments which have led to improvement of the paper. The financial support from the Educational Ministry of Japan (Grant No. 375098, 1978) is appreciated.

References

1 Fletcher, L. S., Briggs, D. G., and Page, R. H., "Heat Transfer in Separated and Reattached Flows: an Annotated Review," *Israel Journal of Technology*, Vol. 12, 1974, pp. 236–261.

2 Ota, T., and Kon, N., "Heat Transfer in the Separated and Reattached Flow on a Blunt Flat Plate," ASME JOURNAL OF HEAT TRANSFER, Vol. 96, 1974, pp. 459–462.

3 Ota, T., and Kon, N., "Heat Transfer in an Axisymmetric Separated and Reattached Flow Over a Longitudinal Blunt Circular Cylinder," ASME JOURNAL OF HEAT TRANSFER, Vol. 99, 1977, pp. 155–157.

4 Ota, T., and Kon, N., "Heat Transfer in the Separated and Reattached Flow Over Blunt Flat Plates—Effects of Nose Shape," *International Journal of Heat and Mass Transfer*, Vol. 22, 1979, pp. 197–206.

5 Sparrow, E. M., and Kalejs, J. P., "Local Convective Transfer Coefficients in a Channel Downstream of a Partially Constricted Inlet," *International Journal of Heat and Mass Transfer*, Vol. 20, 1977, pp. 1241–1249.

6 Koram, K. K., and Sparrow, E. M., "Turbulent Heat Transfer Downstream of an Unsymmetric Blockage in a Tube," ASME JOURNAL OF HEAT TRANSFER, Vol. 100, 1978, pp. 588–594.

7 Seki, N., Fukusako, S., and Hirata, T., "Turbulent Fluctuations and Heat Transfer for Separated Flow Associated With a Double Step at Entrance to an Enlarged Flat Duct," ASME JOURNAL OF HEAT TRANSFER, Vol. 98, 1976, pp. 588–593.

8 Gosman, A. D., Pun, W. M., Runchal, A. K., Spalding, D. B., and Wolfshtein, M., *Heat and Mass Transfer in Recirculating Flows*, Academic Press, London, 1969.

9 Launder, B. E., and Spalding, D. B., *Lectures in Mathematical Models of Turbulence*, Academic Press, London, 1972.

10 Ota, T., and Itasaka, M., "A Separated and Reattached Flow on a Blunt Flat Plate," ASME *Journal of Fluids Engineering*, Vol. 98, 1976, pp. 79–86.

11 Kottke, V., Blenke, H., and Schmidt, K. G., "Einfluβ von Anströmprofil und Turbulenzintensität auf die Umströmung Längsangeströmter Platten Endlicher Dicke," *Wärme- und Stoffübertragung*, Vol. 10, 1977, pp. 159–174.

12 Kottke, V., Blenke, H., and Schmidt, K. G., "Bestimmung des Örtlichen und Mittleren Stoffübergangs an Längsangeströmten Platten Endlicher Dicke mit Ablösen und Wideranlegen der Strömung," *Wärme- und Stoffübertragung*, Vol. 10, 1977, pp. 217–232.

13 Hinze, J. O., *Turbulence*, McGraw-Hill, New York, 1975.

14 Ota, T., Kon, N., Hatakeyama, S., and Sato, S., "Measurements of Turbulent Shear Stress and Heat Flux in an Axisymmetric Separated and Reattached Flow over a Longitudinal Blunt Circular Cylinder," *Bulletin of JSME*, Vol. 23, 1980, to be published.

15. Ota, T., and Narita, M., "Turbulence Measurements in a Separated and Reattached Flow Over a Blunt Flat Plate," ASME *Journal of Fluids Engineering*, Vol. 100, 1978, pp. 224–228.

16 Klebanoff, P. S., "Characteristics of Turbulence in a Boundary Layer With Zero Pressure Gradient," NACA Report 1247, 1955.

17 Ota, T., Kon, N., and Kikuchi, S., "Temperature and Velocity Fields in the Separated and Reattached Flow over Blunt Flat Plates," *Bulletin of JSME*, Vol. 23, 1980, pp. 402–408.

18 Johnson, D. S., "Velocity and Temperature Fluctuation Measurements in a Turbulent Boundary Layer Downstream of a Stepwise Discontinuity in Wall Temperature," ASME *Journal of Applied Mechanics*, Vol. 26, 1959, pp. 325–336.

19 Reynolds, A. J., "The Prediction of Turbulent Prandtl and Schmidt Numbers," *International Journal of Heat and Mass Transfer*, Vol. 18, 1975, pp. 1055–1069.

20 Blom, J., "Experimental Determination of the Turbulent Prandtl Number in a Developed Temperature Boundary Layer," *Heat Transfer—1970*, Vol. 2, FC2.2, Elsevier, Amsterdam, 1970.

21 Simpson, R. L., Whitten, D. G., and Moffat, R. J., "An Experimental Study of the Turbulent Prandtl Number of Air With Injection and Suction," *International Journal of Heat and Mass Transfer*, Vol. 13, 1970, pp. 125–143.

22 Antonia, R. A., Danh, H. Q., and Prabhu, A., "Response of a Turbulent Boundary Layer to a Step Change in Surface Heat Flux," *Journal of Fluid Mechanics*, Vol. 80, 1977, pp. 153–177.

23 Fulachier, L., "Contribution à L'étude des Analogies des Champs Dynamique et Thermique dans une Couche Limite Turbulente: Effect de L'aspiration," Thèse Docteur ès Sciences, Université de Provence, 1972.

J. Andreopoulos[1]
P. Bradshaw
Department of Aeronautics
Imperial College, London

The Thermal Boundary Layer Far Downstream of a Spanwise Line Source of Heat

Measurements are presented of velocity and temperature fluctuation statistics in two-dimensional boundary layers over nominally adiabatic, smooth, and rough surfaces far downstream of spanwise line sources of heat. All quantities are found to scale satisfactorily on u_τ, δ and ΔT_{max}. The generation term in the transport equation for the mean-square temperature fluctuation reaches a maximum at a distance of about 0.7δ above the surface and the turbulent Prandtl number is about 1.0 in the outer layer falling to zero near the surface. The outer part of the thermal layer behaves like a uniformly heated wall flow and the results are relevant to the central region of the plume from a point source of heat or pollutants, which will be approximately two-dimensional at large distances from the source.

1 Introduction

The general problem of turbulent transport of scalar quantities like heat or mass is of great importance in engineering or meteorological studies. In particular, studies of atmospheric pollution, where the source of heat or contaminant is inside the atmospheric boundary layer and comparatively close to the surface, require a more detailed description of the turbulent heat or pollutant fluxes. If the Reynolds analogy between heat and momentum was valid for any flow situation, one could expect that the predictions of such flows would be simple. In fact, this analogy is not always valid and the various prediction methods need accurate velocity-temperature (or concentration) correlation measurements. The analogy between heat and pollutant transfer in turbulent flow is virtually exact if density changes can be neglected; in general, it is much easier to measure temperature fluctuations than concentration fluctuations.

The present experiment is an attempt to investigate the thermal boundary layer far downstream of a line source of heat over rough and smooth surfaces. A previous experiment similar to the present work is that of Poreh and Cermak [1]. They measured mean concentration of ammonia emitted from a surface line source in air in a nonself-preserving velocity boundary layer; measurements of fluctuating concentrations are not reported. They divided the flow field into four zones with different features according to the ratio of plume thickness to boundary layer thickness. Their measurements were carefully reviewed by Morkovin [2], who concluded that the eddy diffusivities when viewed as properties of quasi-similar fields can account for the characteristics of layer developing inside another layer. Some of the present results are comparable to those of Poreh and Cermak for their "final zone", where the edge of the plume has reached that of the boundary layer. Wieghardt [3] measured mean temperature distribution behind point and line sources of the surface, but only for the zones where the plume thickness is less than the boundary layer thickness.

The roughness effects on the hydrodynamic flow field are restricted within ten roughness heights from the wall surface and are discussed in detail by Andreopoulos and Bradshaw [4]. So the main effect of roughness on plume spread is to increase u_τ and, therefore, the mixing rate throughout the boundary layer.

The effect of surface roughness on the transport of heat in a heated boundary layer has been investigated by Pimenta, et al. [5] while an experiment with an elevated point source of heat above a rough wall made by Nakayama and Bradshaw [6] showed some similarities with the present work.

2 Experimental Arrangements and Techniques

The experimental program was carried out in the 91 × 91 cm closed circuit low speed wind tunnel of the Department of Aeronautics at a free stream velocity of 33.5 m/s. The free stream turbulence level in the tunnel was less than 0.05 percent at this speed. A flat plate was installed in the wind tunnel at mid height. All the measurements were made at the end of the plate which has a length of 3.08 m and thickness 28 mm and is made from plywood. The plate thickness and construction were chosen to minimize heat transfer from one side to the other. The heat was introduced by three nichrome wires a few millimeters from the surface near the streamlined leading edge of the plate. The boundary layer thickness at the trailing edge of the plate was at least 51 mm so that the heated wakes of the wires were fully mixed into the turbulent flow; if the plume is fully mixed, the height of the source is, of course, immaterial. Two sets of experiments were carried out: one with a smooth surface and a second with a rough surface. For the latter, the surface of the plate was covered with sand paper which has a maximum grain size of about 1.4 mm and a backing thickness of about 0.25 mm. The corresponding shift of logarithmic velocity profile is $\Delta U/u_\tau = 11.5$. For both experiments heat input was the same, ~2 kW; the heating wires were supplied from two autotransformers, the current and voltage being measured by AVO Model 8 Avometers.

Mean temperature profiles were measured with Chromel-Alumel thermocouples connected to a COMARK differential thermometer. One thermocouple was used by monitoring the free stream temperature continuously. Turbulence measurements were made with DISA 55D01 constant temperature anemometers and DISA miniature-cross-wire probes type 55A38 with 5 μm platinum wires. Temperature fluctuations were measured by a 1 μm "cold" wire (resistance thermometers) mounted on a probe clamped to the side of the cross-wire-probe. The cold wire was operated with heating currents of 1.6 and 1 mA for the smooth and rough wall flow, respectively. Its output voltage was compensated for thermal inertia by a conventional operational amplifier network. The time constant is a function of the instantaneous velocity normal to the temperature wire. The compensator must be set at each operating point because of the velocity variation across the layer. However, Smits [14] estimated that an error of 10 percent in the mean velocity will cause an error of only 3 percent in the sensitivity at high frequencies and the error in broad band temperature fluctuation measurements will be much less than this.

The heating current for the rough wall case was reduced to avoid undesirable velocity fluctuations on the temperature wire. The ratio of the temperature sensitivity to velocity was found experimentally to be of the order of 2.13×10^{-3} C°/m/s. Another estimate of the relative sensitivity dT/dU obtained by using Wyngaard's [12] formula was twice the previously measured value. The same order of difference

---

[1] Present address: SFB 80, Universität Karlsruhe, W. Germany.

Contributed by the Heat Transfer Division for publication in the JOURNAL OF HEAT TRANSFER. Manuscript received by The Heat Transfer Division February 11, 1980.

is found in Wyngaard's comparisons between the measured and the estimated values and is considered to cause negligible velocity effects on the temperature wire.

A "temperature correction" on the x-wire instantaneous signals has been applied. It is based on the value of the instantaneous temperature and is described by Dean and Bradshaw [13]. The hot-wire signals together with those from the cold wire were recorded on an analogue tape recorder and digitized later using the departmental facilities (for details see Andreopoulos [7]). A roughly steady state of the thermal field was reached only after two hr running, since the thermal capacity of the plate, the wind tunnel, and its surroundings was high.

The temperature and the velocity fields were found to be uniform in the spanwise direction and the flux Richardson number, which characterizes the ratio of the buoyant production to the shear production of turbulent kinetic energy, was found to be very small—on the order of 0.0013, for both smooth and rough wall flows.

3 Results and Discussion

The results are presented in Figs. 1–16 and normalized by the maximum temperature difference $\Delta T_{\max} = T_{\max} - T_e$, the friction velocity u_τ, and the boundary layer thickness, δ. Since the turbulent Prandtl number is expected to be of the order of unity, the instantaneous edge of the thermal boundary layer coincides almost exactly with the instantaneous edge of the velocity boundary layer; any difference can be ascribed to the differences between molecular diffusion of momentum and heat in the viscous superlayer and, in a fluid with a molecular Prandtl number near unity, is likely to be very small. Therefore, the mean thicknesses are related so that δ can be used for both. The skin friction coefficients were 0.0024 and 0.0052 for the smooth and rough surface respectively while the boundary layer thicknesses δ_{995} were 51.5 and 73.94 mm, respectively. The enthalpy thicknesses evaluated from the relation

$$\delta_H = \int_0^\infty \frac{U}{U_e}\,\frac{T-Te}{\Delta T_{\max}}\,dy \qquad (1)$$

were found to be 0.50δ and 0.529δ for the smooth and rough case, respectively.

The wall temperatures T_w were evaluated from

$$\frac{T_w - T_e}{\Delta T_{\max}} = \frac{U_e}{u_\tau}\,\mathrm{St}\int_0^\infty \frac{U}{U_e}\,\frac{T-T_e}{\Delta T_{\max}}\,d\left(\frac{y}{\delta}\right) \qquad (2)$$

where the Stanton numbers are (0.00142 and 0.00308, respectively and found to be $T_w - T_e = 0.02\ \Delta T_{\max}$ for the smooth surface and $T_w - T_e = 0.03196\ \Delta T_{\max}$ for the rough surface. The mean temperature profiles on the two surfaces are shown in Fig. 1. In the region outside the inner layer ($y > 0.2\ \delta$) and up to $0.9\ \delta$, there is a difference between the rough and smooth wall cases which is present in some other quantities, such as $\overline{v\vartheta}$. This can be attributed to the different rate of heat losses through the wall, although in both cases $d\ T/dy$ very close to the wall is very high, indicating that the plate is a good insulator. In fact, a rough check on the rate of heat losses evaluated as the difference

$$\text{input heat power} - \int_0^\infty c_p \rho T U dy$$

shows that, for the smooth wall case, the losses are 0.4 kW and for the rough, only 0.020 kW. The ratio of the two heat fluxes is like the ratio of $\delta_H \Delta T_{\max}$, and is about 1.19. Because of the higher heat flux, the rough case is bound to have higher $\Delta T/\Delta T_{\max}$ than the smooth case. Apart from that, it has to compensate for the lower U/U_e as well. In Fig. 1 Poreh and Cermak's results are presented for comparison. Since the scatter is significant, only points from a mean line through their data are plotted. The agreement with the present smooth case results is quite good, and indicates, as was expected, that the height of the heat sources from the wall has already been "forgotten" by the flow.

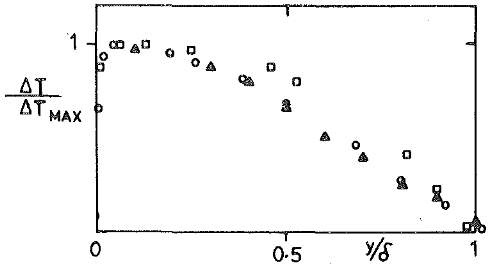

Fig. 1 Mean temperature profiles: ○ smooth wall, □ rough wall, ▲ Poreh and Cermak

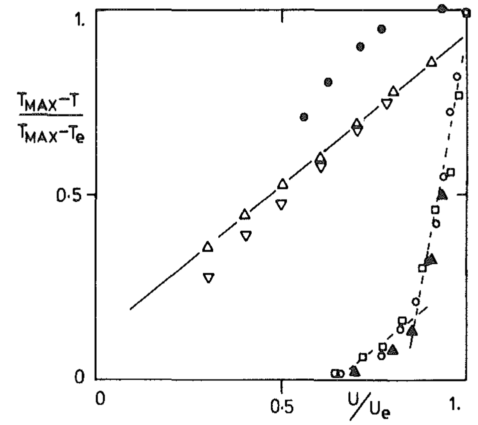

Fig. 2 Mean temperature versus mean velocity: △ Pimenta, et al., ▽ Johnson, ● Blackwell. Other symbols as in Fig. 1

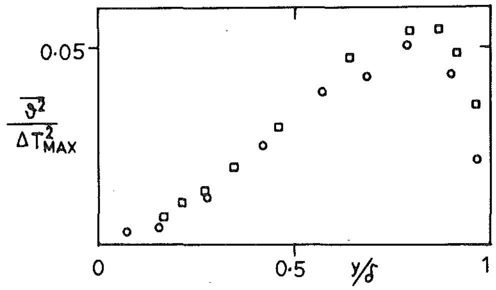

Fig. 3 Mean square temperature fluctuation. Symbols as in Fig. 1

Nomenclature

c_f = skin-friction coefficient, $\tau_w/(0.5\ U_e{}^2\rho)$
c_p = specific heat at constant pressure
Q = heat transfer per unit area per unit time
$\mathrm{Pr}_t = (-\overline{uv}/dU/dy)/(-\overline{v\vartheta}/dT/dy)$ turbulent Prandtl number
$\mathrm{St} = (Q_w/\Theta_\tau)/(Q/T_w - T_e) = (T_w - \tau_e)u_\tau/\int_0^\infty U(T - T_e)dy$, Stanton number
T = temperature (mean)
Θ_τ = friction temperature, $Q_w/c_p u_{\tau\rho}$
u,v,w = fluctuating velocity components in x,y,z directions
U,V,W = mean velocity components in x,y,z directions
u_τ = friction velocity
x,y,z = coordinates: x streamwise, y normal to surface
$\Delta T = T - T_e$
δ = boundary layer thickness
ϑ = fluctuating temperature
ν = kinematic viscosity
ρ = density
τ = shear stress

Subscripts

e = value at boundary layer edge
w = value at surface
max = maximum value

The same mean temperature results are plotted against mean velocity in Fig. 2. Usually these plots are a straight line meaning that the turbulent Prandtl number is 1 as in the results of Pimenta, et al. [5] for a heated rough wall case. The present results do not show exactly this feature. In fact, they exhibit two distinct regions with almost constant dT/dU each. The first region has the same dT/dU as Pimenta, et al. and is extended up to 0.85 δ, a point where the intermittency is 0.5. The second region is probably affected by the highly intermittent character of the flow and has three times greater dT/dU than the first region; in order to maintain Prandtl number equal to 1, $\overline{uv}/\overline{v\vartheta}$ has to vary inversely, and in proportion, to dT/dU between the two regions. Exactly similar behavior characterizes Poreh and Cermak's results, while the results of Blackwell [8] for a smooth heated wall show some similarities to the dual behavior of dT/dU in the present results. In Fig. 2, the results of Johnson [9] are also plotted to indicate the behavior of a thermal layer when only partially mixed inside a boundary layer. Plots in these coordinates are useful in giving an estimate of dT/dU. So any differences in level among the results in Fig. 2 may not be important although they can be attributed to the quite different boundary conditions. But T/U is strictly a function of u_τ/Θ_τ and any comparison should take that into account.

Figure 3 shows the $\overline{\vartheta^2}$ distribution. The inner layer fluid is well mixed so that $\overline{\vartheta^2}$ is small; in the outer intermittent region, however, partly mixed fluid alternates with cold free-stream fluid and $\overline{\vartheta^2}$ reaches a maximum at $y = 0.85\ \delta$, almost the point with intermittency of 0.5 or maximum crossing frequency and also very close to the point of maximum dT/dU.

In Figs. 4–7, the second order velocity-correlation or correlation coefficients are shown. There are some differences between rough and smooth wall cases in $\overline{u\vartheta}$ and $\overline{v\vartheta}$ plots, similar to those that appeared in the mean temperature profiles. These differences are expected as a higher heat flux is required in the rough wall case, because the boundary layer grows faster and a greater rate of heat transfer in the outer layer is needed to maintain self-preservation. Very close to the wall, $\overline{u\vartheta}$ falls to smaller values on the rough wall than on the smooth wall. (The $\overline{u\vartheta}$ correlation coefficient does not indicate any difference between the two cases.) It is worth noting that $\overline{u\vartheta}$ remains negative throughout the boundary layer while $\overline{v\vartheta}$ changes sign very close to the wall (indicating heat losses to the wall) but not exactly at the point where dT/dy changes. Turning to the dimensionless parameters, the ratio $\overline{u\vartheta}/\overline{v\vartheta}$ in the region above $y = 0.5\ \delta$ has a value of -2.0 for both cases, which is in agreement with that found by Pimenta, et al. close to a uniformly heated surface. In this sense, the present "plume" flow field indicates similar behavior to a heated wall flow. For comparison, the results of Pimenta, et al. and Antonia, et al. [15] for half heated wall have been plotted in Figs. 4 and 6. There are some differences between the present results and the heated wall cases especially in $\overline{v\vartheta}$ for $y \angle 0.5\ \delta$. In this region, $\overline{v\vartheta}$ drops quicker than $\overline{u\vartheta}$ and it behaves like the viscous sublayer region of the heated wall case, resulting in a rise in the $\overline{u\vartheta}/\overline{v\vartheta}$. Even in the outer layer there are some differences in $R_{u\vartheta}$ and $R_{v\vartheta}$ between the present flow and that of Pimenta, et al. $R_{v\vartheta}$ in the present flow reaches a maximum value of $+0.38$ while the heated wall flow has a maximum value of $+0.62$ which seems to be very large since R_{uv} is only -0.5 at most. In the outer layer, $R_{u\vartheta}$ in the present case reaches values of -0.62 while Pimenta's value is consistently -0.75 throughout the boundary layer even close to the wall where, according to Launder [10], a high value of $R_{u\vartheta}$ is due to the diminishing effectiveness of the mean strain distruction of $\overline{u\vartheta}$ as the wall is approached. Close to the wall in the present case $R_{u\vartheta}$ drops, basically because $\overline{u^2}$ and $\overline{\vartheta^2}$ drop while $\overline{u\vartheta}$ is roughly constant. For comparison, the results of Fabris [11], in the wake of a heated cylinder, are plotted in Figs. 5 and 7. His $R_{u\vartheta}$ agrees with the present results (both have a maximum value of -0.62) and his $R_{v\vartheta}$ is appreciably higher but his R_{uv} is rather high (maximum value of 0.54). Kovasznay and Ali [16] obtained correlation coefficients in a heated self-preserving two-dimensional symmetrical turbulent wake of a flat plate. The scatter in their results is significant and the lack of symmetry (stickly antisymmetry) between the lower and the upper half of the symmetrical wake in $R_{v\Theta}$ and R_{uv} make a direct comparison rather difficult. Their $R_{v\vartheta}$ for the lower side of the wake is something be-

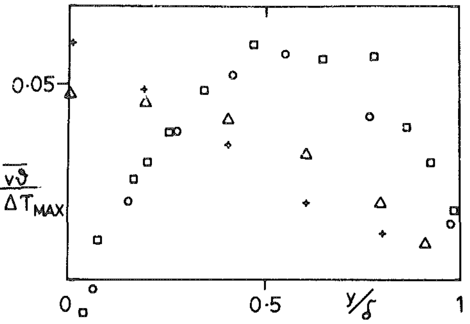

Fig. 4 $\overline{v\vartheta}$ profile. Symbols as in Fig. 1, + Antonia, et al.

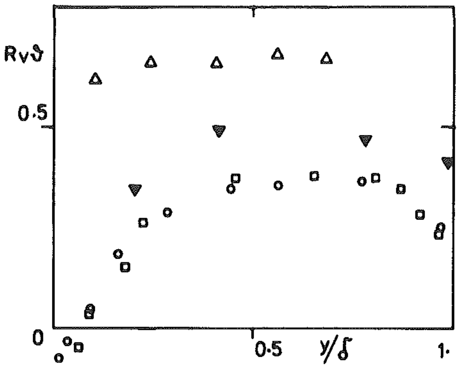

Fig. 5 $R_{v\vartheta}$ profile, ▼ Fabris. Other symbols as in Fig. 2

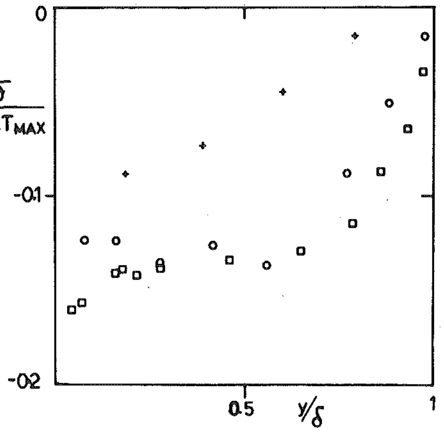

Fig. 6 $\overline{u\vartheta}$ profile, symbols as in Fig. 4

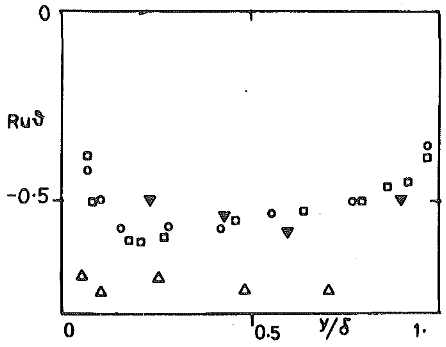

Fig. 7 $R_{u\vartheta}$ profile, symbols as in Fig. 5

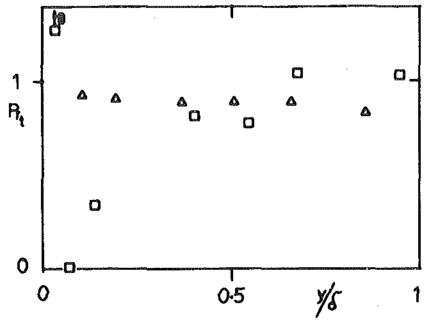

Fig. 8 Prandtl number profile: □ rough wall, △ Pimenta, et al.

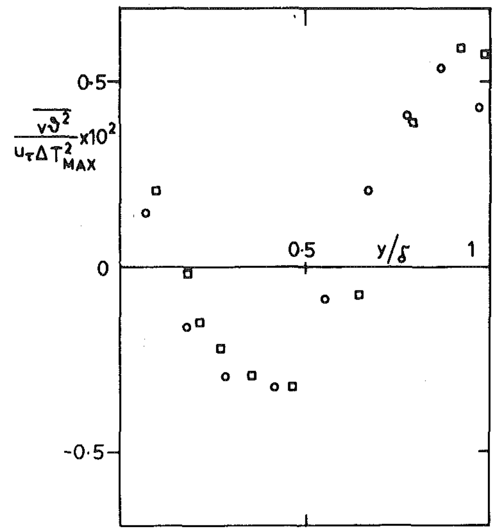

Fig. 9 Triple product $\overline{v\vartheta^2}$, symbols as in Fig. 1

tween 0.36 and 0.5 and for the upper side is 0.83. Apart from that their R_{uv} increases from 0.4 in the boundary layer at the trailing edge to 0.6 in the wake which is considered to be rather high in the light of α new concept of the turbulent near wake that the outer parts of the wake do not change in their turbulent structure significantly with x as it has been proposed by Andreopoulos and Bradshaw [17]. The turbulent Prandtl number is plotted in Fig. 8 together with that of Pimenta's, et al. experiment. In the outer part of the boundary layer Pr_t reaches a value of 1 (while the most popular value was found to be around 0.9) and is continually decreasing towards the wall. Very close to the wall the values of Pr_t are suspicious since they jump from 0 to infinity, because of the change in sign of $\overline{v\vartheta}$.

In Figs. 9–16 some of the third order velocity temperature correlations are presented. The $\overline{v\vartheta^2}$ correlation represents the normal transport of ϑ^2 by v-fluctuations in the turbulent transport term $d\overline{v\vartheta^2}/dy$ in the transport equation. The $\overline{u\vartheta^2}$ is the streamwise transport by u of ϑ^2 and appears in the longitudinal diffusion term $d\overline{u\vartheta^2}/dx$. In the present case, or anywhere where the thin shear layer approximation is valid we expect $d\overline{u\vartheta^2}/dx \ll d\overline{v\vartheta^2}/dy$. If we define a lateral convection velocity of $\overline{\vartheta^2}$ like $v_\theta = \overline{v\vartheta^2}/\overline{\vartheta^2}$ we obtain a better picture of the turbulent transport of $\overline{\vartheta^2}$. This structural parameter is plotted in Fig. 10. For $y > 0.6\ \delta$, $\overline{\vartheta^2}$ is transported outwards, towards the free stream, as in the case for all transported quantities in the outer part of a growing boundary layer. Nearer the surface, where the fluid is well mixed and $\overline{\vartheta^2}$ is smaller, $\overline{\vartheta^2}$ is transported (again down its gradient) towards the surface. For $y < 0.15\ \delta$ approximately, transport is again outwards; this is probably the result of slight heat transfer to the wall, leading to significant dT/dy and $\overline{\vartheta^2}$ generation very close to the surface.

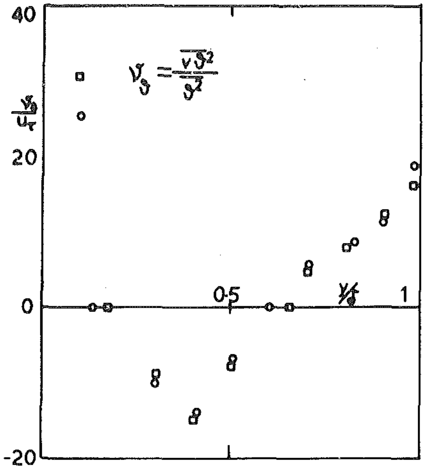

Fig. 10 Bulk transport velocity $v_{\vartheta^2} = \overline{v\vartheta^2}/\overline{\vartheta^2}$, symbols as in Fig. 1

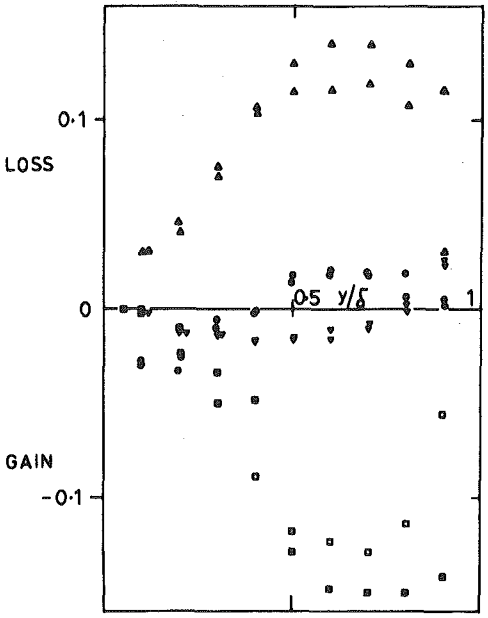

Fig. 11 d balance, □ generation $2_{v\vartheta}\ T/dy\ \delta/u_\tau\ \Delta T_{max}$; ▽ mean transport $2v\vartheta dT/D\overline{\vartheta^2}/Dt\ \delta/u_\tau \Delta T_{max}$; ○ turbulent transport $d\overline{v\vartheta^2}/dy\ \delta/u_\tau/\Delta T_{max}$; △ conductive destruction $2\epsilon_\vartheta \delta/u_\tau \Delta T_{max}$. Plain symbols-smooth case, filled symbols-rough case

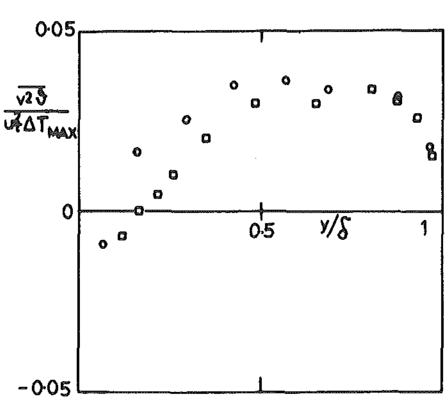

Fig. 12 Triple product $\overline{v^2\vartheta}$, symbols as in Fig. 1

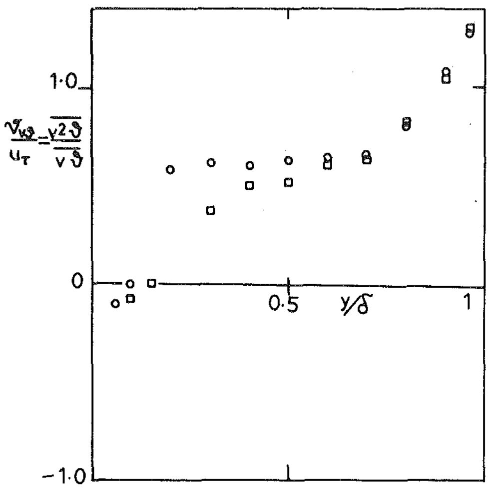

Fig. 13. Bulk transport velocity $\nu_{v\vartheta}$, symbols as in Fig. 1

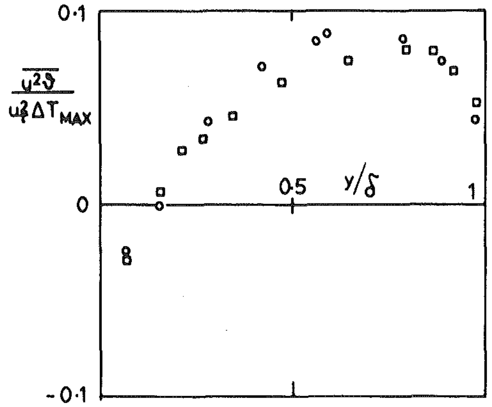

Fig. 14 Triple product $\overline{u\vartheta^2}$, symbols as in Fig. 1

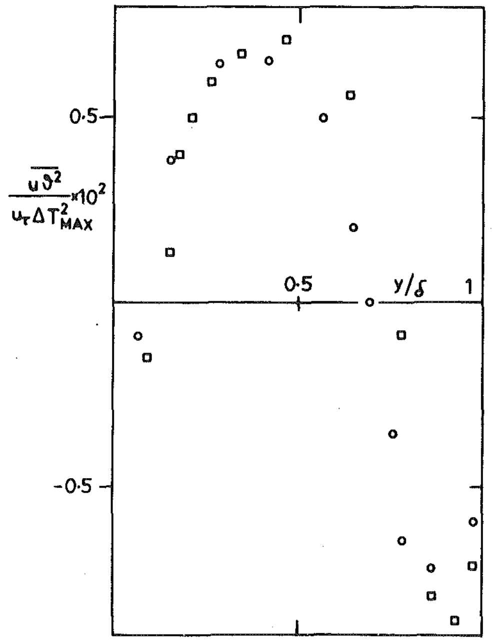

Fig. 15 Triple product $\overline{u^2\vartheta}$, symbols as in Fig. 1

The balance of the various terms involved in the $\overline{\vartheta^2}$ transport equation is shown in Fig. 11. Since $dT/dy \gg dT/dx$, the generation is approximated by $\overline{v\vartheta}dT/dy$ only. The molecular diffusion is also completely neglected since it is two orders of magnitude less than the other terms. The thermal dissipation or distruction $2\epsilon_\vartheta$ is obtained by difference and all terms are nondimensionalized by $\delta/u_\tau\Delta T_{\max}$. The maximum of the generation term occurs at $y = 0.7\ \delta$; recall that in the case of a heated wall flow the generation of $\overline{\vartheta^2}$ reaches a maximum very close to the wall. Here the $\overline{\vartheta^2}$ generation is drastically reduced for $y < 0.7\ \delta$, because both $\overline{v\vartheta}$ and dT/dy are small nearer the surface. For y less than $0.8\ \delta$ the mean flow transport term is a gain in the control volume sense ($D\overline{\vartheta^2}/Dt < 0$); it reaches a maximum at about $0.4\ \delta$ and then dies out close to the wall. Near to the wall there is a gain by turbulent transport which supplies the destruction (thermal conductivity) term since generation is negligible. At the outer edge, i.e., for $y > 0.75\ \delta$, turbulent transport is small, while mean transport has a significant loss ($D\overline{\vartheta^2}/Dt > 0$) almost equal to the dissipation in the smooth case. This is in contrast to the turbulent energy balance in which mean and turbulent transport are roughly equal and opposite, and larger than the other terms. As would be expected, the $\overline{\vartheta^2}$ balance is almost the same for both smooth and rough cases when normalized on u_τ.

The plot of the bulk convection velocity of $\overline{v\vartheta}$ (Fig. 13) illustrates the transport of $\overline{v\vartheta}$ by v. It reaches a positive maximum at the outer edge—considerably larger than the entrainment velocity which is about $8u_\tau$—while near the wall $\overline{v\vartheta}$ is transported towards the wall, as in the case of $\overline{\vartheta^2}$. Figures 14–16 show the streamwise transport velocities of $\overline{\vartheta^2}$, $\overline{u\vartheta}$, $\overline{v\vartheta}$; the sum of the transport velocity and the mean velocity of the fluid is an acceptable, though not unique, definition of the convection velocity of the temperature fluctuation pattern. The convection velocities of the three quantities behave in qualitatively the same way as each other, the convection velocity of the turbulent energy, $\overline{q^2u}/\overline{q^2} + U$ being more than the mean velocity in the inner layer but less in the outer layer. However, there are detailed differences and, in view of the odd behavior of $\overline{v\vartheta}$ in the adiabatic wall flow, the convection velocity of $\overline{\vartheta^2}$ is probably the most representative. Note that the difference between the mean velocity and the convection velocity is not attributable to molecular convection; although heat is almost a permanent contaminant moving with the fluid, high temperature regions may be preferentially correlated with, say, low u—component velocity leading to negative $\overline{u\vartheta}$, and similarly regions of large ϑ^2 correlated with regions, of say, low u lead to negative $\overline{u\vartheta^2}$.

4 Conclusions

The above measurements are believed to give a good picture of the second and third order temperature-velocity correlations and corresponding structural parameters, in smooth and rough wall boundary layers far downstream of a line source of heat. Previous measurements, such as those of Wieghardt [3] and Poreh and Cermak [1], include only mean concentration results. The outmost part of the thermal layer

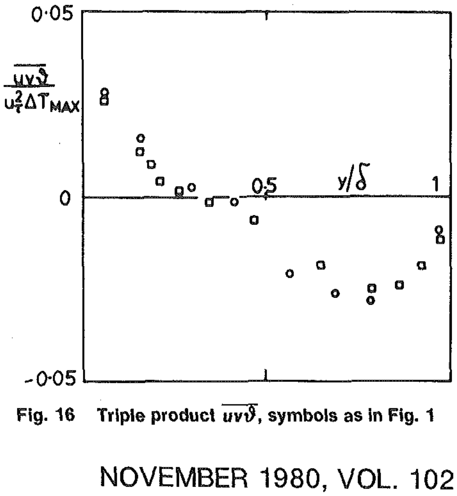

Fig. 16 Triple product $\overline{uv\vartheta}$, symbols as in Fig. 1

behaves like a heated-wall layer (the exact source of the heat transported into the outer layer by the large eddies being nearly immaterial) and the heat transfer exhibits similarities with momentum transfer. The temperature-velocity correlation coefficients $R_{u\vartheta}$ and $R_{v\vartheta}$ are a bit less than those of a uniformly heated wall experiment of Pimenta, et al. [5] (which may be rather high).

The maximum rate of generation of temperature fluctuations occurs at about 0.7 δ while the mean square temperature fluctuation itself peaks at roughly 0.9 δ. The turbulent Prandtl/Schmidt number Pr_t reaches a value close to unity in the outer half of the layer, and is in agreement with previous results for heated walls. Nearer the wall the characteristics are very different from those of a heated-wall layer since the fluid is well mixed and temperature fluctuations are comparatively small. The wall in the present experiment was not perfectly adiabatic and results for $y < 0.1\ \delta$ approximately are not trustworthy; in any case, attempts to evaluate Pr_t in the region close to the wall are fruitless since the heat flux rate and temperature gradient both tend to zero, but the trend Pr_t is towards a value of zero near the nominally adiabatic wall.

Acknowledgments

We wish to express our gratitude for the financial support of the Science Research Council and the Greek State Scholarship Establishments (IKY).

References

1 Poreh, M., and Cermak, J. E., "Study of Diffusion from a Line Source in a Turbulent Boundary Layer," *International Journal of Heat and Mass Transfer,* Vol. 7, 1964, pp. 1083–1095.

2 Morkovin, M. V., "On Eddy Diffusivity, Quasi Similarity and Diffusion Experiments in Turbulent Boundary Layers," *International Journal of Heat Mass Transfer,* Vol. 8, 1965, pp. 129–145.

3 Wieghardt, K., "Über Ausbreitungsvorgänge in Turbulenten Reibungsschienen," *Zeitschrift fuer Angewandte Mathematik und Mechanik,* Vol. 27, 1948, pp. 346–355.

4 Andreopoulos, J., and Bradshaw, P., "Measurements of Turbulence Structure in the Boundary Layer on a Rough Surface," *Boundary Layer Methodology* (in press), 1980.

5 Pimenta, M. M., Moffat, R. J., and Kays, W. M., "The Turbulent Boundary Layer: an Experimental Study of the Transport of Momentum and Heat with the Effect of Roughness, "Report No HMT-21, Thermosciences Division, Stanford University, 1975.

6 Nakayama, A., and Bradshaw, P., Contract Report (CGEB), 1979.

7 Andreopoulos, J., "Symmetric and Asymmetric Near Wake of a Flat Plate," Ph.D. Thesis, London University, 1978.

8 Blackwell, B. F., Kays, W. M., and Moffat, R. J., "The Turbulent Boundary Layer on a Porous Plate: an Experimental Study of the Heat Transfer Behaviour with Adverse Pressure Gradients," Report No HMT-16, Thermosciences Division, Stanford University, 1972.

9 Johnson, D. S., "Velocity and Temperature Fluctuation Measurements in a Turbulent Boundary Layer Downstream of a Stepwise Discontinuity in Wall Temperature," *ASME Journal of Applied Mechanics,* Vol. 26, 1959, pp. 325–336.

10 Launder, B. E., *Topics in Applied Physics,* Vol. 12, Editor P. Bradshaw, Springer Verlag, Berlin, 1976.

11 Fabris, G., "Conditional Sampling Study of the Turbulent Wake of Cylinder: Part 1," *Journal of Fluid Mechanics,* Vol 94, No. 4, 1979, pp. 673–709.

12 Wyngaard, J. C., "The Effect of Velocity Sensitivity on the Temperature Derivatives Statistics in Isotropic Turbulence," *Journal of Fluid Mechanics,* Vol. 48, 1971, pp. 763–769.

13 Dean, R. B., and Bradshaw, P., "Measurements of Interacting Shear Layers in a Duct," *Journal of Fluid Mechanics,* Vol. 78, 1976, pp. 641–676.

14 Smits, A., "Further Developments of the Hot Wire and LASER Methods in Fluid Mechanics, Ph.D Thesis, University of Melbourne, 1974.

15 Antonia, R. A., Dahn, H. Q., and Prabhu, A., "Response of a Turbulent Boundary Layer to a Step Change in Surface Heat Flux," *Journal of Fluid Mechanics,* Vol. 80, 1977, pp. 153–177.

16 Kovasznay, L. S. G., and Ali, F., "Structure of the Turbulence in the Wake of a Heated Flat Plate," *Proceedings of the 5th International Heat Transfer Conference,* ii, 99, Tokyo, 1974.

17 Andreopoulos, J., and Bradshaw, P., "Measurements of Ineracting Turbulent Shear Layers in the Near Wake of a Flat Plate," *Journal of Fluid Mechanics,* Vol. 100, 1980, pp. 639–668.

P. M. Abdul Majeed
Assistant Professor,
Department of Mechanical Engineering,
Regional Engineering College,
Calicut, Kerala 673 601 India

Analysis of Heat Transfer During Hydrair Cooling of Slab-Shaped Food Products

Part I: Theoretical Investigations

Hydrair cooling of perishable food products is expected to incorporate the advantages of both air cooling and hydrocooling processes. This technique consists of passing cold air over a product which is continuously wetted by a spray of chilled water. In this paper, a mathematical model for the hydrair cooling of slab-shaped food products is proposed. The set of differential equations for heat transfer through the product and the wetting liquid are solved simultaneously, using finite difference method. It is observed that the process of hydrair cooling is advantageous at lower values of the film Reynolds number for higher Biot number values. The cooling speed and the governing parameters are correlated.

Introduction

Hydrair cooling, which consists of passing cold air over the product which is continuously wetted by a spray of chilled water, is under preliminary stages of investigation and is expected to combine the advantages of both air cooling and hydrocooling. This process has been experimentally studied by some investigators [1–3] and has been reported to be even better than hydrocooling under certain operating conditions. However, analytical studies of this process yielding time-temperature histories and cooling times are not reported in literature.

Cooling of food packages is quite common in the food industry. For purpose of analysis, such packages can be treated as slabs. In this paper, a mathematical model of the hydrair cooling of food products which can be approximated to the shape of slabs is presented. The energy equation in dimensionless form for the product and for the water film are solved simultaneously using finite difference technique. The results are obtained in terms of dimensionless parameters covering the product properties and processing conditions encountered in food cooling practice.

Theoretical Analysis

Description of the Physical Model. The physical model used for the analysis of the problem is represented in Fig. 1. The product having an initial temperature of T_{p0} is exposed to a film of water having an initial temperature of T_{f0}. Cold air with a wet bulb temperature, T_a flows over the wetted product yielding a uniform surface heat transfer coefficient, h. The product has thickness $2b$, length L and a large width compared to the thickness. The liquid film over the product has uniform thickness, δ. Both heat transfer and mass transfer take place from the surface of the liquid film to the stream of cold air.

Formulation of the Problem. The coordinate system for the analysis is shown in Fig. 1. Application of the continuity momentum and energy equations to the layer of flowing liquid results in the governing equation of the form

$$\alpha_f \frac{\partial^2 T_f}{\partial {y_f}^2} = v_x \frac{\partial T_f}{\partial x_f} + \frac{\partial T_f}{\partial t} \tag{1}$$

where v_x denotes the velocity at any point y_f in the liquid film. For smooth, laminar two-dimensional flow over a vertical surface, v_x is given by [4],

$$v_x = \frac{g}{\nu_f}\left(y_f - \frac{{y_f}^2}{2}\right) \tag{2}$$

Equation (1) suggests that a two-dimensional temperature profile prevails within the liquid film, the x-direction gradient being due to the flow of the liquid. However, the velocity of the liquid film being very small, the gradient in the x-direction will not be appreciable. Moreover, a stagnant layer of liquid can be expected to exist at the product-liquid interface. Thus a uniform temperature can be assumed to exist at the product-liquid interface and the heat transfer in the product can be considered unidimensional.

The one-dimensional conduction equation in the slab is written as,

$$\frac{\partial^2 T_p}{\partial {y_p}^2} = \frac{1}{\alpha_p}\frac{\partial T_p}{\partial t} \tag{3}$$

The initial and boundary conditions of equation (1) are obtained as follows.

The initial uniform temperature within the liquid film yields

$$T_f = T_{f0} \text{ at } t = 0 \text{ for } 0 \le y_f \le \delta \text{ and } 0 \le x_f \le L \tag{4}$$

A continuous flow of water is assumed from the top of the product to maintain a film of flowing water. This gives the condition,

$$T_f = T_{f0} \text{ at } x_f = 0 \text{ for } 0 < y_f \le \delta \text{ and } t \ge 0 \tag{5}$$

At the surface of the water film, the energy exchange with the air stream takes place by a combination of sensible and latent heat transfer.

The latent heat transfer which accompanies the mass transfer is a function of the moisture content, W of the air stream and the total heat transfer per unit area due to the sensible and latent heat transfers can be expressed as [5],

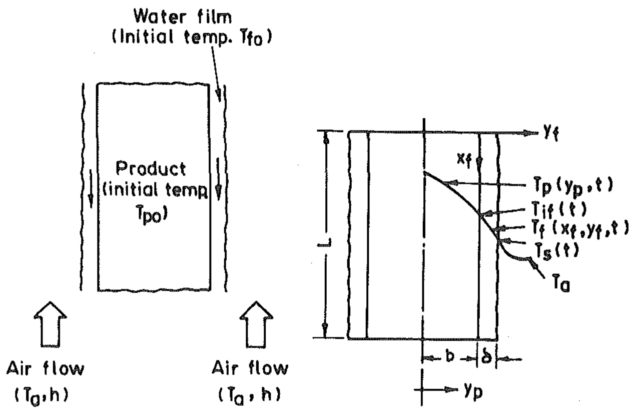

Fig. 1(*a*) Physical model **Fig. 1(*b*)** Coordinate system

Fig. 1 Physical model and coordinate system

Contributed by the Heat Transfer Division for publication in the JOURNAL OF HEAT TRANSFER. Manuscript received by the Heat Transfer Division November 19, 1979.

$$dQ = h(T_s - T_a) + \frac{h}{C_p + WC_{pw}} H'_{fg}(W_s - W) \tag{6}$$

Stoecker [5] has shown that the right hand side of the above equation can be expressed, with sufficient accuracy as a function of the difference between the enthalpy of the saturated film and the enthalpy of the unsaturated air. Thus, an energy balance at the liquid-air interface yields

$$-k_f \frac{\partial T_f}{\partial y_f} = \frac{h}{C_p + WC_{pw}} (H_s - H_a)$$

$$\text{at } y_f = \delta \text{ for } x_f > 0 \text{ and } t > 0 \tag{7}$$

Where H_a is the specific enthalpy of the free stream air which is generally unsaturated. The enthalpy of unsaturated air can be represented with sufficient accuracy by the enthalpy of saturated air at its thermodynamic wet bulb temperature [6]. The enthalpy of saturated air can be expressed as a function of the temperature by a second degree polynomial as,

$$H = A_0 + A_1 T + A_2 T^2 \tag{8}$$

At the product-water interface, a good thermal contact between the two is assumed to exist, resulting in the same temperature for both product and water film. Thus,

$$T_p = T_{if} \text{ at } y_p = b \text{ for } 0 < x_f \leq L \text{ and } t > 0 \tag{9}$$

$$T_f = T_{if} \text{ at } y_f = 0 \text{ for } 0 < x_f \leq L \text{ and } t > 0 \tag{10}$$

Equations (1, 4, 5, 7) and (9) completely define the problem of heat conduction in the liquid film.

Based on the physical model, the following initial and boundary conditions are written

$$T_p = T_{p0} \text{ at } t = 0 \text{ and } 0 \leq y_p \leq b \tag{11}$$

$$\frac{\partial T_p}{\partial y_p} = 0 \text{ at } y_p = 0 \text{ and } t > 0 \tag{12}$$

$$-k_p \frac{\partial T_p}{\partial y_p} = -k_f \frac{\partial T_f}{\partial y_f} \text{ at } y_p = b \text{ for } t > 0 \tag{13}$$

Equations (3, 11, 12) and (13) completely define the problem of heat conduction within the product.

In order to obtain the results in a generalized form, the governing equations and boundary conditions are nondimensionalized using the following definitions.

$$\left.\begin{array}{c}
x_f^* = \dfrac{x_f}{L} \quad y_f^* = \dfrac{y_f}{\delta} \quad y_p^* = \dfrac{y_p}{b} \quad \delta^* = \dfrac{\delta}{b} \quad b^* = \dfrac{b}{L} \\[2ex]
T_p^* = \dfrac{T_p - T_a}{T_{p0} - T_a} \quad T_f^* = \dfrac{T_f - T_a}{T_{f0} - T_a} \quad T_s^* = \dfrac{T_s - T_a}{T_{f0} - T_a} \\[2ex]
T_{if}^* = \dfrac{T_{if} - T_a}{T_{f0} - T_a} \quad R_T = \dfrac{T_{f0} - T_a}{T_{p0} - T_a} \quad \mathrm{Bi} = \dfrac{h\,b}{k_p} \quad k^* = \dfrac{k_p}{k_f} \\[2ex]
\alpha^* = \dfrac{\alpha_p}{\alpha_f} \quad t^* = \dfrac{\alpha_p t}{b^2}
\end{array}\right\} \tag{14}$$

Upon introduction of equations (8) and (14), the governing equations and boundary conditions take the following dimensionless form.

Product

$$\frac{\partial^2 T_p^*}{\partial y_p^{*2}} = \frac{\partial T_p^*}{\partial t^*} \tag{15}$$

$$T_p^* = 1 \text{ at } t^* = 0 \text{ for } 0 \leq y_p^* \leq 1 \tag{16}$$

$$\frac{\partial T_p^*}{\partial y_p^*} = 0 \text{ at } y_p^* = 0 \text{ for } t^* \geq 0 \tag{17}$$

$$\frac{\partial T_p^*}{\partial y_p^*} = \frac{R_T}{k^*\,\delta^*} \frac{\partial T_f^*}{\partial y_f^*} \text{ at } y_p^* = 1 \text{ for } t^* > 0 \tag{18}$$

Liquid film

$$\frac{\partial^2 T_f^*}{\partial y_f^{*2}} = D_1 \frac{\partial T_f^*}{\partial t^*} + D_2 \left(y_f^* - \frac{y_f^{*2}}{2}\right) \frac{\partial T_f^*}{\partial x_f^*} \tag{19}$$

$$T_f^* = 1 \text{ at } t^* = 0 \text{ for } 0 \leq y_f^* \leq 1 \text{ and } 0 \leq x_f^* \leq 1 \tag{20}$$

$$T_f^* = 1 \text{ at } x_f^* = 0 \text{ for } 0 < y_f^* \leq 1 \text{ and } t^* \geq 0 \tag{21}$$

$$T_f^* = T_{if}^* \text{ at } y_f^* = 0 \text{ for } 0 < x_f^* \leq 1 \text{ and } t^* > 0 \tag{22}$$

$$\frac{\partial T_f^*}{\partial y_f^*} = -[E_1 T_s^* + E_2 T_s^{*2}] \text{ at } y_f^* = 1 \tag{23}$$

$$\text{for } 0 < x_f^* \leq 1 \text{ and } t^* > 0$$

where

$$D_1 = \alpha^* \delta^{*2} \tag{24}$$

$$D_2 = 3 \,\mathrm{Pr}_f \,\mathrm{Re}_f \, b^* \delta^* \tag{25}$$

In equation (25), Re_f denotes the film Reynolds number given by [4]

$$\mathrm{Re}_f = \frac{g\delta^3}{3\nu_f^2} \tag{26}$$

In equation (23),

$$E_1 = \mathrm{Bi}\, k^* \delta^* \left(\frac{A_1 + 2 A_2 T_a}{C_p + WC_{pw}}\right) \tag{27}$$

and

$$E_2 = \mathrm{Bi}\, k^* \delta^* A_2 \left(\frac{T_{f0} - T_a}{C_p + WC_{pw}}\right) \tag{28}$$

In the above equations, though E_1 and E_2 are dimensionless, the temperature parameters T_{f0} and T_a still appear explicitly. These are nondimensionalized by defining a new temperature parameter, T^+ as follows.

$$T^+ = \frac{A_2 T}{C_p + WC_{pw}} \tag{29}$$

The specific heat of air at constant pressure, C_p, is assumed to be constant at 1 kJ/kg-K. The quantity WC_{pw} may be assumed constant at 0.021 kJ/kg-K.

The coefficients of equation (8) for the range of wet bulb temperature from −10 to +10°C are

Nomenclature

b = half thickness of product
Bi = Biot number
C_p = specific heat of dry air
C_{pw} = specific heat of water vapour
g = acceleration due to gravity
h = convective heat transfer coefficient
H = specific enthalpy of moist air
H_{fg}' = enthalpy of evaporation of water at the temperature of wetted surface.
k = thermal conductivity
L = height of the product
Pr = Prandtl number
Re_f = film Reynolds number
R_T = temperature ratio defined in equation (14)
t = time
T = temperature
v_x = velocity of film flow
W = humidity ratio defined as mass of water vapour in air per unit mass of dry air
x,y = coordinate distances
Z = half-cooling time of dimensionless time, t^*
α = thermal diffusivity
δ = film thickness
ν = kinematic viscosity

Subscripts

0 = initial condition
a = air wet bulb
f = water film
if = product water interface
p = product
s = air water interface

Superscripts

$*$ = nondimensional quantity defined in equation (14)
$+$ = nondimensional independent parameter defined in equation (29)

$$A_0 = 9.30770 \quad A_1 = 1.75289 \quad A_2 = 0.02193 \tag{30}$$

which yield H in kJ/kg.

On substitution of the above constants, equations (27) and (28) transform into,

$$E_1 = \mathrm{Bi}\, k^*\, \delta^*\, (1.70918 + 2\, T_a{}^+) \tag{31}$$

$$E_2 = \mathrm{Bi}\, k^*\, \delta^*\, R_T\, (T_{p0}{}^+ - T_a{}^+) \tag{32}$$

Method of Solution. The solution of the differential equations for the product and the film given respectively by equations (15) and (19) is obtained using a finite difference method which approximates the derivatives in the differential equation with finite difference analogues at each nodal point, thereby reducing the solution of the differential equation to the solution of a set of algebraic equations. An implicit form of the finite difference method, namely, the backward difference scheme, has been chosen as it does not have a restriction on the size of the time step for stability. The algebraic equations formed, constituted a tri-diagonal set of equations which is solved using Thomas algorithm [7]. The procedure adopted for the simultaneous solution of the two differential equations is as follows.

Initially, a value is assumed for $T_{if}{}^*$ in equation (22) to solve the energy equation of the film. $\partial T_f/\partial y_f{}^*$ at $y_f{}^* = 0$ is then determined along $x_f{}^* = 0$ from which an average value of $\partial T_f{}^*/\partial y_f{}^*$ over $x_f{}^* = 0$ to 1 is calculated. This is used in equation (18) and the energy equation for the product is solved. The value of $T_p{}^*$ at $y_p{}^* = 1$ so obtained is compared with the value corresponding to the assumed value of $T_{if}{}^*$. If they are different, another value of $T_{if}{}^*$ is chosen and the procedure is repeated. This is continued until the assumed value and the one calculated from the solution of equation (15) agree within allowable tolerance. In the actual computation, an iteration technique described in [8] is used by which the correct value of $T_{if}{}^*$ is, in most cases, obtained in three trials.

Results and Discussion

The results are computed for the following governing parameters.

1 The dimensionless wet bulb temperature of air, $T_a{}^+$ is varied from 0.04 to 0.2 in increments of 0.04. This corresponds to a wet bulb temperature range of 2–10°C.

2 The dimensionless initial water temperature, $T_{f0}{}^+$ is varied from 0.1 to 0.4 in increments of 0.1. This corresponds to a temperature range of 5–20°C.

3 Biot number is varied from 0.1 to 10.0 as 0.1, 1.0, 5.0 and 10.0. This range of Bi values covers air velocities up to 5 m/s, characteristic dimension of the product up to 30 cm and thermal properties of a wide variety of products.

4 The film Reynolds number, Re_f is varied from 0.1 to 1000 as 0.1, 1.0, 10.0, 100 and 1000. This corresponds to a film thickness range of 0.04–0.9 mm.

The above ranges of parameters cover the processing conditions, product sizes and thermophysical properties normally encountered in precooling practice.

As the main emphasis in the analysis is on the effect of process parameters, the product-dependent parameters such as $T_{p0}{}^+$, k^*, α^*, δ^* and b^* are given representative values during computation.

For the above values of variables, analytical results are obtained in terms of dimensionless temperature within the product against dimensionless time parameter. The analysis also yields the temperature profile across the product sections.

Figure 2 shows typical temperature profile within the product at different times. The sudden temperature drop seen at the product surface is the result of direct contact with the water film and the accompanying high initial heat transfer potential existing at the surface.

Figure 3 shows the effect of variation of Re_f at a low value of $T_a{}^+$. At the chosen values of other parameters, there is no effect of Re_f for its values greater than 1. Also, the final product temperature approaches the initial water temperature, indicated by R_T for $\mathrm{Re}_f > 1$. $\mathrm{Re}_f < 10$ results in a higher product temperature in the beginning of the cooling process than for $\mathrm{Re}_f \geq 10$. This is because, in the beginning of cooling, higher heat flux from the product produces a higher interface temperature than T_{f0} due to the insufficiency of film flow for carrying away all the heat. However, at the later stages of cooling, the interaction of air with water film helps to reduce the film temperature in the case of low Re_f.

The effect of varying Re_f at a high value of T_a is given in Fig. 4. This condition represents a smaller temperature difference between water and air. Here also, the trend in cooling characteristics is similar to that in Fig. 3. Cooling with low Re_f is slower because of low interaction between air and water due to low value of Bi.

Figure 5 shows the effect of varying Re_f at a low value of Bi. It is found that the cooling rate increases with Re_f up to a value of $\mathrm{Re}_f = 10$, beyond which the influence of Re_f is negligible. The increase in cooling rate with Re_f is due to the condition of low Bi considered here which stipulates a low heat transfer coefficient. Hence the contribution of air in the cooling process is not significant and the cooling rate is mainly dependent on the liquid flow rate which increases with Re_f.

The effect of varying Re_f at a high value of Bi is presented in Fig. 6. It may be seen that the trend in cooling characteristics is reversed in this case compared to that at low value of Bi. Due to the high Bi considered, the influence of air will be significantly felt in the cooling of the film at lower values of Re_f. Hence the cooling rate is higher at low values of Re_f.

In Fig. 7 the effect of variation of Bi is given at two different values of T_{f0}. It may be seen that for values of other parameters considered, variation of Bi over a wide range produces very little effect on the cooling characteristics for $T_{f0}{}^+ = 0.1$ whereas for $T_{f0}{}^+ = 0.4$, the influence of Bi is significant. This is because, in the latter case, the temperature difference between water and air is high, which results in higher heat transfer potential. This produces greater cooling at higher Bi values. However, it may be seen that the smaller difference between air and water produces faster cooling rates.

The effect of Bi variation at a low and a high value of Re_f is shown in Fig. 8. As may be seen, there is considerable increase in the rate of

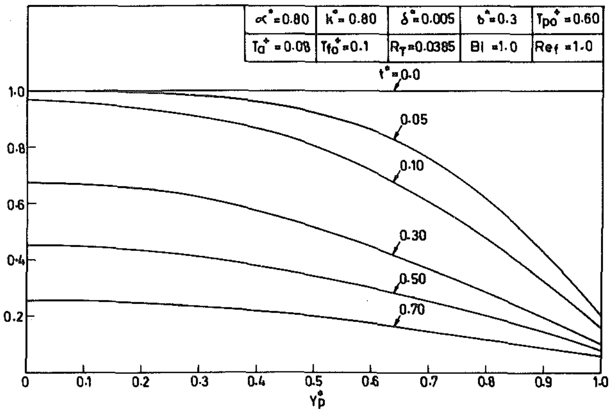

Fig. 2 Typical temperature profile within product

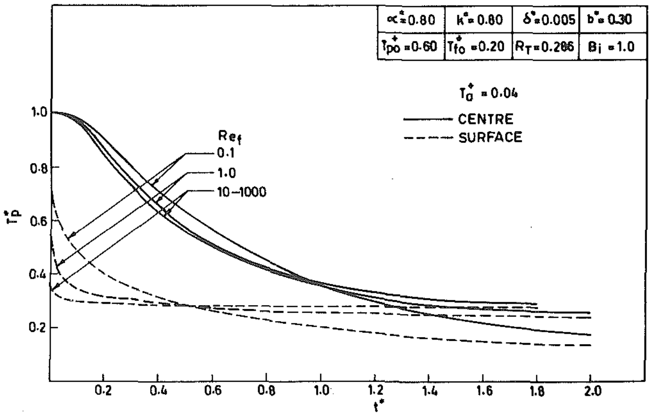

Fig. 3 Effect of film Reynolds number at low $T_a{}^+$

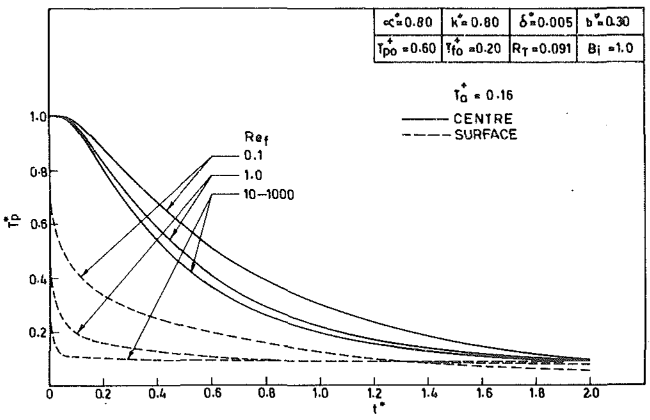

Fig. 4 Effect of film Reynolds number at high T_a^+

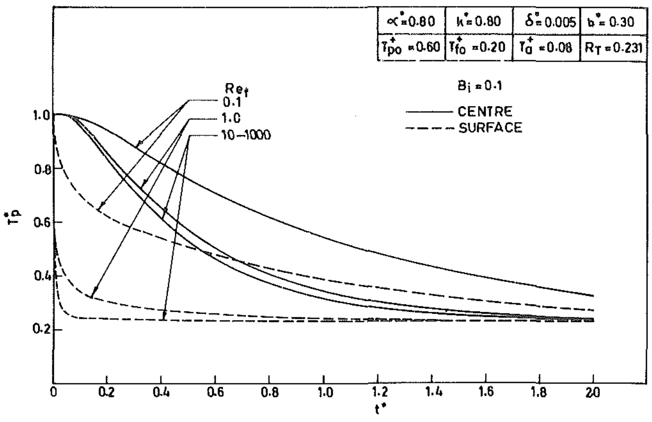

Fig. 5 Effect of film Reynolds number at low Bi

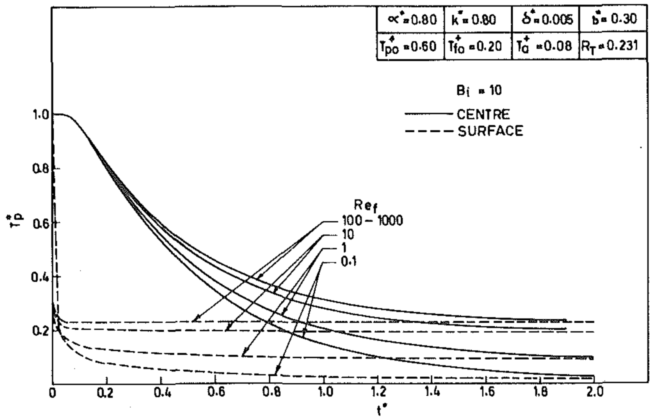

Fig. 6 Effect of film Reynolds number at high Bi

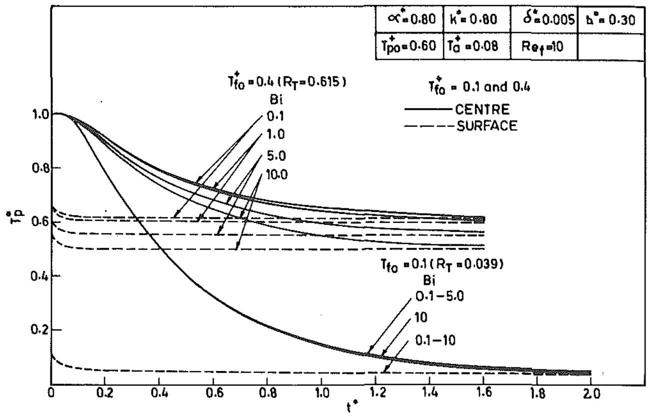

Fig. 7 Effect of Biot number for low and high values of T_{f0}^+

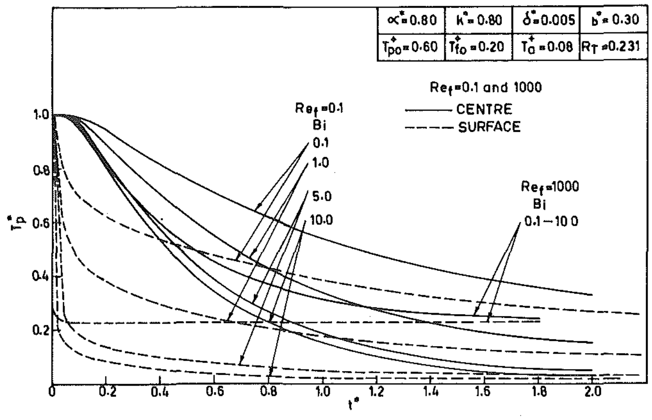

Fig. 8 Effect of Biot number for low and high values of Re$_f$

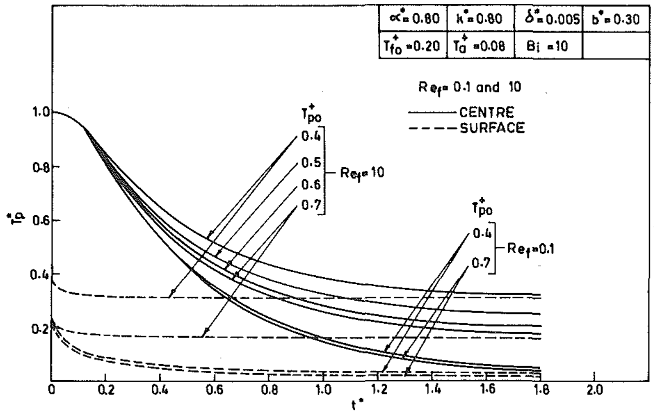

Fig. 9 Effect of initial product temperature

cooling as Bi is increased. This is due to the fact that at high Bi, there is more effective interaction of air and water, resulting in the fast reduction in the film temperature which approaches the air temperature represented by 0 on the T_p* scale. This can be seen from the curves for surface temperature. At very high Re$_f$, variation of Bi does not influence cooling because the high flow rate associated with high Re$_f$ is not influenced by the air flow.

Effect of parameters such as T_{p0}^+, k^*, α^*, δ^* and b^* have also been studied by varying them over wide ranges for fixed values of other parameters. It is observed that only a negligible effect on the cooling characteristics is produced by these parameters with the exception of T_{p0}^+.

Figure 9 shows the effect of variation of T_{p0}^+ on the cooling characteristics. It may be observed that the cooling rate increases with T_{p0}^+ at Re$_f$ = 10 whereas at Re$_f$ = 0.1, the effect of T_{p0}^+ on the cooling rate is seen to be not significant. Since, as indicated earlier, at higher Re$_f$, the cooling is mainly dependent on T_{f0}, as T_{p0} increases for a given T_{f0}, the temperature gradient within the product also increases resulting in faster cooling rates. At lower Re$_f$, due to the smaller film thickness, the film temperature is influenced by the temperature of both product and air. Hence, as T_{p0} increases, the actual film temperature also increases because there is no appreciable change in the temperature gradient within the product. This results in the cooling rate being unaffected significantly as T_{p0}^+ is changed.

The preceding discussions reveal that the major influencing parameters on the hydrair cooling process are Re$_f$, Bi, T_{p0}^+ and the difference $(\Delta T)_{a,f}$ between the initial temperature of water and the wet-bulb temperature of the air defined by,

$$(\Delta T)_{a,f} = T_{f0}^{+} - T_a^{+} \tag{33}$$

With a view to correlate the factors that affect the cooling, the first half cooling time, $Z_{0.5}$ is taken to indicate the cooling speed. In conventional cooling practice, half-cooling time is a measure of cooling speed. In hydrair cooling, due to the variation of the temperatures of water film during the cooling period, it is observed that half-cooling time does not remain constant throughout the cooling process. However, the first half-cooling time may be taken to compare the rate of cooling under different conditions. Of the variables affecting cooling, it has been shown that the value of the film Reynolds number Re_f governs the pattern in which the different parameters affect the cooling rate. Thus, it may be seen that when Re_f is included, the variables become uncorrelatable. Hence a correlation of the first half-cooling time, $Z_{0.5}$ with $(\Delta T)_{a,f}$, Bi and T_{p0}^{+} is obtained for different constant values of Re_f.

In the discussion on the effect of varying Re_f it is shown that hydrair cooling is effective only at lower values of Re_f. This is because only at low Re_f the presence of air influences cooling and the product temperature tends to the wet bulb temperature of air at higher Bi values. At high values of Re_f, due to the greater liquid flow rate, even higher air velocities have only very little effect on the liquid temperature. The influence on product temperature is therefore correspondingly less. Hence for purpose of correlation, three constant values in the lower range are chosen for Re_f, namely, 0.2, 0.5 and 1.0. The correlation is obtained by the multiple linear regression analysis and is of the form

$$Z_{0.5} = a_1(\Delta T)_{a,f}^{a_2}\,\mathrm{Bi}^{a_3}\,T_{p0}^{+a_4} \tag{34}$$

The coefficients a_1, a_2, a_3 and a_4 are given in Table 1.

Table 1 $Z_{0.5} = a_1(\Delta T)_{a,f}^{a_2}\,\mathrm{Bi}^{a_3}\,T_{p0}^{+a_4}$

Product Geometry	Re_f	a_1	a_2	a_3	a_4	Correlation coefficient
SLAB	0.2	0.7116	0.0773	−0.1777	−0.0946	0.987
	0.5	0.6714	0.1057	−0.1033	−0.1492	0.970
	1.0	0.6942	0.1421	−0.0668	−0.1506	0.949

The correlation covers values of $(\Delta T)_{a,f}$ up to 0.16, Bi up to 5.0, T_{p0}^{+} from 0.4 to 0.7 and is applicable over wide ranges of α^*, k^*, δ^* and b^* as it is found that the effect of varying these parameters has negligible influence on cooling.

The correlation can be used for quick estimation of the first half-cooling time of products when the processing conditions and product properties are known. This would also be useful in obtaining an idea about the relative performance of the hydrair cooling process compared to other precooling techniques.

The accuracy of the analytical prediction has been established with the help of elaborate experimentation, the details of which will be presented in a subsequent report. However, for purpose of comparison, the predicted and measured responses obtained for an experimental model for a typical set of governing parameters are given in Table 2.

Concluding Remarks

An analysis which yields the time temperature histories during hydrair cooling of slab-shaped food products is presented. The cooling speed and the governing parameters are correlated. It has been observed that hydrair cooling process is beneficial at lower values of film Reynolds number, i.e. at lower film flow rates, for smaller differential between air and water temperatures. The cooling effect is pronounced at higher value of Biot number, i.e., at higher air velocities.

References

1 Henry, F. E. and Bennett, A. H., "Hydrair Cooling Vegetable Products in Unit Loads," *Trans. ASRAE*, Vol. 16, No. 4, 1973, p. 731.

2 Bennett, A. H., and Wells, J. M., "Hydrair Cooling—A New Pre-Cooling Method with Special Application for Waxed Peaches," *Journal of American Society of Horticultural Science*, Vol. 101, No. 4, July 1976, p. 428.

3 Henry, F. E., Bennett, A. H., and Segall, K. H., "Hydrair Cooling—A New Concept for Pre-Cooling Pallet Loads of Vegetables," *Trans. ASHRAE*, Vol. 82, pt. 2, 1976, p. 541.

4 Fulford, G. D., "The Flow of Fluids in Thin Films," *Advances in Chemical Engineering*, Vol. 5, 1964, p. 151.

5 Stoecker, W. F., *Refrigeration and Airconditioning*, T.M.H., 1977, p. 252.

6 *ASHRAE Guide and Data Book* (*Fundamentals*), ASHRAE, New York 1971.

7 Von Rosenberg, D. U., *Methods for the Numerical Solutions of Partial Differential Equations*, American Elsevier, 1969.

8 Abdul Majeed, P. M., "Studies on Heat Transfer during Hydrair cooling of Food Products," Ph.D. Dissertation, Dept. of Mech. Engg., Indian Inst. of Tech., Madras, India, 1979.

Table 2 Comparison of predicted and measured response at center of product

Product—Food Model Size—12 × 12 × 2 cm
Composition—100 water:40 sugar:3 agar (by weight)

$T_{p0}^{+} = 0.764$ $T_{f0}^{+} = 0.252$ $T_a^{+} = 0.235$ Bi $= 0.545$ $\mathrm{Re}_f = 0.19$

t^*	0.0	0.2	0.4	0.6	0.8	1.0	1.2	1.4	1.6	1.8	2.0
T_p^* Predicted	1.000	0.900	0.710	0.550	0.435	0.340	0.265	0.210	0.165	0.130	0.105
T_p^* Measured	1.000	0.810	0.650	0.520	0.415	0.325	0.260	0.205	0.160	0.125	0.100

Journal of Heat Transfer

Technical Notes

This section contains shorter technical papers. These shorter papers will be subjected to the same review process as that for full papers.

Variances in Solar Collector Performance Predictions Due to Different Methods of Evaluating Wind Heat Transfer Coefficients

J. W. Ramsey[1] and M. Charmchi[1]

Nomenclature

A = surface area of collector
C = circumference of collector
h_w = wind-related heat transfer coefficient
I = solar flux incident on the collector
k = thermal conductivity of ambient air
q_u = rate of useful heat collection per unit collector area
T_a = ambient temperature
T_{in} = fluid inlet temperature

Introduction

Any analysis of a flat-plate solar collector requires knowledge of the wind-related heat transfer coefficient at the outer surface of the outermost cover of the collector, h_w. Most papers follow the recommendations of recent texts [1, 2, 3] and evaluate the h_w by employing the average heat transfer coefficients based on the equation

$$h_w = 5.7 + 3.8\,U_\infty;\ \mathrm{W/m^2 \cdot {}^\circ C} \qquad (1)$$

where U_∞ is the wind velocity (m/s). It has been pointed out previously [4] that equation (1) is inappropriate for the evaluation of h_w since it neglects the effects of wind direction and collector dimensions.

Experimentally determined average heat transfer coefficients for forced convection airflow over square and rectangular plates that are inclined at various angles of attack to the oncoming flow have been reported in [4] and [5], respectively. Fortunately, the wind-related heat transfer coefficients were found to be quite insensitive to the angle of attack and to the aspect ratio of the plate, and a global correlation equation was proposed [5]

$$h_w = 0.86\,\frac{k}{L_c}\,\mathrm{Re}_{L_c}{}^{1/2}\mathrm{Pr}^{1/3} \qquad (2)$$

with the characteristic dimension, L_c, defined as

$$L_c = 4\,A/C \qquad (3)$$

The Reynolds number range investigated extended from about 20,000 to 100,000. The strict adherence of the data to a half-power Reynolds number dependence facilitates extrapolation of the results to higher Reynolds numbers.

The data of [4 and 5] clearly demonstrate that equation (1) is inappropriate for evaluating h_w for solar collectors, (e.g., at U_∞ = 4.5 m/s the value of h_w calculated using equation (1) is 3.8 times greater than that calculated using equation (2)). However, the question of how important this is to the estimated performance of the entire collector was not addressed previously. In the present study, the operating performance of four different collector configurations are predicted using both the inappropriate and appropriate relations to evaluate h_w.

Collector Geometry and Analysis Model

All four of the collectors analyzed were of the basic liquid heating type shown schematically in Fig. 1. The differences between them were in the type of collector plate surface coating and the number of covers employed. Specifically, the four combinations analyzed are: one or two covers and a selectively absorbing surface coating, and one or two covers and a nonselectively absorbing surface coating. These combinations span a broad range of expected performance and, thus, provide a comprehensive picture of the effect of the prediction method used for h_w. The solar absorptance and infrared emittance of the selective coating were taken as 0.95 and 0.1, respectively. In the case of the nonselective coating, both the solar absorptance and infrared emittance were assumed to be 0.95. The covers were 0.32 cm thick sheets of glass. The inner cover was positioned with a space of 2.54 cm between it and the collector plate. The cover spacing for the two-cover configurations was also 2.54 cm.

The dimensions and materials for all four of the collectors analyzed were as follows: a 0.076 cm thick steel collector plate with integral tubes positioned with center-to-center spacings of 7.62 cm, inner and outer tube diameters of 0.49 cm and 0.78 cm, respectively, tube and collector length of 1.83 m, and a 7.62 cm thick layer of insulation (thermal conductivity = 0.041 W/m·°C) on the back side of the collector plate.

The analysis of the collectors was performed using the well-documented Hottel, Whillier and Bliss (HWB) approach [1–3]. Using this model, the rate of useful heat delivered by the collector per unit absorber area is expressed by

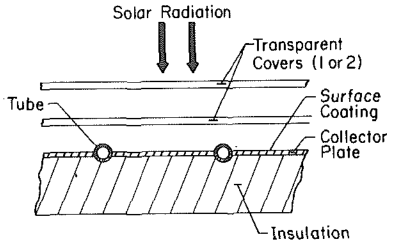

Fig. 1 Schematic of the generalized collector configuration for which the analysis was performed

---

[1] Department of Mechanical Engineering, University of Minnesota, Minneapolis, Minn 55455.

Contributed by the Heat Transfer Division for publication in the JOURNAL OF HEAT TRANSFER. Manuscript received by the Heat Transfer Division June 10, 1980.

$$q_u = F_R[(\tau\alpha)_e I - U_L(T_{\text{in}} - T_a)] \tag{4}$$

Since the details of the HWB model are well documented, the present discussion will concentrate on how the heat transfer coefficient at the outer surface of the collector affects the collector performance factors, U_L, F_R and $(\tau\alpha)_e$ which appear in equation (4).

The quantity U_L is the overall heat loss coefficient which includes conduction through the insulation, radiation and natural convection between the plates, and radiation and convection between the top cover plate and the environment. Therefore, the value of U_L is directly dependent on h_w.

The quantity F_R is referred to as the heat removal factor which is the ratio of the actual energy delivered by the collector to the energy which would have been delivered if the entire collector plate had been at the temperature of the fluid entering the collector. One of the parameters which appears in the defining equation for F_R is U_L. Since h_w is one of the ingredients of U_L, it follows, at least in principle, that F_R depends on h_w. Later, it will be shown numerically that this dependence is small. The effective transmittance absorptance product, $(\tau\alpha)_e$, which appears in equation (4) is a radiation property and is not affected by h_w.

Illustrative calculations will now be performed to demonstrate how q_u/I, F_R and U_L are affected by the equations used to compute h_w.

Results and Discussion

In performing the calculations, the general procedure summarized in [1] was followed. However, one significant difference was that the natural convection heat transfer in the air space between plates was evaluated using the results of more recent investigations [6]. The working fluid in the collector was water and a mass flow rate per unit collector surface area of 0.0135 kg/s·m^2 was used for all calculations. The characteristic length, L_c, used in evaluating h_w from equation (2) was 3.18 m (collector dimensions 1.83 m × 12.2 m (6 ft × 40 ft)). The collectors were assumed to be at an angle of 60 deg from the horizontal. Calculations were carried out for incident flux levels ranging from 200 to 1000 W/m^2 taken in steps of 100 W/m^2. Three of the collectors were evaluated at inlet and ambient temperatures of 85 and 20 °C, respectively. The fourth collector was evaluated at respective inlet and ambient temperatures of 50 and 0 °C.

Table 1 presents a summary of the results obtained for a wind speed of 4.5 m/s (approximately 10 mph). The sets of U_L and F_R values which result when h_w is appropriately or inappropriately evaluated, using the respective equations (2) or (1), are included. The h_w values obtained using equation (2) are 6.0 and 5.9 W/m^2·°C for ambient temperatures of 20 and 0 °C, respectively. The h_w calculated from equation (1) is 22.8 W/m^2·°C, a value 3.8 times too large.

The values of F_R and U_L contained in Table 1 are averages of the results for those flux levels that yielded a positive energy collection. In all cases, the variations in F_R and U_L with respect to incident flux level were less than 1 percent. The transmittance absorptance product is included for completeness. The errors in U_L resulting from the use of equation (1) vary from 5 to 27 percent for the range of collector designs analyzed. It can also be seen in Table 1 that variations in h_w have only a minor effect on F_R.

Predictions of the useful energy delivered by the four collectors are presented in a commonly used format (i.e., q_u/I as a function of $(T_{\text{in}} - T_a)/I$) in Figs. 2 and 3. In the case of the collector with two covers and a selectively absorbing coating (upper curves, Fig. 2), the method of evaluating h_w has little effect on the predicted energy collection rate, but the results shown in Fig. 2 for the case of a nonselective absorber show greater sensitivity to h_w. In Fig. 3, the results for single-cover collectors indicate a much greater sensitivity to h_w than did the results for two-cover collectors.

In normal use, flat plate collectors are forced to operate for a significant fraction of the time at relatively low incident solar flux levels, which corresponds to large abscissa values in Figs. 2 and 3. For these operating conditions it is seen that the errors in predicted performance are greatest.

To further illustrate this point, calculations were made of the rate of energy collection throughout a mild January day in Minneapolis, Minn. (T_a = 0 °C, U_∞ = 4.5 m/s) using a south facing, single-cover

Table 1 Values of U_L and F_R for wind speed of 4.5 m/s

Collector*	Appropriate h_w		Inappropriate h_w	
	F_R	U_L, W/m^2·°C	F_R	U_L, W/m^2·°C
Two covers, selective coating (T_{in} = 85°C, T_a = 20°C)	0.929	2.95	0.927	3.11
One cover, selective coating (T_{in} = 85°C, T_a = 20°C)	0.908	3.89	0.899	4.35
Two covers, nonselective coating (T_{in} = 85°C, T_a = 20°C)	0.897	4.51	0.885	5.07
One cover, nonselective coating (T_{in} = 50°C, T_a = 0°C)	0.863	6.04	0.833	7.64

* $(\tau\alpha)_e$ is 0.765 for two covers and 0.849 for one cover

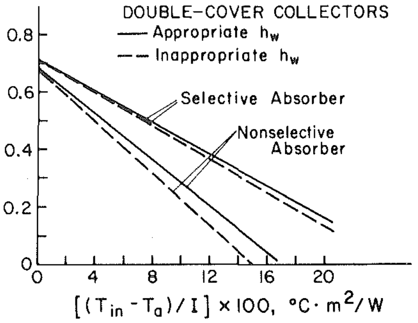

Fig. 2 Predicted performance for double-cover solar collectors

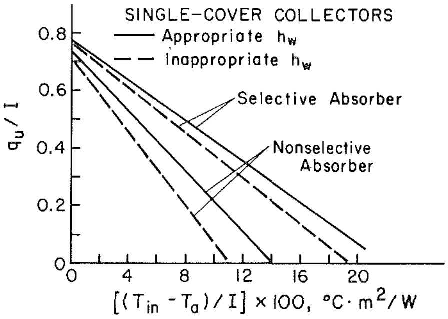

Fig. 3 Predicted performance for single-cover solar collectors

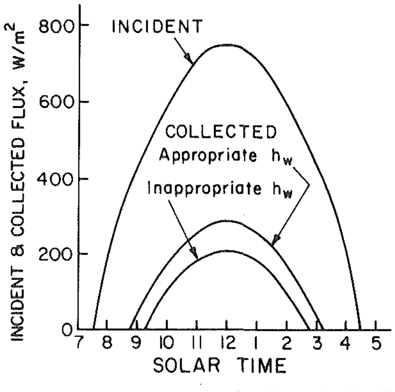

Fig. 4 Daily variation of the incident and collected solar flux for a single-cover, nonselectively coated solar collector (T_{in} = 50 °C, T_a = 0 °C)

Table 2 Effect of wind speed on h_w, U_L and F_R for a collector having a single cover and a nonselective absorber coating

U_∞, m/s	h_w, W/m^2·°C	U_L, W/m^2·°C	F_R
2.25	4.2	5.70	0.870
4.50	5.9	6.04	0.863
6.75	7.3	6.25	0.859

collector with a nonselective absorber coating operating at a fluid inlet temperature of 50 °C. The Liu-Jordan model [7] was used to predict the instantaneous values of the direct, diffuse and ground reflected solar flux incident on the collector, (the ground reflectance was taken as 0.2). By assuming quasi-steady state conditions, the instantaneous rate at which useful energy is collected can be calculated from a modified form of equation (4)

$$q_u = F_R(\tau\alpha)_e[K_D I_D + K_d I_d + K_r I_r] - F_R U_L(T_{\text{in}} - T_a) \qquad (5)$$

where the subscripts D, d and r refer to the direct, diffuse and ground reflected solar radiation respectively. The K coefficients are angle of incidence modifiers which account for the decrease in the effective transmittance absorptance product as the angle of incidence increases. In the present study, it was assumed that the angle of incidence correction for $(\tau\alpha)_e$ is similar to that for the transmission of glass and the K values were evaluated using the procedure recommended by ASHRAE [8].

The daily variation of the incident solar flux on the collector and the corresponding collection rates are presented in Fig. 4. Marked differences exist in the collector output predictions (lower two curves, Fig. 4). Using the inappropriate value of h_w, as calculated from equation (1), results in a shorter collection period plus substantially lower collection rates during the operating period. Overall, this leads to a 37 percent underprediction of the energy delivered for the entire day.

The effect of wind speed on collector performance was checked by analyzing the single-cover, nonselective absorber configuration at additional wind speeds of 2.25 and 6.75 m/s. The results are presented in Table 2. Increasing the wind speed by a factor of three increases the h_w by a factor of the square-root of three, as prescribed by equation (2). This in turn causes a ten percent increase in U_L and only a 1.3 percent decrease in F_R.

Conclusion

Based on the foregoing illustrative examples, it can be concluded that it is of benefit to evaluate the wind-related heat transfer coefficient, h_w, using equation (2).

References

1 Duffie, J. A., and Beckman, W. A., *Solar Energy Thermal Processes*, Wiley-Interscience, New York, 1974, pp. 120–158.

2 Kreith, F., and Kreider, J. F., *Principles of Solar Engineering*, McGraw-Hill, New York, 1978, pp. 203–226.

3 Lunde, P. J., *Solar Thermal Engineering*, Wiley, New York, 1980, pp. 120–165.

4 Sparrow, E. M., and Tien, K. K., "Forced Convection Heat Transfer at an Inclined and Yawed Square Plate—Application to Solar Collectors," ASME JOURNAL OF HEAT TRANSFER, Vol. 99, 1977, pp. 507–512.

5 Sparrow, E. M., Ramsey, J. W., and Mass, E., "Effect of Finite Width on Heat Transfer and Fluid Flow About an Inclined Rectangular Plate," ASME JOURNAL OF HEAT TRANSFER, Vol. 101, 1979, pp. 199–205.

6 Hollands, K. G. T., Konicek, L., Unny, T. E., and Raithby, G. D., "Free Convection Heat Transfer Across Inclined Air Layers," ASME JOURNAL OF HEAT TRANSFER, Vol. 98, 1976, pp 189–193.

7 Jordan, R. C., and Liu, B. Y. H., *Applications of Solar Energy for Heating and Cooling of Buildings*, ASHRAE, New York, 1977, Chapter V.

8 *ASHRAE Handbook of Fundamentals*, ASHRAE, New York, 1977, p. 26.26.

A Parametric Study of Prandtl Number and Diameter Ratio Effects on Natural Convection Heat Transfer in Horizontal Cylindrical Annuli

T. H. Kuehn[1] and R. J. Goldstein[2]

Nomenclature

D = cylinder diameter
g = gravitational acceleration
h = local heat transfer coefficient on either inner or outer cylinder, $q/(T_i - T_o)$
k = fluid thermal conductivity
k_{eq} = local equivalent conductivity on either inner or outer cylinder, q/q_{cond}
L = annular gap, $(D_o - D_i)/2$
Nu_{D_i} = local inner cylinder Nusselt number, $h_i D_i/k$
Nu_{D_o} = local outer cylinder Nusselt number, $h_o D_o/k$
Pr = Prandtl number
q = heat transfer per unit area, $h(T_i - T_o)$
Q = heat transfer per unit length, $\bar{h}_i \pi D_i(T_i - T_o)$, $\bar{h}_o \pi D_o(T_i - T_o)$
Ra_{D_i} = inner cylinder Rayleigh number, $g\beta D_i^3(T_i - T_o)/\nu\alpha$
Ra_{D_o} = outer cylinder Rayleigh number, $g\beta D_o^3(T_i - T_o)/\nu\alpha$
Ra_L = gap Rayleigh number, $g\beta L^3(T_i - T_o)/\nu\alpha$
T = temperature
U = radial velocity
u = dimensionless radial velocity, UL/α
V = angular velocity
v = dimensionless angular velocity, VL/α
α = thermal diffusivity
β = thermal coefficient of volumetric expansion
θ = angle, top of cylinder 0 deg, bottom 180 deg
ν = kinematic viscosity

Subscripts

cond = conduction
conv = convection
i = inner cylinder
o = outer cylinder

Superscript

$-$ = mean value

Introduction

Natural convection in horizontal annuli continues to receive attention because of the interesting flow patterns that develop and the numerous heat transfer applications. Although correlations for the mean heat transfer coefficient have been presented [1–3], no parametric studies have been reported that investigate the effect of the Prandtl number and diameter ratio over the ranges needed for many applications. In the present study, the Prandtl number and diameter ratio are each varied over several orders of magnitude ($0.001 \leq \text{Pr} \leq 1000$, $1.0 \leq D_o/D_i \leq \infty$) to determine their influence on the natural convection flow and local and mean heat transfer in a horizontal annulus.

Numerical Procedure

An explicit successive overrelaxation finite difference technique is employed to solve the governing equations for steady laminar flow in two dimensions between two horizontal, concentric, isothermal cylinders. The method follows the basic procedure given in [4]. Since some coefficients become negative at small values of Pr or in regions of high velocity, which leads to instability, a hybrid technique has been introduced which changes from central to upwind differencing in regions where the coefficients become negative. This technique allows solutions to be obtained at very low values of Pr and very large D_o/D_i. An outline of this procedure is given in [5].

Several grid spacings are used depending on D_o/D_i and Pr. The

[1] Assistant Professor, Department of Mechanical Engineering and Engineering Research Institute, Iowa State University, Ames, Iowa 50011.

[2] Professor and Head, Department of Mechanical Engineering, University of Minnesota, Minneapolis, Minn 55455.

Contributed by the Heat Transfer Division for publication in the JOURNAL OF HEAT TRANSFER. Manuscript received by the Heat Transfer Division June 6, 1979.

collector with a nonselective absorber coating operating at a fluid inlet temperature of 50 °C. The Liu-Jordan model [7] was used to predict the instantaneous values of the direct, diffuse and ground reflected solar flux incident on the collector, (the ground reflectance was taken as 0.2). By assuming quasi-steady state conditions, the instantaneous rate at which useful energy is collected can be calculated from a modified form of equation (4)

$$q_u = F_R(\tau\alpha)_e[K_DI_D + K_dI_d + K_rI_r] - F_RU_L(T_{\text{in}} - T_a) \qquad (5)$$

where the subscripts D, d and r refer to the direct, diffuse and ground reflected solar radiation respectively. The K coefficients are angle of incidence modifiers which account for the decrease in the effective transmittance absorptance product as the angle of incidence increases. In the present study, it was assumed that the angle of incidence correction for $(\tau\alpha)_e$ is similar to that for the transmission of glass and the K values were evaluated using the procedure recommended by ASHRAE [8].

The daily variation of the incident solar flux on the collector and the corresponding collection rates are presented in Fig. 4. Marked differences exist in the collector output predictions (lower two curves, Fig. 4). Using the inappropriate value of h_w, as calculated from equation (1), results in a shorter collection period plus substantially lower collection rates during the operating period. Overall, this leads to a 37 percent underprediction of the energy delivered for the entire day.

The effect of wind speed on collector performance was checked by analyzing the single-cover, nonselective absorber configuration at additional wind speeds of 2.25 and 6.75 m/s. The results are presented in Table 2. Increasing the wind speed by a factor of three increases the h_w by a factor of the square-root of three, as prescribed by equation (2). This in turn causes a ten percent increase in U_L and only a 1.3 percent decrease in F_R.

Conclusion

Based on the foregoing illustrative examples, it can be concluded that it is of benefit to evaluate the wind-related heat transfer coefficient, h_w, using equation (2).

References

1 Duffie, J. A., and Beckman, W. A., *Solar Energy Thermal Processes*, Wiley-Interscience, New York, 1974, pp. 120–158.

2 Kreith, F., and Kreider, J. F., *Principles of Solar Engineering*, McGraw-Hill, New York, 1978, pp. 203–226.

3 Lunde, P. J., *Solar Thermal Engineering*, Wiley, New York, 1980, pp. 120–165.

4 Sparrow, E. M., and Tien, K. K., "Forced Convection Heat Transfer at an Inclined and Yawed Square Plate—Application to Solar Collectors," ASME JOURNAL OF HEAT TRANSFER, Vol. 99, 1977, pp. 507–512.

5 Sparrow, E. M., Ramsey, J. W., and Mass, E., "Effect of Finite Width on Heat Transfer and Fluid Flow About an Inclined Rectangular Plate," ASME JOURNAL OF HEAT TRANSFER, Vol. 101, 1979, pp. 199–205.

6 Hollands, K. G. T., Konicek, L., Unny, T. E., and Raithby, G. D., "Free Convection Heat Transfer Across Inclined Air Layers," ASME JOURNAL OF HEAT TRANSFER, Vol. 98, 1976, pp 189–193.

7 Jordan, R. C., and Liu, B. Y. H., *Applications of Solar Energy for Heating and Cooling of Buildings*, ASHRAE, New York, 1977, Chapter V.

8 *ASHRAE Handbook of Fundamentals*, ASHRAE, New York, 1977, p. 26.26.

A Parametric Study of Prandtl Number and Diameter Ratio Effects on Natural Convection Heat Transfer in Horizontal Cylindrical Annuli

T. H. Kuehn[1] and R. J. Goldstein[2]

Nomenclature

D = cylinder diameter
g = gravitational acceleration
h = local heat transfer coefficient on either inner or outer cylinder, $q/(T_i - T_o)$
k = fluid thermal conductivity
k_{eq} = local equivalent conductivity on either inner or outer cylinder, q/q_{cond}
L = annular gap, $(D_o - D_i)/2$
Nu_{D_i} = local inner cylinder Nusselt number, h_iD_i/k
Nu_{D_o} = local outer cylinder Nusselt number, h_oD_o/k
Pr = Prandtl number
q = heat transfer per unit area, $h(T_i - T_o)$
Q = heat transfer per unit length, $\bar{h}_i\pi D_i(T_i - T_o)$, $\bar{h}_o\pi D_o(T_i - T_o)$
Ra_{D_i} = inner cylinder Rayleigh number, $g\beta D_i{}^3(T_i - T_o)/\nu\alpha$
Ra_{D_o} = outer cylinder Rayleigh number, $g\beta D_o{}^3(T_i - T_o)/\nu\alpha$
Ra_L = gap Rayleigh number, $g\beta L^3(T_i - T_o)/\nu\alpha$
T = temperature
U = radial velocity
u = dimensionless radial velocity, UL/α
V = angular velocity
v = dimensionless angular velocity, VL/α
α = thermal diffusivity
β = thermal coefficient of volumetric expansion
θ = angle, top of cylinder 0 deg, bottom 180 deg
ν = kinematic viscosity

Subscripts

cond = conduction
conv = convection
i = inner cylinder
o = outer cylinder

Superscript

— = mean value

Introduction

Natural convection in horizontal annuli continues to receive attention because of the interesting flow patterns that develop and the numerous heat transfer applications. Although correlations for the mean heat transfer coefficient have been presented [1–3], no parametric studies have been reported that investigate the effect of the Prandtl number and diameter ratio over the ranges needed for many applications. In the present study, the Prandtl number and diameter ratio are each varied over several orders of magnitude ($0.001 \leq \text{Pr} \leq 1000$, $1.0 \leq D_o/D_i \leq \infty$) to determine their influence on the natural convection flow and local and mean heat transfer in a horizontal annulus.

Numerical Procedure

An explicit successive overrelaxation finite difference technique is employed to solve the governing equations for steady laminar flow in two dimensions between two horizontal, concentric, isothermal cylinders. The method follows the basic procedure given in [4]. Since some coefficients become negative at small values of Pr or in regions of high velocity, which leads to instability, a hybrid technique has been introduced which changes from central to upwind differencing in regions where the coefficients become negative. This technique allows solutions to be obtained at very low values of Pr and very large D_o/D_i. An outline of this procedure is given in [5].

Several grid spacings are used depending on D_o/D_i and Pr. The

---

[1] Assistant Professor, Department of Mechanical Engineering and Engineering Research Institute, Iowa State University, Ames, Iowa 50011.

[2] Professor and Head, Department of Mechanical Engineering, University of Minnesota, Minneapolis, Minn 55455.

Contributed by the Heat Transfer Division for publication in the JOURNAL OF HEAT TRANSFER. Manuscript received by the Heat Transfer Division June 6, 1979.

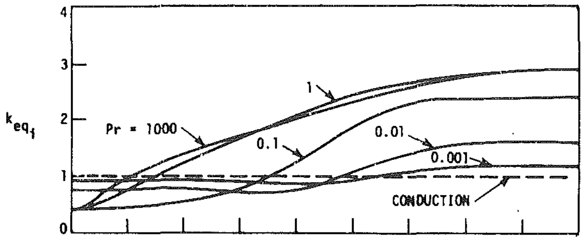

Fig. 1(*a*) Inner cylinder

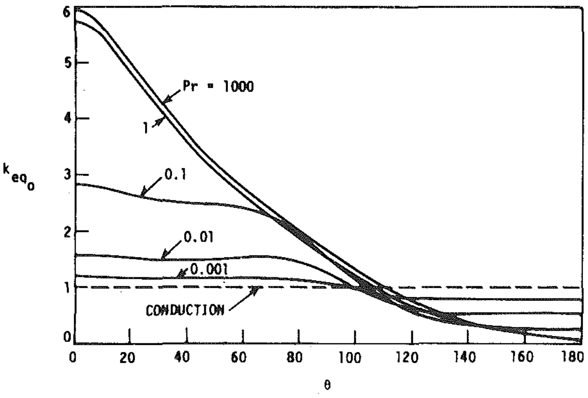

Fig. 1(*b*) Outer cylinder

Fig. 1 Effect of Prandtl number on local heat transfer coefficients, $Ra_L = 10^4$, $D_o/D_i = 2.6$

basic grid has a radial spacing of $L/20$ near the cylinders and $L/10$ in the interior with a uniform angular spacing of 10 deg. At large Rayleigh numbers the radial spacing was reduced to $L/80$ near the walls and the angular spacing decreased to 2.5 deg in the plume.

Results and Discussion

Effect of Prandtl Number. Fifteen solutions were obtained at a constant Rayleigh number and diameter ratio ($Ra_L = 10^4$, $D_o/D_i = 2.6$) with $0.001 \leq Pr \leq 1000$. The flow and heat transfer were analyzed between the limits of conduction at the lowest Pr and fully developed boundary layer flow at the highest Pr.

As the Prandtl number decreases below 1.0 and center of rotation moves down without the appearance of multiple eddies and the dimensionless velocities become similar with their magnitudes proportional to $(Ra\ Pr)^{1/2}$. As the Prandtl number increases above 1.0 the dimensionless velocities become invariant.

The temperature distribution approaches the pure conduction limit as $Pr \rightarrow 0$ and is very close to that limit when $Pr = 0.001$. The temperature profiles are almost independent of Prandtl number when $Pr \geq 1.0$ with thermal boundary layers adjacent to both cylinders.

The local heat transfer coefficients on the two cylinders are shown in Fig. 1 for the entire range of Prandtl number investigated. The distribution on the inner cylinder at large Prandtl number resembles that on a single horizontal cylinder in boundary layer natural convection flow. The local maximum occurs at the stagnation point ($\theta = 180$ deg) with the minimum at the plume separation point ($\theta = 0$ deg). The distribution becomes more uniform and approaches the conduction limit as $Pr \rightarrow 0$. The heat transfer coefficients do not change appreciably when $Pr > 1$ in contrast to external natural convection boundary layer flows where a variation of 20 percent can exist between $Pr = 1.0$ and $Pr = 1000$ [6].

The local heat transfer on the outer cylinder is governed primarily by the impinging thermal plume near $\theta = 0$ at large values of Prandtl number. The plume weakens as $Pr \rightarrow 0$ which results in coefficients that are more uniform and close to the conduction limit. The Prandtl number has virtually no effect on heat transfer in the region, 80 deg $< \theta <$ 130 deg, until the conduction limit is approached.

Effect of Diameter Ratio. The diameter ratio, D_o/D_i, was increased from a value near unity to as large a value as would still give convergence. The Prandtl number remained fixed at $Pr = 0.7$. Values for Ra_{D_i} were set at 10^0, 10^2 or 10^4. These solutions simulate natural convection around a cylinder of fixed size and temperature as the outer cylinder diameter is increased.

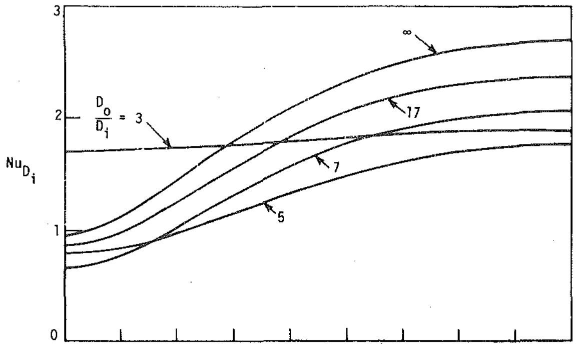

Fig. 2(*a*) Inner cylinder

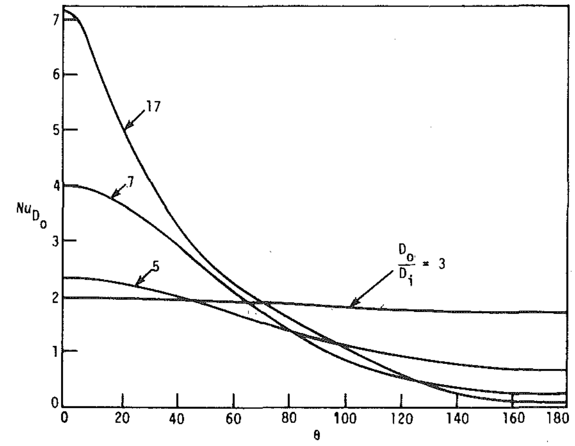

Fig. 2(*b*) Outer cylinder

Fig. 2 Effect of diameter ratio on local heat transfer coefficients, $Ra_{D_i} = 10^2$, $Pr = 0.7$

The flow circulation is very weak with the center of rotation near $\theta = 90$ deg when $D_o/D_i \simeq 1.0$. The temperature distribution and heat transfer are identical to that of pure conduction. As the diameter ratio increases the flow becomes stronger and the center of rotation moves above 90 deg. This increased flow changes the temperature field and local heat transfer coefficients but the mean equivalent conductivity remains close to 1.0. Further increases in diameter ratio result in increased velocities which create thermal boundary layers on both cylinders, and the mean heat transfer increases above that for pure conduction. As the diameter ratio becomes very large, the flow and heat transfer from the inner cylinder approach the values obtained with natural convection about a single horizontal cylinder in an infinite fluid medium [5].

Local heat transfer coefficients for both cylinders are shown in Fig. 2 as a function of diameter ratio for $Ra_{D_i} = 10^2$. The curves for $D_o/D_i = 3$ are essentially that for pure conduction. The transition from conduction occurs near $D_o/D_i = 5$. The local heat transfer coefficients on the inner cylinder approach the free cylinder distribution as $D_o/D_i \rightarrow \infty$. In contrast to the inner cylinder, the local heat transfer coefficients on the outer cylinder do not approach a limiting value but continuously increase near the top ($\theta \simeq 0$ deg) and decrease near the bottom ($\theta \simeq 180$ deg) as the diameter ratio increases.

Mean heat transfer coefficients are plotted in Fig. 3 as a function of diameter ratio for the three values of Ra_{D_i} investigated. The shaded area corresponds to a region of unsteady flow delineated by Powe, Carley and Bishop [7]. The present numerical method should not give valid results in this region. Heat transfer is by conduction alone at small diameter ratios. The conduction curve is also the lower bound of the heat transfer at any specific diameter ratio. The transition between conduction and convection, which is also the condition of the minimum mean heat transfer coefficient at any given value of Ra_{D_i}, occurs when $Ra_L \simeq 10^3$. The mean Nusselt number should asymptotically approach the free cylinder value shown on the right-hand

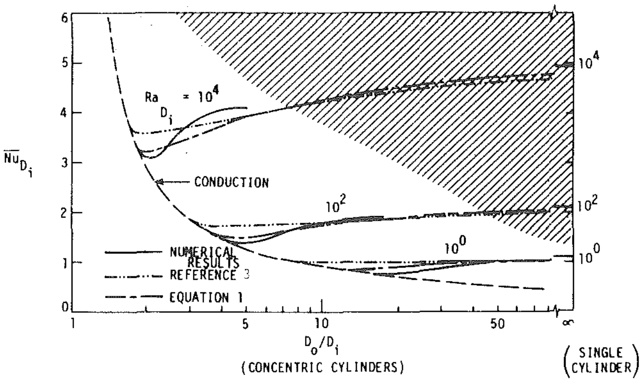

Fig. 3 Influence of diameter ratio on the mean heat transfer coefficient, Pr = 0.7. Shaded area is region of unsteady flow [7].

side of Fig. 3 as $D_o/D_i \rightarrow \infty$. Curves from two heat transfer correlations are shown for comparison.

Mean Heat Transfer Correlation

Mean heat transfer correlations have been developed for natural convection between horizontal cylinders using a double boundary layer concept [2, 3]. These correlations are general in scope but require an iterative procedure to solve for the mean temperature between the boundary layers.

The flow recirculation in a cavity causes the heat transfer to increase over what the double boundary layer model predicts. This increase has been incorporated into the model by basing the Rayleigh numbers, Ra_{D_i} and Ra_{D_o}, on the total temperature difference between the cylinders rather than on the temperature difference across the respective boundary layers. This reduces the complexity of the correlation by eliminating the need for iteration. The Prandtl number does not affect the local heat transfer in the outer cylinder boundary layer region nearly as much as for the inner cylinder, so the Prandtl number variation was removed from the correlation for the outer cylinder boundary layer.

The resulting correlation valid for laminar flow is

$$\overline{\mathrm{Nu}}_{D_{i\mathrm{conv}}} = \frac{2}{\ln\left[\dfrac{1+\dfrac{2}{0.518\mathrm{Ra}_{D_i}{}^{1/4}\left[1+\left(\dfrac{0.559}{\mathrm{Pr}}\right)^{3/5}\right]^{-5/12}}}{1-\dfrac{2}{0.587\mathrm{Ra}_{D_o}{}^{1/4}}}\right]} \tag{1a}$$

$$\overline{\mathrm{Nu}}_{D_{i\mathrm{cond}}} = \frac{2}{\ln\,(D_o/D_i)} \tag{1b}$$

$$\overline{\mathrm{Nu}}_{D_i} = (\mathrm{Nu}_{D_{i\mathrm{cond}}}{}^{15} + \mathrm{Nu}_{D_{i\mathrm{conv}}}{}^{15})^{1/15} \tag{1c}$$

When Pr = 0.7, this correlation fits the numerical results at various diameter ratios better than the correlation given in [3] as shown in Fig. 3. The relative minimum heat transfer at a given value of Ra_{D_i} is predicted fairly well, which is important in many engineering applications. The standard deviation between the present correlation and the fifteen numerical solutions over the range of Prandtl number investigated is 8.6 percent with the maximum deviation of 13 percent occurring near Pr = 0.02. Although this does not fit the solutions at various Prandtl numbers as well as the correlation given in [3], equation (1) is recommended when only approximate results are desired.

Acknowledgment

The authors wish to acknowledge the National Science Foundation for support under Grant NSF/ENG-7721626, a grant of computer time from the University of Minnesota Computer Center, an NDEA IV Fellowship for one of the authors (Thomas H. Kuehn), and partial support from the Engineering Research Institute of Iowa State University.

References

1 Powe, R. E., "Bounding Effects on the Heat Loss by Free Convection from Spheres and Cylinders," ASME JOURNAL OF HEAT TRANSFER, Vol. 96, 1974, pp. 558–560.

2 Raithby, G. D., and Hollands, K. G. T., "A General Method of Obtaining Approximate Solutions to Laminar and Turbulent Free Convection Problems," *Advances in Heat Transfer*, Vol. 11, 1975, pp. 265–315.

3 Kuehn, T. H., and Goldstein, R. J., "Correlating Equations for Natural Convection Heat Transfer Between Horizontal Circular Cylinders," *International Journal of Heat and Mass Transfer*, Vol. 19, 1976, pp. 1127–1134.

4 Kuehn, T. H., and Goldstein, R. J., "An Experimental and Theoretical Study of Natural Convection in the Annulus Between Horizontal Concentric Cylinders," *Journal of Fluid Mechanics*, Vol. 74, 1976, pp. 695–719.

5 Kuehn, T. H., and Goldstein, R. J., "Numerical Solution to the Navier-Stokes Equations for Laminar Natural Convection about a Horizontal Isothermal Circular Cylinder," to be published in *International Journal of Heat and Mass Transfer*, 1980.

6 Churchill, S. W., and Chu, H. H. S., "Correlating Equations for Laminar and Turbulent Free Convection from a Horizontal Cylinder," *International Journal of Heat and Mass Transfer*, Vol. 18, 1975, pp. 1049–1053.

7 Powe, R. E., Carley, C. T., and Bishop, E. H., "Free Convective Flow Patterns in Cylindrical Annuli," ASME JOURNAL OF HEAT TRANSFER, Vol. 91, 1969, pp. 310–314.

The Experimental Measurement of Natural Convection Heat Transfer in Triangular Enclosures Heated or Cooled from Below

R. D. Flack[1]

Nomenclature

$\overline{\mathrm{Gr}}$ = Grashof number $g\beta(T_H - T_C)H^3/\nu_m{}^2$
h_U = local heat transfer coefficient along upper-side wall
$\bar{h}_U$ = average heat transfer coefficient along upper-side wall
k = thermal conductivity of air
ℓ = distance between upper and lower walls at a given x
$\overline{\mathrm{Nu}}_U$ = overall Nusselt number, $\bar{h}_U H/k_m$
q'' = heat transfer per unit area (W/m^2)
$\overline{\mathrm{Ra}}$ = Rayleigh number, $\overline{\mathrm{Gr}}\,\mathrm{Pr}_m$
T_m = mean temperature, $(T_H + T_C)/2$
β = volumetric coefficient of expansion, $1/T$
ν = kinematic viscosity

Subscripts

C,H = conditions at the cold and hot walls
CL = evaluated at enclosure centerline
U,L = conditions at the upper and lower walls

Introduction

Previously, many investigators studied free convection in various two-dimensional enclosures; the literature is reviewed in reference [1]. Recently, Flack, et al. [1, 2] studied the heat transfer rates and flow patterns in triangular geometries which were heated and cooled on opposing sides and which had adiabatic floors. These represented attic spaces with solar collectors on one side. However, the results of these studies cannot be readily adapted to conventional attic spaces, i.e., cool roof and heated floor or vice versa. In this paper heat transfer in triangular enclosures was experimentally studied. The geometries were heated or cooled from the bottom. The present geometry, thus, represents the conventional attic space of a house during winter or summer conditions, respectively.

Apparatus, Procedure, and Analysis

The air-filled enclosure was very similar to that used in [1] and

---

[1] Assistant Professor, Department of Mechanical and Aerospace Engineering, University of Virginia, Charlottesville, Va. 22901, Assoc. Mem. ASME.

Contributed by the Heat Transfer Division for publication in the JOURNAL OF HEAT TRANSFER. Manuscript received by the Heat Transfer Division April 9, 1980.

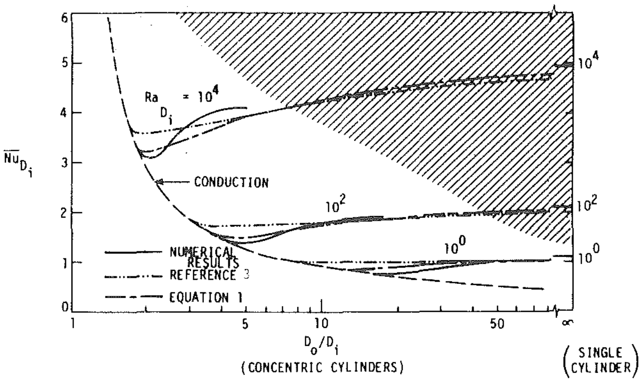

Fig. 3 Influence of diameter ratio on the mean heat transfer coefficient, Pr = 0.7. Shaded area is region of unsteady flow [7].

side of Fig. 3 as $D_o/D_i \to \infty$. Curves from two heat transfer correlations are shown for comparison.

Mean Heat Transfer Correlation

Mean heat transfer correlations have been developed for natural convection between horizontal cylinders using a double boundary layer concept [2, 3]. These correlations are general in scope but require an iterative procedure to solve for the mean temperature between the boundary layers.

The flow recirculation in a cavity causes the heat transfer to increase over what the double boundary layer model predicts. This increase has been incorporated into the model by basing the Rayleigh numbers, Ra_{D_i} and Ra_{D_o}, on the total temperature difference between the cylinders rather than on the temperature difference across the respective boundary layers. This reduces the complexity of the correlation by eliminating the need for iteration. The Prandtl number does not affect the local heat transfer in the outer cylinder boundary layer region nearly as much as for the inner cylinder, so the Prandtl number variation was removed from the correlation for the outer cylinder boundary layer.

The resulting correlation valid for laminar flow is

$$\overline{\mathrm{Nu}}_{D_{i\mathrm{conv}}} = \frac{2}{\ln\left[\dfrac{1+\dfrac{2}{0.518\mathrm{Ra}_{D_i}{}^{1/4}\left[1+\left(\dfrac{0.559}{\mathrm{Pr}}\right)^{3/5}\right]^{-5/12}}}{1-\dfrac{2}{0.587\mathrm{Ra}_{D_o}{}^{1/4}}}\right]} \tag{1a}$$

$$\overline{\mathrm{Nu}}_{D_{i\mathrm{cond}}} = \frac{2}{\ln\,(D_o/D_i)} \tag{1b}$$

$$\overline{\mathrm{Nu}}_{D_i} = (\mathrm{Nu}_{D_{i\mathrm{cond}}}{}^{15} + \mathrm{Nu}_{D_{i\mathrm{conv}}}{}^{15})^{1/15} \tag{1c}$$

When Pr = 0.7, this correlation fits the numerical results at various diameter ratios better than the correlation given in [3] as shown in Fig. 3. The relative minimum heat transfer at a given value of Ra_{D_i} is predicted fairly well, which is important in many engineering applications. The standard deviation between the present correlation and the fifteen numerical solutions over the range of Prandtl number investigated is 8.6 percent with the maximum deviation of 13 percent occurring near Pr = 0.02. Although this does not fit the solutions at various Prandtl numbers as well as the correlation given in [3], equation (1) is recommended when only approximate results are desired.

Acknowledgment

The authors wish to acknowledge the National Science Foundation for support under Grant NSF/ENG-7721626, a grant of computer time from the University of Minnesota Computer Center, an NDEA IV Fellowship for one of the authors (Thomas H. Kuehn), and partial support from the Engineering Research Institute of Iowa State University.

References

1 Powe, R. E., "Bounding Effects on the Heat Loss by Free Convection from Spheres and Cylinders," ASME JOURNAL OF HEAT TRANSFER, Vol. 96, 1974, pp. 558–560.

2 Raithby, G. D., and Hollands, K. G. T., "A General Method of Obtaining Approximate Solutions to Laminar and Turbulent Free Convection Problems," *Advances in Heat Transfer*, Vol. 11, 1975, pp. 265–315.

3 Kuehn, T. H., and Goldstein, R. J., "Correlating Equations for Natural Convection Heat Transfer Between Horizontal Circular Cylinders," *International Journal of Heat and Mass Transfer*, Vol. 19, 1976, pp. 1127–1134.

4 Kuehn, T. H., and Goldstein, R. J., "An Experimental and Theoretical Study of Natural Convection in the Annulus Between Horizontal Concentric Cylinders," *Journal of Fluid Mechanics*, Vol. 74, 1976, pp. 695–719.

5 Kuehn, T. H., and Goldstein, R. J., "Numerical Solution to the Navier-Stokes Equations for Laminar Natural Convection about a Horizontal Isothermal Circular Cylinder," to be published in *International Journal of Heat and Mass Transfer*, 1980.

6 Churchill, S. W., and Chu, H. H. S., "Correlating Equations for Laminar and Turbulent Free Convection from a Horizontal Cylinder," *International Journal of Heat and Mass Transfer*, Vol. 18, 1975, pp. 1049–1053.

7 Powe, R. E., Carley, C. T., and Bishop, E. H., "Free Convective Flow Patterns in Cylindrical Annuli," ASME JOURNAL OF HEAT TRANSFER, Vol. 91, 1969, pp. 310–314.

The Experimental Measurement of Natural Convection Heat Transfer in Triangular Enclosures Heated or Cooled from Below

R. D. Flack[1]

Nomenclature

$\overline{\mathrm{Gr}}$ = Grashof number $g\beta(T_H - T_C)H^3/\nu_m{}^2$
h_U = local heat transfer coefficient along upper-side wall
$\bar{h}_U$ = average heat transfer coefficient along upper-side wall
k = thermal conductivity of air
ℓ = distance between upper and lower walls at a given x
$\overline{\mathrm{Nu}}_U$ = overall Nusselt number, $\bar{h}_U H/k_m$
q'' = heat transfer per unit area (W/m^2)
$\overline{\mathrm{Ra}}$ = Rayleigh number, $\overline{\mathrm{Gr}}\,\mathrm{Pr}_m$
T_m = mean temperature, $(T_H + T_C)/2$
β = volumetric coefficient of expansion, $1/T$
ν = kinematic viscosity

Subscripts

C,H = conditions at the cold and hot walls
CL = evaluated at enclosure centerline
U,L = conditions at the upper and lower walls

Introduction

Previously, many investigators studied free convection in various two-dimensional enclosures; the literature is reviewed in reference [1]. Recently, Flack, et al. [1, 2] studied the heat transfer rates and flow patterns in triangular geometries which were heated and cooled on opposing sides and which had adiabatic floors. These represented attic spaces with solar collectors on one side. However, the results of these studies cannot be readily adapted to conventional attic spaces, i.e., cool roof and heated floor or vice versa. In this paper heat transfer in triangular enclosures was experimentally studied. The geometries were heated or cooled from the bottom. The present geometry, thus, represents the conventional attic space of a house during winter or summer conditions, respectively.

Apparatus, Procedure, and Analysis

The air-filled enclosure was very similar to that used in [1] and

---

[1] Assistant Professor, Department of Mechanical and Aerospace Engineering, University of Virginia, Charlottesville, Va. 22901, Assoc. Mem. ASME.

Contributed by the Heat Transfer Division for publication in the JOURNAL OF HEAT TRANSFER. Manuscript received by the Heat Transfer Division April 9, 1980.

consisted of two constant temperature water tanks for the upper-side walls and another constant temperature water tank for the lower boundary, as shown in Fig. 1(*a*). The ideal enclosure is represented by Fig. 1(*b*).

The upper tanks were connected and water was circulated through the tanks and a reservoir by a centrifugal pump. Water was also circulated through the bottom tank and a second reservoir. The two reservoirs were maintained at constant temperature. One was heated with heating coils, while the second was maintained at room temperature or was filled with ice. When the lower wall was heated, the cool reservoir was maintained at room temperature. The temperatures of the walls were measured with copper constantan thermocouples and were uniform within 0.5°C.

The same three geometries as studied in [1] were examined here. Also, the Wollaston prism schlieren interferometer used by Flack, et al. [1] was utilized to make the heat transfer measurements.

When the lower wall was heated, the upper-side walls were maintained at approximately 20°C. The temperature of the lower wall was then increased from 20°C by 3 to 4°C increments. Eventually, the flow became turbulent due to the large temperature differences. The turbulence became apparent by the randomly fluctuating fringe patterns. Once the flow became turbulent, the tests were terminated.

When the upper walls were heated, two sets of tests were run. First, the lower boundary was maintained at approximately 20°C and second, the lower boundary was maintained at approximately 0°C. Four temperatures were used for the upper walls: approximately 35, 50, 65 and 80°C. When the upper walls were heated, the flow remained stable and laminar for all cases considered.

Analysis of the resulting interferograms has been thoroughly described in [1]. For the total heat transfer rates the uncertainty was typically 8 percent. Also, at worst, 6 percent of the measured heat transfer was lost through the glass end plates.

To complement the heat transfer data, approximate flow patterns were determined for a few of the cases as in [2]. The chamber was uniformly illuminated and the motions of particles were qualitatively observed. Also, the velocities at a few selected points were measured using the laser velocimeter described in reference [2]. The velocity measurements were made primarily to aid in the general understanding of the structure and direction of the flow.

In this paper overall (or average) heat transfer data are reduced and presented. The present data were reduced similarly to data for rectangular enclosures [3,4]. The correlating parameters are defined in the nomenclature. The temperature profiles along the apparatus centerline were also found in the present study.

Results

Cooled from Below. The first condition to be discussed is when the base was cooled and the upper-side walls were heated. For these conditions the flow was always stable and laminar. Typical local heat flux data along one upper-side wall are shown in Fig. 2 for one geometry ($\theta_1 = 45$ deg) and $\overline{\mathrm{Gr}} = 2.84 \times 10^6$. The experimental data are compared to the heat fluxes calculated for simple one-dimensional heat transfer i.e., $q_{1DC}'' = k_m(T_H - T_C)/l$, where l is the distance between the upper and lower walls at any x. For small values of x/L the experimental data agree with the simple theory. For $0.1 \gtrsim x/L \gtrsim 0.3$ the experimental data are typically 30 percent higher than for simple conduction. For $0.5 \gtrsim x/L$ the experimental data are nearly zero and lower than for simple conduction.

Also shown in Fig. 2 is the qualitative flow pattern for the same conditions. It should be noted that the maximum fluid velocities were low (on the order of 10 percent) as compared to those measured in reference [2] for the two upper-side walls heated and cooled. The measured heat transfer rates should not be significantly higher than for simple conduction for such low velocities. This fact is born out in Fig. 2 as the measured rates are, at a maximum, 40 percent higher. For convection dominated flows in enclosures the heat transfer rates are typically 200–1000 percent higher [4]. Similar results were found for other geometries and conditions and results are not presented for the sake of brevity.

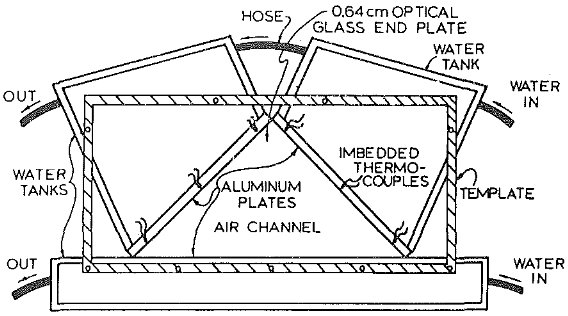

Fig. 1(*a*) Enclosure schematic

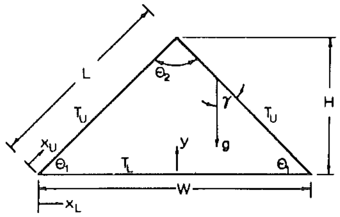

Fig. 1(*b*) Idealized enclosure

Fig. 1 Triangular enclosure apparatus

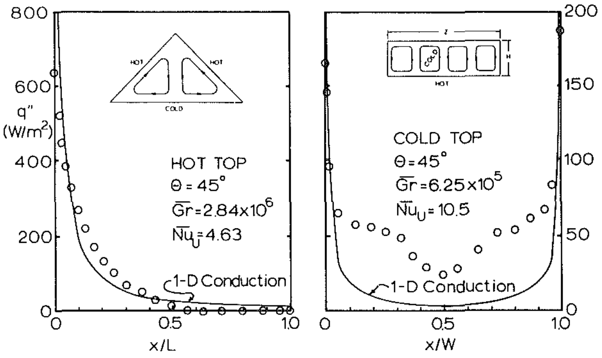

Fig. 2 Typical local heat flux distributions

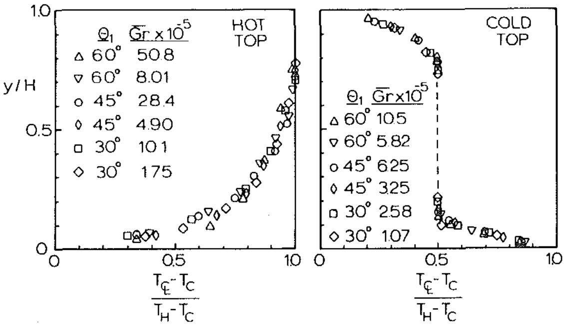

Fig. 3 Typical nondimensionalized centerline temperature profiles

Temperature profiles at the centerline of the enclosure were also found. Typical nondimensionalized results are presented in Fig. 3 for six conditions. All results are nearly identical as shown, regardless of the Grashof number or the geometry. For values of y/H greater than approximately 0.6 the centerline temperature is essentially equal to T_U, which indicates why very low heat transfer rates were measured near the apex; very little driving potential is present near the top.

Reduced heat transfer data is presented in Fig. 4. Included in Fig. 4 are the correlated data presented in reference [1] (with converted parameters) for triangular enclosures with heated and cooled upper-side walls, calculated simple one-dimensional conduction rates, and data for cooled tops/heated bottom (to be discussed in the next subsection). In reference [1] the authors based the nondimensional

Table 1 Transition Grashof numbers

θ_1	$\overline{\mathrm{Gr}}_t \times 10^{-5}$
30 deg	3.01
45 deg	8.88
60 deg	10.5

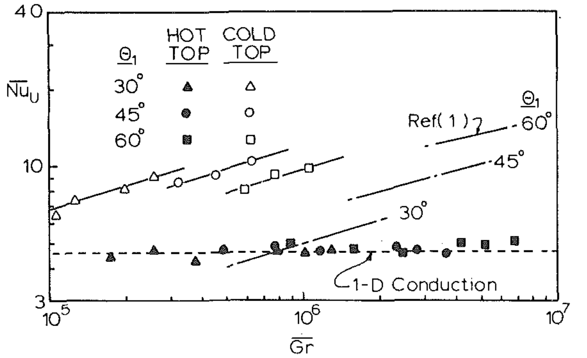

Fig. 4 Nusselt number correlations for triangular enclosures

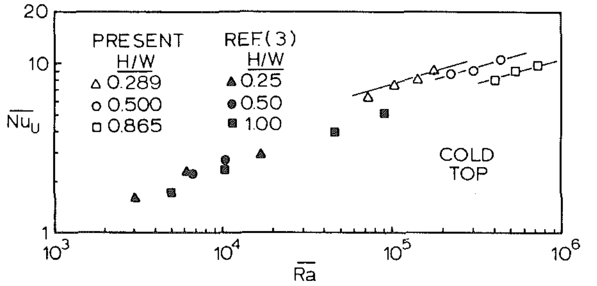

Fig. 5 Comparison of triangular enclosure data (heated from below) to horizontal rectangular enclosure data [3]

parameters on L and included a cosine correction term often used for inclined plates. However, the present geometry is more representative of an air layer between horizontal flat plates than it is of flow over inclined plates. For this reason the nondimensional parameters are based on H and the cosine correction is not included in this paper.

As shown in Fig. 4, very little dependence of the Nusselt number on Grashof number is found, regardless of geometry. These data are compared to the total heat transfer rates calculated for simple one-dimensional conduction. The experimental data are in good agreement with the simple conduction heat transfer and maximum differences are only 10 percent and due primarily to measurement uncertainties.

Heated from Below. The second condition to be discussed is for a heated base and cooled upper-side walls. For these conditions the flow was initially laminar, but as the Grashof number was increased, the flow became turbulent. These transition Grashof numbers are listed in Table 1 for the three geometries considered.

In Fig. 2 typical local heat flux data are presented ($\theta_1 = 45$ deg, $\overline{\mathrm{Gr}} = 6.25 \times 10^5$) for the bottom wall. The data are again compared to fluxes calculated for simple one-dimensional conduction heat transfer. For small values of x/W the experimental data again agree well with the simple theory. For $0.05 \lesssim x/W \lesssim 0.95$ the data are typically 500 percent higher than for simple conduction. This indicates considerable convection occurred.

Qualitative center plane axial flow patterns are also shown in Fig. 2 for the same conditions. Four Bėrnard cells were present while laminar flow existed. Similar flow patterns were observed for the other geometries and Grashof numbers tested here.

Nondimensionalized centerline temperature profiles are presented in Fig. 3. Again results are nearly the same regardless of geometry or Grashof number. Large temperature gradients are present near the top and bottom of the enclosure. For $0.2 \lesssim y/H \lesssim 0.8$ the temperature is nearly constant and equal to T_m.

Table 2 Constants in equation (1)

H/W	θ_1	C_1	C_2
0.289	30 deg	0.22	0.30
0.500	45 deg	0.19	0.30
0.865	60 deg	0.15	0.30

Finally, reduced data are presented in Fig. 4. For this thermal condition, the reduced data are a function of both geometry and Grashof number. The data are curve fitted with an equation of the form

$$\overline{\mathrm{Nu}}_U = C_1\, \overline{\mathrm{Gr}}^{C_2} \qquad (1)$$

For the geometries and ranges in Grashof numbers studied here the values of C_1 and C_2 are summarized in Table 2 and these lines are shown in Fig. 4.

In Fig. 4, the present Nusselt number data are, in general, higher than the data presented in reference [1]. Also, the dependence of $\overline{\mathrm{Nu}}_U$ on θ_1 for the present data is the opposite of what it was in [1]. Namely, presently for a given value of $\overline{\mathrm{Gr}}$, $\overline{\mathrm{Nu}}_U$ increases with decreasing θ_1, while in [1] the Nusselt number decreased. This change in trend is due to the fact that for the present work as θ_1 decreases the average distance between the heated (bottom) and cooled (upper) walls decreases. In reference [1] as θ_1 decreased, the average distance between the heated (one upper-side) wall and the cooled (the other upper-side) wall increased. Thus, the trends of the changing distance between the heated and cooled walls with θ_1 are opposite for the present work and that in [1], which result in opposite trends in the reduced data.

It is interesting to note that the present data for $\theta_1 = 60$ deg corresponds well with data for $\theta_1 = 60$ deg in reference [1] as shown in Fig. 4. For $\theta, = 60$ deg the average distance between the two upper-side walls is the same as between the upper walls and the bottom, since the triangle is equilateral. The flow patterns are significantly different for the two geometries, however. Bėrnard cells existed for the present data, but were absent in [1]. Thus, the similarity between the two sets of data is encouraging, but generalizing the similarity as a function of the average distance between the heated and cooled surface is not possible without further studies for larger value of θ_1.

Data were also correlated as in [1], but is not presented for the sake of brevity. Different constants were found for equation (1), but they were still dependent on θ_1.

In Fig. 5 the present triangular enclosure data are compared to horizontal rectangular enclosure data (heated from below) [3]. Ozoe, et al. [3] tested several aspect ratios with silicone oil for Rayleigh numbers from 3×10^3 to 10^5. The present data ($\overline{\mathrm{Ra}} > 7.5 \times 10^4$) are in good qualitative agreement with the data in reference [3]. The results for the rectangular enclosures are seen to be minimally dependent on the aspect ratio, although it appears that data for small aspect ratios ($H/W = 0.25$) are slightly higher than for data with $H/W = 1.00$ (by approximately 15 percent at $\overline{\mathrm{Ra}} = 10^4$). The present data follow the same trend only the the dependence of $\overline{\mathrm{Nu}}_U$ on H/W is stronger for the present data due the different geometry (approximately 45 percent variation in C_1).

Acknowledgment

This research was sponsored in part by the National Science Foundation under grant No. SER78-00201.

References

1 Flack, R. D., Konopnicki, T. T., and Rooke, J. H., "The Measurement of Natural Convective Heat Transfer in Triangular Enclosures," ASME JOURNAL OF HEAT TRANSFER, Vol. 101, No. 4, Nov. 1979, pp. 648–654.

2 Flack, R. D., and Witt, C. L., "Velocity Measurements in Two Natural Convection Air Flows Using a Laser Velocimeter," ASME JOURNAL OF HEAT TRANSFER, Vol. 101, No. 2, May 1979, pp. 256–260.

3 Ozoe, H., Sayama, H., and Churchill, S. W., "Natural Convection in an Inclined Rectangular Channel at Various Aspect Ratios and Angles-Experimental Measurements," *Int. J. of Heat Mass Transfer,* Vol. 18, No. 12, Dec. 1975, pp. 1425–1431.

4 MacGregor, R. K., and Emergy, H. A., "Free Convection Through Vertical Plane Layers-Moderate and High Prandtl Number Fluids," ASME JOURNAL OF HEAT TRANSFER, Vol. 91, 1969, pp. 391–403.

Turbulent Natural Convection at High Prandtl Numbers

E. Ruckenstein[1] and J. D. Felske[1]

Nomenclature

c_p = specific heat
g = gravitational acceleration
h = heat transfer coefficient
k = thermal conductivity
ℓ = characteristic length
q_0 = heat flux at the wall
T = mean temperature
T_0, T_∞ = wall and ambient temperatures
T' = fluctuation of temperature
u,v = x and y components of mean velocity
u', v' = fluctuations of the x and y velocity components
u^* = scaling velocity
x = coordinate along the plate
y = distance from the surface
α = thermal diffusivity
β = coefficient of thermal expansion
ϵ_h = eddy diffusivity for heat
ν = kinematic viscosity
ρ = density of the fluid
τ_0 = wall shear stress
Pr = Prandtl number
Nu_ℓ = Nusselt number
Gr*, Gr = Grashof numbers defined by equations (22) and (24)

Introduction

The phenomenon of turbulent natural convection near a heated vertical surface has been the subject of many experimental, theoretical, and computational studies. The theoretical and computational studies have employed a variety of approaches. The first analytical study was made by Eckert and Jackson [1] using the integral technique with temperature and velocity profiles appropriate to the natural convective flow. Bayley [2] and Kato, et al. [3] postulated the variations of the eddy diffusivities with distance from the plate and then performed integrations across the boundary layer. Noto and Matsumoto [4] used the concept of local similarity and the eddy diffusivity expression of Kato, et al. [3] to numerically integrate the resulting one dimensional equation. Cebeci and Khattab [5] carried out a "similarity" transformation, retained the nonsimilar terms and assumed distributions for the eddy diffusivity for momentum and for the turbulent Prandtl number in performing their numerical computations. George and Capp [6] used scaling arguments and the method of matched asymptotic expansions, to derive analytical expressions for the velocity and temperature distributions in an intermediate sublayer as well as asymptotic heat transfer and friction laws. The boundary layer equations were directly programmed and numerically solved by Mason and Seban [7] using a mixing length model for the eddy diffusivity and by Plumb and Kennedy [8] and Lin and Churchill [9] using turbulent kinetic energy (K-ϵ) models.

Predictions for a wide range of Prandtl numbers may be generated from these latter numerical techniques. However, physical insight into the transport processes may easily be lost in an approach to the problem which is purely numerical. Hence, it is desireable to obtain analytical results which possess a theoretically sound foundation even if such results can only be obtained for limiting cases. For large Prandtl numbers, simple analytical expressions for the heat transfer coefficient have been derived for various geometries in laminar and turbulent forced convection and also in laminar natural convection. The goal of our present work is to derive an analytical expression for the heat transfer coefficient for a high Prandtl number fluid in turbulent natural convection adjacent to a heated vertical surface. As in all the analytical and numerical studies, a turbulence closure model is required. We will use the concept of eddy diffusivity and borrow a scaling law from forced turbulent convection.

Governing Equations

The time-averaged boundary layer equations for the conservation of mass, momentum and energy are given under the Boussinesq approximation as

$$\frac{\partial u}{\partial x} + \frac{\partial v}{\partial y} = 0 \tag{1}$$

$$u\frac{\partial u}{\partial x} + v\frac{\partial u}{\partial y} = \frac{\partial}{\partial y}\left(\nu\frac{\partial u}{\partial y} - \overline{u'v'}\right) + g\beta(T - T_\infty) \tag{2}$$

$$u\frac{\partial T}{\partial x} + v\frac{\partial T}{\partial y} = \frac{\partial}{\partial y}\left(\alpha\frac{\partial T}{\partial y} - \overline{v'T'}\right) \tag{3}$$

where the primed variables are fluctuating quantities and the unprimed are time averaged. The overbar denotes, as usual, the time average.

When the Prandtl number is large, the thermal layer will be much thinner than the hydrodynamic layer. In addition, as in laminar natural convective flows, the edge of the thermal layer will be much closer to the wall than the point of maximum velocity. Therefore, within this layer the convective transport of heat and momentum will be small compared to the transport by molecular and eddy diffusion. Then, from equation (3), the heat flux is seen to be constant across the thermal layer and is given by

$$q_0/\rho c_p = -\alpha\frac{\partial T}{\partial y} + \overline{v'T'} \tag{4}$$

By introducing the eddy diffusivity for heat

$$\epsilon_h(y) = \frac{-\overline{v'T'}}{\partial T/\partial y} \tag{5}$$

the temperature distribution may be determined by integration to be

$$T(y) - T_0 = -\frac{q_0}{\rho c_p \alpha}\int_0^y \frac{dy}{1 + \text{Pr}\dfrac{\epsilon_h(y)}{\nu}} \tag{6}$$

For large Prandtl numbers, the integrand in the above expression is significantly different from zero only near the surface—where ϵ_h/ν is very small. Outside the thermal layer the integrand is negligible. Therefore $(T_0 - T_\infty)$ may be determined by letting $y \to \infty$ in the above expression while retaining for ϵ_h/ν the expression valid very near the wall. Using this result for $(T_0 - T_\infty)$, the Nusselt number may then be written as

$$\text{Nu}_\ell = \frac{q_0}{(T_0 - T_\infty)}\frac{\ell}{k} = \left[\frac{1}{\ell}\int_0^\infty \left[\frac{dy}{1 + \text{Pr}\dfrac{\epsilon_h(y)}{\nu}}\right]\right]^{-1} \tag{7}$$

where ℓ is an arbitrary reference length and $\epsilon_h(y)$ is the thermal eddy diffusivity distribution in the region very close to the wall.

The Eddy Diffusivity Near the Wall

The determination of the heat transfer coefficient from equation (7) requires first an expression for $\epsilon_h(y)$ appropriate to the near wall region. The variation of the eddy diffusivity for heat in this region may be determined from equation (5) by expanding both $\overline{v'T'}$ and $\partial T/\partial y$ in Taylor series and then dividing. The value of the correlation itself $(\overline{v'T'})$ is zero at the surface. Its first two derivatives

$$\frac{\partial\overline{v'T'}}{\partial y} = \overline{v'\frac{\partial T'}{\partial y}} + \overline{T'\frac{\partial v'}{\partial y}} \tag{8}$$

$$\frac{\partial^2\overline{v'T'}}{\partial y^2} = \overline{v'\frac{\partial^2 T'}{\partial y^2}} + 2\,\overline{\frac{\partial v'}{\partial y}\frac{\partial T'}{\partial y}} + \overline{T'\frac{\partial^2 v'}{\partial y^2}} \tag{9}$$

---

[1] Faculty of Engineering and Applied Science, State University of New York at Buffalo, Amherst, NY 14260.

Contributed by the Heat Transfer Division for publication in the JOURNAL OF HEAT TRANSFER. Manuscript received by the Heat Transfer Division April 2, 1980.

are also seen to be zero at that point since, from the turbulent continuity equation:

$$\left.\frac{\partial v'}{\partial y}\right|_0 = -\left.\frac{\partial u'}{\partial x}\right|_0 - \left.\frac{\partial w'}{\partial z}\right|_0 = 0 \qquad (10)$$

Taking the third derivative and evaluating it at $y = 0$ with the use of equation (10) yields

$$\left.\frac{\partial^3(\overline{v'T'})}{\partial y^3}\right|_0 = 3\left.\overline{\frac{\partial T'}{\partial y}\frac{\partial^2 v'}{\partial y^2}}\right|_0 \qquad (11)$$

Hence the expansion for $\overline{v'T'}$ begins with the third order term (just as for forced flows [10])

$$\overline{v'T'} = \frac{1}{2}\left.\left(\overline{\frac{\partial T'}{\partial y}\frac{\partial^2 v'}{\partial y^2}}\right)\right|_0 y^3 + \ldots \qquad (12)$$

In the expansion for the temperature distribution, $(\partial T/\partial y)_0 = -q_o/k$ by definition and $(\partial^2 T/\partial y^2)_0 = 0$ from equation (3) applied at the surface. By differentiating the energy equation and evaluating it at the surface it results that $(\partial^3 T/\partial y^3)_0 = (\tau_o/\alpha\mu) dT_o/dx$. Hence, the expansion for the temperature gradient becomes

$$\frac{\partial T}{\partial y} = -(q_o/k) + \left(\frac{1}{2\alpha}\frac{\tau_o}{\mu}\frac{dT_o}{dx}\right)y^2 + \ldots \qquad (13)$$

Again, the results have the same form as for forced flows.

Substituting equations (12) and (13) into equation (5) and expressing the result in terms of dimensionless variables, the variation of the eddy diffusivity near the surface may be written as

$$\epsilon_h/\nu = \gamma y^{+3} \qquad (14)$$

in which γ is at most a function of the Prandtl number, $y^+ = yu^*/\nu$ and u^* is a scaling velocity. If it is now assumed that the shear velocity based on the wall shear stress $\sqrt{\tau_o/\rho}$ is the appropriate scaling velocity in the near wall region, then

$$y^+ = y\sqrt{\tau_o/\rho}/\nu \qquad (15)$$

and the thermal eddy diffusivity in the natural convective flow then has the same form near the wall as it does in forced flows.

For large Prandtl numbers it is reasonable to assume that γ is constant. This is equivalent to assuming that the turbulent Prandtl number is independent of the molecular Prandtl number. Such an approximation, however, has been found acceptable for the prediction of heat transfer coefficients for large Prandtl numbers [11]. In the computations and comparisons at the end of the note it will be assumed that $\gamma = 6.8 \times 10^{-4}$, the value indicated by Kato, et al. [3]. Derivation of the following results, however, only requires that γ be independent of y^+.

The Heat Transfer Coefficient

Using the above distribution for the eddy diffusivity, the temperature distribution may then be determined from equation (6) as

$$T(y) - T_o = -\frac{q_o}{\rho c_p \alpha}\frac{p}{3}\left\{\frac{1}{2}\ell n\left[\frac{(y+p)^3}{y^3+p^3}\right] + \sqrt{3}\tan^{-1}\left(\frac{2y-p}{p\sqrt{3}}\right) + \frac{\pi\sqrt{3}}{6}\right\} \qquad (16)$$

where

$$p = \frac{\nu/\sqrt{\tau_o/\rho}}{(\gamma \mathrm{Pr})^{1/3}} \qquad (17)$$

The above temperature distribution is of the same form as the concentration distribution near a wall determined by Lin, et al. [12] in their investigation of mass transfer in turbulent forced flows in a tube. (They had also taken $\epsilon \sim y^3$ near the wall.)

Using equation (16) in the limit $y \to \infty$, the Nusselt number may be determined from equation (7) as

$$\mathrm{Nu}_\ell = \frac{3\sqrt{3}}{2\pi}\frac{\sqrt{\tau_o/\rho}\,\ell}{\nu}(\gamma \mathrm{Pr})^{1/3} \qquad (18)$$

Since the near wall eddy diffusivity expression, equation (14), is valid for both forced and natural convection and since the assumption of a constant heat flux across the thermal layer is valid in either case at large Prandtl numbers, the above expression for the Nusselt number applies equally to forced and natural flows alike (as long as the Prandtl number is very large). It is only the relationship between the shear stress and the characteristic flow velocity which differs. In a forced flow the shear stress is related to either the free stream velocity (for boundary layer flows) or to the average velocity (for the flow in a pipe) and can be determined without consideration of the energy equation. For natural convective flows, Eckert and Jackson [1] assumed that the dependency of the wall shear stress on the characteristic velocity and layer thickness was the same as in forced flows. In the present study, however, a shear stress relation need not be assumed. On the contrary, a relationship between the shear stress and the heat flux can be derived as follows.

For the large Prandtl number fluids under consideration here, the temperature distribution is derived directly from the energy equation and expressed in terms of the unknown wall shear stress (equation (16)). With this temperature distribution, the shear stress may then be determined by integrating the momentum equation, equation (2), across the full extent of the flow with the result

$$\frac{\tau_o}{\rho} = \int_0^\infty g\beta(T - T_\infty)dy - \frac{d}{dx}\int_0^\infty u^2\,dy \qquad (19)$$

Far from the leading edge the flow becomes developed and the profiles no longer change with distance. In this region the acceleration of the fluid is negligible and the momentum equation becomes a simple balance between viscous and buoyant forces

$$\frac{\tau_o}{\rho} = \int_0^\infty g\beta(T - T_\infty)dy \qquad (20)$$

Then, substituting the temperature distribution from equation (16), the shear stress is found to be related to the heat flux by

$$\frac{\tau_o}{\rho} = \left(\frac{\pi}{6\sqrt{3}}\right)^{1/2}\left[\frac{g\beta(q_o/\rho c_p)}{\alpha}\right]^{1/2}\frac{\nu}{(\gamma \mathrm{Pr})^{1/3}} \qquad (21)$$

Substituting this into equation (18), the Nusselt number is thereby given by

$$\mathrm{Nu}_\ell = \left(\frac{3\sqrt{3}}{2\pi}\right)^{3/4}(\gamma \mathrm{Pr})^{1/6}\,\mathrm{Gr}_\ell{}^{*1/4} \qquad (22)$$

where

$$\mathrm{Gr}_\ell^* = \frac{g\beta(q_o/\rho c_p)\ell^4}{\alpha\nu^2} \qquad (22)$$

The above equation can also be written as

$$\mathrm{Nu}_\ell = \left(\frac{3\sqrt{3}}{2\pi}\right)(\gamma \mathrm{Pr})^{2/9}\,\mathrm{Gr}_\ell{}^{1/3} \qquad (23)$$

where

$$\mathrm{Gr}_\ell = \frac{g\beta(T_o - T_\infty)\ell^3}{\nu^2} \qquad (24)$$

Comparison to Numerical Studies

Using the value for γ which Kato, et al. [3] have indicated ($\gamma = 6.8 \times 10^{-4}$) the Nusselt number in the limit of large Prandtl numbers becomes

$$\mathrm{Nu}_\ell = 0.164\,\mathrm{Pr}^{2/9}\mathrm{Gr}_\ell{}^{1/3} \qquad (25)$$

where it should be recalled that ℓ is an arbitrary reference length and may, for example, be taken as the length of the plate L or the distance from the leading edge x. The above theoretical result may be compared directly to the numerical solutions given by Kato, et al. [3] and Noto and Matsumoto [4]. However, a meaningful comparison with experimental data (such as those of Fujii, et al. [13]) is not possible since the fluids used in those experiments have highly variable properties.

Table 1 Nusselt numbers predicted by equation (27), by Kato, et al. [3] and by Noto and Matsumoto [4]

		Nu_x		
Pr	Gr_x	Fig. 5 of reference [4]	Present equation (27)	Fig. 4 of reference [3]
10^2	10^8		211	200
	10^{10}	940	980	1050
	10^{12}		4551	5450
10^3	10^8		352	345
	10^{10}	1560	1635	1650
	10^{12}		7591	8400
10^4	10^8		588	570
	10^{10}	2580	2728	2800
	10^{12}		12662	13700

In Table 1 the Nusselt numbers predicted by equation (25) are compared with the numerical results presented in Fig. 4 of Kato, et al. [3] and also with the numerical results presented in Fig. 5 of Noto and Matsumoto [4] (available only for $Gr_x = 10^{10}$). The results of the present closed form theoretical solution are seen to be in excellent agreement with the two numerical studies.

References

1 Eckert, E. R. G., and Jackson, T. W., "Analysis of Turbulent Free Convection Boundary Layer on a Flat Plate," NACA Tech. Note 2207, 1950.

2 Bayley, F. J., "An Analysis of Turbulent Free-Convection Heat Transfer," *Proceedings of the Institute of Mechanical Engineers*, Vol. 169, No. 20, 1955, pp. 361–368.

3 Kato, H., Nishiwaki, M., and Hirata, M., "On the Turbulent Heat Transfer by Free Convection from a Vertical Plate," *International Journal of Heat and Mass Transfer*, Vol. 11, 1968, pp. 1117–1125.

4 Noto, K., and Matsumoto, R., "Turbulent Heat Transfer by Natural Convection Along an Isothermal Vertical Flat Surface," ASME JOURNAL OF HEAT TRANSFER, Vol. 97, 1975, pp. 621–624.

5 Cebeci, T. and Khattab, A., "Prediction of Turbulent Free-Convective Heat Transfer from a Vertical Flat Plate," ASME JOURNAL OF HEAT TRANSFER, Vol. 97, 1975, pp. 469–471.

6 George, W. K., and Capp, S. P., "A Theory for Natural Convection Turbulent Boundary Layers Next to Heated Vertical Surfaces," *International Journal of Heat and Mass Transfer*, Vol. 22, 1979, pp. 813–826.

7 Mason, H. B., and Seban, R. A., "Numerical Predictions for Turbulent Free Convection from Vertical Surfaces," *International Journal of Heat and Mass Transfer*, Vol. 17, 1974, pp. 1329–1336.

8 Plumb, O. A., and Kennedy, L. A., "Application of a K-ε Turbulence Model to Natural Convection from a Vertical Isothermal Surface," ASME JOURNAL OF HEAT TRANSFER, Vol. 99, 1977, pp. 79–85.

9 Lin, S. J. and Churchill, S. W., "Turbulent Free Convection from a Vertical, Isothermal Plate," *Numerical Heat Transfer*, Vol. 1, 1978, pp. 129–145.

10 Tien, C. L., "A Note on Distributions of Temperature and Eddy Diffusivities for Heat in Turbulent Flow Near a Wall," *Zeitschrift fuer Angewandte Mathematik und Physik*, Vol. 15, 1964, pp. 63–66.

11 Azer, N. Z. and Chao, B. T., "A Mechanism of Turbulent Heat Transfer in Liquid Metals," *International Journal of Heat and Mass Transfer*, Vol. 1, 1960, pp. 121–138.

12 Lin, C. S., Moulton, R. W. and Putnam, G. L., "Mass Transfer Between Solid Wall and Fluid Streams," *Industrial and Engineering Chemistry*, Vol. 45, 1953, pp. 636–640.

13 Fujii, T., Takeuchi, M., Fujii, M., Suzaki, K. and Uehara, H., "Experiments on Natural Convection Heat Transfer from the Outer Surface of a Vertical Cylinder to Liquids," *International Journal of Heat and Mass Transfer*, Vol. 13, 1970, pp. 753–787.

Mixed Convection about a Vertical Surface in Cross-Flow: a Similarity Solution

R. Eichhorn[1] and M. M. Hasan[2]

Nomenclature

g = gravitational acceleration
h = heat transfer coefficient
Gr_z = Grashof Number, $g\beta|T_w - T_\infty|z^3/\nu$
Nu_x = Nusselt number, hx/k
Re_x = Reynolds number, Ux/ν; $U = u_1 x^m$
T = Temperature, $T_w - T_\infty = Nz^n$
u, v, w = velocities in (x, y, z) directions, respectively
x, y, z = coordinate system
γ = angle of wedge vertex to vertical
ξ_x, ξ_z = dimensionless coordinates
$\xi = \xi_x/\xi_z$
ϕ, Ψ = stream functions

Introduction

There has been relatively little work published on problems in which buoyancy acts along a surface in a direction that makes an angle with the direction of a forced flow [1–5]. The present paper presents an analytical study of a combined forced and free convection boundary layer problem with the two flows perpendicular to each other. The problem is formulated for flow over a wedge. Numerical computations were made for a forced flow arising from a two-dimensional stagnation line and a free convection flow arising from a surface temperature that varies linearly with the vertical coordinate. Results are presented for Pr = 0.7 and 6 over a range that varies from forced flow dominant to free convection dominant.

Analysis

Consider a wedge of opening angle $\pi\beta$ whose vertex lies in a vertical plane and makes an angle γ with the vertical coordinate. We assume a Falkner-Skan type of forced flow over the surface of the wedge and a free convection flow in the vertical direction. The equations of motion are relatively simple and admit a similarity solution where either $\gamma = 0$ or $\pi/2$, so our attention will be restricted to these two cases. Figure 1 shows the two flows considered. In each case the x coordinate is measured along the wedge from the vertex in the direction in which the forced flow occurs. The y coordinate is normal to the surface. The wall temperature is allowed to vary only in the vertical direction: i.e., in the z direction in case a ($\gamma = 0$) and in the x direction in case b ($\gamma = \pi/2$).

The case $\gamma = \pi/2$ has been considered by Sparrow, et al. [6] for uniform wall temperature and uniform wall heat flux distributions ($\beta = 2/3$ and 3/4, respectively) and by Gunness and Gebhart [7] who also included the normal pressure gradient effect.

The boundary layer equations for the case $\gamma = \pi/2$ are given in [6] and [7] with g_x of [6] replaced by gsin $(\pi\beta/2)$. For the case $\gamma = 0$, they are given by

$$\frac{\partial u}{\partial x} + \frac{\partial v}{\partial y} + \frac{\partial w}{\partial z} = 0 \tag{1}$$

$$u\frac{\partial u}{\partial x} + v\frac{\partial u}{\partial y} + w\frac{\partial u}{\partial z} = U\frac{dU}{dx} + \nu\frac{\partial^2 u}{\partial y^2} \tag{2}$$

$$u\frac{\partial w}{\partial x} + v\frac{\partial w}{\partial y} + w\frac{\partial w}{\partial z} = \nu\frac{\partial^2 w}{\partial y^2} + g\beta(T - T_\infty) \tag{3}$$

$$u\frac{\partial T}{\partial x} + v\frac{\partial T}{\partial y} + w\frac{\partial T}{\partial z} = \alpha\frac{\partial^2 T}{\partial y^2} \tag{4}$$

The boundary conditions for equations (1) to (4) are

$$\begin{gathered} u = v = w = 0,\ T = T_w \text{ at } y = 0 \\ u \to U,\ w \to 0,\ T \to T_\infty \text{ as } y \to \infty \end{gathered} \tag{5}$$

For the $\gamma = 0$ case, two stream functions Ψ and ϕ may be defined to cope with the three dimensional flow [8]

$$u = \frac{\partial \psi}{\partial y},\ v = -\frac{\partial \psi}{\partial x} - \frac{\partial \phi}{\partial z} \text{ and } w = \frac{\partial \phi}{\partial y} \tag{6}$$

The following substitutions transform the (x, y, z) coordinates to (ξ_x,

---

[1] Dean of Engineering, University of Kentucky, Lexington, Ky. Fellow ASME.

[2] Research Assistant, Department of Mechanical Engineering, University of Kentucky, Lexington, Ky. Student Mem. ASME.

Contributed by the Heat Transfer Division for publication in the JOURNAL OF HEAT TRANSFER. Manuscript received by the Heat Transfer Division January 23, 1980.

Table 1 Nusselt numbers predicted by equation (27), by Kato, et al. [3] and by Noto and Matsumoto [4]

Pr	Gr_x	Nu_x Fig. 5 of reference [4]	Present equation (27)	Fig. 4 of reference [3]
	10^8		211	200
10^2	10^{10}	940	980	1050
	10^{12}		4551	5450
	10^8		352	345
10^3	10^{10}	1560	1635	1650
	10^{12}		7591	8400
	10^8		588	570
10^4	10^{10}	2580	2728	2800
	10^{12}		12662	13700

In Table 1 the Nusselt numbers predicted by equation (25) are compared with the numerical results presented in Fig. 4 of Kato, et al. [3] and also with the numerical results presented in Fig. 5 of Noto and Matsumoto [4] (available only for $Gr_x = 10^{10}$). The results of the present closed form theoretical solution are seen to be in excellent agreement with the two numerical studies.

References

1 Eckert, E. R. G., and Jackson, T. W., "Analysis of Turbulent Free Convection Boundary Layer on a Flat Plate," NACA Tech. Note 2207, 1950.

2 Bayley, F. J., "An Analysis of Turbulent Free-Convection Heat Transfer," *Proceedings of the Institute of Mechanical Engineers,* Vol. 169, No. 20, 1955, pp. 361–368.

3 Kato, H., Nishiwaki, M., and Hirata, M., "On the Turbulent Heat Transfer by Free Convection from a Vertical Plate," *International Journal of Heat and Mass Transfer,* Vol. 11, 1968, pp. 1117–1125.

4 Noto, K., and Matsumoto, R., "Turbulent Heat Transfer by Natural Convection Along an Isothermal Vertical Flat Surface," ASME JOURNAL OF HEAT TRANSFER, Vol. 97, 1975, pp. 621–624.

5 Cebeci, T. and Khattab, A., "Prediction of Turbulent Free-Convective Heat Transfer from a Vertical Flat Plate," ASME JOURNAL OF HEAT TRANSFER, Vol. 97, 1975, pp. 469–471.

6 George, W. K., and Capp, S. P., "A Theory for Natural Convection Turbulent Boundary Layers Next to Heated Vertical Surfaces," *International Journal of Heat and Mass Transfer,* Vol. 22, 1979, pp. 813–826.

7 Mason, H. B., and Seban, R. A., "Numerical Predictions for Turbulent Free Convection from Vertical Surfaces," *International Journal of Heat and Mass Transfer,* Vol. 17, 1974, pp. 1329–1336.

8 Plumb, O. A., and Kennedy, L. A., "Application of a K-ε Turbulence Model to Natural Convection from a Vertical Isothermal Surface," ASME JOURNAL OF HEAT TRANSFER, Vol. 99, 1977, pp. 79–85.

9 Lin, S. J. and Churchill, S. W., "Turbulent Free Convection from a Vertical, Isothermal Plate," *Numerical Heat Transfer,* Vol. 1, 1978, pp. 129–145.

10 Tien, C. L., "A Note on Distributions of Temperature and Eddy Diffusivities for Heat in Turbulent Flow Near a Wall," *Zeitschrift fuer Angewandte Mathematik und Physik,* Vol. 15, 1964, pp. 63–66.

11 Azer, N. Z. and Chao, B. T., "A Mechanism of Turbulent Heat Transfer in Liquid Metals," *International Journal of Heat and Mass Transfer,* Vol. 1, 1960, pp. 121–138.

12 Lin, C. S., Moulton, R. W. and Putnam, G. L., "Mass Transfer Between Solid Wall and Fluid Streams," *Industrial and Engineering Chemistry,* Vol. 45, 1953, pp. 636–640.

13 Fujii, T., Takeuchi, M., Fujii, M., Suzaki, K. and Uehara, H., "Experiments on Natural Convection Heat Transfer from the Outer Surface of a Vertical Cylinder to Liquids," *International Journal of Heat and Mass Transfer,* Vol. 13, 1970, pp. 753–787.

Mixed Convection about a Vertical Surface in Cross-Flow: a Similarity Solution

R. Eichhorn[1] **and M. M. Hasan**[2]

Nomenclature

g = gravitational acceleration
h = heat transfer coefficient
Gr_z = Grashof Number, $g\beta|T_w - T_\infty|z^3/\nu$
Nu_x = Nusselt number, hx/k
Re_x = Reynolds number, $Ux/\nu;\ U = u_1x^m$
T = Temperature, $T_w - T_\infty = Nz^n$
u, v, w = velocities in (x, y, z) directions, respectively
x, y, z = coordinate system
γ = angle of wedge vertex to vertical
ξ_x, ξ_z = dimensionless coordinates
$\xi = \xi_x/\xi_z$
ϕ, Ψ = stream functions

Introduction

There has been relatively little work published on problems in which buoyancy acts along a surface in a direction that makes an angle with the direction of a forced flow [1–5]. The present paper presents an analytical study of a combined forced and free convection boundary layer problem with the two flows perpendicular to each other. The problem is formulated for flow over a wedge. Numerical computations were made for a forced flow arising from a two-dimensional stagnation line and a free convection flow arising from a surface temperature that varies linearly with the vertical coordinate. Results are presented for Pr = 0.7 and 6 over a range that varies from forced flow dominant to free convection dominant.

Analysis

Consider a wedge of opening angle $\pi\beta$ whose vertex lies in a vertical plane and makes an angle γ with the vertical coordinate. We assume a Falkner-Skan type of forced flow over the surface of the wedge and a free convection flow in the vertical direction. The equations of motion are relatively simple and admit a similarity solution where either $\gamma = 0$ or $\pi/2$, so our attention will be restricted to these two cases. Figure 1 shows the two flows considered. In each case the x coordinate is measured along the wedge from the vertex in the direction in which the forced flow occurs. The y coordinate is normal to the surface. The wall temperature is allowed to vary only in the vertical direction: i.e., in the z direction in case a ($\gamma = 0$) and in the x direction in case b ($\gamma = \pi/2$).

The case $\gamma = \pi/2$ has been considered by Sparrow, et al. [6] for uniform wall temperature and uniform wall heat flux distributions ($\beta = 2/3$ and $3/4$, respectively) and by Gunness and Gebhart [7] who also included the normal pressure gradient effect.

The boundary layer equations for the case $\gamma = \pi/2$ are given in [6] and [7] with g_x of [6] replaced by gsin $(\pi\beta/2)$. For the case $\gamma = 0$, they are given by

$$\frac{\partial u}{\partial x} + \frac{\partial v}{\partial y} + \frac{\partial w}{\partial z} = 0 \tag{1}$$

$$u\frac{\partial u}{\partial x} + v\frac{\partial u}{\partial y} + w\frac{\partial u}{\partial z} = U\frac{dU}{dx} + \nu\frac{\partial^2 u}{\partial y^2} \tag{2}$$

$$u\frac{\partial w}{\partial x} + v\frac{\partial w}{\partial y} + w\frac{\partial w}{\partial z} = \nu\frac{\partial^2 w}{\partial y^2} + g\beta(T - T_\infty) \tag{3}$$

$$u\frac{\partial T}{\partial x} + v\frac{\partial T}{\partial y} + w\frac{\partial T}{\partial z} = \alpha\frac{\partial^2 T}{\partial y^2} \tag{4}$$

The boundary conditions for equations (1) to (4) are

$$\begin{gathered} u = v = w = 0,\ T = T_w \text{ at } y = 0 \\ u \to U,\ w \to 0,\ T \to T_\infty \text{ as } y \to \infty \end{gathered} \tag{5}$$

For the $\gamma = 0$ case, two stream functions Ψ and ϕ may be defined to cope with the three dimensional flow [8]

$$u = \frac{\partial \psi}{\partial y},\ v = -\frac{\partial \psi}{\partial x} - \frac{\partial \phi}{\partial z} \text{ and } w = \frac{\partial \phi}{\partial y} \tag{6}$$

The following substitutions transform the (x, y, z) coordinates to $(\xi_x,$

---

[1] Dean of Engineering, University of Kentucky, Lexington, Ky. Fellow ASME.

[2] Research Assistant, Department of Mechanical Engineering, University of Kentucky, Lexington, Ky. Student Mem. ASME.

Contributed by the Heat Transfer Division for publication in the JOURNAL OF HEAT TRANSFER. Manuscript received by the Heat Transfer Division January 23, 1980.

$\xi_z, \eta(x, y)$), for a free stream velocity and wall temperature that vary according to the power laws $U = u_1 x^m$ and $T_w - T_\infty = Nz^n$

$$\eta = (u_1/\nu)^{1/2} x^{(m-1)/2} y = \mathrm{Re}_x{}^{1/2} y/x$$
$$\xi_x = (\nu/u_1)^{1/2} x^{(1-m)/2} = x/\mathrm{Re}_x{}^{1/2} \tag{7}$$
$$\xi_x = z^{(1-n)/4}/C = z/(\mathrm{Gr}_z/4)^{1/4}$$

In addition, dimensionless stream functions $F(\xi_x, \xi_z, \eta)$, $G(\xi_x, \xi_z, \eta)$ and a temperature function $H(\xi_x, \xi_z, \eta)$ are defined as

$$F = \psi/(u_1 \nu)^{1/2} x^{(m+1)/2} \tag{8}$$
$$G = \phi/4\nu C z^{(n+3)/4} \tag{9}$$
$$H = (T - T_\infty)/(T_w - T_\infty) = (T - T_\infty)/Nz^n \tag{10}$$
$$\text{where } C = (g\beta |N|/4\nu^2)^{1/4} \tag{11}$$

The absolute value of N is used in equation (11) to permit consideration of wall temperatures that are higher ($N > 0$) or lower ($N < 0$) than the ambient temperature.

Introducing (6) to (10) in equations (2) to (4), we obtain, for $N > 0$,

$$F''' + \left(\frac{m+1}{2}\right) FF'' + m(1 - F'^2) + \frac{\xi_x}{\xi_z}(n+3)F''G = \left(\frac{1-m}{2}\right)\xi_x(F'F'_{\xi_x} - F''F_{\xi_x}) + \xi_x(1-n)(G'F'_{\xi_z} - F''G_{\xi_z}) \tag{12}$$

$$G''' - \left(\frac{m-1}{2}\right) F'G' + \left(\frac{m+1}{2}\right) FG'' + \frac{\xi_x}{\xi_z}(n+3)(GG'' - G'^2) + \left(\frac{\xi_x}{\xi_z}\right)^3 H = \left(\frac{1-m}{2}\right)\xi_x(F'G'_{\xi_x} - G''F_{\xi_x}) + (n-1)\xi_x(G''G_{\xi_z} - G'G'_{\xi_z}) \tag{13}$$

$$H'' + \mathrm{Pr}\left[\left(\frac{m+1}{2}\right) FH' + \frac{\xi_x}{\xi_z}((n+3)GH' - 4nHG')\right] = \mathrm{Pr}\left(\frac{1-m}{2}\right)\xi_x(F'H_{\xi_x} - H'F_{\xi_x}) + \mathrm{Pr}(n-1)\xi_x(H'G_{\xi_z} - G'H_{\xi_z}) \tag{14}$$

And the transformed boundary conditions are

$$\left.\begin{aligned} &F(\xi_x, \xi_z, 0) = F'(\xi_x, \xi_z, 0) = G(\xi_x, \xi_z, 0) = G'(\xi_x, \xi_z, 0) = 0 \\ &H(\xi_x, \xi_z, 0) = 1 \\ &F'(\xi_x, \xi_z, \infty) = 1,\ G'(\xi_x, \xi_z, \infty) = H(\xi_x, \xi_z, \infty) = 0 \end{aligned}\right\} \tag{15}$$

In the foregoing equations, primes denote partial differentiation with respect to η and subscripts ξ_x and ξ_z denote partial differentiation with respect to those variables.

For $N < 0$, only the term $(\xi_x/\xi_z)^3 H$ in equation (13) changes sign. In this circumstance, we merely need to replace ξ_z by $-\xi_z$ and G by $-G$ to obtain a set of equations and boundary conditions identical to equations (12–15). This fact implies that there is no distinction between flows for which the fluid motion caused by free convection is vertically up or vertically down, at least when forced convection is dominant.

Equations (12–15) may be solved for various combinations of m and n by using one of several solution methods appropriate for nonsimilar equations.

In the case $m = n = 1$, equations (12–14) reduce to ordinary differential equations and ξ_x and ξ_z become parameters independent of x and z, respectively. Only for this particular choice of m and n does the problem under consideration admit a similarity solution. The parameters ξ_x and ξ_z then appear only as the ratio ξ_x/ξ_z in the transformed equations. This ratio measures the relative magnitude of the free convection effect to the forced convection effect. In physical terms the flow is represented by a two-dimensional stagnation line flow in the x-direction and a surface temperature varying linearly in the z direction. For each flow, considered separately, the boundary layer thickness and the heat transfer coefficient are uniform over the surface.

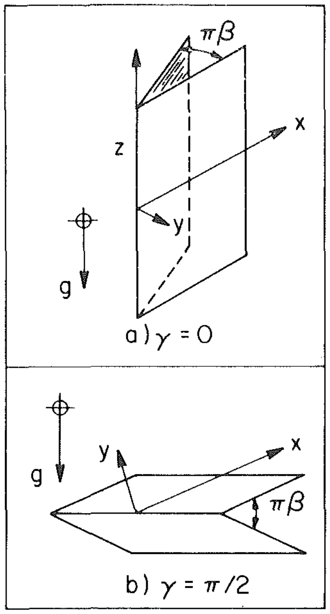

Fig. 1 Physical model and coordinate system

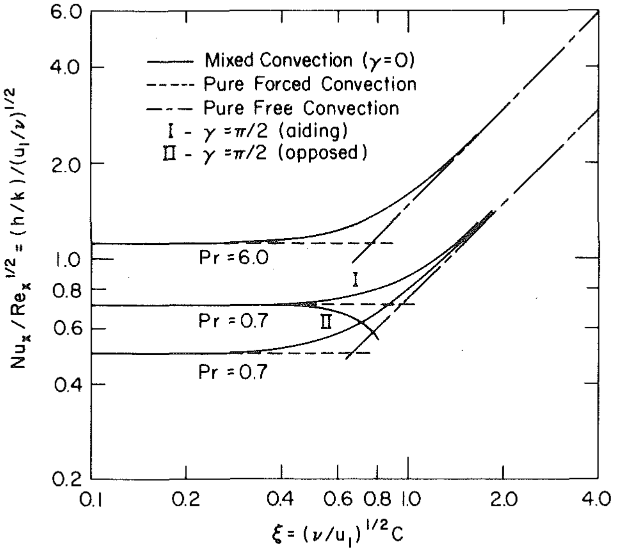

Fig. 2 Nusselt number results for Pr = 0.7 and 6.0

In their consideration of the case $\gamma = \pi/2$, Sparrow, et al. [6] show that a variety of wedge angles and surface temperature distributions lead to similar solutions. They found a relation between m and n given by $m = (n+1)/2$, and presented results for $(m, n) = (2/3, 0)$ and $(3/4, 1/5)$.

Results and Discussion

For the vertical stagnation line case $\gamma = 0$, and $m = n = 1$, numerical solutions were carried out for Prandtl numbers of 0.7 and 6.0. For each Pr, the quantity $\xi (= \xi_x/\xi_z)$ was varied from 0 to 2, thus spanning the range from pure forced convection to dominant free convection.

The primary physical quantity of interest is the heat transfer rate. It can be written in terms of the variables of the analysis, as indicated in Fig. 2. Values of $\mathrm{Nu}_x/\mathrm{Re}_x{}^{1/2}$ as a function of the parameter ξ are plotted as solid lines in Fig. 2 for Pr = 0.7 and 6.0. These values are also listed in Table 1 as are the dimensionless wall shear stresses, $F''(\xi, 0)$ and $G''(\xi, 0)$.

Figure 2 also contains straight lines that represent $\mathrm{Nu}_x/\mathrm{Re}_x{}^{1/2}$ for pure forced convection flow and for pure free convection flow. The equations of these limiting lines are

Table 1 Skin friction and heat transfer results for Pr = 0.7 and 6.0 $m = n = 1, \gamma = 0$

	Pr = 0.7			Pr = 6.0		
ξ	$-H'(\xi,0)$	$F''(\xi,0)$	$G''(\xi,0)$	$-H'(\xi,0)$	$F''(\xi,0)$	$G''(\xi,0)$
0.0	0.49586	1.23258	0.0	1.11468	1.23258	0.0
0.2	0.49712	1.23284	0.00598	1.11612	1.23269	0.00331
0.4	0.51469	1.23642	0.04649	1.13700	1.23420	0.02618
0.5	0.53816	1.24145	0.08753	1.16686	1.23633	0.05110
0.6	0.57350	1.24951	0.14339	1.21555	1.23997	0.08423
0.7	0.61934	1.26086	0.21318	1.28424	1.24537	0.12842
0.8	0.67325	1.27547	0.29579	1.37116	1.25261	0.18235
0.9	0.73293	1.29319	0.39039	1.47296	1.26166	0.24541
1.0	0.79661	1.31384	0.49648	1.58608	1.27245	0.31703
1.2	0.93149	1.36313	0.74217	1.83480	1.29869	0.48436
1.4	1.07211	1.42176	1.03194	2.10132	1.33043	0.68246
1.6	1.21582	1.48832	1.36560	2.37719	1.36686	0.91060
2.0	1.50790	1.64042	2.16462	2.94211	1.45130	1.45616

Table 2 Skin friction and heat transfer results for Pr = 0.7, $m = n = 1, \gamma = \pi/2$

	Aiding		Opposing	
ξ	$-H'(\xi,0)$	$F''(\xi,0)$	$-H'(\xi,0)$	$F''(\xi,0)$
0.0	0.70898	1.23258	0.70898	1.23258
0.1	0.70900	1.23278	0.70895	1.23239
0.2	0.70938	1.23579	0.70857	1.22938
0.3	0.71100	1.24876	0.70693	1.21634
0.4	0.71531	1.28349	0.70244	1.18102
0.5	0.72412	1.35577	0.69264	1.10543
0.6	0.73926	1.48421	0.67347	0.96370
0.7	0.76212	1.68842	0.63692	0.71509
0.8	0.79329	1.98721	0.55868	0.27193
0.9	0.83247	2.39759		
1.0	0.87874	2.93460		
1.2	0.98783	4.44228		
1.4	1.11188	6.66123		
1.6	1.24489	9.54433		
1.8	1.38331	13.33925		

$$\mathrm{Nu}_x/\mathrm{Re}_x{}^{1/2} = \left.\begin{matrix} 0.49586 \text{ for } \mathrm{Pr} = 0.7 \\ 1.11468 \text{ for } \mathrm{Pr} = 6.0 \end{matrix}\right\} \begin{matrix} \text{forced convection:} \\ m = 1 \end{matrix} \qquad (16)$$

$$\mathrm{Nu}_x/\mathrm{Re}_x{}^{1/2} = \left.\begin{matrix} 0.74680\,\xi \text{ for } \mathrm{Pr} = 0.7 \\ 1.45702\,\xi \text{ for } \mathrm{Pr} = 6.0 \end{matrix}\right\} \begin{matrix} \text{free convection:} \\ n = 1 \end{matrix} \qquad (17)$$

Figure 2 shows that for small values of the parameter ξ the Nusselt number results merge with the asymptotes for pure forced convection. For increasing values of the parameter ξ, the Nusselt number for mixed convection flow is higher than it could be in either of the component flows. The greatest deviation of the Nusselt number from the envelope formed by the two limiting lines occurs at the intersection of these lines. These deviations are approximately 23 percent for Pr = 0.7 and 20 percent for Pr = 6.0.

New results for $\gamma = \pi/2$, $m = n = 1$ were obtained in this study from solutions to the equations in the present notation given by Sparrow, et al. [6]. The heat transfer results are given in Table 2 for Pr = 0.7 and are plotted in Fig. 2. Of course, it is possible to distinguish between aiding and opposing flows, in this case. By extrapolating $F''(\xi, 0)$ to zero, we found separation to occur at $\xi \simeq 0.82$, in the opposing flow case.

The forced convection asymptotes ($\xi \rightarrow 0$) for $\gamma = 0$ and $\gamma = \pi/2$ are different from each other because the thermal boundary conditions are different. When $\gamma = 0$, the wall temperature is uniform in the flow direction; when $\gamma = \pi/2$, the wall temperature varies linearly in the flow direction.

Conclusions

1 Mixed convection about a vertical surface leads to a similar solution of the boundary layer equations only for the case of a vertical stagnation line and a linearly varying wall temperature in the vertical direction. The dimensionless heat transfer rate depends only on the parameter $\xi = (\nu/u_1)^{1/2}C$ and is uniform over the surface.

2 In the flows considered here, there is no distinction between the heat transfer and skin friction results for wall temperatures that are higher or lower than the ambient temperature. This conclusion is not restricted to cases for which there are similar solutions.

3 Solutions for Pr = 0.7 and 6.0 show a heat transfer rate greater than that achieved for either flow acting alone, but less than their sums.

References

1 Young, R. J., and Yang, K. T., "Effect of Small Cross-Flow and Surface Temperature Variation on Laminar Free Convection Along a Vertical Place," ASME *Journal of Applied Mechanics*, 1963, pp. 252–256.

2 Yao, L. S., and Catton, I., "Bouyancy Cross-Flow Effect on Longitudinal Boundary Layer Flow Along a Heated Horizontal Hollow Cylinder," ASME JOURNAL OF HEAT TRANSFER, Vol. 99, 1977, pp. 122–124.

3 Oosthuizen, P. H., and Madan, S., "The Effect of Flow Direction on Combined Convective Heat Transfer from Cylinder to Air," ASME JOURNAL OF HEAT TRANSFER, Vol. 93, 1971, pp. 240–242.

4 Oosthuizen, P. H., and Taralis, D. N., "Combined Convection Heat Transfer from Vertical Cylinders in a Horizontal Fluid Flow," ASME Paper No. 76-HT-41, 1976.

5 Yao, L. S., and Chen, F. M., "Analysis of Convective Heat Loss from the Receiver of Solar Power Plants, "ASME Paper No. 79-WA/HT-36, 1979.

6 Sparrow, E. M., Eichhorn, R., and Gregg, J. L., "Combined Forced and Free Convection in a Boundary Layer Flow," *Physics of Fluids*, Vol. 2, No. 3, 1959, pp. 319–328.

7 Gunness, R. C., and Gebhart, B., "Combined Forced and Natural Convection Flow for the Wedge Geometry," *International Journal of Heat-Mass Transfer*, Vol. 8, 1965, pp. 43–53.

8 Moore, F. K., "Three Dimensional Compressible Boundary Layer Flow," NACATN2279, Mar. 1951.

Heat Transfer from Rotating Bodies of Arbitrary Contour

Aryadi Suwono[1]

I Introduction

In a recent paper by the author [1], the velocity distribution in the steady laminar boundary layer flow induced by a rotating body of revolution of arbitrary shape in an infinite incompressible fluid at rest was investigated. The analysis employs a suitable coordinate transformation and the governing momentum equation is expressed in term of a sequence of universal functions which depend only on the class of the body shape and not on details of the contour. The results have been applied to a rotating sphere, and the flow characteristics obtained agree very well with the experimental data even only a few terms of the series was used.

In the present investigation, using the results of reference [1], the thermal boundary layer characteristics for rotating bodies of revolution of arbitrary shape heated to a uniform surface temperature T_0 in an infinite incompressible fluid of undisturbed temperature T_∞ at rest have been examined numerically. The solution is given in terms of series of universal functions.

2 Development of Basic Equations

Let x, y, and z be distances along the surface in a meridian plane, normal to the surface and along the surface in a plane normal to the axis of rotation, respectively, of a nonrotating orthogonal curvilinear coordinate system with the corresponding velocity components u, v, and w. Neglecting dissipation, in dimensionless terms of stretched coordinates and normalizing velocities and temperatures, the steady incompressible flow and energy equations under the usual boundary layer approximations are given by

$$\frac{\partial \bar{u}}{\partial \bar{x}} + \frac{\partial \bar{v}}{\partial \bar{y}} + \frac{\bar{u}}{\bar{r}}\frac{d\bar{r}}{d\bar{x}} = 0 \qquad (1)$$

$$\bar{u}\frac{\partial \bar{u}}{\partial \bar{x}} + \bar{v}\frac{\partial \bar{u}}{\partial \bar{y}} - \frac{\bar{w}^2}{\bar{r}}\frac{d\bar{r}}{d\bar{x}} = \frac{\partial^2 \bar{u}}{\partial \bar{y}^2} \qquad (2)$$

$$\bar{u}\frac{\partial \bar{w}}{\partial \bar{x}} + \bar{v}\frac{\partial \bar{w}}{\partial \bar{y}} + \frac{\bar{u}\bar{w}}{\bar{r}}\frac{d\bar{r}}{d\bar{x}} = \frac{\partial^2 \bar{w}}{\partial \bar{y}^2} \qquad (3)$$

$$\bar{u}\frac{\partial \overline{T}}{\partial \bar{x}} + \bar{v}\frac{\partial \overline{T}}{\partial \bar{y}} = \mathrm{Pr}^{-1}\frac{\partial^2 \overline{T}}{\partial \bar{y}^2} \qquad (4)$$

In equation (4), Pr denotes the Prandtl number, ν/α, where ν and α are the kinematic viscosity and thermal diffusivity. The stretched coordinates and the normalizing quantities are defined by

$$\bar{x} = \frac{x}{L}, \quad \bar{y} = \mathrm{Re}^{1/2}\frac{y}{L}, \quad \bar{z} = \frac{z}{L}$$

$$\bar{u} = \frac{u}{\omega L}, \quad \bar{v} = \mathrm{Re}^{1/2}\frac{v}{\omega L}, \quad \bar{w} = \frac{w}{\omega L} \qquad (5)$$

$$\overline{T} = \frac{T - T_\infty}{T_0 - T_\infty}$$

where L, ω, and Re are the characteristic length, angular velocity of rotation and Reynold number $\mathrm{Re} = \omega L^2/\nu$

The appropriate boundary conditions are

$$\bar{y} = 0 \quad \bar{u} = \bar{v} = 0 \quad \bar{w} = \overline{T} = 1$$

$$y \to \infty \quad \bar{u}, \bar{w}, \overline{T} \to 0 \qquad (6)$$

The solution of (1–3) subject to the boundary conditions (6) has been found [1] by introducing the transformation of variables

$$\xi = \int_0^{\bar{x}} [\bar{r}(\bar{x})]^3 d\bar{x}, \quad \eta = \frac{\bar{r}^2}{(2\xi)^{1/2}}\bar{y} \qquad (7)$$

$$f(\xi, \eta) = \frac{\bar{\psi}(\bar{x}, \bar{y})}{(2\xi)^{1/2}}, \quad g(\xi, \eta) = \frac{\bar{r}\bar{\phi}(\bar{x}, \bar{y})}{(2\xi)^{1/2}} \qquad (8)$$

where $\bar{\psi}(\bar{x}, \bar{y})$ and $\bar{\phi}(\bar{x}, \bar{y})$ are dimensionless stream functions defined by

$$\bar{u} = \frac{1}{\bar{r}}\frac{\partial \bar{\psi}}{\partial \bar{y}}, \quad \bar{v} = -\frac{1}{\bar{r}}\frac{\partial \bar{\psi}}{\partial \bar{x}}, \quad \bar{w} = \frac{\partial \bar{\phi}}{\partial \bar{y}} \qquad (9)$$

and following by writing the solution in the form

$$f(\xi, \eta) = \sum_{n=0}^{\infty} f_n(\eta)\xi^{an}, \quad g(\xi, \eta) = \sum_{n=0}^{\infty} g_n(\eta)\xi^{an} \qquad (10)$$

where a is a positive constant to be determined from the expansion of the principal function $P(\xi) = 2\xi\bar{r}/d\bar{r}d\xi$, which appears in the transformed equations, over the variable ξ

$$P(\xi) = \sum_{n=0}^{\infty} P_n \xi^{an} \qquad (11)$$

It has been identified that if the dimensionless meridional profil of the surface $\bar{r}$ satisfies the relation

$$\bar{r}(\bar{x}) = x^p \sum_{n=0}^{\infty} \bar{r}_n \bar{x}^{qn} \qquad (12)$$

where q is also a positive constant, a is given by

$$a = \frac{q}{3p + 1} \qquad (13)$$

In term of new variables the energy equation (4) is written as

$$P_r^{-1}\overline{T}'' + f\overline{T}' = 2\xi \frac{\partial(\overline{T}, f)}{\xi(\xi, \eta)} \qquad (14)$$

Here, and in the equations which follow, primes denote partial differentiation with respect on η and $\partial(,)/\partial(\xi, \eta)$ is the Jacobian. The appropriate boundary condition are

$$\eta = 0 \; \overline{T} = 1 \quad \text{and} \quad \eta \to \infty \; \overline{T} \to 0 \qquad (15)$$

It should be noted that the flow is similar when $\bar{r} = \bar{r}_0\bar{x}^p$. For this case, the Jacobian in equation (14) vanishes and the temperature profile is also similar. It can be shown by a simple transformation that the transformed momentum and energy equations can be expressed identical to those of Dorfman and Serazetdinov [5] when the dissipation terms are omitted. For $p = 1$, it reduces to the case of a rotating disk or cone and reference [5] shows that the results agree with those obtained in a previous study by Sparrow and Gregg [7].

To obtain the solution for the energy equation subject to its bondary conditions (15), expand $\overline{T}(\xi, \eta)$ in a form similar to that of f or g, i.e.,

$$\overline{T}(\xi, \eta) = \sum_{n=0}^{\infty} \overline{T}_n(\eta)\xi^{an} \qquad (16)$$

Insertation of eqation (16) into equation (14) and comparison of equal powers of ξ, a system of ordinary linear differential equations is obtained for the determination of $\overline{T}_n(\eta)$,

$$\mathrm{Pr}^{-1}\overline{T}_0'' + f_0\overline{T}_0' = 0 \qquad (17)$$

$$\mathrm{Pr}^{-1}\overline{T}_n'' + f_0\overline{T}_n' - 2\,\mathrm{an}\,f_0\overline{T}_n + (1 + 2\,an)\overline{T}_0'f_n$$
$$= \sum_{m=1}^{n-1} \{2am\overline{T}_m f_{n-m}' - (1 + 2am)f_m\overline{T}_{n-m}\} \qquad (18)$$

with

$$\overline{T}_0(0) = 1 \quad \overline{T}_n(0) = 0 \text{ for } n > 0$$

$$\overline{T}_0(\infty), \overline{T}_n(\infty) \to 0 \qquad (19)$$

Furthermore, in order to make use the numerical results of flow characteristics tabulated in reference [1], which are given in terms of series of universal functions, i.e., depend only on parameters p and q, equation (16) will be written as

---

[1] Department of Mechanical Engineering, Institute of Technology of Bandung, P.O. Box 481, Bandung, Indonesia.

Contributed by the Heat Transfer Division for publication in the JOURNAL OF HEAT TRANSFER. Manuscript received by the Heat Transfer Division, August 8, 1979.

Table 1 Wall derivatives of functional coefficients for Pr = 0.72, 1, 100 and $q = 2$

	Pr = 0.72				Pr = 1				Pr = 100			
P_0	$-T_0(0)$	$-\overline{T}'_{1,1}(0)$	$-\overline{T}'_{2,2}(0)$	$\overline{T}'_{2,1}(0)$	$-\overline{T}'_0(0)$	$-\overline{T}'_{1,1}(0)$	$-\overline{T}'_{2,2}(0)$	$-\overline{T}'_{2,1}(0)$	$-\overline{T}'_0(0)$	$-\overline{T}'_{1,1}(0)$	$-\overline{T}'_{2,2}(0)$	$\overline{T}_{2,1}(0)$
1/2	0.232336	0.080990	0.089393	0.102056	0.280190	0.103101	0.113375	0.124240	1.900095	0.973726	1.043155	0.889887
1/4	0.209305	0.186045	0.184884	0.299405	0.251401	0.231185	0.230571	0.368138	1.653160	1.894463	1.929306	2.766315
1/6	0.194143	0.268029	0.258254	0.573222	0.232850	0.331459	0.320984	0.706408	1.514152	2.633486	2.630902	5.374460
1/8	0.183187	0.341302	0.324055	0.918208	0.219544	0.421148	0.402108	1.132581	1.419390	3.297109	3.261185	8.661124
1/10	0.174737	0.409228	0.385184	1.329428	0.209320	0.504314	0.477481	1.640588	1.348515	3.913086	3.846579	12.581414
1/12	0.167926	0.473347	0.442965	1.803284	0.201099	0.582826	0.548728	2.225998	1.292462	4.494690	4.399568	17.101250
1/14	0.162261	0.534528	0.498150	2.336950	0.194271	0.657749	0 616776	2.885317	1.246434	5.049668	4.927417	22.193781
1/16	0.157436	0.593343	0.551237	2.928159	0.188462	0.729777	0.682236	3.615742	1.207600	5.583103	5.434904	27.837346
1/18	0.153252	0.650187	0.602570	3.575007	0.183429	0.799394	0.745533	4.414927	1.174156	6.098544	5.925362	34.013686
1/20	0.149570	0.705350	0.652404	4.275867	0.179003	0.866950	0.806980	5.280839	1.144889	6.598624	6.401267	40.707247

Table 2 Comparison of different predictive methods on local heat transfer parameter, $\mathrm{Nu}/\mathrm{Re}^{1/2}$, for a rotating sphere (Pr = 1)

	According to Banks [2]				According to reference [3]						Calculated from equation (25)		
$\bar{x}$	1 Term	2 Terms	3 Terms	4 Terms	1 Term	2 Terms	3 Terms	4 Terms	5 Terms	6 Terms	1 Term	2 Terms	3 Terms
0.0	0.3963	0.3963	0.3963	0.3963	0.3963	0.3963	0.3963	0.3963	0.3963	0.3963	0.3963	0.3963	0.3963
0.2	0.3963	0.3932	0.3932	0.3932	0.3963	0.3923	0.3923	0.3934	0.3934	0.3933	0.3936	0.3931	0.3931
0.4	0.3963	0.3839	0.3838	0.3838	0.3963	0.3806	0.3803	0.3844	0.3844	0.3849	0.3857	0.3829	0.3836
0.6	0.3963	0.3684	0.3682	0.3681	0.3963	0.3616	0.3601	0.3688	0.3687	0.3709	0.3727	0.3688	0.3677
0.8	0.3963	0.3467	0.3460	0.3458	0.3963	0.3362	0.3316	0.3456	0.3449	0.3513	0.3546	0.3483	0.3455
1.0	0.3963	0.3188	0.3171	0.3163	0.3963	0.3052	0.2947	0.3140	0.3116	0.3248	0.3316	0.3230	0.3173
1.2	0.3963	0.2848	0.2813	0.2788	0.3963	0.2699	0.2498	0.2734	0.2670	0.2896	0.3042	0.2936	0.2842
1.4	0.3963	0.2445	0.2380	0.2318	0.3963	0.2318	0.1977	0.2241	0.2099	0.2428	0.2725	0.2607	0.2477
$\pi/2$	0.3963	0.2053	0.1949	0.1826	0.3963	0.1981	0.1486	0.1758	0.1510	0.1919	0.2427	0.2305	0.2149

$$\overline{T}(\xi,\eta) = \overline{T}_0(\eta) + P_1\overline{T}_{1,1}(\eta)\xi^a + \{P_2\overline{T}_{2,2}(\eta) + P_1^2\overline{T}_{2,1}(\eta)\}\xi^{2a} + \ldots \quad (20)$$

The equation (17) remains unchanged, but the equation (18) is modified. The first two terms are given by

$$\mathrm{Pr}^{-1}\overline{T}''_{1,1} + f_0\overline{T}'_{1,1} - 2af'_0\overline{T}_{1,1} + (1+2a)\overline{T}'_0 f_{1,1} = 0 \quad (21)$$

$$\mathrm{Pr}^{-1}\overline{T}''_{2,2} + f_0\overline{T}'_{2,2} - 4af'_0\overline{T}_{2,2} + (1+4a)T'_0 f_{2,2} = 0 \quad (22)$$

$$\mathrm{Pr}^{-1}\overline{T}''_{2,1} + f_0\overline{T}'_{2,1} - 4af'_0\overline{T}_{2,1} + (1+4a)T'_0 f_{2,1} = 2af'_{1,1}\overline{T}_{1,1} - (1+2a)f_{1,1}\overline{T}'_{1,1} \quad (23)$$

with the boundary conditions

$$T_0(0) = 1 \quad \overline{T}_{1,1}(0) = \overline{T}_{2,2}(0) = \overline{T}_{2,1}(0) = 0$$

$$T_0(\infty), \overline{T}_{1,1}(\infty), \overline{T}_{2,2}(\infty), \overline{T}_{2,1}(\infty) \to 0 \quad (24)$$

3 Results

Equations (17, 21, 22), and (23) with boundary conditions (24) have been integrated numerically following the Runge-Kutta-Merson procedure, with the error maximum of intergration less than 10^{-7} in each step, for Pr = 0.72, 1, 10, 100, $q = 1, 2$ and various values of $P_0 = 2p/(3p+1)$. The quantities of wall derivatives for Pr = 0.72, 1, 100 and $q = 2$ are given in Table 1 (others may be obtained from the author). Now, by simply assembling the values given in Table 1 as coefficients of a series, the surface heat flux q_s from a rotating body of revolution of arbitrary shape in a fluid at rest can be calculated. In term of the local Nusselt number, it is given by

$$\frac{\mathrm{Nu}}{\mathrm{Re}^{1/2}} = \frac{q_s L}{\mathrm{Re}^{1/2}K(T_0 - T_\infty)} = -\frac{\bar{r}^2}{(2\xi)^{1/2}}[\overline{T}'_0(0) + P_1\overline{T}'_{1,1}(0)\xi^a + \{P_2\overline{T}'_{2,2}(0) + P_1^2\overline{T}'_{2,1}(0)\}\xi^{2a} + \ldots] \quad (25)$$

4 Application to rotating spheres

Consider an example of application of the results to the well studied case of a rotating sphere. If the radius of sphere R is taken as a characteristic length, $\bar{r}$, ξ, p, q, P_0, P_1, P_2, and are given by

$$\bar{r} = \sin\bar{x},\ \xi = \frac{\cos^3\bar{x}}{3} - \cos\bar{x} + \frac{2}{3}$$

$$p = 1, \quad q = 2, \quad P_0 = 1/2, \quad P_1 = -\frac{1}{6}, \quad P_2 = -\frac{11}{72}, \quad a = 1/2 \quad (26)$$

The results of $\mathrm{Nu}/\mathrm{Re}^{1/2}$ calculated from equation (22) at various points for Pr = 1 are tabulated in Table 2. These results are compared with the values obtained using the Blasius series [2] and those predicted by Dorfman and Mironova [3]. The degree of convergence of each method is indicated by showing the effect of individual terms. The convergence of the present method is some what faster. The disagreement of the three methods in the region $1 < \bar{x} < \pi$ may be due to this fact, it should be noted that in the Blasius series, the solution is expressed in the form of series expansion over $0 < \bar{x} < \pi/2$, and over $0 < \xi(\bar{x}) < 1$ in the method proposed by Dorfman and Mironova [3], compared with the variable used for expansion in the present analysis $0 < \xi < 2/3$. The most interesting is the fact that the first term of the present method give already a better approximation compared with that of Banks [2] or Dorfman and Mironova [3] where the first term give only the solution for a rotating disk. This is due to inclusion of the effect of the body shape in the first term through the transformed variable ξ. Accounting that near the equator the boundary layer analysis can not be applied due to the effect of flow eruption, for many purpose the use of the first term can be justified. It should be noted that alternatively for the rotating sphere case, q in the equation (26) can be taken equal to 1, and since the sine function has the expansion form $\sum_{n=0}^{\infty} x^{2n+1}/(2n+1)!$ then p should be taken equal to 1 and accordingly $r_1 = r_3 = \ldots = r_{2n+1} = 0$. However it is evidence that more terms are required to achieve a certain accuracy.

The experiments on the heat transfer from a rotating sphere have been carried out by Kreith, et al. [4]. The results obtained is correlated by the equation

$$\overline{\mathrm{Nu}} = 0.86\,\mathrm{Pr}^{0.4}\mathrm{Re}^{1/2} \quad (27)$$

to within 15 percent. Integration of equation (22) over the sphere surface yields $\overline{\mathrm{Nu}} = 0.552\,\mathrm{Re}^{1/2}$ for Pr = 0.72 which agrees with prediction of Dorfman and Serazetdinov [5] and slightly higher than that obtained by Banks [2] but much below the experimental data. This discrepancy can still not be explained. Dorfman and Serazetnov believe that this may be due to the effect of natural convection and eruption at the equator which are not taken into account in calculations.

Banks [2] proposed, based on the results of average Nusselt number calculated for Pr = 0.72 and 1, a relation similar to equation (27) by replacing the constant 0.86 by 0.58. A careful examination shows that this relation is valid only for a limited variation of Prandtl number. Using the calculation results of average Nusselt number for Pr = 0.72,

(continued on page 789)

rameter σ increases. This is due to irreversible conversion of mechanical energy to thermal one.

References

1 Lin, S. H., "Heat Transfer to Plane Non-Newtonian Couette Flow," *International Journal of Heat and Mass Transfer,* Vol. 22, 1979, p. 1117.

2 Middleman, S., *Fundamentals of Polymer Processing,* McGraw-Hill, New York, 1977.

3 Fredrickson, A. G., and Bird, R. B., "Non-Newtonian Flow in an Annuli," *Industrial and Engineering Chemistry,* Vol. 50, 1958, p. 347.

4 Bird, R. B., Armstrong, R. C., and Hassager, O., *Dynamics of Polymeric Liquids,* John Wiley, New York, 1977.

5 Lapidus, L., *Digital Computation for Chemical Engineers,* McGraw-Hill, New York, 1962.

6 Hong, S. N., and Mathews, J. C., "Heat Transfer to Non-Newtonian Fluids in Laminar Flow through Concentric Annuli," *International Journal of Heat and Mass Transfer,* Vol. 12, 1969, p. 1699.

Suwono Continued

1, 10, 100 and the result for a very large Prandtl number calculated assymtotically using Lighthill's hypothesis (see for example reference [6]), it is possible to construct an empirical formulae which is valid for larger variation of Prandtl number. It is found that the following relation.

$$\overline{\mathrm{Nu}} = 1.021\,\mathrm{Re}^{1/2}\,\mathrm{Pr}^{1/3}\,[1 - 0.244\,\mathrm{Pr}^{-1/3} - 0.139\,\mathrm{Pr}^{-2/3} + 0.035\,\mathrm{Pr}^{-1}] \quad \text{for } \mathrm{Pr} > 0.72 \qquad (28)$$

Correlates to within 2 percent of the calculation results.

5 Acknowledgment

The computation of numerical results were made possible though funds from the Alexander von Humboldt Foundation.

References

1 Suwono, A., "Laminar Boundary Layer Flow Near Rotating Bodies of Arbitary Contour," *Acta Mecanica* (forthcoming).

2 Banks, W. H. H., "The Thermal Laminar Boundary Layer on a Rotating Sphere," *Zeitschrift fuer Angewandte Mathematik und Mechanik,* Vol. 16, 1965, pp. 780–788.

3 Dorfman, L. A., and Mironova, V. A., "Solution of Equations for The Heat Mass Transfer," Vol. 13, 1970, pp. 81–92.

4 Kreith, F., Roberts, L. G., Sullivan, J. A., and Sinha, S. N., "Convection Heat Transfer and Flow Phenomena of Rotating Spheres," *International Journal Heat Mass Transfer,* Vol. 5, 1963, pp. 881–885.

5 Dorfman, L. A., and Serazetdinov, A. Z., "Laminar Flow and Heat Transfer Near Rotating Axisymmetric Surface," *International Journal Heat Mass Transfer,* Vol. 8, 1965, pp. 317–327.

6 Lighthill, M. J., "Contribution to The Theory of Heat Transfer Through a Laminar Boundary Layer," *Proceedings of the Royal Society* London A, Vol. 202, 1950, pp. 359–377.

7 Sparrow, E. M., and Gregg, J. L., "Mass Transfer, Flow and Heat Transfer about a Rotating Disk," ASME JOURNAL HEAT TRANSFER, Vol. 82, 1960, pp. 294–302.

Turbulent Heat Transfer to a Rotating Disk: a Review and Extension of Dorfman

M. C. Johnson[1]

Nomenclature

T = temperature
T_w = temperature of disk wall
T_∞ = temperature of rotating fluid core
R = radius
Z = axial distance from rotating disk
W = angular velocity of disk
q = heat flux
V_R = velocity of fluid in radial direction
$V_{R_{\mathrm{AVE}}}$ = average radial velocity at a particular radius
V_∞ = tangential velocity of fluid in core
V_Z = velocity of fluid in axial direction
δ_T = thermal boundary layer size
δ = momentum boundary layer size
ρ = fluid density
c_p = fluid heat capacity
$Pr = \mu c_p/K$ (Prandtl number)
μ = fluid viscosity
h = film coefficient
$\mathrm{Re} = (WR - V_\infty)R\rho/\mu$ (Reynolds number)
$\mathrm{St} = \mathrm{Nu}/\mathrm{Pr\,Re}$ (Stanton number)
ν = kinematic viscosity

Introduction

Heat transfer from a rotating disk to the rotating fluid adjacent to it is defined by the boundary layer energy equation

$$\rho c_p \left(V_R \frac{\partial T}{\partial R} + V_Z \frac{\partial T}{\partial z}\right) = \frac{\partial q}{\partial z} \tag{1}$$

Normally, the heat flux at the disk wall is found using Reynolds analogy. Reynolds analogy applies when the form of the tangential momentum equation and the energy equation are shown to be exactly similar. As shown by Dorfman [1], the Reynolds analogy also requires the tangential momentum and energy boundary conditions to be exactly similar. For a rotating disk, these conditions can be generalized as follows [2].

$$\begin{aligned} \frac{\partial T_\infty/\partial R}{T_w - T_\infty} &= \frac{\partial/\partial R(RV_\infty)}{R^2W - RV_\infty} \\ \frac{\partial/\partial R(T_w - T_\infty)}{T_w - T_\infty} &= \frac{\partial/\partial R(R^2W - RV_\infty)}{R^2W - RV_\infty} \end{aligned} \tag{2}$$

For the case of a disk rotating in a quiescent atmosphere, these conditions become

$$\begin{aligned} T_w - T_\infty &= C_0R^2 \\ T_\infty &= C_1 \end{aligned} \tag{3}$$

In general, these boundary conditions are not met, and it is necessary to look elsewhere for a solution of the boundary layer energy equation.

Dorfman's Method

Dorfman [1] considered the case of a disk rotating in a quiescent atmosphere ($V_\infty = 0$). He integrated the boundary layer energy equation (1) across the thermal boundary layer and introduced the continuity equation, yielding

$$d/dR\left[R\int_0^{\delta_T} V_R(T - T_\infty)dz\right] = -\left.\frac{Rq}{\rho c_p}\right|_{z=0} \tag{4}$$

or, in the dimensionless form

$$\frac{1}{WR^2(T_w - T_\infty)}\, d/dR\left[R\int_0^{\delta_T} V_R(T - T_\infty)dz\right] = \mathrm{St} \tag{4a}$$

The primary difficulty in solving this equation is the assumption of a model for the wall heat flux, which Dorfman assumes in the following form

$$q|_{z=0} = \text{constant}\cdot\left[\int_0^{\delta_T} V_R(T - T_\infty)dz\right]^{-m} \tag{5}$$

where m is a constant to be determined experimentally.

The assumption of (5) reduces equation (4) to a separable nonlinear differential equation.

The actual form of Dorman's assumption is

$$\mathrm{St}^{-1} = A(\mathrm{Pr})(\mathrm{Re}^{**})^m \tag{6}$$

$A(\mathrm{Pr})$ is a function of the Prandtl number and Re^{**} is a thermal Reynolds number using a weighted thermal boundary layer size as a characteristic dimension. It is defined in the next section.

Equation (6) can be rearranged in the form

$$q = \frac{\rho c_p WR(T_w - T_\infty)}{A(\mathrm{Pr})}\left[\frac{\rho}{\mu(T_w - T_\infty)}\int_0^{\delta_T} V_R(T - T_\infty)dz\right]^{-m} \tag{7}$$

Substituting this expression into equation (4), separating variables, assuming constant fluid properties and integrating, an expression for the Stanton number can be found.

$$\mathrm{St} = \frac{\mathrm{Re}^{-m/m+1}(T_w - T_\infty)^m R^{m(m+3)/m+1}}{[A(\mathrm{Pr})]^{1/m+1}} \times \left[\int_0^R (T_w - T_\infty)^{m+1}R^{m+2}dR\right]^{-m/m+1} \tag{8}$$

This equation represents a general expression for the Stanton number. Now m and $A(\mathrm{Pr})$ must be determined empirically. Although any data correlation could be used, it will be convenient to use one such that the disk temperature distribution is rigidly defined. Such conditions exist for the Reynolds analogy.

Dorfman gives an expression for the Stanton number of a disk rotating in a quiescent atmosphere for Reynolds analogy conditions (turbulent flow) [1].

$$\mathrm{St} = 0.0267\,\mathrm{Pr}^{-0.4}\mathrm{Re}^{-0.2} \tag{9}$$

As shown in equation (3), the Reynolds analogy temperature distribution on a disk rotating in a quiescent atmosphere is parabolic ($T_w = C_0R^2 + T_\infty$). Substituting this expression for T_w into equation (8), and rearranging in the form of equation (9), the required empirical constants are found to be

$$\begin{aligned} m &= 0.25 \\ A(\mathrm{Pr}) &= 135.7\,\mathrm{Pr}^{0.5} \end{aligned} \tag{10}$$

Therefore, for turbulent flow conditions, the expression for the Stanton number for a rotating disk in a quiescent atmosphere is

$$\mathrm{St} = \frac{\mathrm{Pr}^{-0.4}\mathrm{Re}^{-0.2}T_w - T_\infty)^{0.25}R^{0.65}}{53.14\left[\int_0^R (T_w - T_\infty)^{1.25}R^{2.25}dR\right]^{0.2}} \tag{11}$$

An application of this equation for temperature distributions of the form: $T_w - T_\infty = BR^m$ is discussed in reference [3].

Improved Method

Arbitrary Fluid Core Rotation and Density Variations. Dorfman considered only the case of a disk rotating in a quiescent atmosphere. He defined the thermal Reynolds number as

---

[1] Department of Mechanical Engineering, Massachusetts Institute of Technology, Cambridge, Massachusetts 02139.

Contributed by the Heat Transfer Division for publication in the JOURNAL of HEAT TRANSFER. Manuscript received by The Heat Transfer Division December 14, 1979.

$$\mathrm{Re}^{**} = \frac{WR\delta_T^{**}}{\nu}$$

and the integral thermal boundary layer thickness as

$$\delta_T^{**} = \int_0^{\delta_T} \frac{V_R(T - T_\infty)dz}{WR(T_w - T_\infty)}$$

A simple extension of Dorfman's method can be effected by allowing for arbitrary fluid core rotation. This can be done by replacing the wheel speed (WR) with the relative speed ($WR - V_\infty$). The thermal Reynolds number then becomes

$$\mathrm{Re}^{**} = \frac{(WR - V_\infty)\delta_T^{**}}{\nu}$$

and the integral thermal boundary layer thickness becomes

$$\delta_T^{**} = \int_0^{\delta_T} \frac{V_R(T - T_\infty)dz}{(WR - V_\infty)(T_w - T_\infty)}$$

Using these forms in equation (6) and allowing for density variations, equation (11) for the Stanton number becomes

$$\mathrm{St} = \frac{\mathrm{Pr}^{-0.4}(T_w - T_\infty)^{0.25}R^{0.25}\mu^{0.2}}{(53.14)\left[\int_0^R \rho R^{1.25}(WR - V_\infty)(T_w - T_\infty)^{1.25}dR\right]^{0.2}} \qquad (12)$$

Beginning of Boundary Layer Growth. Dorfman assumes that boundary layer growth begins at $R = 0$. This is not always the case. A common example can be found in the compressor disk cavities of a gas turbine engine. Mid-compressor air is bled into these cavities for cooling purposes. The air enters at the outer diameter of the disk cavities and exits at the bores in the center of the disks. On the disks, a boundary layer develops which begins at the outer diameter, flows radially inward and exits at the disk bores.

This modifies equation (12) as follows

$$\mathrm{St} = \frac{\mathrm{Pr}^{-0.4}(T_w - T_\infty)^{0.25}R^{0.25}\mu^{0.2}}{(53.14)\left[\int_{R_0}^R \rho R^{1.25}(WR - V_\infty)(T_w - T_\infty)^{1.25}dR\right]^{0.2}} \qquad (13)$$

R_0 is the radius where boundary layer growth begins.

Variations in Fluid Core Temperature. If the fluid core temperature (T_∞) cannot be considered a constant, equation (4) needs to be modified

$$d/dR\left[\rho R \int_0^{\delta_T} V_R(T - T_\infty)dz\right] + R\rho \int_0^{\delta_T} V_R \frac{dT_\infty}{dR} dz = -\left.\frac{Rq}{c_p}\right|_{z=0} \qquad (14)$$

or, as in equation (4*a*), in terms of Stanton number

$$\frac{1}{R(T_w - T_\infty)(WR - V_\infty)\rho}\left[d/dR\left(\rho R \int_0^{\delta_T} V_R(T - T_\infty)dz\right) + R\rho \int_0^{\delta_T} V_R \frac{dT_\infty}{dR} dz\right] = \mathrm{St} \qquad (14a)$$

Substitution of assumption (7) into equation (14) will lead to a differential equation which is no longer separable. To solve the resulting equation it is necessary to make several new assumptions.

1 Assume a shape for the radial velocity profile in the boundary layer:

$$V_R = 2.45V_{R_{\mathrm{AVE}}}(Z/\delta)^{1/7}[1 - (Z/\delta)] \qquad (15)$$

2 Assume a shape for the temperature profile in the boundary layer:

$$T = T_w + (T_\infty - T_w)(Z/\delta)^{1/7} \qquad (16)$$

3 Assume that the thermal boundary layer size is greater than or equal to the momentum boundary layer size:

$$\delta_T \geq \delta \qquad (17)$$

Using these assumptions along with equations (7) and (14) yields

$$\eta^m\left[\frac{d\eta}{dR} + \frac{k\eta}{T_w - T_\infty}\frac{dT_\infty}{dR}\right] = \frac{\rho^{m+1}\nu^m(T_w - T_\infty)^{m+1}(RW - V_\infty)R^{m+1}}{A(\mathrm{Pr})} \qquad (18)$$

where

$$\eta = R\rho(RW - V_\infty)(T_w - T_\infty)\delta_T^{**}$$

k is a constant arising from the integration of the product of the radial velocity and temperature boundary layer profiles.

This equation can be solved by the introduction of an integrating factor

$$\exp\left[(m + 1)k \int \frac{dT_\infty/dR}{T_w - T_\infty} dR\right]$$

Using the integrating factor, equation (18) can be integrated. Following the technique used to derive equation (11) yields equation (19).

For temperature profiles whose shape is known to be different from that assumed in equation (16), equation (19) can be changed to reflect this by changing the constant k introduced in equation (18).

The only experimental results available are for the isothermal disk rotating in a constant temperature environment [4]. For that case, equation (19) reduces to match the experimental results.

References

1 Dorfman, L. A., *Hydrodynamic Resistance and the Heat Loss of Rotating Solids*, pp. 87–98, Oliver and Boyd, 1963.

2 Lord, W., personal communication.

3 Harnett, J. P., Shing-Hwa Tsai, H. N. Jantscher, "Heat Transfer to a Nonisothermal Disk with a Turbulent Boundary Layer", ASME JOURNAL OF HEAT TRANSFER, Vol. 87, 1965, pp. 362–368.

4 Kreith, F. *Principles of Heat Transfer*, Intext Educational Publishers, 1973, pp. 404, 405.

$$\mathrm{St} = \frac{\mathrm{Pr}^{-0.4}R^{0.25}(T_w - T_\infty)^{0.25}\mu^{0.2}\exp\left(1.22\int \frac{dT_\infty/dR}{T_w - T_\infty} dR\right)}{(53.14)\left[\int_{R_0}^R \rho R^{1.25}(T_w - T_\infty)^{1.25}(WR - V_\infty)\exp\left(6.1\int \frac{dT_\infty/dR}{T_w - T_\infty} dR\right) dR\right]^{0.2}} \qquad (19)$$

Experimental Observations of Flow Instability During Turbulent Flow Freezing in a Horizontal Tube

S. B. Thomason[1] and J. C. Mulligan[2]

Introduction

Unsteady freezing processes are of importance in many applications generally and, notably, of specific importance to such technology development as liquid metal cooling and desalination by freeze crystallization. During some recent work in this area, in which experiments on the effects of turbulent-flow on freezing in tube flow were carried out, an unexpected oscillatory phenomenon was discovered. The objective of the experiments was to obtain transient and steady-state heat transfer and pressure-drop data for the controlled case in which the wall temperature of a tube containing a fully-developed turbulent flow is instantaneously lowered to a uniform and constant temperature below the freezing point of the liquid. It was anticipated that the subsequent response would be a transient phase-change process leading to either a steady state with flow in the tube as presented in references [1–4], or to a complete blockage of the tube. On several occasions during the investigation, however, a third and unanticipated periodic response was observed. This response is presented and discussed here.

Experiments

The experiments were conducted using water as the freezing medium and, essentially, the same apparatus as described in reference [1]. Briefly, the water flow system consisted of inlet and exit constant-head reservoirs connected by a continuous entrance section 171.1 cm long and a jacketed test section 116.0 cm long, constructed of copper tubing 1.45 cm in inside diameter with a wall thickness of 0.07 cm. An upstream constant-temperature bath coupled with the inlet reservoir permitted the setting and control of inlet temperature, T_{w1}. Tube wall temperature was controlled by a methanol coolant, which was circulated in the jacket at a sufficiently large flow rate to minimize both the temperature rise of the coolant (usually less than 0.2°C) and nonuniformities in tube wall temperature. The heat transfer coefficient, h, on the coolant side typically was relatively large. The inlet water temperature was held constant at 5.6°C and the exit static pressure at 7.9 cm of water during all experiments reported here, except one in which the inlet water temperature was 7.2°C. The water level in the upstream reservoir, $(\Delta h + 7.9)$ cm, which was used to control the overall pressure drop across the system, Δh cm, and the coolant temperature, T_c, were varied to produce different initial water flow rates (Reynolds numbers, Re_{Di}) and tube-wall temperatures, respectively.

When the desired initial water flow rate and coolant temperature were set, the experiment was initiated by starting the coolant circulation through the cooling jacket, thus lowering the tube-wall temperature below 0°C in a manner closely approximating a step change. The instant at which freezing began in the experiments was accurately detected by monitoring the response pulse from three thermocouples imbedded along the tube wall. Each thermocouple pulsed rapidly, almost simultaneously, at the instant freezing started indicating the instant of initiation as well as confirming that the ice layer formed along the full length of the tube uniformly. The static pressure at the test section inlet, P_0 cm, was then recorded continuously and reported as a dimensionless pressure, P^*, defined as $2(P_0 - 7.9)/\rho v^2$ where v is the mean inlet velocity. The later quantity is related to the test section inlet pressure by the entrance section characteristic equation $\text{Re}_D = 652.7\,(\Delta P)^{0.55}$, where ΔP is the entrance section pressure drop $(\Delta h + 7.9 - P_0)$ cm, and Re_D is the instantaneous pipe Reynolds number. Thus, values of P^* can easily be translated into comparable flow rates, Re_D, by computation. The time, τ, used in displaying the results represents the dimensionless liquid-phase Fourier number $\alpha_l t/r_w^2$.

Results and Discussion

Various combinations of coolant temperature, initial water flow rate, and inlet temperature, resulted in some distinctly different types of freezing response, as demonstrated by the selected pressure-drop versus time curves reported here. When the combination of these boundary conditions was not too severe, a smooth and relatively rapid transient occurred in which a true steady-state frozen shell was achieved and maintained within the tube. Responses of this type, which were expected, were obtained under a variety of conditions and are being reported under separate title. An example of such a pressure-drop response curve is shown by curve 1 in Fig. 1.

As the combination of coolant temperature, initial water flow rate, and inlet temperature was varied to cause more severe freezing, a most interesting and unexpected flow response was observed. Distinct and significant oscillations in flow rate, pressure drop, and wall temperature began occurring in the transient icing process. Curves 2 and 3 in Fig. 1 show results of two experiments at essentially the same initial Reynolds number and inlet temperature which illustrate this unstable oscillatory response. Both were obtained by slightly reducing coolant temperature and each ultimately approaches steady state. In these cases, the oscillations are seen to be very regular and tend to damp just as the steady state is reached. Under somewhat more severe coolant temperatures the oscillations become more extreme, as illustrated in Fig. 2, and somewhat random in the early periods of the transient although the regular damping trend always persisted.

With the boundary conditions adjusted downward to even more conducive conditions, the most interesting phenomenon of the entire series of experiments resulted. In a very narrow range of coolant temperature, for a given initial water flow rate and inlet temperature, almost perfectly periodic pressure-drop and flow-rate variations occurred. The experimental pressure-drop results plotted in Fig. 3 are for such a case where the coolant temperature alone was slightly lowered, the period being approximately 35 min ($\Delta\tau \simeq 6$) and the total oscillation corresponding to 12.5 cm of water ($\Delta P^* \simeq 20$ and Re_D variation of 3720 to 4660). These oscillations were observed for approximately 3 hr and appeared to be quite regular. Similar periodic results for a somewhat lower coolant temperature as well as lower water flow rate are shown in Fig. 4. This experiment, which was carried out at a slightly higher inlet temperature, took place over a time span of approximately 2 1/2 hr and displayed a period of 29 min ($\Delta\tau \simeq 4$) and an oscillation of approximately 4.7 cm of water ($\Delta P^* \simeq 9.5$ and Re_D variation of 3960 to 4200). The differences in the two sets of periodic data reported here result essentially from the slightly different inlet flow rates, inlet water temperatures, and coolant temperatures which were imposed. The occurrance of this phenomenon in the experiments seemed to be extremely sensitive to coolant temperature and only moderately sensitive to initial water flow rate. Unfortunately, the experimental apparatus did not permit a clear definition of the separate effects of these variables.

When the boundary conditions were further reduced, beyond the narrow limits of the periodic regime, the periodic freezing process began to break up and become unstable with pressure-drop patterns appearing wildly oscillatory and random in amplitude, extremely temperature sensitive and sometimes rapidly approaching freeze blockage on an upswing of pressure. With further slight reductions in the conditions, the freezing displayed a more stable and predictable transient leading definitely to freeze blockage, even though still with some oscillatory behavior. Such a response is illustrated by curve 1 of Fig. 5, wherein the transition was produced by slightly lowering coolant temperatures. Finally, as explained in relation to Fig. 1, if the conditions were sufficiently extreme a smooth and rapid transient leading directly to freeze blockage occurred, without any signs of os-

---

[1] Assistant Professor, Department of Mechanical Engineering, Virginia Polytechnic Institute and State University, Blacksburg, Va. 24061.

[2] Professor, Department of Mechanical and Aerospace Engineering, North Carolina State University, Raleigh, N. C. 27650.

Contributed by the Heat Transfer Division for publication in the JOURNAL of HEAT TRANSFER. Manuscript received December 3, 1979.

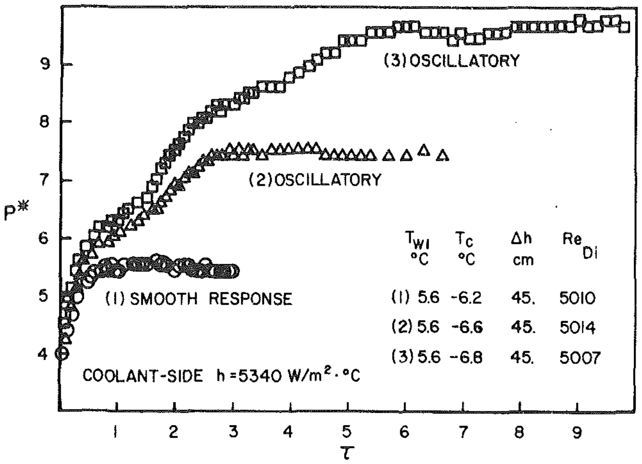

Fig. 1 Representative experimental pressure-drop transients terminating in a steady state

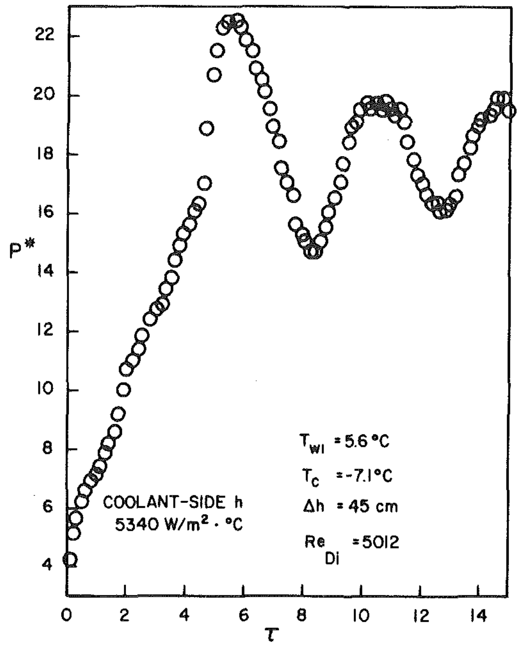

Fig. 2 Illustration of initially magnified pressure-drop oscillations which randomly damped to steady state

cillation. Such responses are illustrated in curves 2 and 3 of Fig. 5.

The controlled variables of coolant temperature, inlet water temperature and upstream and downstream pressure head were constantly monitored and carefully controlled, eliminating any cyclic variations to which the freeze oscillations might be attributed. Also, the freeze oscillations were reproduced a number of times and carefully observed for several hours to insure their actual existence. Thus, it is believed that the data presented here represent a true demonstration of the existence of essentially a third regime of freezing in turbulent tube flow, in addition to the two previously defined in laminar flow studies [4]. That is, conditions may be such that (1) a steady state occurs finally, (2) a freeze blockage occurs finally, or (3) a stable periodic state of alternate freezing and melting occurs. The conditions which are pertinent are such variables as the external coolant temperature and convective conductance, and inlet water temperature, the initial water flow rate (Reynolds number), the tube diameter and length, and the physical relationship between water flow rate and inlet pressure as dictated by the characteristic equation of the upstream flow system. The fact that the flow rate varies with the pressure drop should additionally have an influence on the actual frequency of the oscillation within the periodic regime. In the experiments presented here, with the exception of that depicted in Fig. 4, all variables were held constant except coolant temperature.

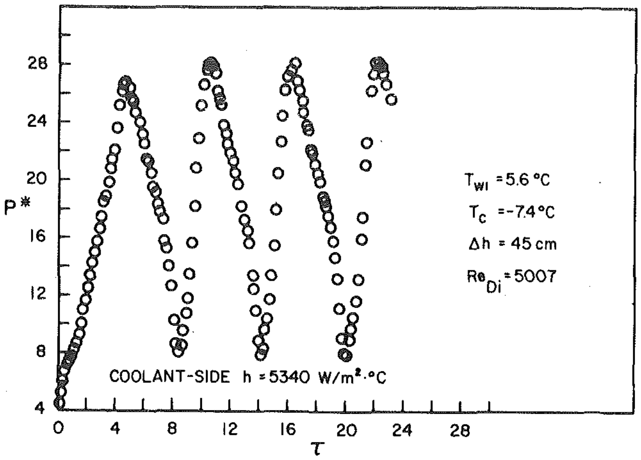

Fig. 3 Periodic pressure-drop oscillation occurring with an actual period of 35 min and a peak-to-peak amplitude of 12.5 cm of water

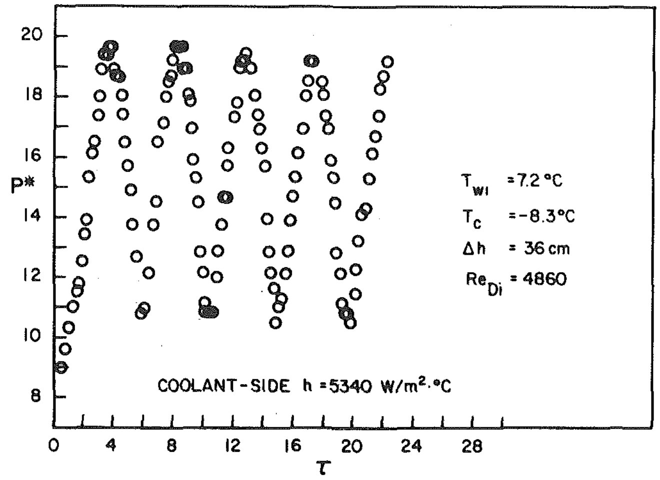

Fig. 4 Periodic pressure-drop oscillation occurring with an actual period of 29 min and a peak-to-peak amplitude of 4.7 cm of water

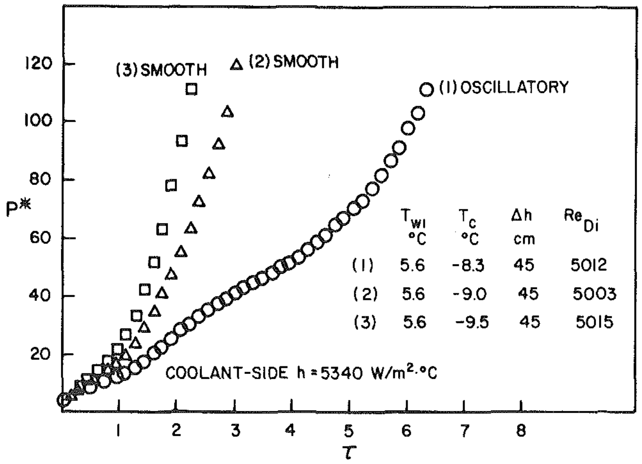

Fig. 5 Typical cases of pressure-drop transients leading to complete blockage

No single mechanism could be isolated as the cause of this unanticipated oscillatory behavior. An instability caused by a phenomenon associated with the inlet ice-free zone, which has been shown to exist by Zerkle [5], is one course of speculation. It has been suggested to the authors that it may even be related in part to an anisotropic behavior of the ice layer as found by Savino and Siegel [6]. A more likely explanation is that the phenomenon is related to a relaminarization and separation instability similar to that recently reported by Gilpin [3]. A "banded" or wavy-ice structure was shown to occur in tubes when freezing occurs with flow Reynolds numbers near transition. A periodic regime of pressure fluctuations could conceivably occur when the wavelength of the resulting ice structure is of the order of the tube length.

Acknowledgment

The authors wish to acknowledge that this work was performed under NSF Grant GK 38131 and, partially, in concert with related work performed under Contract No. 14-34-0001-9530, OWRT, U. S. Department of the Interior.

References

1 Thomason, S. B., Mulligan, J. C., and Everhart, J., "The Effect of Internal Solidification on Turbulent Flow Heat Transfer and Pressure Drop in a Horizontal Tube," ASME JOURNAL OF HEAT TRANSFER, Vol. 100, 1978, pp. 387–394.

2 Gilpin, R. R., "The Effects of Dendritic Ice Formation in Water Pipes," *International Journal of Heat and Mass Transfer,* Vol. 20, 1977, pp. 693–699.

3 Gilpin, R. R., "the Morphology of Ice Structure in a Pipe at or Near Transition Reynolds Numbers," *AIChE Symposium,* Series 189, Vol. 75, 1979, pp. 89–94.

4 Des Ruisseaux, N., and Zerkle, R. D., "Freezing in Hydraulic Systems," ASME Paper No. 68-HT-24, 1968.

5 Zerkle, R. D., "The Effect of External Thermal Insulation on Liquid Solidification in a Tube," *Proceedings of the Sixth Southeastern Seminar on Thermal Sciences,* Raleigh, N. C., Apr. 13–14, 1970, pp. 1–19.

6 Savino, J. M., and Siegel, R., "Experimental and Analytical Study of the Transient Solidification of a Warm Liquid Flowing Over a Chilled Flat Plate," NASA TN D-4015, 1967.

Solidification in Two-Phase Flow

D. J. Petrie,[1] J. H. Linehan,[2]
M. Epstein,[1] G. A. Lambert,[1]
and L. J. Stachyra[1]

Nomenclature

a = crust thermal diffusivity
A = heat flux parameter
B = latent heat parameter
c = crust heat capacity
h = convective heat transfer coefficient
j = superficial gas velocity
k = crust thermal conductivity
L = latent heat of fusion
q = convective heat flux
T_c = methanol coolant temperature (−70°C)
T_ℓ = liquid temperature
T_{MP} = fusion temperature
T_W = wall temperature
t = time
α = void fraction
δ = crust thickness
δ_{ss} = steady-state crust thickness
δ_w = wall thickness (0.238 cm)
τ = dimensionless time
Δ = dimensionless crust thickness
θ = dimensionless wall temperature

1 Introduction

If, in the process of solidification, the liquid phase contains a gas in solution, the gas will be rejected at the phase interface due to the difference in solubility of the gas in the liquid and solid. The evolution of the gas may result in the entrapment of gas bubbles in the solid phase by the advancing solidification front [1]. The resulting porosity alters the properties of the solid [2]. If gas is present in the body of the liquid as a discontinuous phase, it is not clear at present what effect the two-phase mixture will have on the solidification process. The problem of predicting solidification rates in a two-phase mixture arises in safety studies for the fast breeder reactor [3] and in the design of air bubblers as ice control devices for cold-water ports and harbors [4, 5].

A study of the transient solidification of a Wood's metal-nitrogen gas mixture in a cold tube was performed by Greene, et al. [6, 7]. The authors postulated the entrapment of nitrogen gas bubbles within the solid phase and concluded from their experimental results that the rate of solidification may be several times faster for the two-phase case than for the corresponding single phase case.

This paper presents the results of an experiment designed to measure directly the growth of an ice layer (crust) in a water-nitrogen gas mixture.

2 Experiment

A planar test section on which ice crusts were grown was vertically suspended in a pool of water contained within a Lucite bubble column of square cross-section (5.08 cm by 5.08 cm). Nitrogen gas bubbles were formed at a perforated plate located at the bottom of the column. The pressure in the column was atmospheric. A schematic of the apparatus is shown in Fig. 1. The test section was constructed from a copper block 7.62 cm in length and 0.635 cm thick. A serpentine coolant channel was milled into one face of the block. The freezing surface was 0.238 cm thick. Thermocouples (±1°C) were used to measure the test section temperature and were located in the freeze plate 0.2 cm from the freezing surface. The entire test section except for the freeze surface was cast in epoxy material to insulate the edges and back of the test section. The coolant supply line, connecting the coolant reservoir with the test section, was insulated with rubber tubing. A lateral-traversing thermocouple probe (not shown in Fig. 1), similar to that developed by Savino and Siegel [8], was used to measure the instantaneous ice crust thickness as a function of time.

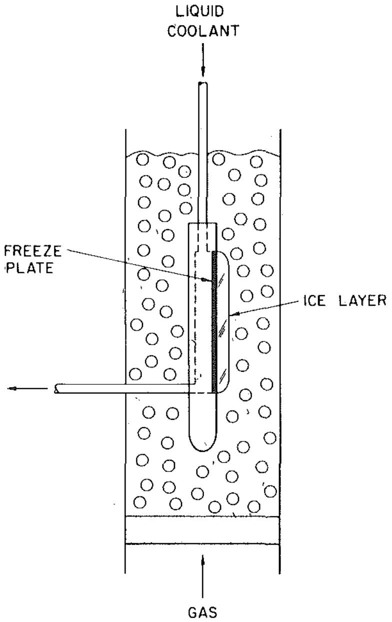

Fig. 1 Schematic diagram of the test section showing an ice layer growing on the freeze plate in an ice-water mixture

---

[1] Reactor Analysis and Safety Division, Argonne National Laboratory, 9700 South Cass Ave., Argonne, IL 60439.

[2] Marquette University, Milwaukee, Wis.

Contributed by The Heat Transfer Division for publication in the JOURNAL OF HEAT TRANSFER. Manuscript received by the Heat Transfer Division May 22, 1980.

[3] Void fraction was calculated as the difference between the height of the expanded pool and the initial height of the pool with zero gas flow divided by the expanded pool height.

odic regime of pressure fluctuations could conceivably occur when the wavelength of the resulting ice structure is of the order of the tube length.

Acknowledgment

The authors wish to acknowledge that this work was performed under NSF Grant GK 38131 and, partially, in concert with related work performed under Contract No. 14-34-0001-9530, OWRT, U. S. Department of the Interior.

References

1 Thomason, S. B., Mulligan, J. C., and Everhart, J., "The Effect of Internal Solidification on Turbulent Flow Heat Transfer and Pressure Drop in a Horizontal Tube," ASME JOURNAL OF HEAT TRANSFER, Vol. 100, 1978, pp. 387–394.

2 Gilpin, R. R., "The Effects of Dendritic Ice Formation in Water Pipes," *International Journal of Heat and Mass Transfer*, Vol. 20, 1977, pp. 693–699.

3 Gilpin, R. R., "the Morphology of Ice Structure in a Pipe at or Near Transition Reynolds Numbers," *AIChE Symposium*, Series 189, Vol. 75, 1979, pp. 89–94.

4 Des Ruisseaux, N., and Zerkle, R. D., "Freezing in Hydraulic Systems," ASME Paper No. 68-HT-24, 1968.

5 Zerkle, R. D., "The Effect of External Thermal Insulation on Liquid Solidification in a Tube," *Proceedings of the Sixth Southeastern Seminar on Thermal Sciences*, Raleigh, N. C., Apr. 13–14, 1970, pp. 1–19.

6 Savino, J. M., and Siegel, R., "Experimental and Analytical Study of the Transient Solidification of a Warm Liquid Flowing Over a Chilled Flat Plate," NASA TN D-4015, 1967.

Solidification in Two-Phase Flow

D. J. Petrie,[1] J. H. Linehan,[2] M. Epstein,[1] G. A. Lambert,[1] and L. J. Stachyra[1]

Nomenclature

a = crust thermal diffusivity
A = heat flux parameter
B = latent heat parameter
c = crust heat capacity
h = convective heat transfer coefficient
j = superficial gas velocity
k = crust thermal conductivity
L = latent heat of fusion
q = convective heat flux
T_c = methanol coolant temperature (−70°C)
T_ℓ = liquid temperature
T_{MP} = fusion temperature
T_W = wall temperature
t = time
α = void fraction
δ = crust thickness
δ_{ss} = steady-state crust thickness
δ_w = wall thickness (0.238 cm)
τ = dimensionless time
Δ = dimensionless crust thickness
θ = dimensionless wall temperature

1 Introduction

If, in the process of solidification, the liquid phase contains a gas in solution, the gas will be rejected at the phase interface due to the difference in solubility of the gas in the liquid and solid. The evolution of the gas may result in the entrapment of gas bubbles in the solid phase by the advancing solidification front [1]. The resulting porosity alters the properties of the solid [2]. If gas is present in the body of the liquid as a discontinuous phase, it is not clear at present what effect the two-phase mixture will have on the solidification process. The problem of predicting solidification rates in a two-phase mixture arises in safety studies for the fast breeder reactor [3] and in the design of air bubblers as ice control devices for cold-water ports and harbors [4, 5].

A study of the transient solidification of a Wood's metal-nitrogen gas mixture in a cold tube was performed by Greene, et al. [6, 7]. The authors postulated the entrapment of nitrogen gas bubbles within the solid phase and concluded from their experimental results that the rate of solidification may be several times faster for the two-phase case than for the corresponding single phase case.

This paper presents the results of an experiment designed to measure directly the growth of an ice layer (crust) in a water-nitrogen gas mixture.

2 Experiment

A planar test section on which ice crusts were grown was vertically suspended in a pool of water contained within a Lucite bubble column of square cross-section (5.08 cm by 5.08 cm). Nitrogen gas bubbles were formed at a perforated plate located at the bottom of the column. The pressure in the column was atmospheric. A schematic of the apparatus is shown in Fig. 1. The test section was constructed from a copper block 7.62 cm in length and 0.635 cm thick. A serpentine coolant channel was milled into one face of the block. The freezing surface was 0.238 cm thick. Thermocouples (±1°C) were used to measure the test section temperature and were located in the freeze plate 0.2 cm from the freezing surface. The entire test section except for the freeze surface was cast in epoxy material to insulate the edges and back of the test section. The coolant supply line, connecting the coolant reservoir with the test section, was insulated with rubber tubing. A lateral-traversing thermocouple probe (not shown in Fig. 1), similar to that developed by Savino and Siegel [8], was used to measure the instantaneous ice crust thickness as a function of time.

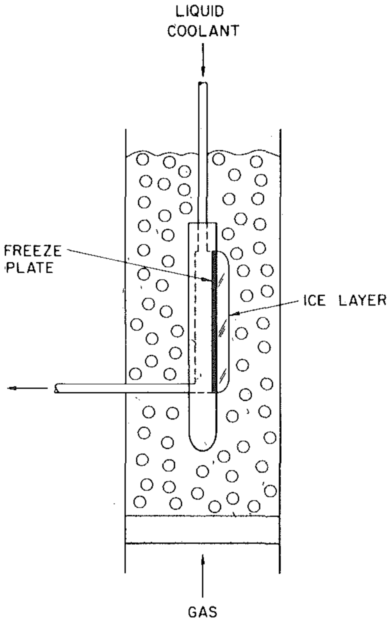

Fig. 1 Schematic diagram of the test section showing an ice layer growing on the freeze plate in an ice-water mixture

---

[1] Reactor Analysis and Safety Division, Argonne National Laboratory, 9700 South Cass Ave., Argonne, IL 60439.

[2] Marquette University, Milwaukee, Wis.

Contributed by The Heat Transfer Division for publication in the JOURNAL OF HEAT TRANSFER. Manuscript received by the Heat Transfer Division May 22, 1980.

[3] Void fraction was calculated as the difference between the height of the expanded pool and the initial height of the pool with zero gas flow divided by the expanded pool height.

The thermocouple probe was constructed by mounting a 30 gauge chromel-alumel thermocouple within a 13 cm long, 0.32 cm o.d. tube. The bare-bead junction, extending 1.0 cm beyond the tube, was trimmed to minimize the response time, flattened slightly, and supported by epoxy. The lateral displacement of the probe from the freezing surface was measured using a micrometer (±0.005 cm). During an experiment, the probe was initially located at a distance from the plate equal to the selected displacement increment used in subsequent measurements. The probe temperature was recorded on a strip-chart recorder. When the ice crust contacted the probe, as determined by watching the strip-chart recorder, the probe was moved laterally away from the crust a distance equal to the displacement increment. Thus, the strip-chart recording provided a means of determining the times of successive equal increments of crust thickness. A more detailed description of this procedure including representative tracings from the experiments is given in [9]. The water pool temperature was measured with a mercury thermometer (±0.1°C).

Two water pool temperatures were studied; in one case the water was at 0°C (saturated), in the other case the water pool was maintained at 14°C (superheated). The experiments covered a range of nitrogen gas volume (void) fractions from 0 to 90 percent. Void fractions[3] from 0 to 65 percent were obtained by simply bubbling nitrogen gas through the perforated plate at superficial velocities ranging from 0 to 12 cm/s into ordinary tap water. Foams having void fractions between 80 and 90 percent were produced by adding a small quantity of Kodak Photo-Flow solution to the pool in the ratio of about 2 drops to 150 ml of water. The ice growth transient was initiated by suddenly allowing the coolant (methyl alcohol at −70°C) to flow into the test section channel. The plate temperature- and crust thickness-time histories were recorded during the experiment. Over the course of an experiment with saturated water (~1 min.), the freeze plate temperature decreased to approximately −65°C and the resulting instantaneous crust thickness was approximately 0.65 cm. In the experiments with superheated water, the crust thickness grew more slowly in comparison to the experiments with saturated water due to the convective heat transport into the crust from the two-phase mixture. In these latter experiments, the crust thickness achieved a steady-state value after approximately three min.

3 Results and Discussion

The measured (dimensionless) crust thickness as a function of dimensionless time is shown in Fig. 2 for water maintained at 0°C. The data flags in this figure represent the standard deviation of a total of 18 runs in which the void fraction was varied from 0.0 to 90 percent. The coolant flowrate was fixed in the experiment so that the freeze plate experienced approximately the same cooling transient during each run. The freeze plate temperature-time curve can be found in reference [9]. For a given crust thickness, the measured times and void fractions for the 18 runs were subjected to a linear regression analysis. It was found that the slope of the regression line was not statistically different from zero. Thus, it can be concluded that, in these experiments, the void fraction does not determine the time for a given crust thickness to be achieved. The small variation in the measurements can be attributed to the small variations in the coolant flow rate from run to run. In addition, the physical characteristics of the ice crusts retrieved from the bubble column after the experiments did not change over the entire range of void fractions investigated. Thus, solidification of a two-phase structure (solid plus gas), as postulated in references [6] and [7] for the freezing of gas-liquid flows in a tube, was not indicated by the post-test observations.

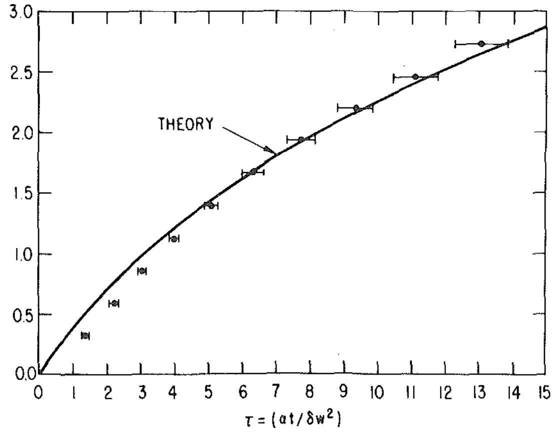

Fig. 2 Dimensionless crust thickness versus dimensionless time for ice growing in a two-phase water-nitrogen gas mixture maintained at 0°C. The data flags represent 18 runs covering the void fraction range 0–90 percent

The dark line in Fig. 2 is based on calculations of ice growth into saturated water in the absence of voids. The theory is based on solving the one-dimensional heat conduction equation in the crust using an accurate collocation technique [10]. The resulting governing equation is

$$\frac{d\Delta}{d\tau} = -\left(\frac{1}{\Delta} + \frac{1}{2}\frac{A}{B}\right) + \left\{\left(\frac{1}{\Delta} - \frac{1}{2}\frac{A}{B}\right)^2 + \frac{2}{B}\frac{\theta}{\Delta^2}\right\}^{1/2} \qquad (1)$$

where

$$\theta(\tau) = \frac{T_W(\tau) - T_{MP}}{T_c - T_{MP}} \quad \text{(dimensionless plate temperature)} \qquad (2)$$

$$\Delta(\tau) = \frac{\delta(\tau)}{\delta_w} \quad \text{(dimensionless crust thickness)} \qquad (3)$$

$$\tau = \frac{at}{\delta_w{}^2} \quad \text{(dimensionless time)} \qquad (4)$$

$$A = \frac{q\delta_w}{k(T_{MP} - T_c)} \quad \text{(dimensionless convective heat flux)} \qquad (5)$$

$$B = \frac{L}{c(T_{MP} - T_c)} \quad \text{(dimensionless latent heat)} \qquad (6)$$

For the case of a saturated liquid, A is set equal to zero. To solve equation (1) the measured wall temperature-time variation was used. The theory is seen to agree favorably with the data. All this strongly implies that the ice growth rate is the same in all runs studied, and is thus independent of the nitrogen gas void fraction, at least up to 90 percent. At early times, the crust thickness is overpredicted by the model probably due to the formation of a metastable, subcooled water layer adjacent to the freezing surface. For low gas void fractions, it was observed that the formation of an ice crust did not occur until the plate temperature decreased several degrees below 0°C and then a crust "flashed" on the surface. Presumably, this phenomenon also occurred at higher void fractions but the presence of the bubbles obscured visual observation.

In the experiments conducted with superheated water at 14°C, a steady-state ice crust was achieved when the conduction heat flux through the crust equaled the convective heat flux to the crust from the two-phase mixture at $\tau \rightarrow \infty$. The measured local crust thickness at the center of the freeze plate as a function of time is shown in Fig. 3 with A as a parameter. It is apparent that the steady-state crust thickness is a function of the superficial gas velocity j, varying from 0.724 cm for $j = 0.1$ cm/s to 0.152 cm for $j = 12.0$ cm/s. Since the steady-state crust thickness, δ_{ss}, is related to the convective heat transfer coefficient by

$$q = h(T_\ell - T_{MP}) = \frac{k(T_{MP} - T_W)}{\delta_{ss}}, \qquad (7)$$

it can be concluded that the convective heat transfer coefficient is increased when the superficial gas velocity is increased. This result is in agreement with studies concerned with the enhancement of convective heat transfer in liquids by gas injection [11, 12]. Values of the convective heat transfer coefficient can be calculated from equations (5) and (7) and the values of A given in Fig. 3.

The dark lines in Fig. 3 represent the predictions obtained with equation (1) wherein the convective heat-transfer coefficient h (or dimensionless parameter A) was evaluated using equation (7) together with the measured values of δ_{ss}. This method of determining steady-state heat transfer coefficients from ice crust thickness measurements is well established [13]. Experimental studies involving

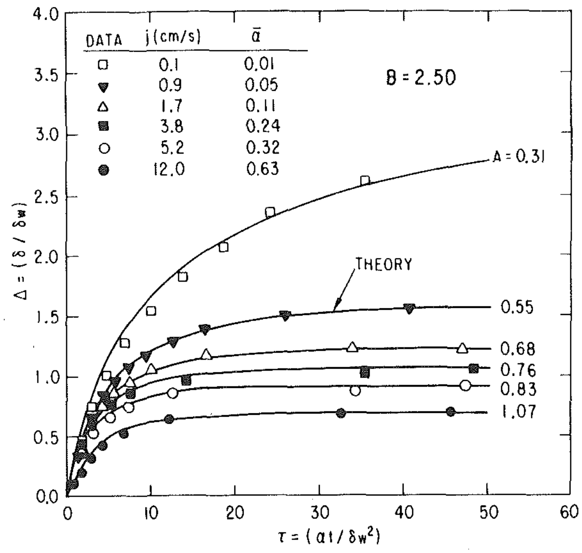

Fig. 3 Dimensionless crust thickness versus dimensionless time for ice growing in a two phase water-nitrogen gas mixture maintained at 14°C, using the superficial gas velocity (or convective heat flux) as a parameter

solidification in pure liquids with forced flow have demonstrated that heat convection is relatively undisturbed by the moving freeze boundary [8, 14]. The good agreement between theory and experiment shown in Fig. 3 is a clear indication that this is also the case for the two-phase solidification experiments reported herein.

4 Conclusions

The following conclusions may be made for the experiments reported herein. For void fractions up to 90 percent, the presence of a discontinuous gas phase in a saturated flowing liquid does not affect the freezing of the liquid on a vertical surface. The crust surface remains smooth and the void in the two-phase mixture is not trapped in the crust in contradistinction to the result of the evolution of a gas resulting from differences in gas solubility in the liquid and solid. For experiments with void fractions from 0 to 65 percent, the two phase flow regimes varied from bubbly flow to churn-turbulent flow and the resulting vigorous agitation at the crust surface presumably prevented the bubbles in the discontinuous phase from attaching themselves to the solid-liquid interface and being incorporated into the solid. However, in the experiments involving foams, it was visually observed that the two phase structure was relatively stagnant. Also, it was found that the crust growth rate and the smooth crust surface was the same as for the experiments at lower void fractions. Thus, it can be concluded that the two-phase fluid mechanics of the relatively stagnant foam structure; that is, water moving in the thin lamallae between the bubbles toward the crust and bubbles moving away from the crust is not important and that conduction in the crust remained the controlling phenomenon. The effect of gas bubbling on the freezing of a flowing, superheated liquid on a vertical surface is to enhance the convective heat transfer from the liquid to the crust. The crust surface remains smooth in this case with no evidence of entrapment of the void. In both cases, the crust growth behavior can be modeled by ignoring the presence of voids (except for the void flux-induced enhancement of the convective heat flux).

Acknowledgment

This work was performed under the auspices of the U.S. Department of Energy.

References

1 Chalmers, B., *Principles of Solidification*, John Wiley and Sons, 1964, p. 186.

2 Colangelo, V. J., and Heiser, F. A., *Analysis of Metallurgical Failures*, John Wiley and Sons, 1974, p. 278.

3 Epstein, M., "Melting, Boiling and Freezing: The "Transition Phase," in Fast Reactor Safety Analysis," in *Symposium on the Thermal and Hydraulic Aspects of Nuclear Reactor Safety, Vol. 2—Liquid Metal Fast Breeder Reactors*, ASME, New York, 1977, pp. 171–193.

4 Michel, B., "Winter Regime of Rivers and Lakes," Cold Regions Sciences and Engineering Monograph II-B1a, U.S. Army Cold Regions Research and Engineering Laboratory, Hanover, NH, 1971.

5 Yen, Y. C., "Heat-Transfer Characteristics of a Bubble-Induced Water Jet Impinging on an Ice Surface," *International Journal Heat Mass Transfer*, Vol. *18*, 1975, pp. 917–924.

6 Greene, G. A., Jones, O. C., and Kazimi, M. S., "Effects of Noncondensable Void Fraction on Freezing of Fluids," *Transactions of the American Nuclear Society*, Vol. *27*, 1977, p. 546; see also BNL-NUREG-24486R, Apr 1978.

7 Green, G. A., Jones, O. C., Kazimi, M. S., Ginsberg, T., and Barry, J. J., "Analysis and Measurement of Solidification Dynamics of Flowing Two-Phase Noncondensable Mixtures," *Transactions of the American Nuclear Society*, Vol. *28*, 1978, p. 465.

8 Savino. J. M., and Siegel, R., "Experimental and Analytical Study of the Transient Solidification of a Warm Liquid Flowing Over a Chilled Plate," NASA TN D-4015, 1967.

9 Petrie, D. J., "Solidification in Two-Phase Flow," M. S. Thesis Marquette Univ., June 1980.

10 Stephen, K., "Influence of Heat Transfer on Melting and Solidification in Forced Flow," *International Journal of Heat Mass Transfer*, Vol. *12*, 1969, pp. 199–214.

11 Chu, Y. C., and Jones, B. G., "Convective Heat Transfer Coefficient Enhancement in Two-Phase Nonboiling Flow," *Transactions of the American Nuclear Society*, Vol. *33*, 1979, pp. 960–961.

12 Luk, A. C. H., Ganguli, A., and Bankoff, S. G., "Simulation of Boiling Pools with Internal Heat Sources by Gas Injection," Northwestern University Report, COO, 2554–6, 1977.

13 Hirata, T., Gilpin, R. R., Cheng, K. C., and Gates, E. M., "The Steady State Ice Layer Profile on a Constant Temperature Plate in a Forced Convection Flow—I: Laminar Regime," *International Journal of Heat Mass Transfer*, Vol. *22*, 1979, pp. 1425–1433.

14 Nansteel, M. W., and Wolgemuth, C. M., "An Investigation of a Two-Phase, Moving Boundary System with Convection at the Solid-Liquid Interface," *AIChE Symposium Series on Heat Transfer*, Vol. *75*, No. 189, 1979, pp. 112–119.

Heat Transfer to Generalized Couette Flow of a Non-Newtonian Fluid in Annuli with Moving Inner Cylinder

S. H. Lin[1] and D. M. Hsieh[1]

Introduction

In a previous work, Lin [1] investigated the heat transfer to a generalized non-Newtonian Couette flow between parallel plates. That problem is of practical significance because of its potential applications in the processing of a number of industrially important non-Newtonian fluids, such as polymer melts and solutions and liquid foods. It is noted that the problem of heat transfer to a plane non-Newtonian Couette flow occurs in plate coating with polymers [2]. A corresponding problem of comparable practical importance is the wire or tube coating. The polymer flow in the latter coating problem takes place between two concentric cylinders in which the outer cylinder is motionless while the inner cylinder moves in the flow direction. This is exemplified by a process in which the wire surface is to be coated with a layer of polymer.

In spite of the practical significance of this coating problem, it has received very little attention in the past. Literature in connection with this coating heat transfer problem is virtually not available. Studies of the heat transfer characteristics of this problem can lead to better understanding of the process performance which in turn can facilitate process equipment design. The present study is an attempt to investigate this problem.

Velocity Distribution of Flow

Like the plane non-Newtonian Couette flow, the present flow

---

[1] Department of Chemical Engineering, Polytechnic Institute of New York, Brooklyn, New York 11201; S. H. Lin is currently with General Electric Company, 100 Woodlawn Avenue, 11-336, Pittsfield, MA 01201.

Contributed by the Heat Transfer Division for publication in the JOURNAL OF HEAT TRANSFER. Manuscript received by The Heat Transfer Division, May 2, 1980.

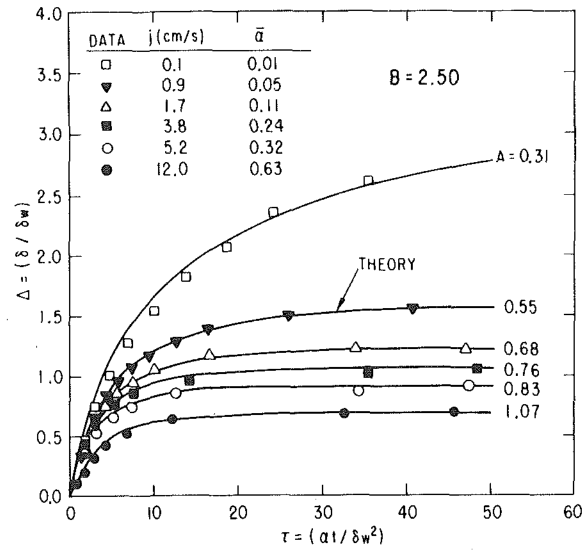

Fig. 3 Dimensionless crust thickness versus dimensionless time for ice growing in a two phase water-nitrogen gas mixture maintained at 14°C, using the superficial gas velocity (or convective heat flux) as a parameter

solidification in pure liquids with forced flow have demonstrated that heat convection is relatively undisturbed by the moving freeze boundary [8, 14]. The good agreement between theory and experiment shown in Fig. 3 is a clear indication that this is also the case for the two-phase solidification experiments reported herein.

4 Conclusions

The following conclusions may be made for the experiments reported herein. For void fractions up to 90 percent, the presence of a discontinuous gas phase in a saturated flowing liquid does not affect the freezing of the liquid on a vertical surface. The crust surface remains smooth and the void in the two-phase mixture is not trapped in the crust in contradistinction to the result of the evolution of a gas resulting from differences in gas solubility in the liquid and solid. For experiments with void fractions from 0 to 65 percent, the two phase flow regimes varied from bubbly flow to churn-turbulent flow and the resulting vigorous agitation at the crust surface presumably prevented the bubbles in the discontinuous phase from attaching themselves to the solid-liquid interface and being incorporated into the solid. However, in the experiments involving foams, it was visually observed that the two phase structure was relatively stagnant. Also, it was found that the crust growth rate and the smooth crust surface was the same as for the experiments at lower void fractions. Thus, it can be concluded that the two-phase fluid mechanics of the relatively stagnant foam structure; that is, water moving in the thin lamallae between the bubbles toward the crust and bubbles moving away from the crust is not important and that conduction in the crust remained the controlling phenomenon. The effect of gas bubbling on the freezing of a flowing, superheated liquid on a vertical surface is to enhance the convective heat transfer from the liquid to the crust. The crust surface remains smooth in this case with no evidence of entrapment of the void. In both cases, the crust growth behavior can be modeled by ignoring the presence of voids (except for the void flux-induced enhancement of the convective heat flux).

Acknowledgment

This work was performed under the auspices of the U.S. Department of Energy.

References

1 Chalmers, B., *Principles of Solidification*, John Wiley and Sons, 1964, p. 186.

2 Colangelo, V. J., and Heiser, F. A., *Analysis of Metallurgical Failures*, John Wiley and Sons, 1974, p. 278.

3 Epstein, M., "Melting, Boiling and Freezing: The "Transition Phase," in Fast Reactor Safety Analysis," in *Symposium on the Thermal and Hydraulic Aspects of Nuclear Reactor Safety, Vol. 2—Liquid Metal Fast Breeder Reactors*, ASME, New York, 1977, pp. 171–193.

4 Michel, B., "Winter Regime of Rivers and Lakes," Cold Regions Sciences and Engineering Monograph II-B1a, U.S. Army Cold Regions Research and Engineering Laboratory, Hanover, NH, 1971.

5 Yen, Y. C., "Heat-Transfer Characteristics of a Bubble-Induced Water Jet Impinging on an Ice Surface," *International Journal Heat Mass Transfer*, Vol. *18*, 1975, pp. 917–924.

6 Greene, G. A., Jones, O. C., and Kazimi, M. S., "Effects of Noncondensable Void Fraction on Freezing of Fluids," *Transactions of the American Nuclear Society*, Vol. *27*, 1977, p. 546; see also BNL-NUREG-24486R, Apr 1978.

7 Green, G. A., Jones, O. C., Kazimi, M. S., Ginsberg, T., and Barry, J. J., "Analysis and Measurement of Solidification Dynamics of Flowing Two-Phase Noncondensable Mixtures," *Transactions of the American Nuclear Society*, Vol. *28*, 1978, p. 465.

8 Savino. J. M., and Siegel, R., "Experimental and Analytical Study of the Transient Solidification of a Warm Liquid Flowing Over a Chilled Plate," NASA TN D-4015, 1967.

9 Petrie, D. J., "Solidification in Two-Phase Flow," M. S. Thesis Marquette Univ., June 1980.

10 Stephen, K., "Influence of Heat Transfer on Melting and Solidification in Forced Flow," *International Journal of Heat Mass Transfer*, Vol. *12*, 1969, pp. 199–214.

11 Chu, Y. C., and Jones, B. G., "Convective Heat Transfer Coefficient Enhancement in Two-Phase Nonboiling Flow," *Transactions of the American Nuclear Society*, Vol. *33*, 1979, pp. 960–961.

12 Luk, A. C. H., Ganguli, A., and Bankoff, S. G., "Simulation of Boiling Pools with Internal Heat Sources by Gas Injection," Northwestern University Report, COO, 2554–6, 1977.

13 Hirata, T., Gilpin, R. R., Cheng, K. C., and Gates, E. M., "The Steady State Ice Layer Profile on a Constant Temperature Plate in a Forced Convection Flow—I: Laminar Regime," *International Journal of Heat Mass Transfer*, Vol. *22*, 1979, pp. 1425–1433.

14 Nansteel, M. W., and Wolgemuth, C. M., "An Investigation of a Two-Phase, Moving Boundary System with Convection at the Solid-Liquid Interface," *AIChE Symposium Series on Heat Transfer*, Vol. *75*, No. 189, 1979, pp. 112–119.

Heat Transfer to Generalized Couette Flow of a Non-Newtonian Fluid in Annuli with Moving Inner Cylinder

S. H. Lin[1] and D. M. Hsieh[1]

Introduction

In a previous work, Lin [1] investigated the heat transfer to a generalized non-Newtonian Couette flow between parallel plates. That problem is of practical significance because of its potential applications in the processing of a number of industrially important non-Newtonian fluids, such as polymer melts and solutions and liquid foods. It is noted that the problem of heat transfer to a plane non-Newtonian Couette flow occurs in plate coating with polymers [2]. A corresponding problem of comparable practical importance is the wire or tube coating. The polymer flow in the latter coating problem takes place between two concentric cylinders in which the outer cylinder is motionless while the inner cylinder moves in the flow direction. This is exemplified by a process in which the wire surface is to be coated with a layer of polymer.

In spite of the practical significance of this coating problem, it has received very little attention in the past. Literature in connection with this coating heat transfer problem is virtually not available. Studies of the heat transfer characteristics of this problem can lead to better understanding of the process performance which in turn can facilitate process equipment design. The present study is an attempt to investigate this problem.

Velocity Distribution of Flow

Like the plane non-Newtonian Couette flow, the present flow

---

[1] Department of Chemical Engineering, Polytechnic Institute of New York, Brooklyn, New York 11201; S. H. Lin is currently with General Electric Company, 100 Woodlawn Avenue, 11-336, Pittsfield, MA 01201.

Contributed by the Heat Transfer Division for publication in the JOURNAL OF HEAT TRANSFER. Manuscript received by The Heat Transfer Division, May 2, 1980.

problem consists of two driving forces: namely, the axial pressure and the moving inner cylinder. The non-Newtonian flow with axial pressure gradient and with stationary inner and outer cylinders was considered by Frederickson and Bird [3] and Bird, et al. [4] and the a detailed procedure for calculating the velocity distribution and the flow rate was developed by those authors. However, the generalized case with both axial pressure gradient and moving inner cylinder has not been dealt with in the literature and hence development of the velocity distribution equations is in order.

Assuming a steady state, one-dimensional flow, the momentum balance equation can be represented by

$$\frac{1}{r}\frac{d}{dr}(r\tau) = -\frac{dP}{dz} \tag{1}$$

where τ is the shear stress, P the pressure, r the radial coordinate and z the axial coordinate. Integration of the above equation assuming a constant axial pressure gradient leads to

$$\tau = \left(-\frac{dP}{dz}\right)r + \frac{c}{r} \tag{2}$$

The velocity distribution for the present annular flow can be divided into two cases. If the axial pressure gradient is not big enough, the maximum velocity of flow will occur at the moving inner cylinder. On the other hand, if the axial pressure gradient becomes sufficiently large, a maximum velocity will be generated between the two cylinders. These two cases are shown in Fig. 1 in which β is the reciprocal of the dimensionless pressure gradient parameter. The velocity distribution for the former case will be developed first.

If the maximum velocity of flow occurs at the moving inner cylinder, the velocity gradient is negative over the whole flow region. The shear stress for a power-law model then can be written as

$$\tau = m\left(-\frac{dv}{dr}\right)^n \tag{3}$$

in which m is the consistency index and n the pseudoplastic index. Equation (3) can be combined with equation (2) to yield

$$\frac{dv}{dr} = -\alpha^{1/n}\left(R - \frac{A^2}{R}\right)^{1/n} \tag{4}$$

where α is defined as $(-r_0/2\mathrm{m})(dP/dz)$, A equal to $(-c/m\alpha r_0)^{1/2}$ and R the dimensionless radial coordinate, r/r_0. Integration of equation (4) gives

$$U = 1 - \frac{1}{\beta}\int_k^R \left(R - \frac{A^2}{R}\right)^{1/n} dR \tag{5}$$

with β being equal to $V/r_0\alpha^{1/n}$, k the dimensionless inner radius and V the constant inner cylinder velocity. It is noted that equation (5) satisfies the condition $U = 1$ at $R = k$. The constant parameter A can be determined by using the condition $U = 0$ at $R = 1$. Hence, from equation (5),

$$\int_k^1 \left(R - \frac{A^2}{R}\right)^{1/n} dR = \beta \tag{6}$$

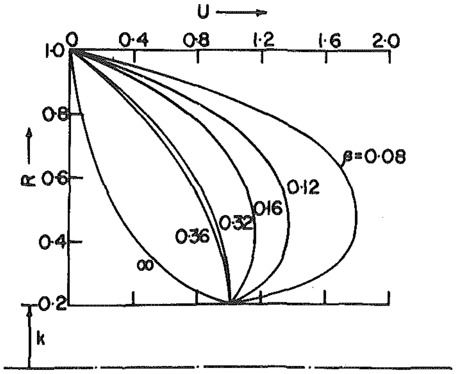

Fig. 1 Velocity distributions for different values of β with $k = 0.2$ and $n = 0.6$

The numerical values of A could not be obtained explicitly from equation (6) and were evaluated by an iterative method [5].

When the maximum velocity takes place between the two cylinders, the velocity distribution can be divided into two regions. The first region is between the outer cylinder and the point of maximum velocity. The velocity gradient in this region is negative and hence equation (4) still is applicable. Integration of this equation using the condition $v_1 = 0$ at $r = r_0$ yields

$$U_1 = \frac{1}{\beta}\int_R^1 \left(R - \frac{A^2}{R}\right)^{1/n} dR;\ \lambda \le R \le 1 \tag{7}$$

In the second region between the point of maximum velocity and the inner cylinder, the velocity gradient becomes positive and the shear stress equation then can be rewirtten as

$$\tau = -m\left(\frac{dv_2}{dr}\right)^n \tag{8}$$

Combination of equations (2) and (8) and integration using the condition $v_2 = V$ at $r = kr_0$ gives

$$U_2 = 1 + \frac{1}{\beta}\int_k^R \left(\frac{A^2}{R} - R\right)^{1/n} dR;\ k \le R \le \lambda \tag{9}$$

It is noted that A is in fact equal to λ since the maximum velocity occurs at $R = \lambda$. The constant parameter A for this case can be estimated by equating equation (7) to equation (9) at $R = \lambda$. Hence it is obtained

$$\int_A^1 \left(R - \frac{A^2}{R}\right)^{1/n} dR - \int_k^A \left(\frac{A^2}{R} - R\right)^{1/n} dR = \beta \tag{10}$$

The numerical values of A were similarly obtained by an iterative method from equation (10) in terms of n, k and ρ. Several tables of the A values have been computed for the present numerical heat transfer study.[2]

The Heat Transfer Model

The steady-state, two-dimensional heat transfer equation with constant physical properties and negligible axial conduction can be represented by

$$\rho C_p v\frac{\partial T}{\partial z} = k_1\left(\frac{\partial^2 T}{\partial r^2} + \frac{1}{r}\frac{\partial T}{\partial r}\right) - \tau\left(\frac{dv}{dr}\right) \tag{11}$$

in which ρ is the fluid density, C_p the heat transfer capacity, k_1 the thermal conductivity and T the temperature. The third term on the right hand side denotes the viscous dissipation which is rather important in the non-Newtonian heat transfer process and was also considered in the previous work [1].

For simplicity, equation (11) can be cast into dimensionless form

$$U(R)\frac{\partial\theta}{\partial Z} = \frac{\partial^2\theta}{\partial R^2} + \frac{1}{R}\frac{\partial\theta}{\partial R} + \sigma f(R) \tag{12}$$

where θ is the dimensionless temperature $(T - T_1)/(T_0 - T_1)$, Z the dimensionless axial distance $zk_1/\rho C_p V r_0^2$ and T_1 and T_0 the inner cylinder wall and inlet fluid temperatures, respectively. The viscous dissipation function $f(R)$ is given by

$$f(R) = \left(R - \frac{A^2}{R}\right)^{(n+1)/n} \tag{13}$$

for the first case with maximum velocity at the inner cylinder and

$$f(R) = \left(R - \frac{A^2}{R}\right)^{(n+1)/n};\ A \le R \le 1 \tag{14}$$

$$= \left(\frac{A^2}{R} - R\right)^{(n+1)/n};\ k \le R \le A \tag{15}$$

for the second case with maximum velocity between the two cylinders.

The inlet and boundary conditions for equation (12) are given by

---

[2] The tables of the A values can be obtained from the authors.

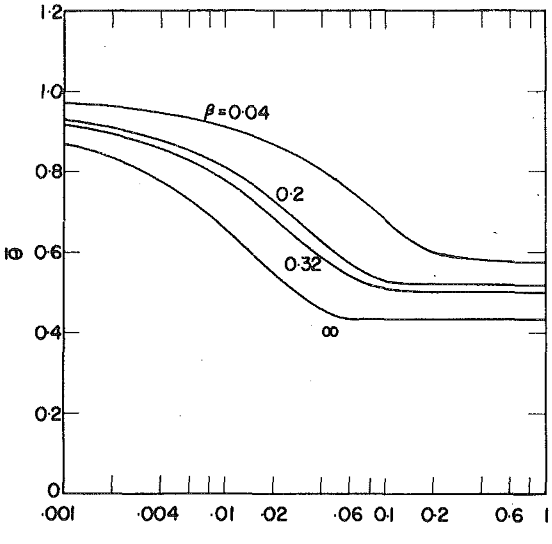

Fig. 2 **The dimensionless bulk temperature versus the dimensionless axial distance with $k = 0.4$, $n = 0.8$ and $\sigma = 0$**

$$Z = 0; \theta = 1 \tag{16}$$

$$R = 0; \frac{\partial \theta}{\partial R} = 0 \tag{17}$$

$$R = 1; \theta = 1 \tag{18}$$

Although other boundary conditions, such as constant heat flux or insulation at the cylinder wall, can also be used, no attempt was made here to adopt them. The Nusselt number at the cylinder wall is defined as

$$\mathrm{Nu} = -\frac{2r_0}{T - T_m}\left(\frac{\partial T}{\partial r}\bigg|_{r=r_0 \text{ or } kr_0}\right) \tag{19}$$

which can be rendered in dimensionless form as

$$\mathrm{Nu}_i = \frac{2}{\bar{\theta}}\left(\frac{\partial \theta}{\partial R}\bigg|_{R=k}\right) \tag{20}$$

for the inner cylinder wall and

$$\mathrm{Nu}_0 = \frac{2}{\bar{\theta}_{-1}}\left(\frac{\partial \theta}{\partial R}\bigg|_{R=1}\right) \tag{21}$$

for the outer cylinder wall. The dimensionless temperature $\bar{\theta}$ is defined as

$$\bar{\theta} = \frac{\int_k^1 \theta U(R) dR}{\int_k^1 U(R) dR} \tag{22}$$

The dimensionless heat transfer equation along with the boundary conditions was solved by the implicit Crank-Nicolson finite difference method [5] to generate the local temperature data which were in turn employed to evaluate the bulk temperature and the Nusselt numbers from equations (20, 21) and (22).

Discussion of Results

In order to ascertain the accuracy of the implicit finite difference scheme used in this work, several runs were made for the problem of heat transfer to non-Newtonian flow in annuli without pressure gradient as a special case so that comparison can be made with the previous results [6]. The present numerical solutions and those of Hong and Mathews [6] are essentially identical.

Figure 2 demonstrates the effect of the reciprocal of the dimensionless pressure gradient group β on the dimensionless bulk temperature. According to definition, small β corresponds to a high pressure gradient and hence the flow will be faster as β decreases. Fast flow reduces the residence time the fluid stays inside the channel and hence reduces the heat loss. In the meantime, a fast flow tends to increase heat transfer through the inner cylinder. For this particular case, the latter effect seems to be of minor significance as compared to the effect of fluid residence time and so a higher bulk temperature is maintained as β increases.

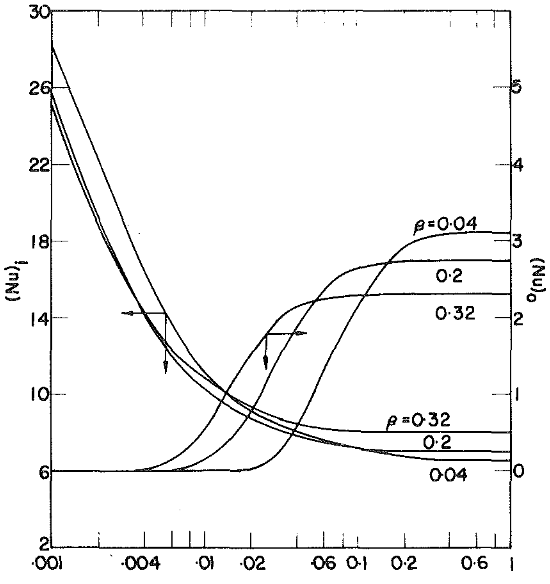

Fig. 3 **The Nusselt numbers versus the dimensionless axial distance with $k = 0.4$, $n = 0.8$ and $\sigma = 0$**

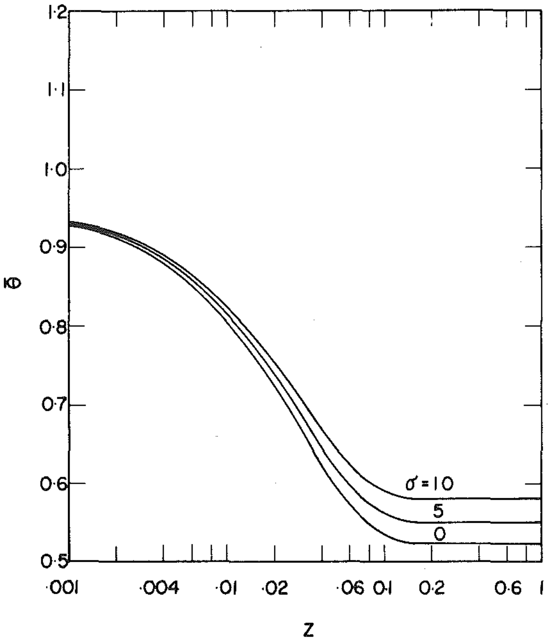

Fig. 4 **The dimensionless bulk temperature versus the dimensionless axial distance with $k = 0.4$, $\beta = 0.2$ and $n = 0.8$**

The effect of β on the Nusselt numbers pertaining to the same physical parameters of Fig. 2 is displayed in Fig. 3. At the inner cylinder wall, the Nusselt number decreases steadily from the channel entrance and tapers off as Z becomes sufficiently large. Appearance of a constant inner Nusselt number at large Z is presumably due to the fully development of temperature profile. The outer Nusselt number shows a different characteristic. It increases with increasing Z until full development of temperature profile is reached.

It is well known that the viscous diisipation can be rather significant in many practical circumstances because of high apparent viscosity of non-Newtonian fluids. Figure 4 shows that the dimensionless bulk temperature is significantly increased as the viscous dissipation parameter σ increases. This is due to irreversible conversion of mechanical energy to thermal one.

References

1 Lin, S. H., "Heat Transfer to Plane Non-Newtonian Couette Flow," *International Journal of Heat and Mass Transfer,* Vol. 22, 1979, p. 1117.

2 Middleman, S., *Fundamentals of Polymer Processing,* McGraw-Hill, New York, 1977.

3 Fredrickson, A. G., and Bird, R. B., "Non-Newtonian Flow in an Annuli," *Industrial and Engineering Chemistry,* Vol. 50, 1958, p. 347.

4 Bird, R. B., Armstrong, R. C., and Hassager, O., *Dynamics of Polymeric Liquids,* John Wiley, New York, 1977.

5 Lapidus, L., *Digital Computation for Chemical Engineers,* McGraw-Hill, New York, 1962.

6 Hong, S. N., and Mathews, J. C., "Heat Transfer to Non-Newtonian Fluids in Laminar Flow through Concentric Annuli," *International Journal of Heat and Mass Transfer,* Vol. 12, 1969, p. 1699.

Suwono Continued

1, 10, 100 and the result for a very large Prandtl number calculated assymtotically using Lighthill's hypothesis (see for example reference [6]), it is possible to construct an empirical formulae which is valid for larger variation of Prandtl number. It is found that the following relation.

$$\overline{\mathrm{Nu}} = 1.021\,\mathrm{Re}^{1/2}\,\mathrm{Pr}^{1/3}\,[1 - 0.244\,\mathrm{Pr}^{-1/3} - 0.139\,\mathrm{Pr}^{-2/3} + 0.035\,\mathrm{Pr}^{-1}] \quad \text{for } \mathrm{Pr} > 0.72 \qquad (28)$$

Correlates to within 2 percent of the calculation results.

5 Acknowledgment

The computation of numerical results were made possible though funds from the Alexander von Humboldt Foundation.

References

1 Suwono, A., "Laminar Boundary Layer Flow Near Rotating Bodies of Arbitary Contour," *Acta Mecanica* (forthcoming).

2 Banks, W. H. H., "The Thermal Laminar Boundary Layer on a Rotating Sphere," *Zeitschrift fuer Angewandte Mathematik und Mechanik,* Vol. 16, 1965, pp. 780–788.

3 Dorfman, L. A., and Mironova, V. A., "Solution of Equations for The Heat Mass Transfer," Vol. 13, 1970, pp. 81–92.

4 Kreith, F., Roberts, L. G., Sullivan, J. A., and Sinha, S. N., "Convection Heat Transfer and Flow Phenomena of Rotating Spheres," *International Journal Heat Mass Transfer,* Vol. 5, 1963, pp. 881–885.

5 Dorfman, L. A., and Serazetdinov, A. Z., "Laminar Flow and Heat Transfer Near Rotating Axisymmetric Surface," *International Journal Heat Mass Transfer,* Vol. 8, 1965, pp. 317–327.

6 Lighthill, M. J., "Contribution to The Theory of Heat Transfer Through a Laminar Boundary Layer," *Proceedings of the Royal Society* London A, Vol. 202, 1950, pp. 359–377.

7 Sparrow, E. M., and Gregg, J. L., "Mass Transfer, Flow and Heat Transfer about a Rotating Disk," ASME JOURNAL HEAT TRANSFER, Vol. 82, 1960, pp. 294–302.

Journal of Heat Transfer Discussion

On the Minimum Film Boiling Conditions for Spherical Geometries[1]

V. K. Dhir.[2] The authors have developed expressions for the minimum film boiling heat fluxes and the film boiling heat transfer coefficients on spheres submerged in pools of saturated or subcooled liquids. In Fig. 7 of the paper, the authors show that the minimum heat flux data of Dhir and Purohit [1] are well bounded by their models for complete wetting and no wetting of the sphere surface. As communicated to the authors also, an error appears to have been made either while calculating or while plotting equation (27). Figure 1 shows how the theory will compare with the data when no wetting of the sphere is assumed to occur. It is noted that for subcooled water, the predicted heat fluxes are much higher than the data. The disagreement between theory and the data increases with subcooling. For water subcooling of 30°C, the predicted heat flux is about 60 percent higher than the data. In Fig. 1 the heat fluxes given by equation (27) for completely wettable surface are not plotted because it is now known what instantaneous contact temperatures were used by the authors. Nevertheless the predicted heat fluxes will be even higher if the surface was assumed to be completely wettable.

The experimentally observed film boiling heat transfer coefficients near the minimum are compared in Fig. 2 with those predicted by equation (38) of the paper for the nonwetting surface. In calculating the heat transfer coefficients from equation (38), the wall temperature is taken to be the minimum film boiling temperature as reported in reference [1]. With subcooled water, the heat transfer coefficient predicted for a wetting surface will be about the same as for a nonwetting surface, since at the observed minimum film boiling temperature equation (33) predicts the weighting factor for the contact area to be very small. Again it is seen that for water subcoolings of 10–30°C, the predicted heat transfer coefficients are about twice the observed values. As reported in reference [1] and also plotted in Fig. 2, the analysis of Dhir and Purohit yields film boiling heat transfer coefficients that are about 25–40 percent lower than the data. It should also be pointed out that the way the equations (27) and (38) for minimum heat flux and the film boiling heat transfer coefficient are written, the minimum film boiling temperature for subcooled liquids cannot be determined using the two equations as one could do for the saturated liquids.

In conclusion, contrary to the authors' claim, equations (27) and (38) do not compare well with the film boiling data obtained on 24.5 mm dia stainless steel spheres submerged in a pool of subcooled water.

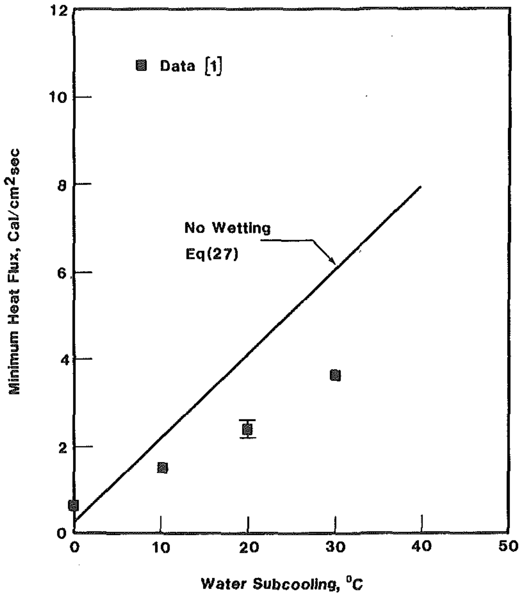

Fig. 1 Comparison of observed and predicted minimum heat flux on 25.4 mm stainless steel spheres submerged in a pool of water

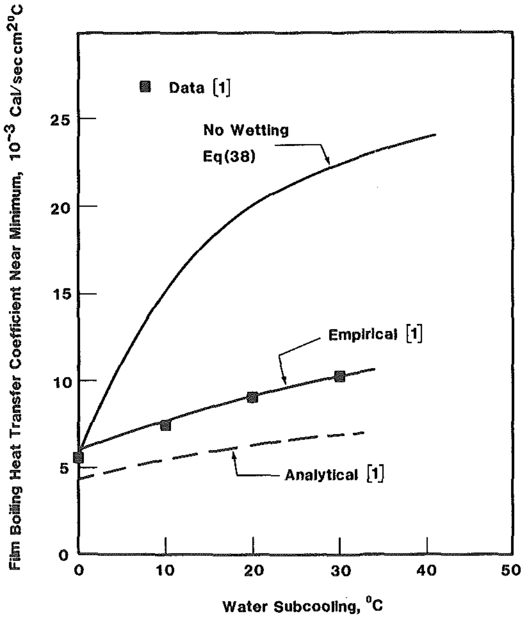

Fig. 2 Comparison of observed and predicted film boiling heat transfer coefficient on 25.4 mm stainless steel spheres

---

[1] By F. S. Gunnerson and A. W. Cronenberg, published in the May 1980 issue of the JOURNAL OF HEAT TRANSFER, Vol. 102, No. 2, pp. 335–341.

[2] Chemical, Nuclear, and Thermal Engineering Department, School of Engineering and Applied Science, University of California, Los Angeles, Calif. 90024.

Additional Reference

1 Dhir, V. K., and Purohit, G. P., "Subcooled Film Boiling Heat Transfer from Spheres," ASME Paper No. 77-HT-78 presented at AIChE/ASME Heat Transfer Conference, Salt Lake City, Utah, 1977. Also published in *Nuclear Engineering and Design*, Vol. 47, No. 1, May 1978.

Authors' Closure

The authors appreciate Professor Dhir's interest and comments on the subject paper. From his discussion, we recognize an error in equation (24) describing the subcooling contribution to the minimum heat flux. The heat transfer into the subcooled liquid during the period of bubble release was initially estimated by a single-dimension analysis, where the liquid temperature gradient was integrated over the period of bubble release. For larger spheres or flat plate heaters, where multiple vapor domes are present, two-dimensional analysis is required where four bubbles per unit heater ($\sim\lambda^2$) are considered rather than two for single-dimension analysis. This results in an expression for the subcooling contribution to the minimum heat flux which is one half of that expressed by equation (24). Therefore, for correct analysis, the factor 2 which appears in equation (24) and subsequently in the subcooling contributions of equations (27, 36) and (38) should be omitted. Our calculations and figures within the original manuscript reflect this correction and are therefore correct as shown.

Since Professor Dhir was unaware of the error in equation (24) his calculations are high by a factor of 2, as illustrated in Figs. 1 and 2 of his discussion.

ERRATA

Erratum: C. F. Delale, "Lower Bound Estimate for Droplet Size in Two-Phase Dispersed Flow," published in the August 1980 issue of the JOURNAL OF HEAT TRANSFER, pp. 501–507.

Equation (A6) should read

$$\left.\frac{h_d(T_v - T_{\mathrm{sat}})}{U_\ell \mathrm{d}}\right|_{\substack{q_\ell=0\\ q_r=0}} \tag{A6}$$